Biochemical characterization of RAS-like proteins and their modulators

Inaugural-Dissertation

For the attainment of the title of doctor in the faculty of Mathematics and Natural Sciences at the Heinrich Heine University Düsseldorf

Presented by

Niloufar Mosaddeghzadeh

From

Booshehr, Iran

Düsseldorf, November 2022

From the Institute of Biochemistry and Molecular Biology II

At the Heinrich Heine University Düsseldorf

Published by permission of the

Faculty of Mathematics and Natural Sciences

At Heinrich Heine University Düsseldorf

1st Supervisor: Prof. Dr. Reza Ahmadian

2nd Supervisor: Prof. Dr. Georg Groth

Date of the oral examination:

CONTENT

LIST OF ABBREVIATIONS

Abbreviation	Long form
Aa	Amino acid
ACK	Activated CDC42 kinase
AKT	Proteinkinase B
AlF4	Tetrafluoroaluminate
ARF	ADP ribosylation factor
ARP2/3	Actin related protein 2/3
BCR	Breakpoint cluster region
CDC42	Cell division control protein 42 homolog
CNTD1	Cyclin N-terminal domain
CR	Conserved regions
DEP1/2	Dishevelled, Eg-10 and Pleckstrin domain
Dia	Diaphanous-related formin
EGFR	Epidermal growth factor receptor
ERK	Extracellular-signal regulated kinase
F	Farnesyl
BAR	Bin-Amphiphysin-RVS
GAP	GTPase activating protein
GDI	Guanine nucleotide dissociation inhibitor
GDP	Guanosin-di-phosphate
GEF	Guanine-nucleotide exchange factor
GG	Geranylgeranyl
GGA	Golgi localized, gamma ear-containing, ARF-binding protein
GRD	RAS-GAP related domain
GTP	Guanosine-Tri-phosphate
HACE	HECT domain and ankyrin repeat containing E3 ubiquitin protein ligase
HRAS	Harvey Rat sarcoma virus
HVR	Hypervariable region
IPP5P	Inositol polyphosphate 5-phosphatase
IQGAP	IQ motif containing GTPase activating protein
kDa	Kilo dalton
KRAS	Kirsten rat sarcoma virus
MEK	Mitogen-activated protein kinase
MLC	Myosin light chain
mTOR	Mammalian target of rapamycin
mTORC	Mammalian target of rapamycin complex
NADPH	Nicotinamide adenine dinucleotide phosphate
NFκB	Nuclear factor 'kappa-light-chain-enhancer' of activated B-cells
NMR	Nuclear magnetic resonance
OCRL	Lowe Oculocerebrorenal syndrome protein
PAK	P21 activated kinase
PDK1	Phosphoinositide-dependent protein kinase 1
PH	Pleckstrin homology
PI3K	Phosphoinositide 3-kinases
PIP	Phosphatidylinositolphosphate
PKN	Seine/threonine protein kinase N
PTM	Posttranslational modification
RAB	Ras related in brain
RAC	Ras-related C3 botulinum toxin substrate

RAF	Rapidly growing fibrosarcoma
RAL GDS	Ral guanine nucleotide dissociation stimulator
RAN	Ras-related nuclear
RAS	Rat sarcoma
RBD	RAS binding domain
RGL	RAS related GDP dissociation stimulator like
RHO	Ras Homolog
RHOA/B/C	Ras homolog family member A/B/C
RIN	RAS and RAB interactor
ROCK	RHO associated protein kinase
ROS	Reactive oxygen species
RTK	Receptor tyrosine kinase
SH	Src homology
SIN1	Stress-activated MAP kinase-interacting protein 1
WAVE	WASP family verprolin homologous protein
WRCH	Wnt-1 responsive CDC42 homolog

Amino Acid	Three letter code	Letter code
Alanine	Ala	A
Arginine	Arg	R
Asparagine	Asn	N
Aspartic acid	Asp	D
Cysteine	Cys	C
Glutamine	Gln	Q
Glutamic acid	Glu	E
Glycine	Gly	G
Histidine	His	H
Isoleucine	Ile	I
Leucine	Leu	L
Lysine	Lys	K
Methionine	Met	M
Phenylalanine	Phe	F
Proline	Pro	P
Serine	Ser	S
Threonine	Thr	T
Tryptophan	Trp	W
Tyrosine	Tyr	Y
Valine	Val	V

SUMMARY

The RAS GTPases superfamily manifests several roles in diverse cellular processes such as proliferation, differentiation, trafficking, adhesion, and migration. RAS GTPases cycle between being GDP bound (inactive state) and GTP bound (active state), which is regulated by two classes of proteins – GAPs and GEFs – which accelerate the slow intrinsic GTP hydrolysis and promote the slow intrinsic nucleotide exchange rates, respectively. Activated RAS GTPases associate with their downstream effectors to wind up their cellular functions, and perturbation in their functions is often reported in cancer and developmental disorders, so-called RASopathies. Novel mutations in ARF3 GTPases were identified in patients suffering from different levels of neurodegeneration. Our structural-functional analyses of ARF3 variants indicated that their nucleotide exchange rates had increased drastically. We were able to prove that the discovered variants are located in the nucleotide-binding pocket, which interferes with the protein functions by stabilizing the protein in GTP-bound form, and subsequently disturbs the Golgi integrity. The HRAS germline mutations, in particular Gly12Ser substitution, lead to the constitutively active forms of HRAS and are associated with Costello syndrome, a complex developmental disorder. It was already known that active HRAS interacts with RIN1 and enhances the RAB5 GTPases activation, as well as ABL1/2 tyrosine kinases, which are signaling modulators in endosomal sorting and cytoskeletal dynamics processes. In our study, we discovered that HRAS Gly12Ser elevates the RIN1-dependent RAB5A activation, and subsequently disturbs the integrins concentration and localization in keratinocytes, which underly the molecular pathogenesis for dermatological findings in Costello syndrome. RHO GTPases, a family of RAS GTPases, have extra regulators, so-called RHOGDIs, which bind to their isoprenoid moiety and sequester them away from the membrane and establish a cytosol pool of RHO GTPases. We inspected the RHOGDI specificity of several RHO GTPases through a structure-function assessment. We discovered that the RHOGDI association with RHO GTPases relies on the positively charged residues and their proximity in the polybasic region and two distinct negatively charged clusters in RHOGDI, which create an electrostatic force to extract RHO GTPases from the membrane. IQGAPs are scaffold proteins, which tether several proteins into specific complexes and safeguard the strength, efficiency, and specificity of signal transduction. Characterization of IQGAP1 and 2 interaction networks with various RHO GTPases showed that both IQGAPs bind CDC42 and RAC1-like proteins, but not the other RHO GTPases due to several residues outside the switch regions. In-depth mutational analyses clarified that the RGCT domain of IQGAPs is responsible for high-affinity binding to the switch region of CDC42. Our studies proved that the GRD domain of IQGAPs is in direct contact with the insert helix of CDC42 and binds to CDC42 in a nucleotide-independent manner.

ZUSAMMENFASSUNG

Die Superfamilie der RAS-GTPasen spielt bei verschiedenen zellulären Prozessen wie Proliferation, Differenzierung, Trafficking, Adhäsion und Migration eine wichtige Rolle. RAS-GTPasen wechseln zwischen GDP-Bindung (inaktiver Zustand) und GTP-Bindung (aktiver Zustand), was durch zwei Klassen von Proteinen - GAPs und GEFs - reguliert wird, die die langsame intrinsische GTP-Hydrolyse beschleunigen bzw. die langsamen intrinsischen Nukleotidaustauschraten fördern. Aktivierte RAS-GTPasen arbeiten mit ihren nachgeschalteten Effektoren zusammen, um ihre zellulären Funktionen zu erfüllen, und eine Störung ihrer Funktionen wird häufig bei Krebs und Entwicklungsstörungen, den so genannten RASopathien, beobachtet. Neuartige Mutationen in ARF3-GTPasen wurden bei Patienten mit verschiedenen Stufen der Neurodegeneration identifiziert. Unsere strukturell-funktionellen Analysen der ARF3-Varianten zeigten, dass ihre Nukleotidaustauschraten drastisch erhöht waren. Wir konnten nachweisen, dass die entdeckten Varianten in der Nukleotidbindungstasche lokalisiert sind, was die Proteinfunktionen beeinträchtigt, indem sie das Protein in GTP-gebundener Form stabilisiert und anschließend die Golgi-Integrität stört. Die HRAS-Keimbahnmutationen, insbesondere die Gly12Ser-Substitution, führen zu den konstitutiv aktiven Formen von HRAS und werden mit dem Costello-Syndrom, einer komplexen Entwicklungsstörung, in Verbindung gebracht. Es ist bereits bekannt, dass aktives HRAS mit RIN1 interagiert und die Aktivierung der RAB5-GTPasen sowie der ABL1/2-Tyrosinkinasen verstärkt, die Signalmodulatoren bei endosomalen Sortier- und Zytoskelettdynamikprozessen sind. In unserer Studie entdeckten wir, dass HRAS Gly12Ser die RIN1-abhängige RAB5A-Aktivierung erhöht und in der Folge die Konzentration und Lokalisierung von Integrinen in Keratinozyten stört, was die molekulare Pathogenese der dermatologischen Befunde beim Costello-Syndrom erklärt. RHO-GTPasen, eine Familie von RAS-GTPasen, verfügen über zusätzliche Regulatoren, so genannte RHOGDIs, die an ihren Isoprenoid-Anteil binden, sie von der Membran absondern und einen Zytosol-Pool von RHO-GTPasen bilden. Wir untersuchten die RHOGDI-Spezifität mehrerer RHO-GTPasen durch eine Struktur-Funktions-Bewertung. Wir entdeckten, dass die RHOGDI-Assoziation mit RHO-GTPasen auf positiv geladenen Resten und deren Nähe in der polybasischen Region und zwei verschiedenen negativ geladenen Clustern in RHOGDI beruht, die eine elektrostatische Kraft erzeugen, um RHO-GTPasen aus der Membran zu ziehen. IQGAPs sind Gerüstproteine, die mehrere Proteine zu spezifischen Komplexen zusammenbinden und die Stärke, Effizienz und Spezifität der Signaltransduktion sicherstellen. Die Charakterisierung der Interaktionsnetzwerke von IQGAP1 und 2 mit verschiedenen RHO-GTPasen zeigte, dass beide IQGAPs CDC42 und RAC1-ähnliche Proteine binden, nicht aber die anderen RHO-GTPasen, was an mehreren Resten außerhalb der Schalterregionen liegt. Eingehende Mutationsanalysen ergaben, dass die RGCT-Domäne der IQGAPs für die hochaffine Bindung an die Schalterregion von CDC42 verantwortlich ist. Unsere Studien haben gezeigt, dass die GRD-Domäne von IQGAPs in direktem Kontakt mit der Insertionshelix von CDC42 steht und auf nukleotidunabhängige Weise an CDC42 bindet.

1. INTRODUCTION

1.1 RAS GTPASES SUPERFAMILY

The RAS (Rat sarcoma) superfamily of small guanosine triphosphatases (GTPases) is composed of over 150 members in humans and governs a variety of fundamental cellular processes [1]. RAS GTPases usually act as molecular switches (Figure 1B) and cycle between a GDP (guanosine-diphosphate) bound and GTP (guanosine-triphosphate) bound state [2]. The RAS superfamily constitutes several subfamilies such as RAS, RHO (RAS homolog), RAB (RAS related in the brain), RAN (RAS related nuclear), and ARF (ADP ribosylation factor) (Figure 1A), which share similar sequence elements, and display an overall three dimensional structure [3]. In the RAS family, HRAS, KRAS, and NRAS are the most extensively studied members. The majority of RAS GTPases share a set of conserved G motifs (GDP/GTP-binding domain) that start from the N-terminus and are identified as; G1, GXXXXGKS/T or P-loop; G2, containing a conserved T; G3, DXXGQ/H/T; G4, N/TKXD; and G5, C/SAK/L/T [4]. All these ensemble motifs build up a 20kDa G domain, which has a conserved structure among all the RAS superfamily proteins [1]. The G2 motif, together with the G3 motif, creates flexible regions called switch I (SWI) and II (SWII) respectively, which change their conformation upon binding to GDP or GTP nucleotides [5,6]. Their switch mechanism between GDP and GTP nucleotides is tightly regulated by 1) Guanine-nucleotide exchange factors (GEFs) that accelerate the exchange of bound GDP nucleotides for GTP, and 2) GTPase activating proteins (GAPs) that stimulate the slow intrinsic GTP hydrolysis by offering an essential catalytic arginine [7]. Membrane association is a very crucial step that allows RAS proteins to initiate signal transduction [8]. As a first step they are targeted to the plasma membrane by posttranslational modification of the C-terminal CAAX motif, where C is a Cys, A is mainly an aliphatic amino acid, and the X residue determines which type of prenylation should occur to these proteins [9,10]. Once X is Ser, Met, Ala, or Gln, the RAS protein acquires a farnesyl (F) moiety, while the presence of Leu alters the modification by Geranylgeranyl (GG) moiety [9]. This prenylation facilitates the targeting and binding of the RAS protein to the membrane, where it engages with other proteins in order to transduce the signal, which was initiated by extracellular stimuli [11].

GTP-bound RAS proteins execute their function through binding to their effector proteins, such as the well-known proteins RAF (Rapidly growing fibrosarcoma), RAL-GDS (RAL guanine nucleotide dissociation stimulator), and RGL (RAL GDP dissociation stimulator like), and RIN (RAS and RAB interactor) [12–15]. RIN1 interacts with RAS directly, and it has been reported that RIN1 can compete with RAF1 to associate with RAS [16,17].

RAS proteins govern many signal transduction cascades including RAF/MEK (Mitogen-activated protein kinase)/ERK (Extracellular signal-regulated kinases) and PI3K (Phosphoinositide 3-kinases)/AKT (protein kinase B) pathways, that play a fundamental role in these pathways in different cellular processes including proliferation, differentiation, apoptosis, and survival (Figure 1) [18–24]. The phosphoinositide kinases (PIK) phosphorylate the inositol ring of phosphatidylinositol (PtdnIns), which is a component of the eukaryotic cell membrane and is important in various cellular events, including survival, proliferation, and cytoskeleton organization [25]. The PIKs constitute three general families and are termed as PI3Ks, PI4Ks, and PIPSKs [26]. PI3K can be activated through growth factors, and generates PIP3 (Phosphatidylinositol-3,4,5-triphosphate), which recruits the

protein kinase AKT to the plasma membrane [27]. AKT is fully activated by double phosphorylation on Thr308 and Ser473 through PDK1 (Phosphoinositide-dependent protein kinase 1) and mTORC2 complex (mammalian target of rapamycin complex 2), respectively [27–29]. The PI3K-AKT and mTOR signaling cascades regulate cancer hallmarks including cell cycle, survival, motility, metabolism, and genomic instability [25,30,31]. The mTORC1 and mTORC2 complexes play a crucial role in diverse cellular processes in response to a variety of intracellular and extracellular stimuli [32]. Aberrations in the RAS signaling pathway are associated with a set of clinically related developmental disorders distinguished by facial dysmorphism, cardiac diseases, abnormal growth, irregular cognitive deficits, and ectodermal and musculoskeletal anomalies, categorized as RASopathies [33–35].

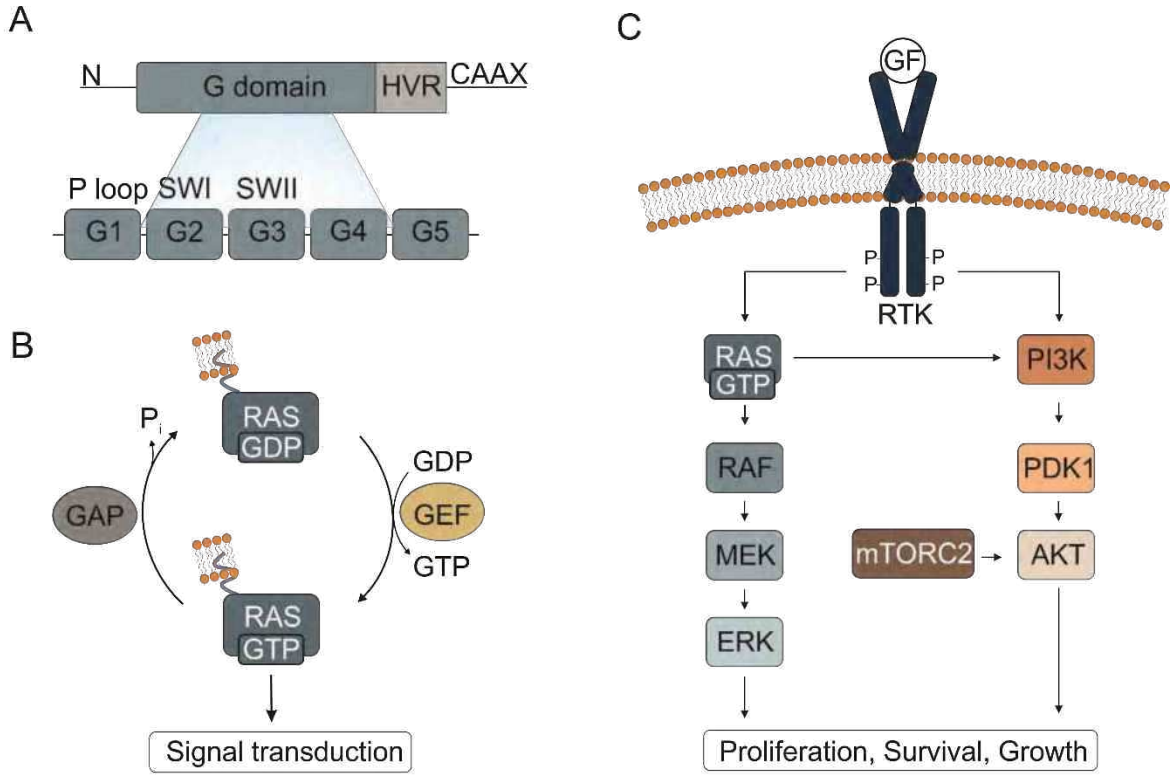

Figure 1. RAS superfamily of small GTPases. (A) The core G domain is comprised of 5 motifs, that are engaged in GDP/GTP binding and hydrolysis. The membrane targeting motif of the RAS superfamily is encrypted in HVR. (B) The active/inactive states of RAS superfamily members are tightly controlled by GAPs and GEFs regulators. (C) Schematic RAS signaling pathway displaying the downstream effectors, as well as upstream activators. Growth factors (GF) bind to receptor tyrosine kinase (RTK) and initiate the activation of RAS, which leads to the activation of the RAF-MEK-ERK cascade. Activated RAF-MEK-ERK results in various cellular functions, including proliferation, survival, and growth. PI3K generates PIP3 and provides a docking site for PDK1 and mTORC2. PDK1 and mTORC2 phosphorylate AKT at Thr308 and Ser473, respectively.

1.2 ARF GTPases

ARF GTPases are distinguished by possessing a unique N-terminal extension that folds as an amphipathic helix, and an N-terminal myristoyl group, which play a key role in membrane association and dissociation [36,37].

ARF GTPases are ubiquitously expressed and mediate crucial functions, like bidirectional membrane trafficking, namely endocytosis, and exocytosis, as well as the recruitment and activation of enzymes, namely phosphatidylinositol (PtdIns) kinases (PIK) that can modify the membrane lipid composition [38–40]. The lipid modification of ARF GTPases is a myristoylation process on a Gly residue of the N-terminus, which directs them to the membrane [40,41].

ARF1 and ARF3 are localized mainly at the Golgi apparatus, particularly at the cis and trans Golgi networks, respectively [42]. They execute their function in the secretory membrane transport systems by interacting with their effectors such as adaptor proteins, Golgi-localized γ-adaptin ear-containing proteins (GGAs), or coat proteins [38,40]. ARF GTPases can tether non-coat Golgi apparatus specific proteins such as golgin-160, which determine Golgi apparatus integrity [43]. ARF GTPases fine-tune several indispensable processes through the regulation of the Golgi apparatus structure and function, cargo sorting, and membrane trafficking. This highlights their central role in the normal development and homeostasis of organelles.

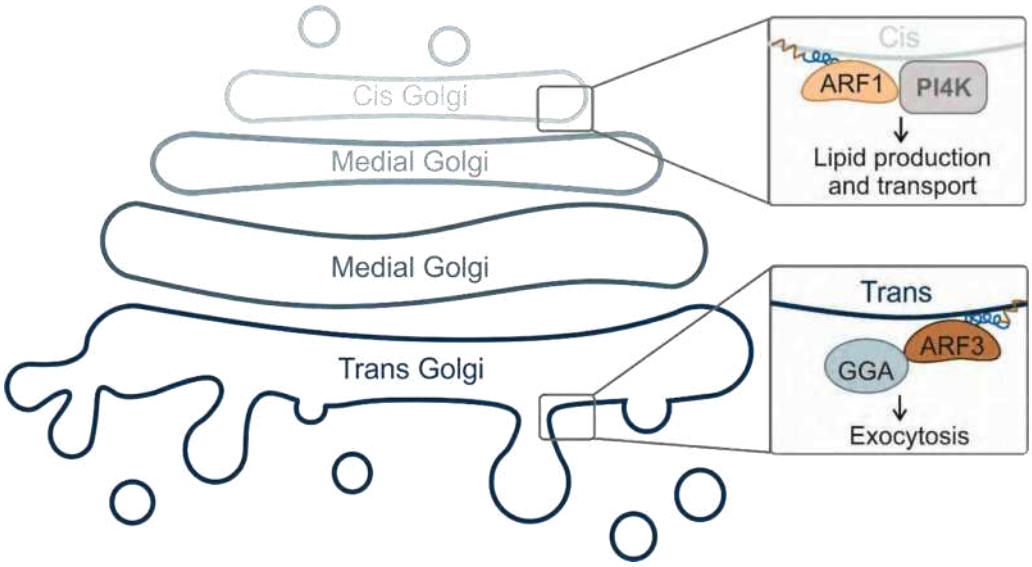

Figure 2. ARF GTPases localization and function at the Golgi apparatus. ARF1 localizes at cis Golgi and ARF3 localizes at the trans Golgi network. ARF1 activates PI4K and subsequently regulates lipid production and transport, and ARF3 influences exocytosis and membrane trafficking through association with GGAs.

1.3 RHO FAMILY

The RHO families are comprised of 20 canonical members, that are divided into six subfamilies according to their sequence homology: RHO (RHOA, RHOB, and RHOC); RAC (Ras-related C3 botulinum toxin substrate) (RAC1, RAC1B, RAC2, RAC3, and RHOG); CDC42 (Cell division control protein 42 homolog) (CDC42, G25K, TC10, TCL, WRCH1, and WRCH2); RHOD (RHOD, RIF); RND (RND1, RND2, and RND3); and RHOH [44].

Activated RHO GTPases participate in essential cellular processes and biochemical functions including actin cytoskeleton reorganization, microtubule dynamics, gene expression, and the regulation of enzymatic activities [45,46]. In the context of mechanotransduction, the majority of studies target RHOA, CDC42, and RAC1 proteins to

grasp their impact on the actin cytoskeleton. These three proteins are the most studied and best-characterized members of the RHO GTPases [46–50].

A major structural component that makes RHO GTPases different from other RAS GTPases, is the presence of an insert helix, located between residues 122 and 135 (CDC42 numbering) [51]. An insert helix is a surface-exposed and dynamic region and is highly variable among different members of RHO GTPases [52]. The latest studies implied the significance of the insert region for RHO GTPases in interaction with effectors, which is important for downstream signaling and exerting effector function [53–55].

RHO proteins are post-translationally modified at the C-terminus by prenylation or palmitoylation, which affects their subcellular localization and their association with specific membranes [56]. In addition, RHO GTPases can be phosphorylated or ubiquitylated, which affects their downstream signaling or their turnover (Table 1) [57].

Table 1. Overview of post-translational modifications of RHO, RAC, and CDC42 GTPases. These modifications affect RHO GTPases membrane localization, and in some cases modulate the GDP-GTP exchange.

	Prenylation	Palmitoylation	Ubiquitination	Phosphorylation
RHOA	GG	-	K6-7 K51	S188 T127
RHOB	GG/F	+	K6 K 7	S185
RHOC	GG	-	-	S73
RAC1	GG	-	T108, Y64, S71	K147 K166
RAC2	GG	-	-	-
RAC3	GG	-	K166	-
RHOG	GG	-	-	-
CDC42	GG	-	-	Y64 S185
TC10	GG	+	-	T197
TCL	GG	+	-	-
WRCH1	-	+	K177, K248	Y254
WRCH2	-	+	-	-

1.3.1 RHO

RHOA, RHOB, and RHOC are highly homologous and their amino acid sequences are 88% identical [58,59]. However, the C-termini of these three proteins, particularly the HVR, are quite different and this dissimilarity is reflected in their localization [60]. RHOA and RHOC are localized mainly at the plasma membrane or cytosol, while RHOB stays predominantly at late endosomes and lysosomes [61].

Different stimuli comprising growth factors, cytokines, and UV irradiation can upregulate RHOB protein levels [62]. Previous reports indicated how the downregulation of RHOA or RHOC enhances RHOB expression [63,64]. Aligned with other studies, these findings

emphasize that RHOB turnover is fast and, unlike the other RHO GTPases, which are relatively stable, RHOB has a shorter half-life [62,65]. Previous reports implied that RHOB is required for the initiation of apoptosis in transformed cells upon DNA damage [66]. RHOB has an impact on the proliferation and adhesion of transformed cells [67]. Due to similar effector binding regions, RHOA and RHOB can share several potential effectors such as mDIA, NF-κB, and protein kinase C-related kinase (PKC) [65,68].

RHOC interacts with RHOA effectors, in particular ROCK (RHO-associated protein kinase) and Citron kinase, with an even higher affinity [69,70]. Studies have shown that the constitutively active RHOC (G14V) binds ROCK1 better than RHOA (G14V), which may indicate different contributions of RHOA and RHOC to cell motility [58,70].

Activated RHOA results in the assembly of contractile actin-myosin filaments called stress fibers, which are required for intercellular tension, and focal adhesion complexes which are hotspots for mechanotransduction (Figure 3) [48].

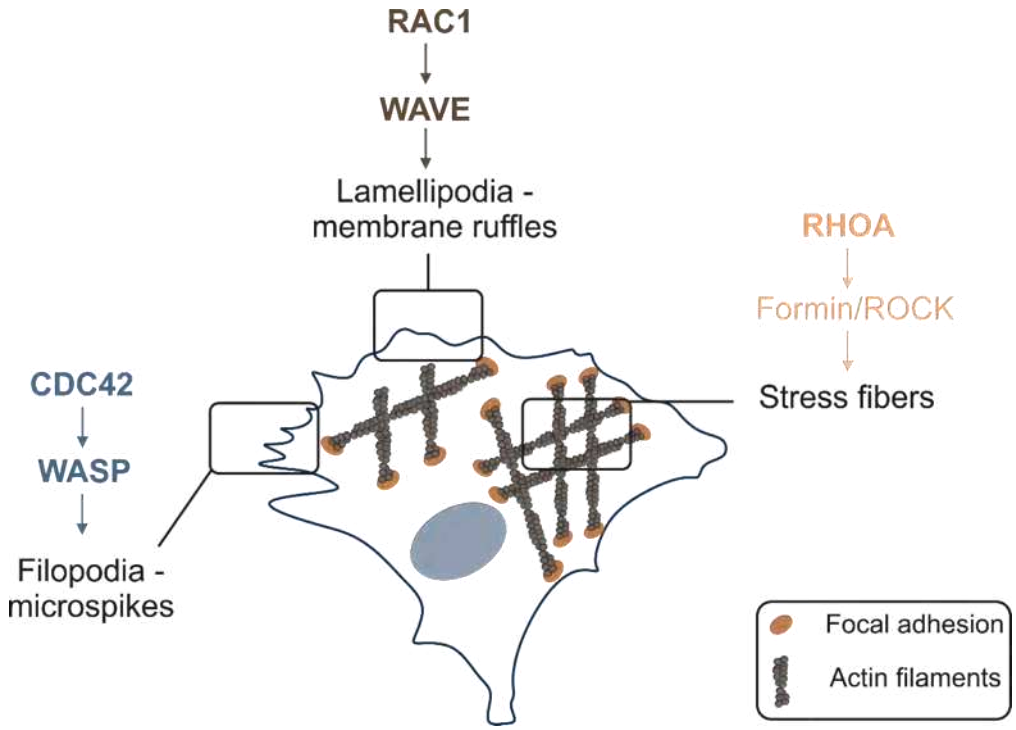

Figure 3. Signal transduction pathways involved in the formation of filopodia, lamellipodia, and stress fibers, mediated by CDC42, RAC1, and RHOA respectively. RHOA, CDC42, and RAC1 can modulate the signaling pathway that links membrane receptors to the cytoskeleton by assembling focal adhesions.

The crystal structures of RHOA in complex with GTPase binding domains (GBDs) of ROCK or PKN (RHO associated protein kinase) have been dissolved and it has been shown that these domains form α-helical coiled-coils, which are positioned in a parallel and anti-parallel manner, respectively [71,72]. GTP-bound RHOA activates PKN through its C-terminus and prompts actin-myosin II contractility in neuronal cells [73]. To generate stress fibers and focal adhesions, RHOA required at least ROCKs and DIA (Diaphanous-related formin) in its downstream path [47,74]. ROCKs are Ser/Thr kinases and regulate the induction of

stress fiber, through their substrates like MLC (Myosin light chain) and MBS (Myosin binding substrate) of MLC phosphatase [75]. Inhibition of MLC phosphatase takes place by phosphorylation and results in an increase in MLC phosphorylation and subsequently induces the actin filament cross-linking activity of myosin II [45,75,76]. It has been shown that ROCK function alone is not adequate as it stands for RHO-induced stress fiber assembly [77]. It has been shown that the presence of ROCK combined with DIA, a member of the formin-homology (FH) family, is essential for stress fiber formation [47,78,79]. DIA interacts with a profiling-actin complex on the growing ends of actin filaments and promotes the linear elongation of actin networks [45,80].

Although several proteins are described as potential downstream effectors for RHOA, and their cellular implications have been examined, only a few investigations have been undertaken to understand their activation mechanism.

1.3.2 RAC

Even though mammalian RAC1, RAC2, and RAC3 are encoded by different genes, they share around 90% identity in their respective amino acid sequences [81,82]. Unlike these three paralogs, RHOG, another member of the RAC family, is more divergent and it is about 70% identical to RAC1 [56]. RAC1b is an alternatively spliced isoform of RAC1, which is distinguished by a 19 amino acid in-frame insertion directly after the switch II region, and was identified in the skin and epithelial tissues from the intestinal tract and breast cancer [83–85]. It has been revealed that the 19 amino acid insertion induces an open conformation in the switch I region, in which the switch I region obtains a distance of 6.5 A° to the nucleotide-binding site, and this results in an accelerated GEF-independent GDP/GTP exchange and a deficient GTP hydrolysis [85,86].

RAC2 is mainly expressed in hematopoietic cells, and it has been proposed that it is responsible for the regulation of the oxidative burst in these cells together with RAC1 [87]. Any downregulation or inactivation of RAC2 is linked to several neutrophilic, phagocytic, and lymphocytic defects which might stem from RAC2-specific activation of NADPH (Nicotinamide adenine dinucleotide phosphate) oxidase [88–92]. Both RAC1 and RAC3 are ubiquitously expressed and therefore regulate a broad range of cellular processes [82].

All the RAC proteins induce the formation of lamellipodia and membrane ruffles (Figure 3), probably through interaction with the WAVE (WASP family verprolin homologous protein) regulatory complex (WRC) which is a five-subunit protein complex [93,94]. The WAVE complex interacts with and activates the ARP2/3 (Actin-related protein) complex via its C-terminal acidic domain, and the activation of the heptameric ARP2/3 complex leads to the initiation of branched filaments at the end of existing actin filaments [95–97]. It has been proposed that RAC1 can localize the WAVE complex to the periphery to promote actin nucleation through ARP2/3 [45,47,98].

Since actin cytoskeletal dynamics regulate vesicular trafficking, the role of RAC1 in the generation of actin-rich membrane protrusion during endocytosis has been studied numerous times [99,100]. Moreover, RAC1 activity is recognized as indispensable for the activation of NADPH oxidase in phagocytic cells during phagocytosis [101,102].

As in other proteins, a counterbalance between synthesis and degradation regulates the expression of RHO GTPases. Ubiquitination governs the degradation process of RAC1 and other RHO GTPases (Table 1) [103]. RAC1 ubiquitination became a focus of studies with

the discovery of HACE1 (HECT domain and ankyrin repeat containing E3 ubiquitin protein ligase) ubiquitin ligase as a tumor suppressor [103,104]. It appeared that the loss of HACE1 was correlated with breast cancer progression due to increased RAC1 activity levels and as a result of enhanced levels of reactive oxygen species and cell migration [104,105].

Besides the plasma membrane and cytosol, RAC1 can localize to the nuclear envelope and nucleoplasm [106,107]. Lanning et al. discovered that the polybasic sequence of RAC1 HVR is the nuclear localization signal (NLS) motif, and described that the difference in NLS sequence alters the nuclear accumulation of different GTPases [106,108,109].

Together with CDC42 and RHO, RAC1 regulates the formation and maintenance of adherens junctions in epithelial cells [110,111]. IQGAPs (IQ motifs containing GTPase activating protein) are scaffolding proteins and play a significant role in protein complex assembly and signaling networks [112–117]. IQGAP1 overexpression results in decreased E-cadherin mediated cell-cell adhesion and leads to weak adhesion [118]. IQGAP1 interacts with β-catenin and dissociates the α-catenin from the cadherin-catenin complex in epithelial cells [115,118]. GTP-bound RAC1 and CDC42 interact with IQGAP1 and hinder its association with β-catenin and accordingly maintain E-cadherin mediated cell-cell adhesion [115,119].

Given the essential roles of RACs, it is not surprising how deficient RAC activity is associated with various diseases including cancer.

1.3.3 CDC42

CDC42 stands out as playing a crucial role in establishing cell polarity, migration, cell cycle, and proliferation in all eukaryotic cells, regardless of the biological context [120–122]. CDC42 induces the formation of filopodia and microspikes (Figure 3) through its association with members of the Wiskott-Aldrich syndrome family of proteins (WASPs), like N-WASP or WASP [123–125]. WRCH1 is the only member of the CDC42 subfamily that does not induce filopodia formation and interacts with neither WASP nor N-WASP [56,126].

Distinct pools of CDC42 have been discovered in various subcellular membrane compartments including the plasma membrane, the Golgi complex, and the endoplasmic reticulum [127–129]. CDC42's role in the Golgi pool has been studied several times and the majority of findings suggest that the Golgi pool acts as a reservoir for particular circumstances [127,130].

Many CDC42 and RAC effectors contain a conserved 18 amino acid binding motif that has been termed CRIB (CDC42/RAC-interactive binding), comprises eight conserved residues within a stretch of 16 to 18 amino acids, and constructs the consensus region of the larger G-protein binding domain (GBD) [131,132]. The CRIB motif exists in ACK (Activated CDC42 kinase), WASP, and PAKs (p21 activated kinase), and it appears to take the Asp38 in the switch I region as the recognition residue for RAC/CDC42 from RHO [47,133].

In the switch II region of RHO GTPases, there are Leu69 and Leu72, which form critical hydrophobic contacts with a majority of effectors, and it has been suggested that they are crucial for the CRIB-containing effectors [134,135]. The electrostatic steering regions and GBDs of CRIB-containing effectors can also keep the intramolecular interactions under control [125,132].

IQGAPs, which are recognized as RAC and CDC42 binding proteins, are found in three paralogs; IQGAP1, IQGAP2, and IQGAP3 with similar domains expressed in mammalians [117,136–139]. IQGAP1 is the most studied member of this family and is ubiquitously expressed [140]. IQGAPs possess several domains which interact with numerous proteins in multiple functions to shield the strength, efficiency, and specificity of signal transduction [115,138,141–143]. IQGAPs consist of an N-terminal calponin homology domain (CHD), a coiled-coil repeat region (CC), a tryptophan-containing proline-rich motif-binding region (WW), 4 isoleucine/glutamine-containing motifs (IQ), a RASGAP-related domain (GRD), a RASGAP C-terminal domain (RGCT), and a very C-terminal domain (CT) [115,116,140,144].

The crystal structure of a GRD fragment in complex with the constitutively active form of CDC42 has been published and it has been demonstrated that GRD adopts a RASGAP-like structure [145]. However, the IQGAP GRD domain is considered an inactive RASGAP due to the absence of crucial catalytic and structural features of a functional GAP [145,146].

It has been reported that the C-terminal region of IQGAP1 is involved in CDC42 and RAC1 interaction [136,147,148]. Although studies indicated that IQGAP1 binds to both GTP/GDP CDC42, it associates only with RAC in a GTP-bound form [144,148]. It has been shown that IQGAP1 mutants defective in CDC42 binding resulted in aberrant multipolar morphology and altered polarization and migration [149]. These findings endorse the significance of IQGAP-CDC42 interaction in cell polarity and migration [150].

Heterozygous mutations in CDC42 have been discovered to cause neurodevelopmental phenotypes, comprising facial dysmorphism, intellectual disability, cardiac effects, and hematological and immunological abnormalities [22,151]. The collection of these phenotypes is representative of Noonan syndrome, which is classified as a RASopathy, and here in the case of CDC42, their upregulated function leads to a disturbance in the RAS signal flow [22]. Overexpression of CDC42 and the other RHO GTPases is reported in several cancers, and due to their central roles in cell architecture and motility, they become potential targets in therapeutic strategies [152–154].

1.3.4 Regulation of RHO GTPases

The GDP/GTP cycle of RHO GTPases is regulated by three structurally distinct and functionally unrelated classes of proteins (Figure 4): 1) GEFs accelerate the slow intrinsic exchange of GDP to GTP and switch on the signal transduction in stimulated cells; 2) GAPs promote the slow intrinsic GTP hydrolysis activity and switch off the signal transduction; 3) GDIs sequester RHO GTPases farther from the membrane by interacting with their isoprenoid moiety and constitute an inactivated cytosolic reservoir [44,155–157].

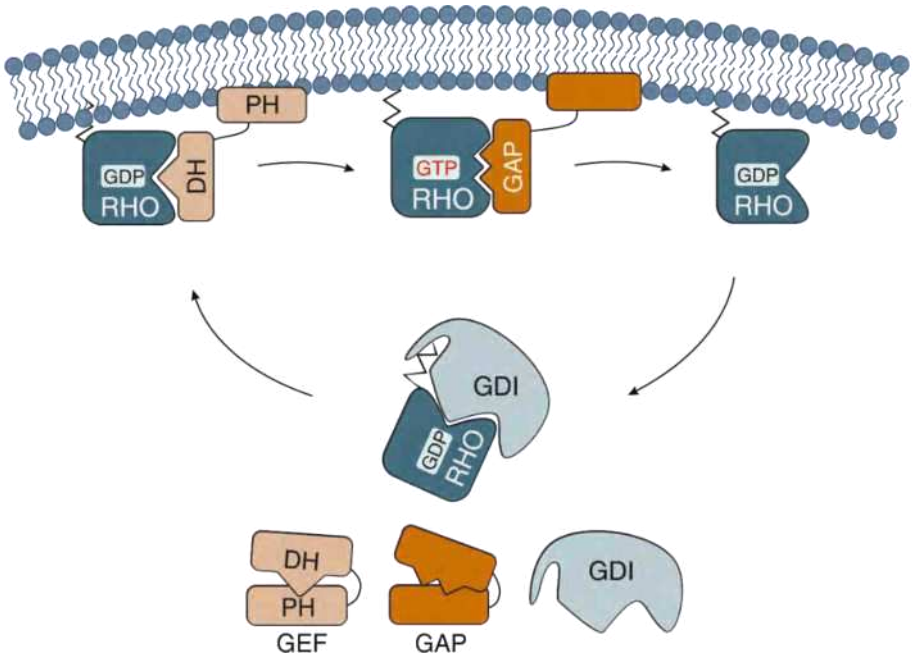

Figure 4. Summary of RHO GTPases regulation through GEF, GAP, and GDI. In resting cells, GDIs bind to RHO GTPases lipid moiety and displace them from the membrane. GEFs associate with RHO GTPases in stimulated cells and accelerate the GDP/GTP exchange. GAPs promote the slow intrinsic GTP hydrolysis activity of RHO GTPases and switch off signal transduction.

1.3.4.1 Guanine nucleotide exchange factors (GEFs)

GEFs are classified into two families based on their structural differences: DBL homology (DH) containing proteins, and dedicator of cytokinesis (DOCK) proteins [155,156]. In general, GEFs bind to their respective RHO GTPases selectively and diminish their affinity for GDP, resulting in GDP displacement and eventual GTP association [158,159].

The nucleotide exchange reaction takes place in several steps: first a low-affinity docking complex forms between GEF and the GDP-bound RHO GTPase [160]. Then GDP dissociates from the primary complex, forming a binary complex of GEF and nucleotide-free RHO GTPase [159,161]. This intermediate complex does not last or accumulate in the cell, as it dissociates due to the high intracellular concentration of GTP, resulting in the formation of GTP-bound RHO GTPases [158,162]. Dominant negative variants of RHO proteins (Thr17 in CDC42 is substituted with asparagine) create a tight complex with their cognate GEFs and hamper the activation of endogenous RHO GTPases [163].

The DBL protein, a prototype of the DBL GEF family, was isolated as an oncogenic product from diffuse B-cell lymphoma cells during an oncogene screening [164]. The unique DH domain in the DBL family is considered a very efficient catalytic machine, which can promote the nucleotide exchange of RHO GTPases 10^7-fold [155]. The X-ray and NMR analyses showed that the DH domain consists of a unique extended bundle of alpha helices which is composed of three conserved regions (CR), namely CR1, CR2, and CR3 [165]. The CR1 and CR3 regions are solvent-exposed until they form a complex with RHO GTPases [166]. Often, the DH domain is followed by a pleckstrin homology (PH) domain, which aids the DBL GEFs anchoring to the membrane through phosphoinositides and directs them towards the relevant RHO GTPases, which are already at the membrane [155]. The PH domain can bind to the DH domain and hamper the catalytic activity of the DH domain and rule as a regulatory domain [44,167].

Out of 74 DBL proteins, nine of them lack the C-terminal tandem PH domain, three of them contain a membrane-bending domain, and around seven of 20 studied DBL proteins did not manifest any GEF activity [166]. Besides the DH-PH tandem motif, the DBL family is comprised of several other domains, which serve in: interaction with other proteins, association with membrane lipids, autoregulation, and subcellular localization [57,168,169]. 74 DBL proteins have been reported in humans, which can be monospecific, bispecific, or oligospecific for a wide range of RHO GTPases [166].

The DOCK family is classified into four subfamilies: DOCK-A, DOCK-B, DOCK-C, and DOCK-D, which are comprised of a total of eleven members and encompass two DOCK homology regions (DHRs) [170,171]. DHR-1 binds to certain phospholipids like PtdIns(3,4,5)P3 and mediates the membrane association, while DHR-2 is the catalytic domain of DOCK GEF [172,173]. DOCK-A and DOCK-B exclusively mediate GEF activity for RAC, while DOCK-C and DOCK-D mainly activate CDC42 [174]. The DOCK family arranges fundamental cellular processes that are dependent or independent of their GEF activity, such as brain development, cell migration, phagocytosis, and cardiovascular development [174–176].

1.3.4.2 GTPase-activating proteins (GAPs)

The RHOGAP family is determined by the presence of a conserved catalytic GAP domain, which is solely adequate to interact with RHO GTPases and accelerate the GTP hydrolysis reaction by several orders of magnitude [3,177,178]. 190 amino acids constitute the GAP domain of the RHOGAP family and there is a high sequence homology within the family [179]. Since RHOGAPs and RASGAPs look almost equivalent in their tertiary structure, it has been proposed that their GAP domains are evolutionarily related [179–181].

A conserved arginine residue, known as arginine finger, from the GAP domain is inserted into the GTP-binding pocket of a cognate RHO GTPase and stabilizes the partial negative charges that develop at the transition state [157]. Then it positions the conserved glutamine from the switch II region (Glu61 in CDC42) to activate a water molecule for a nucleophilic attack on the γ-phosphate of GTP [157,180,182]. Crystallographic analyses revealed that switch I, switch II, and P-loop of RHO GTPases are part of the contacted surfaces with RHOGAP [2,135].

In the very first studies, the crystal structure of the GAP domain of p50-RHOGAP in a complex with RHOA•GDP•ALF_4 was solved [183]. BCR, p50RHOGAP, and p190 were the very first to be identified and are also the most studied members of this family [184–186].

The majority of the RHOGAP family members embody several functional domains and motifs other than the GAP domain, which are involved in membrane targeting or autoregulation [157,187]. Masking the arginine finger is an elegant way to hinder GAP activity [188]. The best example is ARHGAP1, which contains phospholipid binding domain sec14, which can either bind to the GAP domain and block its activity or direct ARHGAP1 to endosomes [189]. The other prevalent domains are CC, P, SRC homology 3, PH, and BAR/F-BAR [44,178,190].

The catalytic activity and substrate selectivity depend upon several mechanisms including phosphorylation, lipid binding, subcellular distribution, and protein-protein interaction [188,191–193].

RHOGAPs are extensively expressed, and according to database searches, 66 distinct RHOGAP domain-containing proteins have been identified. Among the discovered GAP domain-containing proteins, some proteins are incapable of promoting GTP hydrolysis, due to a lack of the arginine finger [44,178]. These catalytically inactive RHOGAPs include OCRL1, INPP5P, FAM13B, ARHGAP36, CNTD1, and DEP1/2 which are incapable of terminating the RHO GTPases signaling by stimulating the GTP hydrolysis [44,178]. However, studying the GAP activity of several RHOGAPs for RHO GTPases suggested that the RHOGAPs do not show a definite selectivity towards particular RHO GTPases [178].

RHOGAPs are primarily considered tumor suppressors, as a dysfunctional RHOGAP can result in uncontrolled RHO GTPase signaling and subsequently elevated transformation and cancer progression [194–196]. Therefore, targeting RHOGAPs becomes interesting in the case of cancers with downregulated or inactivated RHOGAPs [196]. It has been proposed, that targeting the C1 domain of β2-chimerin might regenerate the GAP activity of β2-chimerin to deactivate RAC1 in cancer cells [196,197]. Nevertheless, proposing this solution to restore the GAP activity and tumor suppressor function demands a more physiologically relevant environment to provide more evidence for targeting these proteins.

1.3.4.3 Guanine nucleotide dissociation inhibitors (GDIs)

Unlike the other regulators, only three genes encode RHOGDI in mammals [198]. RHOGDI1 (or RHOGDIα) is the most studied member of the family; it is ubiquitously expressed and can interact with several RHO GTPases [199]. RHOGDI2 (or RHOGDIβ, or LY-GDI) is predominantly expressed in hematopoietic cells and it interacts with several RHO GTPases with a lower affinity than RHOGDI1 [200]. RHOGDI3 (GDIγ) is mainly expressed in the brain, lungs, pancreas, kidneys, and testes [201]. The unique N-terminal extension of RHOGDI3 anchors it to the Golgi complex and other cellular membranes [202]. Despite the prenylation of RHO GTPases, a considerable proportion of these proteins remain in the cytosol, and several proofs consider RHOGDI as the reason [203,204]. This leads to a faster localization and activation of RHO GTPases at any membrane in the cell in reply to certain stimuli [203,204]. It has been shown that in the absence of RHOGDI, the RHO GTPases reservoir would not last and would be degraded by proteasomes [203]. Therefore, the stability of RHO GTPases in the cytosol is owed to their interaction with RHOGDI.

A multi-step binding mechanism has been described for RHOGDI-RAC1 association: 1) RHOGDI associates with highly conserved switch regions of RAC1 through its switch binding domain; 2) the polybasic region of RAC1 is attracted to both the N-terminal of RHOGDI and Geranylgeranyl binding domain; 3) both the N-terminal domain and Geranylgeranyl binding domain of RHOGDI create intermolecular charge forces towards the positively charged HVR of RAC1, and 4) the Geranylgeranyl moiety of RAC1 is positioned towards the hydrophobic cavity of RHOGDI which is located between the Geranylgeranyl binding domain and C-terminal of RHOGDI. Subsequently, the Geranylgeranyl moiety is pulled out of the membrane and the RHO GTPases dissociate from the membrane [205,206].

Previous studies showed that particular protein-protein interactions induce RHOGDI-RHO GTPases dissociation. It has been reported that ezrin-radixin-moesin (ERM) proteins, RHO GEFs, and the p75 neurotrophin receptor can separate RHO GTPases from RHOGDI by competing to interact with RHOGDIs [207–210]. Moreover, phosphorylation of RHOGDIs

reduces their affinity for RHO GTPases and results in the release of RHO GTPases and their subsequent activation [206,207].

Alterations in RHOGDI's expression level have been implicated in several cancers, including hepatocellular carcinoma, pancreatic cancers, and Hodgkin's lymphoma cell lines [211–213].

A recent comprehensive study led to the determination of a pseudo-natural product called Rhonin, which hinders RHOGDI activity and enhances the GTP-bound RHO GTPases [214].

2 THESIS AIMS

Structural-functional studies have revealed the significance of RAS GTPases in the regulation of numerous cellular processes. Their dysfunction is frequently reported in cancer as well as developmental and neurological disorders. Several missense variants of ARF3 GTPases were identified in patients suffering from different levels of neurodegeneration. Constitutive HRAS activation results in Costello syndrome, a rare developmental disorder, identified by distinct facial dysmorphism, cardiac malfunction, and cutaneous manifestations. The discovery of mutations in ARF3 GTPases and HRAS raises questions about their role in the pathogenesis of neurological disorders and Costello syndrome, respectively. This thesis aimed to characterize the ARF3 and HRAS mutations biophysically to decipher the molecular mechanisms behind the pathogenesis of the reported disorders.

RHOGDIs represent a special class of regulatory proteins for RHO GTPases, which regulate the spatiotemporal localization of RHO GTPases. However, the exact mechanism of selective RHO GTPases extraction from the membrane by RHOGDI stayed obscure. Therefore, we aimed to determine the structural parameters, which define the GDI function and puzzle out the mechanistic details of RHO GTPases regulation by RHOGDI.

IQGAPs are multidomain proteins and are considered special effectors for RHO GTPases. Until now, the selectivity criteria of these interactions has been a subject of controversial debate. Moreover, the relevance of the interaction of IQGAP distinct domains remains unknown. Hence, another aim of this thesis was to investigate structural differences in RHO GTPases, which define the selectivity of IQGAPs and characterize the binding properties of the GRD domain of IQGAPs and the GRD contacting surface on the CDC42 GTPase. Addressing these questions will advance our knowledge about the structural-functional relationship in the integrity of signal transduction and uncover molecular details of dysregulated signaling pathways.

CHAPTER II. THE RHO FAMILY GTPASES: MECHANISMS OF REGULATION AND SIGNALING

Niloufar Mosaddeghzadeh, Mohammad Reza Ahmadian

DOI: 10.3390/cells10071831

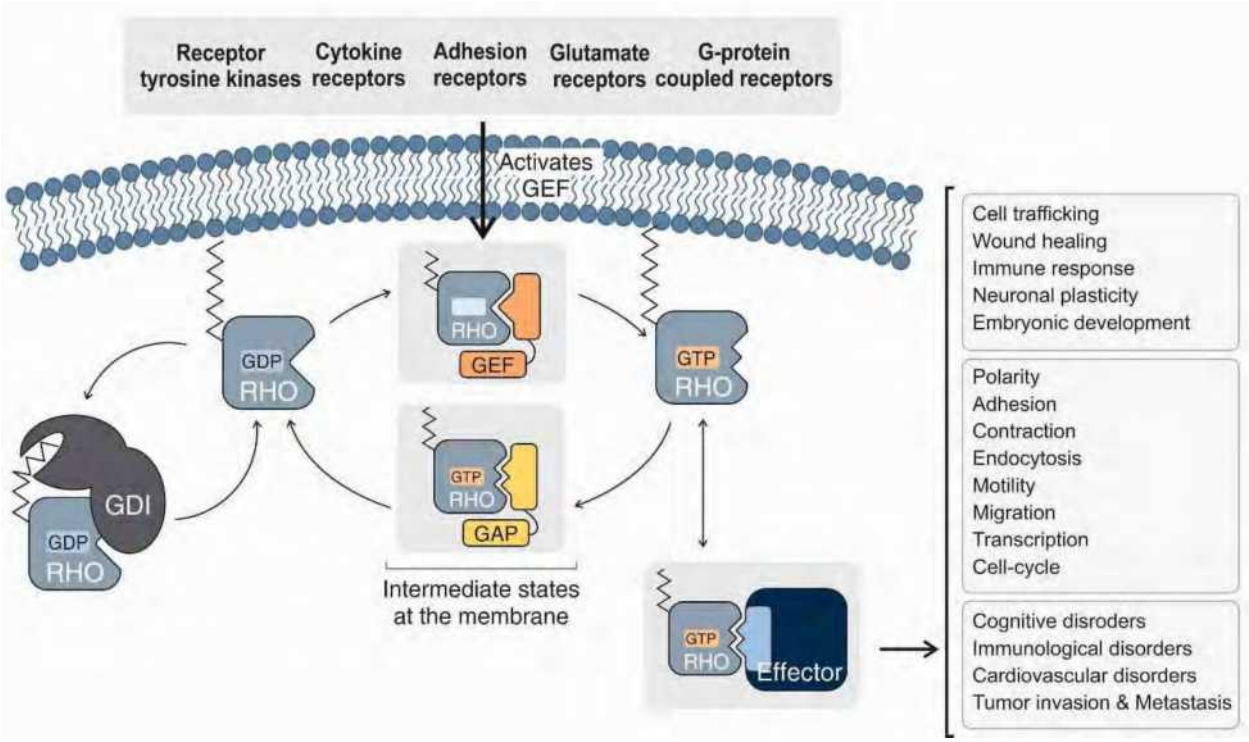

Status:	Published in July 2021
Journal:	Cells
Impact factor:	7.66
Contribution:	80% Drafting, writing, and finalizing the manuscript, literature research, preparing and illustrating the figures.

cells

MDPI

Review

The RHO Family GTPases: Mechanisms of Regulation and Signaling

Niloufar Mosaddeghzadeh and Mohammad Reza Ahmadian *

Institute of Biochemistry and Molecular Biology II, Medical Faculty of the Heinrich Heine University, Universitätsstrasse 1, Building 22.03.05, 40225 Düsseldorf, Germany; mosaddeg@uni-duesseldorf.de
* Correspondence: reza.ahmadian@hhu.de

Abstract: Much progress has been made toward deciphering RHO GTPase functions, and many studies have convincingly demonstrated that altered signal transduction through RHO GTPases is a recurring theme in the progression of human malignancies. It seems that 20 canonical RHO GTPases are likely regulated by three GDIs, 85 GEFs, and 66 GAPs, and eventually interact with >70 downstream effectors. A recurring theme is the challenge in understanding the molecular determinants of the specificity of these four classes of interacting proteins that, irrespective of their functions, bind to common sites on the surface of RHO GTPases. Identified and structurally verified hotspots as functional determinants specific to RHO GTPase regulation by GDIs, GEFs, and GAPs as well as signaling through effectors are presented, and challenges and future perspectives are discussed.

Keywords: CDC42; effectors; RAC1; RHOA; RHOGAP; RHOGDI; RHOGEF; RHO signaling

Citation: Mosaddeghzadeh, N.; Ahmadian, M.R. The RHO Family GTPases: Mechanisms of Regulation and Signaling. *Cells* **2021**, *10*, 1831. https://doi.org/10.3390/cells10071831

Academic Editor: Bor Luen Tang

Received: 9 April 2021
Accepted: 13 July 2021
Published: 20 July 2021

1. Introduction

The RHO (RAS homolog) family is an integral part of the RAS superfamily of guanine nucleotide-binding proteins. RHO family proteins are crucial for several reasons: (i) approximately 1% of the human genome encodes proteins that either regulate or are regulated by direct interaction with RHO proteins; (ii) they control almost all fundamental cellular processes in eukaryotes including morphogenesis, polarity, movement, cell division, gene expression, and cytoskeleton reorganization [1]; and (iii) they are associated with a series of human diseases (Figure 1) [2].

The RHO family of proteins functions as molecular switches in the cell and cycle between being in a GDP-bound, inactive state and a GTP-bound, active state [3]. Invaluable insights have been gained by structural and biochemical studies of RHO GTPases and their complexes with interacting partners thus far, increasing our understanding of both how the switch mechanism of the RHO GTPases is regulated and how a RHO GTPase can interact with four classes of structurally and functionally unrelated protein families (Figure 1) [3]. The cellular regulation of this cycle involves guanine nucleotide exchange factors (GEFs), which accelerate intrinsic GDP/GTP exchange, and GTPase-activating proteins (GAPs), which stimulate intrinsic GTP hydrolysis activity [4]. The formation of the active GTP-bound state of the GTPase is accompanied by a conformational change in two regions (known as switch I and II), which provides a platform for the selective interaction with structurally and functionally diverse proteins (the so-called downstream effectors; Table 1) that initiate a network of cytoplasmic and nuclear signaling cascades [5,6]. A prerequisite of RHO protein function is membrane association, which is achieved by isoprenylation, a posttranslational modification. In this respect, RHO proteins are regulated by a third control mechanism that directs their membrane targeting to specific subcellular sites. Specifically, guanine nucleotide dissociation inhibitors (GDIs) bind selectively to prenylated RHO proteins and control their cycle between the cytosol and membrane. Activation of RHO proteins results in their association with effector molecules that subsequently activate

a wide variety of downstream signaling cascades, thereby regulating many important physiological and pathophysiological processes in eukaryotic cells [7].

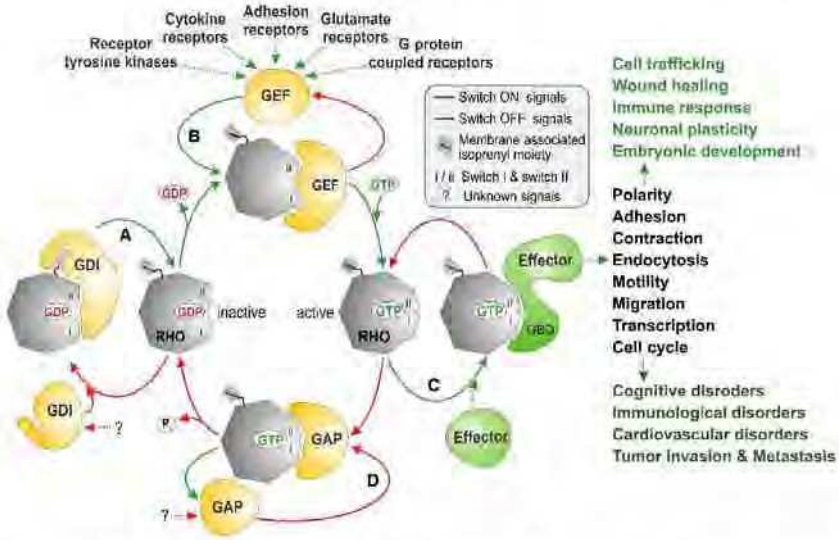

Figure 1. Molecular principles of RHO GTPase regulation and signaling. Most RHO GTPases (20 canonical human members) act as molecular switches by cycling between a GDP-bound, inactive state and a GTP-bound, active state. They interact specifically with four structurally and functionally unrelated classes of proteins: (**A**) In resting cells, guanine nucleotide dissociation inhibitors (GDIs; 4 human members) sequester RHO in the cytoplasm, away from the membrane, by binding to the lipid anchor and thus creating an inactivated cytosolic pool; (**B**) in stimulated cells, different classes of membrane receptors activate guanine nucleotide exchange factors (GEFs; 85 human members: 74 DBL and 11 DOCK family proteins), which in turn activate RHO by accelerating the intrinsic exchange of GDP for GTP and switch ON signal transduction; (**C**) active GTP-bound RHO interacts through the GTPase-binding domain (GBD) with and activates downstream targets (effectors; >70 human members) to cause a variety of intracellular pathways, which control a multitude of biochemical processes involved in the regulation of different biological (dys)functions; (**D**) GTPase-activating proteins (GAPs; 66 human members) negatively regulate RHO by stimulating its slow intrinsic GTP hydrolysis activity and switch OFF signal transduction. Notably, all RHO-interacting proteins recognize and bind RHO at consensus-binding sites called switch I and II.

The molecular mechanisms of RHO GTPase regulation have been well characterized, but our understanding of the signal transduction to downstream targets and, most notably, the autoinhibitory mechanisms of GEFs, GAPs, and effectors remain unclear. Very important and challenging, the elucidation of these critical control mechanisms will open new directions for the design of additional therapeutic interventions.

Signaling by these GTPases is controlled by other mechanisms including post-translational modifications such as phosphorylation, ubiquitylation, sumoylation, and acetylation (see for more details [8,9]).

Table 1. RHO GTPases, potential effectors and their functions in mammalian cells.

RHO GTPases	Effector Proteins	Function	Functions and Effects	References
RHOA	ROCK I/II	Ser /Thr kinase	Actin myosin contraction, Stress fiber formation	[10,11]
	Citron kinase	Ser /Thr kinase	Cytokinesis	[12]
	MBS	Phosphatase subunit	MLC inactivation	[13]
	DIA 1/2	Formin-like proteins	Actin polymerization	[10]
RHOB	Integrin β1	Cell surface receptor	Cell adhesion and migration	[14]
RHOC	FMNL3	Formin like proteins	Migration, Invasion	[15]
RHOH	Kaiso	Transcription factor	TCR activation	[16]
RAC1	PAK1/2/3 *	Ser /Thr kinase	JNK activation, Actin filament stabilization	[17]
	MLK 2/3 *	Ser /Thr kinase	JNK activation	[18,19]
	WAVE	Scaffold	Actin organization	[20]
	p70 S6 kinase *	Ser /Thr kinase	Translation regulation	[21]
	IQGAP1/2 *	Scaffold	Actin/cell-cell contacts	[22,23]
	MEKK1/4 *	Ser /Thr kinase	JNK activation	[24]
	POR1	Scaffold	Actin organization	[25]
	$p67^{phox}$ *	Scaffold	ROS generation	[26]
	PI3 kinase	Lipid kinase	PIP3 levels	[27]
	DAG kinase	Lipid kinase	PA levels	[28,29]
	PLCβ2 *	Lipase	DAG and IP3 levels	[30]
RAC1B	$p120^{ctn}$	Catenin	Cellular transformation	[31]
RAC2	LFA-1	Cell surface receptor	B cell adhesion	[32]
RAC3	GIT1	ARF GAP and scaffold	Regulation of cell adhesion and differentiation	[33]
RHOG	Kinectin	Kinesin receptor	Microtubule dependent transport	[34]
CDC42	N-WASP	Scaffold	Actin organization	[35]
	PAK4	Ser/Thr kinase	Actin organization	[36]
	MRCKα/β	Ser/Thr kinase	Actin organization	[37]
TCL	GIT-PIX complex	Scaffold	Stabilization of focal adhesion	[38,39]
RHOD	Plexin A1/B1	Semaphorin co-receptor	Growth cone formation	[40]
RIF	DIA 1/2	Formin-like proteins	Actin organization	[40,41]
RND1	Stathmin2	Neuronal growth associated proteins	Microtubule depolymerization, Neurite extension	[42]
RND2	Rapostlin	Formin-binding protein	Neurite branching	[43]
RND3	Socius	Scaffold	Loss of stress fibers	[44]
	ROCK1	Ser/Thr kinase	Actomyosin contractility	[45,46]

* Proteins shown with an asterisk are shared effectors for both RAC1 and CDC42.

2. The RHO Family and the Molecular Switch Mechanism

Members of the RHO family have emerged as key regulatory molecules that couple changes in the extracellular environment to intracellular signal transduction pathways. To date, 20 canonical members of the RHO family have been identified in humans and can be categorized into distinct subfamilies based on their sequence homology: RHO (RHOA, RHOB, and RHOC); RAC (RAC1, RAC1B, RAC2, RAC3, and RHOG); CDC42 (CDC42, G25K, TC10, TCL, WRCH1, and WRCH2); RHOD (RHOD, RIF); RND (RND1, RND2, and RND3); and RHOH [47].

RHO family proteins are approximately 21–25 kDa in size. They typically contain a conserved GDP-/GTP-binding domain, called the G domain, and a C-terminal hypervariable region (HVR) ending with a consensus sequence known as CAAX (C is cysteine, A is any aliphatic amino acid, and X is any amino acid) (Figure 2). The G domain consists of five conserved sequence motifs (G1 to G5) that are involved in nucleotide binding and hydrolysis [48]. In the cycle between the inactive and active states, at least two regions of the protein, switch I (G2) and switch II (G3), undergo structural rearrangement and transmit an "OFF" to "ON" signal [3]. Subcellular localization, which is known to be critical for the biological activity of RHO proteins, is achieved through a series of posttranslational modifications at a cysteine residue in the CAAX motif including isoprenylation (geranylgeranyl or farnesyl), endoproteolysis, and carboxyl methylation [49].

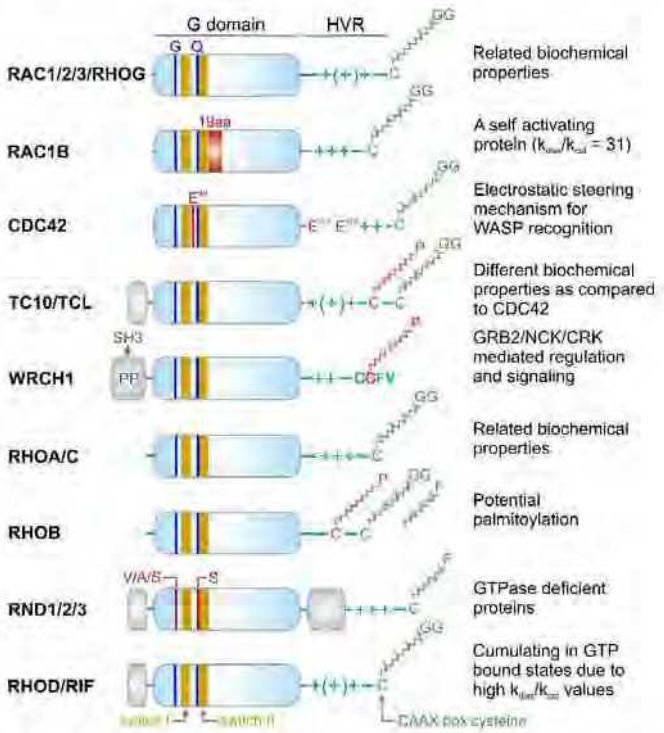

Figure 2. Domains, signature motifs, and post-translational modification of RHO GTPases. RHO GTPases contain a highly conserved G domain, which is responsible for GDP/GTP binding and GTP hydrolysis. Switch I and switch II regions are the consensus binding sites for GEFs, GAPs, GDIs, and effectors, and undergo conformational changes upon the nucleotide exchange and hydrolysis [3]. rest

of captionAll members of the RHO family contain conserved glycine 12 (G) and glutamine 61 (Q; RAC1 numbering), except for the RND proteins, which contain, among other deviations, other residues at these positions. This is why RND proteins constantly remain in the GTP bound state [50]. Other signatures are, for example, a 19-amino acid insertion next to the switch II region in RAC1B with drastic biochemical consequences [51], and glutamic acids (E) in CDC42 crucial for a selective WASP interaction [52]. Some members have amino acid insertion outside the G domain (yellow boxes) with yet unknown properties. The N-terminal insertion in WRCH1 contains proline-rich motifs responsible for interaction with SH3-containing adaptor proteins [53]. Most members have comparable biochemical properties such as nucleotide binding, exchange, and hydrolysis. In contrast to most members, which end up under resting conditions in an inactive GDP-bound state, RAC1B, RHOD, and RIF cumulate in the GTP-bound state due to a faster intrinsic nucleotide exchange reaction (k_{dis}) compared to the intrinsic GTP hydrolysis reaction (k_{cat}) [54]. The C-terminal hypervariable region (HVR) contains the terminal CAAX box, which undergoes posttranslational modification by geranylgeranylation (GG) or alternatively farnesylation (F) in the case of RHOB and the RND proteins at the conserved cysteine (green). Additional modification by a palmitoyl (P) moiety has been reported for RHOB, and the CDC42-related proteins TC10, TCL, and WRCH1. These modifications lead to the membrane anchorage of the members, a process that is stabilized and potentiated through variable numbers of positively charged arginine and lysine residues (+).

Once an isoprenoid moiety is added to CAAX, a RHO protein is translocated to the endoplasmic reticulum, where RCE1 cleaves the AAX tripeptide tail, and then, RHO undergoes carboxymethylation by ICMT [55] RHO proteins can also be phosphorylated, which can affect their association with their regulators or effectors or influence their membrane stability [56–58].

A characteristic region of RHO family GTPases is the insert helix (amino acids 124–136, RHOA numbering), which may play a role in effector activation and downstream processes [59].

Although the majority of the RHO family proteins are remarkably inefficient GTP-hydrolyzing enzymes, in quiescent cells, they accumulate in an inactive state because GTP hydrolysis by RHO proteins is, on average, two orders of magnitude faster than GDP/GTP exchange [47]. These different intrinsic activities provide the basis for a two-state molecular switch mechanism, which greatly depends on the regulatory functions of GEFs and GAPs. Eleven of the 20 RHO family members possess classical molecular switches, namely, RHOA, RHOB, RHOC, RAC1, RAC2, RAC3, RHOG, CDC42, G25K, TC10, and TCL [47].

Atypical RHO family members including RND1, RND2, RND3, RAC1B, RHOH, WRCH1, RHOD, and RIF have been proposed to accumulate in the GTP-bound form in cells [47]. RND1, RND2, RND3, and RHOH constitute a completely distinct group of proteins within the RHO family (Figure 2) [60], as they do not share several essential amino acids including Gly-12 (RAC1 numbering) in the G1 motif (a phosphate-binding loop or P-loop) and Gln-61 in the G3 motif or switch II region, which are critical in GTP hydrolysis. Thus, they can be considered GTPase-deficient RHO-related GTP-binding proteins [61]. RHOD and RIF are involved in the regulation of actin dynamics [41] and exhibit much faster nucleotide exchange than GTP hydrolysis. WRCH1, a CDC42-like protein that has been reported to be a fast-cycling protein, resembles RAC1B, RHOD, and RIF in this regard (Figure 2) [47]. These atypical members do not possess the classical switch mechanism and, therefore, may be regulated through other mechanisms.

3. Regulation of RHO Family GTPases

3.1. Guanine Nucleotide Dissociation Inhibitors (GDIs)

Despite the vast number of RHOGEFs and RHOGAPs, only three GDIs exist in the human genome. The RHOGDI family includes ubiquitously expressed GDI1 (or RHOGDIα) [62]; GDI2 (GDIβ, LY-GDI or D4-GDI), mainly in hematopoietic tissue [63]; and GDI3 (or GDIγ), which is usually expressed in human cerebral, lung, and pancreatic tissue [64]. An N-terminal extension that anchors GDI3 to the membrane of Golgi vesicles distinguishes this isoform from the others [65].

Several studies in recent decades have provided information about the structure and function of GDIs and proposed that they act as shuttles for RHO GTPase [8,66–68]. The shuttling process is initiated by the release of RHO GTPases from donor membranes, the formation of inhibitory cytosolic GDI-RHO GTPase complexes, and the delivery of RHO GTPases to the membranes of subcellular compartments [66,67].

It has been demonstrated that the isoprenylation process in cells can be regulated by GDIs [69]. GDI mediates the release of RHO GTPases from the membrane, maintains them in an inactivated state, and safeguards them against degradation or nonspecific activation by RHOGEFs [25,29,30]. Different structural studies have revealed two sites of GDI and RHO GTPase interaction [70–74]. First, an N-terminal regulatory arm of GDI binds to the switch region of RHO GTPases and inhibits GDP dissociation and GTP hydrolysis. Second, the N-terminus of GDI attracts the positively charged RHO hypervariable region, which is engaged with negatively charged phospholipids of the membrane and initiates the insertion of the geranylgeranyl moiety on the RHO GTPases into a hydrophobic pocket in the GDI molecule, leading to membrane release [75].

3.2. *Guanine Nucleotide Exchange Factors (GEFs)*

GEFs are able to selectively bind to their respective RHO proteins and accelerate the exchange of tightly bound GDP for GTP [8]. Typically, GEFs profoundly reduce the affinity of RHO proteins for GDP, leading to its displacement from GDP and subsequent association with GTP [76,77]. This reaction involves several stages including an intermediate state in which the GEF is in the complex with the nucleotide-free RHO protein. This intermediate does not accumulate in the cell and rapidly dissociates because of the high intracellular GTP concentration, leading to the formation of the active RHO-GTP complex. The main principle driving this mechanism is based on the binding affinity of nucleotide-free RHO protein being significantly greater for GTP than for GEF proteins [76,78]. Cellular activation of RHO proteins and their cellular signaling can be selectively uncoupled from GEFs through the overexpression of dominant-negative mutants of RHO proteins (e.g., threonine 19 in RHOA is replaced with asparagine) [79]. Dominant-negative mutants form a tight complex with their cognate GEFs, preventing them from activating endogenous RHO proteins. RHOGEFs are classified into two distinct families: DBL homology (DH) domain-containing proteins, and dedicator of cytokinesis (DOCK) proteins [80,81].

3.2.1. DBL Family GEFs

RHOGEFs of the diffuse B-cell lymphoma (DBL) family directly activate the proteins of the RHO family [82]. The prototype of this GEF family is the DBL protein, which was isolated as an oncogenic product from diffuse B-cell lymphoma cells in an oncogene screen [83] and was later reported to act on CDC42 [84]. Human DBL family proteins have recently been grouped into functionally distinct categories based on both their catalytic efficiencies and their sequence–structure relationship [47]. Members of the DBL family are characterized by a unique DBL homology (DH) domain [85–88].

The DH domain is a highly efficient catalytic machine [80] that is able to accelerate the nucleotide exchange of RHO proteins by as much as 10^7-fold. The DH domain is often followed by a pleckstrin homology (PH) domain, indicating its essential and conserved function. A model for PH domain-assisted nucleotide exchange has been proposed for some GEFs such as DBL, DBS, and TRIO [80]. Thus, the PH domain serves multiple roles in signaling events by anchoring GEFs to the membrane (via phosphoinositides) and directing them toward their respective GTPase partners, which are on the membrane [80].

Through a search for DH domain-containing proteins in the human genome, 74 DBL proteins have been identified (Figure 3) [47]. Interestingly, nine of these DBL proteins lack the C-terminal tandem PH domain, and three of these proteins contain a membrane bending and tubulating BAR (BIN/amphiphysin/RVS) domain, and seven of 20 investigated DBL proteins do not exhibit any GEF activity (Figure 3) [47]. In addition to the DH-PH tandem motif, DBL family proteins are highly diverse and contain additional domains with different

functions (Figure 3) including SH2, SH3, CH, RGS, PDZ, and/or IQ domains, which enable their interaction with other proteins; BAR, PH FYVE, C1, and C2 domains, which enable their interaction with membrane lipids; and other functional domains such as Ser/Thr kinase, RASGEF, RHOGAP, and RANGEF [82]. These additional domains have been implicated in autoregulation, subcellular localization, and connection to upstream signaling molecules [40,49,50]. Spatiotemporal regulation of DBL proteins has been suggested as a mechanism that specifically initiates the activation of substrate RHO proteins and controls a broad spectrum of normal and pathological cellular functions [89]. Thus, it is evident that members of the DBL protein family are attractive therapeutic targets for a variety of diseases [90,91].

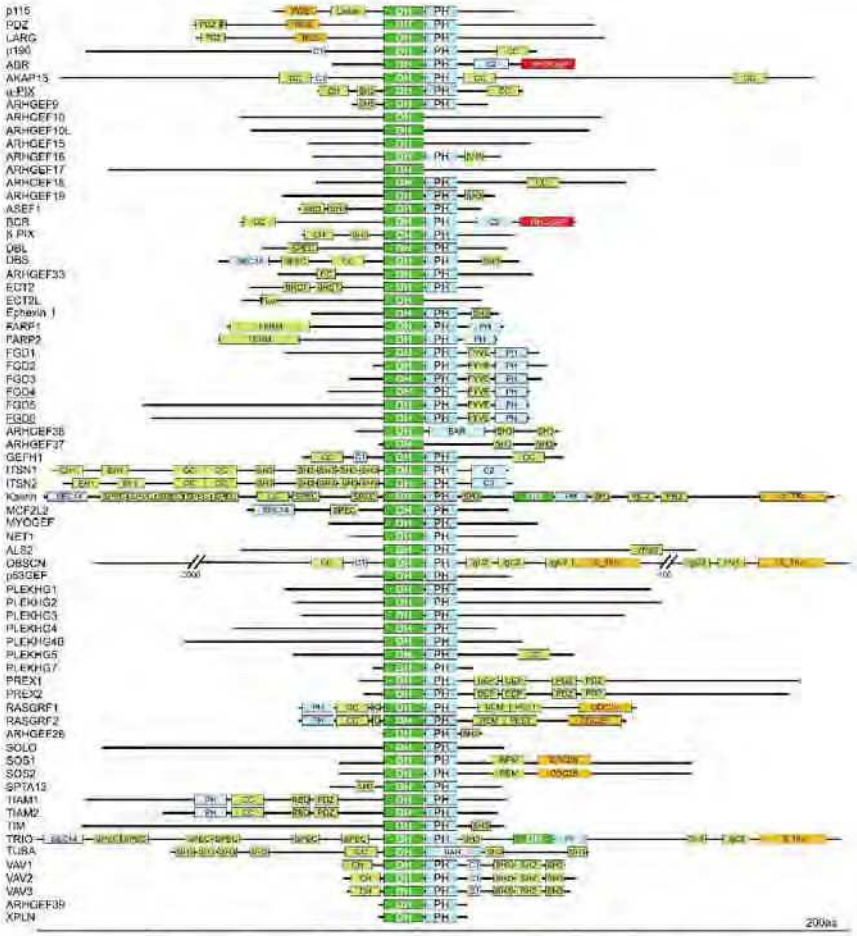

Figure 3. Domain organization of DBL family proteins. The DBL family RHOGEFs are mostly multimodular proteins and have a number of functional domains that may mediate cross talk between RHO proteins and other signaling pathways. DH domains are almost always found with a PH domain in the C-terminus. Some DBL proteins contain two DH–PH cassettes, while some DBL proteins lack tandem PH domains. Functional domains, in addition to the catalytic DH domain (green), are probably involved in lipid and membrane binding (blue), protein interactions (bright green), and enzymatic activities (red and orange). A scale of amino acid numbers in increments of 200 is shown at the bottom. Underlined proteins do not exhibit activity under cell-free conditions [47].

3.2.2. Structural and Functional Characteristics of the DH domain

The DH domain is the signature of DBL family proteins. The catalytic guanine nucleotide exchange activity of DBL family proteins is realized entirely within the DH domain, which is not only sufficient for catalytic activity but also critical for substrate specificity [47,92]. The catalytic DH domain consists of approximately 200 residues, and as determined by x-ray and NMR analyses of the DH domain in several DBL proteins, it is composed of a unique extended bundle of 10–15 alpha helices [93]. This helical fold is mainly composed of three conserved regions, CR1, CR2, and CR3, each of which is 10–30 residues long and forms separate alpha helices that are packed together [45,53]. The CR1 and CR3 regions are solvent exposed until complexed with RHO proteins [47]. Except for these three conserved regions (CR1, CR2, and CR3) in DH domains, DBL family members share little homology with each other [87].

3.2.3. The Tandem PH Domain in DBL Proteins

In the majority of DBL family proteins, the catalytic DH domain is followed by a PH domain consisting of approximately 100 residues (Figure 3), and even though the identity of the PH domain among members of the DBL family is less than 20%, the PH-domain containing DBL proteins share a similar three-dimensional structure with two orthogonal antiparallel β-sheets and a folded C-terminal α-helix that cover one end [94,95]. The PH domain was originally identified in a number of cytoplasmic signaling proteins that displayed homology with a region repeated in pleckstrin [96,97]. The DH-PH tandem is a signature motif of the DBL family, indicating that the PH domain has an essential and conserved function [85,88]. The tandem PH domain can act as a "membrane-targeting device" due to its ability to bind phosphoinositides [98]. It can also bind directly to RHO proteins and potentiate the DH-catalyzed nucleotide exchange reaction [92,93]. In contrast, the PH domains have been shown to bind and inhibit the activity of the DH domain [99,100]. In addition to its membrane-targeting properties, emerging evidence suggests that the PH domain may also play important regulatory roles by serving as a protein–protein interaction module [101].

3.2.4. A Plethora of DBL Family Proteins

It is evident that DBL family proteins are more abundant and varied in cells than RHO family proteins. To date, 74 DBL proteins have been reported in humans, and they are classified into different subfamilies: 46 DBL proteins are monospecific for RHO-, RAC-, and CDC42-selective proteins, five are bispecific for RHO- and CDC42-selective proteins, and six are oligospecific for all three RHO protein subgroups [47]. Since there are many more DBL proteins and many of them can activate more than one RHO protein, the activation of RHO proteins catalyzed by DBL family proteins constitutes a level of regulation in which the signaling pathways can converge or diverge toward one or more RHO proteins [7]. This multifunctionality suggests that at least one representative of each DBL subfamily is expressed in all mammalian cells, but they may act at distinct subcellular sites.

3.3. *DOCK Family of RHOGEFs*

The 11 members of the DOCK family can be categorized into four subfamilies: DOCK-A, DOCK-B, DOCK-C, and DOCK-D [81,102]. DOCK GEFs have two conserved domains: lipid-binding DOCK homology region 1 (DHR-1), which facilitates DOCK localization to membrane compartments, and catalytic DOCK homology region 2 (DHR-2), which induces the GDP-GTP exchange reaction [81,102–104]. It has been proposed that DOCK GEFs activate RAC1 and CDC42 proteins, but not other RHO proteins [105,106].

DOCK proteins orchestrate important processes in brain development including neuron, microglial, and Schwann cell development and functions [102,107]. DOCK2 and DOCK8 play significant roles in immune responses such as the chemotactic responses of T cells and B cells, ROS production in neutrophils, and migration of mature dendritic

cells [81]. Li et al. demonstrated that DOCK1 forms a complex with ELMO1, RAC1, RAC2, and Gαi2, which initiates actin polymerization in breast cancer cells [108].

DOCK2 has been indicated to increase amyloid beta plaque formation, which makes this protein a potential Alzheimer's therapeutic target [109,110]. Janssen et al. showed that in T cells, DOCK8 can form a complex with WASP and ARP2/3 and link TCR to the actin cytoskeleton to form a synapse for T cell responses [111].

Overall, DOCK GEFs play pivotal roles in different biological processes that can be dependent or independent of their GEF activity.

3.4. GTPase-Activating Proteins (GAPs)

Hydrolysis of bound GTP is the timing mechanism that terminates signal transduction of RHO family proteins and enables their return to an inactive, GDP-bound state [87]. The intrinsic GTPase reaction is usually slow but can be stimulated to accelerate by several orders of magnitude through interaction with RHO-specific GAPs [112,113]. The RHOGAP family is identified by the presence of a conserved catalytic GAP domain that is sufficient for engaging RHO proteins and mediating accelerated catalysis [114,115]. The GAP domain inserts a conserved arginine residue, termed an "arginine finger", into the GTP-binding site of the cognate RHO protein to stabilize the transition state and catalyze the GTPase reaction [74,76,77]. This mechanism is similar to that of other small GTP-binding proteins including RAS, RAB, and ARF, although the sequence and folding of the respective GAP families differ from other GTP-binding proteins [115,116]. Masking the catalytic arginine finger is an elegant mechanism for the inhibition of GAP activity. This action has also been recently discovered in the tumor suppressor protein DLC1, an RHOGAP, which is competitively and selectively inhibited by the SH3 domain in p120RASGAP [117,118].

The first RHOGAP discovered, p50RHOGAP, was identified through a biochemical analysis of human spleen cell extracts in the presence of recombinant RHOA [119]. The majority of RHOGAP family members typically harbor several other functional domains and motifs that are implicated in tight regulation and membrane targeting (Figure 4) [74,82,83]. Numerous mechanisms have been shown to affect the specificity and catalytic activity of RHOGAPs (e.g., intramolecular autoinhibition [120], posttranslational modification [121], and regulation by interaction with lipid membranes [122] and proteins [118]).

RHOGAP insensitivity has been frequently analyzed through the substitution of either amino acid that is critical for GTP hydrolysis by RHO proteins (e.g., Gly14 or Gln63 in RHOA), and these mutations generate proteins known as constitutively active mutants [123,124]. In other mutants, the catalytic arginine residue of the GAP domain is replaced with an alanine residue [113,124]. The latter approach is, in principle, very useful under cell-free conditions but not optimal in cells because an Arg-to-Ala mutant may provide a readout similar to that of the wild-type protein as it interferes with downstream signaling by competing with effector(s) for binding to RHO proteins. These RHOGAP mutants are able to bind persistently to their target protein, sequestering the target, which most likely leads to a readout similar to that of activated wild-type RHOGAP. Therefore, it has recently been suggested that mutating critical "binding determinants", particularly Lys319 and Arg323 (p50 numbering), may be a better strategy than substituting the catalytic arginine [114]. Charge reversal of these residues most likely leads to loss of RHOGAP association with its substrate RHO protein and thus abrogates the activity of the GAP domain. This outcome renders mutagenesis not only a tool for determining the specificity of RHOGAPs, but also for investigating GAP domain-independent function(s) of the RHOGAPs.

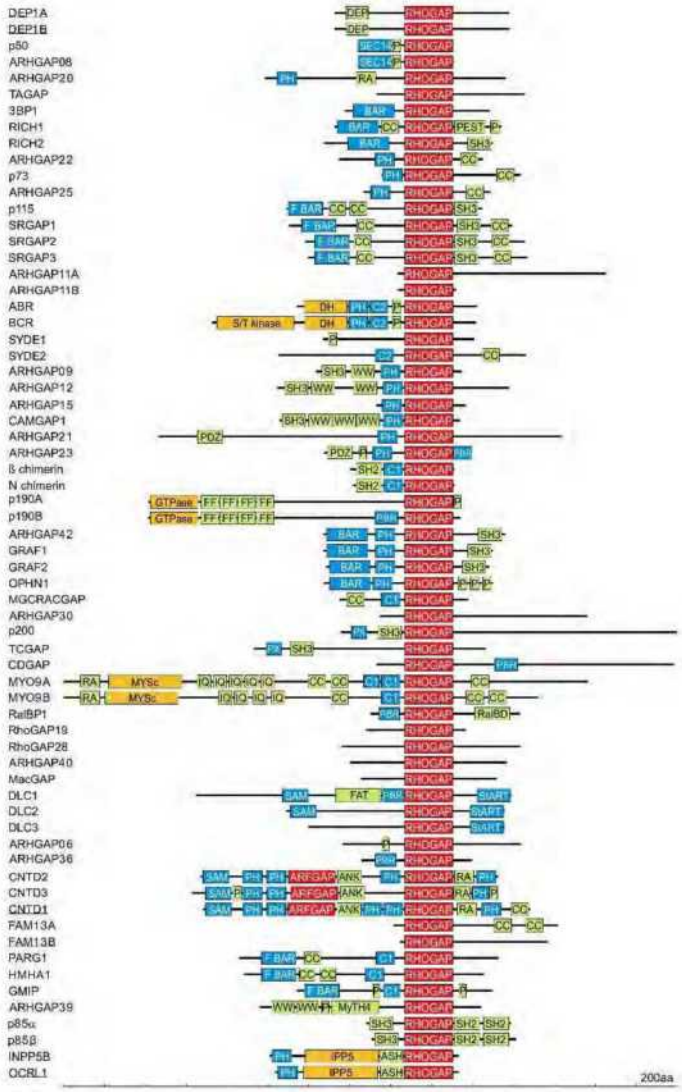

Figure 4. Domain organization of the RHOGAP family proteins (adapted from Amin et al., 2016 [114]). RHOGAPs are mostly multimodular proteins and have a number of functional domains that may mediate cross talk between RHO proteins and other signaling pathways. Functional domains, in addition to the catalytic GAP domain (red), are probably involved in lipid and membrane binding (blue), protein interactions (bright green), and enzymatic activities (red and orange). A scale of amino acid numbers in increments of 200 is shown at the bottom. Underlined proteins are GAP-like proteins with no RHOGAP activity [114].

3.4.1. RHOGAP Family Proteins

The GTPase reaction is of great medical significance, since any disruption of this reaction such as that caused by inhibitory mutations in genes encoding GAP proteins results in persistent downstream signaling. The discovery that GAPs are required for GTPase downregulation was made on the basis that microinjection of recombinant GTP-bound RAS into living cells results in faster GTP hydrolysis than is realized in vitro [125]. The first discovered RHOGAP, p50RHOGAP, was identified by biochemical analysis of human spleen cell extracts with recombinant RHOA [119], and this discovery led to the identification of other RHOGAP-containing proteins such as chimaerin and BCR, whose amino acid sequences are related to p50RHOGAP [126]. Since then, more than 66 RHOGAP-containing proteins have been identified in humans [114,127] The RHOGAP family is identified by the presence of a conserved catalytic GAP domain that is sufficient for RHOGAP interaction with RHO proteins and, in most cases, stimulation of the intrinsic GTP hydrolysis reaction of RHO GTPases [113]. In addition to their signature RHOGAP domain, most RHOGAP family members frequently harbor several other functional domains (Figure 4). The majority of these domains can be classified into the following three major groups: (i) lipid- and membrane-binding domains; (ii) peptide- and protein-interacting domains; and (iii) catalytic domains with enzymatic activities. The most widespread domains are PH, CC, P, SRC homology 3, and BAR/F-BAR (Figure 4). These domains are implicated in regulation, membrane targeting, localization, and potential phosphorylation sites and indicate the complexity of the regulation of GTPase activity. Thirteen GAPs lack any additional putative domains but contain highly variable regions in their N- and C-termini (Figure 4). It is possible that these regions consist of motifs that have not yet been identified, and these regions may contribute to their specific function in the cell.

3.4.2. Structural and Functional Characteristics of the RHOGAP Domain

The GAP domain of the RHOGAP family consists of approximately 190 amino acids and shares high sequence homology within the family. Although the RHOGAP domain shares no similarities to RASGAP family members at the amino acid level, RHOGAPs and RASGAPs resemble each other in their tertiary structure [128,129]. Comparative structural analysis of the RHOGAP domain with other GAPs of RAS subfamilies has suggested that GAP domains in RAS and RHO family proteins are evolutionarily related [128,130] and that the catalytic domains of RHOGAPs share a core structural fold. The RHOGAP domain is made up of seven α-helices. The functional characteristic of the RHOGAP domain is a pair of conserved basic residues: catalytic arginine (the arginine finger) and lysine (Arg282 and Lys319 in p50RHOGAP numbering) [114,131].

3.4.3. The Mechanism by Which the GAP Domain Mediates GTP Hydrolysis

Crystallographic studies of RHOGAP domains in complex with CDC42 bound to GppNHp, RHOA/CDC42 bound to GDP·AlF_4 [76,77,95] and RHOA bound to GDP·MgF_3 [132] have provided insights into the catalytic mechanism of GTP hydrolysis upon stimulation. The GTPase reaction, as part of the switch mechanism, leads to changes in the conformation of the GTPase, especially in flexible and mobile loops known as switch regions. RHOGAP interacts with the switch I and II regions [3,133] and the P-loop of the RHO protein. The GAP domain accelerates the intrinsic GTP hydrolysis by RHO proteins in two ways. First, it directly contributes to catalysis by inserting catalytic arginine in the GAP domain into the active site of the RHO protein. This establishes contacts with the main-chain carbonyl of Gly12 (RAC1 numbering) and helps stabilize the GTP-hydrolysis transition state [134]. Second, this interaction stabilizes the negative charges formed during the transition state of GTP hydrolysis and positions the catalytic glutamine residue (Gln61 RAC1 numbering) of the RHO protein to enable its coordination with nucleophilic water molecules [129,135]. RHOGAP also stabilizes the switch regions of the RHO protein by interacting with residues associated with its intrinsic GTPase activity [113]. ARHGAP36, CNTD1, DEP1, DEP2, FAM13B, INPP5P [136], and OCRL1 lack an arginine finger, which makes them catalytically

inactive (Figure 4) [114]. ARHGAP36 is involved in GLI transcription factor activation, but this function proceeds independent of its GAP domain. CNTD1 lacks RHOGAP activity and acts as an ARF6 GAP. DEP1 and DEP2 coordinate cell cycle progression and interfere with RHOA action and signaling even though they lack RHOGAP activity. OCRL1 has been shown to interact with GTP-bound RAC1 without stimulating hydrolysis. p85α and p85β (85-kDa regulatory subunits of phosphoinositide 3-kinases) are also RHOGAP-like proteins (Figure 4), as they do not show any detectable GAP activity toward different RHO proteins [28]. A prerequisite of GAP function is that the GAP domain position its catalytic residue Arg282 (p50 numbering); therefore, GAPs include a number of amino acids that are critical for binding and stabilizing the protein complex. Both p85 isoforms lack most of binding determinants (e.g., Arg323, Asn391, Val394, and Pro398) as well as the conserved amino acids around the arginine finger [114].

3.4.4. Overabundance and Diversity

Using database searches, 66 distinct RHOGAP domain-containing proteins were found to be encoded in the human genome, whereas the number of RHO family proteins that need to be regulated by GAPs was 18 (excluding constitutively active RHO proteins). The overabundance of RHOGAPs implies that they must be tightly regulated in the cell to prevent RHO proteins from being accidentally turned off. Of the 66 RHOGAPs, 57 proteins have a common catalytic domain capable of terminating RHO protein signaling by stimulating the slow intrinsic GTP hydrolysis (GTPase) reaction (Figure 4). Investigation of the sequence-structure-function relationship between RHOGAPs and RHO proteins by combining in vitro data with in silico data has revealed that the RHOGAP domain itself is nonselective, and in some cases, it is rather inefficient under cell-free conditions. This finding suggests that other domains in RHOGAPs confer substrate specificity and fine-tunes their catalytic efficiency in cells [114].

3.4.5. Regulation and GAP Proteins Functions

RHOGAPs are widely expressed, which makes their apparent redundancy questionable. Therefore, cells must regulate RHOGAPs very tightly to prevent unwanted events that switch off signaling. To ensure stringent regulatory control, RHOGAPs are modulated at different levels, indicating that regions outside the RHOGAP domain most likely determine the specificity of RHOGAPs (Figure 4). Numerous mechanisms have been shown to affect the catalytic activity and substrate specificity of RHOGAPs (e.g., autoinhibition (GRAF and OPHN1) [120]); posttranslational regulation such as phosphorylation (p190GAP and MgcRACGAP) [121]; lipid binding via PH or C2 domains [122]; protein–protein interactions (DLC1/p120RASGAP) [117,118] and subcellular distribution through specific colocalization of RHOGAPs with RHO proteins at the membrane, for example, with a scaffolding protein (Figure 4) [137].

4. Downstream Effectors of RHO GTPases

The ability of RHO GTPases to control a wide range of intracellular signaling pathways is attributed to their association with their cellular targets: effector proteins (Figure 5, Table 1). In contrast to regulators that interact with RHO GTPases to modulate their switch function, effectors require GTPases to be in a specific conformation to realize their own intrinsic function. To date, more than 70 potential effectors have been identified for RHOA, RAC1, and CDC42 [58].

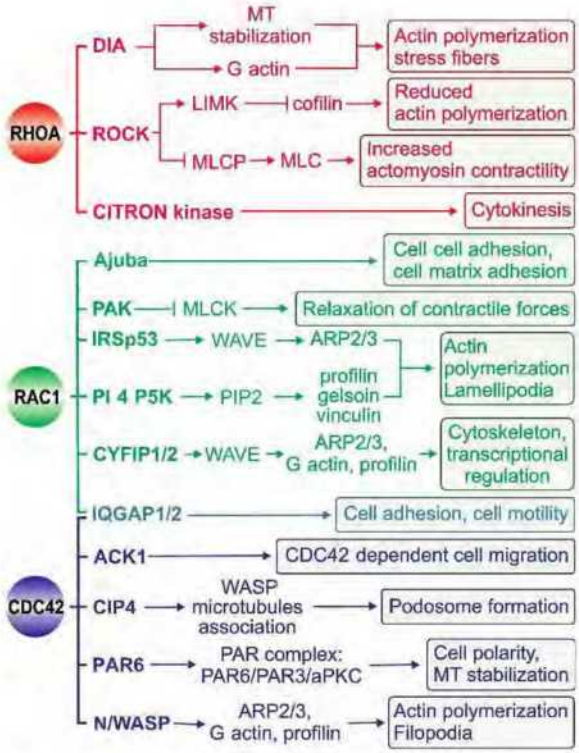

Figure 5. Regulation of actin-based motility by RHOA, RAC1, and CDC42. Activated CDC42, RAC, and RHO bind to and specifically activate their downstream effectors, which are either kinases (e.g., ROCK, PAK, and PI5K) or scaffolding proteins (e.g., DIA, WASP, IRSp53, and IQGAP). These effector proteins activate diverse signaling pathways with distinct effects on the actin cytoskeleton and cellular morphology. An important aspect of cell motility is the equilibrium between the myosin light chain (MLC) and phosphorylated MLC, which is tightly regulated.

The effector proteins are either kinases or scaffolding proteins (Figure 5, Table 1). Kinases form an important class of RHO effectors and result in downstream phosphorylation cascades. Different RHO-associated serine/threonine kinases such as PAK (p21-activated kinase), ROCK (RHO-associated coiled-coil kinase), CRIK (citron kinase), and PKN (protein kinase novel) interact with and are regulated by their partner GTPases [138–140]. Another group of effectors comprise scaffolding proteins, which probably form a framework for signaling cascades, especially through filamentous actin dynamics. IQ motif-containing GTPase-activating protein 1 (IQGAP1) [141], mammalian homolog of Drosophila diaphanous 1 (DIA1), Wiskott-Aldrich syndrome protein (WASP), and Rhotekin (RTKN) are the most extensively investigated effectors in this regard and facilitate complex formation in cells [142].

4.1. Structural Characteristics of RHO GTPase-effector Interactions

The crystal structures of the GTPase-binding domains (GBDs) of PKN and RHO kinase (ROCK) in complex with RHOA revealed that the domains, as predicted from their primary structure, form α-helical coiled coils that are arranged in an antiparallel and parallel fashion, respectively [143,144]. A 13-residue left-handed coiled coil in the

C-terminal portion of the ROCK-CBD, which is considered the minimal sequence required for RHO-interacting motif activity, binds exclusively to the switch and α2 regions of RHOA. In contrast, the RHOA-PKN complex has two possible contact sites on RHOA [143]: contact site 1 consists of the α1, β2/β3, and α5 regions of RHOA, whereas contact site 2 overlaps remarkably well with the ROCK-binding site. The structures of CDC42 in complex with effector proteins containing a CDC42/RAC-interactive binding (CRIB) motif such as PAK1 and WASP, which have been determined mostly by NMR spectroscopy due to their high flexibility [145–149], have shown that the GBD in this class of effectors makes extensive contact with the surface of RHO GTPases. Specifically, GBD binds through its β-hairpin and C-terminal α-helix to the α1, switch I, and II regions and wraps around the α5 and β2 regions of the GTPase with its extended N-terminus, which encompasses the CRIB motif. The basic region of WASP, immediately upstream of the CRIB motif, has been shown to generate favorable electrostatic steering forces to unique glutamate residues in CDC42 (Glu49, Glu171, and Glu178) that control the accelerated WASP-CDC42 association reaction (Figure 2) [52,150]. This process is a prerequisite for WASP activation and a critical step in the temporal regulation and integration of WASP-mediated cellular responses (Figure 5).

Two other effectors, arfaptin and $p67^{phox}$, have novel structures and contact sites on the GTPase [151,152]. Arfaptin forms an elongated crescent-shaped dimer with three helix coiled-coils that makes contact with the switches I and II and α2 regions of RAC1, regardless of its nucleotide-bound state [152], and structurally mimics the DH domain of Tiam1 [153]. $p67^{phox}$ has an α-helical domain that consists of four tetratricopeptide repeat (TPR) motifs, which bind α1, the N-terminal residues of switch I, and the G3 and G5 loops, but not the switch II region or the principal parts of switch I [151]. It has been proposed that the switch regions might be the contact sites for a third protein that is associated with the Rac1-GTP-$p67^{phox}$ complex [154,155].

The mechanism of effector activation of the GTPase–effector complex structures mentioned thus far have not been clarified; however, intramolecular autoinhibition and exposure of their functional domains are known to be required. A common feature of effector complexes is that, with the exception of $p67^{phox}$, they all make intensive contact with the switch/α2 regions of RHO GTPases, which indicates that this region probably serves as the platform for the GTP-dependent recognition of effectors. Two invariant leucine residues (Leu69 and Leu72), which form crucial hydrophobic contacts with almost all effector domains, have been proposed as essential elements for the CDC42/RAC-mediated activation of CRIB-containing effectors [148]. A different activation mechanism has been implicated for the RHO-specific effectors PKN and ROCK, with other domains that bind cooperatively to sites outside the switch regions of RHOA [156].

4.2. RHO GTPase-Mediated Effector Signaling

The fact that effectors commonly contact distinct residues within the highly conserved switch I and II regions of RHO GTPases [3,5] strongly suggests that other domains bind cooperatively to sites outside the switch regions [3,156]. This possibility might explain the cellular specificity of RHO GTPase–effector interactions. Pioneering experiments by Alan Hall and colleagues showed that the reorganization of the actin cytoskeleton is regulated by proteins in the RHO family including CDC42, RAC1, and RHOA (Figure 5) [157]. CDC42 and RAC1 activation, in turn, activates the ARP2/3 complex indirectly via WASP and WAVE to induce branched actin filament networks and the formation of tight bundles of parallel filaments that form the core in filopodia and the formation of a network of diagonally oriented actin filaments that give rise to thin sheets of lamellipodia. RHOA activation leads to the activation of ROCK and DIA and the organization of actomyosin bundles into stress fibers as well as the formation of focal adhesions [1,5]. Coordination of the distinct roles of these GTPases is crucial for regulating cell migration, as demonstrated by wound closure in a fibroblast monolayer: CDC42 regulates cell polarity, RAC1 regulates the protrusion of lamellipodia at the leading edge, and RHO regulates the turnover of highly organized structures termed focal adhesions (reviewed in [7,158–163]).

Moreover, RHO GTPases control signal transduction pathways that influence gene expression including the serum response factor (SRF), nuclear factor κB (NFκB) transcription factor, c-JUN N-terminal kinase (JNK), and p38 milogen-activated protein kinase pathways [19,166]. It has been reported that several enzyme activities can be altered by RHO GTPases. RAC1 can bind directly to $p67^{phox}$, a component of the NADPH oxidase complex, and activate NADPH oxidase activity to generate reactive oxygen species (ROS) (Table 1) [167]. The BCR gene produces a 160 kDa product called $p160^{bcr}$, which encompasses several distinct domains. p160 exhibited GAP activity toward RAC1, RAC2, and CDC42 GTPases. An early study has shown that BCR regulates RAC-mediated superoxide production by the NADPH-oxidase system of leukocytes [168].

5. Conclusions

Abnormal activation of RHO proteins has been shown to play a crucial role in cancer, infectious and cognitive disorders, and cardiovascular diseases. However, several studies must be performed to gain understanding into the complexity of RHO protein signaling. (i) The RHO family comprises 20 signaling proteins, of which only RHOA, RAC1, and CDC42 have been comprehensively studied thus far. The functions of the less-characterized members of this protein family await detailed investigation. (ii) Despite intensive research over the past two decades, the mechanisms by which RHOGDIs associate and extract RHO proteins from the membrane and the factors displacing the RHO protein from the complex with RHOGDI remain to be elucidated. (iii) A tremendous number of 20 RHO-regulating proteins (85 GEFs and 66 GAPs) exist in the human genome. How these regulators selectively recognize their RHO protein targets is not well understood, and the majority of GEFs and GAPs in humans remain uncharacterized. (iv) GDIs, GEFs, GAPs, and effectors, despite their structural diversity, share consensus binding sites within the switch I and II regions [3]. However, all these RHO-binding partners require contact with other regions, not their shared binding region, to realize their specificity for different RHO proteins. (v) A major challenge ahead, which has not been fully addressed thus far, will be gaining an understanding of the spatial temporal regulation of RHO GTPase activity and the interaction of RHO proteins with distinct downstream effectors. (vi) Most GEFs and GAPs need to be regulated and their activation is generally achieved through the release of autoinhibitory elements [92,120]. With a few exceptions [4], the operating principles of these autoregulatory mechanisms remain obscure. (vii) A better understanding of the specificity and the mode of action of the regulatory proteins as well as the selective recruitment and activation of effectors to specific subcellular sites is not only fundamentally important for understanding many aspects of RHO biology, but is also the master key to unlocking the identity of key targets useful in developing drugs against a variety of diseases caused by aberrant RHO protein functions. This regards the spatiotemporal features whose understanding is afflicted with major conceptual shortcomings. Future models should consider both the emerging principle of biomolecular condensates (or non-membrane-bound organelles) that are assembled in liquid-liquid phase separation [169,170] and the modulating principle of accessory proteins [171–173], which appears to safeguard the strength, efficiency, and specificity of signal transduction.

Author Contributions: N.M. and M.R.A. contributed to the conception and design of the article, prepared the figures and Table 1, and provided critical revision of the article and final approval of the accepted version for publication. All authors have read and agreed to the published version of the manuscript.

Funding: This study was supported by the German Research Foundation (Deutsche Forschungsgemeinschaft or DFG; AH 92/8-1); the German Research Foundation (Deutsche Forschungsgemeinschaft or DFG) through the International Research Training Group "Intra and interorgan communication of the cardiovascular system" (grant number: IRTG 1902-p6); the European Network on Noonan Syndrome and Related Disorders (NSEuroNet, grant number: 01GM1621B); and the German Federal Ministry of Education and Research (BMBF) German Network of RASopathy Research (GeNeRARe, grant numbers: 01GM1902C).

Acknowledgments: We are grateful to our colleagues Mamta Jaiswal and Ehsan Amin for the stimulating discussion.

Conflicts of Interest: The authors declare no conflict of interest.

Abbreviations

ABD	APC binding domain
ACK1	Activated CDC42 kinase 1
AlF_4	Tetrafluoroaluminate
ANK	Ankyrin-repeat
ARP2/3	Actin related protein 2/3
ASH	ASPM-SPD-2-Hydin
BAR	BIN–Amphiphysin–RVS
BCR	Breakpoint cluster region
BRCT	BRCA1 C-terminal domain
C1	DAG-binding domain
C2	Calcium/lipid-binding domain
CC	Coiled-coil
CDC25	Catalytic RASGEF domain
CDC42	Cell division control protein 42
CH	Calponin homology
CIP4	CDC42 interacting protein
CNTD1	Cyclin N-terminal domain-containing protein
CYFIP1/2	Cytoplasmic FMR-1 interacting protein 1/2
DAG kinase	Diacyglycerol kinase
DAG	Diacylglycerol
DBL	Diffuse B-cell lymphoma
DEP	Dishevelled, Egl-10 and Pleckstrin domain
DH	DBL homology
DIA	Diaphanous-related formin
DLC1	Deleted in liver Cancer
EH1	EPS15 homology
F-BAR	Extended Fes-CIP4 homology (FCH)-BAR
Fa	Farnesyl moiety
FERM	4.1 protein/ezrin/radixin/moesin
FF	Conserved phenylalanines
FMNL3	Formin-like protein 3
FYVE	FAB1/YOTB/VAC1/EEA1
GAPs	GTPase activating proteins
GDIs	Guanine nucleotide dissociation inhibitors
GDP	Guanosine-5′-diphosphate
GEFs	Guanine nucleotide exchange factors
GG	Geranylgeranyl moiety
GIT	G protein-coupled receptor kinase-interactor 1
GppNHp	Guanosine-5′-[(β, γ)-imido] triphosphate, Trisodium salt
GTP	Guanosine-5′-triphosphate
GTPase	GTP-binding and hydrolyzing domain
GTPase	Guanine triphosphatase
HVR	Hypervariable region
ICMT	Isoprenylcystein carboxyl methyltransferase
IP3	Inositol triphosphate
IPP5	Inositol polyphosphate 5-phosphatase
IQ	Isoleucine-glutamine-rich
IQGAP	IQ motif-containing GTPase activating proteins
IRSp53	Insulin receptor substrate 53 kDa
kDa	Kilodalton
LFA-1	Leukocyte function associated molecule 1 alpha

IgC2	Immunoglobulin C-2 Type
LIMK	LIM domain kinase
MBS	Myosin binding subunit
MEKK	Mitogen Activated Protein kinase kinase kinase
MgF_3	Magnesium fluoride
MLC	Myosin light chain
MLCK	Myosin light chain kinase
MLCP	Myosin light chain phosphatase
MLK	Mixed lineage kinase
MRCK	Myotonic dystrophy kinase related- CDC42 binding Kinase
MT	Microtubule
MYSc	Myosin head domain
MyTH4	Myosin tail homology 4
OCRL1	Lowe oculocerebrorenal syndrome protein
OPHN1	Oligophrenin
P	Proline-rich
PA	Phosphatidic acid
PAK	p21 activated kinase
P	Palmitoyl moiety
PAR6	Partitioning defective 6 homolog
PBR	Polybasic region
PDZ	PSD95/DLG/ZO-1
PEST	Proline-glutamic acid-serine-threonine-rich
PH	Pleckstrin homology
PI3 kinase	Phosphatidylinositol 3-kinase
PI4P5K	Phosphatidylinositol 4, phosphate 5 kinase
PIP2	Phosphatidylinositol 4,5 biphosphate
PIP3	Phosphatidylinositol-3,4,5-triphosphate
PIX	p21-activated protein kinase exchange factor
PLC	Phospholipase C
POR1	Partner of RAC1
RA	RAS association domain
RAC	RAS-related C3 botulinum toxin substrate
RALBD	RAL-binding domain
RBD	RAS-binding domain
Rce1	RAS converting enzyme
REM	RAS exchanger motif
RGS	Regulator of G protein signaling
RHO	RAS homolog
ROCK	RHO-associated protein kinase
S_TKc	Serine/Threonine protein kinase catalytic domain
SAM	Sterile alpha motif
SEC14	Phosphoinositide binding
SH	SRC homology
SH2	SRC homology 2
SH3	SRC homology 3
SPEC	Spectrin repeat
StART	Steroidogenic acute regulatory protein-related lipid transfer
TCR	T cell receptor
VPS9	Vacuolar protein sorting-associated 9
WASP	Wiskott-Aldrich Syndrome Protein
WAVE	WASP family verprolin homologous protein
WW	Conserved tryptophans

References

1. Jaffe, A.B.; Hall, A. Rho GTPases: Biochemistry and biology. *Annu. Rev. Cell Dev. Biol.* **2005**, *21*, 247–269. [CrossRef]
2. Ellenbroek, S.I.J.; Collard, J.G. Rho GTPases: Functions and association with cancer. *Clin. Exp. Metastasis* **2007**, *24*, 657–672. [CrossRef]
3. Dvorsky, R.; Ahmadian, M.R. Always look on the bright site of Rho: Structural implications for a conserved intermolecular interface. *EMBO Rep.* **2004**, *5*, 1130–1136. [CrossRef] [PubMed]
4. Cherfils, J.; Zeghouf, M. Regulation of small GTPases by GEFs, GAPs, and GDIs. *Physiol. Rev.* **2013**, *93*, 269–309. [CrossRef] [PubMed]
5. Bishop, A.L.; Hall, A. Rho GTPases and their effector proteins. *Biochem. J.* **2000**, *348*, 241–255. [CrossRef]
6. Burridge, K.; Wennerberg, K. Rho and Rac Take Center Stage. *Cell* **2004**, *116*, 167–179. [CrossRef]
7. Etienne-Manneville, S.; Hall, A. Rho GTPases in cell biology. *Nature* **2002**, *420*, 629–635. [CrossRef]
8. Hodge, R.G.; Ridley, A.J. Regulating Rho GTPases and their regulators. *Nat. Rev. Mol. Cell Biol.* **2016**, *17*, 496–510. [CrossRef] [PubMed]
9. Knyphausen, P.; Kuhlmann, N.; de Boer, S.; Lammers, M. Lysine-acetylation as a fundamental regulator of ran function: Implications for signaling of proteins of the ras-superfamily. *Small GTPases* **2015**, *6*, 189–195. [CrossRef]
10. Watanabe, N.; Kato, T.; Fujita, A.; Ishizaki, T.; Narumiya, S. Cooperation between mDia1 and ROCK in Rho-induced actin reorganization. *Nat. Cell Biol.* **1999**, *1*, 136–143. [CrossRef]
11. Maekawa, M.; Ishizaki, T.; Boku, S.; Watanabe, N.; Fujita, A.; Iwamatsu, A.; Obinata, T.; Ohashi, K.; Mizuno, K.; Narumiya, S. Signaling from Rho to the actin cytoskeleton through protein kinases ROCK and LIM-kinase. *Science* **1999**, *285*, 895–898. [CrossRef] [PubMed]
12. Madaule, P.; Eda, M.; Watanabe, N.; Fujisawa, K.; Matsuoka, T.; Bito, H.; Ishizaki, T.; Narumiya, S. Role of citron kinase as a target of the small GTPase Rho in cytokinesis. *Nature* **1998**, *394*, 491–494. [CrossRef]
13. Kimura, K.; Ito, M.; Amano, M.; Chihara, K.; Fukata, Y.; Nakafuku, M.; Yamamori, B.; Feng, J.; Nakano, T.; Okawa, K.; et al. Regulation of myosin phosphatase by Rho and Rho-associated kinase (Rho- kinase). *Science* **1996**, *273*, 245–248. [CrossRef] [PubMed]
14. Vega, F.M.; Colomba, A.; Reymond, N.; Thomas, M.; Ridley, A.J. RhoB regulates cell migration through altered focal adhesion dynamics. *Open Biol.* **2012**, *2*. [CrossRef]
15. Vega, F.M.; Fruhwirth, G.; Ng, T.; Ridley, A.J. RhoA and RhoC have distinct roles in migration and invasion by acting through different targets. *J. Cell Biol.* **2011**, *193*, 655–665. [CrossRef] [PubMed]
16. Mino, A.; Troeger, A.; Brendel, C.; Cantor, A.; Harris, C.; Ciuculescu, M.F.; Williams, D.A. Small GTPases RhoH participates in a multi-protein complex with the zinc finger protein kaiso that regulates both cytoskeletal structures and chemokine-induced T cells. *Small GTPases* **2018**. [CrossRef]
17. Bagrodia, S.; Cerione, R.A. PAK to the future. *Trends Cell Biol.* **1999**, *9*, 350–355. [CrossRef]
18. Nagata, K.I.; Puls, A.; Futter, C.; Aspenstrom, P.; Schaefer, E.; Nakata, T.; Hirokawa, N.; Hall, A. The MAP kinase kinase kinase MLK2 co-localizes with activated JNK along microtubules and associates with kinesin superfamily motor KIF3. *EMBO J.* **1998**, *17*, 149–158. [CrossRef] [PubMed]
19. Teramoto, H.; Coso, O.A.; Miyata, H.; Igishi, T.; Miki, T.; Silvio Gutkind, J. Signaling from the small GTP-binding proteins Rac1 and Cdc42 to the c- Jun N-terminal kinase/stress-activated protein kinase pathway: A role for mixed lineage kinase 3/protein-tyrosine kinase 1, a novel member of the mixed lineage kinase family. *J. Biol. Chem.* **1996**, *271*, 27225–27228. [CrossRef]
20. Miki, H.; Suetsugu, S.; Takenawa, T. WAVE, a novel WASP-family protein involved in actin reorganization induced by Rac. *EMBO J.* **1998**, *17*, 6932–6941. [CrossRef]
21. Chou, M.M.; Blenis, J. The 70 kDa S6 kinase complexes with and is activated by the Rho family G proteins Cdc42 and Rac1. *Cell* **1996**, *85*, 573–583. [CrossRef]
22. Fukata, M.; Watanabe, T.; Noritake, J.; Nakagawa, M.; Yamaga, M.; Kuroda, S.; Matsuura, Y.; Iwamatsu, A.; Perez, F.; Kaibuchi, K. Rac1 and Cdc42 capture microtubules through IQGAP1 and CLIP-170. *Cell* **2002**, *109*, 873–885. [CrossRef]
23. Fukataf, M.; Kuroda, S.; Fujii, K.; Nakamura, T.; Shoji, I.; Matsuura, Y.; Okawa, K.; Iwamatsu, A.; Kikuchi, A.; Kaibuchi, K. Regulation of cross-linking of actin filament by IQGAP1, a target for Cdc42. *J. Biol. Chem.* **1997**, *272*, 29579–29583. [CrossRef] [PubMed]
24. Fanger, G.R.; Johnson, N.L.; Johnson, G.L. MEK kinases are regulated by EGF and selectively interact with Rac/Cdc42. *EMBO J.* **1997**, *16*, 4961–4972. [CrossRef]
25. Van Aelst, L.; Joneson, T.; Bar-Sagi, D. Identification of a novel Rac1-interacting protein involved in membrane ruffling. *EMBO J.* **1996**, *15*, 3778–3786. [CrossRef]
26. Diekmann, D.; Abo, A.; Johnston, C.; Segal, A.W.; Hall, A. Interaction of Rac with p67phox and regulation of phagocytic NADPH oxidase activity. *Science* **1994**, *265*, 531–533. [CrossRef] [PubMed]
27. Bokoch, G.M.; Vlahos, C.J.; Wang, Y.; Knaus, U.G.; Traynor-Kaplan, A.E. Rac GTPase interacts specifically with phosphatidylinositol 3-kinase. *Biochem. J.* **1996**, *315*, 775–779. [CrossRef] [PubMed]
28. Tolias, K.F.; Cantley, L.C.; Carpenter, C.L. Rho family GTPases bind to phosphoinositide kinases. *J. Biol. Chem.* **1995**, *270*, 17656–17659. [CrossRef] [PubMed]

29. Houssa, B.; De Widt, J.; Kranenburg, O.; Moolenaar, W.H.; Van Blitterswijk, W.J. Diacylglycerol kinase θ binds to and is negatively regulated by active RhoA. *J. Biol. Chem.* **1999**, *274*, 6820–6822. [CrossRef] [PubMed]
30. Illenberger, D.; Schwald, F.; Pimmer, D.; Binder, W.; Maier, G.; Dietrich, A.; Gierschik, P. Stimulation of phospholipase C-β2 by the Rho GTPases Cdc42Hs and Rac1. *EMBO J.* **1998**, *17*, 6241–6249. [CrossRef] [PubMed]
31. Singh, A.; Karnoub, A.E.; Palmby, T.R.; Lengyel, E.; Sondek, J.; Der, C.J. Rac1b, a tumor associated, constitutively active Rac1 splice variant, promotes cellular transformation. *Oncogene* **2004**, *23*, 9369–9380. [CrossRef] [PubMed]
32. Arana, E.; Vehlow, A.; Harwood, N.E.; Vigorito, E.; Henderson, R.; Turner, M.; Tybulewicz, V.L.L.J.; Batista, F.D. Activation of the Small GTPase Rac2 via the B Cell Receptor Regulates B Cell Adhesion and Immunological-Synapse Formation. *Immunity* **2008**, *28*, 88–99. [CrossRef]
33. Hajdo-Milasinovic, A.; van der Kammen, R.A.; Moneva, Z.; Collard, J.G. Rac3 inhibits adhesion and differentiation of neuronal cells by modifying GIT1 downstream signaling. *J. Cell Sci.* **2009**, *122*, 2127–2136. [CrossRef]
34. Vignal, E.; Blangy, A.; Martin, M.; Gauthier-Rouvière, C.; Fort, P. Kinectin Is a Key Effector of RhoG Microtubule-Dependent Cellular Activity. *Mol. Cell. Biol.* **2001**, *21*, 8022–8034. [CrossRef]
35. Rohatgi, R.; Ma, L.; Miki, H.; Lopez, M.; Kirchhausen, T.; Takenawa, T.; Kirschner, M.W. The interaction between N-WASP and the Arp2/3 complex links Cdc42-dependent signals to actin assembly. *Cell* **1999**, *97*, 221–231. [CrossRef]
36. Abo, A.; Qu, J.; Cammarano, M.S.; Dan, C.; Fritsch, A.; Baud, V.; Belisle, B.; Minden, A. PAK4, a novel effector for Cdc42Hs, is implicated in the reorganization of the actin cytoskeleton and in the formation of filopodia. *EMBO J.* **1998**, *17*, 6527–6540. [CrossRef] [PubMed]
37. Leung, T.; Chen, X.-Q.; Tan, I.; Manser, E.; Lim, L. Myotonic Dystrophy Kinase-Related Cdc42-Binding Kinase Acts as a Cdc42 Effector in Promoting Cytoskeletal Reorganization. *Mol. Cell. Biol.* **1998**, *18*, 130–140. [CrossRef]
38. Wilson, E.; Leszczynska, K.; Poulter, N.S.; Edelmann, F.; Salisbury, V.A.; Noy, P.J.; Bacon, A.; Rappoport, J.Z.; Heath, J.K.; Bicknell, R.; et al. RhoJ interacts with the GIT-PIX complex and regulates focal adhesion disassembly. *J. Cell Sci.* **2014**, *127*, 3039–3051. [CrossRef]
39. Ackermann, K.L.; Florke, R.R.; Reyes, S.S.; Tader, B.R.; Hamann, M.J. TCL/RhoJ plasma membrane localization and nucleotide exchange is coordinately regulated by amino acids within the N terminus and a distal loop region. *J. Biol. Chem.* **2016**, *291*, 23604–23617. [CrossRef] [PubMed]
40. Aspenström, P. Atypical Rho GTPases RhoD and Rif integrate cytoskeletal dynamics and membrane trafficking. *Biol. Chem.* **2014**, *395*, 477–484. [CrossRef]
41. Gad, A.K.B.; Aspenström, P. Rif proteins take to the RhoD: Rho GTPases at the crossroads of actin dynamics and membrane trafficking. *Cell. Signal.* **2010**, *22*, 183–189. [CrossRef]
42. Li, Y.H.; Ghavampur, S.; Bondallaz, P.; Will, L.; Grenningloh, G.; Puschel, A.W. Rnd1 regulates axon extension by enhancing the microtubule destabilizing activity of SCG10. *J. Biol. Chem.* **2009**, *284*, 363–371. [CrossRef]
43. Fujita, H.; Katoh, H.; Ishikawa, Y.; Mori, K.; Negishi, M. Rapostlin is a novel effector of Rnd2 GTPase inducing neurite branching. *J. Biol. Chem.* **2002**, *277*, 45428–45434. [CrossRef] [PubMed]
44. Katoh, H.; Harada, A.; Mori, K.; Negishi, M. Socius Is a Novel Rnd GTPase-Interacting Protein Involved in Disassembly of Actin Stress Fibers. *Mol. Cell. Biol.* **2002**, *22*, 2952–2964. [CrossRef] [PubMed]
45. Riento, K.; Totty, N.; Villalonga, P.; Garg, R.; Guasch, R.; Ridley, A.J. RhoE function is regulated by ROCK I-mediated phosphorylation. *EMBO J.* **2005**, *24*, 1170–1180. [CrossRef]
46. Riou, P.; Villalonga, P.; Ridley, A.J. Rnd proteins: Multifunctional regulators of the cytoskeleton and cell cycle progression. *BioEssays* **2010**, *32*, 986–992. [CrossRef] [PubMed]
47. Jaiswal, M.; Dvorsky, R.; Ahmadian, M.R. Deciphering the molecular and functional basis of Dbl family proteins: A novel systematic approach toward classification of selective activation of the Rho family proteins. *J. Biol. Chem.* **2013**, *288*, 4486–4500. [CrossRef]
48. Wittinghofer, A.; Vetter, I.R. Structure-Function Relationships of the G Domain, a Canonical Switch Motif. *Annu. Rev. Biochem.* **2011**, *80*, 943–971. [CrossRef] [PubMed]
49. Roberts, P.J.; Mitin, N.; Keller, P.J.; Chenette, E.J.; Madigan, J.P.; Currin, R.O.; Cox, A.D.; Wilson, O.; Kirschmeier, P.; Der, C.J. Rho family GTPase modification and dependence on CAAX motif-signaled posttranslational modification. *J. Biol. Chem.* **2008**, *283*, 25150–25163. [CrossRef]
50. Fiegen, D.; Blumenstein, L.; Stege, P.; Vetter, I.R.; Ahmadian, M.R. Crystal structure of Rnd3/RhoE: Functional implications. *FEBS Lett.* **2002**, *525*, 100–104. [CrossRef]
51. Fiegen, D.; Haeusler, L.C.; Blumenstein, L.; Herbrand, U.; Dvorsky, R.; Vetter, I.R.; Ahmadian, M.R. Alternative Splicing of Rac1 Generates Rac1b, a Self-activating GTPase. *J. Biol. Chem.* **2004**, *279*, 4743–4749. [CrossRef]
52. Hemsath, L.; Dvorsky, R.; Fiegen, D.; Carlier, M.F.; Ahmadian, M.R. An electrostatic steering mechanism of Cdc42 recognition by Wiskott-Aldrich syndrome proteins. *Mol. Cell* **2005**, *20*, 313–324. [CrossRef]
53. Kazemein Jasemi, N.; Herrmann, C.; Estirado, E.M.; Gremer, L.; Willbold, D.; Brunsveld, L.; Dvorsky, R.; Ahmadian, M. The intramolecular allostery of GRB2 governing its interaction with SOS1 is modulated by phosphotyrosine ligands. *Biochem. J.* **2021**. [CrossRef]
54. Ahmadian, M.R.; Jaiswal, M.; Fansa, E.K.; Dvorsky, R. New insight into the molecular switch mechanism of human Rho family proteins: Shifting a paradigm. *Biol. Chem.* **2013**, *394*, 89–95. [CrossRef]

55. Winter-Vann, A.M.; Casey, P.J. Post-prenylation-processing enzymes as new targets in oncogenesis. *Nat. Rev. Cancer* **2005**, *5*, 405–412. [CrossRef] [PubMed]
56. Lang, P.; Gesbert, F.; Delespine-Carmagnat, M.; Stancou, R.; Pouchelet, M.; Bertoglio, J. Protein kinase A phosphorylation of RhoA mediates the morphological and functional effects of cyclic AMP in cytotoxic lymphocytes. *EMBO J.* **1996**, *15*, 510–519. [CrossRef]
57. Forget, M.A.; Desrosiers, R.R.; Gingras, D.; Béliveau, R. Phosphorylation states of Cdc42 and RhoA regulate their interactions with Rho GDP dissociation inhibitor and their extraction from biological membranes. *Biochem. J.* **2002**, *361*, 243–254. [CrossRef] [PubMed]
58. Bustelo, X.R.; Sauzeau, V.; Berenjeno, I.M. GTP-binding proteins of the Rho/Rac family: Regulation, effectors and functions in vivo. *BioEssays* **2007**, *29*, 356–370. [CrossRef] [PubMed]
59. Rose, R.; Weyand, M.; Lammers, M.; Ishizaki, T.; Ahmadian, M.R.; Wittinghofer, A. Structural and mechanistic insights into the interaction between Rho and mammalian Dia. *Nature* **2005**, *435*, 513–518. [CrossRef] [PubMed]
60. Troeger, A.; Chae, H.D.; Senturk, M.; Wood, L.; Williams, D.A. A unique carboxyl-Terminal insert domain in the hematopoietic-Specific, gtpase-Deficient rho gtpase rhoh regulates post-Translational processing. *J. Biol. Chem.* **2013**, *288*, 36451–36462. [CrossRef]
61. Garavini, H.; Riento, K.; Phelan, J.P.; McAlister, M.S.B.; Ridley, A.J.; Keep, N.H. Crystal structure of the core domain of RhoE/Rnd3: A constitutively activated small G protein. *Biochemistry* **2002**, *41*, 6303–6310. [CrossRef] [PubMed]
62. Xie, F.; Shao, S.; Zhang, B.; Wang, H.; Liu, B. Role of Rho-specific guanine nucleotide dissociation inhibitor α regulation in cell migration. *Acta Histochem.* **2017**, *119*, 183–189. [CrossRef]
63. Griner, E.M.; Theodorescu, D. The faces and friends of RhoGDI2. *Cancer Metastasis Rev.* **2012**, *31*, 519–528. [CrossRef] [PubMed]
64. De León-Bautista, M.P.; Del Carmen Cardenas-Aguayo, M.; Casique-Aguirre, D.; Almaraz-Salinas, M.; Parraguirre-Martinez, S.; Olivo-Diaz, A.; Del Rocio Thompson-Bonilla, M.; Vargas, M. Immunological and functional characterization of RhoGDI3 and its molecular targets RhoG and RhoB in human pancreatic cancerous and normal cells. *PLoS One* **2016**, *11*, e0166370. [CrossRef]
65. Brunet, N.; Morin, A.; Olofsson, B. RhoGDI-3 regulates RhoG and targets this protein to the Golgi complex through its unique N-terminal domain. *Traffic* **2002**, *3*, 342–358. [CrossRef]
66. Garcia-Mata, R.; Boulter, E.; Burridge, K. The "invisible hand": Regulation of RHO GTPases by RHOGDIs. *Nat. Rev. Mol. Cell Biol.* **2011**, *12*, 493–504. [CrossRef]
67. DerMardirossian, C.; Bokoch, G.M. GDIs: Central regulatory molecules in Rho GTPase activation. *Trends Cell Biol.* **2005**, *15*, 356–363. [CrossRef] [PubMed]
68. Moissoglu, K.; Schwartz, M.A. Spatial and temporal control of Rho GTPase functions. *Cell. Logist.* **2014**, *4*, e943618. [CrossRef] [PubMed]
69. Tnimov, Z.; Abankwa, D.; Alexandrov, K. RhoGDI facilitates geranylgeranyltransferase I-mediated RhoA prenylation. *Biochem. Biophys. Res. Commun.* **2014**, *452*, 967–973. [CrossRef]
70. Grizot, S.; Fauré, J.; Fieschi, F.; Vignais, P.V.; Dagher, M.C.; Pebay-Peyroula, E. Crystal structure of the Rac1 - RhoGDI complex involved in NADPH oxidase activation. *Biochemistry* **2001**, *40*, 10007–10013. [CrossRef] [PubMed]
71. Scheffzek, K.; Stephan, I.; Jensen, O.N.; Illenberger, D.; Gierschik, P. The Rac-RhoGDI complex and the structural basis for the regulation of Rho proteins by RhoGDI. *Nat. Struct. Biol.* **2000**, *7*, 122–126. [CrossRef]
72. Dransart, E.; Olofsson, B.; Cherfils, J. RhoGDIs revisited: Novel roles in Rho regulation. *Traffic* **2005**, *6*, 957–966. [CrossRef]
73. Hoffman, G.R.; Nassar, N.; Cerione, R.A. Structure of the Rho family GTP-binding protein Cdc42 in complex with the multifunctional regulator RhoGDI. *Cell* **2000**, *100*, 345–356. [CrossRef]
74. Longenecker, K.; Read, P.; Derewenda, U.; Dauter, Z.; Liu, X.; Garrard, S.; Walker, L.; Somlyo, A.V.; Nakamoto, R.K.; Somlyo, A.P.; et al. How RhoGDI binds Rho. *Acta Crystallogr. Sect. D Biol. Crystallogr.* **1999**, *55*, 1503–1515. [CrossRef] [PubMed]
75. Mosaddeghzadeh, N.; Kazemein Jasemi, N.S.; Majoleé, J.; Zhang, S.C.; Hordijk, P.L.; Dvorsky, R.; Ahmadian, M.R. New insights into the specificity of the RHO GTPase-GDI interaction: An electrostatic force mechanism. *J. Biol. Chem.* **2021**. Under revision.
76. Cherfils, J.; Chardin, P. GEFs: Structural basis for their activation of small GTP-binding proteins. *Trends Biochem. Sci.* **1999**, *24*, 306–311. [CrossRef]
77. Guo, Z.; Ahmadian, M.R.; Goody, R.S. Guanine nucleotide exchange factors operate by a simple allosteric competitive mechanism. *Biochemistry* **2005**, *44*, 15423–15429. [CrossRef] [PubMed]
78. Hutchinson, J.P.; Eccleston, J.F. Mechanism of nucleotide release from Rho by the GDP dissociation stimulator protein. *Biochemistry* **2000**, *39*, 11348–11359. [CrossRef]
79. Heasman, S.J.; Ridley, A.J. Mammalian Rho GTPases: New insights into their functions from in vivo studies. *Nat. Rev. Mol. Cell Biol.* **2008**, *9*, 690–701. [CrossRef]
80. Rossman, K.L.; Der, C.J.; Sondek, J. GEF means go: Turning on Rho GTPases with guanine nucleotide-exchange factors. *Nat. Rev. Mol. Cell Biol.* **2005**, *6*, 167–180. [CrossRef]
81. Kunimura, K.; Uruno, T.; Fukui, Y. DOCK family proteins: Key players in immune surveillance mechanisms. *Int. Immunol.* **2020**, *32*, 5–15. [CrossRef]
82. Cook, D.R.; Rossman, K.L.; Der, C.J. Rho guanine nucleotide exchange factors: Regulators of Rho GTPase activity in development and disease. *Oncogene* **2014**, *33*, 4021–4035. [CrossRef]

83. Srivastava, S.K.; Wheelock, R.H.P.; Aaronson, S.A.; Eva, A. Identification of the protein encoded by the human diffuse B-cell lymphoma (dbl) oncogene. *Proc. Natl. Acad. Sci. USA* **1986**, *83*, 8868–8872. [CrossRef]
84. Hart, M.J.; Eva, A.; Evans, T.; Aaronson, S.A.; Cerione, R.A. Catalysis of guanine nucleotide exchange on the CDC42Hs protein by the dbloncogene product. *Nature* **1991**, *354*, 311–314. [CrossRef] [PubMed]
85. Aittaleb, M.; Boguth, C.A.; Tesmer, J.J.G. Structure and function of heterotrimeric G protein-regulated Rho guanine nucleotide exchange factors. *Mol. Pharmacol.* **2010**, *77*, 111–125. [CrossRef] [PubMed]
86. Hoffman, G.R.; Cerione, R.A. Signaling to the Rho GTPases: Networking with the DH domain. *FEBS Lett.* **2002**, *513*, 85–91. [CrossRef]
87. Jaiswal, M.; Dubey, B.N.; Koessmeier, K.T.; Gremer, L.; Ahmadian, M.R. Biochemical assays to characterize rho GTPases. *Methods Mol. Biol.* **2012**, *827*, 37–58. [CrossRef] [PubMed]
88. Viaud, J.; Gaits-Iacovoni, F.; Payrastre, B. Regulation of the DH-PH tandem of guanine nucleotide exchange factor for Rho GTPases by phosphoinositides. *Adv. Biol. Regul.* **2012**, *52*, 303–314. [CrossRef]
89. Dubash, A.D.; Wennerberg, K.; García-Mata, R.; Menold, M.M.; Arthur, W.T.; Burridge, K. A novel role for Lsc/p115 RhoGEF and LARG in regulating RhoA activity downstream of adhesion to fibronectin. *J. Cell Sci.* **2007**, *120*, 3989–3998. [CrossRef] [PubMed]
90. Bos, J.L.; Rehmann, H.; Wittinghofer, A. GEFs and GAPs: Critical Elements in the Control of Small G Proteins. *Cell* **2007**, *129*, 865–877. [CrossRef]
91. Vigil, D.; Cherfils, J.; Rossman, K.L.; Der, C.J. Ras superfamily GEFs and GAPs: Validated and tractable targets for cancer therapy? *Nat. Rev. Cancer* **2010**, *10*, 842–857. [CrossRef]
92. Jaiswal, M.; Gremer, L.; Dvorsky, R.; Haeusler, L.C.; Cirstea, I.C.; Uhlenbrock, K.; Ahmadian, M.R. Mechanistic insights into specificity, activity, and regulatory elements of the regulator of G-protein signaling (RGS)-containing Rho-specific guanine nucleotide exchange factors (GEFs) p115, PDZ-RhoGEF (PRG), and lenkemia-associated RhoGEF (LARG). *J. Biol. Chem.* **2011**, *286*, 18202–18212. [CrossRef]
93. Liu, X.; Wang, H.; Eberstadt, M.; Schnuchel, A.; Olejniczak, E.T.; Meadows, R.P.; Schkeryantz, J.M.; Janowick, D.A.; Harlan, J.E.; Harris, E.A.S.; et al. NMR structure and mutagenesis of the N-terminal Dbl homology domain of the nucleotide exchange factor Trio. *Cell* **1998**, *95*, 269–277. [CrossRef]
94. Erickson, J.W.; Cerione, R.A. Structural Elements, Mechanism, and Evolutionary Convergence of Rho Protein-Guanine Nucleotide Exchange Factor Complexes. *Biochemistry* **2004**, *43*, 837–842. [CrossRef] [PubMed]
95. Lemmon, M.A.; Ferguson, K.M.; Abrams, C.S. Pleckstrin homology domains and the cytoskeleton. *FEBS Lett.* **2002**, *513*, 71–76. [CrossRef]
96. Haslam, R.J.; Koide, H.B.; Hemmings, B.A. Pleckstrin domain homology. *Nature* **1993**, *363*, 309–310. [CrossRef] [PubMed]
97. Tyers, M.; Haslam, R.J.; Rachubinski, R.A.; Harley, C.B. Molecular analysis of pleckstrin: The major protein kinase c substrate of platelets. *J. Cell. Biochem.* **1989**, *40*, 133–145. [CrossRef] [PubMed]
98. Dinitto, J.; Lambright, D. Membrane and juxtamembrane targeting by PH and PTB domains. *Biochim. Biophys. Acta Mol. Cell Biol. Lipids* **2006**, *1761*, 850–867. [CrossRef] [PubMed]
99. Han, J.; Luby-Phelps, K.; Das, B.; Shu, X.; Xia, Y.; Mosteller, R.D.; Krishna, U.M.; Falck, J.R.; White, M.A.; Broek, D. Role of substrates and products of PI 3-kinase in regulating activation of Rac-related guanosine triphosphatases by Vav. *Science* **1998**, *279*, 558–560. [CrossRef]
100. Nimnual, A.S. Coupling of Ras and Rac Guanosine Triphosphatases Through the Ras Exchanger Sos. *Science* **1998**, *279*, 560–563. [CrossRef]
101. Lemmon, M.A. Pleckstrin homology domains: Not just for phosphoinositides. *Biochem. Soc. Trans.* **2004**, *32*, 707–711. [CrossRef]
102. Shi, L. Dock protein family in brain development and neurological disease. *Commun. Integr. Biol.* **2013**, *6*, e26839. [CrossRef] [PubMed]
103. Goicoechea, S.M.; Awadia, S.; García-Mata, R. I'm coming to GEF you: Regulation of RhoGEFs during cell migration. *Cell Adhes. Migr.* **2014**, *8*, 535–549. [CrossRef]
104. Chang, L.; Yang, J.; Jo, C.H.; Boland, A.; Zhang, Z.; McLaughlin, S.H.; Abu-Thuraia, A.; Killoran, R.C.; Smith, M.J.; Côté, J.F.; et al. Structure of the DOCK2–ELMO1 complex provides insights into regulation of the auto-inhibited state. *Nat. Commun.* **2020**, *11*, 1–17. [CrossRef] [PubMed]
105. Laurin, M.; Côté, J.F. Insights into the biological functions of Dock family guanine nucleotide exchange factors. *Genes Dev.* **2014**, *28*, 533–547. [CrossRef] [PubMed]
106. Côté, J.F.; Vuori, K. Identification of an evolutionary conserved superfamily of DOCK180-related proteins with guanine nucleotide exchange activity. *J. Cell Sci.* **2002**, *115*, 4901–4913. [CrossRef] [PubMed]
107. Miyamoto, Y.; Yamauchi, J. Cellular signaling of Dock family proteins in neural function. *Cell. Signal.* **2010**, *22*, 175–182. [CrossRef]
108. Li, H.; Yang, L.; Fu, H.; Yan, J.; Wang, Y.; Guo, H.; Hao, X.; Xu, X.; Jin, T.; Zhang, N. ARTICLE Association between Gai2 and ELMO1/Dock180 connects chemokine signalling with Rac activation and metastasis. *Nat. Commun.* **2013**. [CrossRef]
109. Cimino, P.J.; Sokal, I.; Leverenz, J.; Fukui, Y.; Montine, T.J. DOCK2 is a microglial specific regulator of central nervous system innate immunity found in normal and Alzheimer's disease brain. *Am. J. Pathol.* **2009**, *175*, 1622–1630. [CrossRef]
110. Cimino, P.J.; Yang, Y.; Li, X.; Hemingway, J.F.; Cherne, M.K.; Khademi, S.B.; Fukui, Y.; Montine, K.S.; Montine, T.J.; Keene, C.D. Ablation of the microglial protein DOCK2 reduces amyloid burden in a mouse model of Alzheimer's disease. *Exp. Mol. Pathol.* **2013**, *94*, 366–371. [CrossRef] [PubMed]

111. Janssen, E.; Tohme, M.; Hedayat, M.; Leick, M.; Kumari, S.; Ramesh, N.; Massaad, M.J.; Ullas, S.; Azcutia, V.; Goodnow, C.C.; et al. A DOCK8-WIP-WASp complex links T cell receptors to the actin cytoskeleton. *J. Clin. Investig.* **2016**, *126*, 3837–3851. [CrossRef] [PubMed]
112. Eberth, A.; Dvorsky, R.; Becker, C.F.W.; Beste, A.; Goody, R.S.; Ahmadian, M.R. Monitoring the real-time kinetics of the hydrolysis reaction of guanine nucleotide-binding proteins. *Biol. Chem.* **2005**, *386*, 1105–1114. [CrossRef] [PubMed]
113. Fidyk, N.J.; Cerione, R.A. Understanding the catalytic mechanism of GTPase-activating proteins: Demonstration of the importance of switch domain stabilization in the stimulation of GTP hydrolysis. *Biochemistry* **2002**, *41*, 15644–15653. [CrossRef] [PubMed]
114. Amin, E.; Jaiswal, M.; Derewenda, U.; Reis, K.; Nouri, K.; Koessmeier, K.T.; Aspenström, P.; Somlyo, A.V.; Dvorsky, R.; Ahmadian, M.R. Deciphering the molecular and functional basis of RHOGAP family proteins: A systematic approach toward selective inactivation of RHO family proteins. *J. Biol. Chem.* **2016**, *291*, 20353–20371. [CrossRef] [PubMed]
115. Scheffzek, K.; Ahmadian, M.R. GTPase activating proteins: Structural and functional insights 18 years after discovery. *Cell. Mol. Life Sci.* **2005**, *62*, 3014–3038. [CrossRef] [PubMed]
116. Scheffzek, K.; Ahmadian, M.R.; Kabsch, W.; Wiesmüller, L.; Lautwein, A.; Schmitz, F.; Wittinghofer, A. The Ras-RasGAP complex: Structural basis for GTPase activation and its loss in oncogenic ras mutants. *Science* **1997**, *277*, 333–338. [CrossRef] [PubMed]
117. Jaiswal, M.; Dvorsky, R.; Amin, E.; Risse, S.L.; Fansa, E.K.; Zhang, S.C.; Taha, M.S.; Gauhar, A.R.; Nakhaei-Rad, S.; Kordes, C.; et al. Functional cross-talk between ras and rho pathways: A ras-specific gtpase-activating protein (p120RasGAP) competitively inhibits the rhogap activity of deleted in liver cancer (DLC) tumor suppressor by masking the catalytic arginine finger. *J. Biol. Chem.* **2014**, *289*, 6839–6849. [CrossRef] [PubMed]
118. Yang, X.Y.; Guan, M.; Vigil, D.; Der, C.J.; Lowy, D.R.; Popescu, N.C. p120Ras-GAP binds the DLC1 Rho-GAP tumor suppressor protein and inhibits its RhoA GTPase and growth-suppressing activities. *Oncogene* **2009**, *28*, 1401–1409. [CrossRef] [PubMed]
119. Garrett, M.D.; Self, A.J.; Van Oers, C.; Hall, A. Identification of distinct cytoplasmic targets for ras/R-ras and rho regulatory proteins. *J. Biol. Chem.* **1989**, *264*, 10–13. [CrossRef]
120. Eberth, A.; Lundmark, R.; Gremer, L.; Dvorsky, R.; Koessmeier, K.T.; McMahon, H.T.; Ahmadian, M.R. A BAR domain-mediated autoinhibitory mechanism for RhoGAPs of the GRAF family. *Biochem. J.* **2009**, *417*, 371–377. [CrossRef]
121. Minoshima, Y.; Kawashima, T.; Hirose, K.; Tonozuka, Y.; Kawajiri, A.; Bao, Y.C.; Deng, X.; Tatsuka, M.; Narumiya, S.; May, W.S.; et al. Phosphorylation by Aurora B converts MgcRacGAP to a RhoGAP during cytokinesis. *Dev. Cell* **2003**, *4*, 549–560. [CrossRef]
122. Ligeti, E.; Dagher, M.C.; Hernandez, S.E.; Koleske, A.J.; Settleman, J. Phospholipids Can Switch the GTPase Substrate Preference of a GTPase-activating Protein. *J. Biol. Chem.* **2004**, *279*, 5055–5058. [CrossRef]
123. Ahmadian, M.R.; Mittal, R.; Hall, A.; Wittinghofer, A. Aluminium fluoride associates with the small guanine nucleotide binding proteins. *FEBS Lett.* **1997**, *408*, 315–318. [CrossRef]
124. Graham, D.L.; Eccleston, J.F.; Lowe, P.N. The conserved arginine in Rho-GTPase-activating protein is essential for efficient catalysis but not for complex formation with Rho-GDP and aluminum fluoride. *Biochemistry* **1999**, *38*, 985–991. [CrossRef] [PubMed]
125. Trahey, M.; Mccormick, F. A cytoplasmic protein stimulates normal N-ras p21 GTPase, but does not affect oncogenic mutants. *Science* **1987**, *238*, 542–545. [CrossRef]
126. Diekmann, D.; Brill, S.; Garrett, M.D.; Totty, N.; Hsuan, J.; Monfries, C.; Hall, C.; Lim, L.; Hall, A. Bcr encodes a GTPase-activating protein for p21rac. *Nature* **1991**, *351*, 400–402. [CrossRef]
127. Lancaster, C.A.; Taylor-Harris, P.M.; Self, A.J.; Brill, S.; Van Erp, H.E.; Hall, A. Characterization of rhoGAP. A GTPase-activating protein for rho-related small GTPases. *J. Biol. Chem.* **1994**, *269*, 1137–1142. [CrossRef]
128. Rittinger, K.; Taylor, W.R.; Smerdon, S.J.; Gamblin, S.J. Support for shared ancestry of GAPs. *Nature* **1998**, *392*, 448–449. [CrossRef]
129. Scheffzek, K.; Ahmadian, M.R.; Wittinghofer, A. GTPase-activating proteins: Helping hands to complement an active site. *Trends Biochem. Sci.* **1998**, *23*, 257–262. [CrossRef]
130. Scheffzek, K.; Lautwein, A.; Kabsch, W.; Ahmadian, M.R.; Wittinghofer, A. Crystal structure of the GTPase-activating domain of human p120GAP and implications for the interaction with Ras. *Nature* **1996**, *384*, 591–596. [CrossRef]
131. Barrett, T.; Xiao, B.; Dodson, E.J.; Dodson, G.; Ludbrook, S.B.; Nurmahomed, K.; Gamblin, S.J.; Musacchio, A.; Smerdon, S.J.; Eccleston, J.F. The structure of the GTPase-activating domain from p50rhoGAP. *Nature* **1997**, *385*, 458–461. [CrossRef]
132. Graham, D.L.; Lowe, P.N.; Grime, G.W.; Marsh, M.; Rittinger, K.; Smerdon, S.J.; Gamblin, S.J.; Eccleston, J.F. MgF3- as a Transition State Analog of Phosphoryl Transfer. *Chem. Biol.* **2002**, *9*, 375–381. [CrossRef]
133. Vetter, I.R.; Wittinghofer, A. The guanine nucleotide-binding switch in three dimensions. *Science* **2001**, *294*, 1299–1304. [CrossRef] [PubMed]
134. Rittinger, K.; Walker, P.A.; Eccleston, J.F.; Nurmahomed, K.; Owen, D.; Laue, E.; Gamblin, S.J.; Smerdon, S.J. Crystal structure of a small G protein in complex with the GTPase- activating protein rhoGAP. *Nature* **1997**, *388*, 693–697. [CrossRef]
135. Rittinger, K.; Walker, P.A.; Eccleston, J.F.; Smerdon, S.J.; Gamblin, S.J. Structure at 1.65 Å of RhoA and its GTPase-activating protein in complex with a transition-state analogue. *Nature* **1997**, *389*, 758–762. [CrossRef] [PubMed]
136. Jefferson, A.B.; Majerus, P.W. Properties of type II inositol polyphosphate 5-phosphatase. *J. Biol. Chem.* **1995**, *270*, 9370–9377. [CrossRef] [PubMed]
137. Bernards, A. GAPs galore! A survey of putative Ras superfamily GTPase activating proteins in man and Drosophila. *Biochim. Biophys. Acta Rev. Cancer* **2003**, *1603*, 47–82. [CrossRef]

138. Amin, E.; Dubey, B.N.; Zhang, S.C.; Gremer, L.; Dvorsky, R.; Moll, J.M.; Taha, M.S.; Nagel-Steger, L.; Piekorz, R.P.; Somlyo, A.V.; et al. Rho-kinase: Regulation, (dys)function, and inhibition. *Biol. Chem.* **2013**, *394*, 1399–1410. [CrossRef] [PubMed]
139. Narumiya, S.; Tanji, M.; Ishizaki, T. Rho signaling, ROCK and mDia1, in transformation, metastasis and invasion. *Cancer Metastasis Rev.* **2009**, *28*, 65–76. [CrossRef]
140. Zhao, Z.S.; Manser, E. PAK and other Rho-associated kinases - Effectors with surprisingly diverse mechanisms of regulation. *Biochem. J.* **2005**, *386*, 201–214. [CrossRef]
141. Hedman, A.C.; Smith, J.M.; Sacks, D.B. The biology of IQGAP proteins: Beyond the cytoskeleton. *EMBO Rep.* **2015**, *16*, 427–446. [CrossRef]
142. Liu, C.A.; Wang, M.J.; Chi, C.W.; Wu, C.W.; Chen, J.Y. Rho/Rhotekin-mediated NF-κB activation confers resistance to apoptosis. *Oncogene* **2004**, *23*, 8731–8742. [CrossRef] [PubMed]
143. Maesaki, R.; Ihara, K.; Shimizu, T.; Kuroda, S.; Kaibuchi, K.; Hakoshima, T. The structural basis of Rho effector recognition revealed by the crystal structure of human RhoA complexed with the effector domain of PKN/PRK1. *Mol. Cell* **1999**, *4*, 793–803. [CrossRef]
144. Dvorsky, R.; Blumenstein, L.; Vetter, I.R.; Ahmadian, M.R. Structural Insights into the Interaction of ROCKI with the Switch Regions of RhoA. *J. Biol. Chem.* **2004**, *279*, 7098–7104. [CrossRef] [PubMed]
145. Abdul-Manan, N.; Aghazadeh, B.; Liu, G.A.; Majumdar, A.; Ouerfelli, O.; Simonovitch, K.A.; Rosen, M.K. Structure of Cdc42 in complex with the GTPase-binding domain of the "Wiskott-Aldrich syndrome" protein. *Nature* **1999**, *399*, 379–383. [CrossRef]
146. Mott, H.R.; Owen, D.; Nietlispach, D.; Lowe, P.N.; Manser, E.; Lim, L.; Laue, E.D. Structure of the small G protein Cdc42 bound to the GTpasebinding domain of ACK. *Nature* **1999**, *399*, 384–388. [CrossRef] [PubMed]
147. Gizachew, D.; Guo, W.; Chohan, K.K.; Sutcliffe, M.J.; Oswald, R.E. Structure of the complex of Cdc42Hs with a peptide derived from P-21 activated kinase. *Biochemistry* **2000**, *39*, 3963–3971. [CrossRef]
148. Morreale, A.; Venkatesan, M.; Mott, H.R.; Owen, D.; Nietlispach, D.; Lowe, P.N.; Laue, E.D. Structure of Cdc42 bound to the GTPase binding domain of PAK. *Nat. Struct. Biol.* **2000**, *7*, 384–388. [CrossRef]
149. Garrard, S.M.; Capaldo, C.T.; Gao, L.; Rosen, M.K.; Macara, I.G.; Tomchick, D.R. Structure of Cdc42 in a complex with the GTPase-binding domain of the cell polarity protein, Par6. *EMBO J.* **2003**, *22*, 1125–1133. [CrossRef] [PubMed]
150. Martinelli, S.; Krumbach, O.H.F.; Pantaleoni, F.; Coppola, S.; Amin, E.; Pannone, L.; Nouri, K.; Farina, L.; Dvorsky, R.; Lepri, F.; et al. Functional Dysregulation of CDC42 Causes Diverse Developmental Phenotypes. *Am. J. Hum. Genet.* **2018**, *102*, 309–320. [CrossRef]
151. Lapouge, K.; Smith, S.J.M.; Walker, P.A.; Gamblin, S.J.; Smerdon, S.J.; Rittinger, K. Structure of the TPR domain of p67(phox) in complex with Rac·GTP. *Mol. Cell* **2000**, *6*, 899–907. [CrossRef]
152. Tarricone, C.; Xiao, B.; Justin, N.; Walker, P.A.; Rittinger, K.; Gamblin, S.J.; Smerdon, S.J. The structural basis of Arfaptin-mediated cross-talk between Rac and Arf signalling pathways. *Nature* **2001**, *411*, 215–219. [CrossRef]
153. Cherfils, J. Structural mimicry of DH domains by Arfaptin suggests a model for the recognition of Rac-GDP by its guanine nucleotide exchange factors. *FEBS Lett.* **2001**, *507*, 280–284. [CrossRef]
154. Diebold, B.A.; Bokoch, G.M. Molecular basis for Rac2 regulation of phagocyte NADPH oxidase. *Nat. Immunol.* **2001**, *2*, 211–215. [CrossRef]
155. Hoffman, G.R.; Cerione, R.A. Rac inserts its way into the immune response. *Nat. Immunol.* **2001**, *2*, 194–196. [CrossRef] [PubMed]
156. Blumenstein, L.; Ahmadian, M.R. Models of the cooperative mechanism for Rho effector recognition: Implications for RhoA-mediated effector activation. *J. Biol. Chem.* **2004**, *279*, 53419–53426. [CrossRef] [PubMed]
157. Hall, A. Rho GTPases and the actin cytoskeleton. *Science* **1998**, *279*, 509–514. [CrossRef] [PubMed]
158. Lawson, C.D.; Ridley, A.J. Rho GTPase signaling complexes in cell migration and invasion. *J. Cell Biol.* **2018**, *217*, 447–457. [CrossRef] [PubMed]
159. Guan, X.; Guan, X.; Dong, C.; Jiao, Z. Rho GTPases and related signaling complexes in cell migration and invasion. *Exp. Cell Res.* **2020**, 388. [CrossRef]
160. Hall, A. Rho family GTPases. *Biochem. Soc. Trans.* **2012**, *40*, 1378–1382. [CrossRef]
161. Schaks, M.; Giannone, G.; Rottner, K. Actin dynamics in cell migration. *Essays Biochem.* **2019**, *63*, 483–495. [CrossRef] [PubMed]
162. Devreotes, P.; Horwitz, A.R. Signaling networks that regulate cell migration. *Cold Spring Harb. Perspect. Biol.* **2015**, *7*. [CrossRef] [PubMed]
163. Zegers, M.M.; Friedl, P. Rho GTPases in collective cell migration. *Small GTPases* **2014**, *5*. [CrossRef]
164. Sadok, A.; Marshall, C.J. Rho gtpases masters of cell migration. *Small GTPases* **2014**, *5*. [CrossRef]
165. Raftopoulou, M.; Hall, A. Cell migration: Rho GTPases lead the way. *Dev. Biol.* **2004**, *265*, 23–32. [CrossRef]
166. Miralles, F.; Posern, G.; Zaromytidou, A.I.; Treisman, R. Actin dynamics control SRF activity by regulation of its coactivator MAL. *Cell* **2003**, *113*, 329–342. [CrossRef]
167. Hordijk, P.L. Regulation of NADPH oxidases: The role of Rac proteins. *Circ. Res.* **2006**, *98*, 453–462. [CrossRef]
168. Voncken, J.W.; van Schaick, H.; Kaartinen, V.; Deemer, K.; Coates, T.; Landing, B.; Pattengale, P.; Dorseuil, O.; Bokoch, G.M.; Groffen, J.; et al. Increased neutrophil respiratory burst in bcr-null mutants. *Cell* **1995**, *80*, 719–728. [CrossRef]
169. Lyon, A.S.; Peeples, W.B.; Rosen, M.K. A framework for understanding the functions of biomolecular condensates across scales. *Nat. Rev. Mol. Cell Biol.* **2021**, *22*, 215–235. [CrossRef] [PubMed]

170. Araki, Y.; Hong, I.; Gamache, T.R.; Ju, S.; Collado-Torres, L.; Shin, J.H.; Huganir, R.L. Syngap isoforms differentially regulate synaptic plasticity and dendritic development. *Elife* **2020**, *9*, 1–28. [CrossRef] [PubMed]
171. Pudewell, S.; Wittich, C.; Kazemein Jasemi, N.S.; Bazgir, F.; Ahmadian, M.R. Accessory proteins of the RAS-MAPK pathway: Moving from the side line to the front line. *Commun. Biol.* **2021**, *4*, 696. [CrossRef] [PubMed]
172. Li, P.; Banjade, S.; Cheng, H.C.; Kim, S.; Chen, B.; Guo, L.; Llaguno, M.; Hollingsworth, J.V.; King, D.S.; Banani, S.F.; et al. Phase transitions in the assembly of multivalent signalling proteins. *Nature* **2012**, *483*, 336–340. [CrossRef] [PubMed]
173. Case, L.B.; Zhang, X.; Ditlev, J.A.; Rosen, M.K. Stoichiometry controls activity of phase-separated clusters of actin signaling proteins. *Science* **2019**, *363*, 1093–1097. [CrossRef] [PubMed]

CHAPTER III. ELECTROSTATIC FORCES MEDIATE THE SPECIFICITY OF RHO GTPASE-GDI INTERACTION

Niloufar Mosaddeghzadeh, Neda S. Kazemein Jasemi, Jisca Majolée, Si-Cai Zhang, Peter L. Hordijk, Radovan Dvorsky, Mohammad R. Ahmadian

DOI:10.3390/ijms222212493

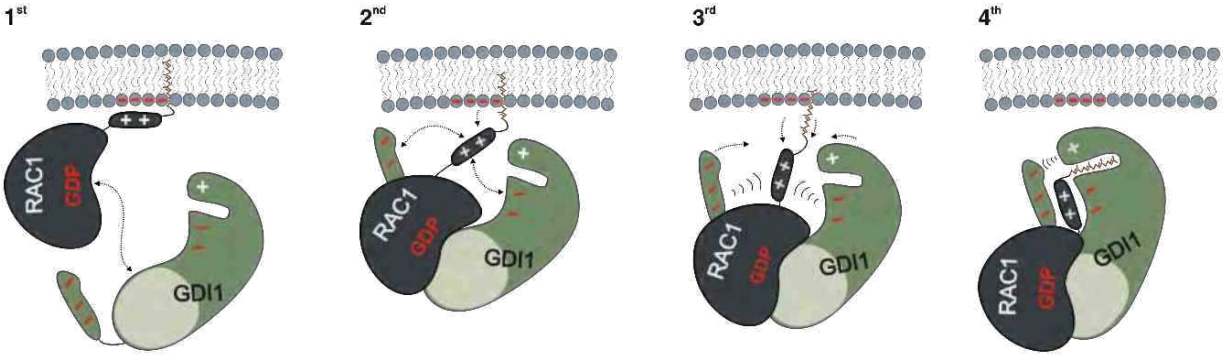

Status:	Published in November 2021
Journal:	International Journal of Molecular Sciences
Impact factor:	6.20
Contribution:	50% Expression and purification of RHO GTPases and RHOGDIs, preparation of nucleotide-free form of RHO GTPases, protein interaction analyses including fluorescence polarization measurements and stopped-flow measurements, preparation and illustration of the figures, drafting and writing the manuscript and discussion.

International Journal of
Molecular Sciences

MDPI

Article

Electrostatic Forces Mediate the Specificity of RHO GTPase-GDI Interactions

Niloufar Mosaddeghzadeh [1], Neda S. Kazemein Jasemi [1], Jisca Majolée [2], Si-Cai Zhang [1], Peter L. Hordijk [2], Radovan Dvorsky [1] and Mohammad Reza Ahmadian [1,3,*]

[1] Institute of Biochemistry and Molecular Biology II, Medical Faculty and University Hospital Düsseldorf, Heinrich Heine University Düsseldorf, 40225 Düsseldorf, Germany; mosaddeg@uni-duesseldorf.de (N.M.); neda.jasemi@hhu.de (N.S.K.J.); sicaichang@gmail.com (S.-C.Z.); radovan.dvorsky@gmail.com (R.D.)
[2] Department of Physiology, Amsterdam UMC, Location VUmc, De Boelelaan, 1108 Amsterdam, The Netherlands; j.majolee@amsterdamumc.nl (J.M.); p.hordijk@amsterdamumc.nl (P.L.H.)
[3] Institute of Future Agriculture, Northwest A&F University, Xianyang 712100, China
* Correspondence: reza.ahmadian@hhu.de; Tel.: +49-211-811-2384

Abstract: Three decades of research have documented the spatiotemporal dynamics of RHO family GTPase membrane extraction regulated by guanine nucleotide dissociation inhibitors (GDIs), but the interplay of the kinetic mechanism and structural specificity of these interactions is as yet unresolved. To address this, we reconstituted the GDI-controlled spatial segregation of geranylgeranylated RHO protein RAC1 in vitro. Various biochemical and biophysical measurements provided unprecedented mechanistic details for GDI function with respect to RHO protein dynamics. We determined that membrane extraction of RHO GTPases by GDI occurs via a 3-step mechanism: (1) GDI non-specifically associates with the switch regions of the RHO GTPases; (2) an electrostatic switch determines the interaction specificity between the C-terminal polybasic region of RHO GTPases and two distinct negatively-charged clusters of GDI1; (3) a non-specific displacement of geranylgeranyl moiety from the membrane sequesters it into a hydrophobic cleft, effectively shielding it from the aqueous milieu. This study substantially extends the model for the mechanism of GDI-regulated RHO GTPase extraction from the membrane, and could have implications for clinical studies and drug development.

Keywords: CDC42; electrostatic steering; G domain; hypervariable region; geranylgeranyl; guanine nucleotide dissociation inhibitors; liposomes; membrane extraction; polybasic motif; RAC1; RAC2; RHOA; RHOGDI

Citation: Mosaddeghzadeh, N.; Kazemein Jasemi, N.S.; Majolée, J.; Zhang, S.-C.; Hordijk, P.L.; Dvorsky, R.; Ahmadian, M.R. Electrostatic Forces Mediate the Specificity of RHO GTPase-GDI Interactions. *Int. J. Mol. Sci.* **2021**, *22*, 12493. https://doi.org/10.3390/ijms222212493

Academic Editor: Claudiu T. Supuran

Received: 25 October 2021
Accepted: 16 November 2021
Published: 19 November 2021

1. Introduction

The RHO family GTPases, most prominently RAC1, CDC42, and RHOA, share two common functional characteristics, membrane anchorage and an on/off switch cycle [1]. They typically contain a conserved GDP/GTP binding domain, called G domain, and a C-terminal hypervariable region (HVR) ending with a consensus sequence known as CAAX (C is cysteine, A is any aliphatic amino acid, and X is any amino acid). Subcellular localization, which is critical for the biological activity of RHO GTPases, is achieved by a series of posttranslational modifications at the cysteine residue in the CAAX motif, including isoprenylation (geranylgeranyl or farnesyl), endoproteolysis and carboxyl methylation [2]. Membrane-associated RHO GTPases act then, with some exceptions [3], as molecular switches by cycling between an inactive GDP-bound state and an active GTP-bound state. This cycle underlies two critical intrinsic functions, GDP-GTP exchange and GTP hydrolysis, which induce structural rearrangements of two regions of the protein, called switch I and switch II [3] (encompassing amino acids 29–42 and 62–68, respectively) and is controlled by two classes of regulatory proteins, guanine nucleotide exchange factors (GEFs) and GTPase activating proteins (GAPs) [4]. RHO GTPases act as dynamic

switches in many developmental and cellular contexts [5] by selectively binding to and activating structurally and functionally diverse effectors. This class of proteins activates a wide variety of downstream signaling cascades [6–9], thereby regulating many important physiological and pathophysiological processes in eukaryotic cells [10–12].

The spatial and temporal activation of RHO GTPases inside a cell is fundamental, for example, to the regulation of local movements and cell-cell contacts that are required for morphogenesis [12]. They are commonly found to cycle between two pools, a membrane-associated and a cytosolic pool. Given the fact that membrane attachment is a prerequisite for the signaling roles of this protein family, it is clear that reversible membrane translocation offers cells a means to regulate the location of the activation event. However, there is a serious handicap to such physical cycling for RHO GTPases. The highly hydrophobic geranylgeranyl (GG) moiety of RHO proteins renders them energetically unfavorable to partition into the cytosol as individual monomers. Post-translationally modified RHO proteins can only detach from membranes if they are assisted by RHO-specific guanine nucleotide dissociation inhibitors (GDIs), that shield the bulky lipid moieties from the aqueous environment of the cytosol [4,13].

In contrast to the tremendous number of the other regulatory proteins of the RHO family (74 GEFs and 66 GAPs) [14,15], only three GDIs exist in the human genome [16]. The GDI family includes the ubiquitously expressed GDI1 (or GDIα) [17], GDI2 (GDIβ, LY-GDI or D4-GDI), which is mainly found in hematopoietic tissue, particularly in B- and T-lymphocytes [18], and GDI3 (or GDIγ) that is preferentially expressed in brain, pancreas, lung, kidney, and testis [19]. Unlike the other two GDIs, GDI3 contains an N-terminal extension that confers anchorage into the membranes of Golgi vesicles [20]. As GDI3 is very similar to GDI1, it can form a complex with all the GDI1 targets [21]. GDI1 and GDI2 contain at their very N-terminus a large number of acidic residues which have been proposed to be essential for their function in the cell [22]. In addition to their physiological expression, GDIs are expressed in several human cancers, including breast, liver, ovarian, pancreatic and myeloid leukemia [13,18,23,24]. Changes in GDI expression levels have shown pro-tumorigenic or anti-tumorigenic effects, that are cell type- and tissue-dependent. One reason for these opposite effects is most probably due to our lack of understanding of the basic mechanism of GDI function and their binding specificities to the different RHO proteins.

Understanding the mechanisms by which signaling events are localized and the physiological consequences of spatial restriction are exerted, is one of the major challenges in cell biology. Comprehensive studies in the last three decades have provided insight into the structure and function of these regulators acting as a shuttle for the RHO GTPases [13,25–27]. The shuttling process, which considerably differs from the KRAS4B^{Far}-PDEδ [28–31], involves the extraction of RHO GTPases from donor membranes, formation of cytosolic GDI-RHO GTPase complexes and delivery of RHO GTPases to the target membranes [13,27]. Accordingly, it has been proposed that GDI regulates the isoprenylation process in the cell [32]. GDI is known to extract RHO GTPases from the membrane, maintain them in an inactivated state, and protect them from both degradation and unspecific activation by RHO-specific GEFs [13,33,34]. Structural studies by different groups have revealed two sites of interaction between GDI and RHO GTPases [35–39]. First, an N-terminal region of the GDIs binds to the switch regions of RHO GTPases leading to the inhibition of both GDP dissociation and GTP hydrolysis. This step involves the Thr35 from the switch I region which would contact the Mg^{2+} ion and has an indispensable role in nucleotide binding of RHO GTPases. The Asp45 residue from the N-terminal region of the GDIs forms a hydrogen bond with this Thr35 residue of switch I region and increases the affinity for the bound GDP nucleotide, that may explain the preference of GDIs for GDP bound form of RHO proteins [37,38]. The first step positions the GDIs hydrophobic pocket toward the membrane surface. In the second step, the geranylgeranyl moiety of RHO GTPases moves out of the membrane and inserts into the hydrophobic pocket of the GDI molecule after which the formed complex moves to the cytosol [36,38]. The mem-

brane release of CDC42•GDI1 complex occurs at a similar rate as the release of CDC42 alone, with the major effect of GDI1 being to impede the re-association of CDC42 with membranes [40]. Moreover, it has been reported that GDI1 binds the isoprenylated RAC1 and RHOA proteins with extremely high binding affinities 0.4 and 0.005 nanomolar affinity, respectively, as compared to non-isoprenylated proteins [41,42]. Although these studies have clearly demonstrated how GDIs interact with and serve as negative regulators of RHO GTPases, yet the basic mechanisms of how they pull the isoprenoid moiety from the membrane remain elusive.

In this study, we investigated the interaction between the three GDI proteins and various members of the RHO GTPase family using structure-function evaluation as well as kinetic and equilibrium measurements. We found clear specificity for the RHO GTPase-GDI interactions, and substantially extended the existing model for binding and membrane extraction of RHO GTPases by GDI1. We found, that: (1) the geranylgeranyl moiety is dispensable for RAC1-GDI1 interaction, (2) seven out twelve RHO family GTPases did not interact with GDI1, (3) a conserved G domain is not rate-limiting for the GDI1 binding, (4) RAC1 polybasic motif dictates GDI1 binding, (5) electrostatic pincer residues of GDI1 grasp RAC1 HVR, and (6) GDI1 buckles RAC1 into its site.

2. Results and Discussion

2.1. Geranylgeranyl Moiety Is Dispensable for RAC1-GDI1 Interaction

To understand the impact of the isoprenyl moiety of RAC1 on GDI1 binding, we compared the biochemical properties of geranylgeranylated RAC1 ($RAC1^{GG}$) from insect cells and non-isoprenylated RAC1 full-length ($RAC1^{FL}$) from *Escherichia coli*. Previous mass spectrometric analysis and liposome sedimentation of intact $RAC1^{GG}$, compared to $RAC1^{FL}$, have revealed a fully modified $RAC1^{GG}$ by geranylgeranylation [34]. Unless otherwise stated, the unmodified RAC1 purified from *E. coli* is designated as $RAC1^{FL}$, the modified RAC1 purified from insect cells as $RAC1^{GG}$, and the unmutated (wild-type) RAC1 as $RAC1^{WT}$ in cell-based experiments.

We determined the GDI association rates with both $RAC1^{GG}$ and $RAC1^{FL}$ using a stopped-flow fluorometric assay. Figure 1A shows a rapid decrease in fluorescence after mixing GDI1 with the RAC1 proteins, which is directly related to the association reaction between the RAC1-GDI1 pairs. Observed rate constants (k_{obs}) obtained by a single exponential fitting increased linearly as a function of the GDI1 concentrations (Figure 1B), and yielded similar association rate constants (k_{on}) for both $RAC1^{GG}$ and $RAC1^{FL}$. The dissociation of the GDI1 from mdGDP-bound RAC1 proteins was measured in a displacement experiment. Observed single exponential fluorescence increase yielded respective dissociation rate constants (k_{off}), which differ only 3-fold (Figure 1C). Notably, the $RAC1^{GG}$-GDI1 interaction showed a biphasic behavior (double exponential kinetics); particularly for the off-rate, an initial rapid increase in fluorescence was followed by a slow plateau phase, which can be attributed to the GG moiety of $RAC1^{GG}$. Calculated dissociation constants (K_d) from the ratio of the k_{off} and k_{on} values (Figure 1D) unexpectedly revealed only a 7-fold higher affinity for $RAC1^{GG}$ vs. $RAC1^{FL}$.

Instead of the simple exponential decrease seen with GAP, there is an initial rapid increase in fluorescence followed by a decrease at a rate similar to that seen at high GAP concentrations. The first phase of the reaction is concentration-dependent, whereas the second is less obviously so. This suggests that an initial association between the proteins leads to an increase in fluorescence, which then decreases on mant-GTP hydrolysis (and consequent dissociation of the proteins) to a level below that of the starting level, in agreement with the observation that the fluorescence of Ras,mant-GDP is lower than that of Ras,mant-GTP. This interpretation means that the mechanism cannot be treated as a very rapid initial equilibration followed by a relatively slow cleavage step, which is the underlying assumption in the analysis of the data obtained with GAP.

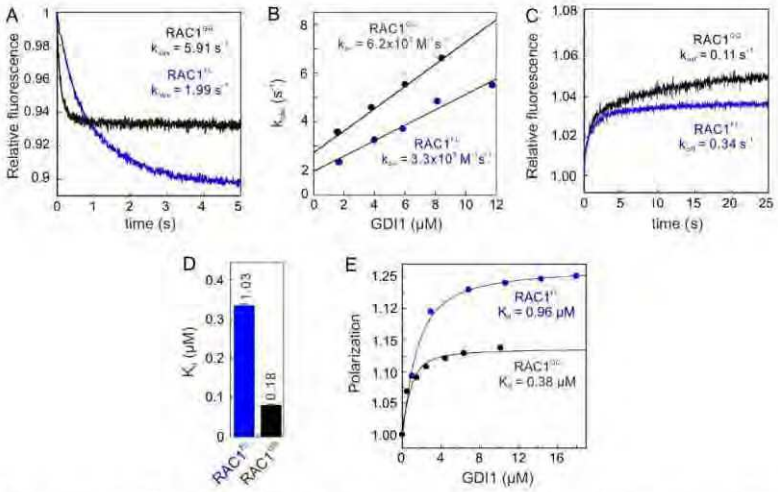

Figure 1. $RAC1^{GG}$ and $RAC1^{FL}$ bind with a similar affinity to GDI1. (**A**) Association of GDI1 (4 μM) with $RAC1^{GG}$ and non-isoprenylated $RAC1^{FL}$ (0.2 μM, respectively). (**B**–**D**) Quantitative measurements of GDI1 interaction with $RAC1^{GG}$ and $RAC1^{FL}$ led to the calculation of the individual binding constants, association rate constant or k_{on} (**B**), dissociation rate constant or k_{off} (**C**), and dissociation constant or K_d directly from the k_{off}/k_{on} ratio (**D**). (**E**) Titration of increasing GDI1 concentrations to $RAC1^{GG}$ and non-isoprenylated $RAC1^{FL}$ (0.2 μM, respectively), using fluorescence polarization, resulted in the determination of the equilibrium K_d values.

This result clearly contradicts existing models which have suggested that the isoprenyl moiety of the RHO GTPases contributes to orders of magnitude higher binding affinity for GDI as compared to unmodified RHO GTPases [41,42]. The studies have determined K_d values of 0.4 nM and 5 pM for the interaction of GDI1 with prenylated RAC1 and RHOA, respectively, as compared to the 180 nanomolar K_d value determined in our study. The reason for the extraordinarily large differences between the binding affinities obviously lies in the proteins and the type of fluorescence reporter groups used in each case. On the one hand, we and Tnimov et al. applied native GDI1 while Newcombe et al. [41] used a coumarin-labeled GDI1 at position cysteine 79, which is actually buried and located in the back side of the C-terminal geranylgeranyl binding domain (GGBD); this modification at this position can drastically alter the confirmation and consequently its biochemical properties of GDI1. On the other hand, native $RAC1^{GG}$ purified from insect cells was used by Newcombe et al. as well as in this study, Tnimov et al. [42] used a cell-free modification approach of $RHOA^{FL}$ and purified geranylgeranyl transferase I and nitrobenzoxadiazole (NBD)-labeled geranyl-pyrophosphate [1]. In this way, the nature of the isoprenyl moiety and the absence of further posttranslational modifications by specific proteolytic removal of the terminal three residues, and carboxylmethylation of prenylted cysteine residue, are largely different from native $RHOA^{GG}$.

Kinetic and equilibrium data revealed that the RAC1-GDI1 interaction is not markedly dependent on the presence of the geranylgeranyl moiety. The binding affinities determined for the RAC1-GDI1 interaction by three different methods indicate that GDI1 binds to non-isoprenylated RAC1 as efficiently as it does to isoprenylated RAC1; $RAC1^{GG}$ exhibited only 2.5 to 4.6-fold lower K_d values compared to $RAC1^{FL}$. Evidently, these data clearly challenge the current regulatory model that the isoprenyl moiety at the C-terminus of RHO GTPases contributes to several orders higher binding affinity of GDI1.

The data presented in this study on similar binding affinity of GDI1 for $RAC1^{GG}$ and $RAC1^{FL}$ is not surprising for two reasons: (1) It is evident that GDI1 recognizes and

binds regions of RAC1 other than the geranylgeranyl moiety in the cell because the latter is inserted into the lipid bilayer and anchors the RAC1 to cellular membranes. Thus, binding of the geranylgeranyl moiety by GDI1 cannot be rate-limiting. (2) GDI1 may not get into a situation where it competes for prenylated and nonprenylated RAC1 simply because nonprenylated RHO GTPases, such as RAC1, may not exist in cells; this has not been reported to our knowledge. Our data can provide an indication of the interaction specificity of GDIs for RHO GTPases. Therefore, we thoroughly investigated the specificity and the structure-function relationships of the three GDIs and various RHO GTPases.

2.2. Conserved G Domain Is Not Rate-Limiting for the GDI1 Binding

The above findings prompted us to unambiguously challenge the paradigm of RAC1 regulation by GDI1. To this end, we investigated the interactions of the three GDI paralogs, GDI1, GDI2 and GDI3, with various non-isoprenylated members of the RHO GTPase family (Table S1; Figure S1). GDI3 was purified as an N-terminal truncated variant lacking the amphipathic helix (amino acids or aa 1-20). Kinetics of association of the GDIs (2 μM) with 0.2 μM mdGDP-bound RHO GTPase was monitored under the same conditions as described above for RAC1. Calculated k_{obs} values for each measurement (Figure S2) were plotted as bar charts in Figure 2A, which clearly show that all three GDIs associated with RAC1, RAC3, RHOG and RHOA under the experimental conditions but apparently not with RAC2, CDC42, TC10, TCL, RHOB, RHOC, RHOD and RIF. GDI2 and GDI3 showed significantly faster association with RAC3 as compared to GDI1. Most remarkably, unlike GDI1 and GDI3, GDI2 was able to bind RAC2. These results clearly indicate for the very first time that GDIs can discriminate between the RHO GTPases by interacting with some but not all the RHO proteins.

To examine binding properties, the respective association rate constants (k_{on}) and the dissociation rate constants (k_{off}) were determined for the interaction of GDI1 with RAC1, RAC3, RHOG and RHOA, and GDI2 with RAC2 under conditions described above (Figures 1A–D and S3A). All kinetic parameters along with calculated dissociation constants (K_d) are summarized in Figure 2B. The data are very similar for the GDI1 interaction with RAC1, RAC3, RHOG and RHOA with K_d values between 0.9 and 3.2 μM. However, GDI2 interactions exhibited similar rate constants for RAC1 and RAC3, which were significantly different from that of GDI1 (Figure 2B). GDI2 exhibited more than 10-fold faster k_{on} values and up to 4-fold slower k_{off} values. GDI2-RAC2 interaction was characterized by a much slower rate of association as compared to RAC1 and RAC3, resulting in a binding affinity of 18.8 μM under the given experimental conditions (Figure 2B).

The biochemical characterization together with structural studies has shown that the RAC paralogs exhibit different properties concerning ligand– and protein–protein interactions [43]. Whereas RAC1 and RAC3 behave almost identically, RAC2 revealed a 25-fold lower nucleotide affinity because of a decreased nucleotide association rate, a slightly higher PAK1 (p21 activated kinase-1, a downstream effector for RAC1 and CDC42) binding affinity, and a significant increase in GEF-catalyzed nucleotide dissociation. These aberrant properties most likely are the consequence of different conformational flexibilities in the switch I region [44].

To understand this result, we have performed integrated sequence-structure analysis for all available GDI structures in complex with RHO GTPases (Table S2) and identified amino acids of the G domain (aa 1–176) involved in RHO GTPase-GDI interactions shown as an interaction matrix in Figure 2C. It reveals that almost all of them are indentical in different RHO GTPases. GDIs appear to mainly contact RHO GTPases through the switch I and II regions, and the α-helix 3 (shown in grey). The same is true also for the GDIs, which apply identical residues, with a few exceptions, to contact RHO GTPases. A major part of the contacts stems from the N-terminal switch binding domain (SWBD in green) and some from the GGBD (in orange; Figure 2D,E). So, identical contact sites do not explain the observed differences in kinetic measurements and this finding rather suggests a GDI1 modulatory region outside the G domain, namely the HVR.

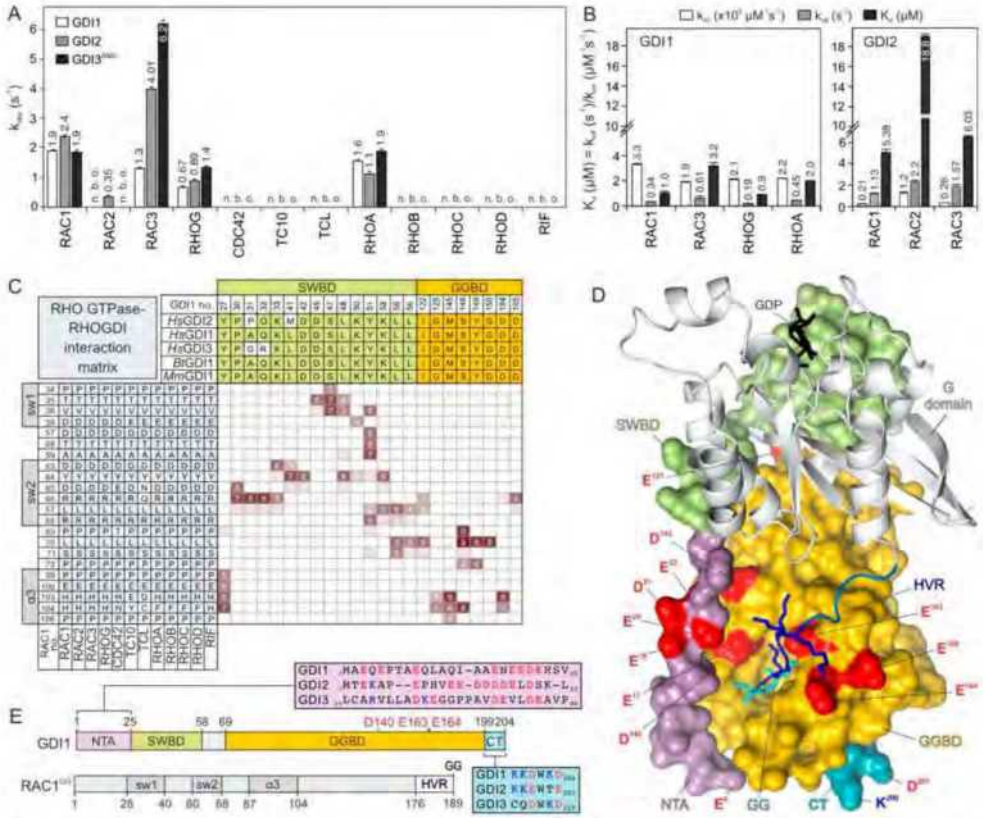

Figure 2. Biochemical and structural view into the RHO GTPase-GDI interactions. (**A**) Kinetics of association of 2 μM GDI proteins (GDI1, GDI2 and GDI3ΔN20) with 0.2 μM mdGDP-bound RHO GTPases (twelve different proteins) was only monitored for RAC1, RAC3, RHOG and RHOA using stopped-flow fluorimetry. GDI2 but not GDI1 and GDI3 associated with RAC2. No binding was observed (n. b. o.) for the other GTPases. Obtained k_{obs} values are the average of four to six independent fluorescence measurements, consisting of 1000 data points each (mean ± S.D.). Kinetic data are shown in Figure S2. (**B**) Individual rate constants were determined, under the same conditions as shown in Figure 1A–C, for the interaction of GDI1 with RAC1, RAC3, RHOG and RHOA, and GDI2 with RAC1, RAC2 and RAC3, respectively. Kinetic data were derived from the average of four to six independent measurements (mean ±S.D.). Kinetic data are shown in Figure S3. (**C**) An interaction matrix of the GDI proteins with twelve RHO family GTPases is generated to determine the frequency of contacts in respective structures. (see Table S2; for more detail see Figure S4). It comprises the amino acid sequence alignments of the RHO proteins (lower left panel) and the GDIs (upper right panel), respectively. Each element corresponds to a possible interaction of RHO residues (row; RAC numbering) and GDI residues (column; GDI1 numbering). The number of actual contact sites between RHO and GDI proteins (with distances of 4 Å or less) were calculated and are indicated with numbers for matrix elements between 1 and 9. (**D**) A detailed view into the structure (PDB code: 1HH4) of GDP-bound $RAC1^{GG}$ (grey ribbon) in complex with GDI1 (surface representation) revealed that the basic HVR (blue) is sandwiched between a series of acidic residues of GDI1 supplied by NTA (purple) and GGBD (orange). (**E**) Schematic diagrams of the domain organizations of GDI1 and $RAC1^{GG}$ illustrate their detailed boundaries. Amino acid sequence alignments of the N-terminal arm (NTA; 25 amino acids) and the C-terminal six residues of the GDI proteins (boxed) highlight negatively and positively charged residues (red and blue). Colors are the same in (**D**).

A comparison of available structures of the RAC1-GDI1 and RAC2-GDI2 complexes revealed a rather high sequence similarity [35,36]. An inspection of full interaction matrix revealed very few amino acid deviations within the RAC G domains (Y/F89) and GDI paralogs (A/P/G31, E/K/R53, A/T/V54; Figure S4). However, Y98 in RAC1 and RAC3 undergoes contacts with H23 and V25 of GDI1 which may not be achieved by F89 in RAC2, that may only contact V25 but not S23. Among the deviations in GDIs, the loop containing A/G31 in GDI1 and GDI3 is in close vicinity of D65/R66 of RAC paralogs, which may, in the case of P31 in RAC2, adopt a different orientation and thereby influence RAC2-GDI2 binding. Residues in SWBD, such as E53 and A54 (GDI1 numbering), appear to be critical for RHO GTPase-GDI interaction. The double mutation of L55/L56 to serines in GDI1 has been shown to drastically decrease its affinity for RAC1 [45].

The interaction matrix showed a conserved interface between RHO GTPases and GDIs, but the missing parts of most structures are, on the one hand, the C-terminal HVR (178–190 aa in RAC1; Figure 2E) [46], and on the other hand, the N-terminal of the GDIs (1–25 aa in GDI1; Figure 2D) [22]. The crystal structure of the $RAC1^{GG}$•GDP•GDI1 complex (PDB code: 1HH4) has remarkably provided the first evidence for the existence of a network of electrostatic interactions between these otherwise highly flexible regions [35]. Accordingly, GDI1 obviously supplies two sets of negatively charged residues to grasp the polybasic motif of RAC1 HVR. These are E109, D140, E163 and E164 of GDI1 GGBD across from E17, E19, E20, D21 and E22 at the flexible NTA of GDI1 (Figure 2E). Thus, it seems that GDI1 applies an electrostatic pincer towards the polybasic motif of RAC1 and extracts it from the membrane. This mechanistic model was next investigated in-depth.

2.3. *RAC1 Polybasic Motif Dictates GDI1 Binding*

A sequence analysis of HVRs of GDI1 associating RHO GTPases ('binders') versus those with no observed GDI1 association ('non-binders') showed clear differences in both numbers and relative positions of positively charged residues (Figure 3A). To examine the impact of HVR on the RHO GTPase-GDI1 interaction, we measured the kinetics of GDI1 association with different HVR variants of RAC1 and RAC2. Remarkably, a loss of RAC1 association was observed with a C-terminal truncated variant lacking HVR-CAAX ($RAC1^{\Delta C10}$) as well as KRKRK-to-EEEEE ($RAC1^{5xE}$; charge-reversal variant) and KRKRK-to-QQKRA (RAC1-to-RAC2 or $RAC1^{RAC2}$ variant). In contrast, a gain of GDI association with RAC2 was observed with QQKRA-to-KRKRK (RAC2-to-RAC1 or $RAC2^{RAC1}$ variant; Figure 3B). These findings were verified by fluorescence polarization experiments (Figure S3A) and obtained data summarized in Figure 3C revealed that (1) $RAC1^{\Delta C10}$ yet bound GDI1 with a 26-fold lower affinity as compared to RAC1, (2) $RAC1^{5xE}$, binding to GDI1 was yet observed with a very low affinity while this was not possible for $RAC1^{RAC2}$, and (3) $RAC2^{RAC1}$ did, in contrast to RAC2, bind GDI1 with an almost similar affinity as determined for RAC1. Taken together aided HVR alteration can completely abolish GDI1 association with RAC1 and revert GDI1 association with RAC2.

The results clearly demonstrate the critical role of the polybasic motif of RAC1 in determining GDI1 binding. It seems that both an increase of overall positive charge in HVR of RAC2 and the distance of the basic residues from the geranylgeranyl site strongly reinforce GDI1 binding affinity. We hypothesize that the GDI1 selectively binds RAC1 polybasic motif to pull the GG moiety from the plasma membrane and direct it into the hydrophobic cavity of its GGBD.

The relative position and the order of the basic residues in HVR seem to contribute to the formation of an electrostatic network (Figure 2E) that may significantly stabilize GDI1 interaction with, for example, RAC1 and RAC3 but not RAC2. Synthetic peptides containing the polybasic motifs of RAC1 (aa 178–188), but not RAC2 (178–188), have been shown to inhibit NADPH oxidase activity in a RAC1-dependent system, and interfere with the translocation of RAC1 proteins to the plasma membrane [47]. While the geranylgeranyl moiety mediates membrane anchorage, the polybasic motif of RAC1 interacts with plasma membrane phosphoinositides and stabilizes its proper orientation [48].

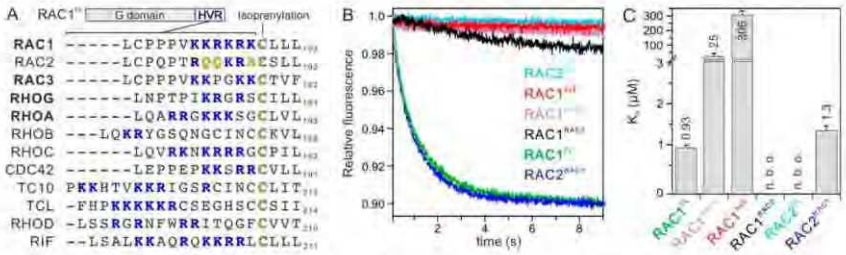

Figure 3. RAC1 HVR generates a selective and high affinity interaction toward GDI1. (**A**) A sequence alignment of hypervariable region (HVR) of RHO GTPases shows significant differences in the frequency of the basic residues (blue). GDI-binding proteins are shown in bold. Critical amino acid deviations in RAC2 are shown in orange. The isoprenylation site (cysteine 189 in RAC1) is highlighted in bold. (**B**) Kinetics of GDI1 association were measured by mixing RAC1 and RAC2 variants (0.2 μM, respectively) with 2 μM GDI1. (**C**) K_d values for the RHO GTPase-GDI1 interaction were determined by titrating RAC1 and RAC2 variants (0.2 μM, respectively) with increasing concentrations of GDI1 using fluorescence polarization (see Figure S5 for more details).

Considering the amino acid sequence identity of the G domain on the one hand (Figure 2C), and the sequence similarities among the hypervariable regions on the other (Figure 3A), it is striking that seven out twelve RHO family GTPases do not interact with GDI1 (Figure 2A). For example, the HVRs of RHOA versus RHOC and RAC3 versus CDC42 look very similar, and yet GDI1 binds one but not the other, under the same experimental condition in this study. An in-depth analysis of the RAC1 and RAC2 variants revealed that the HVR polybasic motif dictates GDI1 binding (Figure 3B,C). The number of positively charged residues appears not to be a binding determining factor since the HVR polybasic motif of the nonbinder RHOC has a higher positive net charge as compared to the binder RHOA (Figure 3A). This is also true if comparing the binder RAC3 with the nonbinder CDC42, which exhibits a much larger amino acid variability with their HVRs. Thus, we assume at this stage that, not the number of positive charges but rather the position of the basic residues relative to the C-terminal cysteine determines the bilateral binding selectivity of the HVR polybasic motif by the negatively charged residues of both GGBD and NTA (Figure 2D,E). This may be the reason for TC10 and RHOD not to interact with GDI1 related to the distance of the polybasic motif to the C-terminal Cysteine (Figure 3A). Notably, Gosser et al. has reported a binding affinity of 1.6 nM between unmodified CDC42 and GDI1, which significantly impaired upon N-terminal deletions of GDI [49]. This value is three orders of magnitude lower than the K_d values we have obtained from kinetic and equilibrium measurements (Figure 1). Gosser et al. have used in addition to mGDP-bound CDC42 also a fluorescein-conjugated GDI at position cysteine 79, which is actually buried and located in the back side of the GGBD; this modification at this position can drastically alter the confirmation and consequently int biochemical properties of GDI1. Moreover, residues next to the positively charged residues within the HVR seem to play a role, too. Glutamines in RAC2 and RIF seem to be deleterious for the interaction with GDI1. Glutamate 181 in CDC42 may exert electrostatic repulsive effects on the GDI binding (Figure 3A). Serine 185 is a phosphorylation site on CDC42, regulating its translocation to the cytosol by favoring its interaction with GDI1 [50]. Future studies will shed light on these issues.

2.4. Electrostatic Pincer Residues of GDI1 Grasp RAC1 HVR

GDI1 function appears to be driven and controlled by electrostatic forces, that attract the polybasic motif of RAC1. To examine this mechanism, we generated different deletion and charge reversal variants of GDI1 and measured both their binding capabilities to $RAC1^{GG}$ and $RAC1^{FL}$, as well as their functional properties to displace $RAC1^{GG}$ from PIP-enriched synthetic liposomes. $GDI1^{E121K}$, which apparently does not contact RAC1

HVR but the switch 2 region (Figure 2E), was used as a control. Kinetic analysis showed that most GDI variants are disabled in associating with RAC1 (Figure 4A). Substitutions of D140, E163 and E164 for lysines or deletion of the N-terminal and very C-terminal amino acids significantly impaired GDI1 binding to isoprenylated and non-isoprenylated RAC1, as compared to GDI1^{WT}. The most drastic effects were observed with 25 and 58 amino acids deleted at the N-terminus (ΔN25 and ΔN58) on the one hand, and double (E163K and E164K or 2E > 2K) and triple (E140K, E163K and E164K or 3E > 3K) mutations, on the other, which did not bind to the RAC proteins under the experimental conditions. Fluorescence polarization measurements verified that most GDI1 variants were yet able to bind RAC1^{FL}, but with up to 145-fold lower binding affinities compared to GDI1^{WT} (Figure 4B). RAC1 binding was completely abolished in the case of ΔN58 and 3E > 3K variants. GDI1$^{\Delta N58}$ not only lacks the very N-terminal acidic resides, that are integral elements of the electrostatic pincer function, but also the switch binding domain (SWBD), which forms multiple contacts with the RAC1 switch regions (Figure 2C,D). GDI1$^{3E>3K}$ most likely creates intermolecular charge repulsion towards positively changed HVR.

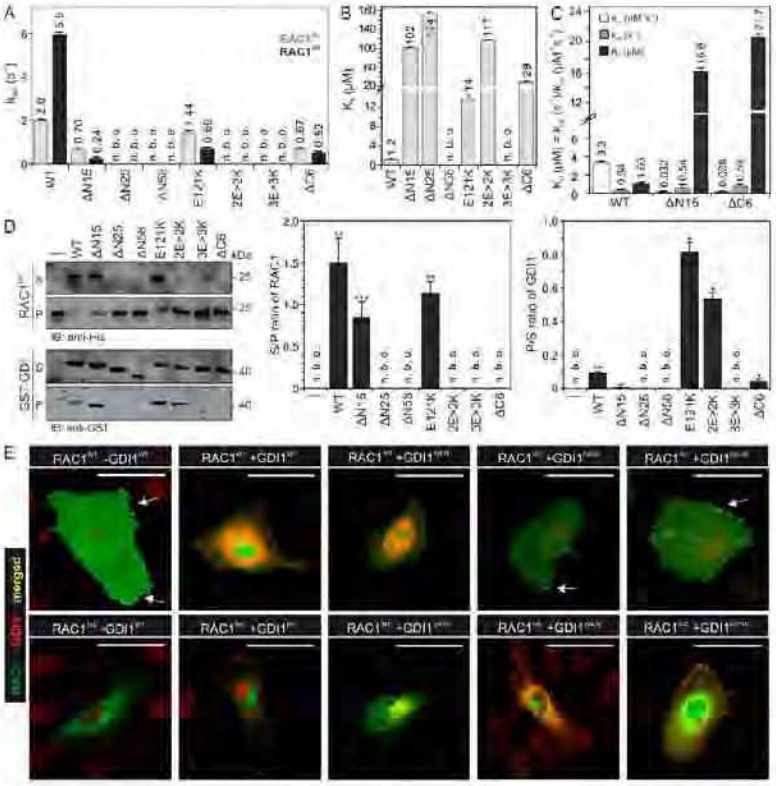

Figure 4. RHOGDI1 grasps basic HVR of RAC1 with multiple negatively charged residues. (**A**) Kinetics of association of 2 μM GDI1 variants with 0.2 μM mdGDP-bound RAC1 was monitored using stopped-flow fluorimetry. The obtained data are the average of four to six independent measurements (mean ± S.D.). Kinetic data are shown in Figure S6. (**B**) K_d values for the interaction between the GDI1 variants and mdGDP-bound RAC1 were determined by fluorescence polarization (See Figure S7 for more details). (**C**) Individual rate constants were determined, under the same conditions as shown in Figure 1A–C, for the interaction of RAC1 with GDI1 WT, ΔN15 and ΔC6,

respectively. Kinetic data were derived from the average of four to six independent measurements (mean ± S.D.). (D) GDI1 variants are, in contrast to $GDI1^{WT}$, impaired in extracting $RAC1^{GG}$ from PIP-enriched synthetic liposomes. The graphs represent densitometric analysis of three independent liposome sedimentation experiments (see Figure S8). Data are expressed as the mean of triplicate experiments ± standard deviation (unpaired t-test, * $p < 0.05$, ** $p < 0.01$, and *** $p < 0.001$). (E) FLAG-GDI1 variants were not able to extract YFP-RAC1 from the plasma membrane of HUVECs. All individual images are illustrated in Figure S9. Scale bar represents 50 µm. Arrow point to colocalization of RAC1 and GDI1 at the membrane ruffles.

To analyze the function of the GDI variants in extracting $RAC1^{GG}$ from the liposomes, we performed a liposome sedimentation assay established previously [34]. Therefore, we mixed PIP-enriched liposomes (200 µm in diameter) with GDP-bound $RAC1^{GG}$ and isolated liposome-bound $RAC1^{GG}$ from the pellet fraction (Figure 4D, first lane) after sedimentation. Next, 1 µM of $RAC1^{GG}$•GDP bound to liposomes was mixed with 2 µM of GDI1 WT and its variants (2 µM, respectively) to measure their ability to displace $RAC1^{GG}$ from the liposomes. Figure 4D shows that $GDI1^{WT}$ quantitatively displaced $RAC1^{GG}$ from the liposomes. In contrast, the majority of the GDI1 variants revealed a significant reduction in their activities, consistently with the kinetic and equilibrium measurements (Figure 4A–C). Particularly, $GDI1^{\Delta N58}$ and $GDI1^{3E>3K}$ were completely disabled in binding and extracting $RAC1^{GG}$ from the liposomes, strongly supporting the notion that GDI1 supplies an electrostatic pincer to grasp RAC1 and pull it out from the plasma membrane. Moreover, $GDI1^{E121K}$ and $GDI1^{2E>2K}$ remained partially associated with liposomes and were sedimented in the pellet fraction (Figure 4D). The fact that these GDI1 variants were able to bind to $RAC1^{GG}$ on the liposomes but could not extract it from the liposomes strongly suggests that an electrostatics-guided binding and extraction mechanism is impaired unilaterally. We think that binding of the GDI1 GGBD with the RAC1 HVR takes it away from its membrane association and release additional basic residues on HVR for the interaction with the negatively charged residues of the GDI1 NTA (the so-called electrostatic pincer; Figure 5). Loss of the GGBD-HVR interaction at this step obviously disabled the GDI1 variants ($GDI1^{E121K}$ and $GDI1^{2E>2K}$), that is associated with $RAC1^{GG}$ on the liposomes, to extract $RAC1^{GG}$ from the membrane.

YFP-RAC1 and FLAG-GDI1 variants were ectopically expressed in HUVECs to analyze the molecular basis of their interactions using immunofluorescence (Figures 4E and S9). In the absence of FLAG-GDI1, YFP-RAC1 was both localized in the cytoplasm and at the plasma membrane (arrowhead). When either $GDI1^{WT}$ or $GDI^{\Delta N15}$ were co-expressed, RAC1 was extracted from the plasma membrane and resided in the cytoplasm. In contrast, $GDI^{\Delta N25}$ and $GDI^{2E>2K}$ interestingly co-localized with RAC1 at the plasma membrane (arrow head), supporting above data that they still bind RAC1, however were disabled in displacing it from the membrane (Figure 4D). The RAC1 localization pattern in co-expression with $GDI^{\Delta N25}$ and $GDI^{2E>2K}$ was similar to the RAC1 localization in the absence of GDI. In contrast, $RAC1^{5xE}$ was exclusively cytosolic both in the absence of GDI1 and in the presence of $GDI^{\Delta N15}$, $GDI^{\Delta N25}$, and $GDI^{2E>2K}$. Co-expression of GDI1 and $RAC1^{5xE}$ seemed to result in the localization of $RAC1^{5xE}$ in the perinuclear structure. Similar to RAC1, co-expression of $RAC1^{5xE}$ without GDI or with $GDI^{\Delta N25}$ and $GDI^{2E>2K}$ resulted in a similar RAC1 localization. Furthermore, $GDI^{\Delta N25}$ co-localization was stronger when co-expressed with $RAC1^{5xE}$ in comparison to its co-expression with RAC1, which is due to the reduction of repulsion that exists between 25 N-terminal amino acids of GDI and HVR of $RAC1^{5xE}$.

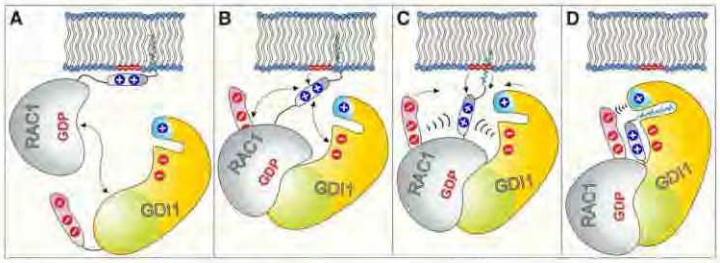

Figure 5. Schematic models of GDI1-regulated RAC1 extraction from the cell membrane. (**A**) GDI1 SWBD (green) recognizes and binds the switch regions of RAC1 to initiate its extraction from the membrane. (**B**) This step is followed by the electrostatic attraction of RAC1 polybasic region through the negatively charged GGBD (orange) and probably also NTA (purple). (**C**) NTA and GGBD are integral elements of the electrostatic pincer function, creating intermolecular charge attraction forces towards positively changed HVR. (**D**) This electrostatic steering mechanism rounds off the GDI1-mediated RAC1 extraction from the membrane by locking the geranylgeranylated C-terminus of RAC1 through the terminal charged regions of GDI1, and safeguarding $RAC1^{GG}$-bound state of the GDI. Coloring is the same as the coloring of GDI1 and RAC1 structures shown in Figure 2D,E. Positive charges are schematically shown as + and negative electrostatics as −. For more details, see the discussion and conclusions.

Both GGBD and NTA of GDI1 provide negatively charged residues as the basic building block of the electrostatic pincer of GDI that grips the RAC1 HVR, pulls the geranylgeranyl moiety out of the membrane and push it into the hydrophobic cavity of GGBD (Figure 5). A prerequisite for ensuring the pincer function is the preceding association of GDI1 via SWBD and also GGBD (Figure 2C). GDI1 variants that lacks negatively charged residues in GGBD ($GDI^{2E>2K}$) or NTA ($GDI^{\Delta N25}$) are able to recognize and bind $RAC1^{GG}$ but are disabled in displacing $RAC1^{GG}$ from the membrane.

The results above are consistent with previous findings and support the concept of an electrostatic pincer mechanism on a subset of RHO family GTPases. An early NMR study has shown that deletion of the highly flexible N-terminal region of GDI1 impairs its ability to extract RAC1 from the plasma membrane in HeLa cells [51]. Mutations of R186 to cysteine in CDC42 HVR has very recently been shown to disrupt its interaction with GDI1 in patients with a novel autoimmune hematological disorder [52]. Thus, electrostatic complementarity between GGBD with the corresponding negative potentials, as shown in this study, and the polybasic region of RAC1, on the one side, and the negative potentials of the N-terminal, rather flexible NTA moving towards the polybasic region from the other side, obviously provide the required forces to facilitate RAC1 displacement from the membrane [35,36,51,53].

2.5. GDI1 Buckles RAC1 into Its Site

A closer look into the $RAC1^{GG}$-GDP-GDI1 complex (PDB code: 1HH4) revealed that the very terminal regions of GDI1 may undergo an electrostatic interaction and thus tighten the complex and avoid dissociation. To examine this hypothesis, we functionally analyzed two flanking deletion variants of GDI1 regarding RAC1 binding and membrane extraction. Kinetic analysis showed that the association rate of $GDI1^{\Delta N15}$ and $GDI1^{\Delta C6}$ were drastically slowed down up to 24-fold, especially for mGDP-bound $RAC1^{GG}$ (Figure 4A). Equilibrium measurements of these terminally deleted variants revealed a massive reduction in the K_d values of 440- and 140-fold, respectively, as compared to $GDI1^{WT}$ (Figure 4B). These GDI1 variants also exhibited a reduced activity in $RAC1^{GG}$ extraction from the liposomes (Figure 4D).

Our findings revealed that completing the RAC1-GDI1 interaction is seemingly based on electrostatic steering, selectively dictated by charge-charge interactions. This mechanism

is notably represented by almost identical k_{off} rates, and more than 100-fold difference in the k_{on} rate for interaction of GDI wt, ΔN15 and ΔC6 with RAC1 (Figure 4C). The kinetic values disclose, for example, the significance of these negatively charged residues of the very N-terminus of GDI1 (E3, E5 and E9; GDI1 residues 1-8 are not visible in the RAC1-GDI1 structure; Figures 2D,E and 4B) in closing up the RAC1 membrane extraction and shielding the geranylgeranyl moiety. Moreover, $GDI1^{\Delta C6}$ exhibited similar attributes to $GDI1^{\Delta N15}$ and $GDI1^{E12K}$ in terms of RAC1 binding capability but has a different effect on RAC1 extraction from the liposomes (Figure 4D). This suggests that the CT motif may have additional roles beyond stabilizing the $RAC1^{GG}$-GDI1 complex through an intramolecular NTA-CT interaction.

These data about the roles of the very N-terminal and C-terminal regions of GDI1, which may hold true for GDI2 and GDI3 due to sequence similarities (Figure 2E), strongly suggest that these regions may act as a 'buckle' that connects them and safeguards RAC1-bound state of the GDI.

3. Conclusions

This study elucidated a distinct and specific mode of GDI function that holds true for only a subset of RHO GTPases. Our data uncovered a latent set of interactions between RAC1 and GDI1, which add additional insight into the multi-step process that facilitates membrane extraction and inhibition of RAC1 activation. We thus hypothesize that GDI1 binds first with its SWBD to the highly conserved switch regions [4] of $RAC1^{GG}$ on the membrane and then by the GGBD the RAC1 HVR associated with the negatively charged phospholipids (Figure 5A,B) [48]. This step may initiate an electrostatic steering mechanism, which, resulting from long-range charge-charge interactions, determines selective recognition of the HVR positive potentials by the GDI1 NTA negative potentials (Figure 5C). This process may generate the required force to pull the geranylgeranyl moiety from the membrane and place it into the GGBD hydrophobic cleft. A last step may be locking $RAC1^{GG}$-GDI1 interaction through the very terminal residues of GDI1 NTA and CT (Figure 5D).

An electrostatic steering mechanism has been previously demonstrated for the interaction between CDC42 and WASP [54,55], and VWF and GPIbα [56]. It results from long-range charge-charge interactions, and dictates selective bimolecular recognition. Notably, electrostatic steering forces control the accelerated association reaction of two molecules, but not the dissociation reaction [54]. This small list of interactions can now be extended to interactions between GDIs and RHO GTPases, such as RAC1.

Our data demonstrated that GDI1 binds essentially similarly to prenylated and non-prenylated RAC1. This is plausible since the geranylgeranyl moiety of RAC1 is inserted into the cellular lipid bilayer and simply prevented from protein interactions. So, what could be the biological implication of the finding that GDI1 binds essentially similarly to RAC1 with and without a geranylgeranyl moiety? The answer probably lies in the specificity of GDIs for RHO GTPases. Our protein interaction and structure-function studies revealed the following insights: (1) The activities of three GDIs do not differ considerably (Figure 2A), pointing to their cell-type specific expression patterns on the one hand and their subcellular localization on the other, providing two GDIs, e.g., GDI1 and GDI3, are expressed at the same time in the same cell. GDI2 showed the highest k_{on} value for RAC2, associating up to 6-fold faster than RAC1 and RAC3. (2) The three GDIs exhibited a clear specificity for the RAC-like proteins, RAC1, RAC2, RAC3 and RHOG, as well as for RHOA, under the experimental conditions used in this study. A systematic analysis of the sequence-structure-function relationships of the RHO GTPase-RHOGDI interaction identified the C-terminal HVR of the RHO GTPases as the key element that ascertains the GDI specificity. (3) Neither GDI1 nor GDI3 but GDI2 exhibited clear selectivity for RAC2, even though this interaction is one of the weakest interactions measured in this study (Figure 2A,B). To explain the RAC2-GDI2 interaction selectivity, which can preferably take place in the hematopoietic system [57,58], we inspected the RHO GTPase-GDI interaction matrix in detail and found

amino acids in GDI2 deviating from those in GDI1 and GDI3, namely Pro28, Leu35, Met38, Asp39, Ala139 and Phe141 (Figure S3). The latter two residues which undergo contact to RHO GTPase HVR may be critical as changes in HVR such as RAC1-to-RAC2 and RAC2-to-RAC1 clearly affected their interaction with GDI1 (Figure 3B,C). This notion goes along with our other data and confirms the central role of HVR in the interaction with GDIs.

Spatiotemporal activation of RHO proteins requires that various regulators are orchestrated. GDI as a membrane cycling factor regulates the state of activation of RHO proteins by displacing them from different membranes and masking them from their activation by GEFs or proteasomal degradation [13,59]. Specific binding of the GDI proteins toward RAC1 in the terms of fast-kinetic elucidates a new mechanism through electrostatic steering between HVR of RAC1 and negatively charged N-terminus of GDI (Figure 5). Nevertheless, HVR determines the kinetics of membrane localization of RHO GTPases [48]. There are genuine data, which showed RAC1 with a strong polybasic region that would be mainly targeted to plasma membrane, but RAC2 and CDC42 with a weaker polybasic region remain in endomembranes [60]. In this context, the high affinity of RAC1 membrane binding calls for a tighter interaction with GDI in order to extract it from membranes.

A number of modulatory proteins and enzyme activities may facilitate or block the GDI-regulated RAC1 extraction from the membrane. A group of proteins that associate with the C-terminal HVR of RAC1 and may interfere with the RhoGDI function, includes CMS/CD2AP [46], β-PIX [61], Pacsin2 [62], NMP1 [63], smgGDS [64], and CaM [65]. The dissociation of RAC1 from GDI1 and its (re)association with the cell membrane still remain unclear.

There are several modulators proposed to fulfill these functions. Potential RhoGDI displacement factors include the neurotrophin receptor p75 ($p75^{NTR}$) and TROY [66–68], and members of the ezrin/radixin/moesin (ERM) protein family [69–71]. Other factors that directly modulate the RhoGDI functions are coronin-1A [72,73], syndecan 4-synectin complex [74], the GAP domain of the RHO regulators BCR and ABR [75,76] and phospholipids, such as phosphoinositide (3,4,5)-trisphosphate (PIP_3) [77]. Phosphorylation of GDI1 by PAK1 at Ser101 and Ser174 has been shown to mediate its dissociation from RAC1 but not RHOA [78]. However, the mechanistic details of such GDI modulators or displacement factors remain unclear.

Enzyme activities that control posttranslational modifications, including phosphorylation, acetylation and sumoylation, add an additional level of complexity to cellular biochemistry and the regulation of the GDI function. 14-3-3τ, a member of the 14-3-3 family, has been shown to promote tumor cell invasion and metastasis by binding to and inhibiting GDI1 [23]. 14-3-3τ binds phosphorylated GDI1 and interferes with its association with RHO proteins, thereby promoting epidermal growth factor (EGF)-induced RHO protein activation. GDI acetylation has also been shown to affect the RHO GTPase-GDI interactions [79], while GDI sumoylation increases this interaction [79,80], which is negatively regulated by the physical interaction of XIAP with GDI [81]. Ubiquitination of GDI by GRAIL, an E3 ligase, does not lead to proteolytic degradation but rather to stabilization of GDI [82].

The structure of uncomplexed GDI1 is yet unknown, raising yet unresolved questions about how the flexible NTA of GDI1 is stabilized and whether GDI1 undergoes conformational changes to open up the hydrophobic cavity of its GGBD.

Very recently, we identified a novel motif in the very C-terminal end of GRB2, consisting of four amino acids, that appears to play a key role in the allosteric regulation of GRB2 signaling from activated receptors to SOS1 activation [83]. It is remarkable that deletion of the CT motif of GDI1 completely abolished the GDI1-induced displacement of RAC1 from the liposomes. We propose that this motif physically binds terminal amino acids of GDI1 NTA and ultimately locks the formed $RAC1^{GG}$-GDI1 complex. However, the CT motif may also contribute to the electrostatic pincer function, by pulling $RAC1^{GG}$ out of the membrane.

While the RAC1 C domain mediates regulation and signaling [4], its HVR, modulated by various posttranslational modifications, finetunes intracellular trafficking, compartmentalization, subcellular localization, interactions, and membrane association by interacting with a variety of proteins [46]. Given this knowledge and the results presented in this study, a crucial and interesting area for future research, is to examine modulatory mechanisms, controlling RAC1 function, which impinges on its C-terminal region. Last but not least, unraveling of the molecular basis of RAC1 regulation may aid in understanding a variety of diseases with the implication of RAC1 deregulation and dysfunction, including atherosclerosis, diabetes and cancer [84].

4. Materials and Methods

4.1. Constructs

Different variants pGEX vectors (pGEX2T and pGEX4T-1) encoding an N-terminal glutathione S-transferase (GST) fusion protein were used to overexpress human GDI1 (acc. no. D13989), GDI2 (acc. no. P52566), and GDI3 (acc. no. Q99819) as well as human RHO-related genes, i.e., RAC1 (acc. no. P63000; aa 1-179), RAC2 (acc. no. P15153; aa 1-192), RAC3 (acc. no. P60763; aa 1-192), RHOG (acc. no. P84095; aa 1-178), RHOA (acc. no. P61586; aa 1-181), RHOB (acc. no. P62745; aa 1-181), RHOC (acc. no. P08134; aa 1-181), CDC42 (acc. no. P60953; aa 1-178), TC10 (acc. no. P17081; aa 2-193), RIF (acc. no. Q9HBH0; aa 1-195), and mouse RHOD (acc. no. P97348; aa 2-193). For baculovirus-insect cell expression, human RAC1 was subcloned into pFastBacHTB vector (Invitrogen, Carlsbad, CA, USA) and fused with an N-terminal hexa-histidine (6xHis) tag. For expression in human cells, RAC1 and GDI1 variants were cloned in pEYFP and pcDNA-FLAG vectors. All RHO GTPase and GDI variants were generated by PCR-based site-directed mutagenesis as described [85].

4.2. Proteins

All proteins were produced using *Escherichia coli* and baculovirus-insect cell expression system as described [34]. Glutathione S-transferase (GST) fusion proteins were isolated by affinity chromatography on a glutathione Sepharose column in the first step and purified by size exclusion chromatography after proteolytic cleavage of GST in the second step [86]. His-tagged proteins were isolated from SF9 insect cells, using affinity chromatography on Ni-NTA columns. The quality of the proteins was analyzed by 12% SDS-PAGE. Protein concentrations were determined using Bradford reagent (Coomassie dye reagent; Sigma, (Steinheim, Germany)), and the GDP concentration in the case of purified RHO GTPases was determined using HPLC [87]. Nucleotide-free RHO proteins were prepared using alkaline phosphatase (Sigma Aldrich, Deisenhofen, Germany)and phosphodiesterase (Sigma Aldrich, Deisenhofen, Germany) at 4 °C as previously described [87]. RHO GTPases were loaded with 2-deoxy-3-O-N-methylanthraniloyl GDP (mdGDP); the fluorescent reporter group methyl-anthraniloyl (m) was attached to the 3'-OH group, and can, due to the lack 2'-OH, not isomerize between 2'- and 3-OH groups as compared to mGDP [88].

4.3. Liposome Assays

The liposomes were freshly prepared to perform liposome sedimentation as described [34]. Briefly, liposome assays were performed by mixing and incubating the liposomes and purified RAC1 proteins. The mixtures were incubated for different time points and centrifuged at different speeds to separate the liposome pellets and supernatants for optimizing the centrifuging force. The liposomes were prepared as a lipid mixture (194 µg), containing 39% (*w*/*w*) phosphatidylethanolamine (PE), 16% (*w*/*w*) phosphatidylcholine (PC), 36% (*w*/*w*) phosphatidylserine (PS), 4% (*w*/*w*) sphingomyelin (SM), and 5% (*w*/*w*) phosphatidylinositol 4,5-bisphosphate (PIP_2), and phosphatidylinositol 3,4,5-trisphosphate (PIP_3), that was dried using light nitrogen stream. The lipids were purchased from Sigma-Aldrich (Munich, Germany). Obtained lipid film was hydrated with 300 µL of a buffer, containing 30 mM HEPES-NaOH pH 7.4, 50 mM NaCl, 3 mM DTT, 5 mM $MgCl_2$.

Sonication (20 s with minimal power, 50% off and 50% on) was employed finally to form liposomes, which were ultimately extruded through a filter with a pore size of 0.2 µm.

4.4. Fluorescence Measurements

Kinetics and equilibrium measurements were performed as described [86]. Briefly, all fluorescence measurements were performed at 25 °C in buffer containing 30 mM Tris/HCl, pH 7.5, 10 mM K_2HPO_4/KH_2PO_4, pH 7.5, 5 mM $MgCl_2$, and 3 mM Dithiothreitol (DTT). The association of mdGDP-bound RHO GTPases (0.2 µM) with RHOGDIs (2 µM or increasing concentrations) was measured in a time-dependent manner using a stopped-flow instrument SF-61, HiTech Scientific (TgK Scientific Limited, Bradford, UK) and SX20 MV, Applied Photophysics (Leatherhead, UK). Emission was detected through a cutoff filter of 408 nm. The observed rate constants were calculated by fitting the data as single exponential decay using the GraFit program (Erithacus software, Staines, UK). Dissociation experiments were performed by displacing the bound GDI from the complex upon adding excess unlabeled GDP-bound RHO proteins. Fluorescence polarization experiments were performed in a Fluoromax 4 fluorimeter (Horiba Jobin Yvon, France) in polarization mode by titrating increasing amounts of different variants of GDI1 to mdGDP-bound RHO proteins (0.2 µM) in a total volume of 200 µL. An excitation wavelength of 360 nm and an emission wavelength of 450 nm were used. The Kd values were calculated by fitting the concentration-dependent binding curve using a quadratic ligand binding equation.

4.5. Sequence and Structural Analysis

Sequence alignments were performed with the BioEdit program using the ClustalW algorithm [89]. The intermolecular contacts were determined (<4.0 Å) between the GDIs and RHO GTPases using available RHO GTPase-GDI complex structures in the Protein Data Bank. A python code has been written using BioPython modules (pairwise2 and SubsMat.MatrixInfo) [90] to calculate inter-molecular distances in PDB structures between the pairs of residues as interaction matrix and synchronise them with sequence alignments of RHO GTPases and GDIs respectively. All structural representations were generated using PyMOL viewer [91].

4.6. Nucleofection and Immunofluorescence Analysis

pYFP-RAC1 and pcDNA3-FLAG-GDI1 plasmids were microporated into HUVECs using the 4D-NucleofectorTM system (Lonza, Cologne, Germany) according to the manufacturer's instructions. After transfection, cells were seeded on fibronectin-coated (5 µg/mL) 2 cm^2 glass coverslips (Thermo Scientific, Menzel-gläser, Germany) and were fixed after 24 h for immunofluorescence analysis. After fixing with warm (37 °C) 4% paraformaldehyde in phosphate buffered saline (PBS) for 15 min followed by three washes with PBS, coverslips were mounted on Mowiol4-88/DABCO solution (Calbiochem, Sigma Aldrich). Cells were permeabilized with 0,2% triton X-100 in PBS for 3 min and blocked for 30 min with 1% HSA in PBS. Hereafter, coverslips were stained with primary anti-FLAG antibody (Sigma, # F7425) in 1% HSA/PBS over night at 4 °C. After washing with PBS, coverslips were incubated with Alexa® 555-conjugated anti-rabbit antibody (# A-31572; Scientific Life Technologies, Darmstadt, Germany) for 1 h at room temperature. Coverslips were mounted with Mowiol4-88/DABCO solution (Calbiochem, Sigma Aldrich). Confocal scanning laser microscopy was performed on a Nikon A1R confocal microscope (Nikon Instruments, Amsterdam, The Netherlands). Cells with moderate expression of the constructs and no aberrant phenotype from non-transfected neighboring cells were imaged. A z-stack image with a total thickness of 2 µm was acquired and images were equally adjusted using ImageJ (Li-CORE Biosciences (Bad Homburg, Germany). The max z-projection is shown with a scale bar representing 50 µm.

Supplementary Materials: The following are available online at https://www.mdpi.com/article/10.3390/ijms222212493/s1.

Author Contributions: M.R.A. conceived and coordinated the study; N.M., N.S.K.J. and S.-C.Z. designed, performed, and analyzed the experiments; J.M. and P.L.H. performed the cell-based experiments; R.D. and M.R.A. performed structural analysis; N.M. and M.R.A. designed and wrote the manuscript. All authors have read and agreed to the published version of the manuscript.

Funding: This study was supported by the German Research Foundation (Deutsche Forschungsgemeinschaft or DFG; grant number: AH 92/8-1), the German Research Foundation (Deutsche Forschungsgemeinschaft or DFG) through the International Research Training Group "Intra- and interorgan communication of the cardiovascular system" (grant number: IRTG 1902-p6), the European Network on Noonan Syndrome and Related Disorders (NSEuroNet, grant number: 01GM1621B); the German Federal Ministry of Education and Research (BMBF)—German Network of RASopathy Research (GeNeRARe, grant numbers: 01GM1902C).

Institutional Review Board Statement: Not applicable.

Informed Consent Statement: Not applicable.

Data Availability Statement: This study includes no data deposited in external repositories.

Acknowledgments: We are grateful to F. Amin, B. Anthony, K. Nouri, K. Sandhoff, M.S. Taha, and C. Wittig for helpful discussions.

Conflicts of Interest: The authors declare that they have no conflict of interest.

References

1. Wennerberg, K.; Der, C.J. Rho-family GTPases: It's not only Rac and Rho (and I like it). *J. Cell Sci.* **2004**, *117*, 1301–1312. [CrossRef] [PubMed]
2. Roberts, P.J.; Mitin, N.; Keller, P.J.; Chenette, E.J.; Madigan, J.P.; Currin, R.O.; Cox, A.D.; Wilson, O.; Kirschmeier, P.; Der, C.J. Rho family GTPase modification and dependence on CAAX motif-signaled posttranslational modification. *J. Biol. Chem.* **2008**, *283*, 25150–25163. [CrossRef] [PubMed]
3. Ahmadian, M.R.; Jaiswal, M.; Fansa, E.K.; Dvorsky, R. New insight into the molecular switch mechanism of human Rho family proteins: Shifting a paradigm. *Biol. Chem.* **2013**, *394*, 89–95. [CrossRef]
4. Dvorsky, R.; Ahmadian, M.R. Always look on the bright site of Rho: Structural implications for a conserved intermolecular interface. *EMBO Rep.* **2004**, *5*, 1130–1136. [CrossRef]
5. Cherfils, J.; Zeghouf, M. Regulation of small GTPases by GEFs, GAPs, and GDIs. *Physiol. Rev.* **2013**, *93*, 269–309. [CrossRef]
6. Bishop, A.L.; Hall, A. Rho GTPases and their effector proteins. *Biochem. J.* **2000**, *348*, 241–255. [CrossRef]
7. White, C.D.; Erdemir, H.H.; Sacks, D.B. IQGAP1 and its binding proteins control diverse biological functions. *Cell. Signal.* **2012**, *24*, 826–834. [CrossRef] [PubMed]
8. Watanabe, T.; Wang, S.; Kaibuchi, K. IQGAPs as Key Regulators of Actin-cytoskeleton Dynamics Mini-review and Review. *Cell Struct. Funct.* **2015**, *40*, 69–77. [CrossRef] [PubMed]
9. Abel, A.M.; Schuldt, K.M.; Rajasekaran, K.; Hwang, D.; Riese, M.J.; Rao, S.; Thakar, M.S.; Malarkannan, S. IQGAP1: Insights into the function of a molecular puppeteer. *Mol. Immunol.* **2015**, *65*, 336–349. [CrossRef]
10. Heasman, S.J.; Ridley, A.J. Mammalian Rho GTPases: New insights into their functions from in vivo studies. *Nat. Rev. Mol. Cell Biol.* **2008**, *9*, 690–701. [CrossRef] [PubMed]
11. Hedman, A.C.; Smith, J.M.; Sacks, D.B. The biology of IQGAP proteins: Beyond the cytoskeleton. *EMBO Rep.* **2015**, *16*, 427–446. [CrossRef]
12. Hall, A. Rho family GTPases. In *Biochemical Society Transactions*; Portland Press: South Portland, ME, USA, 2012; Volume 40, pp. 1378–1382.
13. García-Mata, R.; Boulter, E.; Burridge, K. The "invisible hand": Regulation of RHO GTPases by RHOGDIs. *Nat. Rev. Mol. Cell Biol.* **2011**, *12*, 493–504. [CrossRef] [PubMed]
14. Jaiswal, M.; Dvorsky, R.; Ahmadian, M.R. Deciphering the molecular and functional basis of Dbl family proteins: A novel systematic approach toward classification of selective activation of the Rho family proteins. *J. Biol. Chem.* **2013**, *288*, 4486–4500. [CrossRef]
15. Amin, E.; Jaiswal, M.; Derewenda, U.; Reis, K.; Nouri, K.; Koessmeier, K.T.; Aspenström, P.; Somlyo, A.V.; Dvorsky, R.; Ahmadian, M.R. Deciphering the molecular and functional basis of RHOGAP family proteins: A systematic approach toward selective inactivation of RHO family proteins. *J. Biol. Chem.* **2016**, *291*, 20353–20371. [CrossRef] [PubMed]
16. Dovas, A.; Couchman, J.R. RhoGDI: Multiple functions in the regulation of Rho family GTPase activities. *Biochem. J.* **2005**, *390*, 1–9. [CrossRef] [PubMed]

17. Xie, F.; Shao, S.; Aziz, A.U.R.; Zhang, B.; Wang, H.; Liu, B. Role of Rho-specific guanine nucleotide dissociation inhibitor α regulation in cell migration. *Acta Histochem.* **2017**, *119*, 183–189. [CrossRef]
18. Griner, E.M.; Theodorescu, D. The faces and friends of RhoGDI2. *Cancer Metastasis Rev.* **2012**, *31*, 519–528. [CrossRef]
19. De León-Bautista, M.P.; del.Carmen Cardenas-Aguayo, M.; Casique-Aguirre, D.; Almaraz-Salinas, M.; Parraguirre-Martinez, S.; Olivo-Diaz, A.; del Rocío Thompson-Bonilla, M.; Vargas, M. Immunological and functional characterization of RhoGDI3 and its molecular targets RhoG and RhoB in human pancreatic cancerous and normal cells. *PLoS ONE* **2016**, *11*, e0166370. [CrossRef]
20. Brunet, N.; Morin, A.; Olofsson, B. RhoGDI-3 regulates RhoG and targets this protein to the Golgi complex through its unique N-terminal domain. *Traffic* **2002**, *3*, 342–358. [CrossRef]
21. Ahmad Mokhtar, A.M.B.; Ahmed, S.B.M.; Darling, N.J.; Harris, M.; Moft, H.R.; Owen, D. A Complete Survey of RhoGDI Targets Reveals Novel Interactions with Atypical Small GTPases. *Biochemistry* **2021**, *60*, 1533–1551. [CrossRef]
22. Ueyama, T.; Son, J.; Kobayashi, T.; Hamada, T.; Nakamura, T.; Sakaguchi, H.; Shirafuji, T.; Saito, N. Negative Charges in the Flexible N-Terminal Domain of Rho GDP-Dissociation Inhibitors (RhoGDIs) Regulate the Targeting of the RhoGDI-Rac1 Complex to Membranes. *J. Immunol.* **2013**, *191*, 2560–2569. [CrossRef]
23. Xiao, Y.; Lin, Y.Y.; Ke, S.; Liu, G.E.; Lin, F.-T.; Liu, W.-C. 14-3-3 Promotes Breast Cancer Invasion and Metastasis by Inhibiting RhoGDI. *Mol. Cell. Biol.* **2014**, *34*, 2635–2649. [CrossRef] [PubMed]
24. Harding, M.A.; Theodorescu, D. RhoGDI signaling provides targets for cancer therapy. *Eur. J. Cancer* **2010**, *46*, 1252–1259. [CrossRef]
25. Moissoglu, K.; Schwartz, M.A. Spatial and temporal control of Rho GTPase functions. *Cell. Logist.* **2014**, *4*, e943618. [CrossRef] [PubMed]
26. Hodge, R.G.; Ridley, A.J. Regulating Rho GTPases and their regulators. *Nat. Rev. Mol. Cell Biol.* **2016**, *17*, 496–510. [CrossRef]
27. DerMardirossian, C.; Bokoch, G.M. GDIs: Central regulatory molecules in Rho GTPase activation. *Trends Cell Biol.* **2005**, *15*, 356–363. [CrossRef]
28. Dharmaiah, S.; Bindu, L.; Tran, T.H.; Gillette, W.K.; Frank, P.H.; Ghirlando, R.; Nissley, D.V.; Esposito, D.; McCormick, F.; Stephen, A.G.; et al. Structural basis of recognition of farnesylated and methylated KRAS4b by PDEd. *Proc. Natl. Acad. Sci. USA* **2016**, *113*, E6766–E6775. [CrossRef]
29. Weise, K.; Kapoor, S.; Werkmüller, A.; Möbitz, S.; Zimmermann, G.; Triola, G.; Waldmann, H.; Winter, R. Dissociation of the K-Ras4B/PDEδ complex upon contact with lipid membranes: Membrane delivery instead of extraction. *J. Am. Chem. Soc.* **2012**, *134*, 11503–11510. [CrossRef] [PubMed]
30. Ismail, S.A.; Chen, Y.X.; Rusinova, A.; Chandra, A.; Bierbaum, M.; Gremer, L.; Triola, G.; Waldmann, H.; Bastiaens, P.I.H.; Wittinghofer, A. Arl2-GTP and Arl3-GTP regulate a GDI-like transport system for farnesylated cargo. *Nat. Chem. Biol.* **2011**, *7*, 942–949. [CrossRef]
31. Chandra, A.; Grecco, H.E.; Pisupati, V.; Perera, D.; Cassidy, L.; Skoulidis, F.; Ismail, S.A.; Hedberg, C.; Hanzal-Bayer, M.; Venkitaraman, A.R.; et al. The GDI-like solubilizing factor PDEδ sustains the spatial organization and signalling of Ras family proteins. *Nat. Cell Biol.* **2012**, *14*, 148–158. [CrossRef]
32. Tnimov, Z.; Abankwa, D.; Alexandrov, K. RhoGDI facilitates geranylgeranyltransferase-I-mediated RhoA prenylation. *Biochem. Biophys. Res. Commun.* **2014**, *452*, 967–973. [CrossRef]
33. Robbe, K.; Otto-Bruc, A.; Chardin, P.; Antony, B. Dissociation of GDP dissociation inhibitor and membrane translocation are required for efficient activation of Rac by the Dbl homology-pleckstrin homology region of Tiam. *J. Biol. Chem.* **2003**, *278*, 4756–4762. [CrossRef]
34. Zhang, S.C.; Gremer, L.; Heise, H.; Janning, P.; Shymanets, A.; Cirstea, I.C.; Krause, E.; Nürnberg, B.; Ahmadian, M.R. Liposome reconstitution and modulation of recombinant prenylated human Rac1 by GEFs, GDI1 and Pak1. *PLoS ONE* **2014**, *9*, e102425. [CrossRef] [PubMed]
35. Grizot, S.; Fauré, J.; Fieschi, F.; Vignais, P.V.; Dagher, M.C.; Pebay-Peyroula, E. Crystal structure of the Rac1—RhoGDI complex involved in NADPH oxidase activation. *Biochemistry* **2001**, *40*, 10007–10013. [CrossRef]
36. Scheffzek, K.; Stephan, I.; Jensen, O.N.; Illenberger, D.; Gierschik, P. The Rac-RhoGDI complex and the structural basis for the regulation of Rho proteins by RhoGDI. *Nat. Struct. Biol.* **2000**, *7*, 122–126. [CrossRef] [PubMed]
37. Dransart, E.; Olofsson, B.; Cherfils, J. RhoGDIs revisited: Novel roles in Rho regulation. *Traffic* **2005**, *6*, 957–966. [CrossRef]
38. Hoffman, G.R.; Nassar, N.; Cerione, R.A. Structure of the Rho family GTP-binding protein Cdc42 in complex with the multifunctional regulator RhoGDI. *Cell* **2000**, *100*, 345–356. [CrossRef]
39. Longenecker, K.; Read, P.; Derewenda, U.; Dauter, Z.; Liu, X.; Garrard, S.; Walker, L.; Somlyo, A.V.; Nakamoto, R.K.; Somlyo, A.P.; et al. How RhoGDI binds Rho. *Acta Crystallogr. Sect. D Biol. Crystallogr.* **1999**, *55*, 1503–1515. [CrossRef]
40. Johnson, J.L.; Erickson, J.W.; Cerione, R.A. New insights into how the Rho guanine nucleotide dissociation inhibitor regulates the interaction of Cdc42 with membranes. *J. Biol. Chem.* **2009**, *284*, 23860–23871. [CrossRef] [PubMed]
41. Newcombe, A.R.; Stockley, R.W.; Hunter, J.L.; Webb, M.R. The Interaction between Rac1 and Its Guanine Nucleotide Dissociation Inhibitor (GDI), Monitored by a Single Fluorescent Coumarin Attached to GDI. *Biochemistry* **1999**, *38*, 6879–6886. [CrossRef]
42. Tnimov, Z.; Guo, Z.; Gambin, Y.; Nguyen, U.T.T.; Wu, Y.W.; Abankwa, D.; Stigter, A.; Collins, B.M.; Waldmann, H.; Goody, R.S.; et al. Quantitative analysis of prenylated RhoA interaction with its chaperone, RhoGDI. *J. Biol. Chem.* **2012**, *287*, 26549–26562. [CrossRef]

43. Haeusler, L.C.; Hemsath, L.; Fiegen, D.; Blumenstein, L.; Herbrand, U.; Stege, P.; Dvorsky, R.; Ahmadian, M.R. Purification and biochemical properties of Rac1, 2, 3 and the splice variant Rac1b. *Methods Enzymol.* **2006**, *406*, 1–11.
44. Haeusler, L.C.; Blumenstein, L.; Stege, P.; Dvorsky, R.; Ahmadian, M.R. Comparative functional analysis of the Rac GTPases. *FEBS Lett.* **2003**, *555*, 556–560. [CrossRef]
45. Golovanov, A.P.; Hawkins, D.; Barsukov, I.; Badii, R.; Bokoch, G.M.; Lian, L.-Y.; Roberts, G.C.K. Structural consequences of site-directed mutagenesis in flexible protein domains. *Eur. J. Biochem.* **2001**, *268*, 2253–2260. [CrossRef] [PubMed]
46. Lam, B.D.; Hordijk, P.L. The Rac1 hyper variable region in targeting and signaling-a tail of many stories. *Small GTPases* **2013**, *4*, 78–89. [CrossRef] [PubMed]
47. Joseph, G.; Gorzalczany, Y.; Koshkin, V.; Pick, E. Inhibition of NADPH oxidase activation by synthetic peptides mapping within the carboxyl-terminal domain of small GTP-binding proteins. Lack of amino acid sequence specificity and importance of polybasic motif. *J. Biol. Chem.* **1994**, *269*, 29024–29031. [CrossRef]
48. Maxwell, K.N.; Zhou, Y.; Hancock, J.F. Rac1 Nanoscale Organization on the Plasma Membrane Is Driven by Lipid Binding Specificity Encoded in the Membrane Anchor. *Mol. Cell. Biol.* **2018**, *38*, e00186-18. [CrossRef]
49. Gosser, Y.Q.; Nomanbhoy, T.K.; Aghazadeh, B.; Manor, D.; Combs, C.; Cerione, R.A.; Rosen, M.K. C-terminal binding domain of Rho GDP-dissociation inhibitor directs N-terminal inhibitory peptide to GTPases. *Nature* **1997**, *387*, 814–819. [CrossRef] [PubMed]
50. Forget, M.A.; Desrosiers, R.R.; Gingras, D.; Béliveau, R. Phosphorylation states of Cdc42 and RhoA regulate their interactions with Rho GDP dissociation inhibitor and their extraction from biological membranes. *Biochem. J.* **2002**, *361*, 243–254. [CrossRef]
51. Golovanov, A.P.; Chuang, T.H.; DerMardirossian, C.; Barsukov, I.; Hawkins, D.; Badii, R.; Bokoch, G.M.; Lian, L.Y.; Roberts, G.C.K. Structure-activity relationships in flexible protein domains: Regulation of rho GTPases by RhoGDI and D4 GDI. *J. Mol. Biol.* **2001**, *305*, 121–135. [CrossRef]
52. Lam, M.T.; Coppola, S.; Krumbach, O.H.F.; Prencipe, G.; Insalaco, A.; Cifaldi, C.; Brigida, I.; Zara, E.; Scala, S.; di Cesare, S., et al. A novel disorder involving dyshematopoiesis, inflammation, and HLH due to aberrant CDC42 function. *J. Exp. Med.* **2019**, *216*, 2778–2799. [CrossRef] [PubMed]
53. Keep, N.H.; Barnes, M.; Barsukov, I.; Badii, R.; Lian, L.Y.; Segal, A.W.; Moody, P.C.E.; Roberts, G.C.K. A modulator of rho family G proteins, rhoGDI, binds these G proteins via an immunoglobulin-like domain and a flexible N-terminal arm. *Structure* **1997**, *5*, 623–633. [CrossRef]
54. Hemsath, L.; Dvorsky, R.; Fiegen, D.; Carlier, M.F.; Ahmadian, M.R. An electrostatic steering mechanism of Cdc42 recognition by Wiskott-Aldrich syndrome proteins. *Mol. Cell* **2005**, *20*, 313–324. [CrossRef] [PubMed]
55. Tetley, G.J.N.; Szeto, A.; Fountain, A.J.; Mott, H.R.; Owen, D. Bond swapping from a charge cloud allows flexible coordination of upstream signals through WASP: Multiple regulatory roles for the WASP basic region. *J. Biol. Chem.* **2018**, *293*, 15136–15151. [CrossRef] [PubMed]
56. Jiang, Y.; Fu, H.; Springer, T.A.; Wong, W.P. Electrostatic Steering Enables Flow-Activated Von Willebrand Factor to Bind Platelet Glycoprotein, Revealed by Single-Molecule Stretching and Imaging. *J. Mol. Biol.* **2019**, *431*, 1380–1396. [CrossRef]
57. Didsbury, J.; Weber, R.F.; Bokoch, G.M.; Evans, T.; Snyderman, R. Rac, a Novel Ras-Related Family of Proteins That Are Botulinum Toxin Substrates. *J. Biol. Chem.* **1989**, *264*, 16378–16382. [CrossRef]
58. Scherle, P.; Behrens, T.; Staudt, L.M. Ly-GDI, a GDP-dissociation inhibitor of the RhoA GTP-binding protein, is expressed preferentially in lymphocytes. *Proc. Natl. Acad. Sci. USA* **1993**, *90*, 7568–7572. [CrossRef]
59. Majolée, J.; Podieh, F.; Hordijk, P.L.; Kovačević, I. The interplay of Rac1 activity, ubiquitination and GDI binding and its consequences for endothelial cell spreading. *PLoS ONE* **2021**, *16*, e0254386. [CrossRef]
60. Michaelson, D.; Silletti, J.; Murphy, G.; D'Eustachio, P.; Rush, M.; Philips, M.R. Differential localization of Rho GTPases in live cells: Regulation by hypervariable regions and RhoGDI binding. *J. Cell Biol.* **2001**, *152*, 111–126. [CrossRef]
61. Ten Klooster, J.P.; Jaffer, Z.M.; Chernoff, J.; Hordijk, P.L. Targeting and activation of Rac1 are mediated by the exchange factor β-Pix. *J. Cell Biol.* **2006**, *172*, 759–769. [CrossRef]
62. De Kreuk, B.J.; Nethe, M.; Fernandez-Borja, M.; Anthony, E.C.; Hensbergen, P.J.; Deelder, A.M.; Plomann, M.; Hordijk, P.L. The F-BAR domain protein PACSIN2 associates with Rac1 and regulates cell spreading and migration. *J. Cell Sci.* **2011**, *124*, 2375–2388. [CrossRef]
63. Zoughlami, Y.; van Stalborgh, A.M.; van Hennik, P.B.; Hordijk, P.L. Nucleophosmin1 Is a Negative Regulator of the Small GTPase Rac1. *PLoS ONE* **2013**, *8*, e68477. [CrossRef]
64. Lanning, C.C.; Ruiz-Velasco, R.; Williams, C.L. Novel mechanism of the co-regulation of nuclear transport of SmgGDS and Rac1. *J. Biol. Chem.* **2003**, *278*, 12495–12506. [CrossRef] [PubMed]
65. Xu, B.; Chelikani, P.; Bhullar, R.P. Characterization and Functional Analysis of the Calmodulin-Binding Domain of Rac1 GTPase. *PLoS ONE* **2012**, *7*, e42975. [CrossRef]
66. Yamashita, T.; Tohyama, M. The p75 receptor acts as a displacement factor that releases Rho from Rho-GDI. *Nat. Neurosci.* **2003**, *6*, 461–467. [CrossRef]
67. Lin, Z.; Tann, J.Y.; Goh, E.T.; Kelly, C.; Lim, K.B.; Gao, J.F.; Ibanez, C.F. Structural basis of death domain signaling in the p75 neurotrophin receptor. *Elife* **2015**, *4*, e11692. [CrossRef]
68. Lu, Y.; Liu, X.; Zhou, J.; Huang, A.; Zhou, J.; He, C. TROY interacts with Rho guanine nucleotide dissociation inhibitor α (RhoGDIα) to mediate Nogo-induced inhibition of neurite outgrowth. *J. Biol. Chem.* **2013**, *288*, 34276–34286. [CrossRef]

69. Scoles, D.R. The merlin interacting proteins reveal multiple targets for NF2 therapy. *Biochim. Biophys. Acta* **2008**, *1785*, 32–54. [CrossRef]
70. Takahashi, K.; Sasaki, T.; Mammoto, A.; Takaishi, K.; Kameyama, T.; Tsukita, S.; Tsukita, S.; Takai, Y. Direct interaction of the Rho GDP dissociation inhibitor with ezrin/radixin/moesin initiates the activation of the Rho small G protein. *J. Biol. Chem.* **1997**, *272*, 23371–23375. [CrossRef] [PubMed]
71. Maeda, M.; Matsui, T.; Imamura, M.; Tsukita, S.; Tsukita, S. Expression level, subcellular distribution and Rho-GDI binding affinity of merlin in comparison with ezrin/radixin/moesin proteins. *Oncogene* **1999**, *18*, 4788–4797. [CrossRef] [PubMed]
72. Castro-Castro, A.; Ojeda, V.; Barreira, M.; Sauzeau, V.; Navarro-Lérida, I.; Muriel, O.; Couceiro, J.R.; Pimentel-Muiños, F.X.; del Pozo, M.A.; Bustelo, X.R. Coronin 1A promotes a cytoskeletal-based feedback loop that facilitates Rac1 translocation and activation. *EMBO J.* **2011**, *30*, 3913–3927. [CrossRef] [PubMed]
73. Castro-Castro, A.; Muriel, O.; del Pozo, M.A.; Bustelo, X.R. Characterization of Novel Molecular Mechanisms Favoring Rac1 Membrane Translocation. *PLoS ONE* **2016**, *11*, e0166715. [CrossRef] [PubMed]
74. Elfenbein, A.; Rhodes, J.M.; Meller, J.; Schwartz, M.A.; Matsuda, M.; Simons, M. Suppression of RhoG activity is mediated by a syndecan 4-synectin-RhoGDI1 complex and is reversed by PKCα in a Rac1 activation pathway. *J. Cell Biol.* **2009**, *186*, 75–83. [CrossRef]
75. Kweon, S.-M.; Cho, Y.J.; Minoo, P.; Groffen, J.; Heisterkamp, N. Activity of the Bcr GTPase-activating domain is regulated through direct protein/protein interaction with the Rho guanine nucleotide dissociation inhibitor. *J. Biol. Chem.* **2008**, *283*, 3023–3030. [CrossRef] [PubMed]
76. Ota, T.; Maeda, M.; Okamoto, M.; Tatsuka, M. Positive regulation of Rho GTPase activity by RhoGDIs as a result of their direct interaction with GAPs. *BMC Syst. Biol.* **2015**, *9*, 1–9. [CrossRef]
77. Ugolev, Y.; Berdichevsky, Y.; Weinbaum, C.; Pick, E. Dissociation of Rac1(GDP).RhoGDI complexes by the cooperative action of anionic liposomes containing phosphatidylinositol 3,4,5-trisphosphate, Rac guanine nucleotide exchange factor, and GTP. *J. Biol. Chem.* **2008**, *283*, 22257–22271. [CrossRef]
78. Der Mardirossian, C.; Schnelzer, A.; Bokoch, G.M. Phosphorylation of RhoGDI by Pak1 mediates dissociation of Rac GTPase. *Mol. Cell* **2004**, *15*, 117–127. [CrossRef]
79. Kuhlmann, N.; Wroblowski, S.; Knyphausen, P.; de Boor, S.; Brenig, J.; Zienert, A.Y.; Meyer-Teschendorf, K.; Praefcke, G.J.K.; Nolte, H.; Krüger, M.; et al. Structural and Mechanistic Insights into the Regulation of the Fundamental Rho Regulator RhoGDIα by Lysine Acetylation. *J. Biol. Chem.* **2016**, *291*, 5484. [CrossRef]
80. Yu, J.; Zhang, D.; Liu, J.; Li, J.; Yu, Y.; Wu, X.-R.; Huang, C. RhoGDI SUMOylation at Lys-138 increases its binding activity to Rho GTPase and its inhibiting cancer cell motility. *J. Biol. Chem.* **2012**, *287*, 13752–13760. [CrossRef]
81. Liu, J.; Zhang, D.; Luo, W.; Yu, Y.; Yu, J.; Li, J.; Zhang, X.; Zhang, B.; Chen, J.; Wu, X.-R.; et al. X-linked inhibitor of apoptosis protein (XIAP) mediates cancer cell motility via Rho GDP dissociation inhibitor (RhoGDI)-dependent regulation of the cytoskeleton. *J. Biol. Chem.* **2011**, *286*, 15630–15640. [CrossRef]
82. Su, L.; Lineberry, N.; Huh, Y.; Soares, L.; Fathman, C.G. A novel E3 ubiquitin ligase substrate screen identifies Rho guanine dissociation inhibitor as a substrate of gene related to anergy in lymphocytes. *J. Immunol.* **2006**, *177*, 7559–7566. [CrossRef] [PubMed]
83. Jasemi, N.S.K.; Herrmann, C.; Estirado, E.M.; Gremer, L.; Willbold, D.; Brunsveld, L.; Dvorsky, R.; Ahmadian, M.R. The intramolecular allostery of GRB2 governing its interaction with SOS1 is modulated by phosphotyrosine ligands. *Biochem. J.* **2021**, *478*, 2793–2809. [CrossRef]
84. Olson, M.F. Rho GTPases, their post-translational modifications, disease-associated mutations and pharmacological inhibitors. *Small GTPases* **2018**, *9*, 203–215. [CrossRef] [PubMed]
85. Ahmadian, M.R.; Stege, P.; Scheffzek, K.; Wittinghofer, A. Confirmation of the arginine-finger hypothesis for the GAP-stimulated GTP-hydrolysis reaction of Ras. *Nat. Struct. Biol.* **1997**, *4*, 686–689. [CrossRef]
86. Hemsath, L.; Ahmadian, M.R. Fluorescence approaches for monitoring interactions of Rho GTPases with nucleotides, regulators, and effectors. *Methods* **2005**, *37*, 173–182. [CrossRef]
87. Eberth, A.; Ahmadian, M.R. In vitro GEF and GAP assays. *Curr. Protoc. Cell Biol.* **2009**, *43*, 1–25.
88. John, J.; Sohmen, R.; Feuerstein, J.; Linke, R.; Wittinghofer, A.; Goody, R.S. Kinetics of interaction of nucleotides with nucleotide-free H-ras p21. *Biochemistry* **2002**, *29*, 6058–6065. [CrossRef]
89. Hall, T.A. BioEdit A User-Friendly Biological Sequence Alignment Editor and Analysis Program for Windows 95/98/NT. Nucleic Acids Symposium Series, 41, 95–98. References—Scientific Research Publishing. 1999. Available online: https://www.scirp.org/(S(lz5mqp453edsnp55rrgjct55))/reference/ReferencesPapers.aspx?ReferenceID=1383440 (accessed on 22 February 2021).
90. Cock, P.J.A.; Antao, T.; Chang, J.T.; Chapman, B.A.; Cox, C.J.; Dalke, A.; Friedberg, I.; Hamelryck, T.; Kauff, F.; Wilczynski, B.; et al. Biopython: Freely available Python tools for computational molecular biology and bioinformatics. *Bioinformatics* **2009**, *25*, 1422–1423. [CrossRef]
91. DeLano, W.L. The PyMOL Molecular Graphics System. Delano Scientific, San Carlos. References—Scientific Research Publishing. 2002. Available online: https://www.scirp.org/(S(vtj3fa45qm1ean45vvffcz55))/reference/ReferencesPapers.aspx?ReferenceID=1958992 (accessed on 22 February 2021).

CHAPTER IV. SELECTIVITY DETERMINANTS OF RHO GTPASE BINDING TO IQGAPS

Niloufar Mosaddeghzadeh, Kazem Nouri, Oliver H. F. Krumbach, Ehsan Amin, Radovan Dvorsky, Mohammad Reza Ahmadian

DOI: 10.3390/ijms222212596

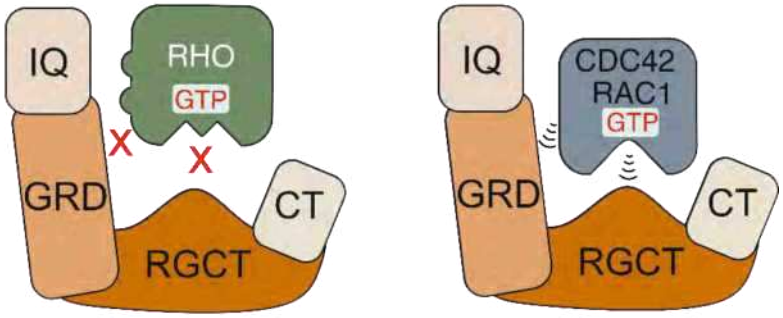

Status:	Published in November 2021
Journal	International Journal of Molecular Sciences
Impact factor:	6.20
Contribution:	45% Expression and purification of RHO GTPases and IQGAPs, preparation of nucleotide-free form of RHO GTPases, protein interaction analyses including fluorescence polarization measurements, stopped-flow measurements, and pull-down assay, preparation of the figures, drafting and writing the manuscript.

International Journal of
Molecular Sciences

MDPI

Article

Selectivity Determinants of RHO GTPase Binding to IQGAPs

Niloufar Mosaddeghzadeh [1,†], Kazem Nouri [1,2,†], Oliver H. F. Krumbach [1], Ehsan Amin [1,3], Radovan Dvorsky [1] and Mohammad R. Ahmadian [1,*]

[1] Medical Faculty, Institute of Biochemistry and Molecular Biology II, University Hospital Düsseldorf, Heinrich Heine University Düsseldorf, 40225 Düsseldorf, Germany; mosaddeg@uni-duesseldorf.de (N.M.); Kazem.nouri@uhnresearch.ca (K.N.); o.krumbach@gmail.com (O.H.F.K.); ehsan.amin@hhu.de (E.A.); radovan.dvorsky@gmail.com (R.D.)
[2] Department of Pathology and Molecular Medicine, McMaster University, Hamilton, ON L8S 4L8, Canada
[3] Medical Faculty, Institute of Neural and Sensory Physiology, University Hospital Düsseldorf, Heinrich Heine University, 40225 Düsseldorf, Germany
* Correspondence: Reza.ahmadian@hhu.de; Tel.: +49-211-811-2384
† These authors equally contributed to this study.

Abstract: IQ motif-containing GTPase-activating proteins (IQGAPs) modulate a wide range of cellular processes by acting as scaffolds and driving protein components into distinct signaling networks. Their functional states have been proposed to be controlled by members of the RHO family of GTPases, among other regulators. In this study, we show that IQGAP1 and IQGAP2 can associate with CDC42 and RAC1-like proteins but not with RIF, RHOD, or RHO-like proteins, including RHOA. This seems to be based on the distribution of charged surface residues, which varies significantly among RHO GTPases despite their high sequence homology. Although effector proteins bind first to the highly flexible switch regions of RHO GTPases, additional contacts outside are required for effector activation. Sequence alignment and structural, mutational, and competitive biochemical analyses revealed that RHO GTPases possess paralog-specific residues outside the two highly conserved switch regions that essentially determine the selectivity of RHO GTPase binding to IQGAPs. Amino acid substitution of these specific residues in RHOA to the corresponding residues in RAC1 resulted in RHOA association with IQGAP1. Thus, electrostatics most likely plays a decisive role in these interactions.

Keywords: IQGAP; scaffold; RHO GTPases; CDC42; RAC1; selective bindings

Citation: Mosaddeghzadeh, N.; Nouri, K.; Krumbach, O.H.F.; Amin, E.; Dvorsky, R.; Ahmadian, M.R. Selectivity Determinants of RHO GTPase Binding to IQGAPs. *Int. J. Mol. Sci.* **2021**, *22*, 12596. https://doi.org/10.3390/ijms222212596

Academic Editor: José Luis Zugaza

Received: 27 October 2021
Accepted: 19 November 2021
Published: 22 November 2021

1. Introduction

IQ motif-containing GTPase-activating proteins (IQGAPs) belong to the class of multidomain scaffold proteins that play central roles in the assembly of protein complexes and signaling networks [1–7]. In humans, three IQGAP paralogs have been described. The ubiquitously expressed IQGAP1 is the best-characterized paralog. IQGAP2 is mostly expressed in the liver, prostate, kidney, thyroid, stomach, testis, platelets, and salivary glands, while IQGAP3 is found in the brain, lung, testis, and intestine [8]. Multiple domains enable IQGAPs to interact with a large number of proteins and to modulate the spatiotemporal distributions of distinct signal-transducing protein complexes, including B/CRAF-MEK1/2-ERK1/2 [9–11], FGFR1-CDC42-NWASP-ARP2/3-actin [12–14], TIAM1-RAC1-PAK6 [15,16], and CDC42/RAC1/CLIP170 [17,18]. IQGAP paralogs share similar domain organization and high sequence homology (Figure 1A). The N-terminal calponin homology domain (CHD) binds F-actin [19]. The polyproline-binding region (WW) binds ERK1/2 [9]. The IQ motif (IQ) binds HER1/2, KRAS, B/CRAF, MEK1/2, and calmodulin [4,20–24]. The RASGAP-related domain (GRD) and RASGAP C-terminal domain (RGCT) bind to CDC42 and RAC1. The C-terminal domain (CT) binds E-cadherin, β-catenin, APC, and CLIP170 [3].

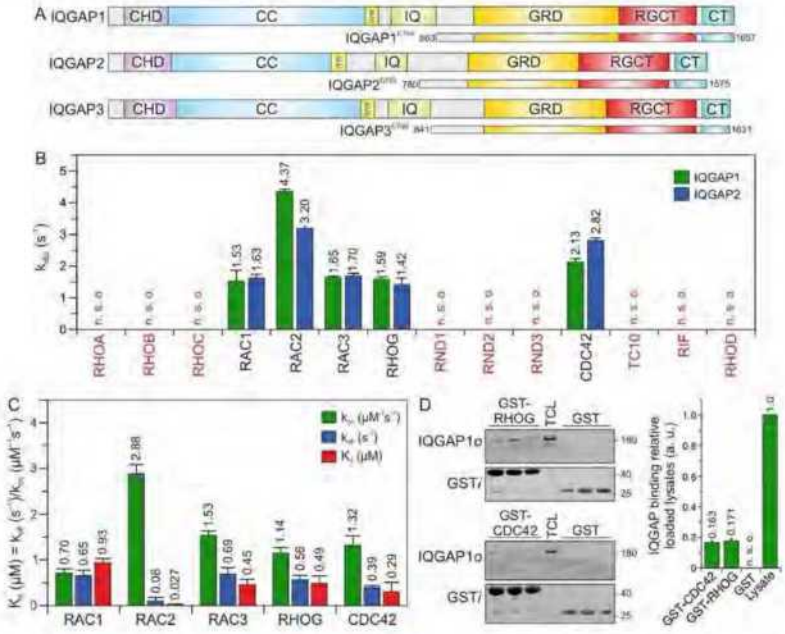

Figure 1. IQGAP1 and IQGAP2 selectively associate with CDC42 and RAC1-like proteins. (**A**) Domain organization of the IQGAP paralogs and their C-terminal fragments assessed in this study (see text for more details). (**B**) The association of IQGAP1^{C794} and IQGAP2^{C795} (2 μM) with various mGppNHp-bound RHO GTPases (0.2 μM) was investigated (Figure S1). The k_{obs} values for the interaction of IQGAP1 and IQGAP2 with several RHO GTPases, shown as bars, illustrate that both IQGAPs associate with CDC42 and RAC1-like proteins. The RHO-like proteins RND1, RND2, RND3, TC10, RIF, and RHOD did not associate with these IQGAPs under these conditions. (**C**) The association rates (k_{on}) were measured using 0.2 μM mGppNHp-bound RHO GTPases with increasing concentrations (2–8 μM) of IQGAP1^{C794}. Dissociation rates (k_{off}) were measured by mixing 2 μM IQGAP1^{C794} complexed with mGppNHp-bound RHO GTPases (0.2 μM) and unlabeled RAC1-GppNHp (10 μM). The individual rate constants were calculated for the interaction of IQGAP1^{C794} with RAC- and CDC42-like proteins, and the results are plotted in bar charts. Association rates (k_{on}), dissociation rates (k_{off}), and dissociation constants (K_d) for IQGAP1^{C794}-RHO protein binding are shown. RAC2 showed the highest binding affinity for IQGAP1^{C794}, followed by CDC42, RAC3, RHOG, and RAC1. The data are expressed as the means ± S.D. All measurements were obtained in duplicate. n. s. o. = no signal observed. Kinetic data, which are summarized in Table S1 and shown in Figure S2, were obtained in triplicate. The data are expressed as the means ± S.D. (**D**) Binding of endogenous IQGAP1 to GppNHp-bound RHOG and CDC42 (left panel) was analyzed in a GST pull-down assay ($n = 3$) using total cell lysate (TCL) of HEK-293 cell (i, input; o, output). GST-CDC42•GppNHp was used as positive control. GST control experiments confirmed the specificity of the interaction between RHOG and IQGAP1. The upper part of the membrane was used for an anti-IQGAP1 immunoblotting, and the lower for an anti-GST. Densitometry analysis of relative IQGAP binding to GST-CDC42 or GST-RHOG (a. u., arbitrary unit) were performed in the next step. Bar charts at the right panel display the quantitation of detected signal in GST-pull down assay from a triplicate experiment.

CDC42 and RAC1 belong to the RHO GTPase family, which includes 20 classical paralogs [25] that control diverse cellular functions [26,27]. RHO GTPases are classified into six subfamilies: the RHO subfamily (RHOA, RHOB, and RHOC); the RAC subfamily (RAC1, RAC1B, RAC2, RAC3, and RHOG); the CDC42 subfamily (CDC42, G25K, TC10, TCL, WRCH1, and WRCH2); the RND subfamily (RND1, RND2, and RND3); and RHOD, RIF, and RHOH, which do not precisely fall into any of these subfamilies [25,28]. The RHOBTB and MIRO subfamilies are atypical members of the RHO family that are

structurally different from classical RHO family members and possess other additional functional domains [29].

RHO GTPases are molecular switches that cycle between an inactive (GDP-bound) and an active (GTP-bound) form [28]. In the active state, they interact with a multitude of target (effector) proteins, such as IQGAPs, to induce cellular responses [30–32]. Interaction with RHO GTPases, such as CDC42 or RAC1, and/or phosphorylation of Ser-1441 and Ser-1443 may release IQGAPs from an autoinhibited state and induce their activated signaling competent state [20,22,23,33]. The interaction of the C-terminal half of IQGAP1, encompassing the GRD, RGCT, and CT domains (hereafter called C794), with RAC1 and CDC42 has been intensively studied by several groups [21,23,33–39]. Despite the common binding properties of CDC42 and RAC1 to IQGAPs, there are significant differences, which may be attributed to divergent IQGAP-RHO GTPase complexes that control distinct cellular processes [23,24,36,40,41]. As the highly flexible switch I and II regions (encompassing amino acids 29–42 and 62–68, respectively), which change their conformation upon GDP to GTP exchange [31], are almost identical in CDC42 and RAC1, the selectivity-determining residues need to be located outside these two regions.

Since its discovery in 1994, IQGAP1 has emerged as a key scaffold protein [42] that links crucial components of multiple cellular processes. Many studies have provided valuable evidence for the interaction between IQGAP1 and CDC42, but the mechanism determining IQGAP binding selectivity for different members of the RHO GTPase family has remained unclear. The following questions were addressed in this study: To what extent do IQGAP paralogs differ in their RHO GTPase-binding characteristics and specificity, and how does IQGAP1 distinguish different RHO GTPases? To this end, we investigated the interactions of IQGAPs with 14 RHO GTPases using the C794 and C795 segments of IQGAP1 and IQGAP2, respectively, which exhibit a sequence identity of 72%. We excluded IQGAP3, RHOH, WRCH1, WRCH2, and TCL from this study because of their low solubility and physical instability. These analyses revealed that IQGAPs bind CDC42 and RAC1-like proteins but not RHO-like proteins. IQGAP1 competition experiments along with mutational and structural analyses revealed three distinct regions proximal to the switch regions that are differentially involved in selective binding of IQGAP1 and 2 to RHO GTPases.

2. Results

2.1. IQGAP1/2 Selectively Bind CDC42 and RAC1-Like Members of the RHO Family

The C-terminal 794 amino acids (aa) of IQGAP1, encompassing the GRD, RGCT, and CT domains, and C795 of IQGAP2, were successfully purified to measure their binding properties over a broad range of RHO GTPases. Interaction studies were performed using time-resolved stopped-flow fluorescence (SFF) spectrometry under previously described conditions [23]. Accordingly, both IQGAPs were associated similarly with the active forms of RAC1, RAC2, RAC3, RHOG, and CDC42, but not with RND1, RND2, RND3, TC10, RHOA, RHOB, RHOC, RHOD, or RIF (Figures 1B and S1A–F).

RND proteins represent a distinct group of proteins within the RHO family. They were purified in their GTP-bound state, but replacing GTP with mGppNHp, 2′/3′-O-(N-methyl-anthraniloyl)- guanosine-5′-[(β,γ)-imido]triphosphate, a slow-hydrolyzing analog of GTP, resulted in complex instability. Therefore, for interaction studies with IQGAPs, we performed indirect competitive assays. We measured the association of $IQGAP1^{C794}$ with RAC1 in the presence and absence of excess GTP-bound RND proteins. As a positive control, we used GppNHp-bound CDC42. In contrast to CDC42, which competitively blocked the IQGAP-RAC1 interaction, no binding of RND proteins was observed (Figure 1B and Figure S1G,H), suggesting that IQGAP1 and IQGAP2 do not interact with these unconventional members of the RHO family.

Given these findings, it was important to investigate the complex formation and binding stoichiometry between CDC42/RAC1 and the IQGAP proteins. LeCour et al. have proposed that constitutively active $CDC42^{Q61L}$ but not $RAC1^{Q61L}$ binds the IQGAP2

(GAP)-related domain (GRD) in a 2:1 ratio to promote IQGAP2 dimerization [41]. Therefore, we performed analytical size-exclusion chromatography using $IQGAP1^{C794}$ and $IQGAP2^{C795}$ alone or mixed with CDC42•GppNHp or RAC1•GppNHp. The elution profiles showed that CDC42, RAC1, and IQGAP1 eluted as dimers, while IQGAP2 eluted mainly as monomers and to some extent as trimers and tetramers (Figure S3A; peaks #1 and #2). The elution profiles of the IQGAPs mixed with CDC42 and RAC1 showed, in addition to RAC1 and CDC42 (peak #1), two peaks (#3 and #5), indicating molecular weights (M_Ws) of 222–235 kDa and elution volumes of 10.2–11.0 mL (Figure S3A). Coomassie-brilliant-blue-stained SDS-PAGE gels revealed that only peak #3 contained IQGAP complexes with RAC1 and CDC42, with an average M_W of 228 kDa that corresponds to a heterotetramer (Figure S3B). $IQGAP2^{C795}$ also eluted as higher oligomers (peak #6), which did not contain either RAC1 or CDC42.

LeCour et al. have reported a high affinity interaction between $CDC42^{Q61L}$ and IQGAP GRD (41). In our previous study, we have shown that $CDC42^{Q61L}$ has a 13-fold stronger interaction with GRD as compared with $CDC42^{WT}$ (23). Therefore, we purified and investigated the stoichiometry of $CDC42^{Q61L}$•GppNHp for its complex formation with IQGAP1 GRD in direct comparison with $CDC42^{WT}$•GppNHp. In the case of $CDC42^{Q61L}$, the elution profile represented two peaks (Figure S4, upper middle panel) for the GRD and $CDC42^{Q61L}$ complex, corresponding to heterotrimeric complex with a stoichiometry of 2:1, as proposed by LeCour et al. [23,41]. However, GRD and $CDC42^{WT}$ complex eluted as a heterotetramer (a 2:2 complex; Figure S4, lower panels).

Overall, the analyses of the size-exclusion chromatography data suggest that under our experimental conditions, the composition of the IQGAP1/2 complexes with both RAC1 and CDC42 corresponds to a 2:2 ratio. Furthermore, the CDC42-GppNHp elution profile at 15.6 and 15.9 mL of elution volume (Figure S3) confirmed the previous observations reported by Zhang et al. regarding the reversible homodimerization of RHO family GTPases [43].

2.2. RAC2 Exhibited the Highest Affinity for IQGAP1

To examine binding properties, the respective association rate constants (k_{on}) and the dissociation rate constants (k_{off}) were determined for the interaction of $IQGAP1^{C794}$ with CDC42 and RAC1-like proteins under the aforementioned conditions (Figures 1C and S2). All the kinetic parameters along with calculated dissociation constants (K_d) are summarized in Table S1. The values are in a range similar to that of wild-type RAC1, RAC3, RHOG, and CDC42, with the exception of RAC2, which strikingly showed a K_d value of 27 nM, the highest affinity for $IQGAP1^{C794}$ (Figure 1C). The rapid association and slow dissociation rates are remarkable, and suggest that the RAC2–IQGAP1 interaction remains stable for a long residence time.

The $IQGAP1^{C794}$ binding of RHOG, in addition to its binding to the RAC and CDC42 proteins, prompted us to investigate the association of RHOG with endogenous IQGAP1 using purified GST-RHOG•GppNHp as bait in a pull-down assay. GST was used as the negative control, and GST-CDC42•GppNHp was used as the positive control. Quantification of the immunoblot analysis using specific antibodies against GST and IQGAP1 showed that cellular IQGAP1 bound RHOG as efficiently as it bound CDC42 (Figure 1D).

Next, we performed an in-depth investigation of the $IQGAP1^{C794}$ interactions with RAC1 and CDC42, which are widely acknowledged to be IQGAP-binding partners.

2.3. Potential Hotspots for IQGAP Binding Appear Outside the Switch Regions

The switch regions (Figure 2A), which are generally known as effector binding sites, are required but not sufficient for effector binding selectivity. The amino acid sequences of these two regions are almost identical, which is particularly notable in comparison to IQGAP1-binding proteins (e.g., members of the RAC subfamily) with nonbinders (e.g., members of the RHO subfamily) (Figure 2B). Thus, a set of specificity-determining residues in RHO GTPase that direct interactions with IQGAPs must reside outside of the switch regions. In this context, notably, the CDC42 subfamily includes both IQGAP binders and

nonbinders. Accordingly, we found four different hotspots, residues 25/26, 45/52, 74, and 85/88 (based on CDC42/RAC numbering), that are highly conserved in IQGAP1 binders and clearly deviate from the corresponding residues in nonbinders (Figure 2B). Notably, we did not consider residues that are quite variable not only between the binders and nonbinders but also within the IQGAP1 binders themselves (e.g., T24, A27, G30, S41; Figure 2B). Moreover, an inspection of the crystal structures of RHO GTPases in five different subfamilies showed that these four sites did not significantly contribute to local structural variations (Figure 2C, upper panel). These residues surround the switch regions and, most interestingly, are all located on the surface of the respective proteins and are thus available for intermolecular interactions (Figure 2C, middle panel).

As almost all amino acids at the selected hotspots in RHOA and RND proteins have charged side chains, electrostatics very likely play a crucial role in complex formation with IQGAP1. With the aim of verifying this hypothesis, we first calculated the electrostatic potentials around these molecules. While the form and magnitude of the electrostatic isosurfaces for cognate RHO GTPases were found to be similar, striking differences were found between their subclasses, with particularly strong negative potentials in the cases of TC10, TCL, RHOA, and RND proteins (Figure 2C, lower panel). The electrostatic surface potentials of 15 different RHO GTPases are shown in Figure S5. Aiming to understand the origin of these differences in the electrostatic potentials of the 15 examined RHO GTPases, we calculated the net charges of their G-domains with −1 attributed to aspartic or glutamic acid and +1 attributed to arginine or lysine. Although RHO GTPases are highly homologous, variations in particular amino acids that might seem negligible from a sequence point of view can lead to a broad span of net protein charges. In the cases of the studied GTPases, the span of electrostatic charges ranges from −9 for RHOB to electrically neutral RIF, clearly explaining the differences in electrostatic potential. The larger the lobe of the negative potential around the protein is, the more negative its net charge. Correlating the electrostatic charge with the binding to IQGAP1, negative charges might discriminate the association with TC10, TCL, RHOA, and RND paralogs. On the other hand, balanced potentials seem to be just a prerequisite for binding, because the charges and corresponding electrostatic potentials of all other GTPases are similar, but RHOD and RIF belong to nonbinders.

2.4. PAK1, $p50^{GAP}$, and DOCK2 Compete with IQGAP1 for Binding RAC1

To further map the $IQGAP1^{C794}$-binding regions on the surface of the RAC1 structure, we performed competitive binding experiments. We repeated the measurement of the $IQGAP1^{C794}$ association with RAC1•mGppNHp in the absence and presence of a 10-fold molar excess of other RAC1-interacting proteins that may be competitors: full-length GDI1, the DBL homology-pleckstrin homology tandem (DH-PH) domain of TIAM1 and TRIO, the DOCK homology region 2 (DHR2) domain of DOCK2, the GAP domain of $p50^{GAP}$, the GTPase-binding domain (GBD) of PAK1, the RAC1-binding domain of plexin-B1 RBD, and the tetratricopeptide repeat (TPR) of $p67^{Phox}$ (Figure 3). These proteins were premixed with $IQGAP1^{C794}$ before rapid mixing with RAC1•mGppNHp in a stopped-flow apparatus. The working model was based on the presumption that if the binding of RAC1 to $IQGAP1^{C794}$ and to RAC1-interacting proteins is mutually exclusive, then the proteins in the mixture will interfere with the ability of $IQGAP1^{C794}$ to associate with RAC1. As shown in Figures 3A and S6, $IQGAP1^{C794}$ association with RAC1•GppNHp was partially abolished with DOCK2 and $p50^{GAP}$, completely abolished with PAK1, and not affected by the other proteins. Notably, GEFs, and most likely DOCK2, do not significantly distinguish between GDP- and GTP- (or GppNHp-) bound RHO GTPases [44].

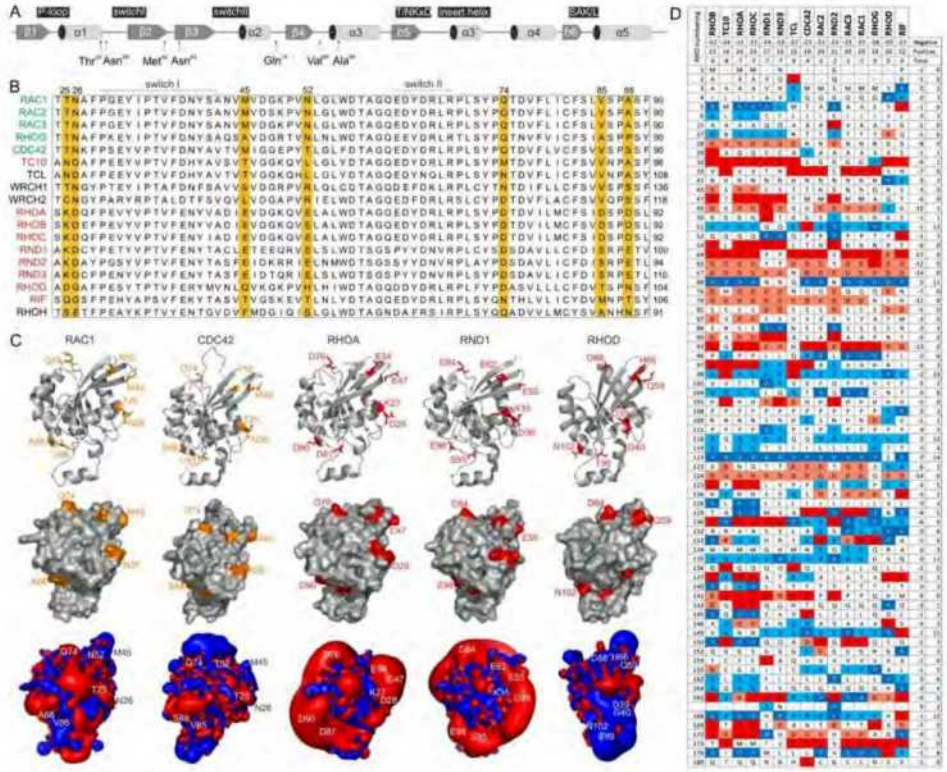

Figure 2. RHO GTPases exhibit significantly different electrostatic properties. (**A**) The G domain organization of RAC1 indicates secondary structure elements, key functional regions and locations of residues crucial for IQGAP1 binding. (**B**) A multiple amino acid sequence alignment of canonical RHO GTPases revealed various residues outside of the switch regions that may determine their differential interactions with IQGAPs. IQGAP binders are colored green, and the nonbinders are colored red. (**C**) Structures in ribbon representation, solvent accessible proteins surfaces and electrostatic potential maps for RAC1 (PDB code, 1MH1), CDC42 (PDB code, 2QRZ), RHOA (PDB code, 1A2B), RND1 (PDB code, 2CLS), and RHOD (PDB code, 2J1L) are shown. Thr-25, Asn-26, Met-45, Asn-52, Gln-74, Val-85, and Ala-88 of RAC1 proposed to determine its specificity for the binding of IQGAPs are located on the surface, negatively charged residues on corresponding positions in, for example, RHOA and RND1 cause significant negative electrostatic potentials. Images were generated with the PyMOL molecular viewer. (**D**) The distribution of charged amino acids vary significantly among RHO GTPases despite their high sequence homology. Sequence alignment of the RHO GTPases used in this study reduced in a way that only loci containing at least one positively charged amino acid, i.e., arginine or lysine, or one negatively charged amino acid, i.e., glutamate or aspartate, were retain, respectively. It demonstrates diverse occurrence of charges in proteins molecules of RHO GTPases that is also reflected on huge differences of electrostatic potentials shown in C. They roughly also correspond to theoretical net charges for whole proteins that were obtained as sums of the +1 or −1 for positively or negatively charged residues, respectively. As only RHOoD and RIF were found to be electrically neutral while all other GTPases possess overall negative net charge, characteristic lobes of negative, red colored electrostatic potentials around the majority of proteins were observed (for reference see also Figure S5).

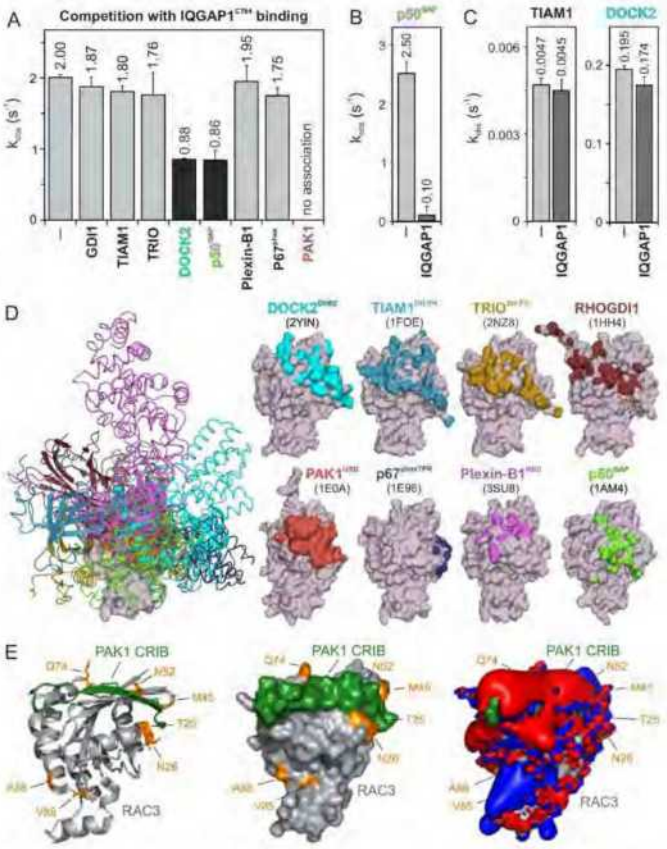

Figure 3. IQGAP1^{C794} competes with DOCK2, p50^{GAP}, and PAK1 for binding RAC1. (**A**) The evaluated observed rate constants (k_{obs}), shown as bars, demonstrate that IQGAP1^{C794} associates with RAC1 regardless of the presence of excess amounts of GDI1, TIAM1, TRIO, Plexin-B1, or p67^{phox}, while the association was blocked in the presence of DOCK2 or p50^{GAP} and completely abolished in the presence of PAK1. (**B**) The p50^{GAP}-stimulated GTPase activity of RAC1 was drastically reduced in the presence of IQGAP1^{C794}. (**C**) TIAM1- and DOCK2-catalyzed nucleotide exchange activity of RAC1 was not significantly changed in the presence of excess amounts of IQGAP1^{C794}. All measurements in (**A**–**C**), which are shown in detail in Figure S6, were obtained in triplicate. The data are expressed as the means + S.D. (**D**) The left panel shows the structure of RAC1 (gray represents the surface) in complex with different RAC and CDC42 interacting partners (in different colored ribbons), including DOCK2^{DHR2}, TIAM1^{DH-PH}, TRIO^{DH-PH}, p50^{GAP}, GDI1, PAK1^{GBD}, p67^{phoxTRP}, and Plexin-B1^{RBD}. The right panel highlights the contact sites of these binding proteins on the surface of RAC1 in the corresponding colors. The protein database identification codes of the respective structures are indicated. (**E**) The complex structure of RAC3 (PDB code, 2IC5) and the CRIB motif of PAK1 (PDB code, 2QME) shows that T25, N26, M45, N52, and Q74 of RAC3 are in close proximity to the CRIB motif-binding region. Electrostatic potentials (right panel) show that the PAK1 CRIB motif generates an overall negative electrostatic surface potential.

In addition, we measured the impact of IQGAP1^{C794} binding to RAC1 on the GEF and GAP activities of TIAM1, DOCK2, and p50^{GAP} (Figure 3B,C). The speculation that GEFs may compete with IQGAP1^{C794} for RAC1•GDP binding is based on the assumption that IQGAP1^{C794} binds to other sites outside the switch regions [40]. No change was observed for the nucleotide exchange reaction catalyzed by TIAM1 or DOCK2 (Figure 3C),

corroborating our previous observation that IQGAP1^{C794}, which binds CDC42•GDP, does interact with RAC1•GDP [23]. In contrast, p50^{GAP}-stimulated GTP hydrolysis activity was drastically inhibited, reduced by 25-fold, in the presence of IQGAP1^{C794} (Figure 3B), confirming the selective and high-affinity binding of IQGAP1^{C794} to RAC1•GTP.

To determine which amino acids of RAC1 are critical for the observed interactions and effects, we first overlaid the extracted structures of the investigated binding proteins (Figure 3D, left panel) with residues that form the interacting interfaces and depicted them on a surface representation of the respective RAC1 structures (Figure 3D, right panel). The interacting interfaces are shown in colors corresponding to the RAC1-binding proteins. We further analyzed the crystal structure of RAC3 in complex with PAK1 GBD, which fully interfered with IQGAP1^{C794} binding to RAC1, and may thus share overlapping binding regions. Remarkably, the residues previously identified by sequence structural analysis as potential (hot)spots for the association of RHO GTPases with IQGAP1^{C794}, namely, T25, N26, M45, N52, and Q74 of RAC3, are located in proximity of the RAC1-binding region of PAK1 GBD (Figure 3E). Visualizing the electrostatic potential of this complex structure showed that PAK1 GBD generates an overall negative electrostatic potential on the surface of RAC3 (Figure 3E, right panel).

2.5. IQGAP1 Binding Hotspots Significantly Vary among RHO GTPases

To identify whether the predicted hotspots determine differences in the interaction of IQGAP1^{C794} with RHO proteins, we replaced these sites in RAC1 and CDC42 with the corresponding amino acids in RHOA (T25K/N26D, M45E/N52E, Q74D, and V85D/S88D) (Figure 2A). Notably, S88 of CDC42 is in the same region as IQGAP2-contacting residues [41]. The interaction of these variants with IQGAP1^{C794} was measured under the same conditions as described above. Strikingly, major changes in the IQGAP1^{C794} binding kinetics were observed for the RAC1 variants but not for the CDC42 variants (Figure 4, left and middle panels). All the variants exhibited slower association kinetics and faster dissociation kinetics (Figure S7). As a result, the overall decrease in the binding affinities of the RAC1 variants for IQGAP1^{C794} ranged between 7- and 17-fold, suggesting that these residues are either part of the RAC1–IQGAP1 binding interface or in close proximity to the IQGAP1-binding sites. To identify the impact of these residues, we generated a RHOA variant containing five substitutions, K27T, D28N, E47M, E54N, and D76Q, to mimic RAC1. Interestingly, this RHOA-to-RAC1 variant was capable of associating with IQGAP1^{C794}, while RHOA^{WT} did not show any association with IQGAP1^{C794} (Figure 4, right panel). These data confirmed the identified sequence-specific binding sites as hotspots.

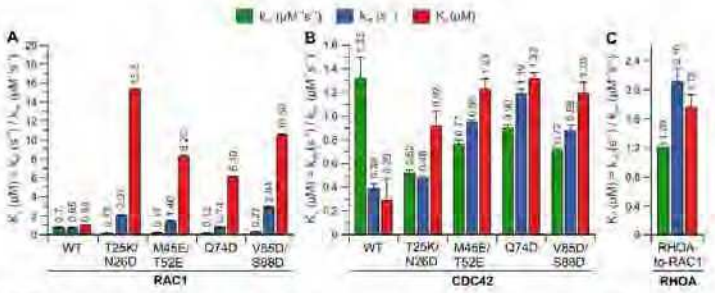

Figure 4. Kinetic measurements of RAC1 and CDC42 variants binding IQGAP1^{C794}. The calculated association rates (k_{on}), dissociation rates (k_{off}), and dissociation constants (K_d) for the interaction of IQGAP1^{C794} with different variants of RAC1 (**A**), CDC42 (**B**), and RHOA (**C**) are plotted as bar charts. All kinetic data are summarized in Table S1 and shown in Figure S7. The data are expressed as the means ± S.D.

3. Discussion

A large number of studies have examined the interaction between IQGAPs and the small GTPases of the RHO family. Among the 20 classical RHO proteins, RAC1 and CDC42 have been extensively studied to characterize their binding behavior with IQGAPs [21,23,33,36,39,45]. Accordingly, IQGAPs are able to interact with different RHO GTPases. To understand the roles of these interactions in the orchestration of signaling events in which IQGAPs serve as scaffold proteins, we explored the selectivity of these interactions. Specifically, we measured the protein–protein interaction of 14 RHO GTPases with $IQGAP1^{C794}$ and $IQGAP2^{C795}$ to identify selectivity determinants. Time-resolved SFT spectrometry was performed to monitor the kinetics of IQGAP associations with RHO GTPases. The results clearly showed that these two IQGAP paralogs bind only CDC42, RHOG and RAC-like proteins. Notably, as RHOG belongs to the same branch of the phylogenetic tree of RHO GTPases that includes RAC1, RAC1B, RAC2 and RAC3, we suggest designating it RAC4.

The comparative analysis of the binding kinetics of the RAC paralogs RAC1, RAC2, and RAC3 with $IQGAP1^{C794}$ showed that RAC2 kinetics with $IQGAP1^{C794}$ were clearly different than those of RAC1 and RAC3, which is consistent with our previous studies. Notably, RAC1 and RAC3 have closely related biochemical properties that differ from those of RAC2. Previous studies reporting results of modeling and normal mode analyses supported the idea that the altered molecular dynamics of RAC2, particularly at the switch I region, may be critical for differences in its behaviors compared to those of RAC1 and RAC3 [46]. In our study, RAC2 exhibited a 4-fold faster k_{on} and an 8-fold lower k_{off}, which resulted in a 34-fold lower K_d value, compared to RAC1 (Figure 1C). An amino acid sequence comparison of the RAC proteins showed that three identical residues in RAC1 and RAC3 were different in RAC2: S48, Y90, and D150 in RAC2 corresponded to G48, F90, and G150 in RAC1 and RAC3, respectively. These residues are located outside the IQGAP1 GRD-binding interface of two CDC42 molecules, which mainly contacts the switch regions [41]. This previous finding and the fact that CDC42 and RAC1 were found to differ in their interactions with IQGAP1 [23,24,40] suggest that RAC proteins may have additional contact sites that differ from those of CDC42. Casteel et al. and Bhattacharya et al. have shown the formation of an IQGAP1 complex with RHOA and RHOC but not with RHOB [47,48]. Our results do not confirm the direct binding of IQGAP1/2 to RHOA/C. In our opinion, the observed interactions of IQGAP1 with RHOA or RHOC appear to be indirect, since these proteins were coimmunoprecipitated from cells overexpressing tagged RHO wild-type proteins and their constitutively active form, or they may have been mediated by an IQGAP1 domain that does not include C794. Evidence supporting an indirect effect is based on our residue-swapping experiment: a variant of RHOA with five substitutions mimicking RAC1 was able to efficiently bind IQGAP1. In contrast, $RHOA^{WT}$ did not bind IQGAP1, validating the identified sequence-specific binding sites as binding hotspots. Our findings also rule out the possibility that some domains other than C794 may mediate binding with RHOA.

Several proteins, including IQGAP3 and the RHO family members RHOH, WRCH1, WRCH2, and TCL, were not investigated in this study because of their limited solubility and stability. Our efforts to purify and characterize these proteins by generating various constructs, particularly IQGAP3, were not successful. In addition, the preparation of mGppNHp-bound RND proteins was not possible due to their instability in the presence of other guanine nucleotides. Purified RND proteins were exclusively GTP-bound, and attempts to hydrolyze GTP to GDP for several days at 25 °C or to exchange GTP for GTP analogs resulted in their precipitation [28,49]. The reason for this outcome is that these proteins are not regulated by a conventional GDP/GTP cycling mechanism and exist in the GTP-bound form in cells [28,49].

A remarkable feature of RHO GTPases is that their regulators (GDIs, GEFs, and GAPs) and effectors, although functionally quite diverse, share a consensus binding site encompassing switch I and II regions [31]. The competition experiments in our study were

based on this basic concept (Figure 3A–C). In contrast to regulators that interact with RHO GTPases to modulate their switch function, the interaction between RHO GTPases and their effectors controls a wide range of intracellular signaling pathways and depends on the kinetics of their interactions, not their binding affinity. In fact, $p67^{phox}$ and Plexin-B1, which bind RAC1 with slightly lower binding affinities of 2.7 and 6.6 µM, respectively [50,51], compared to $IQGAP1^{C794}$, were unable to compete with $IQGAP1^{C794}$, even at 10-fold molar excess. These proteins have an affinity for RAC1 similar to that of $IQGAP1^{C794}$ but different kinetic properties upon binding (a fast k_{on} and a slow k_{off}), as we determined in this study. The observed competitive effects of DOCK2 and $p50^{GAP}$ on $IQGAP1^{C794}$ binding to RAC1•GppNHp seem to be consistent with the presumed importance of the binding kinetics. A previous study showed that very fast GEF- and GAP-catalyzed reactions were both preceded by a much faster association with their cognate GTPase, implying very high k_{on} values [52].

Moreover, the structural properties that characterize the GTPase-binding domains of the effectors and their binding sites are, despite their fundamentally conserved sites, rather diverse. This includes the unexpected features of $p67^{phox}$ contact sites on RAC1. $p67^{phox}$ has an α-helical domain with four tetratricopeptide repeat (TPR) motifs [53] that bind α1, the N-terminal residues of switch I, and the G3 and G5 loops, but not the switch II region or the principal parts of switch I (Figure 3D) [51]. It has also been proposed that the switch regions might be the contact sites for a third protein that is simultaneously associated with the RAC1•GTP•$p67^{phox}$ complex and bound to membrane phospholipids [54,55].

In a comprehensive study, Owen et al. analyzed a multitude of CDC42 and RAC1 variants, particularly variants with changes in the switch regions and the insert helix, to assess their interactions with IQGAP1. Their results suggested that CDC42 and RAC1 associate with IQGAP1 in a significantly different manner [36,40]. Major IQGAP-binding sites in CDC42 are residues in the switch regions, including P34, V36, F37, D38, D63, Y64, R66, and L67, which are basically identical in CDC42 and RAC1. This and another study have shown that the insert helix of CDC42, especially residue Asn-132, may provide an additional binding site for IQGAP2 GRD on CDC42, leading to CDC42 dimerization, which is not evident for RAC1 [24,41]. These data may explain the slightly different binding kinetics of CDC42 and RAC1 towards IQGAP1 (Figure 1B); the faster association rate and slow dissociation rate explain the 3-fold higher binding affinity of CDC42 for IQGAP1 compared to that of RAC1. Using analytical size-exclusion chromatography, we did not observe differences between RAC1 and CDC42 in their complex formation with IQGAP1 or IQGAP2 (Figure S3). All four protein complexes showed an average M_W of 228 kDa, which corresponds to heterotetramers formed in a 2:2 ratio. Our data on residue swapping in RHO GTPases successfully validated the role of hotspot residues identified in the RAC1–$IQGAP1^{C794}$ interaction (Figure 4). Four of seven the hotspots (T25, T52, V85, and S88) investigated in the residue swapping experiments in this study are within the CDC42–IQGAP2 binding interface, while N26, M45, and Q74 are clearly outside but close to the IQGAP2-binding site [24,41]. Our findings support previous research on overlapping RAC1 and CDC42 contact regions, but they also provide additional insights into the possible RAC1–IQGAP interacting interface, which needs to be confirmed by additional structural studies.

LeCour et al. have investigated the IQGAP1 GRD domain in a complex with CDC42Q61L [23,41]. Different groups used this variant of RAC1, CDC42, and RHOA in biophysical studies because it binds to effector proteins with 10- to 30-fold higher affinity. The reason is a tremendous increase and stabilization of an exposed hydrophobic cluster between the switch region in GTP-bound proteins, consisting of P36, V38, and T39 from switch I; Q63, Y66, R68 from switch II; and L69 and L72 from helix α2 [31,56]. This is consistent with the determined binding affinity of IQGAP1 for CDC42Q61L•mGppNHp of 2.37 µM, which is 13-fold higher as compared to the K_d value obtained from IQGAP1 binding to CDC42 [23,41]. In conclusion, we believe that using this variant to characterize RHO GTPase–effector interaction may lead to incorrect conclusions.

In silico analyses of RHO GTPases in this study, based on sequence alignment, comparison of different crystal structures, and electrostatic potentials together with kinetic experiments revealed that significant differences in the IQGAP-binding selectivity can be attributed to a few amino acids deviating between subgroups in the RHO GTPase family. A critical issue that needs to be further considered involves the electrostatics that can either affect bimolecular interactions due to repulsive forces or substantially enhance molecular interactions based on attractive forces, which can contribute to the selectivity and rapid association of two molecules [57–63]. A structural inspection of RHO GTPases revealed that they differ considerably in their electrostatic potentials, as demonstrated by the equipotential contours; even highly related paralogs, such as CDC42 (with a net charge of −4) vs. TC10 (−8), RND1 (−7) vs. RND2 (−2), and RAC1 (−1) vs. RAC2 (−1), are quite different regarding their electrostatic potential distribution (Figures 2D and S5). These differences may have significant effects on interaction selectivity. A remarkable example is the dramatic difference of the k_{on} values of approximately 800-fold for the WASP association with CDC42 and TC10. Unique glutamates in CDC42 (E49, E171, and E178), which are missing in TC10, generate favorable electrostatic steering forces that control the accelerated CDC42–WASP association reaction [45,58]. Notably, RHOC and RHOD are unrelated members of the RHO family with respect to their intrinsic nucleotide exchange and hydrolysis reactions [28] and their interactions with GEFs and GAPs [64,65]. Although RND1 and RND3 show surface potentials similar to RHOA (Figure S5), they are known to antagonize RHOA function [66,67]. A previously performed structure–function analysis showed that GTP-bound RND proteins share a similar fold but striking differences from the conventional members of the RHO family, such as RHOA, especially with regard to interacting interfaces with RHOA regulators and effectors [28,49]. Although a large computational toolbox is currently available for studying the roles played by electrostatics in the regulation of the protein life cycle and protein interactions, electrostatic features are still neglected factors in basic science [59].

Considering the high sequence identity between the RHO GTPases within the switch regions, which are generally acknowledged to be the main binding sites for three classes of regulators and of downstream effectors [31], we proposed that further contact sites outside of the switch regions are required to define the selectivity of the respective interactions. Recently, nine different CDC42 missense mutations causing a phenotype resembling Noonan syndrome have been identified by researchers. Among these mutants, $CDC42^{R66G}$ and $CDC42^{R68Q}$ exhibited defective interactions with IQGAP1 [45]. However, the mutated residues are part of the switch II region and do not significantly differ between RHO GTPases. Another recently described disease, called NOCARH syndrome, caused by a specific missense mutation in $CDC42^{R186C}$, was identified by Lam and colleagues. Biochemical analysis has shown that the interaction of this mutant with IQGAP1 is dramatically diminished [39]. It was thus proposed that this mutant localizes to the Golgi apparatus, since IQGAP1 has been shown to promote CDC42 translocation from the Golgi apparatus to the plasma membrane [68].

In conclusion, our study demonstrated that, in addition to those in the switch regions, distinct residues in CDC42 and RAC1-like proteins are required for their association with $IQGAP1^{C794}$, and these residues are missing in nonbinders. Since IQGAPs are involved in many cellular processes, it will be a great advantage to elucidate the respective mechanisms of their scaffolding functions. Our data shed light on the mechanism of RHO GTPase binding to IQGAPs, allowing us to better understand their physical interactions. The $IQGAP1^{C794}$ interaction with CDC42 and RAC1 was found to be slightly different. These interactions remain a subject of further structural analysis. The binding characteristics of other RHO GTPases, including RAC2 and RHOG, to IQGAP proteins in macrophages and endothelial cells and their roles in differentiation, angiogenesis, barrier function, and inflammation await further investigation [69,70].

4. Materials and Methods

Constructs. Different variants' pGEX vectors (pGEX2T and pGEX4T-1) encoding an N-terminal glutathione S-transferase (GST) fusion protein were used to overexpress human IQGAP1^{C79I} (acc. no. P46940; aa 863–1657), IQGAP1^{GRD} (aa 962–1345), human Plexin B1 RBD (acc. no. O43157; aa 1724–1903), human p67^{phox} TRP (acc. no. P19878; aa 1–203), human PAK1 GBD (acc. No. Q13153; aa 57–141), murine TIAM1 DH-PH (acc. no. Q60610; aa 1033–1404), human TRION DH-PH (acc. no. O75962; aa 1226–1535), and human p50^{GAP} (acc. no. Q07960; aa 198–439), as well as human RHO-related genes, that is, RAC1 (acc. no. P63000; aa 1–179), RAC2 (acc. no. P15153; aa 1–192), RAC3 (acc. no. P60763; aa 1–192), RHOG (acc. no. P84095; aa 1–178), RHOA (acc. no. P61586; aa 1–181), RHOB (acc. no. P62745; aa 1–181), RHOC (acc. no. P08134; aa 1–181), CDC42 (acc. no. P60953; aa 1–178), TC10 (acc. no. P17081; aa 2–193), RND1 (acc. no. Q92730; aa 1–232), RND2 (acc. no. P52198; aa 26–184), RND3 (acc. no. P61587; aa, 1–244), RIF (acc. no. Q9HBH0; aa 1–195), and mouse RHOD (acc. no. P97348; aa 2–193). pET23b was used to express IQGAP2^{C975} (acc. No. Q13576; aa 780–1575), and IQGAP3^{C790} (acc. No. Q13576; aa 841–1631). Human DOCK DHR2 (acc. no. Q92608; 1211–1624) was cloned in the pOPIN vector as previously described [71].

Proteins. All proteins were purified according to established protocols [23]. All proteins, except IQGAP2^{C795}, were isolated as glutathione S-transferase (GST) fusion proteins by affinity chromatography on a glutathione Sepharose column in the first step and purified by size-exclusion chromatography after proteolytic cleavage of GST in the second step [23,72]. IQGAP2^{C795} was purified as a His-tagged protein. This protein was isolated from the supernatant via Ni-NTA affinity purification. Nucleotide-free RHO proteins were prepared using alkaline phosphatase (Roche) and phosphodiesterase (Sigma-Aldrich, St. Louis, MO, USA) at 4 °C as previously described [73]. Fluorescent methyl-anthraniloyl (m) was used to generate mGppNHp-bound RHO proteins; GppNHp is a slow-hydrolyzing analog of GTP. The quality and concentrations of the labeled proteins were determined as previously described [73]. RND proteins, which were isolated in the GTP-bound form, could not be loaded with mGppNHp. GTP degradation by alkaline phosphatase, which is normally used to exchange bound nucleotides with other fluorescent nucleotides, led to their precipitation despite the presence of mGppNHp.

GST pull-down assay. Confluent HEK293 cells cultured on 10 cm dishes were lysed in lysis buffer containing 50 mM Tris-HCl, pH 7.5; 1%, 150 mM NaCl; and 10 mM $MgCl_2$ 1% Igepal Ca-630 supplemented with a protease inhibitor tablet (complete protease inhibitor cocktail, EDTA-free, Merck).

The cell lysates were poured into prechilled tubes and centrifuged at 13,000 rpm for 5 min at 4 °C. Glutathione agarose beads were washed with ice-cold buffer and incubated with 10 micrograms each of GST-RHOG, GST-CDC42-bound GppNHp, and GST alone for 40 min on a rotator at 4 °C. Then, the samples were centrifuged and washed three times with cold buffer containing 50 mM Tris-HCl, pH 7.5; 1%, 150 mM NaCl; and 10 mM $MgCl_2$. The HEK293 cell lysates were added to beads, rotated at 4 °C for 40 min, and later centrifuged and washed three times with cold buffer. The samples were mixed with 1-fold Laemmli buffer, boiled for 10 min at 95 °C and resolved by SDS-PAGE. The separated proteins on 10% SDS-polyacrylamide gels were transferred to a nitrocellulose membrane. The proteins on the membrane were detected by mouse monoclonal anti-IQGAP1 antibody ab56529 (Abcam) and mouse monoclonal anti-GST antibody 2624S (Cell Signaling).

Analytical size-exclusion chromatography. CDC42•GppNHp and RAC1•GppNHp were mixed with IQGAP1^{C794} or IQGAP2^{C795} in a buffer containing 30 mM Tris/HCl, pH 7.5; 150 mM NaCl; and 5 mM $MgCl_2$. Analyses were performed at a flow rate of 0.5 mL/min and a fraction volume of 0.5 mL on a Superdex 200 10/300 column (GE Healthcare Life Sciences) using an ÄKTA purifier. The M_Ws for each eluted peak were calculated based on the calibration curve and the partition coefficient plot (Kav = Ve − V0/Vc − V0) versus the logarithm of the M_Ws; Ve, elution volume number; V0, void volume (=8 mL);

Vc, geometric column volume (=24 mL). The eluted fractions were collected and resolved by SDS-PAGE, and the gels stained with Coomassie brilliant blue.

Fluorescence stopped-flow spectrometry. All kinetic parameters (k_{obs}, k_{on}, and k_{off}) assessed in this study were measured using a previously described kinetic analysis protocol [72]. The kinetic parameters were monitored with a stopped-flow apparatus (Hi-Tech Scientific SF-61 and SX20 MV Applied Photophysics), and the analysis was performed as described [72] using excitation wavelengths of 362 nm (for mant) and 546 nm (for tamra). The emission was detected with a cutoff greater than 408 nm (for mant) and 560 nm (for tamra). The GAP-stimulated GTPase reaction was assessed after 0.2 μM tamraGTP-bound RAC1 was mixed with 10 μM $p50^{GAP}$; tamraGTP is the abbreviation for tetramethylrhodamine-labeled GTP [74]. The GEF-catalyzed nucleotide exchange reaction was assessed after 0.2 μM mGDP-bound RAC1 was mixed with 40 μM GDP and 10 μM TIAM1 or DOCK2. The effector association with the RHO proteins was measured after 0.2 μM mGppNHp-bound RHO proteins were mixed with 2 μM C794 of IQGAP1 or C795 of IQGAP2. Dissociation experiments were performed by displacing the bound effector from the complex upon adding excess unlabeled GppNHp-bound RHO proteins. All measurements were performed in 30 mM Tris-HCl, pH 7.5; 10 mM K_2HPO_4/KH_2PO_4, pH 7.4; 2 mM $MgCl_2$; and 3 mM DTT at 25 °C. The data obtained are averages of at least four independent measurements. Competition experiments were carried out by measuring the association of $IQGAP1^{C794}$ with RAC1•mGppNHp in the presence and absence of excess amounts of RAC-binding proteins: TIAM1 DH-PH, TRIO DH-PH, DOCK2 DHR2, $p50^{GAP}$, PAK1 GBD, plexin B1 RBD, and $p67^{Phox}$ TRP. Previous studies have shown that the association of these proteins with RAC1•mGppNHp, except for IQGAP, does not lead to a change in fluorescence [50,58,65,75], which is a crucial prerequisite for stopped-flow fluorometric competition experiments. The experiment was based on the concept that an increase in fluorescence upon IQGAP association with RAC1•mGppNHp is attenuated by any one of the RAC-binding proteins that compete with IQGAP for the same binding sites. The experimental setup was as follows: syringe 1 contained 4 μM $IQGAP1^{C794}$ and 40 μM of the respective RAC-binding proteins in a premixture, and syringe 2 contained 0.4 μM RAC1•mGppNHp. The two samples were rapidly mixed 1:1 with a dead time of 2 msec and injected into an observation cell at a final volume of 70 μL. The measured rate constants were fitted with a single exponential function using the GraFit program (Erithacus software).

Structural analysis. All sequences related to RHO GTPases were retrieved from the UniProt database. Amino acid sequence alignments were performed in the BioEdit program using the ClustalW algorithm [76]. Model structures of RHO GTPases for which no X-ray or NMR structure was available in the PDB were generated with the program MODELLER [77]. The structures generated with MODELLER were RHOG, RIF, RND2, and TCL, and the following PDB entries were used as template structures: 1I4D, 2J1L, 2REX, and 2ATX. Root-mean-square deviation (RMSD) was calculated with the prompt command in the PyMOL program [78]. Structural analysis and electrostatic potential maps were generated using PyMOL molecular viewer, version 1.5.0.4 (Schrödinger, LLC), and the APBS program [78–80], respectively. The APBS program is based on a standard procedure in which the electrostatic solvation energies of individual moieties are subtracted from the electrostatic energy of the complex. Protein molecules were fully charged in accordance with the CHARMm force field. The refinement consisted of a short procedure for minimization (200 steps) of the complex energy with the fixed structure of the GTPases. The nonlinear Poisson-Boltzmann equation was used in the calculation of binding energies and in the calculation of the electrostatic potential around the GTPases. To compare the electrostatic potentials of proteins with different total charges, the positive and negative charges of the proteins were scaled separately to ensure that the electrostatic potential of each amino acid was +1 and −1, respectively. A value of electrostatic potential at a certain space point indicates the tendency of an electron (i.e., general negative charge) placed at this point to be repulsed (red) or attracted (blue). Triangulation of the electrostatic isosurfaces

for graphic representation was performed using the marching cubes algorithm [81]. The final pictures were generated by the Raster3D package [82]. All APBS calculations were performed with the same parameters: values of electrostatic potential were calculated at the points on the regular 3D grid within the cube with side lengths of 80.0 Å and 60.0 Å for the coarse and fine mesh, respectively, while the number of points in each direction was 128 in both cases. The dielectric constants for the protein and solvent were set to 2.0 and 78.0, respectively.

Supplementary Materials: The following are available online at https://www.mdpi.com/article/10.3390/ijms222212596/s1

Author Contributions: M.R.A. conceived and coordinated the study; N.M., K.N., and O.H.F.K. designed, performed, and analyzed the experiments; R.D. and E.A. performed structural analysis; N.M., K.N., O.H.F.K., and M.R.A. directed the experiments, analyzed the data, and wrote the paper. All authors have read and agreed to the published version of the manuscript.

Funding: This study was supported by the European Network on Noonan Syndrome and Related Disorders (NSEuroNet, grant number: 01GM1621B), the German Research Foundation (Deutsche Forschungsgemeinschaft or DFG) through the International Research Training Group "Intra- and interorgan communication of the cardiovascular system" (grant number: IRTG 1902-p6), the German Federal Ministry of Education and Research (BMBF)—German Network of RASopathy Research (GeNeRARe, grant numbers: 01GM1902C), and the German Research Foundation (DFG, grant number: AH 92/8-1).

Institutional Review Board Statement: Not applicable.

Informed Consent Statement: Not applicable.

Data Availability Statement: All the data are in the manuscript.

Acknowledgments: We thank D. Barford, R.A. Cerione, J.G. Collard, A. Hall, A.W. Püschel, K. Rittinger, H.C. Welch, and A. Wittinghofer for sharing reagents, and the group members at the Institute of Biochemistry and Molecular Biology II of the Heinrich Heine University for discussions.

Conflicts of Interest: The authors declare no conflict of interest.

References

1. Abel, A.M.; Schuldt, K.M.; Rajasekaran, K.; Hwang, D.; Riese, M.J.; Rao, S.; Thakar, M.S.; Malarkannan, S. IQGAP1: Insights into the function of a molecular puppeteer. *Mol. Immunol.* **2015**, *65*, 336–349. [CrossRef] [PubMed]
2. Choi, S.; Anderson, R.A. IQGAP1 is a phosphoinositide effector and kinase scaffold. *Adv. Biol. Regul.* **2016**, *60*, 29–35. [CrossRef] [PubMed]
3. Hedman, A.C.; Smith, J.M.; Sacks, D.B. The biology of IQGAP proteins: Beyond the cytoskeleton. *EMBO Rep.* **2015**, *16*, 427–446. [CrossRef] [PubMed]
4. Smith, J.M.; Hedman, A.C.; Sacks, D.B. IQGAPs choreograph cellular signaling from the membrane to the nucleus. *Trends Cell Biol.* **2015**, *25*, 171–184. [CrossRef]
5. Watanabe, T.; Wang, S.; Kaibuchi, K. IQGAPs as Key Regulators of Actin-cytoskeleton Dynamics Mini-review and Review. *Cell Struct. Funct.* **2015**, *40*, 69–77. [CrossRef]
6. Tanos, B.E.; Yeaman, C.; Rodriguez-Boulan, E. An emerging role for IQGAP1 in tight junction control. *Small GTPases* **2018**, *9*, 375–383. [CrossRef]
7. Nussinov, R.; Zhang, M.; Tsai, C.J.; Jang, H. Calmodulin and IQGAP1 activation of PI3Kα and Akt in KRAS, HRAS and NRAS-driven cancers. *Biochim. Biophys. Acta Mol. Basis Dis.* **2018**, *1864*, 2304–2314. [CrossRef]
8. White, C.D.; Brown, M.D.; Sacks, D.B. IQGAPs in cancer: A family of scaffold proteins underlying tumorigenesis. *FEBS Lett.* **2009**, *583*, 1817–1824. [CrossRef]
9. Roy, M.; Li, Z.; Sacks, D.B. IQGAP1 Binds ERK2 and Modulates Its Activity. *J. Biol. Chem.* **2004**, *279*, 17329–17337. [CrossRef]
10. Roy, M.; Li, Z.; Sacks, D.B. IQGAP1 Is a Scaffold for Mitogen-Activated Protein Kinase Signaling. *Mol. Cell. Biol.* **2005**, *25*, 7940–7952. [CrossRef]
11. Ren, J.G.; Li, Z.; Sacks, D.B. IQGAP1 modulates activation of B-Raf. *Proc. Natl. Acad. Sci. USA* **2007**, *104*, 10465–10469. [CrossRef]
12. Bensenor, L.B.; Kan, H.M.; Wang, N.; Wallrabe, H.; Davidson, L.A.; Cai, Y.; Schafer, D.A.; Bloom, G.S. IQGAP1 regulates cell motility by linking growth factor signaling to actin assembly. *J. Cell Sci.* **2007**, *120*, 658–669. [CrossRef]
13. Le Clainche, C.; Schlaepfer, D.; Ferrari, A.; Klingauf, M.; Grohmanova, K.; Veligodskiy, A.; Didry, D.; Le, D.; Egile, C.; Carlier, M.F.; et al. IQGAP1 stimulates actin assembly through the N-wasp-Arp2/3 pathway. *J. Biol. Chem.* **2007**, *282*, 426–435. [CrossRef]

14. Pelikan-Conchaudron, A.; Le Clainche, C.; Didry, D.; Carlier, M.F. The IQGAP1 protein is a calmodulin-regulated barbed end capper of actin filaments: Possible implications in its function in cell migration. *J. Biol. Chem.* **2011**, *286*, 35119–35128. [CrossRef]
15. Usatyuk, P.V.; Gorshkova, I.A.; He, D.; Zhao, Y.; Kalari, S.K.; Garcia, J.G.N.; Natarajan, V. Phospholipase D-mediated Activation of IQGAP1 through Rac1 regulates hyperoxia-induced p47phox translocation and reactive oxygen species generation in lung endothelial cells. *J. Biol. Chem.* **2009**, *284*, 13339–13352. [CrossRef]
16. Kaur, R.; Yuan, X.; Lu, M.L.; Balk, S.P. Increased PAK6 expression in prostate cancer and identification of PAK6 associated proteins. *Prostate* **2008**, *68*, 1510–1516. [CrossRef]
17. Fukata, M.; Watanabe, T.; Noritake, J.; Nakagawa, M.; Yamaga, M.; Kuroda, S.; Matsuura, Y.; Iwamatsu, A.; Perez, F.; Kaibuchi, K. Rac1 and Cdc42 capture microtubules through IQGAP1 and CLIP-170. *Cell* **2002**, *109*, 873–885. [CrossRef]
18. Watanabe, T.; Wang, S.; Noritake, J.; Sato, K.; Fukata, M.; Takefuji, M.; Nakagawa, M.; Izumi, N.; Akiyama, T.; Kaibuchi, K. Interaction with IQGAP1 links APC to Rac1, Cdc42, and actin filaments during cell polarization and migration. *Dev. Cell* **2004**, *7*, 871–883. [CrossRef]
19. Mateer, S.C.; Morris, L.E.; Cromer, D.A.; Benseñor, L.B.; Bloom, G.S. Actin filament binding by a monomeric IQGAP1 fragment with a single calponin homology domain. *Cell Motil. Cytoskeleton* **2004**, *58*, 231–241. [CrossRef]
20. Grohmanova, K.; Schlaepfer, D.; Hess, D.; Gutierrez, P.; Beck, M.; Kroschewski, R. Phosphorylation of IQGAP1 modulates its binding to Cdc42, revealing a new type of Rho-GTPase regulator. *J. Biol. Chem.* **2004**, *279*, 48495–48504. [CrossRef]
21. Kurella, V.B.; Richard, J.M.; Parke, C.L.; LeCour, L.F.; Bellamy, H.D.; Worthylake, D.K. Crystal structure of the GTPase-activating protein-related domain from IQGAP1. *J. Biol. Chem.* **2009**, *284*, 14857–14865. [CrossRef]
22. Li, Z.; McNulty, D.E.; Marler, K.J.M.; Lim, L.; Hall, C.; Annan, R.S.; Sacks, D.B. IQGAP1 promotes neurite outgrowth in a phosphorylation-dependent manner. *J. Biol. Chem.* **2005**, *280*, 13871–13878. [CrossRef]
23. Nouri, K.; Fansa, E.K.; Amin, E.; Dvorsky, R.; Gremer, L.; Willbold, D.; Schmitt, L.; Timson, D.J.; Ahmadian, M.R. IQGAP1 interaction with RHO family proteins revisited: kinetic and equilibrium evidence for multiple distinct binding sites. *J. Biol. Chem.* **2016**, *291*, 26364–26376. [CrossRef]
24. Sila Ozdemir, E.; Jang, H.; Gursoy, A.; Keskin, O.; Li, Z.; Sacks, D.B.; Nussinov, R. Unraveling the molecular mechanism of interactions of the Rho GTPases Cdc42 and Rac1 with the scaffolding protein IQGAP2. *J. Biol. Chem.* **2018**, *293*, 3685–3699. [CrossRef]
25. Wennerberg, K.; Der, C.J. Rho-family GTPases: It's not only Rac and Rho (and I like it). *J. Cell Sci.* **2004**, *117*, 1301–1312. [CrossRef]
26. Jaffe, A.B.; Hall, A. Rho GTPases: Biochemistry and biology. *Annu. Rev. Cell Dev. Biol.* **2005**, *21*, 247–269. [CrossRef]
27. Haga, R.B.; Ridley, A.J. Rho GTPases: Regulation and roles in cancer cell biology. *Small GTPases* **2016**, *7*, 207–221. [CrossRef]
28. Ahmadian, M.R.; Jaiswal, M.; Fansa, E.K.; Dvorsky, R. New insight into the molecular switch mechanism of human Rho family proteins: Shifting a paradigm. *Biol. Chem.* **2013**, *394*, 89–95. [CrossRef]
29. Beljan, S.; Herak Bosnar, M.; Četković, H. Rho Family of Ras-Like GTPases in Early-Branching Animals. *Cells* **2020**, *9*, 2279. [CrossRef]
30. Bishop, A.L.; Hall, A. Rho GTPases and their effector proteins. *Biochem. J.* **2000**, *348*, 241–255. [CrossRef]
31. Dvorsky, R.; Ahmadian, M.R. Always look on the bright site of Rho: Structural implications for a conserved intermolecular interface. *EMBO Rep.* **2004**, *5*, 1130–1136. [CrossRef] [PubMed]
32. Hall, A. Rho family GTPases. *Biochem. Soc. Trans.* **2012**, *40*, 1378–1382. [CrossRef] [PubMed]
33. Elliott, S.F. Biochemical analysis of the interactions of IQGAP1 C-terminal domain with CDC42. *World J. Biol. Chem.* **2012**, *3*, 53. [CrossRef] [PubMed]
34. Zhang, B.; Wang, Z.X.; Zheng, Y. Characterization of the interactions between the small GTPase Cdc42 and its GTPase-activating proteins and putative effectors: Comparison of kinetic properties of Cdc42 binding to the Cdc42-interactive domains. *J. Biol. Chem.* **1997**, *272*, 21999–22007. [CrossRef]
35. Zhang, B.; Chernoff, J.; Zheng, Y. Interaction of Rac1 with GTPase-activating proteins and putative effectors. A comparison with Cdc42 and RhoA. *J. Biol. Chem.* **1998**, *273*, 8776–8782. [CrossRef]
36. Owen, D.; Campbell, L.J.; Littlefield, K.; Evetts, K.A.; Li, Z.; Sacks, D.B.; Lowe, P.N.; Mott, H.R. The IQGAP1-Rac1 and IQGAP1-Cdc42 interactions: Interfaces differ between the complexes. *J. Biol. Chem.* **2008**, *283*, 1692–1704. [CrossRef]
37. Mataraza, J.M.; Briggs, M.W.; Li, Z.; Frank, R.; Sacks, D.B. Identification and characterization of the Cdc42-binding site of IQGAP1. *Biochem. Biophys. Res. Commun.* **2003**, *305*, 315–321. [CrossRef]
38. Li, R.; Debreceni, B.; Jia, B.; Gao, Y.; Tigyi, G.; Zheng, Y. Localization of the PAK1-, WASP-, and IQGAP1-specifying regions of Cdc42. *J. Biol. Chem.* **1999**, *274*, 29648–29654. [CrossRef]
39. Lam, M.T.; Coppola, S.; Krumbach, O.H.F.; Prencipe, G.; Insalaco, A.; Cifaldi, C.; Brigida, I.; Zara, E.; Scala, S.; Di Cesare, S.; et al. A novel disorder involving dyshematopoiesis, inflammation, and HLH due to aberrant CDC42 function. *J. Exp. Med.* **2019**, *216*, 2778–2799. [CrossRef]
40. Nouri, K.; Timson, D.J.; Ahmadian, M.R. New model for the interaction of IQGAP1 with CDC42 and RAC1. *Small GTPases* **2020**, *11*, 16–22. [CrossRef]
41. LeCour, L.; Boyapati, V.K.; Liu, J.; Li, Z.; Sacks, D.B.; Worthylake, D.K. The Structural Basis for Cdc42-Induced Dimerization of IQGAPs. *Structure* **2016**, *24*, 1499–1508. [CrossRef]
42. Identification of a Human RasGAP-Related Protein Containing Calmodulin-Binding Motifs. Available online: https://pubmed.ncbi.nlm.nih.gov/8051149/ (accessed on 26 February 2021).

43. Zhang, B.; Zheng, Y. Negative regulation of Rho family GTPases Cdc42 and Rac2 by homodimer formation. *J. Biol. Chem.* **1998**, *273*, 25728–25733. [CrossRef]
44. Jaiswal, M.; Gremer, L.; Dvorsky, R.; Haeusler, L.C.; Cirstea, I.C.; Uhlenbrock, K.; Ahmadian, M.R. Mechanistic insights into specificity, activity, and regulatory elements of the regulator of G-protein signaling (RGS)-containing Rho-specific guanine nucleotide exchange factors (GEFs) p115, PDZ-RhoGEF (PRG), and leukemia-associated RhoGEF (LARG). *J. Biol. Chem.* **2011**, *286*, 18202–18212. [CrossRef]
45. Martinelli, S.; Krumbach, O.H.F.; Pantaleoni, F.; Coppola, S.; Amin, E.; Pannone, L.; Nouri, K.; Farina, L.; Dvorsky, R.; Lepri, F.; et al. Functional Dysregulation of CDC42 Causes Diverse Developmental Phenotypes. *Am. J. Hum. Genet.* **2018**, *102*, 309–320. [CrossRef]
46. Haeusler, L.C.; Blumenstein, L.; Stege, P.; Dvorsky, R.; Ahmadian, M.R. Comparative functional analysis of the Rac GTPases. *FEBS Lett.* **2003**, *555*, 556–560. [CrossRef]
47. Bhattacharya, M.; Sundaram, A.; Kudo, M.; Farmer, J.; Ganesan, P.; Khalifeh-Soltani, A.; Arjomandi, M.; Atabai, K.; Huang, X.; Sheppard, D. IQGAP1-dependent scaffold suppresses RhoA and inhibits airway smooth muscle contraction. *J. Clin. Investig.* **2014**, *124*, 4895–4898. [CrossRef]
48. Casteel, D.E.; Turner, S.; Schwappacher, R.; Rangaswami, H.; Su-Yuo, J.; Zhuang, S.; Boss, G.R.; Pilz, R.B. Rho isoform-specific Interaction with IQGAP1 promotes breast cancer cell proliferation and migration. *J. Biol. Chem.* **2012**, *287*, 38367–38378. [CrossRef]
49. Fiegen, D.; Blumenstein, L.; Stege, P.; Vetter, I.R.; Ahmadian, M.R. Crystal structure of Rnd3/RhoE: Functional implications. *FEBS Lett.* **2002**, *525*, 100–104. [CrossRef]
50. Fansa, E.K.; Dvorsky, R.; Zhang, S.C.; Fiegen, D.; Ahmadian, M.R. Interaction characteristics of Plexin-B1 with Rho family proteins. *Biochem. Biophys. Res. Commun.* **2013**, *434*, 785–790. [CrossRef]
51. Lapouge, K.; Smith, S.J.M.; Walker, P.A.; Gamblin, S.J.; Smerdon, S.J.; Rittinger, K. Structure of the TPR domain of p67(phox) in complex with Rac·GTP. *Mol. Cell* **2000**, *6*, 899–907. [CrossRef]
52. Ahmadian, M.R.; Hoffmann, U.; Goody, R.S.; Wittinghofer, A. Individual rate constants for the interaction of Ras proteins with GTPase-activating proteins determined by fluorescence spectroscopy. *Biochemistry* **1997**, *36*, 4535–4541. [CrossRef] [PubMed]
53. D'Andrea, L.D.; Regan, L. TPR proteins: The versatile helix. *Trends Biochem. Sci.* **2003**, *28*, 655–662. [CrossRef] [PubMed]
54. Diebold, B.A.; Bokoch, G.M. Molecular basis for Rac2 regulation of phagocyte NADPH oxidase. *Nat. Immunol.* **2001**, *2*, 211–215. [CrossRef] [PubMed]
55. Hoffman, G.R.; Cerione, R.A. Rac inserts its way into the immune response. *Nat. Immunol.* **2001**, *2*, 194–196. [CrossRef]
56. Dvorsky, R.; Blumenstein, L.; Vetter, I.R.; Ahmadian, M.R. Structural Insights into the Interaction of ROCKI with the Switch Regions of RhoA. *J. Biol. Chem.* **2004**, *279*, 7098–7104. [CrossRef]
57. Sinha, N.; Smith-Gill, S. Electrostatics in Protein Binding and Function. *Curr. Protein Pept. Sci.* **2005**, *3*, 601–614. [CrossRef]
58. Hemsath, L.; Dvorsky, R.; Fiegen, D.; Carlier, M.F.; Ahmadian, M.R. An electrostatic steering mechanism of Cdc42 recognition by Wiskott-Aldrich syndrome proteins. *Mol. Cell* **2005**, *20*, 313–324. [CrossRef]
59. Vascon, F.; Gasparotto, M.; Giacomello, M.; Cendron, L.; Bergantino, E.; Filippini, F.; Righetto, I. Protein electrostatics: From computational and structural analysis to discovery of functional fingerprints and biotechnological design. *Comput. Struct. Biotechnol. J.* **2020**, *18*, 1774–1789. [CrossRef]
60. Bivona, T.G.; Quatela, S.E.; Bodemann, B.O.; Ahearn, I.M.; Soskis, M.J.; Mor, A.; Miura, J.; Wiener, H.H.; Wright, L.; Saba, S.G.; et al. PKC regulates a farnesyl-electrostatic switch on K-Ras that promotes its association with Bcl-XL on mitochondria and induces apoptosis. *Mol. Cell* **2006**, *21*, 481–493. [CrossRef]
61. Zhou, Y.; Hancock, J.F. A novel prenyl-polybasic domain code determines lipid-binding specificity of the K-Ras membrane anchor. *Small GTPases* **2020**, *11*, 220–224. [CrossRef]
62. Connolly, A.; Gagnon, E. Electrostatic interactions: From immune receptor assembly to signaling. *Immunol. Rev.* **2019**, *291*, 26–43. [CrossRef]
63. McLaughlin, S.; Murray, D. Plasma membrane phosphoinositide organization by protein electrostatics. *Nature* **2005**, *438*, 605–611. [CrossRef]
64. Jaiswal, M.; Dvorsky, R.; Ahmadian, M.R. Deciphering the molecular and functional basis of Dbl family proteins: A novel systematic approach toward classification of selective activation of the Rho family proteins. *J. Biol. Chem.* **2013**, *288*, 4486–4500. [CrossRef]
65. Amin, E.; Jaiswal, M.; Derewenda, U.; Reis, K.; Nouri, K.; Koessmeier, K.T.; Aspenström, P.; Somlyo, A.V.; Dvorsky, R.; Ahmadian, M.R. Deciphering the molecular and functional basis of RHOGAP family proteins: A systematic approach toward selective inactivation of RHO family proteins. *J. Biol. Chem.* **2016**, *291*, 20353–20371. [CrossRef]
66. Wennerberg, K.; Forget, M.A.; Ellerbroek, S.M.; Arthur, W.T.; Burridge, K.; Settleman, J.; Der Channing, C.; Hansen, S.H. Rnd proteins function as RhoA antagonists by activating p190 RhoGAP. *Curr. Biol.* **2003**, *13*, 1106–1115. [CrossRef]
67. Chardin, P. Function and regulation of Rnd proteins. *Nat. Rev. Mol. Cell Biol.* **2006**, *7*, 54–62. [CrossRef]
68. Swart-Mataraza, J.M.; Li, Z.; Sacks, D.B. IQGAP1 is a component of Cdc42 signaling to the cytoskeleton. *J. Biol. Chem.* **2002**, *277*, 24753–24763. [CrossRef]
69. Joshi, S.; Singh, A.R.; Zulcic, M.; Bao, L.; Messer, K.; Ideker, T.; Dutkowski, J.; Durden, D.L. Rac2 controls tumor growth, metastasis and M1-M2 macrophage differentiation in vivo. *PLoS ONE* **2014**, *9*, 95893. [CrossRef]

70. Okuyama, Y.; Nagashima, H.; Ushio-Fukai, M.; Croft, M.; Ishii, N.; So, T. IQGAP1 restrains T-cell costimulation mediated by OX40. *FASEB J.* **2020**, *34*, 540–554. [CrossRef]
71. Kulkarni, K.; Yang, J.; Zhang, Z.; Barford, D. Multiple factors confer specific Cdc42 and Rac protein activation by dedicator of cytokinesis (DOCK) nucleotide exchange factors. *J. Biol. Chem.* **2011**, *286*, 25341–25351. [CrossRef]
72. Hemsath, L.; Ahmadian, M.R. Fluorescence approaches for monitoring interactions of Rho GTPases with nucleotides, regulators, and effectors. *Methods* **2005**, *37*, 173–182. [CrossRef]
73. Jaiswal, M.; Dubey, B.N.; Koessmeier, K.T.; Gremer, L.; Ahmadian, M.R. Biochemical assays to characterize rho GTPases. *Methods Mol. Biol.* **2012**, *827*, 37–58. [CrossRef]
74. Eberth, A.; Ahmadian, M.R. In vitro GEF and GAP assays. *Curr. Protoc. Cell Biol.* **2009**, *43*, 14.9.1–14.9.25.
75. Fiegen, D.; Haeusler, L.C.; Blumenstein, L.; Herbrand, U.; Dvorsky, R.; Vetter, I.R.; Ahmadian, M.R. Alternative Splicing of Rac1 Generates Rac1b, a Self-activating GTPase. *J. Biol. Chem.* **2004**, *279*, 4743–4749. [CrossRef]
76. Hall, T.A. BioEdit A User-Friendly Biological Sequence Alignment Editor and Analysis Program for Windows 95/98/NT. *Nucl. Acid Symp. Ser.* **1999**, *41*, 95–98. Available online: https://www.scirp.org/(S(lz5mqp453edsnp55rrgjct55))/reference/ReferencesPapers.aspx?ReferenceID=1383440 (accessed on 22 February 2021).
77. Webb, B.; Sali, A. Comparative protein structure modeling using MODELLER. *Curr. Protoc. Bioinforma.* **2016**, *2016*, 5.6.1–5.6.37. [CrossRef]
78. DeLano, W.L. *The PyMOL Molecular Graphics System*; Delano Scientific: San Carlos, CA, USA, 2002. Available online: https://www.scirp.org/(S(vtj3fa45qm1ean45vvffcz55))/reference/ReferencesPapers.aspx?ReferenceID=1958992 (accessed on 22 February 2021).
79. Holst, M.; Baker, N.; Wang, F. Adaptive multilevel finite element solution of the Poisson-Boltzmann equation I. Algorithms and examples. *J. Comput. Chem.* **2001**, *22*, 475. [CrossRef]
80. Baker, N.A.; Sept, D.; Joseph, S.; Holst, M.J.; McCammon, J.A. Electrostatics of nanosystems: Application to microtubules and the ribosome. *Proc. Natl. Acad. Sci. USA* **2001**, *98*, 10037–10041. [CrossRef]
81. Lorensen, W.E.; Cline, H.E. Marching Cubes: A High Resolution 3D Surface Construction Algorithm. In Proceedings of the 14th Annual Conference on Computer Graphics and Interactive Techniques, SIGGRAPH 1987, Anaheim, CA, USA, 27–31 July 1987; Association for Computing Machinery, Inc.: New York, NY, USA, 1987; Volume 21, pp. 163–169.
82. Merritt, E.A.; Bacon, D.J. Raster3D: Photorealistic Molecular Graphics. *Methods Enzymol.* **1997**, *277*, 505–524. [CrossRef]

CHAPTER V. THE PSEUDO-NATURAL PRODUCT RHONIN TARGETS RHOGDI

Akbarzadeh M, Flegel J, Patil S, Shang E, Narayan R, Buchholzer M, Kazemein Jasemi NS, Grigalunas M, Krzyzanowski A, Abegg D, Shuster A, Ptowski M, Karatas H, Karageorgis G, Mosaddeghzadeh N, Zischinsky ML, Merten C, Golz C, Brieger L, Strohmann C, Antonchick AP, Janning P, Adibekian A, Goody RS, Ahmadian MR, Ziegler S, Waldmann H

DOI: 10.1002/anie.202115193

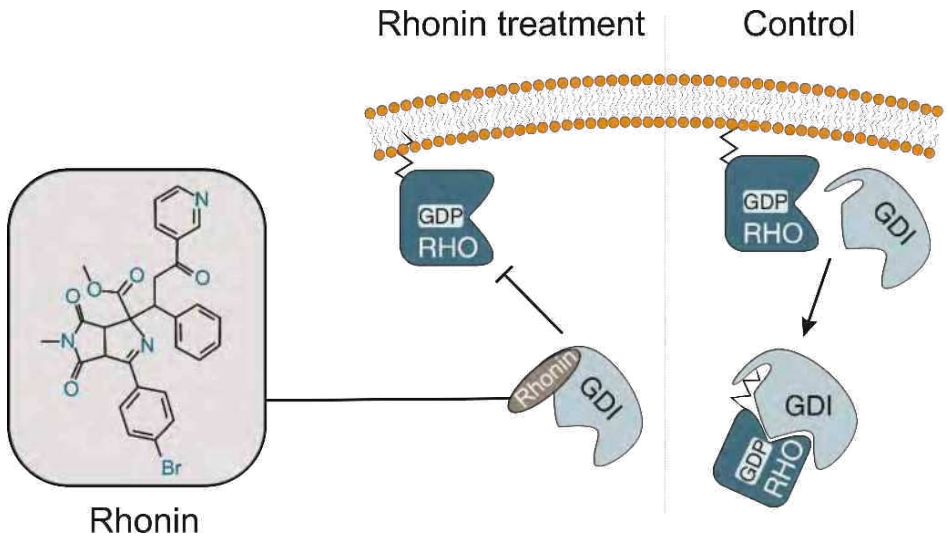

Status:	Published in April 2022
Journal:	Angewandte Chemie International Edition
Impact factor:	16.82
Contribution:	5%
	Purification of RAC1 and RHOGDI1, fluorescence polarization measurements, data evaluation.

Medicinal Chemistry Hot Paper

How to cite: Angew. Chem. Int. Ed. 2022, 61, e202115193
International Edition: doi.org/10.1002/anie.202115193
German Edition: doi.org/10.1002/ange.202115193

The Pseudo-Natural Product Rhonin Targets RHOGDI

*Mohammad Akbarzadeh[+], Jana Flegel[+], Sumersing Patil[+], Erchang Shang, Rishikesh Narayan, Marcel Buchholzer, Neda S. Kazemein Jasemi, Michael Grigalunas, Adrian Krzyzanowski, Daniel Abegg, Anton Shuster, Marco Potowski, Hacer Karatas, George Karageorgis, Niloufar Mosaddeghzadeh, Mia-Lisa Zischinsky, Christian Merten, Christopher Golz, Lucas Brieger, Carsten Strohmann, Andrey P. Antonchick, Petra Janning, Alexander Adibekian, Roger S. Goody, Mohammad Reza Ahmadian, Slava Ziegler, and Herbert Waldmann**

Abstract: For the discovery of novel chemical matter *generally* endowed with bioactivity, strategies may be particularly efficient that combine previous insight about biological relevance, e.g., natural product (NP) structure, with methods that enable efficient coverage of chemical space, such as fragment-based design. We describe the de novo combination of different 5-membered NP-derived N-heteroatom fragments to structurally unprecedented "*pseudo-natural products*" in an efficient complexity-generating and enantioselective one-pot synthesis sequence. The pseudo-NPs inherit characteristic elements of NP structure but occupy areas of chemical space not covered by NP-derived chemotypes, and may have novel biological targets. Investigation of the pseudo-NPs in unbiased phenotypic assays and target identification led to the discovery of the first small-molecule ligand of the RHO GDP-dissociation inhibitor 1 (RHOGDI1), termed Rhonin. Rhonin inhibits the binding of the RHOGDI1 chaperone to GDP-bound RHO GTPases and alters the subcellular localization of RHO GTPases.

Introduction

The discovery of novel chemical matter, which *in general* is endowed with bioactivity and biological relevance, is at the heart of chemical biology. Such compound classes may have new biological targets and modes of action, and, therefore, their bioactivities will best be evaluated in unbiased target-agnostic phenotypic assays followed by target identification and validation.[1]

Strategies for the design of such novel compound classes can draw inspiration from previous insights about the biological relevance of compound classes, as for instance gained by Biology Oriented Synthesis (BIOS). In BIOS, complex natural product (NP) scaffolds are reduced to less complex, synthetically better accessible structures retaining the characteristic properties of the guiding NPs.[2] However,

[*] Dr. M. Akbarzadeh,[+] J. Flegel,[+] Dr. S. Patil,[+] Dr. E. Shang, Prof. Dr. R. Narayan, Dr. M. Grigalunas, A. Krzyzanowski, Dr. M. Potowski, Prof. Dr. H. Karatas, Dr. G. Karageorgis, Prof. Dr. A. P. Antonchick, Dr. P. Janning, Dr. S. Ziegler, Prof. Dr. Dr. h.c. H. Waldmann
Department of Chemical Biology
Max Planck Institute of Molecular Physiology
Otto-Hahn-Straße 11, 44227 Dortmund (Germany)
E-mail: herbert.waldmann@mpi-dortmund.mpg.de

Prof. Dr. R. S. Goody
Max Planck Institute of Molecular Physiology
Otto-Hahn-Straße 11, 44227 Dortmund (Germany)

Dr. M. Akbarzadeh,[+] Dr. M. Buchholzer, Dr. N. S. Kazemein Jasemi, N. Mosaddeghzadeh, Prof. Dr. M. R. Ahmadian
Institute of Biochemistry and Molecular Biology II, Medical Faculty and University Hospital Düsseldorf, Heinrich Heine University Düsseldorf
Universitätsstrasse 1, Building 22.03.05
40225 Düsseldorf (Germany)

Prof. Dr. R. Narayan
School of Chemical and Materials Sciences
IIT Goa, Farmagudi, Ponda, Goa-403401 (India)

Dr. D. Abegg, A. Shuster, Prof. Dr. A. Adibekian
Department of Chemistry, The Scripps Research Institute
130 Scripps Way, Jupiter, FL 33458 (USA)

Dr. M.-L. Zischinsky
Lead discovery center
Otto-Hahn-Str. 15, 44227 Dortmund (Germany)

Prof. Dr. C. Merten
Faculty of Chemistry and Biochemistry, Organic Chemistry II, Ruhr-University Bochum
Universitätsstrasse 150, 44780 Bochum (Germany)

A. Krzyzanowski, Dr. C. Golz, L. Brieger, Prof. Dr. C. Strohmann, Prof. Dr. Dr. h.c. H. Waldmann
Faculty of Chemistry and Chemical Biology
Technical University Dortmund
Otto-Hahn-Straße 6, 44221 Dortmund (Germany)

[+] These authors contributed equally to this work.

BIOS covers only a small fraction of natural product-like chemical space and arrives at compound classes that may retain similar bioactivities to the guiding NPs. These limitations can be overcome by the design and synthesis of "pseudo-natural products" (pseudo-NPs).[3] In the pseudo-NP concept, NP fragments that represent NP structure and properties[4] are combined through de novo combination to afford unprecedented NP-inspired compound classes not accessible by known biosynthesis pathways. Pseudo-NPs inherit characteristic NP structures and properties but go beyond the chemical space explored by nature and, therefore, promise to have unexpected bioactivity and targets.

Five-membered N-heterocycles are defining structural units of numerous natural products with diverse bioactivities. For instance, succinimides occur in the haterumaimides, which have antitumor activity,[5] and the fungal metabolite hirsutellone, which is active against *Mycobacterium tuberculosis* (Figure 1a).[6] Pyrrolines are characteristic structural elements of eudistomin alkaloids with calmodulin antagonist activity (Figure 1a)[7] and the tobacco alkaloid myosmine[8] (Figure 1a). Pyrrolidines occur as isolated scaffolds in various structurally simple alkaloids like nicotine or fused to other scaffolds in structurally more complex alkaloids, such as dendrobine (Figure 1a). Additionally, two pyrrolidines are fused in a bicyclic [2.2.1] arrangement in the nicotin receptor agonist epibatidine (Figure 1a).

Inspired by this diverse occurrence of five-membered N-heterocycles in NPs, we designed and synthesized a pseudo-NP collection that combines these fragments in different connectivities. Phenotypic investigation of bioactivity and target identification led to the discovery of Rhonin, a novel inhibitor of Hedgehog-induced osteogenesis. Rhonin is the first small-molecule ligand of the RHO GDP-dissociation inhibitor1 (RHOGDI1) and inhibits binding of this chaperone to GDP-bound RHO GTPases.

Results and Discussion

Establishment of a Tandem Catalysis Sequence

For the synthesis of a pseudo-NP collection, we aimed to combine 5-membered N-heterocycle fragments in a complexity-generating manner with different connectivities (Figure 1b), i.e., such that i) the fragments do not share atoms and are linked via one bond (monopodal connection; gray bonds, Figure 1b), ii) they share two atoms linked via a common bond (edge fusion; red bonds, Figure 1b) or they may be linked in a bicyclic arrangement sharing three atoms and two bonds (bridge fusion; magenta bonds, Figure 1b). Thereby related but different pseudo-NPs could be synthesized based on a limited set of fragments.

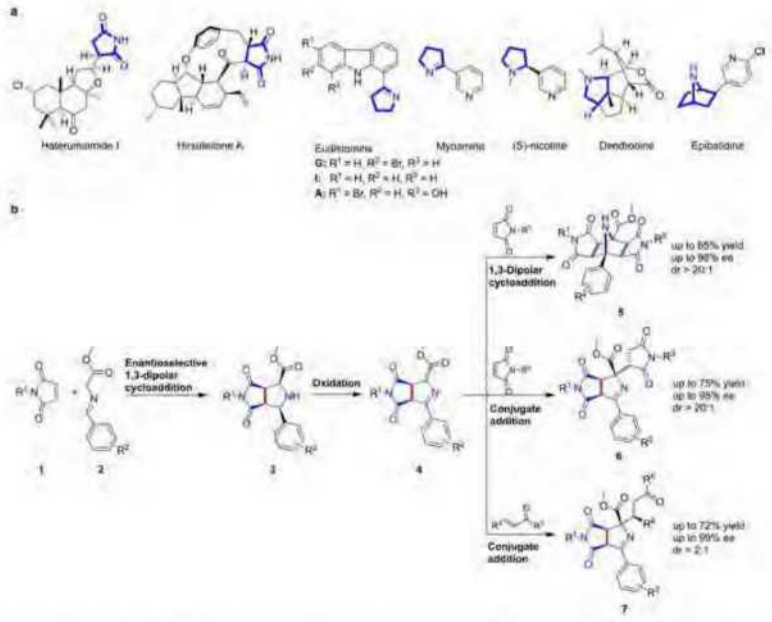

Figure 1. Design of a pseudo-NP collection. a) Representative natural products embodying 5-membered N-heterocycles. b) Tandem catalysis sequence for the synthesis of a pseudo-NP collection containing 5-membered N-heterocycles in different connectivities.

It was initially planned to construct pyrrolidines by means of an enantioselective dipolar cycloaddition of azomethine ylides with maleimides. This would yield an edge-fused pyrrolidine-succinimide pseudo-NP class, i.e., **3**. Subsequent oxidation of the pyrrolidine to an imine would give rise to a succinimide-pyrroline combination **4** which can undergo further transformations. The imine could be converted to a new azomethine ylide which might react with maleimides in a second 1,3-dipolar cycloaddition to yield a double fused pseudo-NP class **5** combining two succinimides with a bicyclic azabicyclo[2.2.1] scaffold, characteristic of epibatidine. Nucleophilic addition to maleimides will generate a pseudo-NP class **6** containing two fragments linked by an edge fusion to a second succinimide fragment via a monopodal connection. Finally, conjugate addition to different α,β-unsaturated electrophiles would yield pseudo-NPs **7** in which a succinimide and a pyrrolidine are combined, and the side chain may contain additional natural product fragments.

Using this divergent synthesis approach, several different pseudo-NP types would be efficiently accessible by the unified strategy. This synthetic strategy offers several attractive features. The metal-catalyzed 1,3-dipolar cycloaddition and the subsequent regio- and chemoselective oxidation could potentially be coupled in a novel tandem catalytic approach in which the metal catalyst used for the cycloaddition could be employed in combination with an oxidizing agent. Such tandem catalysis sequences combining two or more mechanistically distinct chemical reactions are considered to be particularly attractive since they enable expedient generation of molecular complexity and efficiency of the reaction sequence.[9] Hitherto, Δ^1-pyrrolines have been synthesized by means of cycloaddition of Münchnones to electron-deficient alkenes.[10] Thus, the tandem catalysis strategy outlined in Figure 1b also represents a novel method for the synthesis of this compound class.

In order to identify suitable reaction conditions for the tandem catalysis sequence, azomethine ylide **2a** (Figure 2a; R^2=4-Br) was allowed to react with *N*-methylmaleimide **1a** (R^1=Me) in CH_2Cl_2 in the presence of $Cu(CH_3CN)_4PF_6$ as catalyst and (*R*)-Fesulphos [(R_p)-2-(*tert*-butylthio)-1-(diphenylphosphino)ferrocene)] as chiral ligand for the 1,3-dipolar cycloaddition.[11,12] Subsequent addition of TBHP as a terminal oxidant for the Cu^I-catalyzed oxidation gratifyingly yielded the desired pyrroline **4a** (Figure 1b; R^1=Me, R^2=4-Br) in good yield (82%) and with complete regio- and chemoselectivity. The combination of these two steps with the envisaged additional cycloaddition and conjugate addition required careful optimization of the reaction conditions. After substantial experimentation, the use of 1.5 equivalents of both Et_3N and maleimide in CH_2Cl_2 was found to be best for the formation of Michael addition products **6** (Tables S1 and S2). The double cycloaddition to tricyclic products **5** proceeded best in the presence of 0.5 equiv. of DBU in THF (Tables S3–S5). Furthermore, in the presence of CH_2Cl_2 and DBU, nucleophilic addition to acyclic Michael acceptors occurred and products **7** were obtained.

Synthesis of a Pseudo-NP Collection

The successful identification of conditions for the selective formation of the three envisaged compound classes enabled the assembly of a pseudo-NP collection. In the synthesis of double cycloadducts **5** (Figure 2a, conditions A), the aromatic ring of the azomethine ylides **2** can be varied (Figure 2a, **5a–5d**). Electron-donating and -accepting substituents on the phenyl ring were well tolerated and gave the cycloadducts **5a–d** in good yields and with generally excellent enantioselectivity (see Figure 2a). In addition, both aryl and alkyl maleimides could be successfully employed in the reaction in different order and combinations (Figure 2a, **5e**, **5f**).

Under the conditions identified for the Michael addition to unsaturated cyclic electrophiles, a variety of azomethine ylide precursors embodying electron-donating or -withdrawing substituents gave the corresponding products **6** in excellent yields and with high diastereo- and enantioselectivities (Figure 2a, **6a–6e**), regardless of the electronic nature and the position of the substituents on the phenyl ring in the dipole. Acyclic electrophiles, like chalcone and different vinyl- and ethynyl ketones, gave the corresponding products **7** in good yields and with high *ee* (Figure 2a, **7a–7i**). Notably, in the case of styryl-vinyl ketone, a single regioisomer **7e** was obtained in 72% yield. Ethynyl-phenyl ketone yielded the *E*-isomer **7g** in 71% yield. In total 21 pseudo-NPs were synthesized in multi-milligram amounts (typically ca. 5 mg per compound).

The relative configuration of the cycloadducts was unambiguously assigned by means of a crystal structure obtained for *rac*-**6a**. By means of VCD spectroscopy,[13] the absolute configuration of the major diastereomer of **7a** was determined as (*S*)-**7a**. For **7h**, a crystal structure analysis established the *E*-configuration (see the Supporting Information for details). Since the diastereoselectivity of the last functionalization is determined by the two stereocenters established in the first cycloaddition, the absolute configuration of all other compounds was assigned by analogy. For a mechanistic proposal to rationalize the observed direction and level of stereochemical induction (see Scheme S1).

These results demonstrate that the synthesis strategy efficiently yields a pseudo-NP collection including the formation of three stereocenters and a tetrasubstituted carbon atom in a highly efficient one-pot sequence.

Cheminformatic Analysis

The chemical space occupied by the new pseudo-NPs was analyzed by employing the natural-product score (NP-score) distribution.[14] Since the majority of the collection is defined by pyrrolines fused to succinimides, the NP-score was calculated for the sub-library defined by this scaffold and compared with both the score calculated for NPs in ChEMBL[15] and the score calculated for marketed and experimental drugs listed in DrugBank.[16] The pyrroline-derived pseudo-NPs display a narrow distribution in a region of the NP-score graph which is sparsely covered by NPs

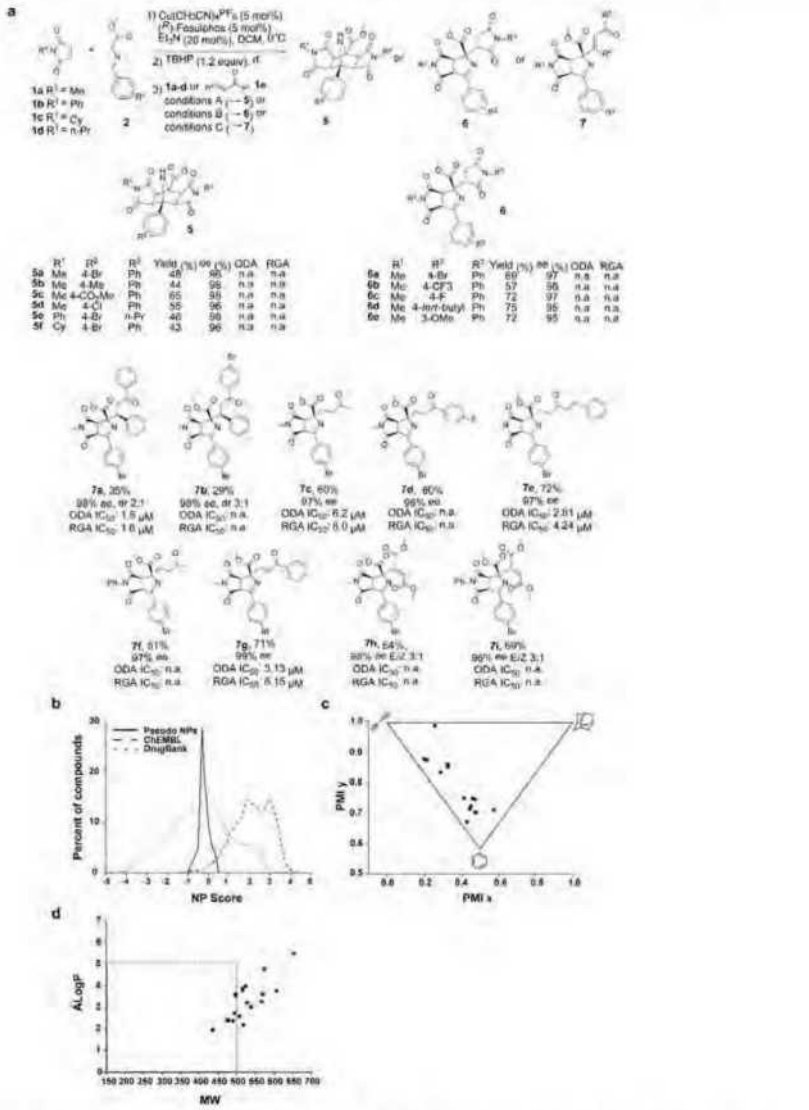

Figure 2. Synthesis of pseudo-NPs that occupy a distinct portion of chemical space. a) Reaction conditions: A) **1a–d** (3 equiv), DBU (0.5 equiv), THF, rt; B) **1a–d** (1.5 equiv), Et_3N (1.5 equiv), DCM, rt; C) **1e** (1.5 equiv), DBU (0.5 equiv), DCM, rt. For **7a**, the yield represents the epimeric mixture of the phenylethyl ketone. ODA: Osteoblast differentiation assay. RGA: Reporter gene assay. All ODA and RGA data are mean values of three independent experiments ($n = 3$). b) NP-likeness score comparison of NPs represented in ChEMBL (dashed curve), Drugbank (dotted curve) and succinimide-pyrroline pseudo-NPs (solid curve). c) PMI plot for succinimide-pyrroline pseudo-NPs. The average of PMI coordinate distribution is shown by a cross. d) ALogP vs MW plot of succinimide-pyrroline pseudo-NPs.

(Figure 2b). The fact that the combination of NP-derived fragments yields compounds with properties diverging from NPs may be counterintuitive. However, the fragment combination generated here is not encountered in nature,

such that the NP-score distribution of these pseudo-NPs should be different to NPs themselves. Comparison to the set of compounds in DrugBank, which represent approved and experimental drugs, demonstrates that the pseudo-NPs display NP-scores in an area populated by synthetically accessible, biologically relevant molecules. However, an additional analysis of the principal moments of inertia (PMI),[17] used as a measure of molecular shape, revealed that the pseudo-NPs described here have a higher degree of three-dimensionality (Figure 2c) compared to typical synthetically accessible compound collections.[18] This observation is supported by the average distance of points from the rod-disc axis calculated to 0.12, as well as the cumulative distance value which was calculated to 2.41 (see Figure S1). Additionally, the average fraction of sp^3 hybridised carbons of these pseudo-NPs was calculated to 0.31, which is within literature suggested range of values[19] (see Table S6). Further analysis using Lipinski-rule-of-5 (Lipinski-Ro5) criteria showed that only 42% of the newly synthesized collection is included within the limits of drug-like space (Figure 2d), indicating that de novo combinations of NP-derived fragments may result in compound collections with enhanced biological relevance even when deviating from established metrics.

The analysis indicates that the succinimide-pyrroline pseudo-NPs may occupy a previously not accessible fraction of NP-inspired chemical space, reflecting the fact that they are not obtainable via current biosynthetic pathways. This novel scaffold may be endowed by design with advantageous physiochemical properties, as the pseudo-NP collection displays a NP-score distribution closer to the region occupied by approved drugs, even if the majority of the collection falls outside the limits of Lipinski-Ro5 space.

Biological Evaluation of the Pseudo-NP Collection

Investigation of biological activity of the pseudo-NP collection in several cell-based assays monitoring modulation of autophagy, Wnt signaling, reactive oxygen species (ROS) induction, Notch signaling and Hedgehog (Hh) signaling revealed that the pyrroline-derived compounds are selective inhibitors of Hh pathway-dependent osteogenesis in pluripotent mouse mesenchymal C3H/10T1/2 cells (see Table S7). Osteogenesis was induced using the Smoothened agonist purmorphamine. Despite the limited number of compounds, trends for structure–activity correlation became apparent. Thus, extension of the ketone part of the most potent hit **7a**, e.g., by introduction of a *para*-Br substituent into the aryl ketone part (to yield **7b**), or by a *para*-F into the phenyl ring (Figure 2a, compare **7a** and **7d**) abolished activity. The configuration of the stereocenter generated in the final conjugate addition to yield, e.g., **7a**, has only minor impact on the bioactivity (Table S7, compare **7a** and its epimer **7a–epi**). A phenyl group is not strictly required in the electrophile for activity, since methyl-vinyl ketone yielded active compound **7e** (Figure 2a and Table S7, **7e**). However, in the presence of a phenyl group derived either from the aryl ketone part or the aryl-vinyl part of the electrophile, activity is higher (compare **7e** to **7a**, **7g** and **7e**). All active cycloadducts were derived from N-methyl maleimide. If the methyl group was replaced by a phenyl substituent, activity was lost (compare **7e** and **7f**). The most potent compound **7a** inhibited Hh-induced osteogenesis with an IC_{50} value of 1.5 ± 0.2 μM (Figure 3a and 3b). Interestingly, **7a** did not inhibit the orthogonal GLI-dependent reporter gene assay in Sonic hedgehog (Shh)-LIGHT2 cells. However, **7a** moderately and partially suppressed the expression of the Hh target genes *Ptch1* and *Gli1* to approx. 50% at a concentration of 5 μM (Figure 3c).

Most Hh pathway inhibitors target the seven-pass transmembrane protein Smoothened (SMO), e.g. Vismodegib and cyclopamine, and often affect SMO ciliary localization.[20] However, **7a** did not displace the SMO binder BODIPY-cyclopamine from SMO (Figure S2) and did not affect the localization of SMO to cilia as indicated by the co-localization of acetylated tubulin (as a ciliary marker) and SMO (Figure 3d). Thus, **7a** inhibits purmorphamine-induced osteogenesis most likely without targeting SMO.

Osteogenesis Inhibitor 7a Targets RHOGDI1

For target identification, affinity probes **8** and **9** (Figure 4a) were synthesized based on the structure–activity relationship. The corresponding Boc-protected analogue of **8** retained significant osteogenesis inhibiting activity (**S10a**, $IC_{50} = 12.0 \pm 1.2$ μM, Table S7), whereas the Boc-protected analogue of **9** was inactive (**S10b**, Table S7). Label-free quantification of proteins that selectively bound to the active probe **8** as compared to the control probe **9** indicated RHO GDP-dissociation inhibitor 1 (RHOGDI1), Filamin-B and Filamin-C as potential targets (Table S8). Subsequent immunoblotting after the pulldown confirmed the selective enrichment of RHOGDI1 but not of Filamin-B and Filamin-C (Figure 4b and Figure S3). Furthermore, excess of **S10a** prevented the enrichment of RHOGDI1 by probe **8** (Figure 4c). These findings point toward RHOGDI1 as a target of **7a**.

RHOGDI1 is a chaperone for geranylgeranylated (GerGer) proteins, in particular the RHO GTPases.[21] The major fraction (90–95%) of prenylated RHO GTPases are maintained in a stable soluble state in the cytosol by RHOGDI1.[22] **7a** directly binds to RHOGDI1 as demonstrated for the fluorescent **7a** derivative **10**, which displays a dissociation constant (K_D) of 3.01 μM and 8.5 μM for RHOGDI1Δ15 and RHOGDI1Δ25, respectively (Figures 4d and 4e). RHOGDI1 can extract GDP-bound inactive RHO GTPases from membranes and sequesters them in the cytosol. In an in vitro liposome sedimentation assay,[23] addition of RHOGDI1 to liposomes loaded with prenylated GDP-bound RAC1 resulted in extraction of RAC1, i.e., RAC1 was detected in the soluble fraction (Figure 4f). However, in the presence of **7a** and RHOGDI1, RAC1 remained bound to the liposomes, i.e., RAC1 was detected in the insoluble fraction. This finding indicates that **7a** inhibits the extraction of RAC1 by RHOGDI1. The

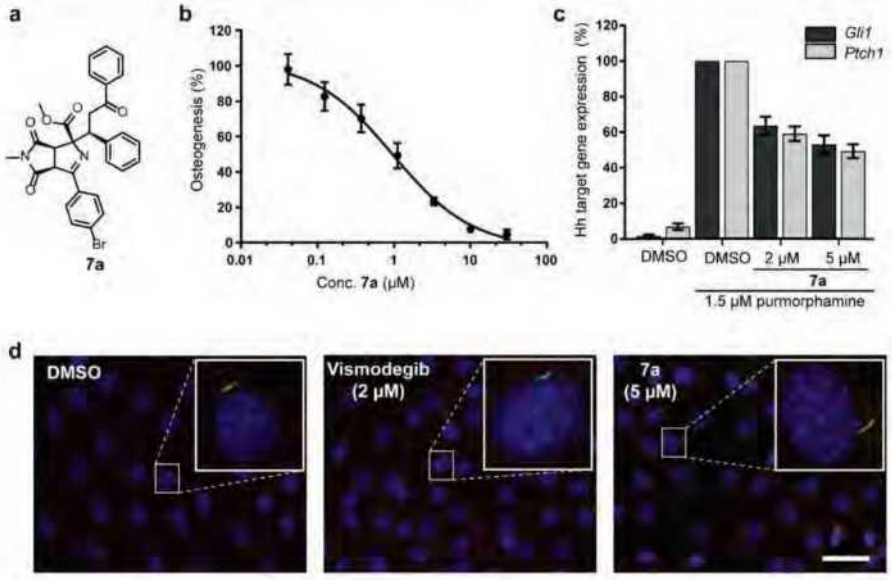

Figure 3. Compound **7a** inhibits Hh-induced osteogenesis. a) Structure of **7a**. b) Hh-induced osteogenesis in C3H/10T1/2 cells. Cells were treated with 1.5 μM purmorphamine and compound **7a** for 96 h prior to detection of alkaline phosphatase activity (mean + SD, $n=3$). c) C3H/10T1/2 cells were treated with purmorphamine (1.5 μM) and of **7a** or DMSO for 96 h prior to detection of the expression of *Ptch1*, *Gli1*, *Ap3d1* and *Gapdh* by means of RT-qPCR. (mean ± SD, $n=3$). d) Detection of SMO in cilia in NIH/3T3 cells. Blue: nuclei; red: SMO; green: acetylated tubulin. Insets: representative single cilia. Scale bar: 10 μm.

structurally similar analog **7d** (Figure 2a), which did not inhibit osteogenesis, also did not inhibit extraction of RAC1 from liposomes (Figure 4f). Similar results were obtained in a liposome flotation assay[24] (Figures S4a and S4b). In addition to RAC1, **7a** also inhibited the RHOGDI1-mediated extraction of RHOA and CDC42 (Figure S4c and S4d). **7a** slowed down the kinetics of geranylgeranylated RAC1 extraction mediated by RHOGDI1 in a surface plasmon resonance (SPR) setup using immobilized synthetic $PI(4,5)P_2$-rich liposomes loaded with geranylgeranylated GDP-bound RAC1, whereas the inactive derivative **7d** did not (Figures S5a–S5c). These results suggest that **7a** may directly modulate the RHOGDI1-RAC1 interaction. To gain insight into the binding site for **7a** on RHOGDI1, competition between fluorescent derivative **10** and prenylated RAC1 was monitored. Addition of prenylated RAC1 to a pre-formed **10**-RHOGDI1 complex reduced fluorescence polarization, indicating displacement of **10** from RHOGDI1 (Figure 4g). However, non-prenylated RAC1 was able to bind RHOGDI1 but could not displace the ligand. Moreover, increasing concentrations of **7a** competed with the binding of RHOGDI1 to a GerGer-RAB1 peptide, which was previously shown to bind to the prenyl-binding pocket of RHOGDI1 (Figure 4h).[25] Probe **10** also bound to RHOGDI2 and RHOGDI3 (Figure 4e). In order to determine selectivity for binding to RHOGDI, displacement of fluorescein-labelled atorvastatin (K_D = 58 nm) from the prenyl-binding pocket of the lipoprotein chaperone PDEδ was investigated.[26] PDEδ preferably binds farnesylated lipoproteins like the RAS and RHEB. **7a** does not compete with fluorescein-labelled atorvastatin for binding to PDEδ (Figure S5d). Moreover, probe **10** binds to PDEδ only at higher concentrations (Figure S5e), thus demonstrating selectivity for RHOGDI.

Compound **7a** exhibited limited solubility in our experiments. To enhance solubility, the phenyl rings attached to the pyrroline part of **7a** were replaced with pyridines. For simplification of derivatization, these compounds were synthesized through an alternative two-step protocol (see the Supporting Information and Scheme S2). The pyridine derivatives were either as potent or more potent than the original compound **7a** in the osteogenesis assay while displaying better kinetic solubility (Table S9).

We selected compound **7l** (280 mg were readily obtained) for further investigations as it most potently inhibited purmorphamine-induced osteogenesis (Figure 5a and 5b), while displaying good kinetic solubility of 47.3 μM (Table S9) and permeability (41.1% flux in a parallel artificial membrane permeability assay: PAMPA). Similar to **7a**, compound **7l** did not suppress GLI-dependent reporter gene expression and only slightly reduced the expression of the Hh target genes *Ptch1* and *Gli1* (Figure 5c and Fig-

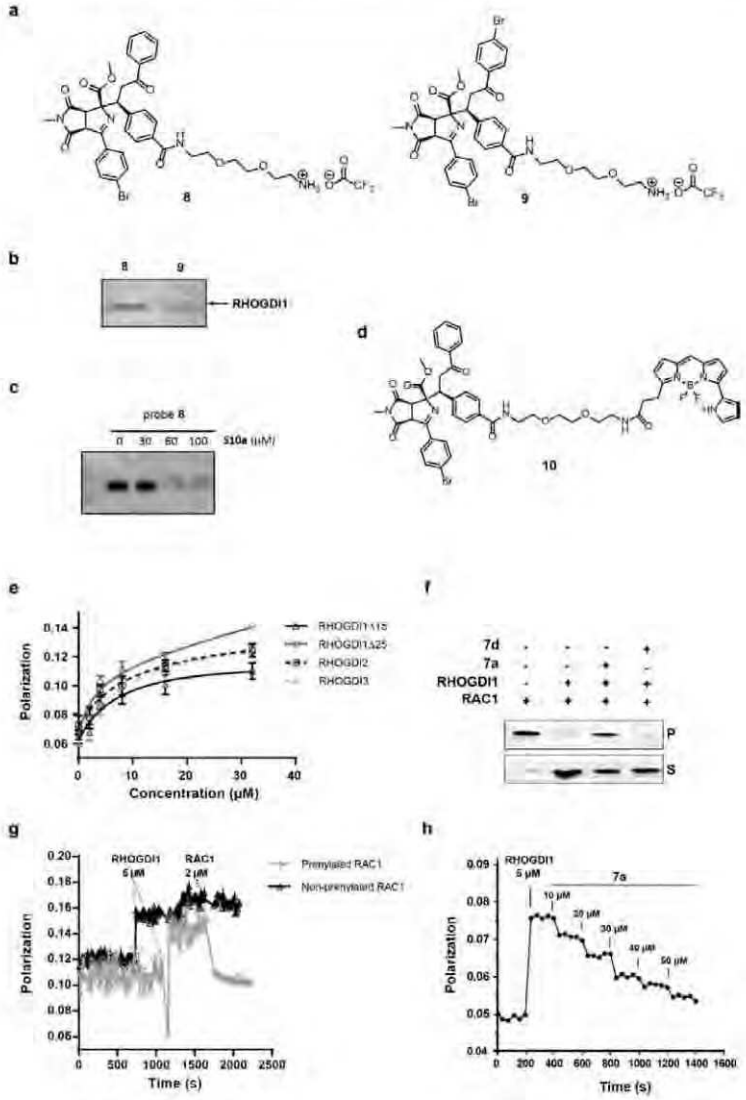

Figure 4. Compound **7a** is a RHOGDI1 inhibitor. a) Structure of the affinity probes **8** and **9**. b) Affinity-based enrichment of RHOGDI1 from NIH/3T3 lysates by probe **8** as compared to probe **9** and detection using a RHOGDI1 antibody. c) Competition pulldown was performed as in b in presence of **S10a** as a competitor. d) Structure of the fluorescent derivative **10**. e) Binding of derivative **10** to RHOGDI1-3. K_D (RHOGDI1Δ15): 8.51 μM, K_D (RHOGDI1Δ25): 3.09 μM; K_D (RHOGDI2): 9.08 μM; K_D (RHOGDI3): 11.45 μM. Fluorescence polarization measurements using **10** and RHOGDI1-3. Representative data (mean values + SD, $n = 3$). f) Displacement of prenylated GDP-bound RAC1 from liposomes by GST-RHOGDI1 in the presence or absence of 50 μM **7a** or inactive derivative **7d** as determined using a liposome sedimentation assay. Representative data ($n = 3$). P: pellet; S: supernatant. g) Competition of derivative **10** with RAC1. Fluorescence polarization measurements after adding 2 μM prenylated RAC1 or non-prenylated RAC1 to 2 μM compound **10** and 5 μM RHOGDI1. Representative data ($n = 3$). h) Fluorescence polarization measurements upon titration of **7a** into a mixture of 5 μM FITC-labelled GerGer-Rab1 peptide and 50 μM RHOGDI1.

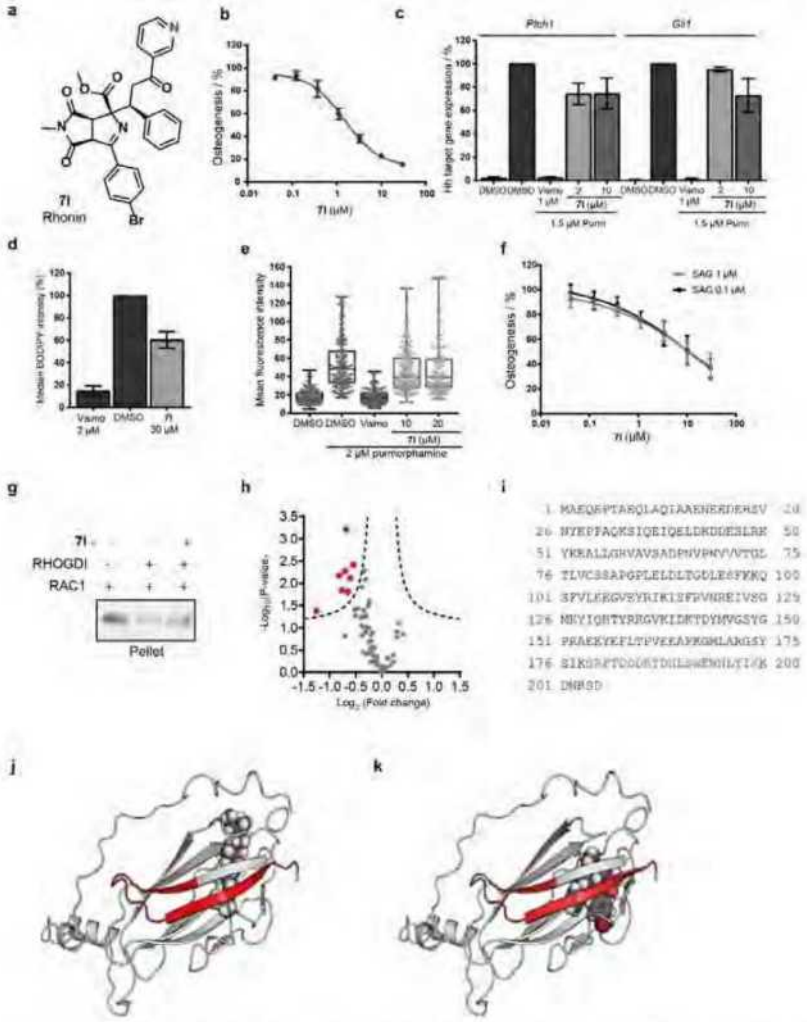

Figure 5. Rhonin (**7l**) inhibits osteogenesis and binds to RHOGDI1. a) Structure of compound **7l** termed Rhonin. b) C3H/10T1/2 cells were treated with 1.5 μM purmorphamine and compound **7l** for 96 h prior to determination of alkaline phosphatase activity. Data are mean values + SD, $n = 3$. c) C3H/10T1/2 cells were treated with purmorphamine (1.5 μM) and **7l** or DMSO for 96 h prior to detection of the expression levels of *Ptch1*, *Gli1*, *Ap3d1* and *Gapdh* using of RT-qPCR (mean values ± SD, $n = 3$). d) SMO binding assay upon treatment of cells with BODIPY-cyclopamine followed by addition of **7l**, Vismodegib or DMSO and quantification of SMO-bound BODIPY-cyclopamine using flow cytometry. e) Ciliary localization of SMO in NIH/3T3 cells. Representative results; each data point represents the intensity value of one single cilium. Statistical significance was evaluated using an unpaired t-test with a confidence interval of 95% ($p \leq$ n.s.). f) Influence of **7l** on osteogenesis in presence of 1 μM or 0.1 μM of SAG and of **7l** (mean values ± SD, $n = 3$). g) Displacement of prenylated GDP-bound RAC1 from synthetic liposomes by GST-RHOGDI1 in the presence or absence of 50 μM **7l** as determined using a liposome sedimentation assay. Representative data ($n = 3$). For uncropped blot see Figure S14. h) Limited proteolysis of RHOGDI1 in presence of 100 μM **7l**. Volcano plot (FDR = 0.05, $S_0 = 0.1$) of the identified and quantified peptides of RHOGDI (≈95% sequence coverage). i) Mapping of proteinase K-protected peptides (amino acids 179–199) in the amino acid sequence of RHOGDI1. Protected lysines detected using the STPyne probe are shown in blue. j) and k) Mapping of proteinase K-protected peptides in the structure of RHOGDI1 with the bound geranylgeranyl group (j) and a computationally predicted model of the RHOGDI1-**7l** complex (k). Red coloration: region protected from proteinase K-mediated proteolysis in presence of compound **7l**. The structures were prepared based on the PDB entry 1HH4.

ure S6a). However, **7l** inhibited the expression of the alkaline phosphatase gene (*Alpl*) which is in line with suppression of osteogenesis (Figure S6b). We detected a partial decrease in BODIPY-cyclopamine fluorescence in SMO-expressing cells (Figure 5d). However, in the presence of **7l** and upon stimulation with purmorphamine, SMO was localized to the cilia (Figure 5e) and cilia formation was not affected (Figure S6c). To further address putative SMO targeting by **7l**, we explored **7l**-mediated suppression of osteogenesis in the presence of low and high concentrations of the SMO agonist SAG. Compounds like Vismodegib that target the heptahelical bundle of SMO, display decreased potency in the presence of high doses of SAG, which itself binds to the heptahelical bundle as well (Figure S6d).[27] Derivative **7l** displayed similar potency in the presence of 0.1 μM and 1 μM SAG and behaved like GANT61 (Figure 5f and Figure S6e). Thus, **7l** does not appear to influence osteogenesis through modulation of SMO.

In agreement with the observations for **7a**, compound **7l** inhibited RHOGDI1-mediated extraction of RAC1 from liposomes (Figure 5g). Whereas non-prenylated TAMRA-GDP-RAC1 bound to RHOGDI1 with a K_D of 5.7 μM, which is in agreement with previous reports,[28] in the presence of **7l** the K_D value for the RHOGDI1-RAC1 interaction increased to 133.3 μM, which indicates that **7l** does interfere with RHOGDI1-RAC1-GDP complex formation (Figures S6f). Based on the obtained results, the measured affinity between probe **10** and RHOGDI1 is K_D= 3.1–8.5 μM (from Figure 4e) and is in line with the K_i for **7l** of ca. 2.2 μM (as determined by the Cheng–Prusoff equation using data from Figures S6f). The K_D for the binding of probe **10** to RHOGDI1 might appear to be too low to interfere with the extremely high affinity GerGer-RAC1/RHOGDI1 interaction (K_D=ca. 10^{-11} M),[29] and this would be true if **7l** and GerGer-RAC1 were competing directly for binding to RHOGDI1 in the absence of other factors. However, as shown in Figure 4f, there is a clear displacement of RAC1 from its complex with RHOGDI1 in the presence of liposomes. The reason for this is that there is already substantial competition for RAC1 binding to RHOGDI1 from the high concentration of lipids that are able to bind RAC1 with relatively high affinity, and this competition can be modified by **7l**. As shown in Figure S7, there is a predicted displacement of RAC1 from RHOGDI1 in the micromolar to hundreds of micromolar range of **7l** concentration. At 50 μM**7l**, ca. 50% of RAC1 is bound to liposomes, in approximate agreement with the results of Figure 4f and Figure 5g. Effectively, **7l** acts as a buffer that reduces the free concentration of RHOGDI1 and this leads to the effects seen.

To map the binding site of **7l** in RHOGDI1, we performed a limited proteolysis analysis of RHOGDI1. Mass spectrometry revealed that several peptides in the 179–199 amino acid sequence were protected from proteinase K-mediated proteolysis in the presence of compound **7l** (Figure 5h and i and Table S10). These proteolysis-protected peptides are located in the protein structure adjacent to the geranylgeranyl binding site (Figure 5j and 5k). This finding suggests binding of **7l** in the GerGer-binding pocket. As the conformotypic peptides contained a lysine residue, we employed the lysine-reactive probe STPyne (Figure S6g) to label lysines in a lysate of HEK293T cells expressing human RHOGDI1. In the presence of compound **7l**, lysines 186 and 199 in RHOGDI1 were less efficiently labeled, thus indicating a limited access of STPyne to these residues due to compound binding (Figure 5i and Table S11). Furthermore, a possible binding pose and contacts of the ligand in the GerGer pocket were predicted using computational methods. Docking into the binding site was performed using an induced fit docking (IFD) methodology, which was followed by a molecular dynamics (MD) simulation with explicit waters. The COSY and NOESY 2D NMR results for **7l** in chloroform clearly show that the imine is the preferred tautomer in solution. An enamine structure was considered for the docking as well because the solution situation may not be directly comparable to the compound in complex with the protein.[30] Ab-initio IFD methodology afforded credible poses for both imine-like and enamine-like tautomers of **7l** in the flexible binding site of RHOGDI1 (Figure S8). The best poses for the two tautomers afforded satisfactory docking scores, with enamine giving somewhat better results. None of the poses generated for the imine matched with the experimentally obtained structure–activity information for the tested compounds, whereas the orientation found for the enamine-like structure seemed to be in agreement with the physical data. The difference in the observed results could be explained by the significant geometry change of the compound core in the two tautomers (Figure S9). Therefore, further calculations and computational analysis were performed with the enamine. The ligand in the resulting pose is stabilized in the protein pocket throughout the entire MD simulation (120 ns; Figure S10 and Table S12). Notable interactions of compound **7l** with the C-terminal β-strand of RHOGDI1 (Trp194, Leu196 and Ile198) were observed (Figure S11 and Video S1), thus, providing a plausible explanation for the observed increase in the proteolytic stability of the terminal protein region in the presence of **7l**. These findings confirm RHOGDI1 as a direct target of compound **7l**. Therefore, compound **7l** was termed Rhonin.

RHOGDI is a Negative Regulator of Osteogenesis

To examine the role of RHOGDI1 in purmorphamine-induced osteogenesis, we depleted RHOGDI1 by means of a small interfering RNA (knockdown efficiency: 88%; Figure S12a). Purmorphamine-mediated osteoblast differentiation was increased upon RHOGDI1 depletion using siRNA (Figure 6a). By analogy, RHOGDI1 knockdown along with simultaneous activation of the Hh pathway increased the levels of the Hh target genes *Ptch1* and *Gli1* (Figure 6b). Conversely, RHOGDI1 overexpression decreased Hh pathway activity (Figure 6c and Figure S12b). These results indicate that RHOGDI1 is a negative regulator of purmorphamine-induced osteogenesis.

Our findings establish a link between RHOGDI1 and osteogenesis. The influence of RHO GTPases on osteoblast

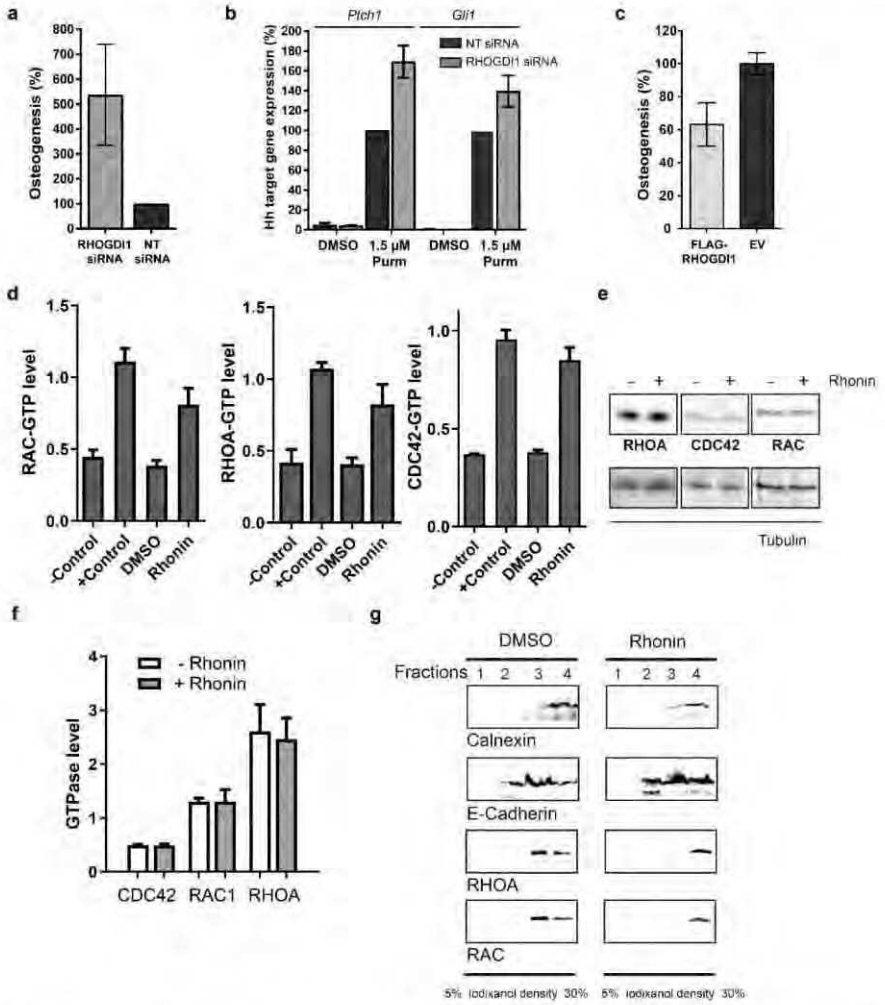

Figure 6. RHOGDI1 is a negative regulator of osteogenesis. a) and b) Influence of RHOGDI1 knockdown. a) Osteogenesis assay upon RHOGDI1 knockdown. NT: control siRNA (mean values ± SD, $n = 3$). Knockdown efficiency: 88%. See also Figure S12a. b) *Ptch1* and *Gli1* expression upon RHOGDI1 knockdown in C3H/10T1/2 cells (mean values ± SD, $n = 3$). c) Influence of RHOGDI overexpression on osteogenesis (mean values ± SD, $n = 3$). See also Figure S12b. d) Detection of GTP-bound RHO GTPases by means of G-LISA upon treatment with 10 µM Rhonin for 24 h.—Control: lysis buffer; + Control: respective constitutively active GTPase (mean values ± SD, $n = 3$). e) and f) Influence of Rhonin (10 µM) on the total cellular levels of RHO GTPases upon treatment for 24 h detected using immunoblotting (e). Quantification of band intensities in relation to the loading control tubulin is shown in f (mean values ± SD, $n = 3$). g) Distribution of RHO GTPases in different cellular fractions upon treatment with Rhonin (10 µM). On a separate gel, calnexin and E-cadherin were detected as markers for ER and plasma membrane, respectively. For uncropped blots see Figure S14.

differentiation is cell- and context-dependent and would depend on the employed system since activity of RHO GTPases will depend on different factors, i.e. phosphorylation, ubiquitination, GEFs, GAPs and possibly other effectors.[31] In human mesenchymal stem cells, RHOA and ROCK were positively correlated with commitment to the osteoblast lineage.[32] We detected suppression of purmorphamine-induced osteogenesis by inhibitors of RAC or ROCK

(see Table S13). RHOGDI1 modulation by Rhonin has an effect on Hh-induced osteogenesis opposite to RHOGDI1 depletion. Such divergence between chemical and genetic perturbations has been observed before and, actually, may differentiate a chemical-biological analysis form a genetic investigation.[33] Genetic knockout or knockdown remove or reduce the target protein, whereas small molecules modulate individual binding sites or functions. RHOGDI1 recognizes its target GTPases via two binding sites. While Rhonin affects binding to the prenyl-binding pocket, RHOGDI1 knockdown abolishes binding to both sites.

Rhonin Activates RHO GTPases by Inhibiting RHOGDI1

Since RHOGDI1 is a regulator of RHO GTPases, small-molecule modulator of RHOGDI1 should affect the activity of RHO GTPases. Rhonin increased the levels of GTP-bound RHO GTPases (Figure 6d), which is in accordance with inhibition of RHOGDI1 activity. Rhonin did not alter the total levels of the three RHO GTPases (Figure 6e and 6f). Interference with RHOGDI1 function should alter the subcellular localization of RHO GTPases.[22] Indeed, treatment with Rhonin led to a shift of the membrane-bound RHO GTPases from the plasma membrane to the endoplasmic reticulum (ER) membrane (Figure 6g). Thus, upon treatment with Rhonin the amount of RHOA and RAC1 at the ER membrane increases. This finding suggests mislocalization of RHO GTPases. RHO GTPases are involved in cell migration which may depend on different RHO GTPases, cell type or stimulus.[34] Therefore, we investigated the migration of NIH/3T3 cells in the presence of Rhonin using a wound healing assay. Similar to the RHOA inhibitor I (C3 toxin), Rhonin moderately inhibited wound closure and, thus, cell migration (Figure S13).

Conclusion

We validate the "pseudo-natural product" concept by the design, synthesis and evaluation of a compound collection that combines five-membered N-heterocycles (i.e. pyrrolidines, pyrrolines and succinimides) characteristic for NP classes with different structure and different biosynthetic origin, in novel arrangements and with different connectivities. The novel pseudo-NP Rhonin proved to be an inhibitor of Hh-induced osteogenesis but does not efficiently target canonical Hh signaling and SMO in particular and may therefore target downstream osteogenic pathways.[35] In conclusion, we report the first small molecule that directly targets RHOGDI, impairs RHOGDI function as well as the activity of RHO GTPases and promises to be an invaluable tool to explore RHO GTPase-related biology.

Acknowledgements

This work was supported by the Max Planck Society and the European Research Council under the European Union's Seventh Framework Programme (FP7/2007-2013, ERC Grant agreement no. 268309), as well as the German Research Foundation (DFG, AH 92/8-1), the Cluster of Excellence RESOLV ("Ruhr Explores Solvation") (EXC-2033, project 390677874; formerly EXC 1069), the International Research Training Group (IRTG 1902, SP6), the European Network on Noonan Syndrome and Related Disorders (NSEuroNet, 01GM1621B), the German Federal Ministry of Education and Research—German Network of RASopathy Research (GeNeRARe, 01GM1902C) and the Scripps Research Institute. We thank Dr. Sonja Sievers and the Compound Management and Screening Center (COMAS), Dortmund, Germany for screening the compounds and Beate Schölermann and Christine Nowak (Max Planck Institute, Dortmund) for technical support. We thank Lena Knauer and Kathrin Louven (Technical University Dortmund) for performing X-ray crystallographic analysis. We are grateful towards Dr. Peter Bieling (Max Planck Institute of Molecular Physiology, Dortmund), Dr. Leif Dehmelt (Technical University Dortmund), Dr. Peter t'Hart (Chemical Genomics Centre, Dortmund) and Dr. Oliver Rocks (Max Delbrück Center for Molecular Medicine, Berlin) for valuable discussions. Open Access funding enabled and organized by Projekt DEAL.

Conflict of Interest

G.K. is an employee of AstraZeneca, U.K.

Data Availability Statement

The data that support the findings of this study are available from the corresponding author upon reasonable request.

Keywords: Inhibitors · Liposomes · Osteogenesis · Proteins · Pseudo-Natural Products · RHOGDI · Small Molecules

[1] a) A. Ursu, H. Waldmann, *Bioorg. Med. Chem. Lett.* **2015**, *25*, 3079; b) B. K. Wagner, S. L. Schreiber, *Cell Chem. Biol.* **2016**, *23*, 3; c) F. Vincent, P. Loria, M. Pregel, R. Stanton, L. Kitching, K. Nocka, R. Doyonnas, C. Steppan, A. Gilbert, T. Schroeter, M. C. Peakman, *Sci. Transl. Med.* **2015**, *7*, 293ps15.
[2] H. van Hattum, H. Waldmann, *J. Am. Chem. Soc.* **2014**, *136*, 11853.
[3] a) G. Karageorgis, E. S. Reckzeh, J. Ceballos, M. Schwalfenberg, S. Sievers, C. Ostermann, A. Pahl, S. Ziegler, H. Waldmann, *Nat. Chem.* **2018**, *10*, 1103; b) G. Karageorgis, D. J. Foley, L. Laraia, H. Waldmann, *Nat. Chem.* **2020**, *12*, 227; c) G. Karageorgis, D. J. Foley, L. Laraia, S. Brakmann, H. Waldmann, *Angew. Chem. Int. Ed.* **2021**, *60*, 15705; *Angew. Chem.* **2021**, *133*, 15837.
[4] B. Over, S. Wetzel, C. Grutter, Y. Nakai, S. Renner, D. Rauh, H. Waldmann, *Nat. Chem.* **2013**, *5*, 21.
[5] M. J. Uddin, S. Kokubo, K. Ueda, K. Suenaga, D. Uemura, *J. Nat. Prod.* **2001**, *64*, 1169.
[6] M. Isaka, N. Rugseree, P. Maithip, P. Kongsaeree, S. Prabpai, Y. Thebtaranonth, *Tetrahedron* **2005**, *61*, 5577.

[7] J. i Kobayashi, H. Nakamura, Y. Ohizumi, Y. Hirata, *Tetrahedron Lett.* **1986**, *27*, 1191.
[8] S. Tyroller, W. Zwickenpflug, E. Richter, *J. Agric. Food Chem.* **2002**, *50*, 4909.
[9] T. L. Lohr, T. J. Marks, *Nat. Chem.* **2015**, *7*, 477.
[10] a) A. D. Melhado, G. W. Amarante, Z. J. Wang, M. Luparia, F. D. Toste, *J. Am. Chem. Soc.* **2011**, *133*, 3517; b) W. Sun, G. Zhu, C. Wu, G. Li, L. Hong, R. Wang, *Angew. Chem. Int. Ed.* **2013**, *52*, 8633; *Angew. Chem.* **2013**, *125*, 8795.
[11] A. P. Antonchick, C. Gerding-Reimers, M. Catarinella, M. Schürmann, H. Preut, S. Ziegler, D. Rauh, H. Waldmann, *Nat. Chem.* **2010**, *2*, 735.
[12] R. Narayan, M. Potowski, Z.-J. Jia, A. P. Antonchick, H. Waldmann, *Acc. Chem. Res.* **2014**, *47*, 1296.
[13] C. Merten, T. P. Golub, N. M. Kreienborg, *J. Org. Chem.* **2019**, *84*, 8797.
[14] P. Ertl, S. Roggo, A. Schuffenhauer, *J. Chem. Inf. Model.* **2008**, *48*, 68.
[15] A. P. Bento, A. Gaulton, A. Hersey, L. J. Bellis, J. Chambers, M. Davies, F. A. Krüger, Y. Light, L. Mak, S. McGlinchey, M. Nowotka, G. Papadatos, R. Santos, J. P. Overington, *Nucleic Acids Res.* **2014**, *42*, D1083.
[16] V. Law, C. Knox, Y. Djoumbou, T. Jewison, A. C. Guo, Y. Liu, A. Maciejewski, D. Arndt, M. Wilson, V. Neveu, A. Tang, G. Gabriel, C. Ly, S. Adamjee, Z. T. Dame, B. Han, Y. Zhou, D. S. Wishart, *Nucleic Acids Res.* **2014**, *42*, D1091.
[17] W. H. B. Sauer, M. K. Schwarz, *J. Chem. Inf. Comput. Sci.* **2003**, *43*, 987.
[18] I. Colomer, C. J. Empson, P. Craven, Z. Owen, R. G. Doveston, L. Churcher, S. P. Marsden, A. Nelson, *Chem. Commun.* **2016**, *52*, 7209.
[19] F. Lovering, J. Bikker, C. Humblet, *J. Med. Chem.* **2009**, *52*, 6752.
[20] T. L. Lin, W. Matsui, *OncoTargets Ther.* **2012**, *5*, 47.
[21] R. Garcia-Mata, E. Boulter, K. Burridge, *Nat. Rev. Mol. Cell Biol.* **2011**, *12*, 493.
[22] E. Boulter, R. Garcia-Mata, C. Guilluy, A. Dubash, G. Rossi, P. J. Brennwald, K. Burridge, *Nat. Cell Biol.* **2010**, *12*, 477.
[23] S.-C. Zhang, L. Gremer, H. Heise, P. Janning, A. Shymanets, I. C. Cirstea, E. Krause, B. Nürnberg, M. R. Ahmadian, *PLoS One* **2014**, *9*, e102425.
[24] J. Bigay, J. F. Casella, G. Drin, B. Mesmin, B. Antonny, *EMBO J.* **2005**, *24*, 2244.
[25] T. Mejuch, G. Garivet, W. Hofer, N. Kaiser, E. K. Fansa, C. Ehrt, O. Koch, M. Baumann, S. Ziegler, A. Wittinghofer, H. Waldmann, *Angew. Chem. Int. Ed.* **2017**, *56*, 6181; *Angew. Chem.* **2017**, *129*, 6277.
[26] A. R. Shepard, R. E. Conrow, I. H. Pang, N. Jacobson, M. Rezwan, K. Rutschmann, D. Auerbach, R. Sriramaratnam, V. W. Cornish, *ACS Chem. Biol.* **2013**, *8*, 549.
[27] J. K. Chen, J. Taipale, K. E. Young, T. Maiti, P. A. Beachy, *Proc. Natl. Acad. Sci. USA* **2002**, *99*, 14071.
[28] A. R. Newcombe, R. W. Stockley, J. L. Hunter, M. R. Webb, *Biochemistry* **1999**, *38*, 6879.
[29] Z. Tnimov, Z. Guo, Y. Gambin, U. T. Nguyen, Y. W. Wu, D. Abankwa, A. Stigter, B. M. Collins, H. Waldmann, R. S. Goody, K. Alexandrov, *J. Biol. Chem.* **2012**, *287*, 26549.
[30] a) Y. C. Martin, *J. Comput.-Aided Mol. Des.* **2009**, *23*, 693; b) P. Pospisil, P. Ballmer, L. Scapozza, G. Folkers, *J. Recept. Signal Transduction* **2003**, *23*, 361; c) A. D. Bochevarov, E. Harder, T. F. Hughes, J. R. Greenwood, D. A. Braden, D. M. Philipp, D. Rinaldo, M. D. Halls, J. Zhang, R. A. Friesner, *Int. J. Quantum Chem.* **2013**, *113*, 2110.
[31] a) R. G. Hodge, A. J. Ridley, *Nat. Rev. Mol. Cell Biol.* **2016**, *17*, 496; b) G. V. Pusapati, J. H. Kong, B. B. Patel, A. Krishnan, A. Sagner, M. Kinnebrew, J. Briscoe, L. Aravind, R. Rohatgi, *Dev. Cell* **2018**, *44*, 271; c) K. Huck, C. Sens, C. Wuerfel, C. Zoeller, I. A. Nakchbandi, *Int. J. Mol. Sci.* **2020**, *21*, 385; d) M. Onishi, Y. Fujita, H. Yoshikawa, T. Yamashita, *Cell Death Dis.* **2013**, *4*, e698; e) D. Harmey, G. Stenbeck, C. D. Nobes, A. J. Lax, A. E. Grigoriadis, *J. Bone Miner. Res.* **2004**, *19*, 661.
[32] R. McBeath, D. M. Pirone, C. M. Nelson, K. Bhadriraju, C. S. Chen, *Dev. Cell* **2004**, *6*, 483.
[33] a) Z. A. Knight, K. M. Shokat, *Cell* **2007**, *128*, 425; b) W. A. Weiss, S. S. Taylor, K. M. Shokat, *Nat. Chem. Biol.* **2007**, *3*, 739.
[34] A. J. Ridley, *Curr. Opin. Cell Biol.* **2015**, *36*, 103.
[35] D. S. Amarasekara, S. Kim, J. Rho, *Int. J. Mol. Sci.* **2021**, *22*, 2851.

Manuscript received: November 25, 2021
Accepted manuscript online: February 16, 2022
Version of record online: March 2, 2022

CHAPTER VI. CDC42-IQGAP INTERACTIONS SCRUTINIZED: NEW INSIGHTS INTO THE BINDING PROPERTIES OF THE GAP-RELATED DOMAIN

Niloufar Mosaddeghzadeh, Silke Pudewell, Farhad Bazgir, Neda S. Kazemein Jasemi, Oliver H. F Krumbach, Lothar Gremer, Dieter Willbold, Radovan Dvorsky, Mohammad R. Ahmadian

DOI: 10.3390/ijms23168842

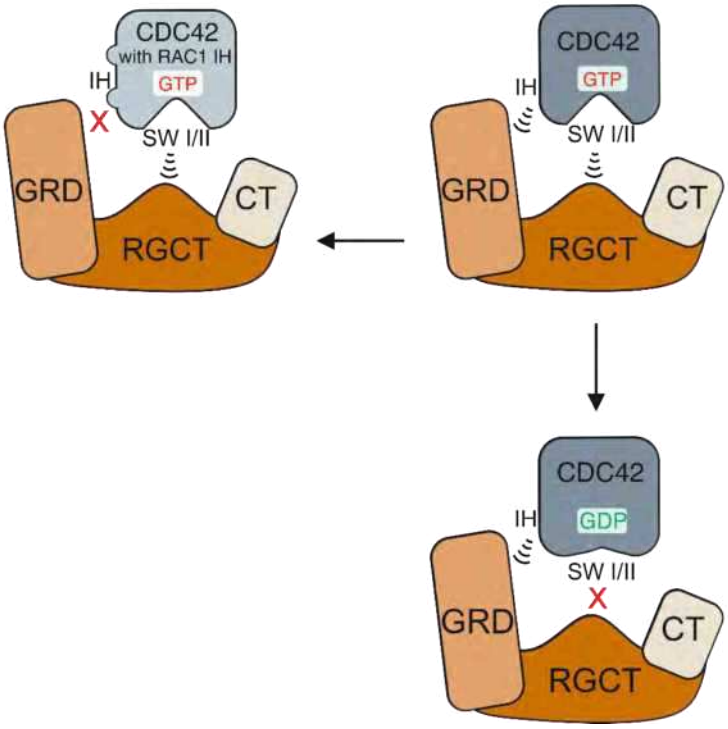

Status:	Published in August 2022
Journal	International Journal of Molecular Sciences
Impact factor:	6.20
Contribution:	50%
	Expression and purification of RHO GTPases and IQGAPs, preparation of nucleotide-free form of RHO GTPases, protein interaction analyses including fluorescence polarization measurements, stopped-flow measurements and pull-down assay, figure preparation and illustration, drafting and writing the manuscript.

International Journal of
Molecular Sciences

MDPI

Article

CDC42-IQGAP Interactions Scrutinized: New Insights into the Binding Properties of the GAP-Related Domain

Niloufar Mosaddeghzadeh [1,†], Silke Pudewell [1,†], Farhad Bazgir [1], Neda S. Kazemein Jasemi [1], Oliver H. F. Krumbach [1], Lothar Gremer [2,3], Dieter Willbold [2,3], Radovan Dvorsky [1,4] and Mohammad R. Ahmadian [1,*]

1 Institute of Biochemistry and Molecular Biology II, Medical Faculty and University Hospital Düsseldorf, Heinrich Heine University Düsseldorf, 40225 Düsseldorf, Germany
2 Institute of Physical Biology, Heinrich Heine University Düsseldorf, 40225 Düsseldorf, Germany
3 Institute of Biological Information Processing, Structural Biochemistry (IBI-7), Forschungszentrum Jülich, 52425 Jülich, Germany
4 Center for Interdisciplinary Biosciences, P. J. Šafárik University, Jesenná 5, 040 01 Košice, Slovakia
* Correspondence: reza.ahmadian@uni-duesseldorf.de; Tel.: +49-211-811-2384
† These authors contributed equally to this work.

Abstract: The IQ motif-containing GTPase-activating protein (IQGAP) family composes of three highly-related and evolutionarily conserved paralogs (IQGAP1, IQGAP2 and IQGAP3), which fine tune as scaffolding proteins numerous fundamental cellular processes. IQGAP1 is described as an effector of CDC42, although its effector function yet re-mains unclear. Biophysical, biochemical and molecular dynamic simulation studies have proposed that IQGAP RASGAP-related domains (GRDs) bind to the switch regions and the insert helix of CDC42 in a GTP-dependent manner. Our kinetic and equilibrium studies have shown that IQGAP1 GRD binds, in contrast to its C-terminal 794 amino acids (called C794), CDC42 in a nucleotide-independent manner indicating a binding outside the switch regions. To resolve this discrepancy and move beyond the one-sided view of GRD, we carried out affinity measurements and a systematic mutational analysis of the interfacing residues between GRD and CDC42 based on the crystal structure of the IQGAP2 GRD-CDC42^{Q61L} GTP complex. We determined a 100-fold lower affinity of the GRD1 of IQGAP1 and of GRD2 of IQGAP2 for CDC42 mGppNHp in comparison to C794/C795 proteins. Moreover, partial and major mutation of CDC42 switch regions substantially affected C794/C795 binding but only a little GRD1 and remarkably not at all the GRD2 binding. However, we clearly showed that GRD2 contributes to the overall affinity of C795 by using a 11 amino acid mutated GRD variant. Furthermore, the GRD1 binding to the CDC42 was abolished using specific point mutations within the insert helix of CDC42 clearly supporting the notion that CDC42 binding site(s) of IQGAP GRD lies outside the switch regions among others in the insert helix. Collectively, this study provides further evidence for a mechanistic framework model that is based on a multi-step binding process, in which IQGAP GRD might act as a 'scaffolding domain' by binding CDC42 irrespective of its nucleotide-bound forms, followed by other IQGAP domains downstream of GRD that act as an effector domain and is in charge for a GTP-dependent interaction with CDC42.

Keywords: CDC42; GAP; GAP-related domain; GRD; GTPase activating protein; IQGAP; nucleotide-independent binding; RASGAP; RHO GTPases; scaffold protein; scaffolding protein; switch regions

Citation: Mosaddeghzadeh, N.; Pudewell, S.; Bazgir, F.; Kazemein Jasemi, N.S.; Krumbach, O.H.F.; Gremer, L.; Willbold, D.; Dvorsky, R.; Ahmadian, M.R. CDC42-IQGAP Interactions Scrutinized: New Insights into the Binding Properties of the GAP-Related Domain. *Int. J. Mol. Sci.* **2022**, *23*, 8842. https://doi.org/10.3390/ijms23168842

Academic Editor: Alexandr Baykov

Received: 23 June 2022
Accepted: 6 August 2022
Published: 9 August 2022

1. Introduction

RHO GTPases act, with some exceptions [1], as molecular switches by cycling between an inactive (GDP-bound) and an active (GTP-bound) state. Their functions at the plasma membrane are usually controlled by three groups of regulatory proteins: guanine nucleotide dissociation inhibitors (GDIs), guanine nucleotide exchange factors (GEFs) and GTPases activating proteins (GAP's) [2]. The formation of the active GTP-bound state of

RHO GTPases, such as CDC42, is accompanied by a conformational change in two regions, known as switch I and II (encompassing amino acids or aa 29–42 and 62–68, respectively); these regions provide a platform for a GTP-dependent, high-affinity association of structurally and functionally diverse effector proteins, e.g., ACK, PAK1, WASP, ROCK1, DIA and IQGAP1, through their so-called GTPase-binding domains (GBDs) [3–13] (reviewed in [14]). GTPase-effector signaling activates further a wide variety of pathways in all eukaryotic cells [2].

A unique feature distinguishing the RHO family from other small GTPase families is the presence of a 12 amino-acid insertion (aa 124–135 in CDC42) that protrudes from the G domain structure by forming a short helix, the so-called insert helix (IH) [15]. This IH is highly charged and variable among the members of the RHO family [15]. The IH has been very recently shown to have larger conformational flexibility in the GDP-bound CDC42 than in the GTP-bound CDC42 [16]. IH is a binding site for RHOGDI1, p50GAP, DIA, FMNL2, PLD1 and IQGAP2 [10,12,17–21], and appears rather essential for downstream activation of RHO GTPases [21–23].

IQGAP1 is ubiquitously expressed and shares a similar domain structure with its human paralogs IQGAP2 and IQGAP3 (Figure 1A), including an N-terminal calponin homology domain (CHD), a coiled-coil repeat region (CC), a tryptophan-containing proline-rich motif-binding region (WW), four isoleucine/glutamine-containing motifs (IQ), a RASGAP-related domain (GRD), a RASGAP C-terminal domain (RGCT) and a very C-terminal domain (CT). IQGAPs interact with a large number of proteins and modulate the spatiotemporal distributions of distinct signal-transducing protein complexes [24–34]. As multidomain scaffold proteins, they safeguard the magnitude, efficiency and specificity of signal transduction [35]. They have been localized at multiple subcellular sites orchestrating different signaling pathways and thus controlling a variety of cellular functions [36–42]. Notably, IQGAP1 has been implicated as a drug target due to its vital regulatory roles in cancer development [42–49] although the molecular mechanism of its functions is unclear.

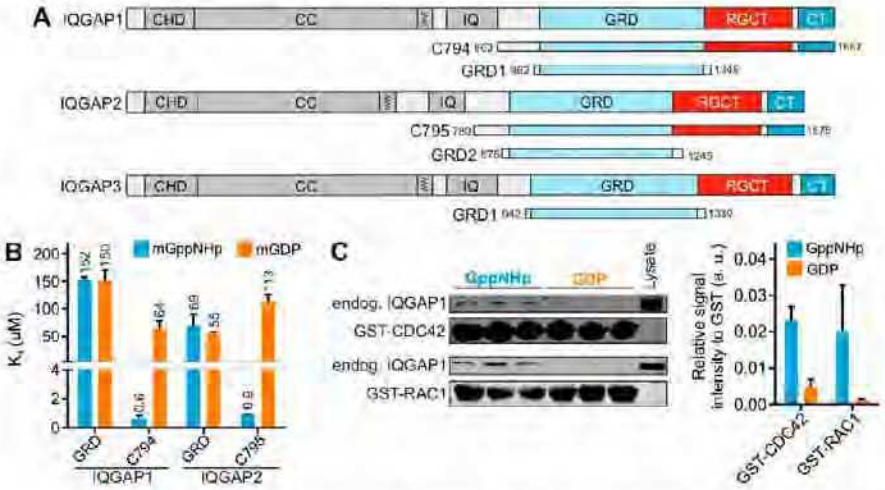

Figure 1. IQGAP GRD binding is nucleotide independent. (**A**) Domain organization of the IQGAP paralogs along with their GRDs and C-terminal fragments assessed in this study (see text for more details). (**B**) Fluorescence polarization analysis of IQGAP1 and IQGAP2 proteins with mGppNHp- and mGDP-bound CDC42. (**C**) Pull-down of endogenous IQGAP1 FL from HEK293 lysates with GppNHp- or GDP-bound GST-CDC42 and GST-RAC1, respectively. Densitometry evaluation of relative IQGAP1 binding to GST-CDC42 proteins (a. u., arbitrary unit) from a triplicate experiment is shown as bar charts.

Earlier studies analyzed the crucial role of IQGAP RGCT in high-affinity binding to the switch regions of the GTP-bound, active CDC42 and proposed it as an IQGAP 'effector domain' [5,50,51]. Accordingly, Swart-Mataraza et al. reported that the CDC42 GppNHp can still bind to IQGAP-ΔGRD (lacking aa 1122–1324) [52]. Moreover, Li et al. mapped the CDC42 and IQGAP binding regions and determined that switch I and surrounding regions (residues 29–55) together with the insert region (residues 122–134) are required for high affinity binding to IQGAP1 [53]. LeCour et al., however, solved a crystal structure of constitutively active CDC42(Q61L) in complex with the IQGAP2 GRD (GRD2) and proposed that CDC42 binds GRD2 from two different sites in a 4:2 stoichiometry [12,54]. One is the 'GAPex-mode binding site' (ex stands for 'extra' subdomains consisting of variable N- and C- terminal flanking regions) and the other is the 'RASGAP-mode binding site' very much resembling the RASGAP and CDC42GAP structures [18,55] with a conserved core domain (GAPc). Analyzing this structure, Ozdemir et al. proposed that CDC42 IH binding to the GAPex-domain induces GRD2 dimerization and changes the RASGAP site allosterically, which subsequently create another interaction interface for CDC42 binding (leading to a 2:1 stoichiometry of GRD2 and CDC42) [54].

A number of biophysical and biochemical studies have provided valuable insights into the structural and binding properties of the C-terminal domains of IQGAP1 (C794) and IQGAP2 (C795), encompassing the GRD, RGCT and CT domains, with CDC42 [12,50,52–54,56–63]. Evidently, all three domains bind with different affinities to CDC42 [5]. However, the mechanistic principles behind these interactions have remained unclear. Moreover, there are conflicting views regarding the assignment of a 'CDC42-specific GBD' for IQGAPs. One model proposes the GRD and its RASGAP-mode binding with the switch regions of CDC42 [12,54,56,58,64], whereas the other model excludes GRD and marks RGCT, located distal to the GRD, as crucial for high-affinity binding to CDC42 in a GTP-dependent manner [5,26,50–52]. Aiming to shed light on this discrepancy and to understand the molecular basis of CDC42-IQGAP interaction we comprehensively investigated the nature of the GRD interaction with CDC42 in this study and determined the role of the IH of CDC42 in contributing to GRD association. Furthermore, we studied the binding characteristics of C794 regarding the switch region and IH contact sites by mutational analysis, and verified the results in cell-based studies with endogenous IQGAP1. Collectively, our results consolidate and refine the importance of IQGAP RGCT as the true GBD in the recognition of CDC42 and its binding in a GTP-dependent manner. The GRD, although not a central effector domain, is evidently necessary for scaffolding CDC42 and facilitating its recruitment to preexisting cues.

2. Results and Discussion

IQGAP1 and IQGAP2 proteins were analyzed in this study to critically evaluate the function of the respective GRD domains. First, we determined the CDC42 binding properties of different IQGAP proteins, including IQGAP1 full-length (FL). Second, we examined the role of amino-acids crucial for the interplay between IQGAP2 and CDC42 using mutational IQGAPs and CDC42 variants. Third, we analyzed the impact of CDC42 IH as an IQGAP binding site. Fourth, we investigated the RASGAP activity of IQGAP1 GRD towards eight different members of the RAS family and examined the introduction of a catalytic arginine finger in the GRD.

2.1. GRD Is Not the Prominent Binding Domain for High IQGAP-CDC42 Affinity

2.1.1. GRD Binds to CDC42 with Very Low Affinity in a Nucleotide-Independent Manner

Different domains and fragments of the IQGAPs, including GRD1 and C794 of IQGAP1, as well as GRD2 and C795 of IQGAP2 (Figure 1A), were purified to determine their binding affinities for mGDP- and mGppNHp-bound CDC42 using fluorescence polarization. Obtained dissociation constants (K_d; Figure 1B) clearly show that all IQGAP constructs are able to bind CDC42 but with different affinities and preferences for the nucleotide-bound forms of CDC42. GRDs of both IQGAPs are low-affinity binders and do

not discriminate between the active and the inactive states of CDC42. Similar observations were made for GRD3 and the CT of IQGAP1 (Supplementary Figure S1). In contrast, C794 and C795, encompassing in addition to both GRD and CT also the central RGCT (Figure 1A), exhibited K_d values of 0.6 and 0.9 μM, respectively, indicating an around 100-fold higher affinity for the GTP-bound active CDC42 as compared to CDC42 GDP (Figure 1B). This result clearly suggests that RGCT but not GRD represents a 'CDC42-specific GBD' for at least IQGAP1 and IQGAP2, by directly associating with the switch regions of CDC42 GTP. Unfortunately, our efforts to obtain IQGAP1 RGCT (aa 1276–1575) and IQGAP3 C790 (aa 841–1631) for determining their binding affinities to the members of the RHO GTPase family, including CDC42, has been remaining unsuccessful [26,51]. Purified IQGAP1 RGCT tends to assemble into higher oligomeric or polymeric states, and, thus, is disabled in binding CDC42 [51].

Several lines of evidence support the crucial role of RGCT rather than GRD as the IQGAP effector domain for CDC42: (i) Here we can show that proteins containing RGCT bind with a more than 100-fold affinity to CDC42 mGppNHp as compared to isolated GRD or CT (Figure 1B and Figure S1), (ii) substitution of the Serine 1443 for glutamate (a phosphomimetic mutation) drastically impaired IQGAP1 binding to CDC42 mGppNHp [5,51]; (iii) an IQGAP1 protein, lacking the GRD (aa1122–1324), only binds CDC42 GppNHp, in contrast to IQGAP1 itself, that binds both GppNHp-bound and GDP-bound CDC42 [52]. The latter has been also demonstrated in other studies [63,64] and support our previous [26,51] and current findings that IQGAP domains, including GRD and CT, bind CDC42 GDP as strong as CDC42 GppNHp (Figure 1B).

2.1.2. Endogenous IQGAP1 also Binds CDC42 GDP

Serum-stimulated HEK293 cells, endogenously expressing IQGAP1 full-length (FL), were now used to carry out a pull-down assay with purified GST-fusion proteins of CDC42 and RAC1 in either GDP-bound or GppNHp-bound forms. IQGAP1 FL bound to these GTPases, regardless of their nucleotide status even though the binding to GDP-bound proteins was observed to be much weaker than the GppNHp-bound proteins (Figure 1C). This pattern corresponds to the binding behavior of C794 and not with the binding of GRD1 alone. Densitometric evaluation of three independent pull-down experiments showed that IQGAP1 FL binding to CDC42 GDP is much stronger than to RAC1 GDP (Figure 1C).

Altogether, our data suggest that IQGAP1 forms a complex with CDC42 through different sites in both nucleotide-dependent and nucleotide-independent manner.

2.2. *Switch Regions of CDC42 Are Not the Main Binding Sites for the GRDs*

Timpson's and our group have provided evidence that the IQGAP RGCT is essential for high affinity binding to the switch regions of the GTP-bound, active CDC42 and thus acts as an IQGAP 'effector domain' [5,50,51]. This critical issue has now been further expanded with additional experiments as described above (Figure 1), and confirms the crucial role of the RGCT as an IQGAP 'effector domain' that selectively associates with CDC42 GTP and carries out the high affinity association. Other groups have, in contrast, used the constitutive active CDC42(Q61L) in their structural and biochemical analysis and proposed that CDC42(Q61L) GTP GRD forms a GTPase-effector complex [12,54,56,57]. Such a role of the GRD in associating with CDC42 GTP is astonishing considering the afore mentioned studies on both GRD1-CT that binds CDC42 with a higher affinity as compared with GRD and an IQGAP1 variant, lacking the RASGAP domain (aa 1122–1324), which equally interacts with CDC42 as compared with IQGAP1 wild type [52]. To clarify this discrepancy, we have carefully examined 'the RASGAP-mode binding site' of CDC42 using mutational approaches coupled with kinetic and equilibrium measurements. Results of this examination are discussed in following subsections.

2.2.1. Mutations in CDC42 Switch Regions Only Mildly Affect GRD Binding

Proposed interacting mode of GRD with the switch regions of CDC42 (RASGAP mode binding) was deduced from the IQGAP2 GRD2 structure in complex $CDC42^{Q61L}$.GTP [12] and two CDC42 mutation variants within the switch I and II regions (2xSW and 8xSW) and a 11-residues mutant variant within the GRD of IQGAP2 C795 (11xGRD) were generated as illustrated in Figure 2A. Identical and highly conserved residues within the interacting interface highlighted in Figure 2B, were all replaced by alanine. All variants were stable in their purified forms and Far-UV CD spectroscopic measurements excluded any improper folding as compared to the wild-type proteins (Supplementary Figure S2).

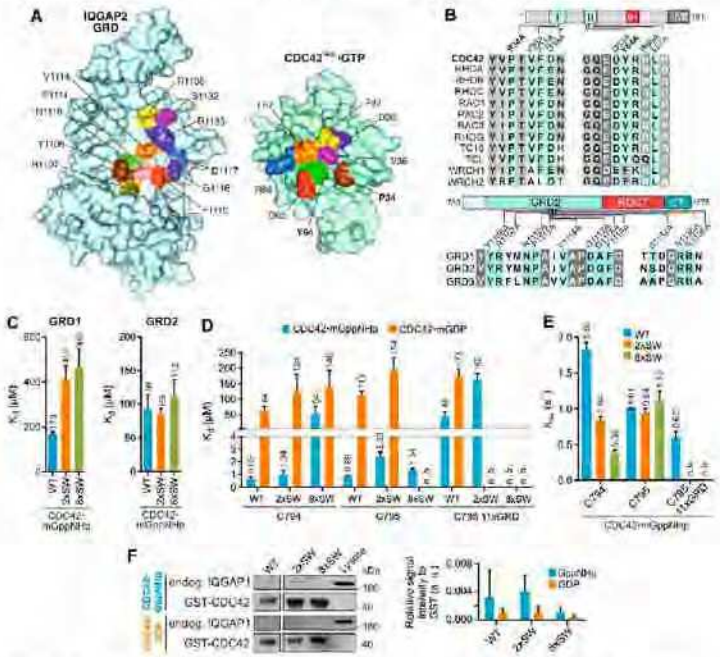

Figure 2. Analysis of CDC42 switch region and IQGAP1 GRD mutants. (**A**) The selection of GRD2 and CDC42 mutations is based on the GRD2/$CDC42^{Q61L}$ structure (PDB: 5CJP). Interacting residues colored on both proteins were selected for mutational analysis. For more details see also Table S1. (**B**) Multiple sequence alignments of switch regions of RHO GTPases and IQGAPs highlight identical or homologous interacting residues that have been replaced in this study by alanine for analyzing their impact on IQGAP binding. Conserved residues are shaded in grey. Mutations in CDC42 switch regions include 2xSW (bolded residues) and 8xSW (all eight residues, as indicated), and 11xGRD in IQGAP2 C795. (**C**) Fluorescence polarization measurements of mGppNHp-bound CDC42 WT, 2xSW and 8xSW with IQGAP1 GRD1 or IQGAP2 GRD2. (**D**) The K_d values for the interactions of IQGAP1 C794, IQGAP2 C795 and C795 11xGRD with the CDC42 variants in mGppNHp- and mGDP-bound form were determined using fluorescence polarization. n.b. stands for no binding observed. C794 and C795 CDC42 WT measurements are included from Figure 1B for simple comparison. (**E**) Observed rate constants (k_{obs}) for the IQGAPs association with mGppNHp-bound CDC42 WT, 2xSW and 8xSW were measured using stopped-flow fluorimetry. (**F**) Pull-down of endogenous IQGAP1 FL from HEK293 lysates with GST-CDC42 in GppNHp-bound or GDP-bound state. Cell lysate was used as an input control. Densitometry evaluation of relative IQGAP1 binding to GST-CDC42 proteins (a. u., arbitrary unit) from triplicate experiments is shown as bar charts.

We first determined the K_d values for the GRD1 and GRD2 interaction with the mGppNHp-bound CDC42 WT, 2xSW and 8xSW. Interestingly, we found a two to three-fold reduction in the binding affinity of GRD1 but no notable reduction for GRD2 with the CDC42 variants as compared to CDC42 WT (Figures 1B, 2C and S3). As the effect of 2x and 8x introduced mutations on the proposed crucial interaction sites of CDC42 and GRD2 did not result in a decrease of affinity, our data clearly indicates that the association of CDC42 switch regions with IQGAP must be through other sites rather than the GRD.

2.2.2. IQGAP C794/C795 Binding Is Impaired by Switch Region and GRD Mutations

Next, we measured the K_d values for the interaction of IQGAP1 C794 or IQGAP2 C795, containing the GRD, RGCT and CT domains, with mGDP-bound and mGppNHp-bound CDC42 variants. Data shown in Figure 2D (Supplementary Figure S4) indicate that the substitution of two amino acids in the switch regions was not sufficient to largely impair the CDC42-C794 interaction. However, mGppNHp-bound, but not mGDP-bound CDC42 8xSW exhibited a drastic reduction (86-fold) in its binding affinity for C794. For mGDP-bound CDC42, introduction of SW mutations only slightly decreased the affinity of C794. The IQGAP2 C795 binding to the CDC42 switch regions was not impaired by neither 2x nor 8x mutants of CDC42 in mGppNHp-bound state. Interestingly, IQGAP2 C795 showed a slightly decreased binding to the mGDP-bound CDC42 2xSW mutant but no binding to the 8xSW mutant, a much different result than obtained for GRD2 binding alone. The data from real-time stopped-flow fluorescence spectrometry (Figure 2E and Figure S5) showed both IQGAPs associated with similar k_{obs} values, as observed in Figure 2D.

The next question addressed was to what extent CDC42 binding of IQGAP1 FL was affected by the switch region mutations. Therefore, endogenous IQGAP1 was pulled down from HEK293 lysates using GDP-bound and GppNHp-bound GST-CDC42 WT, 2xSW and 8xSW. As shown in Figure 2F, IQGAP1 binding to CDC42 did not change with two amino acid substitution of the switch regions but was disrupted with the eight mutations. These experiments support our kinetic and equilibrium measurements and clearly indicate that the switch regions are significant for the IQGAP1 interaction with both GDP-bound and GppNHp-bound CDC42.

Taken together, the presented data suggest a slightly different binding behavior of IQGAP1 and IQGAP2 variants for CDC42. Our results do not support the interacting mode between IQGAP and CDC42 based on the crystal structure [12] and the central role of the GRD in it [54] since the introduction of SW mutations of CDC42 clearly affected C795/C794 binding but only little the GRD binding. We, in contrary, propose that the interactions sites on IQGAP for complex formation with CDC42 GTP are clearly within the RGCT and might be different between IQGAP1 and IQGAP2.

2.3. Insert Helix Contributes to the Binding Affinity of CDC42 for IQGAP1 GRD

The question arises as which regions on CDC42 could bind GRD if we can now exclude the switch regions. A region/site that has attracted our attention is the IH of CDC42 for valid reasons. We have shown that IQGAPs bind to RAC-like and CDC42-like proteins but not to the other members of the RHO family [26] and the IH consistently is a highly variable region among the RHO GTPases (Figure 3A) [15]. Several CDC42-binding proteins, including RHOGDI1, p50GAP, FMNL2 and IQGAP2 have been shown to contact the IH [10,12,17,18,20]. Thus, mutational analysis of the CDC42 IH was performed, using four different single residue mutations and a quadruple mutation (Figure 3A and Table S1). Note that variable residues were replaced in CDC42 by the corresponding residues of RAC1. Most remarkably and in sharp contrast to the SW mutations (Figure 2), all IH mutations abolished GRD1-CDC42 interaction irrespective of the nucleotide-bound states of CDC42 (Figures 3B and S6), which underlines the central role of CDC42 IH in GRD binding. The scenario was rather different for C794, which binds mGDP-bound CDC42 with 3-fold and mGppNHp-bound CDC42 with 20-fold lower affinities (Figure 3B). These

data are consistent with the recent observation by Nussinov and colleagues that the CDC42 IH reveals nucleotide-dependent conformational flexibility [16].

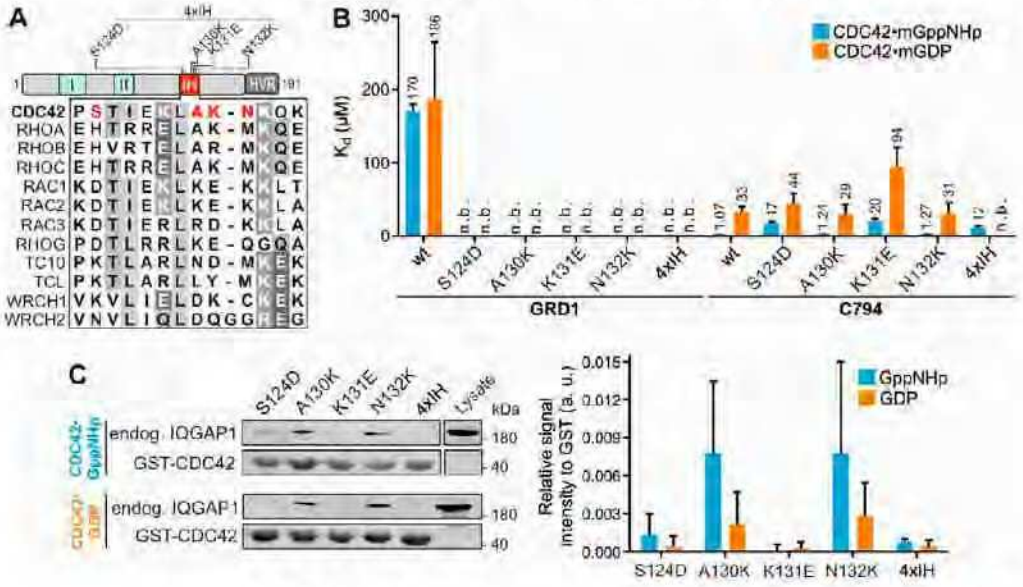

Figure 3. CDC42 IH mutations decrease binding affinity. (**A**) Amino acid alignment of the insert helix of selected members of the RHO GTPase family. CDC42 mutations (red) to RAC1 were introduced outside of the conserved regions (grey). (**B**) Fluorescence polarization data for the interaction of GRD1 and C794 with the CDC42 IH variants. (**C**) Pull-down of endogenous IQGAP1 FL from HEK293 lysates with GST-CDC42 IH variants in both GppNHp-bound and GDP-bound forms. Cell lysate was used as an input control. The pull-down data for GST-CDC42^{wt} is shown in Figure 2F as all pull-down experiments were conducted under the same conditions. Densitometry evaluation of relative IQGAP1 binding to GST-CDC42 proteins (a. u., arbitrary unit) from a triplicate experiment is shown as bar charts.

The data from fluorescence polarization could be verified via pull-down assay. The binding pattern of CDC42 IH mutants with endogenous IQGAP1 followed the same pattern, displaying no binding for A130K and 4xIH and very weak binding for S124D (Figure 3C). Generally, binding could be observed much stronger for GppNHp-bound than for GDP-bound CDC42 variants, supporting the pull-down data shown above (Figure 1C).

Several published studies have shown that mutations of the CDC42 IH impact their properties in binding IQGAPs. Li et al. (1999) have shown that IH deletion in CDC42 impairs its binding affinity for the effectors, in particular IQGAP1 C794 [53]. Owen et al. (2008) investigated the impact of the IH mutations in CDC42^{Q61L} on IQGAP1 C794 binding [56]. Consistent with our findings, they observed a slight decrease in C794 affinity for CDC42^{Q61L} with A130K or N132K. Moreover, Ozdemir et al. also applied the CDC42^{Q61L} variant and suggested the IH together with switch I region to be mainly responsible for its binding to the *ex*-domain of GRD (GRDex) of IQGAP2 [54].

2.4. Q61L Variant Is Not a Wildtype Equivalent for CDC42-IQGAP Interactions

An issue that still needs to be addressed is why are there several discrepancies between the studies regarding the GRD binding property for CDC42? A possible answer to this question is the use of different CDC42 mutants in these studies that are alike, but not equivalent, especially regarding this interaction.

In the GTP-bound CDC42, Q61 acts as a 'catalytic residue' that is involved in hydrogen bonding with a catalytic water molecule, an arginine finger of GAP and the γ-phosphate of GTP, initiating a nucleophilic attack that hydrolyzes GTP (Figure 4A) [18,65]. L61 does not, however, undergo these functionally critical hydrogen bonds but rather points towards protein surface without causing significant structural changes (Figure 4A). As a result, the substitution of Q61 by leucine drastically increases the binding affinity of IQGAPs for $CDC42^{Q61L}$ GTP by up to 15-fold as was clearly demonstrated previously [5,26,51]. Despite this fact, many groups use this CDC42 variant for the interaction analysis of effectors, such as IQGAPs [12,54,56,57]. Thus, we revisited this issue and have comparatively analyzed the interaction of IQGAP1 GRD with $CDC42^{Q61L}$ and $CDC42^{wt}$ using fluorescence polarization and size exclusion chromatography (SEC). Equilibrium measurements shown in Figure 4B clearly revealed that the Q61L mutation results in a strong enhancement of GRD1 and GRD2 binding with the mGppNHp-bound CDC42, but not with mGDP-bound CDC42. The binding affinity of mGppNHp-bound $CDC42^{Q61L}$ rises from a low affinity 186 µM/69 µM binding to a high 2.7 µM/2.5 µM binding for GRD1/GRD2, respectively (Figures 4B and S7). This is a change of 30–50-fold and might explain the huge differences of CDC42 interactions with GRD. Moreover, SEC analysis showed that GRD1 forms a 2:2 stoichiometry with $CDC42^{wt}$ GppNHp but 2:1 stoichiometry with $CDC42^{Q61L}$ GppNHp (Figure 4C–F).The latter is remarkably consistent with the previous reports on a high-affinity binding of IQGAP2 GRD2 with $CDC42^{Q61L}$ GTP and 4:2 and 2:1 stoichiometry, respectively [12,54]. These findings verified the clear difference between $CDC42^{wt}$ and $CDC42^{Q61L}$ and how replacement of Q61 by L changes the binding properties (affinity and stoichiometry) of CDC42 interaction with IQGAP GRDs.

Chen et al. have reported that the Q61L mutation strengthen hydrogen bond interactions between CDC42 and the γ-phosphate of GTP [66]. Analyzing the $Cdc42^{Q61L}$ GTP GRD2 structure, Ozdemir et al. proposed that CDC42 IH binding to the GAPex-domain induces allosteric changes in the RASGAP site, which in turn facilitate GRD dimerization, and enable the second $CDC42^{Q61L}$ to bind to this site (yielding a 2:1 stoichiometry) [54]. Collectively, we recapitulate that $CDC42^{Q61L}$ is not an ideal analog of $CDC42^{wt}$ especially in studying the interaction of the downstream effectors. G12V and Q61L mutations of CDC42 cause GAP insensitivity leading to sustained hyperactivation of CDC42 [16,18,55,65,66]. Thus, we suggest $CDC42^{wt}$ GppNHp and even $CDC42^{G12V}$ GTP variants as more suitable species for the investigation of CDC42-effector interaction rather than $CDC42^{Q61L}$ GTP.

2.5. GRD Lacks the Structural Fingerprints to Induce the GAP Activity

The structure of the RAS-RASGAP complex shows GAP-334 interacting predominantly with the switch regions of RAS [55]. Three regions (finger loop, FLR motif and helix α7/variable loop) constitute structural fingerprints of the RASGAP p120 and neurofibromin that form critical RAS binding sites in order to apply an arginine finger into the active center of RAS [67,68]. Amino acid sequence analysis of these RASGAPs with the three IQGAP paralogs showed that major parts of these fingerprints are different in IQGAPs (Figure 5A). Moreover, the catalytic arginine is missing and there is instead a threonine (T1045 in IQGAP1; Figure 5A). Thus, it is quite understandable why IQGAP1 did not display RASGAP activities towards HRAS [60]. It is, however, known that GAPs specific for other members of the RAS superfamily use other catalytic residues than an arginine (reviewed in [69,70]).

We set out to examine a possible GAP activity of IQGAP1 GRD towards different RAS family GTPases. Figure 5B shows that IQGAP1 GRD is a pseudo-RASGAP domain with no obvious catalytic ability (orange bars). Earlier studies have shown that the substitution of the arginine finger of the RASGAPs to other amino acids completely abolishes their GAP activity [67,68]. Therefore, threonine 1046 of IQGAP1 GRD was replaced by an arginine and the impact of T1046R on the GTP hydrolysis of the eight RAS proteins was measured. Data shown in Figure 5B revealed no apparent GAP activities of $IQGAP1\ GRD^{T1046R}$ (green bars)

as expected for a RASGAP. These data suggest that IQGAPs, besides lacking an arginine finger, do not contain critical RAS-binding residues of the α7/variable loop (Figure 5A).

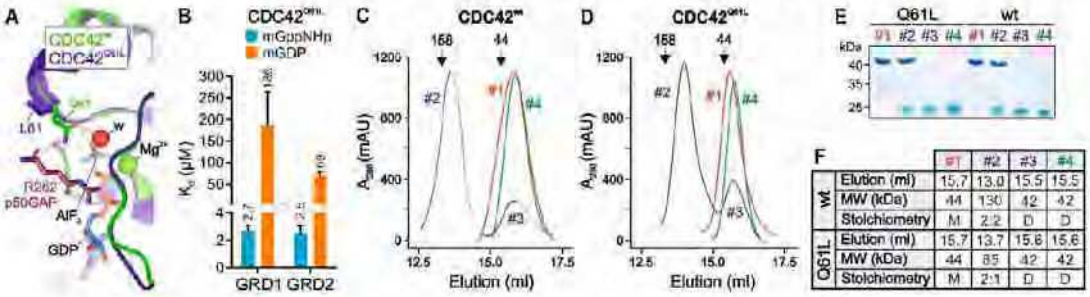

Figure 4. Comparative analysis of IQGAP1 GRD1 interaction with $CDC42^{Q61L}$ and $CDC42^{wt}$. (**A**) Structural overlay of $CDC42^{wt}$ GDP AlF_3 p50GAP (green; PDB: 1GRN) on $CDC42^{Q61L}$ GTP IQGAP2 (blue; PDB: 5CJP) with the focus on Q61 hydrogen bonds (red dashed lines). GDP AlF_3 mimics the transition state of the GTP hydrolysis reaction and is coordinated with the magnesium ion (Mg^{2+}) and the nucleophilic water molecule (w) and the arginine finger (R282) of p50GAP. Aluminum trifluoride (AlF_3) mimics the γ-phosphate of GTP in the transition state. In contrast to L61, Q61 is critical for the catalysis of the GTP hydrolysis reaction through three hydrogen bonds (see text). (**B**) Fluorescence polarization data of IQGAP GRD1 with CDC42 mGppNHp and CDC42 mGDP. (**C**–**F**) IQGAP GRD differently forms complexes with $CDC42^{WT}$ and $CDC42^{Q61L}$, respectively, when applied on an analytical SEC. For this purpose, $CDC42^{WT}$ GppNHp (**C**) or $CDC42^{Q61L}$ GppNHp (**D**) were mixed with IQGAP1 GRD1 and SEC was performed on a Superdex 200 10/300 column using an ÄKTA purifier (flow rate of 0.5 mL/min, fraction volume of 0.5 mL) and a buffer, containing 30 mM Tris/HCl, pH 7.5, 150 mM NaCl, and 5 mM $MgCl_2$. The elution profiles represented one peak for the respective CDC42 proteins (#1), two peaks for the respective mixtures of respective CDC42 proteins with GRD (#2 and #3) and one peak for the GRD1 (#4). (**E**) Coomassie brilliant blue staining of the corresponding elution volumes indicated that only peaks #2 contain GRD1 complexes with $CDC42^{WT}$ or $CDC42^{Q61L}$, respectively. Peaks #3 only contain the CDC42 proteins as compared to the peaks #1 and #4. (**F**) The SEC profiles of $CDC42^{WT}$ and $CDC42^{Q61L}$ are summarized for each peak regarding the elution volume, the molecular weight (MW) and the stoichiometry. M stands for monomeric and D for dimeric. The theoretical MWs of CDC42 (21.2 kDa) and GRD (43 kDa) were calculated using the Expasy Protparam tool. The presented MWs for each peak was calculated based on the calibration curve (aldolase 158 kDa and ovalbumin 44 kDa, respectively) and partition coefficient plot (Kav = Ve − V0/Vc − V0) versus the logarithm of MWs; Ve: elution volume number; V0: void volume (8 mL); Vc: geometric column volume (24 mL)). Accordingly, peaks #2 correspond to a heterotetrameric complex between $CDC42^{WT}$ GppNHp and GRD1 with a MW of 130 kDa, and a heterotrimeric complex of GRD and $CDC42^{Q61L}$ GppNHp with a MW of 85 kDa.

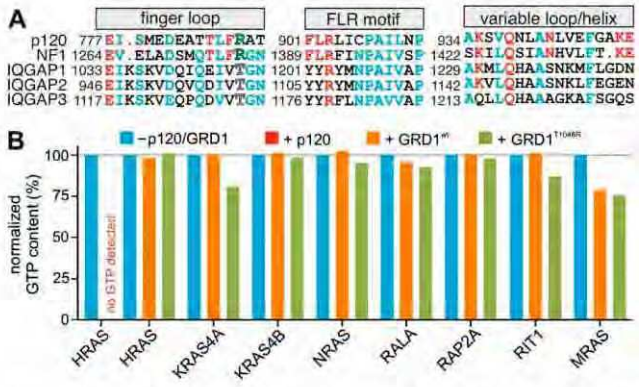

Figure 5. Deviation in RAS-binding residues in GRDs cause lack of RASGAP activity. (**A**) Sequence alignment of human RASGAPs p120, neurofibromin (NF1) and the three IQGAP paralogs highlights distinctive deviations in three signature motifs (grey boxes): the finger loop, FLR region and a7/variable loop. RAS-binding residues are shown in red and conserved residues in blue. The catalytic arginine (green) is substituted by threonine in IQGAPs. The numbers correspond to the amino acids of the respective proteins. (**B**) GTP hydrolysis of various RAS family GTPases was measured in the absence (blue) and in the presence of p120 GAP domain (red; positive control, where no GTP detected) or GRD1^{wt} (orange) and GRD1^{T1046R} (green). The GTP hydrolysis of the RAS proteins (10 μM) was measured via HPLC and the GTP content normalized to 100% before adding p120 or GRD1, respectively, at 100 μM concentrations and 1 min incubation time.

3. Material and Methods

3.1. Constructs

The pGEX4T1 encoding an N-terminal glutathione S-transferase (GST) fusion protein was used to overexpress human IQGAP1 (accession number P46940) GRD1 (aa 962–1345), C794 (aa 863–1657) and CT (aa 1576–1657); human IQGAP2 (accession number Q13576) GRD2 (aa 875–1246) and C795 (aa 780–1575); human IQGAP3 (accession number P60953) GRD3 (aa 942–1330); human CDC42 (accession number P60953; aa 1–178). All constructs and related variants are list in Supplementary Table S1. For purification of these proteins, pGEX-4T1 constructs were transformed in *Escherichia coli* and proteins were isolated via affinity chromatography using a glutathione Sepharose column on a ÄKTA start protein purification system (Cytiva, US) [71]. GST-cleavage was carried out by incubation with thrombin (#T6884-1KU, Sigma Aldrich, Taufkirchen, Germany) at 4 °C until full digestion of the fusion protein. Quality of the proteins were checked via SDS-PAGE and Coomassie staining. CDC42 variants were further verified for their activity in HPLC by determining the amount of bound nucleotide [71]. Nucleotide free proteins were prepared by incubating the proteins with alkaline phosphatase (#P0762-250UN, Sigma Aldrich, Germany) and phosphodiesterase (#P3243-1VL, Sigma Aldrich, Taufkirchen, Germany) at 4 °C [71]. CDC42 variants were labelled with either GDP (#51060, Sigma Aldrich, Taufkirchen, Germany), GppNHp (#NU-401, Jena Bioscience, Jena, Germany), mant-GDP (#NU-204, Jena Bioscience, Jena, Germany) or mant-GppNHp (#NU-207, Jena Bioscience, Jena, Germany).

3.2. Circular Dichroism (CD) Spectrometry

Far-UV-CD spectroscopy of protein samples were performed on a JASCO J-715 CD spectropolarimeter (Jasco, Gross-Umstadt, Germany) using quartz cuvettes (Helma, Mühlheim, Germany) with 1 mm path length. Spectra were recorded at protein concentrations of 20 μM CDC42 WT and variants in 1 mM NaPi buffer, pH 7.0 or 8 μM IQGAP WT and variants in 12.5 mM TRIS/HCl pH 7.4, 37.5 mM NaCl, 1.25 mM $MgCl_2$, at 22 °C with instrument settings as follows: 0.1 nm step size, 50 nm min^{-1} scan speed, 1 nm

band with. Signal-to-noise ratio was improved by accumulation of 10 scans per sample. The mean residue ellipticity $[\theta]_{mrw}$ in deg·cm^2·dmol^{-1} was calculated from the equation $[\theta]_{mrw} = (\theta_{obs} \times MRW)/(c \times d \times 10)$, with θ_{obs}, observed ellipticity (in degrees); c, concentration (in g/mL); d, cell path length (in cm); MRW (mean residue weight), molecular weight divided by number of peptide bonds.

3.3. Cell Culture and Lysis

HEK293 cells were cultured in Dulbecco's Modified Eagle's Medium (DMEM) (# 12320032, Thermo Fisher, Waltham, CA, USA) supplemented with 10 % FBS and 1% Penicillin/Streptomycin in an exponential growth phase at 37 °C with 5% CO_2 and 95% humidity. Lysis was performed by washing the cells with $PBS^{-/-}$ and scraping them down with FISH buffer (50 mM Tris/HCl pH 7.5, 100 mM NaCl, 2 mM $MgCl_2$, 10% glycerol, 20 mM β-glyerolphosphate, 1 mM Na_3VO_4, 1× protease inhibitor cocktail and 1% IGPAL). Cells were lysed for 10 min on ice and then centrifuged for 10 min at 15,000× g. Supernatant was used for affinity pull down measurements.

3.4. GST-Pull-Down

The pull-down of endogenously expressed proteins with purified GST-fused proteins was performed using glutathione agarose beads (#745500.10, Macherey-Nagel, Düren, Germany). Beads were coupled to the GST-fused protein for one hour at 4 °C while mixing and centrifuged for 5 min at 500× g. Excess protein was removed by three washing steps. Coupled beads were incubated with HEK293 lysate for one hour at 4 °C on a rotor and again washed 3 times. In the final step, beads were mixed with 1× Laemmli buffer and proteins were denatured at 95 °C for 5 min. Samples were evaluated via SDS-PAGE and western blotting using anti-GST (own antibody, mouse) and anti-IQGAP1 (NBP1-06529, Novus, Wiesbaden Nordenstadt, Germany, rabbit) primary antibodies and secondary antibodies: IRDye® 800 CW anti-Rabbit IgG and IRDye® 680 RD anti-Mouse IgG from LiCor. Values were analyzed by using multiple t test analysis in GraphPad Prism 6 (one unpaired t test per row, fewer assumptions by analyzing each row individually).

3.5. Fluorescence Stopped-Flow Spectrometry

All kinetic parameters (k_{obs}) evaluated in this study were analyzed using a previously described kinetic analysis protocol [72]. The kinetic parameters were monitored with a stopped-flow apparatus (HiTech Scientific, Applied Photophysics SX20, Leatherhead, UK). The excitation was set for mant at the wavelength of 362 nm, and emission was detected through a cutoff filter of 408 nm. The observed rate constants were calculated by fitting the data as single exponential decay using GraFit program.

3.6. Fluorescence Polarization

To determine the dissociation constant K_d of direct protein–protein interaction (including weak interactions) fluorescence polarization analysis was performed in a Fluoromax 4 fluorimeter (Horiba Scientific, Loos, France). Here, 1 µM mant-GDP or mant-GppNHp labelled CDC42 proteins were prepared in a total volume of 170 µL in a three directional cuvette. Measurement was performed in polarization mode versus time with an excitation wavelength of 360 nm (slit width: 8 µm) and an emission wavelength of 450 nm (slit width: 10 µm). K_d values were calculated in GraFit 5 by fitting the concentration-dependent binding curve using a quadratic ligand binding equation.

3.7. GTP Hydrolysis Measurements

GTP hydrolysis rates of a set of different GTPases in presence and absence of GRD1 and its T1046R mutant containing the arginine residue were measured by high-performance liquid chromatography (HPLC) analysis. GTP-bound HRAS in presence of p120 GAP was used as control. Then, 10 µM of each GTPase in the GTP bound state was injected into the HPLC mixing chamber after 1 min of incubation in absence (intrinsic) and presence

(GAP stimulated) of 100 µM of GRD1 WT and T1046R variant. The GTP content for each measurement was calculated by dividing the intensity of the GTP detection peak to the sum of the intensities of the GTP plus GDF peaks.

4. Conclusions

The exact binding site of the IQGAP GRD and CDC42 is still not completely clear to date. This article provides evidence that the IQGAP GRD does not act as the primary or leading effector binding domain of CDC42 and counterevidence the role of IQGAP GRD in CDC42 binding deduced from a crystal structure of an IQGAP2 GRD2-CDC42Q61L GTP complex. We could show that the GRD does not bind to CDC42 in a nucleotide-dependent manner and that even multiple mutations of the suggested main residues of interaction do not abolish the direct physical interaction in cells and under cell-free conditions. Our data support the binding model of Ozdemir et al. [54] and propose the CDC42 IH as a key binding site for GRD. Furthermore, we shed light once more into the interaction difference of $CDC42^{wt}$ and $CDC42^{Q61L}$ that might be one of the main reasons of the discrepancies in the published data as discussed above. By our comparative measurements of IQGAP1 and IQGAP2 variants, we found differences in their binding strength and specificity towards $CDC42^{wt}$ but also towards various CDC42 variants. Our efforts to investigate also IQGAP3 were so far not successful. The exact binding residues and interaction sites of IQGAP1 and IQGAP2 with the switch regions of CDC42 will still remain to be identified in the future.

Supplementary Materials: The following supporting information can be downloaded at: https://www.mdpi.com/article/10.3390/ijms23168842/s1.

Author Contributions: M.R.A. conceived and coordinated the study; N.M., S.P., F.B., N.S.K.J. and O.H.F.K. designed, performed and analyzed the experiments; N.M., L.G. and D.W. performed the CD experiments; R.D. performed structural analysis; N.M. and M.R.A. directed the experiments, analyzed the data and wrote the paper. All authors have read and agreed to the published version of the manuscript.

Funding: This study was supported by the European Network on Noonan Syndrome and Related Disorders (NSEuroNet, grant number: 01GM1621B to N.S.K.J. and M.R.A.), the German Research Foundation (Deutsche Forschungsgemeinschaft or DFG) through the International Research Training Group 'Intra- and interorgan communication of the cardiovascular system' (grant number: IRTG 1902-p6 701158241 to F.B. and M.R.A.), the German Federal Ministry of Education and Research (BMBF)—German Network of RASopathy Research (GeNeRARe, grant numbers: 01GM1902C to N.M. and M.R.A.), the Research Committee of the Medical Faculty of the Heinrich Heine University (grant number: 9772764 to S.P. and M.R.A) and the Operational Program Integrated Infrastructure ERDF: Open scientific community for modern interdisciplinary research in medicine (OPENMED; grant number: ITMS2014+: 313011V455 to R.D.).

Institutional Review Board Statement: Not applicable.

Informed Consent Statement: Not applicable.

Data Availability Statement: All the data are in the manuscript.

Acknowledgments: We thank Roland Piekorz and Kotsene Loumonvi for support and discussions.

Conflicts of Interest: The authors declare no conflict of interest.

References

1. Ahmadian, M.R.; Jaiswal, M.; Fansa, E.K.; Dvorsky, R. New insight into the molecular switch mechanism of human Rho family proteins: Shifting a paradigm. *Biol. Chem.* **2013**, *394*, 89–95. [CrossRef]
2. Mosaddeghzadeh, N.; Ahmadian, M.R. The RHO Family GTPases: Mechanisms of Regulation and Signaling. *Cells* **2021**, *10*, 1831. [CrossRef] [PubMed]
3. Abdul-Manan, N.; Aghazadeh, B.; Liu, G.A.; Majumdar, A.; Ouerfelli, O.; Simonovitch, K.A.; Rosen, M.K. Structure of Cdc42 in complex with the GTPase-binding domain of the "Wiskott-Aldrich syndrome" protein. *Nature* **1999**, *399*, 379–383. [CrossRef] [PubMed]

4. Mott, H.R.; Owen, D.; Nietlispach, D.; Lowe, P.N.; Manser, E.; Lim, L.; Laue, E.D. Structure of the small G protein Cdc42 bound to the GTpasebinding domain of ACK. *Nature* **1999**, *399*, 384–388. [CrossRef]
5. Nouri, K.; Timson, D.J.; Ahmadian, M.R. New model for the interaction of IQGAP1 with CDC42 and RAC1. *Small GTPases* **2020**, *11*, 16–22. [CrossRef]
6. Morreale, A.; Venkatesan, M.; Mott, H.R.; Owen, D.; Nietlispach, D.; Lowe, P.N.; Laue, E.D. Structure of Cdc42 bound to the GTPase binding domain of PAK. *Nat. Struct. Biol.* **2000**, *7*, 384–388. [CrossRef]
7. Dvorsky, R.; Ahmadian, M.R. Always look on the bright site of Rho: Structural implications for a conserved intermolecular interface. *EMBO Rep.* **2004**, *5*, 1130–1136. [CrossRef]
8. Dvorsky, R.; Blumenstein, L.; Vetter, I.R.; Ahmadian, M.R. Structural Insights into the Interaction of ROCKI with the Switch Regions of RhoA. *J. Biol. Chem.* **2004**, *279*, 7098–7104. [CrossRef] [PubMed]
9. Hemsath, L.; Dvorsky, R.; Fiegen, D.; Carlier, M.F.; Ahmadian, M.R. An electrostatic steering mechanism of Cdc42 recognition by Wiskott-Aldrich syndrome proteins. *Mol. Cell* **2005**, *20*, 313–324. [CrossRef]
10. Rose, R.; Weyand, M.; Lammers, M.; Ishizaki, T.; Ahmadian, M.R.; Wittinghofer, A. Structural and mechanistic insights into the interaction between Rho and mammalian Dia. *Nature* **2005**, *435*, 513–518. [CrossRef]
11. Hall, A. Rho family GTPases. In *Biochemical Society Transactions*; Portland Press: London, UK, 2012; Volume 40, pp. 1378–1382.
12. LeCour, L.; Boyapati, V.K.; Liu, J.; Li, Z.; Sacks, D.B.; Worthylake, D.K. The Structural Basis for Cdc42-Induced Dimerization of IQGAPs. *Structure* **2016**, *24*, 1499–1508. [CrossRef] [PubMed]
13. Owen, D.; Mott, H.R. CRIB effector disorder: Exquisite function from chaos. *Biochem. Soc. Trans.* **2018**, *46*, 1289–1302. [CrossRef] [PubMed]
14. Mott, H.R.; Owen, D. Structures of Ras superfamily effector complexes: What have we learnt in two decades? *Crit. Rev. Biochem. Mol. Biol.* **2015**, *50*, 85–133. [CrossRef] [PubMed]
15. Thapar, R.; Karnoub, A.E.; Campbell, S.L. Structural and Biophysical Insights into the Role of the Insert Region in Rac1 Function. *Biochemistry* **2002**, *41*, 3875–3883. [CrossRef] [PubMed]
16. Haspel, N.; Jang, H.; Nussinov, R. Active and Inactive Cdc42 Differ in Their Insert Region Conformational Dynamics. *Biophys. J.* **2021**, *120*, 306. [CrossRef] [PubMed]
17. Wu, W.J.; Leonard, D.A.; Cerione, R.A.; Manor, D. Interaction between Cdc42Hs and RhoGDI Is Mediated through the Rho Insert Region. *J. Biol. Chem.* **1997**, *272*, 26153–26158. [CrossRef]
18. Nassar, N.; Hoffman, G.R.; Manor, D.; Clardy, J.C.; Cerione, R.A. Structures of Cdc42 bound to the active and catalytically compromised forms of Cdc42GAP. *Nat. Struct. Biol.* **1998**, *5*, 1047–1052. [CrossRef] [PubMed]
19. Lammers, M.; Meyer, S.; Kühlmann, D.; Wittinghofer, A. Specificity of Interactions between mDia Isoforms and Rho Proteins. *J. Biol. Chem.* **2008**, *283*, 35236–35246. [CrossRef] [PubMed]
20. Kühn, S.; Erdmann, C.; Kage, F.; Block, J.; Schwenkmezger, L.; Steffen, A.; Rottner, K.; Geyer, M. The structure of FMNL2–Cdc42 yields insights into the mechanism of lamellipodia and filopodia formation. *Nat. Commun.* **2015**, *6*, 7088. [CrossRef] [PubMed]
21. Walker, S.J.; Brown, H.A. Specificity of Rho insert-mediated activation of phospholipase D1. *J. Biol. Chem.* **2002**, *277*, 26260–26267. [CrossRef] [PubMed]
22. Karnoub, A.E.; Der, C.J.; Campbell, S.L. The Insert Region of Rac1 Is Essential for Membrane Ruffling but Not Cellular Transformation. *Mol. Cell. Biol.* **2001**, *21*, 2847–2857. [CrossRef] [PubMed]
23. Zong, H.; Kaibuchi, K.; Quilliam, L.A. The Insert Region of RhoA Is Essential for Rho Kinase Activation and Cellular Transformation. *Mol. Cell. Biol.* **2001**, *21*, 5287–5298. [CrossRef] [PubMed]
24. Fukata, M.; Watanabe, T.; Noritake, J.; Nakagawa, M.; Yamaga, M.; Kuroda, S.; Matsuura, Y.; Iwamatsu, A.; Perez, F.; Kaibuchi, K. Rac1 and Cdc42 capture microtubules through IQGAP1 and CLIP-170. *Cell* **2002**, *109*, 873–885. [CrossRef]
25. Watanabe, T.; Wang, S.; Noritake, J.; Sato, K.; Fukata, M.; Takefuji, M.; Nakagawa, M.; Izumi, N.; Akiyama, T.; Kaibuchi, K. Interaction with IQGAP1 links APC to Rac1, Cdc42, and actin filaments during cell polarization and migration. *Dev. Cell* **2004**, *7*, 871–883. [CrossRef] [PubMed]
26. Mosaddeghzadeh, N.; Nouri, K.; Krumbach, O.H.F.; Amin, E.; Dvorsky, R.; Ahmadian, M.R. Selectivity determinants of rho gtpase binding to iqgaps. *Int. J. Mol. Sci.* **2021**, *22*, 12596. [CrossRef] [PubMed]
27. Roy, M.; Li, Z.; Sacks, D.B. IQGAP1 Binds ERK2 and Modulates Its Activity. *J. Biol. Chem.* **2004**, *279*, 17329–17337. [CrossRef] [PubMed]
28. Roy, M.; Li, Z.; Sacks, D.B. IQGAP1 Is a Scaffold for Mitogen-Activated Protein Kinase Signaling. *Mol. Cell. Biol.* **2005**, *25*, 7940. [CrossRef] [PubMed]
29. Ren, J.G.; Li, Z.; Sacks, D.B. IQGAP1 modulates activation of B-Raf. *Proc. Natl. Acad. Sci. USA* **2007**, *104*, 10465–10469. [CrossRef] [PubMed]
30. Benseñor, L.B.; Kan, H.M.; Wang, N.; Wallrabe, H.; Davidson, L.A.; Cai, Y.; Schafer, D.A.; Bloom, G.S. IQGAP1 regulates cell motility by linking growth factor signaling to actin assembly. *J. Cell Sci.* **2007**, *120*, 658–669. [CrossRef] [PubMed]
31. Le Clainche, C.; Schlaepfer, D.; Ferrari, A.; Klingauf, M.; Grohmanova, K.; Veligodskiy, A.; Didry, D.; Le, D.; Egile, C.; Carlier, M.F.; et al. IQGAP1 stimulates actin assembly through the N-wasp-Arp2/3 pathway. *J. Biol. Chem.* **2007**, *282*, 426–435. [CrossRef]
32. Kaur, R.; Yuan, X.; Lu, M.L.; Balk, S.P. Increased PAK6 expression in prostate cancer and identification of PAK6 associated proteins. *Prostate* **2008**, *68*, 1510–1516. [CrossRef]

33. Usatyuk, P.V.; Gorshkova, I.A.; He, D.; Zhao, Y.; Kalari, S.K.; Garcia, J.G.N.; Natarajan, V. Phospholipase D-mediated Activation of IQGAP1 through Rac1 regulates hyperoxia-induced p47phox translocation and reactive oxygen species generation in lung endothelial cells. *J. Biol. Chem.* **2009**, *284*, 15339–15352. [CrossRef] [PubMed]
34. Pelikan-Conchaudron, A.; Le Clainche, C.; Didry, D.; Carlier, M.F. The IQGAP1 protein is a calmodulin-regulated barbed end capper of actin filaments: Possible implications in its function in cell migration. *J. Biol. Chem.* **2011**, *286*, 35119–35128. [CrossRef] [PubMed]
35. Pudewell, S.; Wittich, C.; Kazemein Jasemi, N.S.; Bazgir, F.; Ahmadian, M.R. Accessory proteins of the RAS-MAPK pathway: Moving from the side line to the front line. *Commun. Biol.* **2021**, *4*, 696. [CrossRef] [PubMed]
36. Watanabe, T.; Wang, S.; Kaibuchi, K. IQGAPs as Key Regulators of Actin-cytoskeleton Dynamics Mini-review and Review. *Cell Struct. Funct.* **2015**, *40*, 69–77. [CrossRef]
37. Abel, A.M.; Schuldt, K.M.; Rajasekaran, K.; Hwang, D.; Riese, M.J.; Rao, S.; Thakar, M.S.; Malarkannan, S. IQGAP1: Insights into the function of a molecular puppeteer. *Mol. Immunol.* **2015**, *65*, 336–349. [CrossRef] [PubMed]
38. Hedman, A.C.; Smith, J.M.; Sacks, D.B. The biology of IQGAP proteins: Beyond the cytoskeleton. *EMBO Rep.* **2015**, *16*, 427–446. [CrossRef] [PubMed]
39. Smith, J.M.; Hedman, A.C.; Sacks, D.B. IQGAPs choreograph cellular signaling from the membrane to the nucleus. *Trends Cell Biol.* **2015**, *25*, 171–184. [CrossRef]
40. Choi, S.; Anderson, R.A. IQGAP1 is a phosphoinositide effector and kinase scaffold. *Adv. Biol. Regul.* **2016**, *60*, 29–35. [CrossRef] [PubMed]
41. Tanos, B.E.; Yeaman, C.; Rodriguez-Boulan, E. An emerging role for IQGAP1 in tight junction control. *Small GTPases* **2018**, *9*, 375–383. [CrossRef] [PubMed]
42. Nussinov, R.; Zhang, M.; Tsai, C.J.; Jang, H. Calmodulin and IQGAP1 activation of PI3Kα and Akt in KRAS, HRAS and NRAS-driven cancers. *Biochim. Biophys. Acta Mol. Basis Dis.* **2018**, *1864*, 2304–2314. [CrossRef] [PubMed]
43. White, C.D.; Li, Z.; Dillon, D.A.; Sacks, D.B. IQGAP1 Protein Binds Human Epidermal Growth Factor Receptor 2 (HER2) and Modulates Trastuzumab Resistance. *J. Biol. Chem.* **2011**, *286*, 29734. [CrossRef] [PubMed]
44. Liu, C.; Billadeau, D.D.; Abdelhakim, H.; Leof, E.; Kaibuchi, K.; Bernabeu, C.; Bloom, G.S.; Yang, L.; Boardman, L.; Shah, V.H.; et al. IQGAP1 suppresses TβRII-mediated myofibroblastic activation and metastatic growth in liver. *J. Clin. Investig.* **2013**, *123*, 1138–1156. [CrossRef] [PubMed]
45. Jameson, K.L.; Mazur, P.K.; Zehnder, A.M.; Zhang, J.; Zarnegar, B.; Sage, J.; Khavari, P.A. IQGAP1 scaffold-kinase interaction blockade selectively targets RAS-MAP kinase–driven tumors. *Nat. Med.* **2013**, *19*, 626–630. [CrossRef] [PubMed]
46. Choi, S.; Hedman, A.C.; Sayedyahossein, S.; Thapa, N.; Sacks, D.B.; Anderson, R.A. Agonist-stimulated phosphatidylinositol-3,4,5-trisphosphate generation by scaffolded phosphoinositide kinases. *Nat. Cell Biol.* **2016**, *18*, 1324–1335. [CrossRef] [PubMed]
47. Peng, X.; Wang, T.; Gao, H.; Yue, X.; Bian, W.; Mei, J.; Zhang, Y. The interplay between IQGAP1 and small GTPases in cancer metastasis. *Biomed. Pharmacother.* **2021**, *135*, 111243. [CrossRef]
48. Wei, T.; Lambert, P.F. Role of IQGAP1 in Carcinogenesis. *Cancers* **2021**, *13*, 3940. [CrossRef]
49. Rotoli, D.; Díaz-Flores, L.; Gutiérrez, R.; Morales, M.; Ávila, J.; Martín-Vasallo, P. Amotl2, IQGAP1, and FKBP51 Scaffold Proteins in Glioblastoma Stem Cell Niches. *J. Histochem. Cytochem.* **2022**, *70*, 9–16. [CrossRef]
50. Elliott, S.F. Biochemical analysis of the interactions of IQGAP1 C-terminal domain with CDC42. *World J. Biol. Chem.* **2012**, *3*, 53. [CrossRef]
51. Nouri, K.; Fansa, E.K.; Amin, E.; Dvorsky, R.; Gremer, L.; Willbold, D.; Schmitt, L.; Timson, D.J.; Ahmadian, M.R. IQGAP1 interaction with RHO family proteins revisited: kinetic and equilibrium evidence for multiple distinct binding sites. *J. Biol. Chem.* **2016**, *291*, 26364–26376. [CrossRef]
52. Swart-Mataraza, J.M.; Li, Z.; Sacks, D.B. IQGAP1 is a component of Cdc42 signaling to the cytoskeleton. *J. Biol. Chem.* **2002**, *277*, 24753–24763. [CrossRef] [PubMed]
53. Li, R.; Debreceni, B.; Jia, B.; Gao, Y.; Tigyi, G.; Zheng, Y. Localization of the PAK1-, WASP-, and IQGAP1-specifying regions of Cdc42. *J. Biol. Chem.* **1999**, *274*, 29648–29654. [CrossRef] [PubMed]
54. Sila Ozdemir, E.; Jang, H.; Gursoy, A.; Keskin, O.; Li, Z.; Sacks, D.B.; Nussinov, R. Unraveling the molecular mechanism of interactions of the Rho GTPases Cdc42 and Rac1 with the scaffolding protein IQGAP2. *J. Biol. Chem.* **2018**, *293*, 3685–3699. [CrossRef] [PubMed]
55. Scheffzek, K.; Ahmadian, M.R.; Kabsch, W.; Wiesmüller, L.; Lautwein, A.; Schmitz, F.; Wittinghofer, A. The Ras-RasGAP complex: Structural basis for GTPase activation and its loss in oncogenic ras mutants. *Science* **1997**, *277*, 333–338. [CrossRef] [PubMed]
56. Owen, D.; Campbell, L.J.; Littlefield, K.; Evetts, K.A.; Li, Z.; Sacks, D.B.; Lowe, P.N.; Mott, H.R. The IQGAP1-Rac1 and IQGAP1-Cdc42 interactions: Interfaces differ between the complexes. *J. Biol. Chem.* **2008**, *283*, 1692–1704. [CrossRef]
57. Kurella, V.B.; Richard, J.M.; Parke, C.L.; LeCour, L.F.; Bellamy, H.D.; Worthylake, D.K. Crystal structure of the GTPase-activating protein-related domain from IQGAP1. *J. Biol. Chem.* **2009**, *284*, 14857–14865. [CrossRef]
58. Gorisse, L.; Li, Z.; Wagner, C.D.; Worthylake, D.K.; Zappacosta, F.; Hedman, A.C.; Annan, R.S.; Sacks, D.B. Ubiquitination of the scaffold protein IQGAP1 diminishes its interaction with and activation of the Rho GTPase CDC42. *J. Biol. Chem.* **2020**, *295*, 4822–4835. [CrossRef]

59. McCallum, S.J.; Wu, W.J.; Cerione, R.A. Identification of a putative effector for Cdc42Hs with high sequence similarity to the RasGAP-related protein IQGAP1 and a Cdc42Hs binding partner with similarity to IQGAP2. *J. Biol. Chem.* **1996**, *271*, 21732–21737. [CrossRef]
60. Hart, M.J.; Callow, M.G.; Souza, B.; Polakis, P. IQGAP1, a calmodulin-binding protein with a rasGAP-related domain, is a potential effector for cdc42Hs. *EMBO J.* **1996**, *15*, 2997–3005. [CrossRef]
61. Zhang, B.; Chernoff, J.; Zheng, Y. Interaction of Rac1 with GTPase-activating proteins and putative effectors. A comparison with Cdc42 and RhoA. *J. Biol. Chem.* **1998**, *273*, 8776–8782. [CrossRef]
62. Kuroda, S.; Fukata, M.; Nakagawa, M.; Fujii, K.; Nakamura, T.; Ookubo, T.; Izawa, I.; Nagase, T.; Nomura, N.; Tani, H.; et al. Cdc42 and Rac1 Regulate the Interaction of IQGAP1 with β-Catenin. *J. Biol. Chem.* **1999**, *274*, 26044–26050. [CrossRef]
63. Grohmanova, K.; Schlaepfer, D.; Hess, D.; Gutierrez, P.; Beck, M.; Kroschewski, R. Phosphorylation of IQGAP1 modulates its binding to Cdc42, revealing a new type of Rho-GTPase regulator. *J. Biol. Chem.* **2004**, *279*, 48495–48504. [CrossRef] [PubMed]
64. Mataraza, J.M.; Briggs, M.W.; Li, Z.; Frank, R.; Sacks, D.B. Identification and characterization of the Cdc42-binding site of IQGAP1. *Biochem. Biophys. Res. Commun.* **2003**, *305*, 315–321. [CrossRef]
65. Scheffzek, K.; Ahmadian, M.R.; Wittinghofer, A. GTPase-activating proteins: Helping hands to complement an active site. *Trends Biochem. Sci.* **1998**, *23*, 257–262. [CrossRef]
66. Chen, S.; Shu, L.; Zhao, R.; Zhao, Y. Molecular dynamics simulations reveal the activation mechanism of mutations G12V and Q61L of Cdc42. *Proteins Struct. Funct. Bioinform.* **2022**, *90*, 1376–1389. [CrossRef]
67. Ahmadian, M.R.; Stege, P.; Scheffzek, K.; Wittinghofer, A. Confirmation of the arginine-finger hypothesis for the GAP-stimulated GTP-hydrolysis reaction of Ras. *Nat. Struct. Biol.* **1997**, *4*, 686–689. [CrossRef] [PubMed]
68. Ahmadian, M.R.; Kiel, C.; Stege, P.; Scheffzek, K. Structural fingerprints of the Ras-GTPase activating proteins neurofibromin and p120GAP. *J. Mol. Biol.* **2003**, *329*, 699–710. [CrossRef]
69. Scheffzek, K.; Shivalingaiah, G. Ras-specific gtpase-activating proteins—structures, mechanisms, and interactions. *Cold Spring Harb. Perspect. Med.* **2019**, *9*, a031500. [CrossRef]
70. Scheffzek, K.; Ahmadian, M.R. GTPase activating proteins: Structural and functional insights 18 years after discovery. *Cell. Mol. Life Sci.* **2005**, *62*, 3014–3038. [CrossRef]
71. Jaiswal, M.; Dubey, B.N.; Koessmeier, K.T.; Gremer, L.; Ahmadian, M.R. Biochemical assays to characterize Rho GTPases. *Methods Mol. Biol.* **2012**, *827*, 37–58. [CrossRef]
72. Hemsath, L.; Ahmadian, M.R. Fluorescence approaches for monitoring interactions of Rho GTPases with nucleotides, regulators, and effectors. *Methods* **2005**, *37*, 173–182. [CrossRef] [PubMed]

CHAPTER VII. CUTANEOUS MANIFESTATIONS IN COSTELLO SYNDROME: HRAS P. GLY12SER AFFECTS RIN1-MEDIATED INTEGRIN TRAFFICKING IN IMMORTALIZED EPIDERMAL KERATINOCYTES

Nauth T, Bazgir F, Voß H, Brandenstein LI, Mosaddeghzadeh N, Rikassel V, Deden S, Gorzelanny C, Schülter H, Ahmadian MR, Rosenberger G

DOI: 10.1093/hmg/ddac188

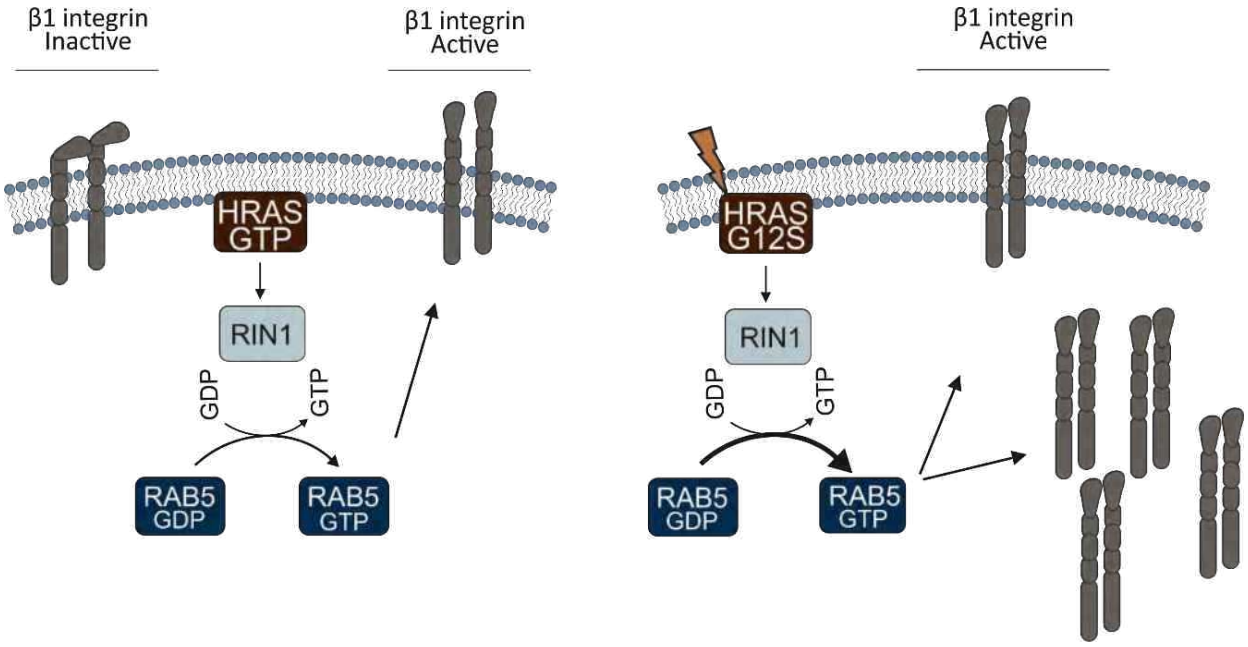

Status:	Published in August 2022
Journal:	Human Molecular Genetics
Impact factor:	6.15
Contribution:	10% Expression and purification HRAS wild type and mutants, RIN1, preparation of nucleotide-free form of HRAS.

Human Molecular Genetics, 2022, Vol. 00, 00, 1–15
https://doi.org/10.1093/hmg/ddac188
Advance access publication date 18 August 2022
Original Article

Cutaneous manifestations in Costello syndrome: HRAS p.Gly12Ser affects RIN1-mediated integrin trafficking in immortalized epidermal keratinocytes

Theresa Nauth[1,†], Farhad Bazgir[2,†], Hannah Voß[1], Laura I. Brandenstein[1], Niloufar Mosaddeghzadeh[2], Verena Rickassel[1], Sophia Deden[1], Christian Gorzelanny[4], Hartmut Schlüter[3], Mohammad R. Ahmadian[2] and Georg Rosenberger[1,*]

[1]Institute of Human Genetics, University Medical Center Hamburg-Eppendorf, 20246 Hamburg, Germany
[2]Institute of Biochemistry and Molecular Biology II, Medical Faculty and University Hospital Düsseldorf, Heinrich-Heine University, 40225 Düsseldorf, Germany
[3]Institute of Clinical Chemistry and Laboratory Medicine, Section Mass Spectrometry and Proteomics, University Medical Center Hamburg-Eppendorf, 20246 Hamburg, Germany
[4]Department of Dermatology and Venereology, University Medical Center Hamburg-Eppendorf, 20246 Hamburg, Germany

*To whom correspondence should be addressed at: Institute of Human Genetics, University Medical Center Hamburg-Eppendorf, Martinistraße 52, 20246 Hamburg, Germany. Tel: +49 40 74105 4594; Fax: +49 40 74105 5338; Email: rosenberger@uke.de

†TN and FB share the first author position.

Abstract

Heterozygous germline missense variants in the HRAS gene underlie Costello syndrome (CS). The molecular basis for cutaneous manifestations in CS is largely unknown. We used an immortalized human cell line, HaCaT keratinocytes, stably expressing wild-type or CS-associated (p.Gly12Ser) HRAS and defined RIN1 as quantitatively most prominent, high-affinity effector of active HRAS in these cells. As an exchange factor for RAB5 GTPases, RIN1 is involved in endosomal sorting of cell-adhesion integrins. RIN1-dependent RAB5A activation was strongly increased by $HRAS^{Gly12Ser}$, and HRAS-RIN1-ABL1/2 signaling was induced in $HRAS^{WT}$- and $HRAS^{Gly12Ser}$-expressing cells. Along with that, $HRAS^{Gly12Ser}$ expression decreased total integrin levels and enriched β1 integrin in RAB5- and EEA1-positive early endosomes. The intracellular level of active β1 integrin was increased in $HRAS^{Gly12Ser}$ HaCaT keratinocytes due to impaired recycling, whereas RIN1 disruption raised β1 integrin cell surface distribution. $HRAS^{Gly12Ser}$ induced co-localization of β1 integrin with SNX17 and RAB7 in early/sorting and late endosomes, respectively. Thus, by retaining β1 integrin in intracellular endosomal compartments, HRAS-RIN1 signaling affects the subcellular availability of β1 integrin. This may interfere with integrin-dependent processes as we detected for $HRAS^{Gly12Ser}$ cells spreading on fibronectin. We conclude that dysregulation of receptor trafficking and integrin-dependent processes such as cell adhesion are relevant in the pathobiology of CS.

Introduction

Costello syndrome (CS) (OMIM #218040), a rare developmental disorder, is characterized by a multiorgan presentation with distinctive facial features, failure-to-thrive, developmental delay, cardiac manifestations and a history of polyhydramnios (1). Moreover, patients show distinct dermatologic features including loose, redundant and soft skin on the neck, hands and feet, deep palmar and plantar creases, hyperpigmentation and prematurely aged skin. With increasing age, patients develop palmoplantar keratoderma and facial papillomata, preferentially in the face and perianal region. Individuals with CS have sparse and curly hair, frontotemporal alopecia, brittle and thin fingernails and toenails as well as spatulate finger pads (1,2). CS is caused by pathogenic heterozygous germline variants in the proto-oncogene HRAS, which cause constitutive HRAS activation (3). Approximately 80% of CS-associated HRAS variants result in the missense change p.Gly12Ser (1).

HRAS acts as molecular switch by alternating between an active guanosine triphosphate (GTP)-bound and inactive guanosine diphosphate (GDP)-bound state. Active HRAS binds to diverse effectors and, thereby, controls a variety of cellular signaling pathways. Amongst HRAS effectors the serine/threonine RAF kinases, the catalytic subunits of phosphoinositide 3-kinases (PIK3CA), phospholipase C1 (PLCE1) and RAL guanine nucleotide dissociation stimulator (RALGDS) are best characterized (4). Less is known about the HRAS effector RAS and RAB interactor 1 (RIN1) and its associated signaling pathways (5,6): binding of active HRAS to RIN1 promotes the activation of RAB5 GTPases (7) and ABL1/2 tyrosine kinases (8). Through these two signaling branches, endosomal sorting events and cytoskeletal dynamics are coordinated (7–12). Translocation of RIN1 between cytoplasmic and membrane compartments is controlled in part by Ser^{351} phosphorylation-dependent binding to 14-3-3 proteins (10,13).

The molecular pathophysiology caused by disease-associated HRAS variants has been investigated in various cell types including neuronal cells, heart muscle cells, fibroblasts and others (14–19). However, up to date the molecular basis for dermatologic/epidermal findings in CS and other RASopathies is largely unknown.

The epithelium of the skin, the epidermis, is composed of four layers of keratinocytes that undergo proliferation and programmed differentiation (20). This process—also known as epidermal stratification—is the prerequisite for a functional and

Received: March 9, 2022. Revised: July 15, 2022. Accepted: August 7, 2022

healthy skin, and HRAS has been shown to be an important modulator in keratinocyte stratification (21,22). The basal keratinocytes are highly proliferative and connect the epidermis with the extracellular matrix (ECM) and the dermis via focal adhesions and hemidesmosomes (20,23). Moreover, keratinocytes are in close contact with neighboring keratinocytes through cell–cell contacts, including adherens junctions, tight junctions, desmosomes and gap junction (20,23). All of these cell–cell and cell–ECM contacts are facilitated by diverse transmembrane and cell adhesion proteins such as cadherins, claudins and integrins (20,23). Transmembrane integrins connect the actin cytoskeleton of the cell with the ECM and transduce signals in both directions. Integrin receptors consist of alpha and beta subunits, and the majority of these heterodimers contain the β1 subunit that plays a central role in the maintenance of epidermal stratification and adhesion to the basement membrane (20–25).

In line with the dynamic nature of the epidermis and to maintain epidermal homeostasis, keratinocytes continuously reorganize their cell–cell contacts and adhesion sites with neighboring cells and to the ECM, respectively (20). For this, a tightly regulated vesicle-based endosomal sorting (trafficking) machinery is essential to internalize, recycle back to the plasma membrane and/or degrade contact and adhesion proteins. Accordingly, the surface availability and activity of integrins in keratinocytes and, consequently, the efficiency to get in contact with the ECM and to appropriately respond to environmental cues is controlled by marked trafficking of these receptors within a cycle of endocytosis, recycling and lysosomal degradation (24,26). Notably, a large proportion of integrins is recycled back to the plasma membrane resulting in a remarkably protein half-life (12–24 hours) (24).

The RAB family of GTPases, in particular the RIN1 effector RAB5, regulates vesicle-dependent cellular distribution of integrins and, thereby, controls cell adhesion and adhesion-dependent processes such as cell spreading and migration (24,27). Spatiotemporal reorganization of the actin cytoskeleton is central for both integrin-dependent cell adhesion and motility (28), and the tyrosine kinases ABL1/2 downstream of RIN1 can promote actin polymerization during these processes (29,30).

Here we provide evidence for a critical function of the HRAS-RIN1 signaling node for adhesion-associated integrin trafficking in immortalized HaCaT keratinocytes, and we add a novel aspect in the molecular pathogenesis of CS.

Results

RIN1 is the quantitatively most prominent and high-affinity effector of HRAS in immortalized HaCaT keratinocytes

As an epidermal cellular model system, we used immortalized human keratinocyte cells (HaCaT) stably expressing HA-tagged $HRAS^{WT}$ (HA-$HRAS^{WT}$) and $HRAS^{Gly12Ser}$ (HA-$HRAS^{Gly12Ser}$), two clones each (indicated as 1 and 2). To identify keratinocyte-specific binding partners of HRAS, we affinity purified HA-$HRAS^{WT}$ and HA-$HRAS^{Gly12Ser}$ from HaCaT lysates and analyzed precipitates by differential quantitative proteomics. In total, 825 proteins were quantified (Supplementary Material, Table S1). A missing value tolerant nonlinear iterative partial least squares (NIPALS) principal component analysis (PCA) demonstrated the clear distinguishability of HA-$HRAS^{WT}$ and HA-$HRAS^{Gly12Ser}$ clones, based on the relative abundance of the proteins in the precipitates, according to principal component 1 (PC1, 78% of the explained variation) and PC2 (27%). Native and empty vector (EV) transfected HaCaT cells formed a separate cluster (Fig. 1A). Quantitative comparison of HA-$HRAS^{WT}$ and HA-$HRAS^{Gly12Ser}$ samples identified 82 significantly differential abundant proteins ($P < 0.05$ or = 1 and FoldChange difference > 1.5, Supplementary Results and Discussion, Supplementary Material, Table S1). Pearson's correlation-based hierarchical clustering was performed for all genes/proteins listed in the WP_RAS_SIGNALING gene-set (www.gsea-msigdb.org). Nineteen known HRAS-associated proteins where found (Fig. 1B). We identified the RAS and RAB interactor 1 (RIN1) (FC difference: 7.8) and Ras-related proteins Rap1a (RAP1A) and Rap1b (RAP1B) as highly abundant in HA-$HRAS^{Gly12Ser}$ vs HA-$HRAS^{WT}$ precipitates (Fig. 1B; Supplementary Material, Table S1). Notably, proteomic analyses of HaCaT cells expressing the oncogenic variant HA-$HRAS^{Gly12Val}$ resulted in a similar but not identical pattern compared with CS-associated HA-$HRAS^{Gly12Ser}$ expressing HaCaT keratinocytes (Supplementary Material, Fig. S1), this suggests mutation-specific consequences in addition to mutation effect overlaps. In this study, we focused on RIN1 (for details see Supplementary Material, Results and Discussion). Co-immunoprecipitation of endogenous RIN1 was increased by approximately 7-fold in HA-$HRAS^{Gly12Ser}$ compared to HA-$HRAS^{WT}$ expressing HaCaT keratinocytes cultured in 10% serum (Fig. 1C). Moreover, we used the GST-tagged RAS association domain of RIN1 (RIN1[RA]) and precipitated HA-tagged HRAS from HaCaT extracts. Whereas HA-$HRAS^{WT}$ was pulled down (PD) weakly, HA-$HRAS^{Gly12Ser}$ strongly co-precipitated with GST-RIN1[RA] demonstrating RIN1 binding with activated HRAS (Fig. 1D). By fluorescence polarization, we detected an approximately 2-fold increased binding affinity of RIN1[RA] with $HRAS^{Gly12Ser}$ vs $HRAS^{WT}$ (Fig. 1E and Supplementary Material, Fig. dS2). The mildly hyperactive $HRAS^{Gly12Gly}$ showed an affinity to RIN1[RA] comparable with $HRAS^{WT}$, while no binding was detected for dominant negative $HRAS^{Ser17Asn}$. Finally, we compared expression of HRAS pathway proteins in HaCaT, HEK-293, HeLa cells as well as primary keratinocytes and primary fibroblasts. RIN1 is strongly expressed in HaCaT cells and primary keratinocytes, however, (very) weakly in primary fibroblasts and in HeLa cells (Fig. 1F). We did not detect RIN1 in HEK-293 cells. Similar to RIN1, strongest expression of HRAS was detected in HaCaT and primary keratinocytes (Fig. 1F). Whereas expression of PI3K and PLCe was robust in (HaCaT and primary) keratinocytes, RALGDS protein levels were moderate, each compared to the remaining cell types (Fig. 1F). RAF1 was well expressed in HEK-293 and HeLa cells but weakly in HaCaT keratinocytes (Supplementary Material, Fig. S3A). Accordingly, expression of HA-$HRAS^{Gly12Ser}$ or HA-$HRAS^{WT}$ did not significantly affect RAF-mediated phosphorylation of MEK1/2 and ERK1/2 (Supplementary Material, Fig. S3B). These data indicate that HRAS-RIN1 signaling is relevant in keratinocyte biology.

HRAS controls RIN1 effector pathways

RIN1 is a guanine nucleotide exchange factor for the RAS-related protein RAB5A and an activator of non-receptor tyrosine-protein kinases ABL1/2 (7,8). To determine HRAS-RIN1 stimulated RAB5A activation, we measured the release of fluorescently labeled GDP (mant-deoxy-GDP) from recombinant RAB5A. In the absence of active HRAS protein, recombinant RIN1[GEF-RA]^{WT} (comprising the guanine exchange factor and RAS association domains) did not affect nucleotide exchange on RAB5A. Upon addition of GppNHp-loaded $HRAS^{WT}$, $HRAS^{Gly12Ser}$ or $HRAS^{Gly12Gly}$, the nucleotide exchange rate of RAB5A was significantly increased by 34-, 52- and 68-fold, respectively (Fig. 2A and Supplementary Material, Fig. S4). As a negative

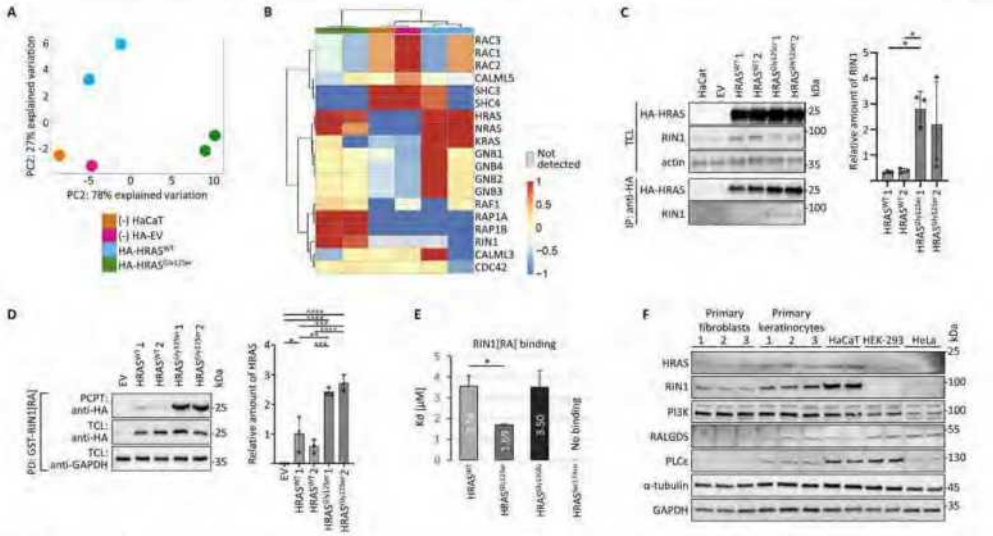

Figure 1. RIN1 is a highly abundant and high-affinity effector of HRAS in HaCaT keratinocytes. (**A**) Distinct proteomic relative quantitative differences between HaCaT keratinocytes expressing $HRAS^{WT}$ and $HRAS^{Gly12Ser}$. HRAS was precipitated with anti-HA magnetic beads and subjected to LC–MS/MS analysis. Scatter plot distribution of $HRAS^{WT}$ (blue) $HRAS^{Gly12Ser}$ (green) native (HaCaT, orange) and EV (pink) transfected (HA-EV) samples for the top two principal components in NIPALS PCA, based on 885 proteins quantified. PC, principle component. (**B**) RIN1 is highly abundant in HA-$HRAS^{Gly12Ser}$ precipitates. Pearson's correlation based hierarchical clustering of $HRAS^{WT}$, $HRAS^{Gly12Ser}$, native (HaCaT) and EV transfected (HA-EV) samples, based on all quantified proteins implemented in the WP_RAS_SIGNALING (www.gsea-msigdb.org) gene-set. The relative protein abundance is coded by colors from red (high abundant) to blue (low abundant). (**C**) RIN1 strongly co-precipitates with $HRAS^{Gly12Ser}$. TCL of HaCaT cells stably expressing HA-tagged HRAS variants and controls were subjected to IP with anti-HA magnetic beads. Co-precipitation and input levels of endogenous RIN1 were assessed by anti RIN1 immunoblotting. Actin was used as loading control. The graph shows relative amounts of co immunoprecipitated RIN1 normalized to immunoprecipitated HA HRAS and to total amounts of RIN1 and HA HRAS in cell lysates ($n = 3$). One way ANOVA, Tukey's multiple comparison test, $P < 0.05$, $n = 3$. (**D**) $HRAS^{Gly12Ser}$ efficiently co precipitates with RIN1 in GTPase pulldown assays. HA HRAS was PD from cell extracts of HaCaT keratinocytes stably expressing HA-$HRAS^{WT}$ or HA-$HRAS^{Gly12Ser}$ by using GST-fused RIN1[RA]. Precipitates (PCPT) and TCL were subjected to immunoblotting as indicated. The graph shows mean relative protein amounts of precipitated HA-HRAS normalized to total HA-HRAS ($n = 3$). One-way ANOVA, Tukey's multiple comparison test, $P < 0.05$. RIN1[RA], Ras and Rab interactor 1 [RAS association domain]. (**E**) RIN1 is a high affinity effector of HRAS. Fluorescence polarization experiments were performed to determine the dissociation constants (Kd) by titrating mantGppNHp bound HRAS variants with increasing concentrations of RIN1[RA]. mantGppNHp is a fluorescent, non hydrolyzable GTP analog under the experimental conditions. (**F**) HaCaT and primary keratinocytes (strongly) express RIN1 and HRAS. TCLs of primary fibroblasts and primary keratinocytes, (derived from three juvenile individuals each), as well as HaCaT keratinocytes, HEK-293 cells and HeLa cells were subjected to immunoblotting as indicated. α-tubulin and GAPDH were used as loading controls. RIN1, RAS and RAB interactor 1; PI3K, phosphoinositide 3-kinase; RALGDS, RAL guanine nucleotide dissociation stimulator; PLCε, phospholipase Cε.

control, we used inactive $HRAS^{Ser17Asn}$. The RIN1[GEF-RA]^{Glu574Ala} variant with reduced RAB5A GEF activity (31) resulted in lower increase of RAB5A nucleotide exchange rates (by 16-, 20- and 38-fold for $HRAS^{WT}$, $HRAS^{Gly12Ser}$ and $HRAS^{Gly12Asp}$, respectively) (Fig. 2A and Supplementary Material, Fig. S4). These findings suggest that the HRAS-RIN1-RAB5 signaling pathway is functional and depends on HRAS activity. As the cellular level of GTP is much higher than GDP, we conclude that increased RAB5A GDP release rates in the presence of $HRAS^{Gly12Ser}$ (or $HRAS^{Gly12Asp}$) compared to $HRAS^{WT}$ likely render RAB5A in an active GTP-bound state. To prove HRAS-RIN1-ABL signaling in immortalized keratinocytes, we generated RIN1-deficient HaCaT cells by using the Type II CRISPR-Cas system with tracrRNAs (32). As read-out, we determined Tyr^{421} phosphorylation of the adaptor protein CRKII, a well established ABL substrate (33). CRKII phosphorylation was significantly reduced in RIN1-deficient HaCaT cells vs native HaCaT cells (Fig. 2B). Conversely, cells stably overexpressing $HRAS^{WT}$ or $HRAS^{Gly12Ser}$ strongly increased CRKII phosphorylation (by 4- to 5-fold) compared with control (EV) cells (Fig. 2B). HRAS-promoted CRKII phosphorylation does require RIN1, because transient overexpression of HA-$HRAS^{WT}$ or HA-$HRAS^{Gly12Ser}$ enhanced CRKII phosphorylation in native HaCaT cells but not in RIN1-deficient HaCaT cells (Fig. 2C). Finally, we detected strong and medium expression of p-CRKII in HaCaT and primary keratinocytes, respectively (Fig. 2D). Thus, HRAS and RIN1 control ABL kinase-mediated downstream signaling in keratinocytes. RIN1 is regulated by the phosphorylation of serine 351 (Ser^{351}), which enhances interaction with 14-3-3 adaptor proteins and reduces RIN1 membrane residence and RAS accessibility (13). Phospho Ser^{351} levels were only tendentially but not significantly reduced in HaCaT cells expressing $HRAS^{Gly12Ser}$ vs $HRAS^{WT}$ (Fig. 2D). However, transiently expressed EGFP-$RIN1^{WT}$ was clearly enriched at the membrane of $HRAS^{Gly12Ser}$ cells (Fig. 2F and Supplementary Material, Fig. S5). Taken together, these data suggest that $HRAS^{Gly12Ser}$ affects RIN1-mediated signaling pathways.

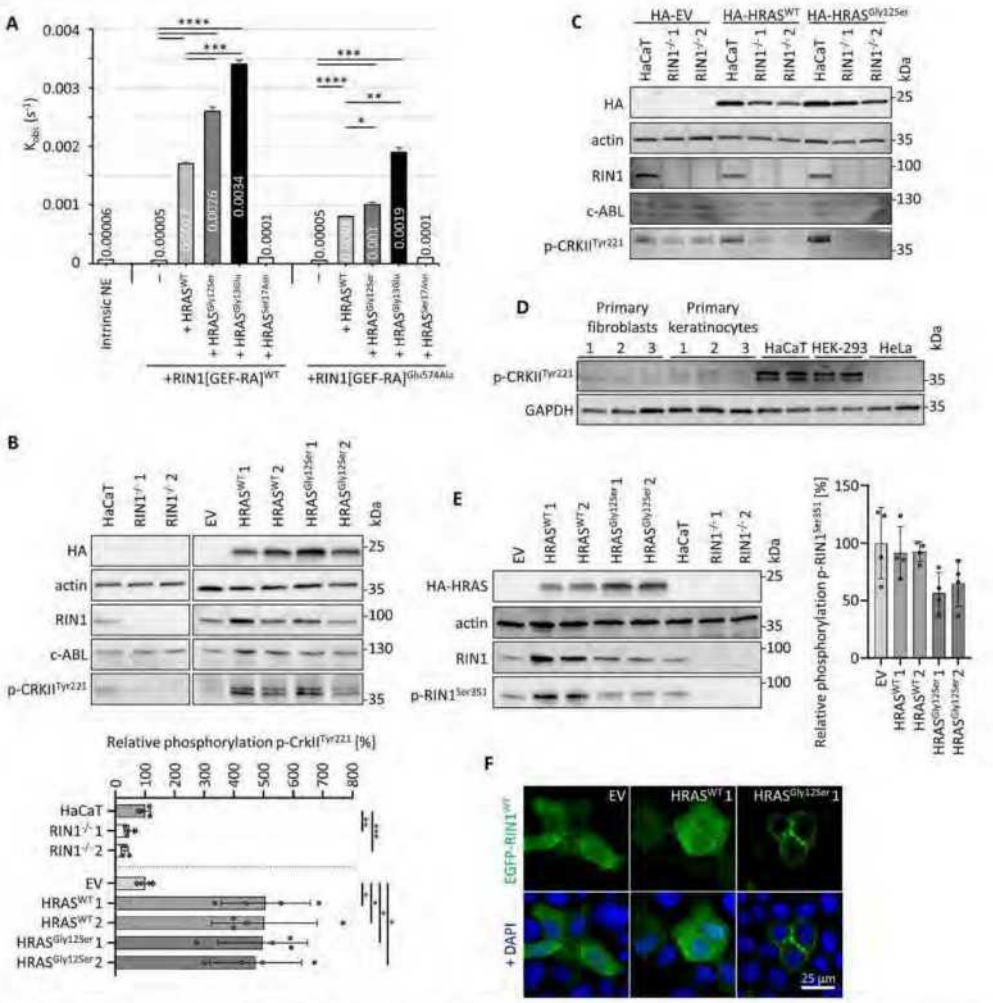

Figure 2. HRAS controls RIN1 effector pathways. (**A**) The HRAS-RIN1-RAB5 signaling axis is functional. The release of mant-deoxy-GDP from RAB5A was measured intrinsically (NE, nucleotide exchange) and in the presence of RIN1[GEF-RA] and HRAS variants as indicated in a fluorimeter instrument. K_{obs} (s^{-1}), observed fluorescent rates per second; *, $P < 0.05$; **, $P < 0.01$; ***, $P < 0.001$; ****, $P < 0.0001$; unpaired 2-tailed *T*-test. (**B**) HRAS stimulates activity of ABL. TCLs of native and RIN1-deficient HaCaT cells as well as HaCaT keratinocytes stably expressing HA-HRAS variants and EV-controls were subjected to immunoblotting as indicated. Phosphorylation levels of the c-ABL substrate CRKII (p-CRKII^{Tyr221}) were normalized to actin. The mean ± SD of four independent experiments ($n = 4$) each is shown relative to native HaCaT controls or EV controls. One-way ANOVA; Sidak's multiple comparison test; *, $P < 0.05$; c-ABL, tyrosine kinase ABL1. (**C**) HRAS promoted CRKII phosphorylation does require RIN1. Native and RIN1-deficient HaCaT cells were transiently transfected with EV (HA-EV), HA-HRAS^{WT} or HA-HRAS^{Gly125Ser} and TCLs were subjected to immunoblotting as indicated. Actin was used as loading control. (**D**) Phospho-CRKII is expressed in HaCaT and primary keratinocytes. TCLs of primary fibroblasts, primary keratinocytes, HaCaT keratinocytes, HEK-293 cells, and HeLa cells were subjected to immunoblotting using anti phospho-CRKII antibody (p-CRKII^{Tyr221}). GAPDH was used as loading control. (**E**) HRAS^{Gly125Ser} reduces RIN1^{Ser351} phosphorylation. Radioimmunoprecipitation assay buffer (RIPA) cell extracts were subjected to immunoblotting with antibodies against phosphorylated and total RIN1. Levels of phosphorylated RIN1^{Ser351} were double normalized to total RIN1 and actin. The graph shows relative phosphorylation of RIN1 (± SD) in four independent experiments ($n = 4$); EV was considered as 100%. One-way ANOVA with Tukey's multiple comparison test ($P < 0.05$) showed no significant difference. (**F**) Expression of HA-HRAS^{Gly125Ser} promotes membrane localization of RIN1. HaCaT cells expressing HRAS^{WT} or HRAS^{Gly125Ser} and control cells (EV) were transiently transfected with EGFP-RIN1^{WT}, fixed and stained with DAPI to visualize nuclei. Cells were imaged by confocal microscopy, scale bar 25 µm.

HRAS affects concentration and/or localization of integrins

Due to strong involvement of RAB5 GTPases and ABL kinases in integrin regulation (24,27–30), we compared levels of β1 and β4 integrin in various cell types. β1 integrin was robustly expressed in primary fibroblasts and keratinocytes, in HaCaT and HeLa cells, but not in HEK 293 cells (Fig. 3A). β4 integrin was detected only in HaCaT and primary keratinocytes but not in primary fibroblasts, HEK-293 and HeLa cells (Fig. 3A). Next, we examined the impact of HRAS and RIN1 on integrin expression in HaCaT cells. Immunoblotting analysis revealed a significant decrease of β4 integrin level in cells expressing $HRAS^{WT}$ or $HRAS^{Gly12Ser}$ compared to control (EV) cells (Fig. 3B). The level of β1 integrin was not significantly affected by the presence of $HRAS^{WT}$ or $HRAS^{Gly12Ser}$ (Fig. 3B). β1 and β4 integrin levels in RIN1-deficient HaCaT keratinocytes were similar to those in HaCaT control cells (Fig. 3B). Integrins are embedded in a dynamic cycle of endocytosis, recycling and degradation; depending on their activation state, they localize in endosomal structures or at the plasma membrane (34). We analyzed the distribution of β1 integrin by immunocytochemistry. Both active and total β1 integrin predominantly localize at the cell membrane in control (EV) and $HRAS^{WT}$ expressing cells (Fig. 3C; Supplementary Material, Fig. S6). HaCaT cells expressing $HRAS^{Gly12Ser}$ showed a strong enrichment of β1 integrin positive vesicles inside the cell body (Fig. 3C and D; Supplementary Material, Fig. S6). Co-staining with RAB5, a marker protein for early endosomes (24,35), revealed co-localization of β1 integrin with RAB5 at these intracellular vesicles (Fig. 3C; Supplementary Material, Fig. S6). We determined moderate occurrence of β1 integrin-positive vesicles in RIN1-deficient cells, however these only marginally colocalized with RAB5 (Fig. 3C and D; Supplementary Material, Fig. S6). Next, we visualized the early endosomal marker protein EEA1 (35). We detected a rather weak co-localization of EEA1 with β1 integrin both, in control (EV) and $HRAS^{WT}$ expressing cells; the size of EEA1 positive vesicles was slightly increased in $HRAS^{WT}$ cells compared to control cells (Supplementary Material, Fig. S7). $HRAS^{Gly12Ser}$ expression was associated with clearly enlarged or clustered EEA1-positive vesicles and partial co-localization with β1 integrin (Supplementary Material, Fig. S7). RIN1 $^{-/-}$ HaCaT keratinocytes showed very small EEA1-positive vesicles with very weak or without β1 integrin co-localization, which was similar to native HaCaT cells (Supplementary Material, Fig. S7). Our data suggest that $HRAS^{Gly12Ser}$ promotes enrichment of β1 integrin in the early endosomal compartment. In addition to HRAS-induced deregulation of β1 and β4 integrin, we detected decreased abundance of α6 and α2 integrins in HaCaT cells expressing $HRAS^{WT}$ (Supplementary Material, Fig. S8A). Finally, immunofluorescence analysis revealed a strong enrichment of E-cadherin positive intracellular vesicles in $HRAS^{Gly12Ser}$ HaCaT cells (Supplementary Material, Fig. S8B). Taken together, altered HRAS signaling may interfere with a central cellular mechanism that controls abundance and distribution of diverse cell contact and adhesion molecules.

$HRAS^{Gly12Ser}$ affects integrin trafficking

Surface availability and activity of integrins is controlled by trafficking within a cycle of endocytosis, recycling and lysosomal degradation (24,26). We used antibody TS2/16 specific for the active conformation, applied flow cytometry (34,36) and determined the amount of active integrin both on the cell surface before internalization and in intracellular compartments after internalization. HaCaT cells stably expressing $HRAS^{WT}$ showed a similar relative amount of active cell surface β1 integrin as control cells (EV) (Fig. 4A). Stable over-expression of active $HRAS^{Gly12Ser}$ slightly but not significantly reduced the relative amount of β1 integrin at the cell surface in both $HRAS^{Gly12Ser}$ cell lines (1 and 2) (Fig. 4A). Quantification of intracellular β1 integrin over time revealed strongest differences between cell clones after 15 min internalization (Supplementary Material, Fig. S9). At this point, the fraction of internalized β1 integrin was increased by approximately 1.5-fold in HaCaT keratinocytes expressing $HRAS^{Gly12Ser}$ vs $HRAS^{WT}$ or control (EV) cells (Fig. 4B). These results suggest that $HRAS^{Gly12Ser}$ affects integrin trafficking by increasing the intracellular fraction of active β1 integrin. To discriminate if $HRAS^{Gly12Ser}$ stimulates endocytosis or impairs recycling of β1 integrin, we performed internalization assays in the presence of the recycling inhibitor primaquine (37). Upon 15 min internalization, the amount of intracellular β1 integrin was similar in HaCaT cells expressing $HRAS^{Gly12Ser}$, $HRAS^{WT}$ or control cells (Fig. 4C). These data suggest that expression of CS-associated HA-$HRAS^{Gly12Ser}$ interferes with recycling of active integrin. Knock out of RIN1 did not affect internalized β1 integrin level, however, cell surface level was slightly—but not significantly—increased (Supplementary Material, Fig. S10). We could support these results by immunocytochemical examination using the marker protein SNX17 (sorting nexin 17) that promotes recycling of the receptor over lysosomal degradation at early and sorting endosomes (24,26,38). Stable expression of $HRAS^{Gly12Ser}$ resulted in increased localization of active/total β1 integrin at SNX17-positive vesicles (Fig. 4D; Supplementary Material, Fig. S11A). Knockout of RIN1 had no effect on this localization (Supplementary Material, Fig. S11B). Inactive β1 integrins are rapidly recycled in a RAB4-dependent manner, whereas active receptors are trafficked through the RAB11 long-loop pathway (26). Expression of $HRAS^{Gly12Ser}$ had no significant effect on the distribution of active/total integrin at RAB4-positive vesicles (Supplementary Material, Fig. S12A) and slightly increased localization of active β1 integrin at RAB11-positive vesicles (Supplementary Material, Fig. S12B). RIN1-deficient cells showed an increased number of RAB4-positive vesicles without β1 integrin co-localization (Supplementary Material, Fig. S12C). Taken together, our data suggest that CS-associated $HRAS^{Gly12Ser}$ enriches β1 integrin in the endosomal compartment on the cost of surface integrin. In line with this, visualization of RAB7, a marker for late endosomes, showed enhanced co-localization with total β1 integrin in $HRAS^{Gly12Ser}$ cells (Supplementary Material, Fig. S13). In contrast, by using lysosomal marker LAMP1 we detected no co-localization with β1 integrin in these cells (Supplementary Material, Fig. S14). We conclude that over-expression of $HRAS^{Gly12Ser}$ disturbs the balance between cell surface and intracellular β1 integrin pools in HaCaT keratinocytes and HRAS-RIN1 signaling regulates β1 integrin availability at the cell surface.

HRAS-RIN1 signaling controls HaCaT keratinocyte spreading on fibronectin

Integrin trafficking is directly implicated in the regulation of cell spreading and cell migration (24,39). We studied the consequences of HRAS-RIN1 signaling on spreading of HaCaT cells on fibronectin-coated coverslips. Cells expressing $HRAS^{WT}$ or $HRAS^{Gly12Ser}$ showed significantly fewer cell protrusions (i.e. filopodia) and a general decreased spreading ability compared to EV transfected cells (Fig. 5A). HaCaT cells deficient for RIN1 are rich of actin bundles, spread very quickly, and were significantly larger compared to native HaCaT cells (Fig. 5B). These findings

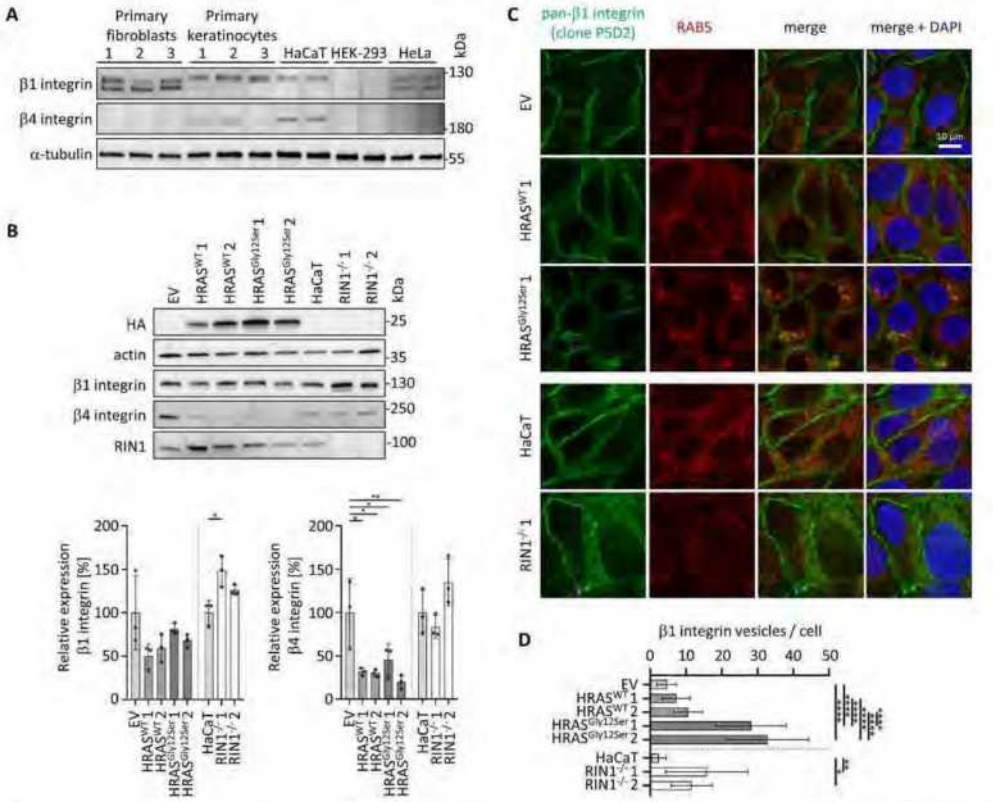

Figure 3. HRAS-RIN1 signaling controls expression and localization of integrins. (**A**) Primary and HaCaT keratinocytes express β1 and β4 integrin. TCLs of primary fibroblasts, primary keratinocytes, HaCaT keratinocytes, HEK-293 cells and HeLa cells were subjected to immunoblotting as indicated. Both, mature (upper band) and precursor (lower band) β1 integrin were detected. α-tubulin was used as loading control. (**B**) HRAS-RIN1 signaling modulates expression of integrins. TCLs of HaCaT keratinocytes stably expressing HA HRAS variants, EV controls, native HaCaT cells and RIN1 deficient cells were subjected to immunoblotting as indicated. Graphs show the mean (± SD) of β1 (left) and β4 (right) integrin levels from three independent experiments relative to EV and HaCaT cells. One-way ANOVA, Tukey's multiple comparison test, $P < 0.05$ was used. (**C**) β1 integrin is enriched in RAB5-positive vesicles in cells expressing HA-HRAS^{Gly12Ser}. HaCaT cells were plated on coverslips, fixed and Rab5 was stained by mouse anti-Rab5 antibody followed by anti-mouse Alexa Fluor 568-conjugated antibody. After blocking, cells were stained by directly conjugated mouse β1 integrin P5D2-Alexa 488. Nuclear DNA was labeled by DAPI. Scale 10 µm. $n = 3$. (**D**) β1 integrin positive vesicles are increased in HA HRAS^{Gly12Ser} HaCaT keratinocytes. HaCaT keratinocytes stably expressing HRAS^{WT}, HRAS^{Gly12Ser} or EV-controls, as well as native HaCaT cells and RIN1 deficient cells were stained for β1 integrin. Microscopic images were analyzed for β1 integrin positive intracellular vesicles with Imaris as described in the methods section. Graph shows mean numbers of β1 integrin positive vesicles per cell (± SD) from 3–5 independent experiments. One-way ANOVA, Tukey's multiple comparison test, $P < 0.05$ was used.

suggest that HRAS RIN1 signaling is a key pathway to control cell spreading.

Discussion

The epidermal manifestation in patients with CS raises the question on the functional impact of CS-associated HRAS variants in keratinocytes, the major cell type in the human skin. We report here for the first time on the crucial function of HRAS RIN1 signaling in endocytic sorting of integrin receptors in immortalized epidermal HaCaT keratinocytes. Expression of the CS-typical HRAS variant p.Gly12Ser essentially affected integrin trafficking, suggesting a role of altered integrin availability in the pathogenesis of the epidermal manifestation in CS. In line with this, β1 integrin dysfunction has been associated with CS typical epidermal manifestations including epidermal thickening, prematurely aged skin, keratosis and papillomata as well hair abnormalities (for details see Supplementary Material, Results and Discussion) (40–45).

HRAS-RIN1 signaling in HaCaT keratinocytes

We showed that the previously less perceived HRAS effector RIN1 is strongly expressed both in permanent and primary keratinocytes and greatly enriched in HRAS^{Gly12Ser} precipitates. RIN1 binds with high affinity and specificity to activated HRAS (6,13,46). Similarly, we found a high binding affinity of RIN1 with HRAS^{Gly12Ser}. It has been demonstrated that RIN1 efficiently competed with RAF1 for binding to activated RAS *in vitro* (13).

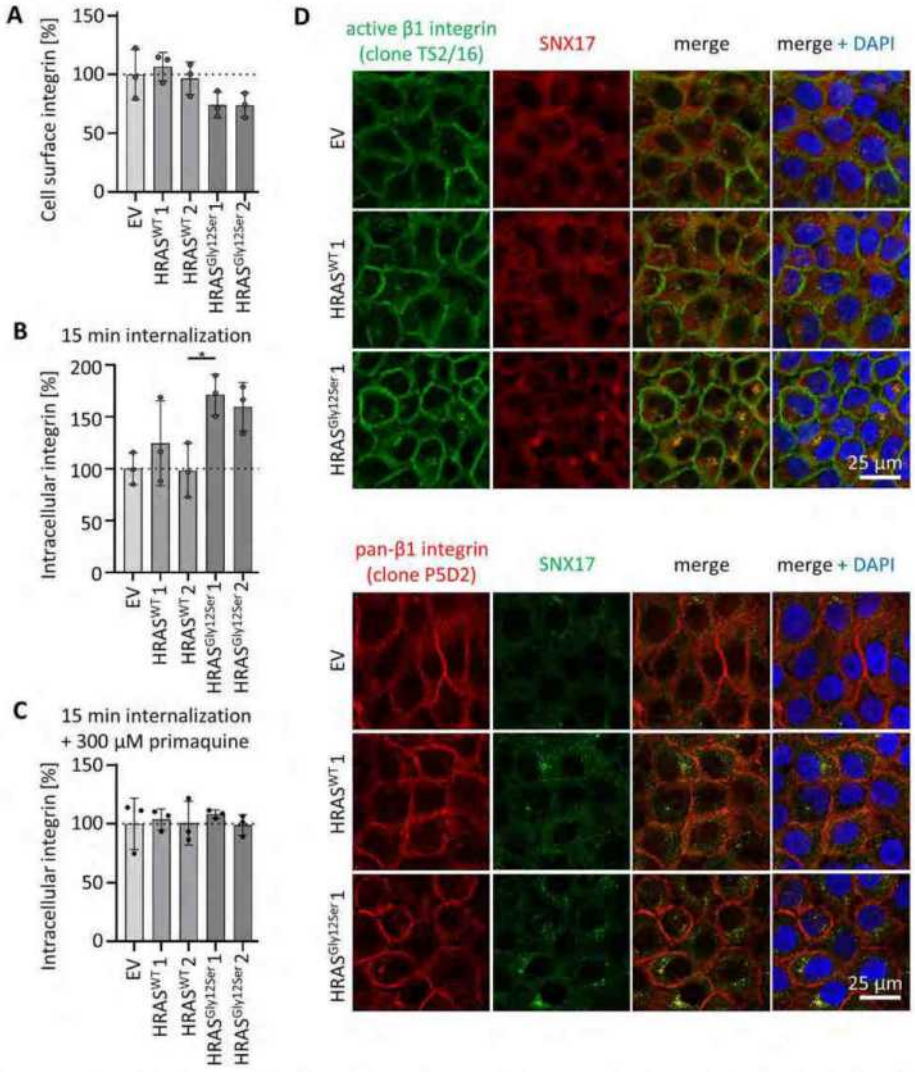

Figure 4. (**A**–**C**) $HRAS^{Gly12Ser}$ interferes with integrin trafficking. Cells were starved, incubated on ice, labeled with antibodies against active β1 integrin (TS2/16-Alexa Fluor 488) and further processed as described in methods. Graphs show the mean (± SD) amounts of β1 integrin on the cell surface before internalization (A), intracellular β1 integrin after 15 min internalization (B) and intracellular β1 integrin after 15 min internalization in the presence of primaquine (C) from three independent experiments each ($n = 3$). After internalization, remaining fluorescence on the cell surface was quenched by acidic wash treatment and fluorescence intensities of internalized β1 integrin (B and C) were normalized against total cell surface fluorescence intensities from (A). Fluorescent intensities of EV-transfected control cells were considered as 100%. *P* values were calculated by one-way ANOVA with Tukey's multiple comparison test ($P < 0.05$). (**D**) β1 integrin is enriched at SNX17-positive vesicles in HaCaT keratinocytes expressing HA-$HRAS^{Gly12Ser}$. HaCaT cells stably expressing HA-HRAS variants or transfected with EV were seeded on coverslips, fixed and stained with rabbit anti-SNX17 antibody followed by anti-rabbit Alexa Fluor 568 (red) and Alexa Fluor 488-conjugated mouse anti β1 integrin TS2/16 (green) antibodies (upper part of the figure). To visualize total β1 integrin, cells were stained with mouse anti-β1 integrin (clone P5D2) and rabbit anti-SNX17 antibody followed by anti-mouse Alexa Fluor 568 (red) and anti-rabbit Alexa Fluor 488 (green) antibodies. Nuclear DNA was labeled by DAPI. Scale 25 µm. $n = 3$.

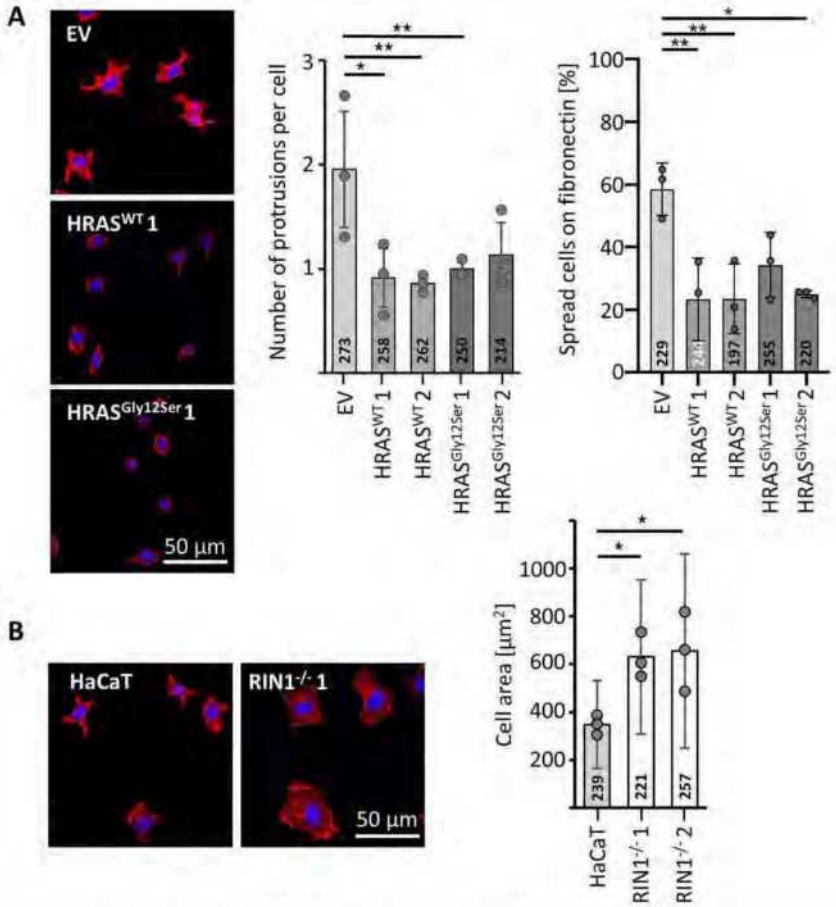

Figure 5. HRAS-RIN1 signaling controls spreading of HaCaT keratinocytes on fibronectin (FN). HaCaT cells stably expressing HA-HRAS variants, EV controls, native HaCaT cells and RIN1 deficient cells were starved and plated on FN coated coverslips. After 60 min, cells were fixed and F-actin was stained by using Texas Red phalloidin. Nuclear DNA was labeled by DAPI. Scale 50 µm. (**A**) Expression of $HRAS^{WT}$ or $HRAS^{Gly12Ser}$ inhibits protrusion formation and spreading. The number of cell protrusions was counted by microscopic analysis of EV transfected and HRAS variant expressing cells. Representative pictures of cells during spreading are given. The left graph shows the mean number (± SD) of actin protrusions per cell (left graph) determined in three independent experiments. The right graph shows the mean number (± SD) of spread cells from three independent experiments. The exact numbers of analyzed cells are given. One-way ANOVA, Tukey's multiple comparison test, $P < 0.05$. (**B**) Knockout of RIN1 promotes cell spreading. Cells were visualized by microscopy and cell areas were measured by using ImageJ. Representative pictures of spreading cells are given. The graph shows the mean areas (± SD) of >200 spread cells determined in three independent experiments each. One-way ANOVA, Tukey's multiple comparison test, $P < 0.05$.

In HaCaT keratinocytes, however, RAF1 was expressed at low levels suggesting that RAF1 is a rather minor competitor of RIN1 in this cell type. Accordingly, RAF-MAPK signaling was only marginally altered by expression of active $HRAS^{Gly12Ser}$ in HaCaT cells. This is in contrast to data from neuronal cells or fibroblasts, in which RAS-RAF kinase signaling was significantly altered by CS-associated HRAS variants (15–17). A particular relevance of the HRAS-RIN1 signaling axis has been demonstrated in neuronal cells, mammary epithelial cells, mouse fibroblasts and in various heterologous cell lines, such as HeLa, HEK293T, NIH3T3 and A549 cells (7,8,10,11,31,47–49). Briefly, binding of active HRAS to RIN1 promotes the activation of RAB5 GTPases (7) and ABL1/2 tyrosine kinases (8). In line with these previous data, we found that HRAS and RIN1 control RAB5- and ABL-kinase-dependent signaling in HaCaT cells. Taken together, our results suggest that RIN1 is a major HRAS effector in epidermal keratinocytes.

HRAS-RIN1 signaling in integrin trafficking

A function of RIN1 in the regulation of endocytic trafficking is well established: RIN1 stimulates ligand induced receptor internalization in fibroblasts, epithelial cells and cancer cells (7,10–12,31,50–52). Moreover, RIN1 has strong impact on endosome

morphology and endosome fusion (7,12,53–55). On the other hand, an involvement of RIN1 in endocytic sorting of integrin receptors has not yet been described in any cell type. A role of HRAS as a regulator of endocytic sorting has not gained much attention to date.

Here, we show that HRAS-RIN1 signaling controls integrin trafficking and, therefore, the availability of integrins on the cell surface of epidermal HaCaT keratinocytes, a cell type that upkeeps a potent and tightly controlled integrin trafficking machinery (23,24). Based on our results we suggest that activation of HRAS-RIN1 signaling enhances the intracellular $\beta1$ integrin fraction at the expense of surface $\beta1$ integrin (for an overview of relevant results, see Supplementary Material, Table S2). In line with this, most of available data indicate that HRAS-RIN1 signaling increases the intracellular fraction of cell surface receptors (10,31,50,51).

There are significant data on the HRAS homologues GTPase RRAS and its involvement in integrin regulation (56). Previous overexpression studies showed that RRAS promotes endocytosis, spatio-temporal clustering and recycling of $\beta1$ integrin (57). Moreover, it was demonstrated that RRAS induces active $\beta1$ integrin endocytosis depending on RIN2 and RAB5 (58). Our data suggest a different function for HRAS-RIN1 signaling in integrin trafficking; activation of this cascade promotes intracellular enrichment of $\beta1$ integrin by acting on trafficking between different endosomal compartments because: First, active/total $\beta1$ integrin was enriched in SNX17-positive vesicles in cells expressing $HRAS^{Gly12Ser}$ (Supplementary Material, Table S2); SNX17 promotes receptor recycling over lysosomal degradation at early and sorting endosomes (24,26,38). In this context, it has previously been shown, that HRAS forms a complex with SNX17 (59), supporting a role of HRAS-RIN1 at early and sorting endosomes. And second, we detected increased levels of active/total $\beta1$ integrin in RAB7-positive vesicles (late endosomes) but not in lysosomes of cells overexpressing $HRAS^{Gly12Ser}$ (Supplementary Material, Table S2). Based on the postulated function of RRAS as a positive regulator of $\beta1$ integrin endocytosis and recycling and, thereby enhancement of integrin function in cell adhesion and spreading (57), we suggest a complementary function for HRAS. The latter rather holds back $\beta1$ integrin in the endosomal compartment and thus decreases its surface availability. In line with this, HRAS and RRAS have been reported to play opposite and counteracting roles in integrin-mediated adhesion in some cell types (60).

The function of HRAS in the epidermis

The epidermal manifestation in patients with CS (1,2) proves a critical function of HRAS signaling in epidermal development and/or homeostasis. Mice expressing an activated $HRAS^{Gly12Val}$ transgene showed aberrant $\beta1$ and $\beta4$ integrin expression and developed massive hyperplastic skin papillomas at sites of wounding (61–63). RAS function in epidermal homeostasis has mainly been attributed to RAF-MAP kinase and PI3 kinase signaling (21,22,63). Here, we put forward the HRAS-RIN1 signaling axis that regulates the expression and/or distribution of integrin receptors. Integrins underlie the ability of keratinocytes for adhesion to the ECM (23–25,39) and an altered cellular distribution of integrin is in well agreement with affected cell adhesion. In line with this, we show that expression of $HRAS^{Gly12Ser}$ affects HaCaT keratinocyte spreading on fibronectin. Notably, overexpression of wild-type HRAS ($HRAS^{WT}$) is also sufficient to induce the observed effects on HaCaT keratinocyte adhesion, suggesting a dose effect in this specific cellular context. Finally, knockout of RIN1 resulted in an overspread HaCaT cell phenotype. We conclude that HRAS-RIN signaling likely controls cell adhesion by acting on integrin availability.

In addition to dysregulated $\beta1$ integrin that is core constituent of focal adhesions (20,23,25), we detected reduced levels of $\beta4$ integrin in HaCaT keratinocytes over-expressing $HRAS^{WT}$ or $HRAS^{Gly12Ser}$. Together with $\alpha6$ integrin, $\beta4$ integrin forms the central core of the hemidesmosome (23). Available data suggest that dysregulation of $\beta4$ integrin results in defective basement membrane adhesion and migration deficits (for details see Supplementary Material, Results and Discussion) (20,25). Since $\beta4$ integrin, similar to $\beta1$ integrin, is sorted via endosomal compartments (64,65), it is plausible, that trafficking defects may affect the cellular distribution and/or amount of $\beta4$ integrin. Moreover, we detected altered expression or distribution of other contact and adhesion molecules in cells overexpressing $HRAS^{WT}$ or $HRAS^{Gly12Ser}$ (for details see Supplementary Material, Discussion). Taken together we suggest that HRAS controls subcellular distribution and availability of various contact and adhesion proteins in keratinocytes.

Integrin mediated adhesion and spreading results in intracellular reactive oxygen species (ROS) production and modulation of various signaling pathways (66–69). Vice versa, intracellular ROS levels have an effect on integrin mediated signaling and thereby influence cell adhesion and migration (70). Oncogenic RAS proteins also promote the generation of ROS, which in turn modulate multiple signaling pathways (71,72). Accordingly, primary fibroblasts from subjects with CS showed increased levels of ROS resulting in enhanced AMP-activated protein kinase α (AMPKα) and p38 activation as well as dysregulated energetic metabolism (73). In conclusion, $HRAS^{Gly12Ser}$ associated defects in integrin trafficking, as we describe in our study for HaCaT keratinocytes, as well as increased ROS levels, as shown in CS fibroblasts (73), may conjointly contribute to specific cellular pathophysiologic features, such as adhesion and migration deficits.

Dysregulated endosomal sorting is a novel pathomechanism in RASopathies

CS belongs to the RASopathies, a group of disorders caused by germline variants in genes encoding components or regulators of RAS signaling pathways. Mostly gain-of function or hyperactivation of the RAS-MAPK pathway is cited to explain the molecular consequences of pathogenic variants. Our data point to a novel aspect in the molecular pathogenesis of RASopathies as we describe HRAS-RIN1 as regulatory signaling axis for (integrin) trafficking in HaCaT keratinocytes. Defective endocytic sorting of receptors, i.e. EGFR and glutamate receptors, has been already proposed and demonstrated as a pathomechanistic basis for Noonan syndrome related phenotypes (74–76). In analogy, bi-allelic pathogenic variants in *RIN2*, an ubiquitously expressed protein that interacts with RAB5 and is involved in the regulation of endocytic trafficking, cause a syndromic disorder characterized by a significant skin manifestation (77). In conclusion, altered endosomal sorting of cell surface receptors may explain certain epidermal manifestations in various RASopathies and related disorders.

Limitations

This study also has limitations. As a cellular model, we used HaCaT cells that is a spontaneously immortalized epithelial cell line with loss-of function variants in tumor protein p53 (TP53) (78,79). TP53 is involved in the regulation of keratinocyte homeostasis (growth, differentiation and senescence) (80), thus it

cannot be excluded that the loss of TP53 influences experimental results in HaCaT cells.

Materials and Methods

Cell culture

The HaCaT keratinocyte cell line is a spontaneously immortalized and non-tumorigenic cell line that maintains typical characteristics of keratinocytes and is widely used for *in vitro* skin models (81). HaCaT cells were cultured in Dulbecco's Modified Eagle Medium (DMEM, Gibco, Thermo Fisher Scientific, Inc., Waltham, MA, USA) containing 10% serum (Sigma-Aldrich, Merck, Darmstadt, Germany) and penicillin-streptomycin (100 U/ml and 100 mg/ml, respectively) (Sigma-Aldrich) at 37°C and 5% CO_2. Human primary keratinocytes were freshly isolated from juvenile foreskin as previously reported (82). Briefly, foreskin tissue was cut into small pieces, which were incubated in trypsin solution (0.25% v/v in phosphate buffered saline, Merck) to separate epidermis and dermis. Mechanical dissociation of the epidermal layer produced a suspension of keratinocytes that were cultivated for 5 days at 37°C and 5% CO_2 in serum-free EpiLife medium (Life Technologies, Thermo Fisher Scientific). Primary fibroblasts obtained from skin biopsies of three juvenile individuals were cultured in DMEM (Gibco, Thermo Fisher Scientific) supplemented with 10% fetal bovine serum (GE Healthcare, Chalfont St Giles, UK) and penicillin–streptomycin (100 U/ml and 100 mg/ml, respectively; ThermoFisher).

Generation of stable cell lines

The coding sequences of HA-tagged $HRAS^{WT}$ (GenBank accession number NM_005343.4) and the *HRAS* mutants c.34G>A (p.Gly12Ser) and c.35G>T (p.Gly12Val) were sub-cloned into pcDNA 3.2 DEST Mammalian Expression Vector (Thermo Fisher Scientific). HaCaT cells were transfected by electroporation using the Neon transfection system (Thermo Fisher Scientific) according to the manufacturer's instructions (pulse voltage 1600 V; pulse width 10 ms; pulse number 3). Cells were selected with 500 μg/ml Geneticin (Gibco, Thermo Fisher Scientific) according to the manufacturer's instructions. Cells were single cell sorted by fluorescence activated cell sorting (FACS) (FACS Aria III; BD Biosciences, San Jose, CA, USA) and single cell clones were analyzed for expression.

Generation of RIN1 knockout cells

Two specific crRNAs targeting RIN1 (Design ID: Hs.Cas9.RIN1.1.AA: CATTGGGCACGTCATACAGT; Hs.Cas9.RIN1.1.AC: CAGATCAGCTGGACTAGGTC), the tracrRNA and Cas9 protein were synthesized by Integrated DNA Technologies (IDT, Inc., Iowa, USA). The assembly of the ribonucleoprotein (RNP) complex and the delivery by Neon electroporation system (Thermo Fisher Scientific) were performed according to the manufacturers' instructions. Briefly, crRNA and tracrRNA were hybridized at the same molar ratios in IDT duplex buffer (30 mM HEPES, pH 7.5; 100 mM potassium acetate) at 95°C for 5 min and were allowed to slowly cool to 20°C. To generate Cas9 RNPs, Cas9 protein and RNAs duplex (crRNA:tracrRNA) were incubated in Resuspension Buffer R (from Neon System Kit) for 20 min at room temperature. 5 x 10^5 HaCaT cells were resuspended in Resuspension Buffer R and RNPs were added. Electroporation was performed with a 10 μL Neon System Kit (pulse voltage 1600 V, pulse width 10 ms, pulse number 3). Cells were grown under normal conditions, single cell sorted into 96 well plates using FACS sorter (FACS Aria III, BD Biosciences) and analyzed for RIN1 knockout clones by immunoblotting.

Sample preparation for proteomics

In-gel digestion was done following established protocols (83). Shrinking and swelling was performed with 100% acetonitrile (ACN) and 100 mM NH_4HCO_3. In-gel reduction was achieved with 10 mM dithiothreitol (dissolved in 100 mM NH_4HCO_3). Alkylation was performed with 55 mM iodacetamide (dissolved in 100 mM NH_4HCO_3). Proteins in the gel pieces were digested by covering them with a trypsin solution (8 ng/μl sequencing-grade trypsin, dissolved in 50 mM NH_4HCO_3 containing 10% ACN) and incubating the mixture at 37°C for overnight. Tryptic peptides were yielded by extraction with 2% formic acid (FA), 80% ACN. The extract was evaporated. For liquid chromatography-mass spectrometry (LC-MS/MS) analysis, samples were dissolved in 20 μL 0.1% FA.

Differential quantitative proteomics

Chromatographic separation of peptides was achieved by nano ultra-performance liquid chromatography (UPLC, nanoAcquity system, Waters, Milford, MA, USA) with a two-buffer system (buffer A: 0.1% FA in water, buffer B: 0.1% FA in ACN). Attached to the UPLC was a peptide trap (180 μm × 20 mm, 100 Å pore size, 5 μm particle size, Symmetry C18, Waters) for online desalting and purification followed by a 25-cm C18 reversed-phase column (75 μm × 200 mm, 130 Å pore size, 1.7 μm particle size, Peptide BEH C18, Waters). Peptides were separated using an 80-min gradient with linearly increasing ACN concentration from 2% to 30% ACN in 65 minutes. The eluting peptides were analyzed on a Quadrupole Orbitrap hybrid mass spectrometer (QExactive, Thermo Fisher Scientific). Here, the ions being responsible for the 12 highest signal intensities per precursor scan (1 × 10^6 ions, 70000 Resolution, 240 ms fill time) were analyzed by MS/MS (higher-energy collisional dissociation (HCD) at 25 normalized collision energy, 1 × 10^5 ions, 17 500 resolution, 50 ms fill time) in a range of 400–1200 m/z. A dynamic precursor exclusion of 20 s was used.

LC-MS/MS data were searched with the Sequest algorithm integrated in the Proteome Discoverer software (v. 2.41.15, Thermo Fisher Scientific) against a reviewed human Swissprot database, obtained in April 2020, containing 20 365 entries. Carbamidomethylation was set as fixed modification for cysteine residues and the oxidation of methionine and pyro-glutamate formation at glutamine residues at the peptide N-terminus, as well as acetylation of the protein N-terminus were allowed as variable modifications. A maximum number of 2 missing tryptic cleavages was set. Peptides between 6 and 144 amino acids where considered. A strict cutoff (false discovery rate (FDR) <0.01) was set for peptide and protein identification.

Constructs, recombinant proteins and nucleotide loading

pGEX vectors were used for bacterial overexpression of RIN1 [GEF-RA] (amino acids 293–716) variants (wild-type and p.Glu574Ala), full length variants of HRAS (wild-type, c.34G>A (p.Gly12Ser), c.38_39delGCinsAA (p.Gly13Glu) and c.50G>A (p.Ser17Asn)] and full length RAB5A. Proteins were isolated as glutathione S-transferase (GST) fusion proteins in *Escherichia coli* BL21 (DE3) and purified after cleavage of the GST tag via gel filtration (Superdex 75 or 200, GE Healthcare). Nucleotide-free and fluorescent nucleotide bound proteins (RAB5A and HRAS) were prepared using alkaline phosphatase (Roche, Basel, Switzerland) and phosphodiesterase (Sigma-Aldrich) at 4°C. Methylanthraniloyl

(mant-) GppNHp (guanosine 5′ β,γ-imidotriphosphate), a non-hydrolysable GTP analog and methylanthraniloyl (mant-) dGDP (deoxyguanosine-5′-diphosphate) were used as fluorescent nucleotides. The mant-GppNHp content of each labeled protein was determined by HPLC using a buffer containing 20–25% acetonitrile. All proteins were analyzed by sodium dodecyl-sulfate polyacrylamide gel electrophoresis (SDS-PAGE) and stored at −80°C.

Fluorescence polarization

Increasing amounts of RIN1[RA] were titrated to mantGppNHp-bound HRAS proteins (1 μM) in a buffer, containing 30 mM Tris/HCl (pH 7.5), 150 mM NaCl, 5 mM $MgCl_2$, 3 mM dithiothreitol and a total volume of 200 μl at 25°C. For excitation, wavelength of 362 nm (slit width: 8 micron) was used for the mant fluorophore and 450 nm was used for emission (slit width: 10 micron). The dissociation constants (Kd) were calculated by fitting the concentration-dependent binding curve using a quadratic ligand-binding equation. Fluorescence experiments were performed in a Fluoromax 4 fluorimeter in polarization mode.

Fluorimeter measurements

Guanine nucleotide exchange reactions were performed with a Fluoromax 4 fluorimeter instrument. The excitation and emission wavelengths for mant-deoxy-GDP were 360 nm and 450 nm, respectively. For nucleotide exchange reactions, 1 μM mant-deoxy-GDP RAB5A, 100 μM GDP, 10 μM RIN1 [GEF-RA] and 1 μM GppNHp-bound HRAS were used in 200 μL of measurement buffer containing 30 mM Tris/HCl, pH 7.5, 10 mM K_2HPO_4/KH_2PO_4, 2 mM $MgCl_2$ and 3 mM dithiothreitol at 25°C.

GTPase pull down assay

The RAS-association (RA) domains of RIN1 (amino acids 624–716) was used to specifically pull down GTP-bound HRAS from cell extracts. Preparation of GST-RA beads, cell lysis and precipitation of GTP-bound GTPases have been described previously (14).

(Co-)Immunoprecipitation

Cells were washed and scraped off in ice-cold PBS. Cell pellets were lysed on ice for 60 min in ice-cold co-immunoprecipitation buffer (50 mM Tris-HCl pH 8.0, 120 mM NaCl, 0.5% Nonidet P40, supplemented with complete Mini Protease Inhibitors and PhosStop (Roche)) and clarified by centrifugation (14 000 rpm, 15 min, 4°C). After removing small aliquots (total cell lysates – TCL), supernatants were incubated with 20 μl Pierce Anti-HA magnetic beads (#88836, Thermo Fisher Scientific) at 4°C with rotation for 60 min. Beads were magnetically separated from cell lysates and subsequently washed (3x) with Co-IP-buffer by rotation for 3 min at room temperature. After final wash, beads were supplemented with sample buffer, heated to 95°C and precipitated proteins were subjected to SDS-PAGE and immunoblotting or to sample preparation for proteomics.

Immunoblotting and antibodies

Cells were cultured as specified, washed with PBS and scraped off in ice-cold PBS. Cell pellets were lysed on ice for 60 min with cell lysis buffer (50 mM Tris-HCl, pH 8.0, 150 mM NaCl, 1% Nonidet P-40, supplemented with complete Mini Protease Inhibitors and PhosStop (Roche)). Cell lysates were clarified by centrifugation (14 000 rpm, 15 min, 4°C) and supernatants were supplemented with sample buffer. Proteins were separated on SDS-polyacrylamide gels and transferred to PVDF membranes. Following blocking (20 mM Tris–HCl, pH 7.4; 150 mM NaCl; 0.1% Tween-20; 5% non-fat dry milk) and washing (20 mM Tris-HCl, pH 7.4; 150 mM NaCl; 0.1% Tween-20), membranes were incubated in primary antibody solution (20 mM Tris–HCl, pH 7.4; 150 mM NaCl; 0.1% Tween-20; 5% BSA or 5% non-fat dry milk) containing the appropriate antibodies. Rabbit polyclonal antibodies against RIN1 (Thermo Fisher Scientific; PA5-57292; 1:1000/Sigma; HPA035491; 1:1000), PI3K (Upstate Biotechnology Inc.; Thermo Fisher Scientific; 06-195; 1:1000), PLCE1 (Abbexa Ltd, Biozol, Cambridge, UK; abx147622; 1:1000), RAF-1 (Santa Cruz Biotechnology Inc., Dallas, Texas, USA; sc-7267; 1:200), RALGDS (Thermo Fisher Scientific; PA5-49099; 1:1000), MEK1/2 (Cell Signaling Tech., Danvers, MA; no. 9122; 1:1000), phospho-MEK1/2 (Ser217/221) (Cell Signaling Tech.; no. 9121; 1:1000), p44/42 MAP Kinase (ERK1/2) (Cell Signaling Tech.; no. 9102; 1:1000), phospho-p44/42 MAP Kinase (ERK1/2) (Thr202/Tyr204) (Cell Signaling Tech.; no. 9101; 1:1000), Akt1/2/3 (Cell Signaling Tech.; no. 9272; 1:1000), phospho-Akt1/2/3 (Ser473) (Cell Signaling Tech.; no. 9271; 1:1000), HRAS (Proteintech; 18 295-1-AP; 1:1000), actin (Sigma; A5060; 1:250), c ABL (Cell signaling; 2862; 1:1000), and p-Crkll Tyr221 (Cell signaling; 3491; 1:1000) as well as rabbit monoclonal phospho-RIN1 antibodies (abcam; ab179976, [EPR2794(2)]) phospho Ser351; 1:1000) were used. Mouse monoclonal antibodies against α-Tubulin (Sigma-Aldrich; clone DM1A, T9026; 1: 3000), GAPDH (abcam, Cambridge, UK; ab8245, 1:10 000), CD29 β1 integrin (BD; 610467, 1:500), CD104 β4 integrin (BD; 611 233; 1:500), RAB5 (BD; 610 724, 1:500) were applied. Rat monoclonal HA-HRP (Roche; 12 013 819 001, 1:10 000) was used to detect HA-HRAS. Membranes were washed and incubated with secondary horseradish peroxidase (HRP) coupled anti-rabbit (NA934V) and anti-mouse (NA931V) antibodies (GE Healthcare; 1: 7500) or with goat anti-mouse IgG StarBright Blue 700 Fluorophore antibodies (BioRad; 12 004 159, 1:10 000). After final washing, proteins were visualized using the ChemiDoc MP Imaging System (Bio-Rad Laboratories, Inc.; Hercules, CA, USA). Data shown are representative of three independent experiments.

Immunocytochemistry and antibodies

HaCaT cells were seeded on coverslips (300 000 cells/3.5 cm^2) and cultivated overnight. For transient expression of RAB4 (pEGFP-C1 Rab4B WT), RAB7 (pmEGFP-C1 Rab7a WT), RAB11 (pmEGFP-C1 RAB11A WT), LAMP1 (plasmid RFP-LAMP1, addgene #1817) and EV RFP-N1 (control), cells were transfected with jetOPTIMUS (1:1.25) for 24 h according to manufacturer's protocol (Polyplus transfection, Illkirch, France). Subsequently, cells were rinsed with PBS, fixed with 4% paraformaldehyde (Sigma-Aldrich) in PBS and washed three times with PBS. After treatment with permeabilization/blocking solution (2% BSA, 3% goat serum, 0.5% Nonidet P40 in PBS), cells were incubated in antibody solution (3% goat serum and 0.1% Nonidet P40 in PBS) containing appropriate primary antibodies: Alexa Fluor 488 or unconjugated mouse monoclonal β1 integrin antibody clone P5D2 (abcam; total β1 integrin; ab193591/ab24693, 1:200); Alexa Fluor 488 or unconjugated mouse monoclonal β1 integrin clone TS2/16 (Santa Cruz Biotechnology; active β1 integrin, TS2/16, sc-53711, 1:100); mouse monoclonal RAB5 antibody (BD Biosciences; 610 724, 1:100); rabbit monoclonal anti-RAB5 antibody (cell signaling Tech., 3547, 1:100); rabbit monoclonal EEA1 (Cell Signaling Tech.; 3288S, 1:100); rabbit polyclonal SNX17 antibody (Novus Biologicals; NBP1-92417, 1:100); rabbit monoclonal E-cadherin antibody

(abcam, ab40772 [EP700Y], 1:250). Cells were washed with PBS and incubated with Fluorophore-conjugated secondary goat anti-mouse Alexa Fluor488 antibody, Alexa Fluor568 antibody or Texas Red-X phalloidin (Life Technologies,) in antibody solution. After extensive washing with PBS, cells were embedded in ProLong Diamond Antifade Mountant with DAPI (P36962, Life Technologies). Fixed samples were analyzed with Zeiss Axiovert 200 M with ApoTome for structured illumination (63x Plan-Apochromat Oil DIC, NA 1.4; Carl Zeiss Microscopy, Jena, Germany) and confocal laser scanning microscopes (Leica TCS SP5/SP8, 63x HC PL APO Oil/CS2, NA 1.4; Leica Microsystems, Wetzlar, Germany) were used for image acquisition, respectively. Confocal images of β1 integrin labeled HaCaT keratinocytes were analyzed for intracellular vesicles using Imaris (v7.6.1, Oxford Instruments, Abingdon, UK). After background subtraction, relevant vesicles were identified applying an automatic threshold based segmentation algorithm (i.e. surface tool), followed by a sphericity filter (sphericity parameter $\geq$ 0.87) on the segmented objects.

Antibody-based integrin internalization assay

Cells were kept under serum-deprived conditions (0.1% serum) for 2–3 h and harvested with StemProAccutase (Thermo Fisher Scientific). Cells were incubated on ice and cell surface β1 integrins were stained with directly conjugated antibody clone TS2/16-Alexa Fluor 488 (detects the active conformation of β1 integrin, sc-53711 AF488, Santa Cruz Biotechnology) or isotype control mouse IgG1, κ (14-4714-82, Invitrogen) diluted 1:100 in FACS-buffer (PBS containing 0.5% BSA and 2 mM EDTA) for 60 min at 4°C and rotation. After 1 h cells were washed twice with FACS-buffer. To start integrin internalization, cells were incubated in pre-warmed media (0.1% serum/DMEM) at 37°C for 15, 30 or 60 min. After internalization, cells were immediately transferred on ice and cooled down. The remaining cell surface bound antibody was removed by acidic wash buffer (0.2 M acetic acid, 0.5 M NaCl, pH 2.2) in three washing steps (3 min each), followed by neutralization with 0.3% BSA/DMEM. In parallel, antibody treated cells were left on ice (0 min internalization) as a control for endocytosis. Controls and isotype controls confirmed functionality and antibody specificity of the internalization assay (data not shown). To measure the total amount of cell surface integrin stained by the β1 integrin antibody, cells were left on ice without acid wash. Fluorescent intensities of total cell surface and internalized β1 integrin of 20000 cells per condition were measured with FACS Canto II (BD Biosciences). Viable, single cells were gated by forward scatter (FSC) and side scatter (SSC) dot blot (Flowing Software by Perttu Terho, Turku Centre for Biotechnology, Finland). Fluorescence intensities of internalized β1 integrin were normalized against total cell surface fluorescence intensities. Relative fluorescent intensities of HaCaT/EV and HaCaT control cells were considered as 100%. To inhibit integrin recycling, cells were treated with 300 μM primaquine during 15 min internalization.

Analysis of cell spreading and protrusion numbers

Cells were kept under serum-deprived conditions (0.1% serum) over night and then seeded on fibronectin-coated coverslips. Beforehand, coverslips were coated with 10 μg/ml fibronectin (F2006, Sigma) in PBS over night at 4°C, washed with PBS and blocked in 1% BSA/PBS for 60 min at 37°C. Cells were harvested with StemProAccutase (Thermo Fisher Scientific), washed with PBS, and seeded in DMEM/0.3% BSA. After 1 h at 37°C, samples were fixed with 4% PFA for 10 min at room temperature and subsequently treated with permeabilization/blocking solution (7% BSA, 3% goat serum, 0.5% Nonidet P40 in PBS), followed by antibody solution (3% goat serum and 0.1% Nonidet P40 in PBS) containing Phalloidin TexasRed (Life Technologies). After extensive washing with PBS cells were embedded in ProLong Diamond Antifade Mountant with DAPI (P36962, Life Technologies). Cells were visualized by using a confocal laser scanning microscope (Leica TCS SP5, 63x HC PL APO Oil CS2, NA 1.4; Leica Microsystems, Wetzlar, Germany) and images were taken. The numbers of spread and not spread cells were determined by visual inspection, with only solitary cells with a clear flat spread out cell morphology being considered as fully spread. The number of cell protrusions (i.e. filopodia) was determined by visual inspection of confocal images and the area of cells was measured using ImageJ area measurement tool.

Statistical analysis

Fluorescent signals on blots from three independent experiments were quantified by densitometric analysis using the Image Lab software (V5.0.0, Bio-Rad Laboratories). A ONE-WAY-ANOVA in combination with Tukey's or Sidak's *post-hoc* multiple comparison test was used to determine the significance of the difference between cells overexpressing $HRAS^{WT}$ and $HRAS^{Gly12Ser}$. Values are presented as the mean ± standard deviation and were considered significant at P-value < 0.05. For differential quantitative proteomics, obtained relative differences of protein abundances where log2 transformed. Median normalization was performed for each sample. Missing value-tolerant NIPALS PCA calculation and visualization were performed, using the MixOmix package implemented in the R software environment (84). Details and background information on NIPALS PCA calculations are described in the Supplementary Materials and Methods. To investigate the abundance distribution of HRAS signaling-associated proteins, Pearson's correlation-based hierarchical clustering was performed, based on all proteins present in the WikiPathways-RAS signaling geneset (85), obtained from the Molecular Signature Database (MsigDB) (86). Heatmap visualization of clustering results was performed using the pheatmap package, implemented in the R software environment. To test for the overrepresentation of GO terms and pathways across differential abundant interactors between WT and Gly12Ser HRAS gene-set enrichment analysis (GSEA) (version 4.1) was used (86). Log2 transformed, centered protein abundances were tested against gene ontology gene-sets (Cellular Component, Biological Process, Molecular function) and curated gene-sets from the WikiPathway database. Permutation was performed based on gene-sets. A weighted enrichment statistic was applied, using the signal-to-noise ratio as a metric for gene ranking. Balancing and normalization where disabled within GSEA. Gene-sets with a P-value < 0.01 and an FDR < 0.25 were considered significantly enriched. Enriched gene-sets where plotted according to their normalized enrichment score using Microsoft Excel. T-testing was performed in Perseus (Version 1.6.5.0). Proteins with a P-value < 0.05, exceeding a FoldChange difference of >1.5 between $HRAS^{WT}$ and $HRAS^{Gly12Ser}$-derived IPs were considered as statistically significant differential abundant.

Supplementary Material

Supplementary Material is available at *HMG* online.

Acknowledgements

cDNA constructs for transient expression of RAB4 (pEGFP-C1 $Rab4B^{WT}$) and RAB7 (pmEGFP-C1 $Rab7a^{WT}$) were obtained from

Juan Bonifacino, for transient expression of RAB11 (pmEGFP-C1 RAB11A^{WT}) from Frederike Harms, and for transient expression of human RIN1 (pEGFP-RIN1^{WT}) from Angelika Haußer.
We thank the UKE Microscopy Imaging Facility and UKE FACS Sorting Core Unit for assistance.

Conflict of interest statement. The authors have declared that no conflict of interest exists.

Funding

This work was supported by the German Federal Ministry of Education and Research (BMBF) within the German Network of RASopathy Research (GeNeRARe; funding codes 01GM1902C and 01GM1902E to FB, MRA and GR); within the European Network on Noonan Syndrome and Related Disorders (NSEuroNet; funding code 01GM1621B to NM and MRA); and by grants from the Deutsche Forschungsgemeinschaft (DFG) [funding codes IRTG 1902-p6 (International Research Training Group 'Intra- and interorgan communication of the cardiovascular system'), INST 337/15-1, INST 337/16-1 and INST 152/837-1].

Ethics Statement

For skin biopsies and juvenile foreskin preparations, informed written consent was obtained from all subjects or their legal guardians under protocols approved by the local ethics board of the Hamburg Medical Chamber (PV7038 and WF-061/12).

Authors' Contributions

G.R. conceived and designed the project. H.S., C.G., M.R.A. and G.R. coordinated and supervised experimental work. T.N., F.B., H.V., L.I.B., N.M., V.R. and S.D. conducted the experiments and acquired and analyzed data. T.N., F.B., H.S., M.R.A. and G.R. interpreted the data and defined follow up experiments. T.N., F.B., H.V., C.G. and G.R. drafted the manuscript with contributions of all authors. M.R.A. and G.R. reviewed and finalized the manuscript.

The research was performed in four laboratories (principle investigators: H.S., C.G., M.R.A. and G.R.). T.N. did most of the experiments and data curation; therefore, she merited the first place in the order of the first authors. The contribution of F.B. was critical for the manuscript (e.g. to demonstrate that the HRAS-RIN1 signaling axis is functional) and it was felt that F.B. merited the second place on the shared first authorship. Both first authors agreed to this order of first authorship.

References

1. Gripp, K.W., Morse, L.A., Axelrad, M., Chatfield, K.C., Chidekel, A., Dobyns, W., Doyle, D., Kerr, B., Lin, A.E., Schwartz, D.D. et al. (2019) Costello syndrome: clinical phenotype, genotype, and management guidelines. *Am. J. Med. Genet. A*, **179**, 1725–1744.
2. Siegel, D.H., Mann, J.A., Krol, A.L. and Rauen, K.A. (2012) Dermatological phenotype in Costello syndrome: consequences of Ras dysregulation in development. *Br. J. Dermatol.*, **166**, 601–607.
3. Gripp, K.W. and Lin, A.E. (2012) Costello syndrome: a Ras/mitogen activated protein kinase pathway syndrome (rasopathy) resulting from HRAS germline mutations. *Genet. Med.*, **14**, 285–292.
4. Simanshu, D.K., Nissley, D.V. and McCormick, F. (2017) RAS proteins and their regulators in human disease. *Cell*, **170**, 17–33.
5. Bliss, J.M., Venkatesh, R. and Colicelli, J. (2006) The RIN family of Ras effectors. *Methods Enzymol.*, **407**, 335–344.
6. Han, L. and Colicelli, J. (1995) A human protein selected for interference with Ras function interacts directly with Ras and competes with Raf1. *Mol. Cell. Biol.*, **15**, 1318–1323.
7. Tall, G.G., Barbieri, M.A., Stahl, P.D. and Horazdovsky, B.F. (2001) Ras-activated endocytosis is mediated by the Rab5 guanine nucleotide exchange activity of RIN1. *Dev. Cell.*, **1**, 73–82.
8. Hu, H., Bliss, J.M., Wang, Y. and Colicelli, J. (2005) RIN1 is an ABL tyrosine kinase activator and a regulator of epithelial cell adhesion and migration. *Curr. Biol.*, **15**, 815–823.
9. Sziber, Z., Lilliom, H., Morales, C.O., Ignacz, A., Rafikat, A.E., Ellwanger, K., Link, G., Szucs, A., Hausser, A. and Schlett, K. (2017) Ras and Rab interactor 1 controls neuronal plasticity by coordinating dendritic filopodial motility and AMPA receptor turnover. *Mol. Biol. Cell.*, **28**, 285–295.
10. Balaji, K., Mooser, C., Janson, C.M., Bliss, J.M., Hojjat, H. and Colicelli, J. (2012) RIN1 orchestrates the activation of RAB5 GTPases and ABL tyrosine kinases to determine the fate of EGFR. *J. Cell Sci.*, **125**, 5887–5896.
11. Balaji, K. and Colicelli, J. (2015) RIN1 regulates cell migration through RAB5 GTPases and ABL tyrosine kinases. *Commun. Integr. Biol.*, **8**, e25421.
12. Barbieri, M.A., Kong, C., Chen, P.I., Horazdovsky, B.F. and Stahl, P.D. (2003) The Src homology 2 domain of Rin1 mediates its binding to the epidermal growth factor receptor and regulates receptor endocytosis. *J. Biol. Chem.*, **278**, 32027–32036.
13. Wang, Y., Waldron, R.T., Dhaka, A., Patel, A., Riley, M.M., Rozengurt, E. and Colicelli, J. (2002) The RAS effector RIN1 directly competes with RAF and is regulated by 14-3-3 proteins. *Mol. Biol. Cell.*, **22**, 916–926.
14. Rosenberger, G., Meien, S. and Kutsche, K. (2009) Oncogenic HRAS mutations cause prolonged PI3K signaling in response to epidermal growth factor in fibroblasts of patients with Costello syndrome. *Hum. Mutat.*, **30**, 352–362.
15. Nihori, T., Aoki, Y., Okamoto, N., Kurosawa, K., Ohashi, H., Mizuno, S., Kawame, H., Inazawa, J., Ohura, T., Arai, H. et al. (2011) HRAS mutants identified in Costello syndrome patients can induce cellular senescence: possible implications for the pathogenesis of Costello syndrome. *J. Hum. Genet.*, **56**, 707–715.
16. Krencik, R., Hokanson, K.C., Narayan, A.R., Dvornik, J., Rooney, G.E., Rauen, K.A., Weiss, L.A., Rowitch, D.H. and Ullian, E.M. (2015) Dysregulation of astrocyte extracellular signaling in Costello syndrome. *Sci. Transl. Med.*, **7**, 286ra266.
17. Paquin, A., Hordo, C., Kaplan, D.R. and Miller, F.D. (2009) Costello syndrome H-Ras alleles regulate cortical development. *Dev. Biol.*, **330**, 440–451.
18. Tidyman, W.E., Lee, H.S. and Rauen, K.A. (2011) Skeletal muscle pathology in Costello and cardio-facio-cutaneous syndromes: developmental consequences of germline Ras/MAPK activation on myogenesis. *Am. J. Med. Genet. C Semin. Med. Genet.*, **157C**, 104–114.
19. Hinek, A., Teitell, M.A., Schoyer, L., Allen, W., Gripp, K.W., Hamilton, R., Weissberg, R., Kluppel, M. and Lin, A.E. (2005) Myocardial storage of chondroitin sulfate-containing moieties in Costello syndrome patients with severe hypertrophic cardiomyopathy. *Am. J. Med. Genet. A*, **133**, 1–12.
20. Simpson, C.L., Patel, D.M. and Green, K.J. (2011) Deconstructing the skin: cytoarchitectural determinants of epidermal morphogenesis. *Nat. Rev. Mol. Cell Biol.*, **12**, 565–580.

21. Drosten, M., Lechuga, C.G. and Barbacid, M. (2013) Genetic analysis of Ras genes in epidermal development and tumorigenesis. *Small GTPases*, **4**, 236–241.
22. Drosten, M., Lechuga, C.G. and Barbacid, M. (2014) Ras signaling is essential for skin development. *Oncogene*, **33**, 2857–2865.
23. Hegde, S. and Raghavan, S. (2013) A skin-depth analysis of integrins: role of the integrin network in health and disease. *Cell Commun. Adhes.*, **20**, 155–169.
24. Moreno-Layseca, P., Icha, J., Hamidi, H. and Ivaska, J. (2019) Integrin trafficking in cells and tissues. *Nat. Cell Biol.*, **21**, 122–132.
25. Rippa, A.L., Vorotelyak, E.A., Vasiliev, A.V. and Terskikh, V.V. (2013) The role of integrins in the development and homeostasis of the epidermis and skin appendages. *Acta Nat.*, **5**, 22–33.
26. De Franceschi, N., Hamidi, H., Alanko, J., Sahgal, P. and Ivaska, J. (2015) Integrin traffic - the update. *J. Cell Sci.*, **128**, 839–852.
27. Yuan, W. and Song, C. (2020) The emerging role of Rab5 in membrane receptor trafficking and signaling pathways. *Biochem. Res. Int.*, **2020**, 4186308.
28. Parsons, J.T., Horwitz, A.R. and Schwartz, M.A. (2010) Cell adhesion: integrating cytoskeletal dynamics and cellular tension. *Nat. Rev. Mol. Cell Biol.*, **11**, 633–643.
29. Woodring, P.J., Hunter, T. and Wang, J.Y. (2003) Regulation of F-actin-dependent processes by the Abl family of tyrosine kinases. *J. Cell Sci.*, **116**, 2613–2626.
30. Khatri, A., Wang, J. and Pendergast, A.M. (2016) Multifunctional Abl kinases in health and disease. *J. Cell Sci.*, **129**, 9–16.
31. Hu, H., Milstein, M., Bliss, J.M., Thai, M., Malhotra, G., Huynh, L.C. and Colicelli, J. (2008) Integration of transforming growth factor beta and RAS signaling silences a RAB5 guanine nucleotide exchange factor and enhances growth factor-directed cell migration. *Mol. Biol. Cell*, **28**, 1573–1583.
32. Chylinski, K., Le Rhun, A. and Charpentier, E. (2013) The tracrRNA and Cas9 families of type II CRISPR-Cas immunity systems. *RNA Biol.*, **10**, 726–737.
33. Colicelli, J. (2010) ABL tyrosine kinases: evolution of function, regulation, and specificity. *Sci. Signal.*, **3**, re6.
34. Arjonen, A., Alanko, J., Veltel, S. and Ivaska, J. (2012) Distinct recycling of active and inactive beta1 integrins. *Traffic*, **13**, 610–625.
35. Jovic, M., Sharma, M., Rahajeng, J. and Caplan, S. (2010) The early endosome: a busy sorting station for proteins at the crossroads. *Histol. Histopathol.*, **25**, 99–112.
36. Su, Y., Xia, W., Li, J., Walz, T., Humphries, M.J., Vestweber, D., Cabañas, C., Lu, C. and Springer, T.A. (2016) Relating conformation to function in integrin $\alpha5\beta1$. *Proc. Natl. Acad. Sci. U. S. A.*, **113**, E3872–E3881.
37. van Weert, A.W., Geuze, H.J., Groothuis, B. and Stoorvogel, W. (2000) Primaquine interferes with membrane recycling from endosomes to the plasma membrane through a direct interaction with endosomes which does not involve neutralisation of endosomal pH nor osmotic swelling of endosomes. *Eur. J. Cell Biol.*, **79**, 394–399.
38. Böttcher, R.T., Stremmel, C., Meves, A., Meyer, H., Widmaier, M., Tseng, H.-Y. and Fässler, R. (2012) Sorting nexin 17 prevents lysosomal degradation of $\beta1$ integrins by binding to the $\beta1$-integrin tail. *Nat. Cell Biol.*, **14**, 584–592.
39. Paul, N.R., Jacquemet, G. and Caswell, P.T. (2015) Endocytic trafficking of integrins in cell migration. *Curr. Biol.*, **25**, R1092–R1105.
40. Brakebusch, C., Grose, R., Quondamatteo, F., Ramirez, A., Jorcano, J.L., Pirro, A., Svensson, M., Herken, R., Sasaki, T., Timpl, R. et al. (2000) Skin and hair follicle integrity is crucially dependent on beta 1 integrin expression on keratinocytes. *EMBO J.*, **19**, 3990–4003.
41. Carroll, J.M., Romero, M.R. and Watt, F.M. (1995) Suprabasal integrin expression in the epidermis of transgenic mice results in developmental defects and a phenotype resembling psoriasis. *Cell*, **83**, 957–968.
42. Bosset, S., Bonnet-Duquennoy, M., Barre, P., Chalon, A., Lazou, K., Kurfurst, R., Bonte, F., Schmebert, S., Disant, F., Le Varlet, B. et al. (2003) Decreased expression of keratinocyte beta1 integrins in chronically sun-exposed skin in vivo. *Br. J. Dermatol.*, **148**, 770–778.
43. Giangreco, A., Goldie, S.J., Failla, V., Saintigny, G. and Watt, F.M. (2010) Human skin aging is associated with reduced expression of the stem cell markers beta1 integrin and MCSP. *J. Invest. Dermatol.*, **130**, 604–608.
44. Ferreira, M., Fujiwara, H., Morita, K. and Watt, F.M. (2009) An activating beta1 integrin mutation increases the conversion of benign to malignant skin tumors. *Cancer Res.*, **69**, 1334–1342.
45. Lee, C.H., Chen, J.S., Sun, Y.L., Liao, W.T., Zheng, Y.W., Chai, C.Y., Chen, G.S. and Yu, H.S. (2006) Defective beta1-integrins expression in arsenical keratosis and arsenic-treated cultured human keratinocytes. *J. Cutan. Pathol.*, **33**, 129–138.
46. Han, L., Wong, D., Dhaka, A., Afar, D., White, M., Xie, W., Herschman, H., Witte, O. and Colicelli, J. (1997) Protein binding and signaling properties of RIN1 suggest a unique effector function. *Proc. Natl. Acad. Sci. U. S. A.*, **94**, 4954–4959.
47. Dhaka, A., Costa, R.M., Hu, H., Irvin, D.K., Patel, A., Kornblum, H.I., Silva, A.J., O'Dell, T.J. and Colicelli, J. (2003) The RAS effector RIN1 modulates the formation of aversive memories. *J. Neurosci.*, **23**, 748–757.
48. Dreosti, B., Huynh, L., Thai, M., Bliss, J.M., Nagaoka, Y., Wang, Y., Ching, T.H., Jiang, M., Martin, K.C. and Colicelli, J. (2010) Regulated expression of the Ras effector Rin1 in forebrain neurons. *Mol. Cell. Neurosci.*, **43**, 108–116.
49. Deininger, K., Eder, M., Kramer, E.R., Zieglgansberger, W., Dodt, H.U., Dornmair, K., Colicelli, J. and Klein, R. (2008) The Rab5 guanylate exchange factor Rin1 regulates endocytosis of the EphA4 receptor in mature excitatory neurons. *Proc. Natl. Acad. Sci. U. S. A.*, **105**, 12539–12544.
50. Hunker, C.M., Giambini, H., Galvis, A., Hall, J., Kruk, I., Veisaga, M.L. and Barbieri, M.A. (2006) Rin1 regulates insulin receptor signal transduction pathways. *Exp. Cell Res.*, **312**, 1106–1118.
51. Tomshine, J.C., Severson, S.R., Wigle, D.A., Sun, Z., Beleford, D.A., Shridhar, V. and Horazdovsky, B.F. (2009) Cell proliferation and epidermal growth factor signaling in non-small cell lung adenocarcinoma cell lines are dependent on Rin1. *J. Biol. Chem.*, **284**, 26331–26339.
52. Trino, S., De Luca, L., Simeon, V., Laurenzana, I., Morano, A., Calvano, A., La Rocca, F., Pietrantuono, G., Bianchino, G., Grieco, V. et al. (2016) Inverse regulation of bridging integrator 1 and BCR-ABL1 in chronic myeloid leukemia. *Tumor Biol.*, **37**, 217–225.
53. Jozic, I., Saliba, S.C. and Barbieri, M.A. (2012) Effect of EGF-receptor tyrosine kinase inhibitor on Rab5 function during endocytosis. *Arch. Biochem. Biophys.*, **525**, 16–24.
54. Galvis, A., Giambini, H., Villasana, Z. and Barbieri, M.A. (2009) Functional determinants of ras interference 1 mutants required for their inhibitory activity on endocytosis. *Exp. Cell Res.*, **315**, 820–835.
55. Jozic, I., Blanco, G. and Barbieri, M.A. (2011) Inhibition of Rab5 activation during insulin receptor-mediated endocytosis. *Curr. Cell. Biochem.*, **1**, 20–32.
56. Weber, S.M. and Carroll, S.L. (2021) The role of R-Ras proteins in normal and pathologic migration and morphologic change. *Am. J. Pathol.*, **191**, 1499–1510.

57. Conklin, M.W., Ada-Nguema, A., Parsons, M., Riching, K.M. and Keely, P.J. (2010) R-Ras regulates beta1-integrin trafficking via effects on membrane ruffling and endocytosis. *BMC Mol. Cell Biol.*, **11**, 14.
58. Sandri, C., Caccavari, F., Valdembri, D., Camillo, C., Veltel, S., Santambrogio, M., Lanzetti, L., Bussolino, F., Ivaska, J. and Serini, G. (2012) The R-Ras/RIN2/Rab5 complex controls endothelial cell adhesion and morphogenesis via active integrin endocytosis and Rac signaling. *Cell Res.*, **22**, 1479–1501.
59. Ghai, R., Mobli, M., Norwood, S.J., Bugarcic, A., Teasdale, R.D., King, G.F. and Collins, B.M. (2011) Phox homology band 4.1/ezrin/radixin/moesin-like proteins function as molecular scaffolds that interact with cargo receptors and Ras GTPases. *Proc. Natl. Acad. Sci. U. S. A.*, **108**, 7763–7768.
60. Kinbara, K., Goldfinger, L.E., Hansen, M., Chou, F.L. and Ginsberg, M.H. (2003) Ras GTPases: integrins' friends or foes? *Nat. Rev. Mol. Cell Biol.*, **4**, 767–776.
61. Greenhalgh, D.A., Rothnagel, J.A., Quintanilla, M.I., Orengo, C.C., Gagne, T.A., Bundman, D.S., Longley, M.A. and Roop, D.R. (1993) Induction of epidermal hyperplasia, hyperkeratosis, and papillomas in transgenic mice by a targeted v-Ha-ras oncogene. *Mol. Carcinog.*, **7**, 99–110.
62. Bailleul, B., Surani, M.A., White, S., Barton, S.C., Brown, K., Blessing, M., Jorcano, J. and Balmain, A. (1990) Skin hyperkeratosis and papilloma formation in transgenic mice expressing a ras oncogene from a suprabasal keratin promoter. *Cell*, **62**, 697–708.
63. Dajee, M., Tarutani, M., Deng, H., Cai, T. and Khavari, P.A. (2002) Epidermal Ras blockade demonstrates spatially localized Ras promotion of proliferation and inhibition of differentiation. *Oncogene*, **21**, 1527–1538.
64. Yoon, S.O., Shin, S. and Mercurio, A.M. (2005) Hypoxia stimulates carcinoma invasion by stabilizing microtubules and promoting the Rab11 trafficking of the alpha6beta4 integrin. *Cancer Res.*, **65**, 2761–2769.
65. Jeong, H., Lim, K.M., Kim, K.H., Cho, Y., Lee, B., Knowles, B.C., Roland, J.T., Zwerner, J.P., Goldenring, J.R. and Nam, K.T. (2019) Loss of Rab25 promotes the development of skin squamous cell carcinoma through the dysregulation of integrin trafficking. *J. Pathol.*, **249**, 227–240.
66. Chiarugi, P. (2008) From anchorage dependent proliferation to survival: lessons from redox signalling. *IUBMB Life*, **60**, 301–307.
67. Goitre, L., Pergolizzi, B., Ferro, E., Trabalzini, L. and Retta, S.F. (2012) Molecular crosstalk between integrins and cadherins: do reactive oxygen species set the talk? *J. Sign. Transduct.*, **2012**, 807682.
68. Mushtaq, U., Bashir, M., Nabi, S. and Khanday, F.A. (2021) Epidermal growth factor receptor and integrins meet redox signaling through P66shc and Rac1. *Cytokine*, **146**, 155625.
69. Svineng, G., Ravuri, C., Rikardsen, O., Huseby, N.E. and Winberg, J.O. (2008) The role of reactive oxygen species in integrin and matrix metalloproteinase expression and function. *Connect. Tissue Res.*, **49**, 197–202.
70. Gregg, D., de Carvalho, D.D. and Kovacic, H. (2004) Integrins and coagulation: a role for ROS/redox signaling? *Antioxid. Redox Signal.*, **6**, 757–764.
71. Bartolacci, C., Andreani, C., El-Gammal, Y. and Scaglioni, P.P. (2021) Lipid metabolism regulates oxidative stress and ferroptosis in RAS-driven cancers: a perspective on cancer progression and therapy. *Front. Mol. Biosci.*, **8**, 706650.
72. Ferro, E., Goitre, L., Retta, S.F. and Trabalzini, L. (2012) The interplay between ROS and Ras GTPases: physiological and pathological implications. *J. Sign. Transduct.*, **2012**, 365769.
73. Carpentieri, G., Leoni, C., Pietraforte, D., Gecchetti, S., Iorio, E., Belardo, A., Pietrucci, D., Di Nottia, M., Pajalunga, D., Megiorni, F. *et al.* (2022) Hyperactive HRAS dysregulates energetic metabolism in fibroblasts from patients with Costello syndrome via enhanced production of reactive oxidizing species. *Hum. Mol. Genet.*, **31**, 561–575.
74. Martinelli, S., De Luca, A., Stellacci, E., Rossi, C., Checquolo, S., Lepri, F., Caputo, V., Silvano, M., Buscherini, F., Consoli, F. *et al.* (2010) Heterozygous germline mutations in the CBL tumor-suppressor gene cause a Noonan syndrome-like phenotype. *Am. J. Med. Genet. A.*, **87**, 250–257.
75. Brand, K., Kentsch, H., Glashoff, C. and Rosenberger, G. (2014) RASopathy-associated CBL germline mutations cause aberrant ubiquitylation and trafficking of EGFR. *Hum. Mutat.*, **35**, 1272–1281.
76. Altmuller, F., Pothula, S., Annamneedi, A., Nakhaei-Rad, S., Montenegro-Venegas, C., Pina-Fernandez, E., Marini, C., Santos, M., Schanze, D., Montag, D. *et al.* (2017) Aberrant neuronal activity-induced signaling and gene expression in a mouse model of RASopathy. *PLoS Genet.*, **13**, e1006684.
77. Basel-Vanagaite, L., Sarig, O., Hershkovitz, D., Fuchs-Telem, D., Rapaport, D., Gat, A., Isman, G., Shirazi, I., Shohat, M., Enk, C.D. *et al.* (2009) RIN2 deficiency results in macrocephaly, alopecia, cutis laxa, and scoliosis: MACS syndrome. *Am. J. Hum. Genet.*, **85**, 254–263.
78. Boukamp, P., Petrussevska, R.T., Breitkreutz, D., Hornung, J., Markham, A. and Fusenig, N.E. (1988) Normal keratinization in a spontaneously immortalized aneuploid human keratinocyte cell line. *J. Cell Biol.*, **106**, 761–771.
79. Lehman, T.A., Modali, R., Boukamp, P., Stanek, J., Bennett, W.P., Welsh, J.A., Metcalf, R.A., Stampfer, M.R., Fusenig, N., Rogan, E.M. *et al.* (1993) p53 mutations in human immortalized epithelial cell lines. *Carcinogenesis*, **14**, 833–839.
80. Abbadie, C., Pluquet, O. and Pourtier, A. (2017) Epithelial cell senescence: an adaptive response to pre-carcinogenic stresses? *Cell. Mol. Life Sci.*, **74**, 4471–4509.
81. Colombo, I., Sangiovanni, E., Maggio, R., Mattozzi, C., Zava, S., Corbett, Y., Fumagalli, M., Carlino, C., Corsetto, P.A., Scaccabarozzi, D. *et al.* (2017) HaCaT cells as a reliable in vitro differentiation model to dissect the inflammatory/repair response of human keratinocytes. *Mediat. Inflamm.*, **2017**, 7435621.
82. Pollok, S., Pfeiffer, A.C., Lobmann, R., Wright, C.S., Moll, I., Martin, P.E. and Brandner, J.M. (2011) Connexin 43 mimetic peptide Gap27 reveals potential differences in the role of Cx43 in wound repair between diabetic and non-diabetic cells. *J. Cell. Mol. Med.*, **15**, 861–873.
83. Shevchenko, A., Tomas, H., Havlis, J., Olsen, J.V. and Mann, M. (2006) In-gel digestion for mass spectrometric characterization of proteins and proteomes. *Nat. Protoc.*, **1**, 2856–2860.
84. Rohart, F., Gautier, B., Singh, A. and Le Cao, K.A. (2017) mixOmics: an R package for 'omics feature selection and multiple data integration. *PLoS Comp. Biol.*, **13**, e1005752.
85. Martens, M., Ammar, A., Riutta, A., Waagmeester, A., Slenter, D.N., Hanspers, K., R, A.M., Digles, D., Lopes, E.N., Ehrhart, F. *et al.* (2021) WikiPathways: connecting communities. *Nucleic Acids Res.*, **49**, D613–D621.
86. Subramanian, A., Tamayo, P., Mootha, V.K., Mukherjee, S., Ebert, B.L., Gillette, M.A., Paulovich, A., Pomeroy, S.L., Golub, T.R., Lander, E.S. *et al.* (2005) Gene set enrichment analysis: a knowledge-based approach for interpreting genome-wide expression profiles. *Proc. Natl. Acad. Sci. U. S. A.*, **102**, 15545–15550.

CHAPTER VIII. DOMINANTLY ACTING VARIANTS IN ARF3 HAVE DISRUPTIVE CONSEQUENCES ON GOLGI INTEGRITY AND CAUSE MICROCEPHALY RECAPITULATED IN ZEBRAFISH

Fasano G, Muto V, Radio C, Venditti M, Mosaddeghzadeh N, Coppola S, Paradisi G, Zara E, Bazgir F, Zigler A, Chillemi G, Bertuccini L, Tinari A, Vetro A, Pantaleoni F, Pizzi S, Conti L, Petrini S, Bruselles A, Prandi I, Mancini C, Chandramouli B, Barth M, Bris C, Milani D, Mariani R, Curry C, Guerrini R, Slavotinek A, Iascone M, Dallapiccola B, Ahmadian M R, Tartaglia M

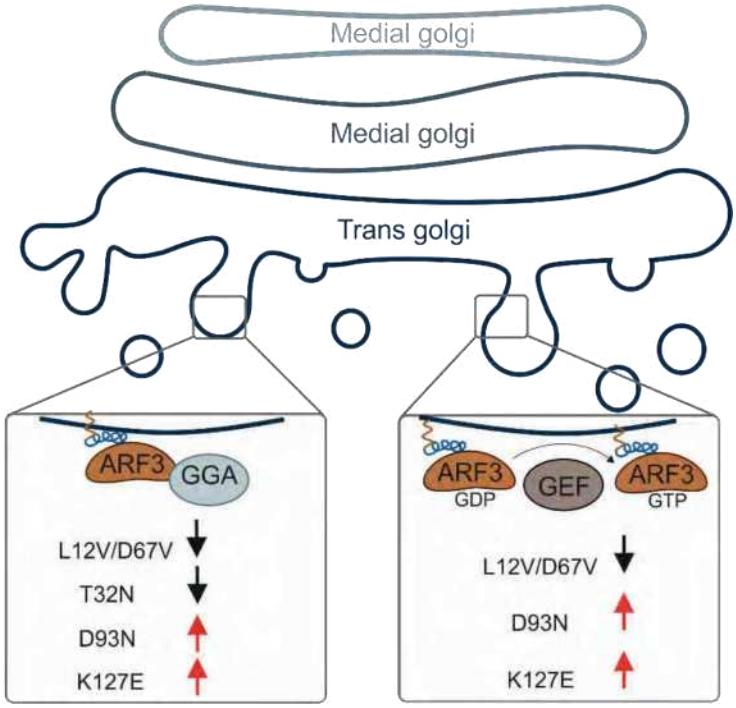

Status:	Accepted in October 2022
Journal:	Nature Communications
Impact factor:	17.69
Contribution:	20%
	Expression and purification of ARF3 wild type and variants in *E. coli* and eukaryotic systems, protein interaction analyses including fluorescence polarization measurements, stopped-flow measurements and pull-down assay, discussion.

Peer review information: *Nature Communications* thanks Vincent El Ghouzzi and the other, anonymous, reviewer(s) for their contribution to the peer review of this work. Peer reviewer reports are available.

Dominant *ARF3* variants disrupt Golgi integrity and cause a neurodevelopmental disorder recapitulated in zebrafish

Giulia Fasano[1*], Valentina Muto[1*], Francesca Clementina Radio[1*], Martina Venditti[1] Niloufar Mosaddeghzadeh[2],Simona Coppola[3], Graziamaria Paradisi[1,4], Erika Zara[1,5], Farhad Bazgir[2], Alban Ziegler[6,7], Giovanni Chillemi[4,8], Lucia Bertuccini[9], Antonella Tinari[10], Annalisa Vetro[11], Francesca Pantaleoni[1], Simone Pizzi[1], Libenzio Adrian Conti[12], Stefania Petrini[12], Alessandro Bruselles[13], Ingrid Guarnetti Prandi[14], Cecilia Mancini[1], Balasubramanian Chandramouli[15], Magalie Barth[6,7], Céline Bris[6,7], Donatella Milani[16], Angelo Selicorni[17], Marina Macchiaiolo[1], Michaela V Gonfiantini[1], Andrea Bartuli[1], Riccardo Mariani[18], Cynthia J Curry[19], Renzo Guerrini[11], Anne Slavotinek[19], Maria Iascone[20], Bruno Dallapiccola[1], Mohammad Reza Ahmadian[2], Antonella Lauri[1#], Marco Tartaglia[#]

Affiliations

[1]Genetics and Rare Diseases Research Division, Ospedale Pediatrico Bambino Gesù, IRCCS, 00146 Rome, Italy.

[2]Institute of Biochemistry and Molecular Biology II, Heinrich Heine University Düsseldorf, Düsseldorf, Germany.

[3]Centro Nazionale Malattie Rare, Istituto Superiore di Sanità, 00161 Rome, Italy.

[4]Department for Innovation in Biological Agro-food and Forest systems (DIBAF), University of Tuscia, 01100 Viterbo, Italy.

[5]Department of Biology and Biotechnology "Charles Darwin", Università "Sapienza", Rome 00185, Italy

[6]UFR Santé de l'Université d'Angers, INSERM U1083, CNRS UMR6015, MITOVASC, SFR ICAT, F-49000 Angers, France.

[7]Département de Génétique, CHU d'Angers, 49000 Angers, France.

[8]Institute of Biomembranes, Bioenergetics and Molecular Biotechnologies, Centro Nazionale delle Ricerche, 70126, Bari, Italy.

[9]Servizio grandi strumentazioni e core facilities, Istituto Superiore di Sanità, 00161 Rome, Italy.

[10]Centro di riferimento per la medicina di genere, Istituto Superiore di Sanità, 00161 Rome, Italy.
[11]Pediatric Neurology, Neurogenetics and Neurobiology Unit and Laboratories, Meyer Children's Hospital, University of Florence, 50139 Florence, Italy.
[12] Confocal Microscopy Core Facility, Ospedale Pediatrico Bambino Gesù, IRCCS, 00146 Rome, Italy.
[13]Dipartimento di Oncologia e Medicina Molecolare, Istituto Superiore di Sanità, 00161 Rome, Italy.
[14]Department of Chemistry and Industrial Chemistry, Università di Pisa, 56124 Pisa, Italy.
[15]Super Computing Applications and Innovation, CINECA, 40033 Casalecchio di Reno, Italy.
[16]Pediatric Highly Intensive Care Unit, Fondazione IRCCS Ca' Granda Ospedale Maggiore Policlinico, 20122 Milan, Italy.
[17]Mariani Center for Fragile Children Pediatric Unit, Azienda Socio Sanitaria Territoriale Lariana, 22100 Como, Italy.
[18]Department of Laboratories, Ospedale Pediatrico Bambino Gesù, IRCCS, 00146 Rome, Italy.
[19]Department of Pediatrics, Division of Medical Genetics, University of California, San Francisco, San Francisco, CA 94143, USA.
[20]Medical Genetics, ASST Papa Giovanni XXIII, 24127 Bergamo, Italy.
*These authors equally contributed to the work.

#Corresponding authors:

Antonella Lauri
Genetics and Rare Diseases Research Division
Ospedale Pediatrico Bambino Gesù
Viale di San Paolo, 15
00146 Rome, Italy
Email: antonella.lauri@opbg.net

Marco Tartaglia
Genetics and Rare Diseases Research Division
Ospedale Pediatrico Bambino Gesù
Viale di San Paolo, 15
00146 Rome, Italy
Email: marco.tartaglia@opbg.net

67 **Abstract**

68 Vesicle biogenesis, trafficking and signaling *via* Endoplasmic reticulum-Golgi network
69 support essential developmental processes and their disruption lead to
70 neurodevelopmental disorders and neurodegeneration. We report that *de novo*
71 missense variants in *ARF3*, encoding a small GTPase regulating Golgi dynamics,
72 cause a developmental disease in humans impairing nervous system and skeletal
73 formation. Microcephaly-associated *ARF3* variants affect residues within the guanine
74 nucleotide binding pocket and variably perturb protein stability and GTP/GDP binding.
75 Functional analysis demonstrates variably disruptive consequences of ARF3 variants
76 on Golgi morphology, vesicles assembly and trafficking. Disease modeling in zebrafish
77 validates further the dominant behavior of the mutants and their differential impact on
78 brain and body plan formation, recapitulating the variable disease expression. In-depth
79 *in vivo* analyses traces back impaired neural precursors' proliferation and planar cell
80 polarity-dependent cell movements as the earliest detectable effects. Our findings
81 document a key role of ARF3 in Golgi function and demonstrate its pleiotropic impact
82 on development.

83 **Introduction**

84 The Golgi apparatus is a polarized, membrane network-built organelle
85 organized as a series of flattened, stacked pouches (*cisternae*) held together by matrix
86 proteins and microtubules and structured into the *cis* and *trans*-Golgi compartments. It
87 is responsible for transporting, modifying, and packaging proteins and lipids into
88 vesicles for their targeted delivery[1–4]. Golgi also provides signaling platforms for the
89 regulation of a wide range of cellular processes (*e.g.*, cell polarity, stress response and
90 mitosis) suggesting a role as a cell sensor and regulator similarly to other organelles,
91 which ultimately orchestrates development[4–6]. Golgi function is highly depending upon
92 its rapid structural remodeling in response to different physiological stimuli, which is
93 attained *via* tightly regulated processes involving ribbon disassembly, tubulovesicular
94 conversion as well as stacks repositioning[4,7]. Of note, stimulus-dependent Golgi

repositioning in the apical radial glia precursors is crucial to maintain stem cell identity, likely controlling polarized trafficking during corticogenesis[8].

In the last years, several Mendelian disorders have causally been related to the defective or aberrant function of components of the transport machinery[9]. In particular, disruption of Golgi organization underlies several diseases, most of which share altered neurodevelopment and early-onset neurodegeneration[10–12]. In these disorders, collectively named "Golgipathies", recurrent features include microcephaly, CNS defects (*e.g.*, delayed myelination, cortical atrophy, abnormal corpus callosum, and pontocerebellar hypoplasia) and developmental delay (DD)/intellectual disability (ID) [12,13]. More generally, defective vesicle formation and unbalanced trafficking have been recognized as prominent patho-mechanisms in several neurodevelopmental disorders with CNS malformations and microcephaly[14–16], and neurodegenerative conditions[17,18].

The six members of the ADP-ribosylation factors (ARF) family of small GTPases (ARF1, ARF3-6, and ARF2, missing in primates) regulate key events of Golgi structure and function, vesicular biogenesis and cargo transport. ARF function is broadly overlapping and redundant in cells[19,20], where they participate in bidirectional membrane trafficking required for endocytosis and anterograde/retrograde transport, including protein recycling to the membranes or their degradation[20–24].

These proteins bind to guanine nucleotides with high affinity and specificity and cycle between a GTP (active) and GDP (inactive)-bound form[22,25]. Similar to other members of the RAS superfamily, release of GDP is stimulated by specific guanine nucleotide exchange factors (ARFGEFs), indirectly favoring binding to GTP[22,26,27]. As a consequence of the conformational change promoted by GTP, the *N*-terminal myristoylated region is exposed, allowing anchoring of the active GTPase to membranes of different organelles, including *cis* and *trans*-Golgi, plasma membrane and endosomes, where these proteins exert their function[22,25,28–30]. Moreover, the conformational rearrangement of the switch 1 [SW1] and switch 2 [SW2] regions controls the interaction with a number of effectors and regulators[30–32]. The intrinsic slow GTPase activity of ARFs is accelerated by specific GTPase-activating proteins (ARFGAPs), which result in protein inactivation and release from membrane[22,29,33,34].

By interacting with coat and adaptor proteins *via* this switch system[1,22], ARF proteins support various steps of the biosynthetic trafficking, such as COP-I vesicle formation and budding, which are essential for anterograde/retrograde cargo

transport[35,36]. ARF proteins can also recruit non-coat Golgi-specific factors to membranes (*e.g.*, Golgin-160 and GCC88)[37], which are fundamental for Golgi structural integrity[38,39], and thereby contribute to the control of Golgi and organelle structural organization and function[20,23,40,41].

The use of constitutively active (CA, GTP-bound) and dominant negative (DN, GDP-bound) ARF mutants as well as ARF silencing in cells has demonstrated the variable consequences of aberrant ARF function on Golgi integrity, morphology, vesicle formation and recycling[20,36], and the redundant roles among the various ARF proteins. CA mutants (*i.e.*, ARF1/3^{Q71L}) produce loss of the Golgi ribbon-like structure with an overall expansion of the Golgi and COP-I compartments due to conspicuous vesiculation[20,23]. Conversely, DN mutants (*e.g.*, ARF3^{N126I}) induce a different pattern of Golgi fragmentation, with dispersion of the coat proteins and COP-I disassembly[20]. The latter resembles the ARF poisoning effect triggered by brefeldin A (BFA), which blocks the normal activation of all ARF proteins by binding ARF1-GDP-GEF[42].

ARF-regulated Golgi dynamics during mitosis is crucial for cell division and cytokinesis[43–45]. Ultimately, by controlling Golgi structure, function, cargo sorting and trafficking, ARFs actively participate to the fine regulation of key events during embryogenesis (*i.e.*, cell polarity establishment and migration during gastrulation, neuronal maturation and tissue morphogenesis)[46]. A hyperactive or reduced *arf1* function in zebrafish results into altered body plan and head development[47,48]. In particular, hyperactive *arf1* induces body plan alterations that are consistent with altered planar cell polarity (PCP)[47].

Notwithstanding their emerging pivotal roles in development, mutations in *ARF* genes have only recently been linked to human disease, with activating missense variants of *ARF1* (MIM: 103180) causing a rare dominant malformation of cortical development resulting from defective neuronal migration (MIM: 618185)[49]. More recently, during the revision of this work, two pathogenic variants in *ARF3* were described in three individuals with a variable neurodevelopmental phenotype, and microcephaly in the most severe case[50].

Here, we report five *de novo* missense *ARF3* variants underlying a similar disorder affecting CNS and skeletal development. *In silico* and *in vitro* analyses provide evidence of a variable impact of mutations on protein stability, activity, Golgi integrity,

vesicle formation and cargo recycling. In-depth investigation in zebrafish corroborates the dominant nature of mutations, confirm a diverse effect on Golgi morphology during early embryogenesis, and recapitulate the variable brain and axial defects observed in patients. Experiments in live embryos further trace back the effect of aberrant ARF3 function to an altered balance of cell proliferation and death within the anterior developing brain and to impaired PCP-dependent cell axes formation.

Results

ARF3 mutations cause a developmental disorder affecting CNS and skeletal formation

In the frame of a research program dedicated to subjects affected by unclassified diseases, trio-based exome sequencing allowed us to identify a previously unreported *de novo ARF3* variant, c.379A>G (p.Lys127Glu; NM_001659.2), as the putative disease-causing event in a girl (Subject 1) with a severe syndromic neurodevelopmental disorder characterized by growth restriction, severe microcephaly, progressive diffuse cortical atrophy, hypoplasia of corpus callosum and other brain anomalies at MRI (*i.e.*, lateral ventricular enlargement, severe brainstem hypoplasia particularly affecting the pons, cerebellar inferior vermis hypoplasia), seizures, profound DD/ID and skeletal involvement (*i.e.*, 11 rib pairs and severe scoliosis), inguinal hernia and congenital heart defects (CHD). (**Supplementary Figure 1, Supplementary Tables 1 and 2 and clinical reports**). Whole exome sequencing (WES) data analysis excluded the presence of other relevant variants compatible with known Mendelian disorders based on their expected inheritance model and associated clinical presentation, and high-resolution SNP array analysis excluded occurrence of genomic rearrangements. The missense change, which had not previously been reported in population databases, affected an invariantly conserved residue among orthologs, paralogs and other structurally related GTPases of the RAS family (**Supplementary Figure 2a**). Through networking and GeneMatcher[51], we identified four additional subjects with *de novo ARF3* missense variants, which had not been reported in ExAC/gnomAD and involved amino acid residues located in regions highly constrained for variation (**Supplementary Table 2, Supplementary Figure 2a,b**). No additional candidate variants in clinically associated genes were identified in any patients (WES statistics and data output, **Supplementary Tables 3-7**). Affected

residues but Leu[12] were conserved among ARF3 orthologs and paralogs, and three of them were also conserved among other RAS GTPases (**Supplementary Figure 2a**). The identified missense variants affected residues whose corresponding positions in other GTPases of the RAS superfamily had previously been associated with human disease (**Supplementary Table 8**). Among these, the same Lys-to-Glu substitution at codon 127 in Subject 1 was recently reported to affect the corresponding residue in ARF1 in a patient with DD, microcephaly, periventricular heterotopia, progressive cerebral atrophy and epilepsy[49].

Affected subjects showed variable degree of DD/ID associated with brain and skeletal anomalies (**Supplementary Figure 1, Supplementary Table 1 and clinical reports**). No characteristic craniofacial gestalt was noted, with only minor craniofacial features reported in single patients, mainly related to microcephaly (**Supplementary Figure 1a,b**). Likewise Subject 1, Subject 2 (p.Leu12Val; p.Asp67Val) showed microcephaly, profound DD/ID, absence of speech and language development, progressive diffuse cortical atrophy with diminished hemispheric white matter, thin corpus callosum, progressive pontocerebellar hypoplasia without involvement of the cerebellar vermis, hypotonia, microsomia, and consistent skeletal defects (**Supplementary Figure 1b,c; Supplementary Table 1 and clinical reports**). A comparable but less severe condition was also observed in Subject 4 (p.Asp93Asn), who manifested hypotonia, severe DD/ID, delayed speech and language development, post-natal microcephaly, thinning of the corpus callosum as well as milder skeletal defects (**Supplementary Figure 1, Supplementary Table 1 and clinical reports**). Subject 3 (p.Pro47Ser) and Subject 5 (p.Thr32Asn) showed the mildest phenotype with DD/ID and delayed (Subject 3) or severely delayed (Subject 5) speech and language development. Subject 3 also shows early-onset seizures and a severe hypoplasia of the anterior part of the temporal lobe associated with hypomyelination and thin corpus callosum, while Subject 5 showed hypoplasia of the corpus callosum, mild white matter involvement in periventricular and supraventricular areas, and a large cisterna magna with a milder skeletal involvement (**Supplementary Figure 1b,c, Supplementary Table 1 and clinical reports**).

Disease-associated *ARF3* variants variably affect protein stability and function

The identified disease-associated variants affected residues spotted throughout the coding sequence except the *C*-terminus region (**Figure 1a**). First, we examined the possible functional consequences of each amino acid substitution using a three-dimensional structure of the GTPase recently solved by X-ray diffraction[52] as reference. All residues except for Leu[12] cluster within or close to the GTP/GDP binding pocket (**Figure 1b**). Lys[127] is one of the four residues of the NKXD motif directly mediating binding to GTP/GDP by binding to the ribose ring[32], and substitution of the positively charged residue with a negatively charge glutamate was predicted to affect nucleotide binding (**Figure 1c**). Similarly, Thr[32] contributes to stabilize the GTP/GDP binding *via* direct hydrogen bonding with one oxygen atom of the α phosphate (**Figure 1c**). While conservative, the Thr to Asn substitution was predicted to result in a steric hindrance. Asp[93] does not directly contact GTP, even though it participates to the overall general structure of the nucleotide binding pocket by a direct hydrogen bond with the lateral chain of Lys[127](**Figure 1c**). The Asp-to-Asn change was anticipated to disrupt the interaction between the two residues, destabilizing GTP/GDP binding (**Figure 1d**). Pro[47] and Asp[67] were predicted to affect ARF3 GTPase activity. Pro[47] is located within the SW1 region, which plays a key role in the catalytic activity of the GTPase and the conformational rearrangement mediating binding to effectors[22,32]. Substitution of this non-polar residue with a polar serine was expected to strongly perturb the functional behavior of the protein. Similarly, Asp[67] participates in the coordination of the Mg^{2+} ion through direct hydrogen bonds with a water molecule[31] (**Figure 1c**), and contributes to the regulation of GDP/GTP binding upon the "inter-switch toggle" mechanism[53]; its substitution with valine was predicted to considerably perturb GTP/GDP binding[30] and the overall organization of the nucleotide binding pocket. Similar pathogenic variants in RAS proteins were predicted to destabilize the binding to GTP/GDP[54,55], and ARF1 substitutions in Lys[127], Asp[67] and Asp[93] were documented to have deleterious effect in yeast[56]. Leu[12] (in *cis* with p.Asp67Val in Subject 2) is located within the flexible *N*-terminal myristoylated alpha helix implicated in membrane-cytoplasm shuttling[22,30], a region that has not been resolved structurally. No obvious consequence could be hypothesized for p.Leu12Val. However, a possible impact on nucleotide binding and GTPase activity cannot be excluded[57]. Of note, while Thr[32], Asp[93] and Lys[127] map regions of the GTPase not directly involved in intermolecular contacts, Pro[47] and Asp[67] lie in regions close to the surface of the

GTPase interacting with effectors/regulators[58], which does not rule out the possibility of a more complex functional behavior of the p.Pro47Ser and p.Asp67Val changes. To explore the structural and functional consequences of these two substitutions, we built a model of ARF3 interacting with the cytosolic coat protein complex (COP) formed by γ-COP (COPG1) and ζ-COP (COPZ1) starting from an available GTP-bound ARF1:COPG1-COPZ1 complex (PDB: 3TJZ) as template[59] (**Figure 1e-h**). The model for the wild-type (WT) ARF3 protein was validated by a 500-ns molecular dynamics (MD) simulation, documenting conservation of all known interactions with GTP and Mg^{2+} (**Figure 1e,f**; **Supplementary Table 9**). The ARF3:COPG1 interface is stabilized by an intermolecular hydrogen bonding network involving Arg^{19}, Thr^{48} and Asn^{84} ARF3 residues (**Supplementary Table 10**). We assessed the structural perturbations due to the introduced p.Pro47Ser and p.Asp67Val changes using the same time-frame. A minor impact on the ARF3 surface interacting with COPG1 was evident in the simulation when introducing the p.Asp67Val substitution (**Figure 1g**; **Supplementary Table 10**). As predicted by the structural inspection, this change resulted instead in a significant rearrangement of the nucleotide binding pocket with a reduction of the interactions of Lys^{127} and Thr^{45} with GTP (**Supplementary Table 9**). The Pro-to-Ser substitution at codon 47 did not significantly affect ARF3 binding to GTP (**Supplementary Table 9**), while a dramatic perturbation of the intermolecular binding network with COPG1 due to a substantial rearrangement of the SW1 region was observed (**Figure 1h**; **Supplementary Table 10**). Consistently, essential dynamics analysis documented a major effect of p.Pro47Ser in terms of global fluctuations and long range correlated movements, compared to the other simulations (**Supplementary Figure 3**). These structural analyses predicted that all variants but p.Leu12Val affect ARF3 GTP/GDP binding and/or the GTPase activity. A more articulated impact on conformational rearrangements mediating binding to effectors was suggested for p.Pro47Ser.

To experimentally validate the predicted consequences on ARF3 function, we examined the protein levels of each mutant in transiently transfected COS-1 cells, basally and after 3 and 6 hour-treatment with the protein synthesis inhibitor, CHX. Immunoblotting analysis documented levels of $ARF3^{D93N}$ and $ARF3^{T32N}$ comparable to the WT protein, while showed a slightly reduced level for $ARF3^{P47S}$ and a marked reduction for $ARF3^{K127E}$ and particularly $ARF3^{L12V/D67V}$ (**Figure 2a**; **Supplementary**

Figure 4a), the latter also confirmed in zebrafish embryos (**Supplementary Figure 4b**), which was not related to a significant reduction in the mRNA levels (**Supplementary Figure 5a**). A similar reduction in expression was confirmed by quantitative imaging analysis in COS-1 cells expressing mCherry-tagged ARF3^{K127E} and ARF3$^{L12V/D67V}$ (**Supplementary Figure 5b-c'**). Treatment with MG132 and bafilomycin A1, partially rescued the reduced levels of ARF3^{K127E} and ARF3$^{L12V/D67V}$, indicating an involvement of both the proteasomal pathway and autophagy in degradation (**Figure 2a'**).

In its active GTP-bound state, ARF3 is able to bind to the Golgi-associated gamma-adaptin ear-containing ARF-binding protein 3 (GGA3) to regulate downstream events controlling *trans*-Golgi function and intracellular trafficking[60]. Thereby, we performed pull-down experiments using the GGA3 protein-binding domain (PBD) on cell lysates from transfected COS-1 cells to compare the relative amounts of GTP-bound fraction of WT and mutant ARF3 proteins. In the same assay, we parallelly assessed ARF3^{Q71L} and ARF3^{T31N} as CA and the DN mutants, respectively[23,41]. Compared to cells expressing ARF3^{WT}, those expressing the ARF3^{K127E}, ARF3$^{L12V/D67V}$ and ARF3^{T32N} mutants showed a statistically significant reduction of the absolute ARF3 GTP-bound fraction, while a significant increase and a trend in the same direction were documented for ARF3^{D93N} and ARF3^{P47S}, respectively (**Figure 2b,c**). Next, by employing a cell-free system and fluorescence polarization we examined the biochemical behavior of a subset of mutants for which we obtained purified proteins. Compared to the WT protein, we observed an increased intrinsic (*i.e.*, GEF-independent) nucleotide exchange for the ARF3^{K127E} and ARF3^{D93N} mutants. A reduced exchange rate was instead registered for ARF3$^{L12V/D67V}$, while ARF3^{T32N} did not show significant alterations (**Supplementary Figure 6a,a'**). By inspecting the GTP hydrolysis of the purified proteins, we failed to note major changes compared to AR3^{WT} (**Supplementary Figure 6b,b'**). Altogether, these data suggest a stabilized GTP-bound conformation and an overall hyperactive behavior for ARF3^{D93N} and, to a minor extent, ARF3^{P47S}, while a DN behavior could be established for the ARF3^{T32N} variant. These findings could not unambiguously functionally classify the ARF3^{K127E}, and ARF3$^{L12V/D67V}$ behavior.

Disease-associated ARF3 mutants differentially impact on Golgi morphology

Next, we assessed the specific Golgi phenotype resulting from overexpression of the individual mutants in cells. Given the role of ARF proteins in maintaining proper Golgi integrity, organization and function[4,20,36,41,61], we performed confocal microscopy analysis of COS-1 cells overexpressing mCherry-tagged WT and ARF3 mutants and labelled for the resident *trans*-Golgi protein Golgin-97[62]. To specifically ascribe the observed phenotype to known dysregulated ARF function and derive possible insights into the mechanism, we directly compared Golgin-97 patterns to that obtained by known CA (p.Q71L) and DN (p.T31N) ARF3 proteins. Four major Golgi morphotypes were identified (**Figure 3a,b**). As expected, $ARF3^{WT}$-expressing cells showed a diffuse cytoplasmic ARF3 localization. Perinuclear (PN) localization of the protein was also observed, partially co-localizing with Golgin-97 (*i.e.*, GTP-bound ARF3), which showed a canonical, compact ribbon-like morphology (**Figure 3a, upper row, Supplementary Figure 7**). Conversely, only in a minority of cells expressing the DN $ARF3^{T31N}$, the *trans*-Golgi was recognizable as a discrete compact entity, while most cells showed partial or total dispersion of Golgin-97 within the cytosol (**Figure 3a, 2nd row, Supplementary Figure 7**), in line with previous reports[41,50] indicating occurrence of massive Golgi disassembly. In striking contrast, cells expressing the CA $ARF3^{Q71L}$ protein showed a compact and expanded Golgin-97 staining, likely reflecting an expansion in size of the *trans*-Golgi (**Figure 3a, 3rd row, Supplementary Figure 7**), as previously reported[23]. Dot plot representation of the Golgin97 mean intensity (I) and area (A) in cells expressing $ARF3^{WT}$, $ARF3^{Q71L}$ and $ARF3^{T31N}$ allowed to classify these distinct Golgi structural rearrangements into discrete classes: compact, expanded, partially or totally dispersed (**Figure 3b, Supplementary Figure 7**), providing an unbiased tool for the Golgi morphology assessment. Notably, altered Golgi morphology was not only characterized by an increase in area, but also by a significant decrease in Golgin-97 signal intensity with respect to compact Golgi. The three altered Golgi morphotypes were variably observed in cells expressing the identified *ARF3* variants, and a variable severity of the phenotype was documented. Cells expressing the $ARF3^{K127E}$, $ARF3^{L12V/D67V}$ and $ARF3^{D93N}$ showed Golgi structural alterations in all analyzed cells, while compact Golgi organization was observed in a fraction of cells expressing the $ARF3^{T32N}$ and $ARF3^{P47S}$ (**Figure 3a,c**), which is suggestive of a milder impact of these mutants, in line with the mild clinical features of patients (**Supplementary Table 1 and clinical reports**). Notably, similar to what was observed

for the DN mutant, ARF3^{K127E}, ARF3$^{L12V/D67V}$ and ARF3^{T32N} mainly induced variable Golgi dispersal, which was observed in all cells expressing either ARF3^{K127E} or ARF3$^{L12V/D67V}$ (**Figure 3a, 4th and 5th row, c**). Cells expressing ARF3^{T32N} were characterized by a milder reorganization of the Golgi with only a minority of cells showing total dispersion (23%, **Figure 3a 6th row, c**). On the other hand, resembling the effect of the CA mutant, ARF3^{D93N} and ARF3^{P47S} showed a significant increase of cells with expanded Golgi (79% and 67%) (**Figure 3a 7th and 8th row, c**). Of note, a more severe effect was documented for ARF3^{D93N}, with a fraction of cells also exhibiting partial dispersion, while a compact Golgi was observed in approximately 30% of cells expressing ARF3^{P47S} (**Figure 3c**). These findings provide evidence of a differential functional impact of the identified ARF3 variants on Golgi structural morphology (**Figure 3c**).

Next, we further investigated Golgi morphology *via* ultrastructure inspection by performing transmission electron microscopy (TEM) on cells expressing ARF3^{K127E} and ARF3^{D93N}, which showed the "fully dispersed" and "expanded" trans-Golgi morphotypes, respectively. While perinuclear Golgi mini-stacks well organized in ribbons were recognizable in cells expressing ARF3^{WT} (**Supplementary Figure 8a,a'**), those expressing ARF3^{K127E} exhibited Golgi fragmentation characterized by an integrity loss of the mini-stacks with numerous diffused vesicles and small cisternae scattered in a wide area (**Supplementary Figure 8 b,b'**). Cells expressing ARF3^{D93N} displayed a different pattern with loss of the typical ultrastructure of Golgi elements and a marked increase in swollen cisternae and a diffuse vesiculation, which were confined within the defined area normally occupied by Golgi (**Supplementary Figure 8 c,c'**). A similar fragmentation pattern had previously been described[4,23,63,64], also for CA ARF and ARF-like mutants[4,23,63,64]. We cannot exclude occurrence of more complex morphological alterations, whose assessment would require electron tomography analysis or 3D super resolution microscopy.

To further validate these findings within an organismal context, we next set out to examine the *trans*-Golgi in zebrafish embryos expressing ARF3^{K127E} and ARF3^{D93N}, for which opposite effects were observed in cells. Zebrafish harbors two paralogs, *arf3a* and *arf3b*, which share common ancestry with mammalian *ARF3* and conservation of the amino acids involved in the identified mutations (**Supplementary Figure 2a**). *arf3a* and *arf3b* are both expressed during early embryonic development,

and *arf3b* shows higher level of expression after maternal-to-zygotic transition (MZT) throughout gastrulation and somitogenesis (**Supplementary Figure 9**), indicating its predominant role during these developmental stages. Next, we overexpressed mRNAs encoding $ARF3^{WT}$, $ARF3^{K127E}$ and $ARF3^{D93N}$, and used specific cellular and subcellular makers to assess *trans*-Golgi morphology in precursor cells of the envelope layer (ELV) in early gastrula (**Figure 4a**). We reasoned that the complexity of the physiological Golgi dynamics *in vivo* and the expected occurrence of fragmented Golgi in proliferating cells[43] might limit our ability to distinguish the specific pathogenic effect of the mutants on Golgi in fish. Thereby, we first verified whether the dispersion of Golgi elements due to expression of $ARF3^{K127E}$ could be observed in early zebrafish embryos. To this aim, we injected mRNAs encoding the mCherry-tagged $ARF3^{WT}$ and $ARF3^{K127E}$ in a first batch of siblings, together with a fluorescent membrane marker and EGFP-tagged GalT (galactosidase T^{65}), a marker of trans-Golgi. By using this marker, we parallelly confirmed $ARF3^{K127E}$-mediated Golgi elements dispersal in a live time lapse of COS-1 cells (**Figure 4a-c**; **Supplementary Movie 1**) and in alive zebrafish embryos (**Figure 4d,e**). In embryos, we observed a diffused distribution of $ARF3^{WT}$ partially overlapping EGFP-GalT staining. The latter was structured in ribbon-like elements. Conversely, in $ARF3^{K127E}$ expressing fish, EGFP-GalT signal distribution appeared less intense and organized in small and large puncta, some of which also co-localized with ARF3 (indicating Golgi-localization) (**Figure 4d,e, Supplementary Figure 10a**). Next, we compared the EGFP-GalT staining associated with $ARF3^{K127E}$ and $ARF3^{D93N}$, using the patterns resulting from CA and DN ARF3 mutants as reference. Again, we observed a reduced number of ribbon-like Golgi in cells expressing $ARF3^{K127E}$ (<20%) as compared to WT, similarly to the DN ARF3-expressing embryos (**Supplementary Figure 10b,c**). Despite the changes in Golgi morphology were subtler in fish injected with $ARF3^{D93N}$, loss of typical Golgi ribbon-like structures was evident. This pattern was accompanied by instances of large EGFP-$GalT^{+}$ structures (39%), also documented in fish expressing the known CA mutant (**Supplementary Figure 10b,c**).

Overall, the collected *in vitro* and *in vivo* findings suggest that the identified pathogenic variants in *ARF3* have a variable dominant impact on protein stability, activity, and Golgi morphology. The Golgi morphotype analysis established the presence of different functional classes of disease-causing ARF3 mutants, broadly ascribing to a

DN or CA mechanism. Notably, their variable strength appeared to correlate with the severity of clinical features observed in patients.

ARF3 mutants impair COP-I vesicle formation and cargo recycling in COS-1 cells

Given the known involvement of ARF GTPases into vesicles budding, endosomal transport and recycling, and considering the observed Golgi phenotypes, we then asked whether and how ARF3 mutants impact on the formation and activity of the endolysosomal compartments along the endocytic-recycling pathway. First, we examined the integrity of COP-I vesicles by immunostaining the β-COP subunit of COP-I. In line with the Golgi phenotypes and previous reports on DN and CA ARF3[20,65], cells expressing ARF3^{K127E} and ARF3$^{L12V/D67V}$ were characterized by a sparse distribution of the signal throughout the cytoplasm, indicating a disassembly of COP-I vesicles. Differently, a large number of cells expressing ARF3^{P47S} and ARF3^{D93N} showed an expanded β-COP signal, which is indicative of an enlarged COP-I compartment. Cells expressing ARF3^{T32N} did not show a clear-cut phenotype, with a minor incidence of cells showing partial/complete disassembly, indicative of a mild effect of the mutant (**Figure 5a,b**).

Next, to follow cargos destiny within the endocytic-recycling pathway, we continuously incubated COS-1 cells with fluorescently labeled transferrin (Tfn) at 37 °C for 5 or 30 minutes to trigger internalization and trafficking of the endocytic vesicles containing labeled Tfn/TfnR complex to the endolysosomal compartment[66]. The subcellular distribution of vesicles in these two time points was assessed by confocal microscopy. In a normal scenario, upon 5 min incubation, Tfn is internalized and found along the endocytic pathway; following longer incubation time, the majority of the Tfn^{+} cargo is expected to have recycled back to the cell surface, such that limited Tfn levels are observed in the PN compartment[67,68]. Upon 5 min incubation, the distribution of Tfn appeared nonuniform in ARF3^{WT} expressing cells, with sparse Tfn^{+} vesicles clusters observed throughout the cell, mostly within the PN space ("semi-clustered"), similarly to non-transfected cells (**Supplementary Figure 11 a,b**). In contrast, a higher fraction of the cells expressing ARF3^{K127E} and ARF3$^{L12V/D67V}$ showed Tfn^{+} vesicles enriched within the PN region ("clustered") (**Supplementary Figure 11 a-b'**). In cells incubated for a longer time with Tfn, both mutants showed an even stronger cargo accumulation (**Figure 6a-b'**; **Supplementary Figure 11c**).

To further assess possible defects in recycling, cells incubated for 30 min with Tfn were stained for Rab5 and Rab11, early (EE) and recycling (RE) endosome markers, respectively[68–71]. The fraction of internalized Tfn co-localizing with Rab5$^+$ vesicles was significant higher in ARF3^{K127E} and ARF3$^{L12V/D67V}$ expressing cells compared to the control cells (**Figure 6c,d**). A similar trend was observed with respect to Rab11, which was statistically significant for ARF3$^{L12V/D67V}$ (**Supplementary Figure 12**). These findings indicate a dominant behavior of ARF3^{K127E} and ARF3$^{L12V/D67V}$ in causing cargo transport delay. None of the other mutants showed altered behavior.

Not recycled Tfn is normally eliminated via the lysosomal pathway[72–75] . To evaluate mis-targeting of the Tfn to lysosomes or overload of the degradative pathway, cells incubated with Tfn for 30 min were stained with the lysosomal marker Lamp2. Compared to cells expressing ARF3^{WT}, only cells expressing ARF3^{D93N} showed a significant increase of the fraction of Tfn colocalized with Lamp2 at the PN. Nevertheless, expression of all mutants except ARF3^{P47S} was associated with a significant increased fraction of Lamp2$^+$ vesicles colocalized with Tfn (**Supplementary Figure 13**). Hence, despite the mutation-specific patterns, lysosomes seem to generally increase their Tfn loading in the majority of the mutants.

Functional validation in zebrafish confirms the pathogenicity and dominant mechanism of action of ARF3 variants

We expanded our *in vivo* validation by investigating a possible variable impact of all the identified ARF3 mutants on embryogenesis. To this aim, myc-tagged WT and mutant *ARF3* mRNAs were microinjected at one-cell stage zebrafish embryos (**Figure 7a**). As anticipated, endogenous *arf3* is detected at early stages of embryogenesis (*i.e.*, before MZT) and it accumulates only later starting at late blastula/early gastrula period (**Supplementary Figure 9**). In the injected embryos, we profiled the expression timing of Myc-tagged protein and determined a subtle expression of both WT and mutant ARF3 before MZT, with a clear increase only later during development. This pattern mimicked the endogenous *arf3* expression (**Supplementary Figure 14**).

Injected embryos were sorted based on the expression of GFP-CAAX (used as injection marker), and developmental progression was followed from early time points of gastrulation till 48 hours post fertilization (hpf) embryos (long-pec stage) (**Figure 7a-b'**), when morphogenesis is nearly completed and sub-compartmentalization of

different neural structures can be appreciated[76]. Embryos expressing each of the tested ARF3 mutants showed significant phenotypic alterations compared to siblings expressing $ARF3^{WT}$ and not injected controls. Compared to normal development (class I), mutant embryos showed variable degree of survival rate and developmental delay (class II) (**Figure 7c-c'', Supplementary Fig.15a**). A statistically significant decrease in the survival rate of embryos expressing $ARF3^{K127E}$ was documented (**Figure 7c'**), and morphogenesis appeared particularly perturbed both at the level of the head and trunk for a significant fraction of embryos. For the majority of the analyzed mutants, a substantial fraction of embryos (≥ 25%) showed mild or severe phenotypes (class III and IV, respectively) that were characterized by reduced head size, with/without microphthalmia, and/or mild shortening and lateral bending of body axis (class III), or considerably reduced head (microcephaly or anencephaly) and eye size, with marked reduction of the trunk, defective body elongation and severe lateral bending (kinked notochord, class IV) (**Figure 7c-c'', Supplementary Fig.15a**).

To validate the mechanism of action and further test the dominant behavior of the *ARF3* variants *in vivo*, we directly compared the observed ARF3 overexpression phenotype with that obtained by downregulating endogenous *arf3 via* translation blocking morpholino (MO) approach, targeting both *arf3a* and *arf3b* maternal and zygotic translation. At 24 hpf, fish injected with MO against *arf3a* and *arf3b* showed a subtler phenotype, with a prevalence of class II phenotype (developmental delay), and only a small percentage (< 8%) of animals showing the characteristic body curvatures observed in fish expressing ARF3 mutants (**Figure 7d,d'**). These defects increased only later in development but remained < 20% on average (**Figure 7d''**). Moreover, contrary to fish expressing ARF3 mutants, we did not observe severely affected embryos among the *arf3* MO-injected embryos (**Figure 7d-d''**) nor significant death (**Supplementary Fig.15b**). Notably, the incidence of the observed phenotype increased with increasing MO doses (**Figure 7d-d''**), and by 48 hpf a significant rescue of the phenotype could be observed when co-injecting mRNA encoding $ARF3^{WT}$ (**Figure 7e-e''**), demonstrating the specificity of the phenotype in relation to *arf3* downregulation.

The MO approach had previously been used as tool to test the genetic mechanism of action *in vivo*, assuming that downregulation of endogenous protein expression alleviates the phenotypes associated with CA mutants but exacerbate the phenotype

of DN mutants[77]. Therefore, we performed a set of experiments in which each of the pathogenic *ARF3* alleles was co-injected with *arf3/b* MO (+MO). When we statistically assessed the incidence of phenotypes in "+MO" conditions against those observed by injecting solely mutant *ARF3* mRNA (-MO), a significant worsening of the most severe traits was documented in for $ARF3^{K127E}$ (class IV), $ARF3^{L12V/D67V}$ and $ARF3^{T32N}$ (both for class III). On the other hand, we observed a significant alleviation of the phenotype (class III) in embryos expressing $ARF3^{D93N}$ and co-injected with *arf3a/b* MO. We did not observe any substantial change in the phenotype severity for $ARF3^{P47S}$ (**Figure 7f**). A ratio between the percentage of embryos showing the most severe traits, including class IV and V (deceased fish) with or without MO confirmed the trend for most of the mutants (**Figure 7f**). Altogether, these data provided *in vivo* evidence of a dominant mechanism of the identified disease-causing variants, clearly distinguishable from the *arf3* loss-of-function effect. Moreover, corroborating the *in vitro* results, these findings support a DN mechanism for p.K127E, p.L12V/p.D67V and p.T32N, and a CA behavior for p.D93N.

Zebrafish embryos expressing ARF3 mutants recapitulate the variable disease severity

To explore further the consequences of *ARF3* mutations on neurodevelopment, we more accurately characterized zebrafish head and brain phenotype. At 24 and 48 hpf, compared to not injected controls and siblings expressing $ARF3^{WT}$, we registered a significant reduction of the head area for p.K127E and p.L12V/D67V, with the most severe cases lacking the frontal part of the brain and eyes (**Figure 7b'**; **Figure 8a,b**). Phenotypic assessment at later stages (4.5 days post fertilization, dpf) documented appearance of microcephaly also in embryos expressing $ARF3^{D93N}$, while none of the other mutants showed significant changes (**Figure 8b'**).

These *in vivo* measurements resembled the variable clinical traits reported in patients, with only Subjects 1 (p.K127E) and Subject 2 (p.L12V/p.D67V) showing severe microcephaly at birth, and Subject 4 (p.D93N) displaying post-natal microcephaly (**Figure 8b'', Supplementary Figure 1, Supplementary Table 1 and clinical reports**).

Next, taking advantage of our live whole-brain/embryos samples, we examined the anterior brain volume in fish exhibiting early- and late-onset microcephaly as well as

embryos expressing ARF3^{P47S}, which was associated to a mild reduction within the developing forebrain in Subject 3 (**Supplementary Figure 1, Supplementary Table 1 and clinical reports**). To this aim, we employed the *NBT:dsRed* transgenic line, labeling differentiated neurons. Volumetric reconstructions from live confocal z-stack acquisitions confirmed a significant reduction of the brain volume for ARF3^{K127E} and ARF3$^{L12V/D67V}$ (**Figure 8c,c'**).

Additional volumetric measurements obtained from fixed specimens at 48 hpf by labeling mature axonal and neuronal structures confirmed the observed brain volume reduction for ARF3^{K127E} (**Supplementary Figure 16**). Of note, despite head measurements documented only a delayed effect of ARF3^{D93N} and did not show significant changes for ARF3^{P47S}, the volumetric analysis of the anterior brain at 48 hpf was able to capture a significant reduction of brain mass for both mutants (**Figure 8c,c'**).

Defective formation of the forebrain commissural fibers of the corpus callosum (CC) is a common feature of all patients. No evolutionary related structure has been described in teleost fish; nevertheless, the anterior commissure (AC) is the major white matter structure within the developing telencephalon. Likewise CC, AC consists of thick axonal bundles connecting the two hemispheres of the telencephalic forebrain[78]. To expand our brain phenotyping, we assessed AC formation in 48 hpf fish injected with WT and mutant *ARF3* mRNA by using staining against anti-acetylated tubulin to visualize the axonal bundles. A significant reduction in the width of the AC lateral bundles was observed for all the ARF3 mutants. A stronger effect was recorded for ARF3^{K127E}, ARF3$^{L12V/D67V}$ and ARF3^{D93N} when the width of the entire AC was considered (**Supplementary Figure 17**).

Altogether, the morphometric parameters measured *in vivo* are consistent with the variable degree of impaired brain development as a distinctive feature of the disease, and support the occurrence of telencephalic white matter defects as a common trait of this new Golgipathy. Our findings further document a severe effect on brain development for the p.K127E and p.L12V/D67V *ARF3* substitutions in zebrafish, which captures the severity of phenotype observed in Subject 1 and 2.

Aberrant ARF3 function induce proliferation and cell cycle defects within the anterior brain

Cortical malformations resulting in microcephaly are often caused by aberrant neurogenesis underlying altered proliferation and cell cycle progression, which ultimately lead to premature stem cell death[79–81]. To test this hypothesis and probe into the mechanism causing reduced brain volume in mutant embryos, we examined the proliferative status and quantified cell death. By performing whole-brain immunohistochemistry using anti-proliferating cell nuclear antigen (PCNA) and anti-phospho-histone 3 (pH3) antibodies, we queried the proliferative and mitotic ability of precursor cells at 48 hpf within the forebrain proliferative zone (pz), which is clearly discernible from ventral confocal images (**Figure 9a,b**). The number of $pH3^+$ cells within this region was significantly reduced in embryos expressing $ARF3^{K127E}$; a similar trend was observed for $ARF3^{L12V/D67V}$ and $ARF3^{D93N}$ expression fish (**Figure 9b,c**). In addition, we detected changes in the overall distribution of proliferative cells within the dorsal brain domain, which ectopically invaded the midbrain territory normally populated by differentiated neurons and nerve bundles (tectal neuropil)[82,83], with a stronger effect observed for $ARF3^{K127E}$ and $ARF3^{D93N}$ (**Supplementary Figure 18a-h**). This pattern indicates the occurrence of a complex impairment of the developmental processes within the anterior brain. No major changes in the total number of $pH3^+$ cells were observed except for an increase in the cerebellum in $ARF3^{D93N}$ expressing fish (**Supplementary Figure 18i-k**).

Next, by assessing the known chromatin morphology by inspecting pH3 staining appearance, we profiled cells with respect to cell cycle stage[84]. Compared to controls, significant alterations in the relative proportion of mitotic cells between early phases (prophase/prometaphase), metaphase or late phases (anaphase/telophase) were observed in embryos expressing the ARF3 mutants with the exception of $ARF3^{P47S}$. Specifically, precursor cells scored a higher percentage of $pH3^+$ cells in prophase/prometaphase at the expenses of later cell cycle stages, suggesting a delay or arrest in early mitosis (**Figure 9b,d,e**).

Precursor cells failing to progress through cell cycle are normally targeted to apoptosis *via* mitotic surveillance systems[85]. Similar mechanisms activated during aberrant neurogenesis deplete the pool of stem cells available for neurogenesis and brain growth, and result in microcephaly[86,87]. To test this possibility, we next assessed cell death rate within the forebrain of our fish mutants by live embryo staining with acridine orange (AO). The analysis showed a significant increase of AO^+ spots (*i.e.*, dying cells

and/or apoptotic bodies) in ARF3^{K127E} and ARF3$^{L12V/D67V}$ expressing fish (**Figure 9f and g, upper graph**). This finding is in line with the clinical and functional *in vivo* data reporting p.K127E and p.L12V/D67V as the ARF3 amino acid substitutions associated with the most severe phenotype characterized by early-onset microcephaly in patients and severe head area reduction in fish, respectively. Increased cell death was also recorded for ARF3^{P47S} and ARF3^{D93N} expressing fish when a larger area of the forebrain including the eyes was examined (**Figure 9g, lower graph**).

Last, given the importance of Golgi for the establishment and the dynamics of mitotic spindles in dividing precursors[88–90], we asked whether spindle aberrations could at least partially explain the cell cycle alterations observed in fish, as previously reported in a number of cortical malformations with microcephaly[91–93]. We took advantage of the transgenic line *Tg(XlEef1a1:dclk2DeltaK-GFP)* marking microtubules in early embryos, and investigated metaphase spindles morphology within the anterior ventral brain in live embryos expressing ARF3^{WT}, ARF3^{K127E} and ARF3^{D93N}, causing early- *vs* late-onset microcephaly. Compared to controls, aberrantly elongated spindle morphology was recorded for both mutants (**Supplementary Figure 19**), indicating a common effect on spindle microtubules organization, likely explaining the similar impact on cell cycle.

Collectively these data suggest a complex impact of different ARF3 mutants on neurogenesis and point to an impaired balance between precursors' cell mitosis and cell death as a mechanism contributing to the observed neurodevelopmental phenotypes.

ARF3 mutants variably impact PCP-dependent axes formation in early zebrafish development

We detailed the morphological defects and developmental processes implicated in the observed body curvature. We focused on the notochord, which supports the body elongation along the anterior to posterior axis (AP) and spine formation[94], and whose altered development has been associated with CA ARF1 in fish[47]. We documented the occurrence of multiple notochord curvatures of variable degrees in animals expressing each of the ARF3 mutants except ARF3^{P47S} (**Figure 10a-c**). Quantification of the degree of bending (180°: normal; 179° ≥ angle ≥ 110°: mild; angle ≤ 109°: severe) showed a similar incidence of mild and severe bending (in > 90% of embryos) in fish

expressing ARF3^{K127E} and ARF3$^{L12V/D67V}$ (**Figure 10b,c**), in line with the overall severity of the skeletal phenotype characterizing subjects 1 and 2 (**Supplementary Figure 1, Supplementary Table 1 and clinical reports**). Overall, all mutants expect ARF3^{P47S} showed a significant higher number of notochord curvatures (**Figure 10c'**).

We further examined the underlying causes of the perturbed body trunk and notochord morphogenesis by tracing back axes establishment in development. First, we examined patterning and morphogenesis in animals in their segmentation stage (15 hpf). During this period, the embryo AP and medio-lateral (ML) axes are already established and somitogenesis occurs. mRNA levels of *Krox20* and *MyoD* (markers of the hindbrain rhombomeres in the anterior cephalic domain and of developing somites from the paraxial mesoderm, respectively) were assessed in whole-mount embryos by *in situ* hybridization (ISH). While proper patterning of cephalic region and paraxial mesoderm was in place, we observed a variable perturbation of the AP and ML axes in the ARF3 mutants (**Figure 10d,e**). Embryos expressing ARF3 mutants showed a clear shortening of the AP length compared to WT (**Figure 10e,f**). Consistently, the number of somites in mutant embryos was also reduced (**Supplementary Figure 20**). Expansion of the paraxial tissue in the ML axis was also apparent for some mutants (**Figure 10e**). The data pointed to a defective convergence-extension (CE) process, which was evident for all mutants except ARF3^{P47S} when the CE index (*i.e.*, the ratio between the AP extend and ML extend of the anterior somites) was assessed (**Figure 10 e,g**). For both AP and ML axes defects, severely affected embryos were more prevalent among those expressing ARF3^{K127E}.

Lastly, benefiting from the transparent and fast zebrafish development, we assessed the time occurrence of axes defects linked to gastrulation (and thereby CE) perturbation by investigating earlier stages (**Supplementary Figure 21a**). Already between 10 - 13 hpf, when segmentation has just started, brain thickenings and tail bud are visible at the very anterior and posterior end of the embryo, respectively, as a result of correctly orchestrated gastrulation movements[76]. By measuring the angle between the developed cephalic and caudal structures at this stage, we documented a reduced embryo elongation (likely due to aberrant /delay gastrulation) for ARF3^{K127E} and ARF3^{D93N} (**Supplementary Figure 21b,c**), indicating an early impact of these mutants on axes formation.

Perturbed cell movements were further confirmed in live embryos expressing ARF3^{K127E}, which exhibited the strongest effect in terms of axis elongation (AP, ML). Early embryos (6 – 7 hpf) showed reduced epiboly and impaired gastrulation, which ultimately resulted in in defective head and tail bud formation (**Supplementary Figure 21d,e**). Of note, cells expressing the mutant appeared mostly round, with a reduced number of protrusions, with respect to cells expressing the WT protein (**Supplementary Figure 21d-f**), suggesting occurrence of altered polarity establishment and cytoskeletal organization as an early molecular event, in line with the emerging roles of Golgi in instructing cell polarity[95].

These *in vivo* findings demonstrate impairment of axes formation of variable degree as a common trait of the mutants causing skeletal deformities in patients, broadly recapitulating the severity of the clinical phenotype, and trace back the mechanism to a compromised PCP-dependent CE cell movement for the severe cases.

Discussion

Controlling organelle stability, targeted trafficking of proteins and lipids and signaling, the highly conserved ARF GTPases contribute to cell polarity, division and migration ultimately instructing development[1,46,47]. Here we identify *de novo* missense *ARF3* variants as the molecular event underlying a clinically variable neurodevelopmental disorder characterized by DD/ID and variable CNS defects as common features. Microcephaly and progressive cerebral atrophy occurred in most affected individuals, while epilepsy and skeletal abnormalities were variably documented as associated traits. The clinical phenotype of this disorder is reminiscent of the condition caused by activating mutations in *ARF1*[49], characterized by DD/ID, microcephaly, delayed myelination, cortical and cerebellar atrophy, periventricular heterotopia and seizures as major features, but also showing periventricular heterotopia. A related neurodevelopmental disorder characterized by DD/ID, progressive microcephaly, failure to thrive, and periventricular heterotopia has been linked to biallelic inactivating variants of *ARFGEF2* (ARPHM, MIM: 608097)[16], encoding ARF-specific GEF stimulating the GTPase activation. Consistent with the observed clinical variability, our *in vitro* data demonstrate variable consequences of the identified disease-causing *ARF3* variants on protein stability, nucleotide binding activity and exchange, as well as on *trans*-Golgi and vesicles integrity and function. The differential impact of DN and

CA on Golgi integrity is supported by *in vivo* validation. Zebrafish models, which recapitulate the pleiotropic effect and the variable strength of each ARF3 variant on developing brain and body axes, offer further insights into the underlying sub-cellular and cellular pathogenic mechanisms.

The activity of ARF3 at the *trans*-Golgi is tightly regulated *via* a conformational switch controlled by reversible GDP-to-GTP binding, which determine Golgi stability and trafficking[22,32]. Our structural inspection indicates that the majority of the disease-causing *ARF3* mutations affect conserved residues involved in GDP/GTP binding/exchange, previously reported to be mutated in other GTPases of the RAS superfamily (*e.g.*, ARF1, HRAS, KRAS, NRAS, MRAS, RRAS, RRAS2), which cause neurodevelopmental syndromes or contribute to oncogenesis[49,96–101] (COSMIC database, **Supplementary Figure 2a and Supplementary Table 8**). Lys^{127} in ARF3 (mutated in Subject 1) is homologous to Lys^{117} in HRAS (MIM: 190020), which if mutated cause Costello syndrome (CS [MIM: 218040])[102]. Pro^{47} (mutated in Subject 3) is homologous to Pro^{34} in HRAS, KRAS and NRAS. The same Pro-to-Ser change have previously been reported as a somatic event in *HRAS* underlying vascular tumors[103], and other changes affecting this residue in KRAS, HRAS and NRAS have been described in RASopathies[104–106] (ClinVar IDs: VCV000040454, VCV001052630, VCV000039647). Furthermore, a missense change affecting the adjacent residue in *ARF1* (p.Thr48Ile) was observed in a patient with clinical features overlapping with the present series[106]. In HRAS and KRAS, mutations affecting Thr^{58}, which is adjacent to the aspartic acid residue homologous to Asp^{67} in ARF3 (mutated in Subject 2), have causally been linked to RASopathies[104,107,108]. Consistent with our findings, a recent report identified two missense changes affecting Asp^{67} and Arg^{99} of ARF3 in patients showing severe microcephaly at birth and progressive cortical and brainstem atrophy and epileptic seizures, and neurodevelopmental delay, cerebellar hypoplasia and epilepsy, respectively[50]. Finally, both p.Pro47Ser and p.Asp67Val affect a conserved hydrophobic region of ARF3 involved in effector binding[24,30,109], with molecular dynamics simulations suggesting a major perturbation exerted by p.Pro47Ser on ARF3 binding to effectors. These considerations stimulate future studies aimed to demonstrate whether effector binding in these mutants is qualitatively and/or quantitatively altered.

Our *in vitro* data show an altered behavior of all ARF3 mutants in terms of stability and GTP binding. Among these, two amino acid changes, p.D93N and p.P47S, were classified as CA, with the former exhibiting the strongest activation, in line with the severe and milder phenotypes observed in patients harboring these variants, respectively. The GTP binding behavior of the p.T32N substitution could be classified as DN, while a more complex behavior emerged for p.K127E and p.L12V/D67V variants. The dramatically accelerated degradation of the two ARF3 mutants and reduced absolute levels of their GTP-bound forms cannot rule out the possibility of a loss-of-function behavior, which is in contrast with the activating role of the p.Lys117Arg substitution in *HRAS* causing upregulation of MAPK signaling in Costello syndrome[102,110]. Similar to this variant, however, biochemical investigation performed on purified proteins in a cell-free system demonstrates an increased nucleotide exchange rate and exclude any significant impact of on the GTPase catalytic activity. The reduced activity of the purified $ARF3^{L12V/D67V}$ is instead in line with the structural prediction, anticipating a destabilization of both GTP and GDP binding via impaired coordination with Mg^{2+}. It should be noted that myristylation is not achieved in the bacterial expression system employed to purify the proteins and the used cell-free assay does not account for the relevance of the lipid bilayer on the structural rearrangement of the GTPase and its and function[20,111]. Future dedicated experiments are required to more accurately examine the biochemistry of these mutants.

To functionally characterize the behavior of ARF3 mutants we profiled their impact on Golgi morphology. While depletion of *ARF1* or *ARF3* was not reported to affect Golgi structure[20], a differential impact of DN and CA forms is known. Golgi fragmentation with dispersion of specific Golgi associated and coat proteins (beta-COP) is reported for DN ARF mutants[20,50,61], while an extension of the Golgi compartment, with swelling of Golgi and COP-I vesicles resulting in a sustained vesiculation has been associated with expression of constitutively active mutants[61,23]. The observed *trans*-Golgi and vesicle morphotypes identify different functional classes, mirroring CA and DN behaviors. The pathophysiological relevance of these findings for embryonic development are supported by *in vivo* analysis of live *trans*-Golgi morphology in early zebrafish embryos overexpressing $ARF3^{K127E}$ and $ARF3^{D93N}$. Nevertheless, the molecular mechanism by which aberrant ARF3 function causes different Golgi fragmentation patterns and the extent to which antero-retrograde transport might be

775 impaired due to defective COP-I assembly and function remains to be determined. In
776 this context, it should be noted that the specific Golgi phenotype shown by p.K127E,
777 p.L12V/D67V and, to a less extend, p.T32N are reminiscent of the BFA-induced effect
778 in cells. Upon treatment with BFA, ARF-GDP-GEF complex titrates the available GEF
779 molecules away from the other ARF proteins, inhibiting their function[42]. Indeed, only
780 co-occurring loss of function of multiple ARF proteins is able to perturb organelle and
781 vesicle integrity[20,112].
782 Defective Golgi stability and activity is an emerging cause of cortical malformation[12].
783 The finding of fragmented Golgi in cells and embryos expressing the disease-
784 associated ARF3 mutants assigns this disorder to the recently defined family of
785 "Golgipathies", a group of heterogenous neurodevelopmental disorders clinically
786 characterized by a wide spectrum of CNS abnormalities[12,13]. Even if not detailed and
787 therefore not easily comparable to our work, the recent functional investigation carried
788 out by Sakamoto *et al.* on two *ARF3* mutations causing a similar neurodevelopmental
789 condition corroborates the present findings.
790 Regulated transport through the endolysosomal system assists the differential
791 targeting of cargos containing signaling molecules, polarity and morphogenic factors
792 to membrane or to *trans*-Golgi network for retrieval or to lysosomal degradation. The
793 importance of a healthy machinery to support this choice is just starting to gain
794 attention in the context of development and disease[73,113]. Of note, our experiments with
795 fluorescently labeled Tfn in combination with staining for EE, RE and lysosomes
796 unravel a cargo accumulation and delayed recycling in cells expressing ARF3 mutants
797 specifically leading to early-onset microcephaly and severe skeletal defects.
798 Interestingly, only an increased lysosomal Tfn cargo delivery seems to occur for
799 p.D93N causing late-onset microcephaly and mild skeletal deformities. The data also
800 suggest a general overload of the lysosomal system for all mutants, the relevance of
801 which should be further investigated. Thereby, besides the clear distinction in Golgi
802 morphological patterns, a variable impact on the efficiency of sorting and transport
803 seem to underlie the variable severity observed in our patients. Adding to our evidence,
804 impaired endosomal trafficking of EGF signaling components and Tfn recycling
805 underlie proliferative defects recently identified as a major cause of a
806 neurodevelopmental disorder with microcephaly[114,115].

The attentive *in vivo* investigation performed here makes a strong case for the importance of correct ARF3 function during a number of processes supporting embryogenesis. First, the extensive phenotypic characterization in zebrafish provides sufficient evidence of the pathogenicity of all the identified *ARF3* variants and their dominant nature. In line with the Golgi phenotype observed *in vitro*, overexpression of ARF3 mutants and downregulation of endogenous *arf3* in zebrafish embryos corroborate the DN (p.K127E, p.L12V/D67V, and p.T32N) and CA (p.D93N) behaviors *in vivo*.

Independently of the specific mechanism of dominance, all mutants modelled in fish recapitulated the involvement of brain and axes malformations, and the variable strength of the disease manifestation. Strikingly, likewise patients, overexpression of $ARF3^{K127E}$ and $ARF3^{L12V/D67V}$ produce early-onset severe microcephaly in fish, while fish expressing $ARF3^{D93N}$ show late-onset microcephaly. Furthermore, in depth brain analysis documents underlying brain volume reduction and validates defective forebrain white matter as a common feature of this neurodevelopmental disease. In line with these results, a severe *vs* mild clinical phenotype was anticipated in the yeast *arf1* mutants involving Lys^{127} and Asp^{93}, documenting complete or incomplete dominant lethal phenotypes, respectively[56].

Mechanistically, our *in vivo* work also provides insights into the processes that might hinder neurogenesis and contribute to the neurodevelopmental defects. Our cell cycle profiling experiments indicate a possible delay of the mitosis in the early stages and an increased cell death within the developing anterior brain for the majority of the ARF3 fish mutants. A "Golgi check point" sensing Golgi integrity and correct segregation has been suggested as an additional level to control cell cycle progression[116], whose contribution to the observed brain growth and morphogenesis defects is worth of further investigation. On the other hand, our forebrain recording during development determined the occurrence of altered spindle morphology in microcephaly-causing ARF3 mutants, which might ultimately underlie mitotic arrest and cell death. Supporting this hypothetic scenario, mitotic arrest resulting in increased apoptosis of cells with aberrant spindle are appreciated as pathological mechanisms underlying conditions characterized by cortical malformations and microcephaly, some of which already successfully modelled in zebrafish[80,81,92,93,117]. The involvement of Golgi function in cell division, microtubule organization and spindle formation is

840 recognized[88,89]. In line with our data, elongated spindles result from depletion of the
841 constituent Golgi proteins, which keep the integrity of the organelle in mouse oocyte[90].
842 The role of ARF1 in mediating Golgi morphological changes during mitosis[43], and the
843 function of class I ARF proteins in controlling proliferation have been reported[118,119],
844 including the ARF3 involvement on cell cycle progression and apoptosis in gastric
845 cancer[118]. Our zebrafish data show variably penetrant effects on cell proliferation and
846 death, especially for p.P47S and p.T32N. This resembles the milder effect of these two
847 mutants observed in cells in terms of GA integrity, vesicles assembly and recycling and
848 anticipated by the mildest clinical traits associated with them. An investigation including
849 a larger sample size might further clarify the presence of subtler effects. Conversely,
850 additional, and not explored mechanisms might produce the mild phenotypes
851 observed.
852 Lastly, strengthening the causal association of the described *ARF3* mutations to the
853 observed skeletal traits, variable degrees of axial malformations have been highlighted
854 in the generated fish models recapitulating the severity of the disease in human.
855 Likewise in patients, similar defects are associated with DN and CA mutations, with
856 p.K127E and p.L12V/D67V producing the most severe effects. Morphometric and live
857 imaging analysis in early embryonic stages traced back the first assessable effect to
858 defective PCP-mediated cell motility. CE movements, which require a fine tuning of
859 cell polarity factors within cells and are needed to shape the AP and ML axes[120–122],
860 are evidently affected by ARF3 mutants. Of note, biosynthetic trafficking and correct
861 function of ER and GA is essential during animal development for regulating
862 morphogens' distribution[46,47,123], and required for cell polarity establishment and
863 migration, as shown *in vitro*[124], nematodes[125] and zebrafish[126]. Consistent with our
864 findings, fish expressing the CA microcephaly-associated ARF1 mutant show similar
865 PCP-related axial defects[47]. Moreover, fish mutants for ARF-interacting COP-I/COP-II
866 coat components exhibit skeletal and notochord abnormalities associated to Golgi
867 disassembly[127,128]. On the other hand, post-Golgi trafficking and sorting of polarity
868 components also contribute to brain development, underlying correct asymmetric cell
869 division and migration in vertebrate neurogenesis, axon arborization and
870 synaptogenesis[46,129]. Along these lines, the impaired function of ARFGEF2 underlying
871 the microcephalic traits observed in patients with ARPHM has been indeed linked to
872 proliferative and migratory defects due to *trans*-Golgi to membrane trafficking of E-

cadherins and beta-catenin[16]. The direct contribution of the impaired recycling found in cells to the observed brain defects *in vivo* remains to be assessed.

In conclusion, our work identifies *ARF3* as a gene implicated, when mutated, in a clinically variable neurodevelopmental disorder belonging to the emerging class of "Golgipathies"[12,13]. Our findings specifically highlight a role of ARF3 in the maintenance of *trans*-Golgi integrity, and document an obligate dependence of early developmental processes and brain morphogenesis on proper function of this GTPase. The generated *in vivo* models represent a tool that can be exploited to deepen our understanding on the pathological mechanisms underlying the disease.

Methods

Subjects

The study has been approved by the local Institutional Ethical Committee of the Ospedale Pediatrico Bambino Gesù IRCCS (OPBG), Rome (1702_OPBG_2018). Subject 1 was analyzed in the frame of a research project dedicated to undiagnosed disorders (Undiagnosed Patients Program, OPBG), while the other subjects were referred for diagnostic genetic testing. Clinical data and DNA samples were collected, stored and used following procedures in accordance with the ethical standards of the declaration of Helsinki protocols, and after signed consents from the participating families. The authors affirm that human research participants provided informed consent for publication of the images in Supplementary Figure 1 and of clinical information potentially identifying individuals.

Exome sequencing analysis

In all families, WES was performed using DNA samples obtained from leukocytes and a trio-based strategy was used. Target enrichment kits, sequencing platforms, data analysis, and WES statistics are reported in **Supplementary Table 3-7** and in the **Supplementary Methods**. WES data processing, read alignment to the GRCh37/hg19 version of genome assembly, and variant filtering and prioritization by allele frequency, predicted functional impact, and inheritance models were performed as previously reported[130–134]. WES data output is summarized in **Supplementary Table 3-7**. Cloning of the genomic portion encompassing the c.34C>G and c.200A>T

missense substitutions (p.Leu12Val and p.Asp67Val; Subject 2) was used to confirm that both variants were on the same allele. Variant validation and segregation were assessed by Sanger sequencing in all the subjects included in the study.

Structural analysis and molecular dynamics simulations

The structural impact of the disease-associated missense changes was assessed using the available three-dimensional structures of human ARF3 complexed with GTP and *V. vulnificus* multifunctional-autoprocessing repeats-in-toxin (MARTX) (PDB 6ii6, https://www.rcsb.org/structure/6ii6)[52]. The structure was visualized using the VMD visualization software v.1.9.3[135].A model of GTP-bound ARF3 interacting with the cytosolic coat protein complex subunits γ-COP (COPG1) and ζ-COP (COPZ1) was built using the SWISS-MODEL automated protein structure homology modeling server (http://swissmodel.expasy.org)[136] using the 2.90 Å resolution X-ray structure (PDB 3TJZ)[59]. Alignment of template and model amino acid sequences is reported in **Supplementary Figure 21.** The p.Asp67Val and p.Pro47Ser mutations were introduced using the UCSF Chimera v.1.15[137]. The side-chain orientations were obtained with the Dunbrack backbone-dependent rotamer library[138], choosing the best rotamer with minimal/no steric clashes with neighboring residues. Following protonation of titratable amino acids at pH=7, proteins were added in cubic boxes and solvated in water. Counter-ions were added to neutralize the charges of the system with the genion GROMACS tool[139]. After energy minimizations, the systems were slowly relaxed for 5 ns by applying positional restraints of 1000 kJ mol^{-1} nm^{-2} to atoms. Unrestrained simulations were carried out for a length of 500 ns with a time step of 2 fs using GROMACS 2020.2. The CHARMM36 all-atom force field[140] was used for the protein description and water molecules were described by TIP3P model[141]. V-rescale temperature coupling was employed to keep the temperature constant at 300 K[142]. The Particle-Mesh Ewald method was used for the treatment of the long-range electrostatic interactions[143]. The first 5 ns portion of the trajectory was excluded from the analysis. All analyzes were performed using GROMACS utilities.

Expression constructs and *in vitro* mRNA synthesis

The full-length coding sequence of WT human ARF3 (NM_001659.3) was obtained by PCR and cloned into the pcDNA3.1/myc-6His eukaryotic expression vector (Life Technologies). The disease-associated substitutions were introduced in the

pcDNA3.1/myc-6His expressing ARF3 WT and into pcDNA3/hArf3(WT)-mCherry (plasmid 79420, Addgene)[144] by site-directed mutagenesis (QuikChange II Site-Directed Mutagenesis Kit, Agilent Technologies, 200522-5). For zebrafish expression experiments, the myc-tagged (*C*-terminus) WT and mutant ARF3 sequences or mCherry-tagged plasmids were subcloned into the pCS-Dest vector (plasmid 22423, Addgene)[144] via LRII clonase-mediated recombination (ThermoFisher, 12538120). pCS-Dest-mKOFP2-CAAX and pCS-Dest-EGFP-GalT were generated by subcloning the ADDGENE plasmids 75155[145] and 11929[146], respectively. Plasmids were digested and linearized with *Kpn*I-HF (NEB New England Biolabs, R3142S), and mRNA was produced using mMessage mMachine SP6 transcription kit and poly(A) tailing kit (Thermo Fisher, AM1340). All cloned sequences were confirmed by bidirectional DNA sequencing.

COS-1 cell culture and transient transfection assays

COS-1 cells (CRL-1650-ATCC) were cultured in Dulbecco' s modified Eagle's medium supplemented with 10% heat-inactivated fetal bovine serum (FBS, GIBCO, 10270-106), 1x sodium pyruvate (EUROCLONE, 11360-039) and 1x penicillin-streptomycin (EUROCLONE, ECB3001D), at 37 °C with 5% CO2. Subconfluent cells were transfected with plasmids encoding myc- or mCherry-tagged WT and mutant ARF3, EGFP-GalT (Addgene, 11929,[146]) and GFP-rab11 (Addgene, Plasmid #12674)[147] using FuGENE 6 (Promega, E2691), according to the manufacturer's instructions.

Zebrafish husbandry

Zebrafish NHGRI, *Tg(Xla.Tubb:DsRed)*[148] and *Tg(XlEef1a1:dclk2DeltaK-GFP)*[149] were cultured following standard protocols. Fish were housed in a water circulating system (Tecniplast ©) under controlled conditions (light/dark 14:10, 28 °C, 350-400 µS, pH 6.8-7.2) and fed daily with dry and live food. All animal experiments were conducted under the approval of the Italian Ministry of Health (DGSA -Direzione generale della sanità animale e dei farmaci veterinari, 23/2019-PR).

ARF3-myc immunoblotting in COS-1 and in zebrafish embryos

Transfected COS-1 cells were lysed in radio-immunoprecipitation assay (RIPA) buffer, pH 8.0, containing phosphatase and protease inhibitors (Sigma-Aldrich, P5726, P0044, P8340). Lysates were kept on ice for 30 min and centrifuged at 16,000 g for 20

966 min at 4 °C. Samples containing an equal amount of total proteins (15 µg) were
967 resolved by 12% sodium dodecyl sulfate (SDS)-polyacrylamide gel (Biorad, 1610185).
968 Proteins were transferred to nitrocellulose membrane using a dry transfer system
969 (Biorad), and blots were blocked with 5% non-fat milk powder (Biorad, 170-6404) in
970 Phosphate-buffered saline (PBS) containing 0.1% Tween-20 for 1 hours at 4 °C and
971 incubated with mouse monoclonal anti-Myc (1:1000, Cell Signaling, 2276S), mouse
972 monoclonal anti-β-tubulin (1:1000, Thermo Fisher, 32-2600), mouse monoclonal anti-
973 GAPDH (1:1000, Santa Cruz, sc-32233) and anti-mouse HRP-conjugated secondary
974 antibody (1:3000, Thermo Fisher, 31450). For zebrafish immunoblots experiments,
975 total protein lysates from a pool of non-injected control zebrafish embryos and from
976 siblings injected with myc-tagged $ARF3^{WT}$ and mutant ARF3 different stage of
977 development were obtained by syringe homogenization in cold lysis buffer (Tris HCl
978 10 mM pH 7.4; EDTA 2 mM; NaCl 150 mM; Triton X-100 1% supplemented with 1X
979 protease inhibitors cocktail (Roche, 11836170001) and equal amounts of protein
980 extracts (40 µg) were separated on a 12% Sodium dodecyl sulfate (SDS)-
981 polyacrylamide gel. The total protein concentration was determined by the Bradford
982 assay (Bio-Rad) using Infinite M Plex (Tecan). After electrophoresis, the proteins were
983 transferred to PVDF membrane using a wet transfer system (Biorad, for myc-tagged
984 ARF3 mutants at 6 and 12 hpf) or nitrocellulose membrane using Trans-Blot Turbo
985 Transfer System (Biorad, myc-tagged ARF3 mutants from 1.75 to 3.7 hpf). Blots were
986 blocked with 5% non-fat milk powder (Biorad) or bovine serum albumin (BSA, Sigma-
987 Aldrich, A8022-100G) in PBS containing 0.1% Tween-20 (Sigma-Aldrich, P2287)
988 overnight at 4°C constantly shaking and incubated with primary antibody in blocking
989 solution. The following primary antibodies were used: mouse monoclonal anti-myc
990 (Cell Signaling, dilution 1:1000, 2276), rabbit polyclonal anti-GAPDH (1:1000,
991 Genetex, GTX124503). Following washes in PBST 0.1%, membranes were incubated
992 with anti-mouse- (1:3000, Thermo Fisher, 31450) and anti-rabbit-HRP-conjugated
993 secondary antibodies (1:3000, Thermo Fisher, 31460). Immunoreactive proteins were
994 detected by an enhanced chemiluminescence (ECL) detection kit (Thermo Fisher,
995 34095) according to the manufacturer's instructions, and an Alliance Mini HD9 with Q9
996 Mini 18.02-SN software (Uvitec) was used for chemiluminescence detection.
997 Uncropped blots are provided in the Source data file and Supplementary information.

In vitro ARF3 protein stability assays

COS-1 cells were seeded at 3×10^5 in 6-well plates and the following day were transfected with WT or mutant myc-tagged ARF3 expression constructs for 24 hours. A subset of transfected cells was then treated with CHX (10 µg/ml) (Sigma-Aldrich, C7698) for 3 and 6 hours and with proteasome inhibitor MG132 (100 µM) (Sigma-Aldrich, C2211) or with the autophagy inhibitor bafilomycin A1 (200 nM) (Sigma-Aldrich, B1793) for 6 hours to assess protein stability and degradation pathways. Alliance Mini HD9 with Q9 Mini 18.02-SN software (Uvitec) was used for chemiluminescence detection. Uncropped blots are provided in the Source data file and Supplementary information.

ARF3 activity (GTP-bound state) assay in COS-1 cells

COS-1 cells (1 x 10^6) were seeded in 100 mm petri dishes and transfected with myc-tagged *ARF3* expression constructs. Twenty-four hours after transfection, cells were washed twice with ice cold PBS and collected in 50 mM Tris (pH 7.4), 150 mM NaCl, 10mM $MgCl_2$, 10% Glycerol, 1% NP-40 with proteases and phosphatase inhibitors (Sigma-Aldrich, P5726, P0044, P8340). Cell lysates were further subjected to pull-down using GGA3-conjugated agarose beads (Cell Biolabs, STA-419) and incubated at 4 °C for 60 min. Control samples were preincubated with 100 µM GDP (Cell Biolabs, 240104) or the GTP analogue guanosine-5'-(γ-thio)-triphosphate (GTPγS) (Cell Biolabs, 240103) for 30 min and then pulled-down according to the manufacturer's instructions (Cell Biolabs, STA-407-1). For immunoblotting analyzes, pulled down samples including GTPγS/GDP controls and whole cell lysates were combined with a 2x sample buffer and denatured at 95 °C for 5 min. Samples were then separated by SDS-PAGE and incubated with mouse monoclonal anti-Myc and mouse monoclonal anti-GAPDH antibodies. GTP-bound protein level was detected by an ECL detection kit (Thermo Fisher, 34577). Alliance Mini HD9 with Q9 Mini 18.02-SN software (Uvitec) was used for chemiluminescence detection. Uncropped blots are provided in the Source data file.

Protein expression and purification, nucleotide exchange and GTP hydrolysis measurements

Proteins were isolated as glutathione S-transferase (GST) fusion proteins in E. *coli* strain CodonPlusRIL, purified after cleavage of the GST tag via gel filtration Superdex

75 or 200 (GE Healthcare, 28989333, 28989335). Nucleotide-free and fluorescent nucleotide-bound ARF3 proteins were using alkaline phosphatase (Sigma-Aldrich, P0762-250UN) and phosphodiesterase (Sigma-Aldrich, P3243-1VL) at 4°C. Various fluorescence reporter groups, including Mant and Tamra, have been coupled to 2´ (3´)-hydroxyl group of the ribose moiety of GDP and GppNHp (Tamra GTP from Jena Bioscience, #NU-820-TAM, MantdGDP from Jena Bioscience, #NU-205L). All proteins were analyzed by SDS-PAGE and stored at -80°C. Fluorescence polarization experiments were performed in a Fluoromax 4 fluorimeter in polarization mode. The excitation and emission wavelengths for Mant-deoxy-GDP were 360 nm (Slid width: 8 µm) and 450 nm (slid width: 10 µm), respectively. For nucleotide exchange reactions, 1 µM Mant-deoxy-GDP ARF3, 100 µM GDP, 10 µM ARFGEF BIG2 were used in 200 µl of measurement buffer containing 30 mM Tris/HCl, pH 7.5, 10 mM K_2HPO_4/KH_2PO_4, 2 mM $MgCl_2$ and 3 mM dithiothreitol at 25°C). For GTP hydrolysis activity 1µM of Tamra-GTP bound proteins were used with the excitation, wavelength of 543 nm (slit width: 8 micron) and emission wavelength of 580 nm (slit width: 10 micron), in a buffer containing 30 mM Tris/HCl (pH 7.5), 150 mM NaCl, 5 mM MgCl2, 3 mM dithiothreitol and a total volume of 200 µl at 25 °C. The observed rate constants (k_{obs}) were calculated by fitting the data as single exponential decay using GraFit software v.5.0.13 [150].

RT-PCR prolife of endogenous *arf3a* and *arf3b* mRNAs in zebrafish embryos

To evaluate gene expression of *arf3a* and *arf3b* paralogs throughout zebrafish embryogenesis, total RNA was isolated from whole embryonic tissue samples at different stages of development (1 – 18 hpf) using TRIzol reagent (Invitrogen, 15596026). The first-strand cDNA was synthesized from total RNA using the SuperScript™ IV First-Strand Synthesis System (Thermo-Fisher, 18091050) according to the manufacturer's protocol and DNAse treatment was performed to avoid genomic DNA contamination. RT-PCR was performed with specific primer sets annealing on conserved regions of *arf3a* and *arf3b* zebrafish paralogs (ENSDART00000103639.5 and ENSDART00000053775.3, respectively) using GoTaq® G2 Green Master Mix (Promega, M7822) (**Supplementary Table 11**). Amplification of the elongation factor 1α (*eif1α*) was used as housekeeping control

gene. Alliance Mini HD9 with Q9 Mini 18.02-SN software (Uvitec) was used for signal detection. Uncropped gels are provided in the Supplementary information.

RT-PCR of *myc-tagged ARF3* in COS-1 cells

To verify the expression of myc-tagged ARF3$^{L12V/D67V}$ and ARF3^{D93N} after transient transfection in COS-1 cells, RNA from transfected cells was extracted using RNeasy Mini Kit (Qiagen, 74104) and the cDNA was retrotranscribed using oligo-dT SuperScript IV System kit (Thermo-Fisher, 18091050) according to manufacturer's protocols. The RT-PCR assay was design to map the boundaries between the C-terminal coding region of ARF3 and the myc-tag sequence (**Supplementary Table 11**), low number of cycle (*i.e.* n = 15) were used in the PCR reaction to avoid PCR plateau phase and signal saturation. RT-PCR on GAPDH gene was used as internal housekeeping control. KAPA2G Fast ReadyMix (Sigma Aldrich, KK5603) was used to amplify the target sequence, according to protocol instructions. Alliance Mini HD9 with Q9 Mini 18.02-SN software (Uvitec) was used for signal detection. Uncropped gels are provided in the Supplementary information.

ARF3 overexpression and arf3a and arf3b downregulation in zebrafish embryos

Injection of *in vitro* synthesized capped mRNAs encoding myc- and mCherry-tagged ARF3 (15 pg, ARF3^{WT}, and mutant ARF3), mKOFP-CAAX (15 pg), H2A-mCherry (15 pg), EGFP-GalT (15 pg), EGFP-CAAX (15 pg) and EGFP-GalT (50 pg) was performed in one-cell stage zebrafish embryos using FemtoJet 4x microinjection system (Eppendorf). mRNA was produced using mMESSAGE mMACHINE™ SP6 Transcription Kit Poly A Tailing Kit (ThermoFisher, AM1340 and AM1350). Injected embryos were cultured under standard conditions at 28 °C in fresh E3 medium and for each batch, not-injected fish were used as controls together with fish injected with the WT form of ARF3 mRNA. To perform *arf3a* and *arf3b* knockdown experiments in zebrafish embryos, 0.3 mM of each antisense morpholino oligonucleotides (MO, Gene Tools LLC) targeted specifically to the translational initiation site of *arf3a* and *arf3b* (resulting in 0.6 mM of MO in total) were co-injected into one cell stage embryos (**Supplementary Table 11**). All the injected fish were monitored every day, survival rate and phenotype were scored at 24 hpf and 48 hpf.

ARF3 protein localization and Trans-Golgi morphology analysis in fixed COS-1 cells

COS-1 cells (20×10^3) were seeded in 24-well cluster plates onto 12-mm cover glasses and transfected with WT or mutant mCherry-tagged ARF3 expression constructs for 48 hours. Cells were then fixed with 4% paraformaldehyde for 10 minutes at room temperature, followed by permeabilization with 0.025% Triton X-100 for 5 minutes at room temperature. Cells were stained with mouse monoclonal anti-Golgin-97 antibody (1:50, Invitrogen, A21270) for 1 hour at room temperature, rinsed twice with PBS and incubated with Alexa Fluor 488 goat anti-mouse secondary antibody (1:200, Invitrogen, A11017) for 1 hour at room temperature. After staining, coverslips were mounted on slides by using Vectashield Antifade mounting medium containing 1.5 µg/ml DAPI (Vector Laboratories, H-1200-10). Images were acquired using a Leica TCS SP8X laser-scanning confocal microscope (Leica Microsystems) using LAS X software v.3.5 equipped with a pulsed and tunable white light laser source, 405 nm diode laser and 2 Internal Spectral Detector Channels (HyD) GaAsP, and an acousto-optical beam splitter (AOBS) allowing separation of multiple fluorescence spectra. Sequential confocal images were acquired using excitation laser lines at 405 nm (for DAPI, emission range 410-480 nm), 488 nm (for Alexa Fluor 488, emission range 500-550 nm) and 594 nm (for mCherry, emission range 600-650 nm), with a HC PL APO CS2 63x (numerical aperture, NA, 1.40) oil immersion objective (Leica Microsystems), a 1024x1024 format image, 0.38 µm pixel size and 400Hz scan speed. Z-reconstructions were obtained from a z-step size of 0.5 µm, with an electronic zoom of 1.8x. Maximum intensity projection (MIP) of z-series was obtained by LAS X software v.3.5. Deconvolution analysis (HyVolution v.2 software, Leica Microsystems) using 'best resolution' algorithm of Golgin-97$^+$ cisternae and vesicles was applied to z-stacks with an electronic zoom of 4x, to improve contrast and resolution of confocal raw images; then surface 3D rendering was generated from the deconvoluted images using LASX 3D Analysis tool (LAS X software v.3.5). Evaluation of different Golgi morphologies was performed by creating different masks with Fiji[151] to determine the Golgi area (Golgin-97$^+$) and identify the cell boundaries (Arf3-mCherry$^+$) in transfected cells. Total cell area, Golgi area and mean intensity (MI) for Golgin-97 were calculated for each cell. Whole cell area was determined using mCherry fluorescence as a mask. Golgi mean intensity (MI of Golgin-97$^+$ area, arbitrary units) *vs.* Golgi area [(Golgin-97$^+$

area/total cell area)*100] were plotted for $ARF3^{WT}$, $ARF3^{Q71L}$ and $ARF3^{T31N}$ and the parameters giving the best separation between the chosen populations were manually selected, as reported in **Figure 3.**

Time-lapse imaging of Golgi dynamics in COS-1 cells

For live imaging, COS-1 cells (10 x 10^4) were seeded into µ-dishes 35 mm (Ibidi) 24 hours before transfection. The day after, cells were co-transfected with WT or mutant mCherry-tagged *ARF3* and EGFP-GalT constructs. Four hours post-transfection, time-lapse acquisitions were performed with a Leica TCS-SP8X confocal microscope (Leica Microsystems) with a PlApo CS2 20x/0.75 objective, using excitation lines at 488 nm (for EGFP, emission range 500-550 nm) and 594 nm (for mCherry, emission range 600-650 nm). Parallel live imaging of control and mutant samples was performed simultaneously using the Mark & Find mode of the LAS X software v.3.5. Cells were monitored every 15 min and imaging was carried out with a 1024x1024 format, 0.38 µm pixel size, scan speed of 600Hz, a zoom magnification up to 1.5 and z-step size of 0.7 µm, Time-lapse microscopy was performed with a stage incubator (OkoLab) allowing to maintain stable conditions of temperature at 37°C, with 5% of CO_2 and humidity during live cell imaging.

Trans-Golgi analysis in live zebrafish embryos

Trans-Golgi morphology was assessed from single confocal images of the animal pole of late gastrulae injected with $ARF3^{WT}$ and ARF3 mutants as well as EGFP-GalT and mKOFP-CAAX mRNA. Images were acquired using a Leica TCS SP8X or Stellaris 5 confocal microscope (Leica Microsystems) equipped with LAS X software v.4.5, a pulsed and tunable white light laser source, 405 nm diode laser, hybrid detectors, and an acousto-optical beam splitter (AOBS) allowing separation of multiple fluorescence spectra, HC FLUOTAR L VISIR 25x/0.95 water-immersion objective, a 1024 x 1024 format at 400 Hz and z-step of 0.75µm using laser line and emission filters as above. Trans-Golgi morphology ($EGFP\text{-}GalT^+$) in each cell was scored independently by two researchers and two different categories of the $EGFP\text{-}GalT^+$ signal were identified: cells showing a "ribbon-like" displayed a recognizable $EGFP\text{-}GalT^+$ ribbon-like or a circular or semi-circular compact structure, while if no circular nor ribbon like structure could be recognized and instead the pattern was more dotted, either with a single large and small dots recognizable or with spread dots distributed randomly inside the

cytoplasm, cells were classified as harboring a "non-ribbon/puncta-like" EGFP-GalT$^+$ staining, as indicated in the main text and in **Supplementary Figure 10**.

Transmission electron microscopy analysis of Golgi morphology

COS-1 cells were seeded at 2×10^5 in 6-well plates and transfected with ARF3 WT, K127E and D93N for 48 hours. Cells were then fixed with 2.5% glutaraldehyde in 0.1 M sodium cacodylate buffer (pH 7.2) 1 hour at RT, washed in buffer and post-fixed in 1% OsO4 in 0.1 M sodium cacodylate buffer for 1 hour at RT. Post-fixed specimens were washed in buffer, dehydrated through a graded series of ethanol solutions (30–100% ethanol) and embedded in Agar Resin Kit (Agar Scientific, R1031). Ultrathin sections, obtained by a UC6 ultramicrotome (Leica), were stained with uranyl acetate and Reynolds' lead citrate and examined at 100kV by a Philips EM 208S Transmission Electron Microscope (FEI- Thermo Fisher) equipped with acquisition system Megaview III SIS camera (Olympus-SIS Milan, Italy) and iTEM3 software.

Assessment of COP-I vesicles assembly, Tfn accumulation and recycling in COS-1 cells expressing WT and mutant ARF3

COS-1 cells (20×10^3) were seeded in 24-well cluster plates onto 12-mm cover glasses and transfected with WT or mutant mCherry-tagged ARF3 expression constructs. After 48 hours of transfection, COS-1 cells were washed and serum starved for 45 minutes at 37°C and were then incubated with 50 µg/ml Alexa Fluor 488 or Alexa Fluor 647 conjugated transferrin (Invitrogen, T13342 and T23366, respectively) in serum-free medium for the indicated time (5 or 30 min). At the end of the 37°C incubation period used to follow intracellular trafficking, the cells were cooled to 4°C, washed twice with ice-cold PBS to remove unbound transferrin, and then incubated twice for 2 min at 4°C with ice-cold stripping buffer (150 mM NaCl, 20 mM HEPES, 5 mM KCl, 1 mM CaCl2, 1 mM MgCl2, pH 5.5) to remove the excess of transferrin bound to the cell surface. To follow the formation of COP-I vesicles and the levels of Tfn present in early endosomes (EE), and lysosomes after 30 min of incubation, cells were fixed with 4% paraformaldehyde for 10 minutes at room temperature, followed by permeabilization with 0.025% Triton X-100 for 5 minutes at room temperature and were then stained with antibodies recognizing COP-I, EE and lysosomal markers overnight for 1 hour at 4°C. These antibodies were used: rabbit polyclonal anti-ß COP (1:2000, Abcam, ab2899), rabbit monoclonal anti-Rab5 (1:200, Cell Signaling, 3547S) and mouse

monoclonal anti-LAMP-2 (1:200, Santa Cruz, sc-18822), respectively. Cells were then rinsed twice with PBS and incubated with Alexa Fluor 633 goat anti-mouse secondary antibody (1:200, Invitrogen, A21050) or Alexa Fluor 488 goat anti-rabbit secondary antibody (1:200, Invitrogen, A11070) for 1 hour at room temperature. To assess the levels of Tfn present in recycling endosomes (RE) after 30 min of incubation, cells were co-transfected with the plasmid encoding the GFP-tagged RE marker Rab11. All the slides were mounted using Vectashield Antifade mounting medium containing 1.5 µg/ml DAPI (Vector Laboratories, H-1200-10). Confocal z-stacks of the cells incubated 5 min with Tfn and of those stained for βCOP or the cells expressing GFP- Rab11 and incubated 30 min with Tfn were obtained using TCS-SP8X confocal microscope (Leica Microsystems) with a HC PL APO CS2 63x (NA 1.40) oil immersion, using excitation lines at 488 nm (for GFP, emission range 500-550 nm), 594 nm (for mCherry, emission range 600-650 nm), 640 (for Alexa Fluor 647, emission range 650-700 nm) and 630 nm (for Alexa Fluor 633, emission range 640-690 nm), a 1024x1024 format at 400Hz, 0.14 µm pixel size, a zoom magnification of 2.5 x and z-step size of 0.7 µm. Confocal z-stacks of the cells stained for Rab5 and Lamp2 at 30 min upon Tfn treatment were obtained using Stellaris 5 (Leica Microsystem), A HC PL APO CS2 63x/1.40 Oil objective was used. Confocal acquisitions were performed using 405, 488, 594, 633-nm laser excitation lines for the different fluorophores used and emission spectra as above. Sequential acquisitions were performed and with a 1024x1024 format at 400 (Rab 5) or 200 Hz (Lamp 2), and a z-step of 0.7 µm. For all the experiments, laser intensity and detectors parameters and offsets were unchanged per each condition of a single experiment. Phenotype categories for cells expressing WT and mutant ARF3 were independently inspected by two researchers and classified as reported in the main text. Briefly, for COP-I vesicles assembly, the number of cells (%) showing "assembled", "disassembled" or "extended" COP-I compartment at the PN were estimated by the occurrence of clustered, absent /highly scattered or increased β-COP$^+$ area, respectively. The β-COP$^+$ area was measured using a manual ROI selection, ROI manager and measurement tool in Fiji. For each cell the β-COP$^+$ area was normalized by the total area of the nucleus and cells with an extended COP-I compartment were estimated by a ratio β-COP$^+$ area/nucleus area. The distribution patterns of the Tfn inside the cytoplasm was scored in replicate for the different incubation times. The Tfn signal distribution inside the cell and its relative clustering at

the perinuclear compartment (PN) was inspected and the number of cells (%) showing different classes of Tfn phenotype was calculated. Three different categories of Tfn distributions were identified (accumulation at the PN = "clustered", presence of a Tfn^+ clusters and sparse dotted signal throughout the cell = "semidispersed", no Tfn^+ clusters visible = "dispersed"). Co-occurrence of Tfn with Rab5, Rab11 or Lamp2 at the PN was quantified using the colocalization algorithm of IMARIS softare v.9.5 (Bitplane) and the built-in thresholding method, which was equally applied to all conditions within each experiment. Manders overlap coefficients were calculated for the fraction of Tfn overlapping the respective fluorophores in a manually selected ROI corresponding to the visible Tfn+ PN cluster and viceversa[152].

Zebrafish body axis, notochord and head phenotyping

Embryos were screened for gross phenotype penetrance and classified as class I ("normal"), class II ("developmental delay"), class III ("mild" microcephaly, with/without microphthalmia and/or mild shortening and lateral bending of body axis) and class IV ("severe" microcephaly/anencephaly with/without microphthalmia and marked trunk deformity, defective body elongation and severe lateral bending) at 24 hpf and 48 hpf, as reported in the main text. For detailed analysis, not injected controls and injected fish at 12 and 15 hpf (for body axis), 30 hpf (for notochord) and 48 hpf (for head size) were embedded in 2% low melting agarose (Sigma-Aldrich) dissolved in E3 medium. Bright-field images were acquired at Leica M205FA microscope (Leica Microsystems) equipped with LAS X software v.3.0, 0.63x magnification (for body axis and head size) and Leica Thunder Imager microscope (Leica Microsystems) with N PLAN 5X/0.12 PHO objective (for notochord) equipped with LAS X software v.3.7. These parameters were assessed: *i)* head size measured by the area surface between the rostral most part of the head and the optic vesicle; *ii)* degree of the notochord angles (plotted in a Rose diagram using Oriana software v.4 [153]) and incidence of embryos showing mild and severe notochord curvatures (calculated on the average degree of all the curvatures per embryo); *iii)* number of notochord curvatures and *iv)* antero-posterior (AP) embryo extension, measured as length from the most anterior region of *Krox20* domain (R3) to the posterior region of *MyoD* domain (paraxial mesoderm) and *v)* convergence-extension index, calculated as the ratio of AP and medio-lateral axes

(ML, calculated as the length of the visible first somite); *vi)* angle between the antero-posterior ends.

Zebrafish live imaging of brain volume and 3D rendering from *Tg(NBT:dsRed)* fish

Live *Tg(NBT:dsRed)* fish injected with WT and mutant ARF3 at 48 hpf were embedded in 2% low melting agarose/E3 medium and imaged using Leica Stellaris 5 confocal microscope (Leica Microsystems) equipped with LAS X software v. 4.5 using a sensitive hybrid detector and keeping minimal laser power (579 nm wavelength). Live z-stacks were performed using HC FLUOTAR L VISIR water immersion 25x/0.95 objective, using excitation lines at 594 nm (emission range 600-650 nm), a 512x 512 format at 400 and 600 Hz and a z-step size of 2.5 µm. Volumetric brain reconstructions and quantifications were obtained using 3D Volume (Blend model) and Surfaces rendering reconstruction algorithm of IMARIS v.9.5 (Bitplane), employing the same parameters for the different individuals.

Whole-mount immunofluorescence in 48hpf zebrafish embryos

Zebrafish embryos were fixed in 4% PFA/PBS (Thermo Fisher, 28908) for 3 hours at room temperature (RT), dehydrated through methanol washes from 25% (in PBS) to 100% and stored at -20°C. Fixed samples were rehydrated back to PBS through serial washes and incubated with 150 mM Tris-HCl pH 9.0 for 5 min at RT and 15 min at 70°C for antigen retrieval. The samples were then permeabilized with 0.8% PBST (Triton, Sigma-Aldrich, X-100) and 1 µg/ml proteinase K (Sigma-Aldrich, P2308) for 40 min at RT (for acetylated α-tubulin and HuC/Elav) or with cold Acetone for 20 min (for PCNA and Phospho-Histone H3, pH3). The samples were post-fixed in 4% PFA/PBS for 20 min at RT and incubated 4 hours in a solution containing 10% of normal goat serum (NGS) and 2% of BSA in 0.8% PBST for 4 hours at 4°C. These primary antibodies were used: mouse anti-acetylated tubulin (1:250, Sigma Aldrich, T7451), rabbit anti-Elavl3+4 (1:100, GeneTex, GTX128365), rabbit anti-PCNA at (1:250, GeneTex, GTX12449), mouse anti-pH3 (1:250, Abcam, ab14955) overnight at 4°C with gentle shaking. These secondary antibodies were used: goat anti-mouse Alexa Fluor 488 (1:1000, Thermo Fisher, A11001), goat anti-rabbit Alexa Fluor 633 (1:1000, Thermo Fisher, A21070), goat anti-rabbit DyLight 594 (1:1000, GeneTex, GTX213110-05). The Stellaris 5 confocal microscope (Leica Microsystem) equipped

with LAS X software v. 4.5 and a HC FLUOTAR L VISIR water immersion 25x/0.95 objective were used for z-stack image acquisition. Ventral z-stacks of embryos stained for acetylated α-tubulin, mounted in 2% low melting agarose/PBS (Sigma-Aldrich, A9414), were acquired with: 499 nm laser line (emission range 510-600 nm), 1024x1024 format at 400 Hz, and 1.5 µm z-step size. Z-stacks of embryos stained for PCNA and pH3, mounted in 90% glycerol/PBS, were acquired sequentially with 591nm and 631nm laser lines and emission range 596-636 and 644-700 nm, respectively. Volumetric brain acquisitions were obtained by scanning with a 1024x1024 format at 200 Hz and 0.5 or 0.7 µm z-step size and with a digital zoom of 2.5 (ventral brain) or by scanning with a 512x512 format at 400 Hz and 2 µm z-step size (dorsal brain). Embryos stained for HuC/Elav were imaged using the confocal microscopes Leica TCS-SP8 or Olympus FV1000 equipped with FV10-ASW version 4.1, 20x/0.75 objective, using laser line 543 (for HuC/Elav, emission range 560-620nm) and 635 nm (for acetylated tubulin, emission range 655-755nm) scanning with a 1024 x 1024 format, a speed of 400 Hz and z-step size of 2 µm.

Analysis of the forebrain anterior commissure

For morphological analyzes of forebrain anterior commissure and its lateral bundles, the medial and lateral width were calculated using the "line selection" tool in Fiji[151] as indicated in the **Supplementary figure 17**.

Analysis of the number of mitotic cells and the pH3 distribution in precursor cells of the developing anterior brain

The number of pH3$^+$ precursor cells (mitotic) was quantified in both ventral and dorsal anterior brain z-stacks of the stained 48 hpf embryos. The number of cells was quantified manually or using the "spot analysis" algorithm of IMARIS software 9.5 (Bitplane) throughout the 3D volume of the confocal acquisitions, applying the same parameters to all the scans. The automatic analysis was manually inspected and corrected. Superficial staining corresponding to large epidermal cells was excluded from the analysis. A 3D rendering in the whole dorsal anterior brain was also performed using the same software and showing the pH3+ cells. For the ventral scans, the pH3 signal positivity and distribution pattern was assessed in precursor cells found within the defined ROI corresponding to the proliferative zone of a ventral portion of the forebrain, clearly discernible in the confocal acquisitions. The total number of pH3+

cells (mitotic) were counted along the full z-stack of the ROI. Following Tang *et al.* (2012)[154], cells at different mitotic phases corresponding to early (prophase + prometaphase), metaphase and late (anaphase + telophase) were scored based on the pH3 signal distribution, indicative of the cell's chromatin topological status. For the dorsal scans, to assess possible alterations of the normal spatial distribution of $pH3^+$ cells within the optic tectum, the number of mitotic cells in different regions (left and right neuropil vs medial proliferative zone and cerebellum), was manually quantified.

Staining and analysis of apoptotic cells in the anterior brain

To assess apoptotic cells in the anterior brain of developing fish expressing WT and mutant ARF3, live staining with acridine orange (AO) was performed. Briefly, microinjected larvae at 48hpf were incubated with 100 µg acridine orange (Sigma-Aldrich, A6014) in E3 medium for 1 hour in the dark at 28°C then washed extensively with E3 and mounted for microscopy in multi-well dishes using 1.5% low melting agarose/E3 (Sigma-Aldrich, A9414). Live z-stacks of the anterior forebrain in *x, y, z* were acquired at the Thunder Imager microscope (Leica Microsystems), using HC PL Fluotar 10x/0.32 DRY objective, 2048x2048 format, 475-nm excitation line and with a z-step of 5 µm. AO^+ spots were counted using the "multi-points" tool of Fiji[151] after adjusting brightness and contrast equally across all the conditions of a single experiment.

Live imaging and analysis of mitotic spindles in precursor cells of the anterior brain

To examine spindle morphology of dividing progenitor cells in zebrafish forebrain, transgenic *Tg(XlEef1a1:dclk2DeltaK-GFP)* fish marking microtubules were injected with mRNA encoding my-tagged $ARF3^{WT}$, $ARF3^{K127E}$ and $ARF3^{D93N}$ together with the mRNA encoding H2AmCherry marking the chromatin. Fish at 1 dpf (~ 30 hpf) were embedded in 1.5% low melting agarose in E3 medium and live confocal *x, y, z, t* acquisitions of the forebrain region were obtained at the Stellaris 5 confocal microscope (Leica Microsystems), with a HC Fluotar VISIR L 25x/0.95 water immersion objective, 488 nm laser line (for GFP, emission range 504nm-600nm), and 594 nm (for mCherry, emission range 625-700 nm) in sequential model and with a format of 512x512 at 400 Hz and with a z-step of 1.5 µm. A time interval (TI) of 4 minutes was set between consecutive scans for ~ 1 hour ($ARF3^{WT}$ and $ARF3^{D93N}$,

acquired with a digital zoom of 1.7) and > 5 hours ($ARF3^{WT}$ and $ARF3^{K127E}$, acquired with a digital zoom of 1). The mitotic spindle's length and width were analyzed using the selection and measurement tools in Fiji[151].

Whole-mount *in situ* hybridization of *Krox20* and *MyoD* mRNA

The fragments of Krox-20 and MyoD cDNA used for riboprobe synthesis were amplified from a zebrafish cDNA preparation by PCR using One Taq DNA polymerase (NEB New England Biolabs, BM0509S) and the primers listed in **Supplementary Table 11**. The PCR fragments were cloned into pGEM-T Easy vector (Promega, A1380) and sequences were confirmed by DNA sequencing. The digoxigenin-labeled antisense riboprobes were synthesized by i*n vitro* transcription with DIG RNA labeling kit SP6/T7 (Roche, 11277073910). *In situ* hybridization analysis in whole-mount zebrafish embryos at 15 hpf was performed as described in Thisse et al.[155]. Briefly, samples were permeabilized with proteinase K treatment (1 µg/ml, Sigma-Aldrich, P2308-25MG) for 2 minutes, pre-incubated in 2% blocking reagent (Roche, 11096176001) and incubated with the transcribed riboprobes (2 ng/µl) in hybridization mix (50% formamide, Sigma-Aldrich, F9037-100ML, 1.3x SSC 20X (175,3gr NaCl, 88,2gr Na Citrate 300mM, PH 7), 100 g/ml heparin, (Sigma-Aldrich, H3149-25KU), 50 µg/ml yeast RNA, Sigma-Aldrich, 10109223001), 0.2% Tween-20,0 (Sigma-Aldrich, P2287), 5% CHAPS (Merck, 850500P-1G), 5 mM EDTA pH 8, Sigma-Aldrich, E7889-100ML) at 65 °C for at least 15 hours. Afterwards, samples were rinsed with scalar dilutions of SSC solutions (25%, 50%, 75%) and incubated with anti-alkaline phosphatase (AP)-conjugated antibody (1:5000, Roche, 11093274-910) for 2 hours at room temperature. Chromogenic staining was developed via BM Purple substrate (Sigma-Aldrich, 11442074001) according to manufacturer's instructions. Specimens were mounted in 90% glycerol and dorsal images were acquired at the Olympus TH4-200 microscope (Olympus) equipped with Olympus cellSens Standard software v.1.14, with C Plan 10X/0.25 RC1 objective or Thunder Imager (Leica Microsystem) with N PLAN 5X/0.12 PHO objective.

Embryo extension analysis at 13 hpf and confocal live imaging of zebrafish embryos during late gastrulation

Overall embryos extension of embryos injected with myc-tagged ARF3 WT and mutants at 13 hpf at the end of gastrulation was estimated by calculating the angle

amplitude between A-P ends (head and tail bud, respectively) from bright field images acquired at Leica M205FA microscope (Leica Microsystems), using the "angle measurement" tool of Fiji[151]. For *in vivo* gastrulae imaging, embryos at mid-gastrula stage were embedded in 2% low melting agarose (Sigma-Aldrich, A9414) in E3 medium. 4D (*x, y, z, t*) fluorescent data were acquired using Leica TCS-SP8 confocal microscope (Leica Mycrosystems) with hybrid detectors and keeping minimal laser power. Time-lapses were acquired with a PlApo CS2 20x/0.75 objective using a 488 nm laser line (for GFP, emission range 495nm-550nm) and 594 nm (for mCherry, emission range 605-680 nm). Z-stacks were obtained with a TI of 30 min, a 1024 x 1024 format at 400Hz and a *z*-step size of 3 µm. Fluorochromes unmixing was performed by acquisition of automated-sequential collection of multi-channel images, to reduce spectral crosstalk between channels, and the same setting parameters were used for all examined samples. Embryo live imaging was performed simultaneously using the Mark & Find mode of the LAS X software.

Statistics and reproducibility

Data were analyzed independently by at least two researchers and statistical assessments were performed using GraphPad software v.9 (Prism). Log-rank (Mantel-Cox) test was used to assess survival in zebrafish mutants and morphants. For phenotypes penetrance assessment Chi-squared test in a 2x2 contingency table was used, performed as pairwise statistical comparisons across experimental conditions as indicated in the text and figures. Normality tests (Anderson-Darling, D'Agostino & Pearson, Shapiro-Wilk and Kolmogorov-Smirnov tests) were run to assess normal distribution of the data. Parametric data with more experimental groups were analyzed with ANOVA test, non-parametric data with Kruskal-Wallis test and specific *post hoc* tests were always used as indicated in the figure legends and **Statistical table 12**. All the analyses were two-tailed.

Image processing

Raw images were analyzed with Fiji[151], LAS X Life Science imaging softwares (Leica Microsystem, v.3, 3.5, 3.7, 4.5), FV10-ASW software v.4.1, Olympus cellSens Standard imaging software v.1.14 (Olympus Life Science) and IMARIS v.9.5 (Bitplane) and processed using Photoshop or Illustrator (Adobe Systems Incorporated) for figure assembly. Image acquisition parameters (laser lines and power, detector settings,

objective used) were maintained equal within each experiment. Brightness and contrast were adjusted equally across whole images and between images belonging to the same experiment. Exceptions are explained here. In Figure 10, due to possible background differences within each imaged well, each brightfield image showing the notochord was individually adjusted for brightness and contrast to allow best notochord visualization. Given the high signal intensity that would shadow the Golgi staining, in Supplementary Figure 10 the brightness of the mKOFP signal (blue) used only for membrane rendering was reduced in post-processing for $ARF3^{K127}$ as compared to $ARF3^{WT}$. All the schematic illustrations were generated by researchers using Illustrator 2021-2022 (Adobe) except for the human brain illustration item in Fig. 8 which was created with BioRender.com and modified in Illustrator 2021-2022 (Adobe).

Data availability

The clinical data were collected after signed consent forms. The entire dataset is included within the manuscript. Given the progressive nature of the disease, additional information eventually collected after this publication will be made available upon request to the corresponding authors (antonella.lauri@opbg.net, marco.tartaglia@opbg.net) and referring clinicians. The sequencing data are available under restricted access for privacy/ethical reasons, access can be obtained contacting the corresponding authors. The ARF3 variants identified in this study have been deposited in the ClinVar database under the following accession codes: SCV002549683 (c.34C>G, p.Leu12Val) [https://www.ncbi.nlm.nih.gov/clinvar/variation/1697208/?oq=SCV002549683&m=NM_001659.3(ARF3):c.34C%3EG%20(p.Leu12Val)], SCV002549684 (c.95C>A, p.Thr32Asn) [https://www.ncbi.nlm.nih.gov/clinvar/variation/1697209/?oq=SCV002549684&m=NM_001659.3(ARF3):c.95C%3EA%20(p.Thr32Asn)], SCV002549685 (c.139C>T, p.Pro47Ser) [https://www.ncbi.nlm.nih.gov/clinvar/variation/1697210/?oq=SCV002549685&m=NM_001659.3(ARF3):c.139C%3ET%20(p.Pro47Ser)], SCV002549686 (c.200A>T, p.Asp67Val) [https://www.ncbi.nlm.nih.gov/clinvar/variation/1697211/?oq=SCV002549686&m=NM_001659.3(ARF3):c.200A%3ET%20(p.Asp67Val)], SCV002549687 (c.277G>A,

p.Asp93Asn) [https://www.ncbi.nlm.nih.gov/clinvar/variation/1697212/?oq=SCV002549687&m=NM_001659.3(ARF3):c.277G%3EA%20(p.Asp93Asn)], and SCV002549688 (c.379A>G, p.Lys127Glu) [https://www.ncbi.nlm.nih.gov/clinvar/variation/1697213/?oq=SCV002549688&m=NM_001659.3(ARF3):c.379A%3EG%20(p.Lys127Glu)]. The UCSC GRCh37/hg19 human genome assembly used as reference for reads alignment is available at https://www.ensembl.org/info/website/tutorials/grch37.html. The dbSNP150, gnomAD V.2.1.1, ClinVar and COSMIC v.96 databases used in this paper are available at https://gnomad.broadinstitute.org/, https://genome.ucsc.edu/cgi-bin/hgTrackUi?db=hg38&g=snp150Common and (https://www.ncbi.nlm.nih.gov/clinvar/), https://cancer.sanger.ac.uk/cosmic, respectively. The raw blots and raw data for the different measures of this study are provided in the Supplementary Information/Source data file. Source data are provided with this paper. Due to the large size of each dataset, all the raw imaging data, supporting the findings of the work are available from the corresponding authors upon request. All the constructs generated in this study will be shared upon request to the corresponding authors.

References

1. D'Souza-Schorey, C. & Chavrier, P. ARF proteins: roles in membrane traffic and beyond. *Nat. Rev. Mol. Cell Biol.* **7**, 347–358 (2006).
2. Cockcroft, S. *et al.* Phospholipase D: a downstream effector of ARF in granulocytes. *Science* **263**, 523–526 (1994).
3. Guo, Y., Sirkis, D. W. & Schekman, R. Protein Sorting at the trans-Golgi Network. *Annu. Rev. Cell Dev. Biol.* **30**, 169–206 (2014).
4. Makhoul, C., Gosavi, P. & Gleeson, P. A. Golgi Dynamics: The Morphology of the Mammalian Golgi Apparatus in Health and Disease. *Front. Cell Dev. Biol.* **7**, 112 (2019).
5. Makhoul, C., Gosavi, P. & Gleeson, P. A. The Golgi architecture and cell sensing. *Biochem. Soc. Trans.* **46**, 1063–1072 (2018).

1473 6. Gosavi, P. & Gleeson, P. A. The Function of the Golgi Ribbon Structure - An Enduring
1474 Mystery Unfolds! *BioEssays News Rev. Mol. Cell. Dev. Biol.* **39**, (2017).
1475 7. Wei, J.-H. & Seemann, J. Golgi ribbon disassembly during mitosis, differentiation and
1476 disease progression. *Curr. Opin. Cell Biol.* **47**, 43–51 (2017).
1477 8. Xie, Z., Hur, S. K., Zhao, L., Abrams, C. S. & Bankaitis, V. A. A Golgi Lipid Signaling
1478 Pathway Controls Apical Golgi Distribution and Cell Polarity during Neurogenesis. *Dev.*
1479 *Cell* **44**, 725-740.e4 (2018).
1480 9. De Matteis, M. A. & Luini, A. Mendelian disorders of membrane trafficking. *N. Engl. J.*
1481 *Med.* **365**, 927–938 (2011).
1482 10. Seifert, W. *et al.* Cohen syndrome-associated protein, COH1, is a novel, giant Golgi
1483 matrix protein required for Golgi integrity. *J. Biol. Chem.* **286**, 37665–37675 (2011).
1484 11. Shamseldin, H. E., Bennett, A. H., Alfadhel, M., Gupta, V. & Alkuraya, F. S. GOLGA2,
1485 encoding a master regulator of golgi apparatus, is mutated in a patient with a
1486 neuromuscular disorder. *Hum. Genet.* **135**, 245–251 (2016).
1487 12. Rasika, S., Passemard, S., Verloes, A., Gressens, P. & El Ghouzzi, V. Golgipathies in
1488 Neurodevelopment: A New View of Old Defects. *Dev. Neurosci.* **40**, 396–416 (2018).
1489 13. Dupuis, N. *et al.* Dymeclin deficiency causes postnatal microcephaly, hypomyelination
1490 and reticulum-to-Golgi trafficking defects in mice and humans. *Hum. Mol. Genet.* **24**,
1491 2771–2783 (2015).
1492 14. Izumi, K. *et al.* ARCN1 Mutations Cause a Recognizable Craniofacial Syndrome Due to
1493 COPI-Mediated Transport Defects. *Am. J. Hum. Genet.* **99**, 451–459 (2016).
1494 15. Halperin, D. *et al.* SEC31A mutation affects ER homeostasis, causing a neurological
1495 syndrome. *J. Med. Genet.* **56**, 139–148 (2019).
1496 16. Sheen, V. L. *et al.* Mutations in ARFGEF2 implicate vesicle trafficking in neural
1497 progenitor proliferation and migration in the human cerebral cortex. *Nat. Genet.* **36**, 69–
1498 76 (2004).

17. Cui, Y., Yang, Z. & Teasdale, R. D. The functional roles of retromer in Parkinson's disease. *FEBS Lett.* **592**, 1096–1112 (2018).
18. Ebanks, K., Lewis, P. A. & Bandopadhyay, R. Vesicular Dysfunction and the Pathogenesis of Parkinson's Disease: Clues From Genetic Studies. *Front. Neurosci.* **13**, 1381 (2019).
19. Liang, J. O. & Kornfeld, S. Comparative activity of ADP-ribosylation factor family members in the early steps of coated vesicle formation on rat liver Golgi membranes. *J. Biol. Chem.* **272**, 4141–4148 (1997).
20. Volpicelli-Daley, L. A., Li, Y., Zhang, C.-J. & Kahn, R. A. Isoform-selective Effects of the Depletion of ADP-Ribosylation Factors 1–5 on Membrane Traffic. *Mol. Biol. Cell* **16**, 4495–4508 (2005).
21. Chavrier, P. & Goud, B. The role of ARF and Rab GTPases in membrane transport. *Curr. Opin. Cell Biol.* **11**, 466–475 (1999).
22. Donaldson, J. G. & Jackson, C. L. ARF family G proteins and their regulators: roles in membrane transport, development and disease. *Nat. Rev. Mol. Cell Biol.* **12**, 362–375 (2011).
23. Zhang, C. J. *et al.* Expression of a dominant allele of human ARF1 inhibits membrane traffic in vivo. *J. Cell Biol.* **124**, 289–300 (1994).
24. Khan, A. R. & Ménétrey, J. Structural biology of Arf and Rab GTPases' effector recruitment and specificity. *Struct. Lond. Engl. 1993* **21**, 1284–1297 (2013).
25. Gillingham, A. K. & Munro, S. The small G proteins of the Arf family and their regulators. *Annu. Rev. Cell Dev. Biol.* **23**, 579–611 (2007).
26. Donaldson, J. G., Finazzi, D. & Klausner, R. D. Brefeldin A inhibits Golgi membrane-catalysed exchange of guanine nucleotide onto ARF protein. *Nature* **360**, 350–352 (1992).
27. Helms, J. B. & Rothman, J. E. Inhibition by brefeldin A of a Golgi membrane enzyme that catalyses exchange of guanine nucleotide bound to ARF. *Nature* **360**, 352–354 (1992).

28. Randazzo, P. A., Yang, Y. C., Rulka, C. & Kahn, R. A. Activation of ADP-ribosylation factor by Golgi membranes. Evidence for a brefeldin A- and protease-sensitive activating factor on Golgi membranes. *J. Biol. Chem.* **268**, 9555–9563 (1993).
29. Antonny, B., Huber, I., Paris, S., Chabre, M. & Cassel, D. Activation of ADP-ribosylation factor 1 GTPase-activating protein by phosphatidylcholine-derived diacylglycerols. *J. Biol. Chem.* **272**, 30848–30851 (1997).
30. Goldberg, J. Structural basis for activation of ARF GTPase: mechanisms of guanine nucleotide exchange and GTP-myristoyl switching. *Cell* **95**, 237–248 (1998).
31. Amor, J. C., Harrison, D. H., Kahn, R. A. & Ringe, D. Structure of the human ADP-ribosylation factor 1 complexed with GDP. *Nature* **372**, 704–708 (1994).
32. Kjeldgaard, M., Nyborg, J. & Clark, B. F. The GTP binding motif: variations on a theme. *FASEB J. Off. Publ. Fed. Am. Soc. Exp. Biol.* **10**, 1347–1368 (1996).
33. Randazzo, P. A. Resolution of two ADP-ribosylation factor 1 GTPase-activating proteins from rat liver. *Biochem. J.* **324 (Pt 2)**, 413–419 (1997).
34. Reinhard, C., Schweikert, M., Wieland, F. T. & Nickel, W. Functional reconstitution of COPI coat assembly and disassembly using chemically defined components. *Proc. Natl. Acad. Sci. U. S. A.* **100**, 8253–8257 (2003).
35. Rothman, J. E. Mechanisms of intracellular protein transport. *Nature* **372**, 55–63 (1994).
36. Popoff, V. *et al.* Several ADP-ribosylation factor (Arf) isoforms support COPI vesicle formation. *J. Biol. Chem.* **286**, 35634–35642 (2011).
37. Gilbert, C. E., Sztul, E. & Machamer, C. E. Commonly used trafficking blocks disrupt ARF1 activation and the localization and function of specific Golgi proteins. *Mol. Biol. Cell* **29**, 937–947 (2018).
38. Munro, S. The golgin coiled-coil proteins of the Golgi apparatus. *Cold Spring Harb. Perspect. Biol.* **3**, a005256 (2011).
39. Kulkarni-Gosavi, P., Makhoul, C. & Gleeson, P. A. Form and function of the Golgi apparatus: scaffolds, cytoskeleton and signalling. *FEBS Lett.* **593**, 2289–2305 (2019).

1553 40. Kondo, Y. *et al.* ARF1 and ARF3 are required for the integrity of recycling endosomes
1554 and the recycling pathway. *Cell Struct. Funct.* **37**, 141–154 (2012).
1555 41. Dascher, C. & Balch, W. E. Dominant inhibitory mutants of ARF1 block endoplasmic
1556 reticulum to Golgi transport and trigger disassembly of the Golgi apparatus. *J. Biol.*
1557 *Chem.* **269**, 1437–1448 (1994).
1558 42. Robineau, S., Chabre, M. & Antonny, B. Binding site of brefeldin A at the interface
1559 between the small G protein ADP-ribosylation factor 1 (ARF1) and the nucleotide-
1560 exchange factor Sec7 domain. *Proc. Natl. Acad. Sci. U. S. A.* **97**, 9913–9918 (2000).
1561 43. Altan-Bonnet, N., Phair, R. D., Polishchuk, R. S., Weigert, R. & Lippincott-Schwartz, J. A
1562 role for Arf1 in mitotic Golgi disassembly, chromosome segregation, and cytokinesis.
1563 *Proc. Natl. Acad. Sci. U. S. A.* **100**, 13314–13319 (2003).
1564 44. Hanai, A. *et al.* Class I Arfs (Arf1 and Arf3) and Arf6 are localized to the Flemming body
1565 and play important roles in cytokinesis. *J. Biochem. (Tokyo)* **159**, 201–208 (2016).
1566 45. Nakayama, K. Regulation of cytokinesis by membrane trafficking involving small
1567 GTPases and the ESCRT machinery. *Crit. Rev. Biochem. Mol. Biol.* **51**, 1–6 (2016).
1568 46. Rodrigues, F. F. & Harris, T. J. C. Key roles of Arf small G proteins and biosynthetic
1569 trafficking for animal development. *Small GTPases* **10**, 403–410 (2019).
1570 47. Carvajal-Gonzalez, J. M. *et al.* The clathrin adaptor AP-1 complex and Arf1 regulate
1571 planar cell polarity in vivo. *Nat. Commun.* **6**, 6751 (2015).
1572 48. Petko, J. A. *et al.* Proteomic and functional analysis of NCS-1 binding proteins reveals
1573 novel signaling pathways required for inner ear development in zebrafish. *BMC*
1574 *Neurosci.* **10**, 27 (2009).
1575 49. Ge, X. *et al.* Missense-depleted regions in population exomes implicate ras superfamily
1576 nucleotide-binding protein alteration in patients with brain malformation. *NPJ Genomic*
1577 *Med.* **1**, (2016).
1578 50. Sakamoto, M. *et al.* De novo ARF3 variants cause neurodevelopmental disorder with
1579 brain abnormality. *Hum. Mol. Genet.* **31**, 69–81 (2021).

1580 51. Sobreira, N., Schiettecatte, F., Valle, D. & Hamosh, A. GeneMatcher: a matching tool for
1581 connecting investigators with an interest in the same gene. *Hum. Mutat.* **36**, 928–930
1582 (2015).
1583 52. Lee, Y. *et al.* Makes caterpillars floppy-like effector-containing MARTX toxins require
1584 host ADP-ribosylation factor (ARF) proteins for systemic pathogenicity. *Proc. Natl. Acad.*
1585 *Sci. U. S. A.* **116**, 18031–18040 (2019).
1586 53. Pasqualato, S., Renault, L. & Cherfils, J. Arf, Arl, Arp and Sar proteins: a family of GTP-
1587 binding proteins with a structural device for 'front-back' communication. *EMBO Rep.* **3**,
1588 1035–1041 (2002).
1589 54. Carta, C. *et al.* Germline missense mutations affecting KRAS Isoform B are associated
1590 with a severe Noonan syndrome phenotype. *Am. J. Hum. Genet.* **79**, 129–135 (2006).
1591 55. Zampino, G. *et al.* Diversity, parental germline origin, and phenotypic spectrum of de
1592 novo HRAS missense changes in Costello syndrome. *Hum. Mutat.* **28**, 265–272 (2007).
1593 56. Click, E. S., Stearns, T. & Botstein, D. Systematic structure-function analysis of the small
1594 GTPase Arf1 in yeast. *Mol. Biol. Cell* **13**, 1652–1664 (2002).
1595 57. Amor, J. C. *et al.* Structures of yeast ARF2 and ARL1: distinct roles for the N terminus in
1596 the structure and function of ARF family GTPases. *J. Biol. Chem.* **276**, 42477–42484
1597 (2001).
1598 58. Ménétrey, J. *et al.* Structural basis for ARF1-mediated recruitment of ARHGAP21 to
1599 Golgi membranes. *EMBO J.* **26**, 1953–1962 (2007).
1600 59. Yu, X., Breitman, M. & Goldberg, J. A Structure-Based Mechanism for Arf1-Dependent
1601 Recruitment of Coatomer to Membranes. *Cell* **148**, 530–542 (2012).
1602 60. Ratcliffe, C. D. H., Sahgal, P., Parachoniak, C. A., Ivaska, J. & Park, M. Regulation of
1603 Cell Migration and β1 Integrin Trafficking by the Endosomal Adaptor GGA3. *Traffic Cph.*
1604 *Den.* **17**, 670–688 (2016).

1605 61. Xiang, Y., Seemann, J., Bisel, B., Punthambaker, S. & Wang, Y. Active ADP-ribosylation
1606 factor-1 (ARF1) is required for mitotic Golgi fragmentation. *J. Biol. Chem.* **282**, 21829–
1607 21837 (2007).
1608 62. Lu, L., Tai, G. & Hong, W. Autoantigen Golgin-97, an effector of Arl1 GTPase,
1609 participates in traffic from the endosome to the trans-golgi network. *Mol. Biol. Cell* **15**,
1610 4426–4443 (2004).
1611 63. Lu, L., Horstmann, H., Ng, C. & Hong, W. Regulation of Golgi structure and function by
1612 ARF-like protein 1 (Arl1). *J. Cell Sci.* **114**, 4543–4555 (2001).
1613 64. Joshi, G., Chi, Y., Huang, Z. & Wang, Y. Aβ-induced Golgi fragmentation in Alzheimer's
1614 disease enhances Aβ production. *Proc. Natl. Acad. Sci. U. S. A.* **111**, E1230-1239
1615 (2014).
1616 65. Manolea, F. *et al.* Arf3 is activated uniquely at the trans-Golgi network by brefeldin A-
1617 inhibited guanine nucleotide exchange factors. *Mol. Biol. Cell* **21**, 1836–1849 (2010).
1618 66. Hsu, V. W., Bai, M. & Li, J. Getting active: protein sorting in endocytic recycling. *Nat.*
1619 *Rev. Mol. Cell Biol.* **13**, 323–328 (2012).
1620 67. Sheff, D., Pelletier, L., O'Connell, C. B., Warren, G. & Mellman, I. Transferrin receptor
1621 recycling in the absence of perinuclear recycling endosomes. *J. Cell Biol.* **156**, 797–804
1622 (2002).
1623 68. Mani, M. *et al.* Developmentally regulated GTP-binding protein 2 coordinates Rab5
1624 activity and transferrin recycling. *Mol. Biol. Cell* **27**, 334–348 (2016).
1625 69. Rink, J., Ghigo, E., Kalaidzidis, Y. & Zerial, M. Rab conversion as a mechanism of
1626 progression from early to late endosomes. *Cell* **122**, 735–749 (2005).
1627 70. Ren, M. *et al.* Hydrolysis of GTP on rab11 is required for the direct delivery of transferrin
1628 from the pericentriolar recycling compartment to the cell surface but not from sorting
1629 endosomes. *Proc. Natl. Acad. Sci. U. S. A.* **95**, 6187–6192 (1998).
1630 71. Takahashi, S. *et al.* Rab11 regulates exocytosis of recycling vesicles at the plasma
1631 membrane. *J. Cell Sci.* **125**, 4049–4057 (2012).

1632 72. Maxfield, F. R. & McGraw, T. E. Endocytic recycling. *Nat. Rev. Mol. Cell Biol.* **5**, 121–132
1633 (2004).
1634 73. Cullen, P. J. & Steinberg, F. To degrade or not to degrade: mechanisms and significance
1635 of endocytic recycling. *Nat. Rev. Mol. Cell Biol.* **19**, 679–696 (2018).
1636 74. Gammella, E. *et al.* Unconventional endocytosis and trafficking of transferrin receptor
1637 induced by iron. *Mol. Biol. Cell* **32**, 98–108 (2021).
1638 75. Johnson, M. B., Chen, J., Murchison, N., Green, F. A. & Enns, C. A. Transferrin receptor
1639 2: evidence for ligand-induced stabilization and redirection to a recycling pathway. *Mol.*
1640 *Biol. Cell* **18**, 743–754 (2007).
1641 76. Kimmel, C. B., Ballard, W. W., Kimmel, S. R., Ullmann, B. & Schilling, T. F. Stages of
1642 embryonic development of the zebrafish. *Dev. Dyn. Off. Publ. Am. Assoc. Anat.* **203**,
1643 253–310 (1995).
1644 77. Zaghloul, N. A. *et al.* Functional analyses of variants reveal a significant role for
1645 dominant negative and common alleles in oligogenic Bardet-Biedl syndrome. *Proc. Natl.*
1646 *Acad. Sci. U. S. A.* **107**, 10602–10607 (2010).
1647 78. Suárez, R., Gobius, I. & Richards, L. J. Evolution and development of interhemispheric
1648 connections in the vertebrate forebrain. *Front. Hum. Neurosci.* **8**, 497 (2014).
1649 79. Zaqout, S. & Kaindl, A. M. Autosomal Recessive Primary Microcephaly: Not Just a Small
1650 Brain. *Front. Cell Dev. Biol.* **9**, (2022).
1651 80. Phan, T. P. & Holland, A. J. Time is of the essence: the molecular mechanisms of
1652 primary microcephaly. *Genes Dev.* **35**, 1551–1578 (2021).
1653 81. Fasano, G., Compagnucci, C., Dallapiccola, B., Tartaglia, M. & Lauri, A. Teleost fish and
1654 organoids: alternative windows into the development of healthy and diseased brains.
1655 *Front. Mol. Neurosci.* doi:doi: 10.3389/fnmol.2022.855786.
1656 82. Gebhardt, C. *et al.* An interhemispheric neural circuit allowing binocular integration in the
1657 optic tectum. *Nat. Commun.* **10**, 5471 (2019).

1658 83. Ito, Y., Tanaka, H., Okamoto, H. & Ohshima, T. Characterization of neural stem cells and
1659 their progeny in the adult zebrafish optic tectum. *Dev. Biol.* **342**, 26–38 (2010).
1660 84. Chippalkatti, R. & Suter, B. 5-Ethynyl-2'-Deoxyuridine/Phospho-Histone H3 Dual-
1661 Labeling Protocol for Cell Cycle Progression Analysis in Drosophila Neural Stem Cells.
1662 *JoVE J. Vis. Exp.* e62642 (2021) doi:10.3791/62642.
1663 85. Phan, T. P. *et al.* Centrosome defects cause microcephaly by activating the 53BP1-
1664 USP28-TP53 mitotic surveillance pathway. *EMBO J.* **40**, e106118 (2021).
1665 86. Barkovich, A. J., Dobyns, W. B. & Guerrini, R. Malformations of cortical development and
1666 epilepsy. *Cold Spring Harb. Perspect. Med.* **5**, a022392 (2015).
1667 87. Chen, J.-F. *et al.* Microcephaly disease gene Wdr62 regulates mitotic progression of
1668 embryonic neural stem cells and brain size. *Nat. Commun.* **5**, 3885 (2014).
1669 88. Kodani, A. & Sütterlin, C. The Golgi protein GM130 regulates centrosome morphology
1670 and function. *Mol. Biol. Cell* **19**, 745–753 (2008).
1671 89. Wei, J.-H., Zhang, Z. C., Wynn, R. M. & Seemann, J. GM130 Regulates Golgi-Derived
1672 Spindle Assembly by Activating TPX2 and Capturing Microtubules. *Cell* **162**, 287–299
1673 (2015).
1674 90. Zhang, C.-H. *et al.* GM130, a cis-Golgi protein, regulates meiotic spindle assembly and
1675 asymmetric division in mouse oocyte. *Cell Cycle Georget. Tex* **10**, 1861–1870 (2011).
1676 91. Ansar, M. *et al.* Bi-allelic Variants in DYNC1I2 Cause Syndromic Microcephaly with
1677 Intellectual Disability, Cerebral Malformations, and Dysmorphic Facial Features. *Am. J.*
1678 *Hum. Genet.* **104**, 1073–1087 (2019).
1679 92. Farag, H. G. *et al.* Abnormal centrosome and spindle morphology in a patient with
1680 autosomal recessive primary microcephaly type 2 due to compound heterozygous
1681 WDR62 gene mutation. *Orphanet J. Rare Dis.* **8**, 178 (2013).
1682 93. Novorol, C. *et al.* Microcephaly models in the developing zebrafish retinal
1683 neuroepithelium point to an underlying defect in metaphase progression. *Open Biol.* **3**,
1684 130065 (2013).

1685 94. Bagwell, J. *et al.* Notochord vacuoles absorb compressive bone growth during zebrafish
1686 spine formation. *eLife* **9**, (2020).
1687 95. Ravichandran, Y., Goud, B. & Manneville, J.-B. The Golgi apparatus and cell polarity:
1688 Roles of the cytoskeleton, the Golgi matrix, and Golgi membranes. *Curr. Opin. Cell Biol.*
1689 **62**, 104–113 (2020).
1690 96. Tate, J. G. *et al.* COSMIC: the Catalogue Of Somatic Mutations In Cancer. *Nucleic Acids*
1691 *Res.* **47**, D941–D947 (2019).
1692 97. Tartaglia, M. & Gelb, B. D. Disorders of dysregulated signal traffic through the RAS-
1693 MAPK pathway: phenotypic spectrum and molecular mechanisms. *Ann. N. Y. Acad. Sci.*
1694 **1214**, 99–121 (2010).
1695 98. Motta, M. *et al.* Activating MRAS mutations cause Noonan syndrome associated with
1696 hypertrophic cardiomyopathy. *Hum. Mol. Genet.* **29**, 1772–1783 (2020).
1697 99. Flex, E. *et al.* Activating mutations in RRAS underlie a phenotype within the RASopathy
1698 spectrum and contribute to leukaemogenesis. *Hum. Mol. Genet.* **23**, 4315–4327 (2014).
1699 100. Niihori, T. *et al.* Germline-Activating RRAS2 Mutations Cause Noonan Syndrome.
1700 *Am. J. Hum. Genet.* **104**, 1233–1240 (2019).
1701 101. Capri, Y. *et al.* Activating Mutations of RRAS2 Are a Rare Cause of Noonan
1702 Syndrome. *Am. J. Hum. Genet.* **104**, 1223–1232 (2019).
1703 102. Denayer, E. *et al.* Mutation analysis in Costello syndrome: functional and structural
1704 characterization of the HRAS p.Lys117Arg mutation. *Hum. Mutat.* **29**, 232–239 (2008).
1705 103. Lim, Y. H. *et al.* Somatic Activating RAS Mutations Cause Vascular Tumors Including
1706 Pyogenic Granuloma. *J. Invest. Dermatol.* **135**, 1698–1700 (2015).
1707 104. Schubbert, S. *et al.* Germline KRAS mutations cause Noonan syndrome. *Nat. Genet.*
1708 **38**, 331–336 (2006).
1709 105. Zenker, M. *et al.* Expansion of the genotypic and phenotypic spectrum in patients
1710 with KRAS germline mutations. *J. Med. Genet.* **44**, 131–135 (2007).

106. Landrum, M. J. *et al.* ClinVar: improving access to variant interpretations and supporting evidence. *Nucleic Acids Res.* **46**, D1062–D1067 (2018).

107. Nava, C. *et al.* Cardio-facio-cutaneous and Noonan syndromes due to mutations in the RAS/MAPK signalling pathway: genotype-phenotype relationships and overlap with Costello syndrome. *J. Med. Genet.* **44**, 763–771 (2007).

108. Gripp, K. W. & Lin, A. E. Costello syndrome: a Ras/mitogen activated protein kinase pathway syndrome (rasopathy) resulting from HRAS germline mutations. *Genet. Med. Off. J. Am. Coll. Med. Genet.* **14**, 285–292 (2012).

109. Merithew, E. *et al.* Structural Plasticity of an Invariant Hydrophobic Triad in the Switch Regions of Rab GTPases Is a Determinant of Effector Recognition*. *J. Biol. Chem.* **276**, 13982–13988 (2001).

110. Denayer, E., de Ravel, T. & Legius, E. Clinical and molecular aspects of RAS related disorders. *J. Med. Genet.* **45**, 695–703 (2008).

111. Northup, J. K., Jian, X. & Randazzo, P. A. Nucleotide exchange factors. *Cell. Logist.* **2**, 140–146 (2012).

112. Pennauer, M., Buczak, K., Prescianotto-Baschong, C. & Spiess, M. Shared and specific functions of Arfs 1-5 at the Golgi revealed by systematic knockouts. *J. Cell Biol.* **221**, e202106100 (2022).

113. Burd, C. & Cullen, P. J. Retromer: a master conductor of endosome sorting. *Cold Spring Harb. Perspect. Biol.* **6**, a016774 (2014).

114. Carpentieri, J. A. *et al.* Endosomal trafficking defects alter neural progenitor proliferation and cause microcephaly. *Nat. Commun.* **13**, 16 (2022).

115. Garcia-Cazorla, A., Oyarzábal, A., Saudubray, J.-M., Martinelli, D. & Dionisi-Vici, C. Genetic disorders of cellular trafficking. *Trends Genet.* **38**, 724–751 (2022).

116. Ayala, I. & Colanzi, A. Structural Organization and Function of the Golgi Ribbon During Cell Division. *Front. Cell Dev. Biol.* **10**, 925228 (2022).

117. Kim, O.-H. *et al.* Zebrafish knockout of Down syndrome gene, DYRK1A, shows social impairments relevant to autism. *Mol. Autism* **8**, 50 (2017).

118. Liu, J. *et al.* ARF3 inhibits proliferation and promotes apoptosis in gastric cancer by regulating AKT and ERK pathway. *Acta Biochim. Pol.* **68**, 223–229 (2021).

119. Boulay, P.-L. *et al.* ARF1 controls proliferation of breast cancer cells by regulating the retinoblastoma protein. *Oncogene* **30**, 3846–3861 (2011).

120. Jessen, J. R. *et al.* Zebrafish trilobite identifies new roles for Strabismus in gastrulation and neuronal movements. *Nat. Cell Biol.* **4**, 610–615 (2002).

121. Roszko, I., Sawada, A. & Solnica-Krezel, L. Regulation of convergence and extension movements during vertebrate gastrulation by the Wnt/PCP pathway. *Semin. Cell Dev. Biol.* **20**, 986–997 (2009).

122. Wallingford, J. B., Fraser, S. E. & Harland, R. M. Convergent extension: the molecular control of polarized cell movement during embryonic development. *Dev. Cell* **2**, 695–706 (2002).

123. Lauri, A., Fasano, G., Venditti, M., Dallapiccola, B. & Tartaglia, M. In vivo functional genomics for undiagnosed patients: the impact of small GTPases signaling dysregulation at pan-embryo developmental scale. *Front. Cell Dev. Biol.* **9**, (2021).

124. Prigozhina, N. L. & Waterman-Storer, C. M. Decreased polarity and increased random motility in PtK1 epithelial cells correlate with inhibition of endosomal recycling. *J. Cell Sci.* **119**, 3571–3582 (2006).

125. Winter, J. F. *et al.* Caenorhabditis elegans screen reveals role of PAR-5 in RAB-11-recycling endosome positioning and apicobasal cell polarity. *Nat. Cell Biol.* **14**, 666–676 (2012).

126. Ulrich, F. *et al.* Wnt11 Functions in Gastrulation by Controlling Cell Cohesion through Rab5c and E-Cadherin. *Dev. Cell* **9**, 555–564 (2005).

127. Sarmah, S. *et al.* Sec24D-dependent transport of extracellular matrix proteins is required for zebrafish skeletal morphogenesis. *PloS One* **5**, e10367 (2010).

128. Coutinho, P. *et al.* Differential requirements for COPI transport during vertebrate early development. *Dev. Cell* **7**, 547–558 (2004).

129. Horton, A. C. *et al.* Polarized Secretory Trafficking Directs Cargo for Asymmetric Dendrite Growth and Morphogenesis. *Neuron* **48**, 757–771 (2005).

130. Pezzani, L. *et al.* Atypical presentation of pediatric BRAF RASopathy with acute encephalopathy. *Am. J. Med. Genet. A.* **176**, 2867–2871 (2018).

131. Ziegler, A. *et al.* Confirmation that variants in TTI2 are responsible for autosomal recessive intellectual disability. *Clin. Genet.* **96**, 354–358 (2019).

132. Radio, F. C. *et al.* SPEN haploinsufficiency causes a neurodevelopmental disorder overlapping proximal 1p36 deletion syndrome with an episignature of X chromosomes in females. *Am. J. Hum. Genet.* **108**, 502–516 (2021).

133. Lin, Y.-C. *et al.* SCUBE3 loss-of-function causes a recognizable recessive developmental disorder due to defective bone morphogenetic protein signaling. *Am. J. Hum. Genet.* **108**, 115–133 (2021).

134. Vetro, A. *et al.* ATP1A2- and ATP1A3-associated early profound epileptic encephalopathy and polymicrogyria. *Brain J. Neurol.* (2021) doi:10.1093/brain/awab052.

135. Humphrey, W., Dalke, A. & Schulten, K. VMD: visual molecular dynamics. *J. Mol. Graph.* **14**, 33–38, 27–28 (1996).

136. Waterhouse, A. *et al.* SWISS-MODEL: homology modelling of protein structures and complexes. *Nucleic Acids Res.* **46**, W296–W303 (2018).

137. Pettersen, E. F. *et al.* UCSF Chimera--a visualization system for exploratory research and analysis. *J. Comput. Chem.* **25**, 1605–1612 (2004).

138. Dunbrack, R. L. Rotamer libraries in the 21st century. *Curr. Opin. Struct. Biol.* **12**, 431–440 (2002).

139. Páll, S. *et al.* Heterogeneous parallelization and acceleration of molecular dynamics simulations in GROMACS. *J. Chem. Phys.* **153**, 134110 (2020).

1790 140. Huang, J. & MacKerell, A. D. CHARMM36 all-atom additive protein force field:
1791 validation based on comparison to NMR data. *J. Comput. Chem.* **34**, 2135–2145 (2013).
1792 141. Mark, P. & Nilsson, L. Structure and Dynamics of the TIP3P, SPC, and SPC/E Water
1793 Models at 298 K. *J. Phys. Chem. A* **105**, 9954–9960 (2001).
1794 142. Bussi, G., Donadio, D. & Parrinello, M. Canonical sampling through velocity
1795 rescaling. *J. Chem. Phys.* **126**, 014101 (2007).
1796 143. Darden, T., York, D. & Pedersen, L. Particle mesh Ewald: An N·log(N) method for
1797 Ewald sums in large systems. *J. Chem. Phys.* **98**, 10089–10092 (1993).
1798 144. Villefranc, J. A., Amigo, J. & Lawson, N. D. Gateway compatible vectors for analysis
1799 of gene function in the zebrafish. *Dev. Dyn. Off. Publ. Am. Assoc. Anat.* **236**, 3077–3087
1800 (2007).
1801 145. Don, E. K. *et al.* A Tol2 Gateway-Compatible Toolbox for the Study of the Nervous
1802 System and Neurodegenerative Disease. *Zebrafish* **14**, 69–72 (2017).
1803 146. Cole, N. B. *et al.* Diffusional mobility of Golgi proteins in membranes of living cells.
1804 *Science* **273**, 797–801 (1996).
1805 147. Choudhury, A. *et al.* Rab proteins mediate Golgi transport of caveola-internalized
1806 glycosphingolipids and correct lipid trafficking in Niemann-Pick C cells. *J. Clin. Invest.*
1807 **109**, 1541–1550 (2002).
1808 148. Peri, F. & Nüsslein-Volhard, C. Live Imaging of Neuronal Degradation by Microglia
1809 Reveals a Role for v0-ATPase a1 in Phagosomal Fusion In Vivo. *Cell* **133**, 916–927
1810 (2008).
1811 149. Tran, L. D. *et al.* Dynamic microtubules at the vegetal cortex predict the embryonic
1812 axis in zebrafish. *Dev. Camb. Engl.* **139**, 3644–3652 (2012).
1813 150. Leatherbarrow, R. J. *GraFit Version 7*. (2010).
1814 151. Schindelin, J. *et al.* Fiji: an open-source platform for biological-image analysis. *Nat.*
1815 *Methods* **9**, 676–682 (2012).

152. Dunn, K. W., Kamocka, M. M. & McDonald, J. H. A practical guide to evaluating colocalization in biological microscopy. *Am. J. Physiol. Cell Physiol.* **300**, C723-742 (2011).

153. Kovach, W. L. Oriana – Circular Statistics for Windows. (2011).

154. Tang, D., Yuan, H., Vielemeyer, O., Perez, F. & Wang, Y. Sequential phosphorylation of GRASP65 during mitotic Golgi disassembly. *Biol. Open* **1**, 1204–1214 (2012).

155. Thisse, C. & Thisse, B. High-resolution in situ hybridization to whole-mount zebrafish embryos. *Nat. Protoc.* **3**, 59–69 (2008).

Acknowledgments

H2A-mCherry:pDest and GFP-CAAX:pDest plasmids were kindly provided by Dr. Mette Handberg-Thorsager (Max Planck Institute of Molecular Cell Biology and Genetics, Dresden, MPI-CBG, Germany). pcDNA3/hArf3(WT)-mCherry was a gift from Kazuhisa Nakayama (Addgene plasmid # 79420; http://n2t.net/addgene:79420; RRID:Addgene_79420) EGFP-GalT was a gift from Jennifer Lippincott-Schwartz (Addgene plasmid # 11929; http://n2t.net/addgene:11929; RRID:Addgene_11929), GFP-rab11 WT was a gift from Richard Pagano (Addgene plasmid # 12674; http://n2t.net/addgene:12674;RRID:Addgene_12674). *Tg(XlEef1a1:dclk2DeltaK-GFP)* was a kind gift from Prof. M. Mione (Laboratory of Experimental Cancer Biology – CIBIO, Trieste, Italy). We acknowledge Cineca ELIXIR-IIB for computing resources, and thank Dr. Giovanna Zambruno for providing support and technical advice on TEM. This work was supported, in part, by Fondazione Bambino Gesù (Vite Coraggiose to M.T.), Italian Ministry of Health (CCR-2017-23669081, RCR-2020-23670068_001 and RCR-2021-23671215 to M.T; RF-2018-12366931 to F.C.R., G.C. and B.D.; Ricerca Corrente 2021, Ricerca Corrente 2022 to A.L., S.C. and M.T., and RF-2013-02355240 to R.G.), Ministero della Salute (Ricerca 5x1000) to A.L. and M.T, Italian Ministry of Research (FOE 2019 to M.T.), the Tuscany Region Call for Health 2018 (DECODE EE, to R.G.), and the European Union Seventh Framework Programme (DESIRE [602531] to R.G.), Istituto Superiore di Sanità (Bando Ricerca Indipendente ISS 2020-2022-ISS20-39c812dd2b3c to S.C).

Author contribution

G.F. designed and performed the *in vivo* experiments and contributed to analyze *in vitro* cell experiments and to write the manuscript. V.M. designed and performed the *in vitro* experiments and contributed to write the manuscript. F.C.R. coordinated the clinical data collection and phenotyping, analyzed the clinical data and contributed to write the manuscript; M.V. performed the *in situ* hybridization assay, contributed to constructs preparation and to the analysis of cells experiments; N.M. performed the cell-free biochemical experiments with F.B.; S.C. designed and performed the Golgi morphological experiments in cells and contributed to the recycling and pull-down experiments with E.Z.; G.P. performed the cell proliferation and death assays in zebrafish; L.A.C. and S.Pe. contributed to the confocal scanning experiments. A.Z., A.V., F.P., S.Pi., A.B., and M.I. generated and analyzed the genomic data; G.C., performed the structural analyses and molecular dynamics simulations with I.G.P. and B.C.; L.B. e A.T. performed the TEM experiments; C.M. performed the ARF3 RT-PCR experiment in COS-1 cells; R.M. contributed to TEM sections preparations; M.B., C.B., D.M., A.Se., M.M., M.V.G., A.B., C.J.C., R.G., A.Sl. and B.D. identified the patients, and collected and analyzed the clinical data; M.R.A. supervised the cell-free biochemical experiments and analyzed the data; A.L. and M.T. conceived, designed, and supervised the project, analyzed the data, wrote and revised the manuscript. G.F., V.M. and F.C.R. equally contributed to the work, M.V. and N.M. equally contributed to the work. A.L. and M.T. jointly coordinated the study.

Competing Interests

The authors declare no competing interests.

Figure legends

Figure 1. Structural organization of ARF3, location of mutated residues and molecular dynamics analyses. (**a**) Domain organization of ARF3 excluding the unstructured *C*-terminal tail. Switch 1, switch 2 and the NKXD fingerpoint motif are highlighted in pink, green and yellow, respectively. The variants identified in affected subjects are also reported; (**b**) 3D structure in two different orientations of GTP-bound ARF3 interacting with the MARTX toxin (PDB 6ii6). Side chains of the ARF3 residues mutated in the affected subjects and GTP are in cyan and red, respectively. Main chain of residues belonging to switch 1, switch 2 and NKXD fingerpoint motif are colored as

above; (**c**) Enlargement of the ARF3 GTP binding pocket with the five mutated residues. The direct hydrogen bond between the N atom in the Lys127 lateral chain and the oxygen atom of the GTP ribose ring is highlighted in dashed line. The Mg^{2+} ion is colored in magenta, while the oxygen atom of the water molecule, mediating the interaction between Asp^{67} and the manganese ion, is shown in light blue color. The two hydrogen bonds between Asp^{67} and the water molecule are highlighted with dotted lines. (**d**) zoom showing the structural organization around residue 93. Left: view of the WT Asp^{93} forming a hydrogen bond with Lys^{127}. Right: structure with the p.Asp93Asn mutation and hydrogen bond breaking. The Mg^{2+} ion is colored in magenta (**e**) Homology model of GTP-bound ARF3 interacting with the cytosolic coat protein complex COPG1-COPZ1 (PDB: 3TJZ) validated by a 500-ns molecular dynamics (MD) simulation. The region of contact between ARF3 and COPG1 (orange color) is shown in e. (**f-h**) MD simulations of wild-type (f), p.Asp67Val (g) and p.Pro47Ser (h) ARF3 complexed with COPG1-COPZ1. Residues involved in the contact are shown with their side chain and colored as the respective protein/region. ARF3 backbone is represented with a diameter proportional to its per-residue fluctuations (RMSF).

Figure 2. Expression, stability and GTPase activity of WT and mutant ARF3 proteins in COS-1 cells. (**a, a'**) Western blot analysis showing the protein levels of myc-tagged $ARF3^{WT}$ and all the identified mutants in transfected COS-1 cells, basally and after treatment with cycloheximide (CHX) (10 µg/ml) for the indicated time points (a), and with MG132 (100 µM), or bafilomycin A1 (200 nM) for six hours (a'). (**b**) Pull-down assay using GGA3-conjugated beads shows ARF3 activation in COS-1 cells transiently transfected with WT or mutant myc-tagged ARF3 expression constructs. Active and total ARF3 levels are monitored using anti-myc antibody. GAPDH and beta-tubulin are used as loading controls. Pull down assays of $ARF3^{WT}$ transfected cells performed in the presence of an excess of GDP and γGTP are used as negative and positive controls, respectively (b, left panel). Pulldown samples in b (left and right), are loaded on different blots and processed parallelly. Representative blots are shown and data are expressed as mean ± SEM of three independent experiments. Two-way ANOVA followed by Tukey's *post hoc* test (a, WT vs. all mutants, ****$p < 0.0001$; a', K127E *vs.* K127E+MG132 **$p=0.0052$; K127E *vs.* K127E+Bafilomycin *$p=0.0195$;

L12V/D67V *vs.* L12V/D67V+MG132 *p=0.0123; L12V/D67V *vs.* L12V/D67V+Bafilomycin *p=0.0411), One-way ANOVA followed by Sidak's *post hoc* test (b left panel, WT *vs.* WT+GTP *p=0.0197), One-way ANOVA followed by Dunnett's *post hoc* test (b, WT *vs.* K127E **p =0.0088; WT *vs.* L12V/D67V **p =0.0058; WT *vs.* D93N **p= 0.0035; WT *vs.* T32N **p = 0.0075; WT vs Q71L ****p<0.0001; WT *vs.* T31N ***p=0.0006) are used to assess statistical significance. (c) Summary table of the data obtained relatively to the stability and activity of the different ARF3 mutants. Source data are provided as a Source Data file.

Figure 3. ARF3 mutants induce variable Golgi morphological alterations in COS-1 cells. (a) Maximum intensity confocal *z*-projections showing immunostaining against Golgin-97 (trans-Golgi marker) (green) performed in fixed COS-1 cells transiently transfected with mCherry-tagged $ARF3^{WT}$, $ARF3^{T31N}$ and $ARF3^{Q71L}$ (DN and CA variants, respectively) or mutants identified (magenta) for 48 hours. Composite colocalization images are shown in the right panels with nuclei (DAPI staining) in blue. The images are representative of three independent experiments. Scale bars = 2 µm (high magnification) and 10 µm (all the other images). (b) Golgi mean intensity and area define distinct Golgi morphotypes. Dot plots of mean intensity (MI) and area of Golgi in cells transiently transfected with mCherry-tagged $ARF3^{WT}$, or $ARF3^{Q71L}$ and $ARF3^{T31N}$ mutants (up, middle, bottom panels) are shown. Golgi MI and area (% of whole cell) of cells were measured based on Golgin-97 staining. Whole cell area was determined using the area covered by mCherry fluorescence as a mask. Representative 3D rendering images of the observed Golgi staining are shown. Cell populations located in different gates are characterized by distinct Golgi morphologies: Compact: A < 2.6 and MI > 1.5 (green gate); expanded Golgi: 2,7 < A < 12 and MI > 0.8, (purple gate); partially dispersed Golgi: 2,7 < A < 12 and MI < 0.8 (pink gate); totally dispersed Golgi: A > 12 and MI < 0.8, (bordeaux gate). (c) Incidence of trans-Golgi morphotypes.The bar graph represents the percentage of cells showing compact, expanded, partially or fully dispersed distribution (part.disp and ful.disp.) of Golgi in mCherry-tagged ARF3 transfected cells, based on the classification described above in b. N of cells = 26 (WT); 22 (Q71L); 29 (T31N); 20 (K127E); 20 (L12V/D67V); 21 (P47S); 28 (D93N) and 27 (T32N). Data are expressed as mean ± SEM of three independent experiments. Two-sided Chi-square's test in a 2×2 contingency table (WT

vs. all mutants, compact vs. all phenotypes ****p < 0.0001) is used to assess statistical significance. Arb.units = arbitrary units. Source data are provided as a Source Data file.

Figure 4. *Trans*-Golgi fragmentation visualized by EGFP-GalT in cells and zebrafish embryos expressing the mutant mCherry-tagged ARF3^{K127E}. (**a**) Schematic representation of the experimental set up in both *in vitro* and *in vivo* systems. COS-1 cells are transfected with DNA constructs expressing WT and mutant ARF3-mCherry (magenta) and EGFP-GalT (*trans*-Golgi maker, green) and analyzed by live confocal microscopy between 4-6 hours post transfection. Zebrafish embryos are injected at 1 cell stage with WT and mutant ARF3-mCherry and EGFP-GalT mRNA. mKOFP-CAAX mRNA is used as membrane marker (cyan). Animals are analyzed by live confocal microscopy during gastrulation (~6-7 hpf). (**b,c**) Maximum intensity projections of confocal images of a single time-lapse experiment (Supplementary Movie 1) performed in transfected COS-1 cells at 15 min (~4 hours post transfection) and 120 min later (~6 hours post transfection) from the start of the time-lapse experiment. The images show diffused EGFP-GalT signal (*trans*-Golgi fragmentation) in ARF3^{K127E} over time (white arrows). Scale bar = 20µm. (**d,e**) 3D image reconstructions from live confocal acquisitions of the animal pole in developing zebrafish embryos expressing ARF3^{WT} and ARF3^{K127E} at the mid-gastrulation stage (~ 6 hpf). White arrowheads indicate a compact *trans*-Golgi morphology surrounding the nucleus ("ribbon") in the EVL cells. Yellow arrowheads indicate cells showing "*punta*" morphology of the TG dispersed throughout the cytosol. Scale bars = 20 µm and 50 µm. The images are representative of embryos from two independent batches. Quantification is shown in Supplementary Fig.10a. Source data are provided as a Source Data file.

Figure 5. Variable impact of *ARF3* mutations on COP-I vesicles assembly. (**a**) Maximum intensity confocal z-projections of COS-1 cells expressing mCherry-tagged ARF3^{WT} and all identified mutants and stained for the β-subunit of COP-I. The right panel shows a magnification of β-COP signal. Nuclei are labeled with DAPI (blue). Yellow and red and purple arrowheads: normal, diffused and expanded β-COP signal, respectively. Scale bar is 10 µm. The images are representative of cells from a single experiment. (**b**) Quantification of the percentage of WT and ARF3 mutant cells

showing different classes of phenotypes as indicated in the legend (compact and expanded: clustered signal visible at the PN region and with a ratio between COP-I area/nucleus area <- 0.25 or > 0.25, respectively). N of cells = 18 (WT); 26 (K127E, compact vs. diffused ****p<0.0001, compact vs. expanded ****p<0.0001); 16 (L12V/D67V, compact vs. diffused ****p<0.0001); 18 (T32N); 15 (D93N, compact vs. expanded ***p=0.0007) and 15 (P47S, compact vs. expanded **p=0.011). Two-sided Chi-square's test in 2x2 contingency table is used to assess statistical significance. Source data are provided as a source data file.

Figure 6. Internalized Tfn accumulates in the perinuclear region and in Rab5+ endosomes of COS-1 cells expressing ARF3^{K127E} and ARF3$^{L12DV/D67V}$ (a) Maximum intensity confocal z-projections showing the distribution of Tfn-488 (black dots) upon 30 min of incubation in COS-1 cells expressing mCherry-tagged ARF3^{WT} and all identified mutants. Red circle indicates Tfn signal at the perinuclear region (PN). Outlines (black in a and yellow in c) depict the boundaries of representative transfected cells. In a the black and white images are rendered by inverting the original LUT in Fiji and nuclei are pseudo-colored (purple) in the images. The images are representative of two independent experiments. (**b-b'**) Incidence of cells showing "clustered", "semi-clustered" or "dispersed" Tfn staining (b) and the ratio of the cells (%) showing "clustered" Tfn phenotype normalized by not-transfected cells (NT) with the same phenotype (b', internal control). N of cells = 42 (WT); 22 (K127E, ****p<0.0001); 33 (L12V/D67V, ***p=0.0002); 31 (P47S); 26 (D93N); and 25 (T32N). Data are expressed as mean ± SEM (b,b') of three (WT) and two (all the other mutants) independent experiments. (**c**) Maximum intensity confocal z-projections showing COS-1 cells expressing ARF3^{WT} and all identified mutants, incubated with Tfn-488 for 30 min followed by immunostaining against Rab5 (marker of early endosomes). For all the panels single channels (ARF3mCherry: gray, Tfn-488: magenta, Rab5: green), the merge showing the co-localization between Tfn and Rab5 is shown. The insets in the white square show a zoom on the PN co-localization signal. Nuclei are stained with DAPI. The images are representative of cells from a single experiment. (**d**) Colocalization analysis showing the spatial co-occurrence of Tfn and Rab5+ signals at the PN region in the z-stacks analyzed, n of cells = 13 (WT; K127E **** p<0.0001; T32N), 16 (L12V/D67V, **p=0.0016; D93N), 21 cells (P47S). The fraction (%) of Tfn^{+}

signal co-localized with Rab5$^+$ vesicles at the PN (thresholded Mander's coefficient M1) is reported as box-and-whisker with median (middle line), 25th–75th percentiles (box), and min-max values (whiskers) of a single experiment. All the data points and the mean ("+") are also shown. Two-sided Chi-square's test in a 2×2 contingency table (semi-clustered and dispersed vs. clustered, b), One-way ANOVA followed by Dunnett's multiple comparison post hoc test (b', d) are used to assess the statistical significance. Source data are provided as a Source Data file.

Figure 7. Expression of mutant ARF3 and downregulation of endogenous *arf3* induce distinct phenotypes in zebrafish. (**a**) Experimental strategy in zebrafish models. Injected with WT and mutant ARF3 at 1 cell stage and phenotyped at different stages. (**b-b'**) Images and close-ups of ARF3^{WT} and ARF3^{K127E} expressing embryos at 24 hpf, co-injected with GFP-CAAX and Phenol-Red (dashed circle depicts cephalic region). (**c**) Bright-field images of embryos expressing WT and mutant ARF3. The images are representative of embryos from two (b,b') and five (c) independent batches. (**c'**) Embryo survival, n of embryos = 246, 114, 53, 86, 85, 161, 114 (not injected, WT, K127E, *p=0.03, L12V/D67V, P47S, D93N, T32N) from pooled batches. (**c''**) Incidence of gross phenotypes at 24 hpf (classes: I, II=yellow arrows, III, IV=gray and black arrows, respectively), n of embryos = 132 (not injected); 69 (WT); 21 (K127E, ****p<0.0001); 58 (L12V/D67V, *p=0.02); 45 (P47S, *p=0.03); 86 (D93N, **p=0.0018); 64 (T32N, ****p<0.0001). Data are expressed as mean ± SEM of four (not injected, WT), three (D93N) and two (K127E, L12V/D67V, P47S, T32N) independent batches. (**d-d''**) Bright field images (d) and phenotype incidence at 24hpf and 48 hpf of *arf3a/arf3b* MO-injected embryos (d',d''). Respectively, in d' and d'' n of embryos = 50, 48 (not injected); 25, 22 (MO 0.4 mM, ***p=0.0002, ****p<0.0001); 31, 27 (MO 0.6 mM ****p<0.0001); 21, 17 (MO 0.8 mM, ****p<0.0001) of one batch. (**e-e''**) Bright-field images (e) and phenotype incidence at 24hpf and 48hpf (e',e'') of *arf3a/arf3b* MO-injected embryos (0.6mM) -/+ ARF3^{WT} mRNA. The images in d and e are representative of embryos of one batch. Respectively in e' and e'', n of embryos = 47 (not injected); 22, 18 (MO 0.6 mM, ****p<0.0001); 17,15 (MO 0.6 mM + ARF3WT, **p=0.0091 in e'') of one batch. (**f**) Phenotype worsening index at 48 hpf (fold-change) for ARF3 mutants (severe + deceased) compared to controls (co-injected with *arf3*

MO). In the scatter plot the values <=0 (green) are found in the "alleviation window" depicted with a green shading. Dots represent the "worsening index" for each experiment, calculated by dividing the percentage of severely diseased fish (class IV-V) in "MO+" condition by the same percentage obtained in "MO-"condition of two (K127E, L12V/D67V, P47S, T32N) or three (D93N) independent batches. The mean effect of MO for each mutation is also shown as bar graph. N of embryos = 21 and 36 (K127E – and + MO *p=0.0307); 58 and 47 (L12V/D67V – and +MO, **p=0.0068); 45 and 54 (P47S – and +MO); 86 (D93N + and - MO, ***p=0.0004); 64 and 35 (T32N – and + MO, *p=0.0370). Data in the bar graphs are expressed as a mean ±SEM of two independent batches. Survival is assessed by Log-Rank (Mantel –Cox) test (c'), Two-sided Chi-square's test in a 2×2 contingency table (class II, III and IV vs. I in c'', d',d'', e',e'') or Two-sided One sample t-test (class III/ IV/V vs. I in f) testing null hypothesis H_0, represented by the expected mean value of the control population, are used to assess statistical significance. Source data are provided as a Source Data file.

Figure 8. Occurrence of microcephaly and reduced brain volume in zebrafish expressing a subset of ARF3 mutants. (a) Bright-field images of the head (purple dashed line) in fish expressing WT and mutant ARF3 at 48 hpf (the inset for $ARF3^{K127E}$ documents a severe case). The images are representative of embryos from two independent batches. (**b-b'**) Head area quantification at 48hpf (b) and 4.5 dpf (b'). In b, set 1: n of embryos = 25 (not injected), 23 (WT); 22 (K127E, ***p=0.0002) and 25 (L12V/D67V, *p=0.0106) of one batch; set 2: n of embryos = 29 (WT);; 28 (P47S); 30 (D93N); 29 (T32N). in b', n of embryos = 30 (not injected); 30 (WT); 27 (P47S); 30 (D93N, ***p=0.0006) and 28 (T32N) of one batch. Data are expressed as box-and-whisker with median (middle line), 25th–75th percentiles (box), and min-max values (whiskers). All the data points and the mean ("+") are also shown. (**b''**) Schematics of the brain volume reduction in human patients harboring a subset of ARF3 mutants and in zebrafish models generated in this study. The human brain in the illustration was created with BioRender.com and modified using Illustrator (Adobe). A summary of OFC and brain malformations data from patients in this study are depicted below (no sign of brain malformation (-), mild (+), moderate (++) and severe (+++) malformations). (c) Volumetric reconstructions (c) and anterior brain volume (white dashed line) from live confocal acquisitions from whole brains of 48hpf *Tg(NBT:dsRed)* fish injected with

mRNA encoding WT and ARF3 mutants. The images are representative of embryos from two independent batches for WT, K127E and L12V/D67V and from one batch for the other mutants. OT: optic tectum, Ce: cerebellum, Fb: forebrain, Mb: midbrain, Hb: hindbrain. (c') Quantification of the brain volume. Set 1: n of embryos = 4 (WT); 4 (K127E, *p=0.0163) from one batch; set 2: n of embryos = 3 (WT); 3 (L12V/D67V, ** p=0.0029); 4 (P47S, *p = 0.0350 and D93N, ***p=0.0010) of one batch. Data are expressed as mean ± SEM. Different datasets for the same measurement are shown in adjacent plots with the internal WT control for each set, not injected controls between batches are not significantly different. One-way ANOVA followed by Dunnett's multiple comparison *post hoc* test (b, left panel; c', right panel), Krustal-Wallis followed by Dunn's multiple comparison *post hoc* test (b, right panel; b'), unpaired t-test with Welch's correction (c', left panel) are used to assess statistical significance. Source data are provided as a source data file.

Figure 9. Increased number of cells in early mitosis and cell death within the developing forebrain of zebrafish expressing a subset of ARF3 mutants (**a**) Schematics of the forebrain (Fb, gray) proliferative zone (pz, cyan) and a confocal scan of the ventral Fb in zebrafish expressing $ARF3^{WT}$ (dashed white circle) showing proliferative and mitotic cells (PCNA and pH3 staining in red and cyan, respectively). Mb: midbrain, Hb: hindbrain (**b**) Maximum intensity *z*-projections from a subset of confocal sections showing pH3+ mitotic cells within the ventral Fb (vFb) in zebrafish expressing WT and mutant ARF3. The images are representative of embryos from one batch. Dashed white line indicates the Fb ventricle, insets show zooms on pH3+ cells. Arrowheads indicate examples of pH3+ cells in different stages of mitosis: early mitosis (purple); metaphase (green) and late mitosis (blue). (**c**) Quantification of the total number of $pH3^+$ cells in pz, n of embryos = 5 (WT and K127E, * p= 0.0217) of one batch. Data are expressed as box-and-whisker with median (middle line), 25th–75th percentiles (box), and min-max values (whiskers). All the data points and the mean ("+") are also shown. (**d,e**) Incidence of $pH3^+$ cells in the different mitosis stages. N of cells = 111 and 110 (WT); 61 (K127E, early mitosis *vs* metaphase *p=0.0168, early *vs* late mitosis ***p=0.0003); 88 (L12V/D67V, early mitosis *vs* metaphase *p=0.0115, early *vs* late mitosis ****p<0.0001); 75 (D93N, early mitosis *vs* metaphase **p=0.0028);

110 (P47S); 109 cells (T32N, early mitosis *vs* metaphase *p=0.0267, early *vs* late mitosis **p=0.0069) from 5 embryos of one batch. Data are expressed as mean ± SEM. In c and e different datasets for the same measurement are shown in adjacent plots with the internal WT control for each set. (**f**) Maximum intensity *z*-projections of the ventral brain stained with the acridine orange (AO). The black and white images are rendered by inverting the original LUT in Fiji. The images are representative of embryos from two independent batches. Orange arrowheads indicate specific staining. vFb pz, ventricle, eyes and olfactory epithelium (OE) are outlined for morphological guidance, * indicates eyes with pigmentation background. (**g**) Quantification of the number of AO+ spots. N of embryos =6 (WT); 5 (K127E, *p=0.0163, *p=0.0461 for upper and lower graphs, respectively); 6 (L12V/D67V, *p=0.0109); 6 (P47S, **p=0.0017 and D93N, *p=0.0387) of one batch. Data are expressed as box-and-whisker with median (middle line), 25th–75th percentiles (box), and min-max values (whiskers). All the data points and the mean ("+") are also shown. Two-sided Chi-square's test in a 2×2 contingency table (e), One-way ANOVA followed by Dunnett's (c and g, upper graph) or Kruskal-Wallis followed by Dunn's (g, lower graph) *post-hoc* tests are used to assess statistical significance. Source data are provided as a source data file.

Figure 10. Aberrant ARF3 function causes axial defects with notochord curvatures and defective axes formation in zebrafish. (**a**) Notochord curvatures of variable severity (purple angles schematics) and bright filed images of WT and mutant ARF3 expressing fish at 30 hpf. The images are representative of embryos from three (WT, K127E and L12V/D67V), two (P47S) and one batch (other mutations). (**b**) Rose diagrams showing notochord angles, n of angles = 17 (WT); 49 (K127E); 32 (L12V/D67V); 31 (P47S); 35 (D93N) and 38 (T32N) pooled from a total n of embryos indicated below (c). Mean vector (μ) ± circular SD are shown. Dark and light violet shadings in the rose diagrams represent mild and severe classes of notochord curvatures, respectively. (**c**) Incidence of embryos with mild or severe notochord curvatures, set 1: n of embryos = 9 (not injected); 17 (WT); 15 (K127E, ****p<0.0001) and 11 (L12V/D67V, ***p=0.0005) of three independent batches; set 2: n. of embryos = 13 (WT); 28 (P47S); 19 (D93N, ***p=0.0003) and 24 (T32N, ****p<0.0001) of one batch. Data are expressed as mean ± SEM (set 1) or mean (set 2). (**c'**) Quantification

of the number of notochord curvatures per embryo from one batch (same n of embryos as in c): K127E, ****p<0.0001; L12V/D67V, **p=0.0015; D93N, **p=0.0022 and T32N, ****p<0.0001. (**d**) Schematics of *Krox20* and *MyoD* expression at 15 hpf. Black square brackets indicate AP and ML axes. R3 and R5: rhombomeres 3 and 5. (**e**) Bright field images showing *Krox20* and *MyoD in situ* mRNA staining (insets show severe cases). The images are representative of embryos from two independent batches for WT, K127E and L12V/D67V and from one batch for the other mutations. (**f**) Quantification of AP embryo extension, set 1: n of embryos = 10 (not injected); 10 (WT); 10 (K127E, ****p<0.0001); 10 (L12V/D67V, **p=0.0078); set 2: n of embryos 18 (WT); 22 (P47S, *p=0.0169); 24 (D93N, * p=0.0207) and 16 (T32N, ***p=0.0002) of one batch. In c' and f data are expressed as box-and-whisker with median (middle line), 25th–75th percentiles (box), and min-max values (whiskers). All the data points and the mean ("+") are also shown. (**g**) Incidence of fish with different convergence and extension (CE) index values (same n of embryos as in f) ****p<0.0001 (K127E and L12V;D67V), **p=0.0015; *p=0.0251 (D93N), *p=0.039 (T32N). Different datasets for the same measurement are shown in adjacent plots with the internal WT control for each set. Not injected controls between batches are not significantly different. Non-parametric Kruskal-Wallis followed by Dunn's multiple comparison *post hoc* test (c', f), Two-sided Chi-square's test in 2x2 contingency table (c, g, normal *vs.* phenotype) are used. Source data are provided as source data file.

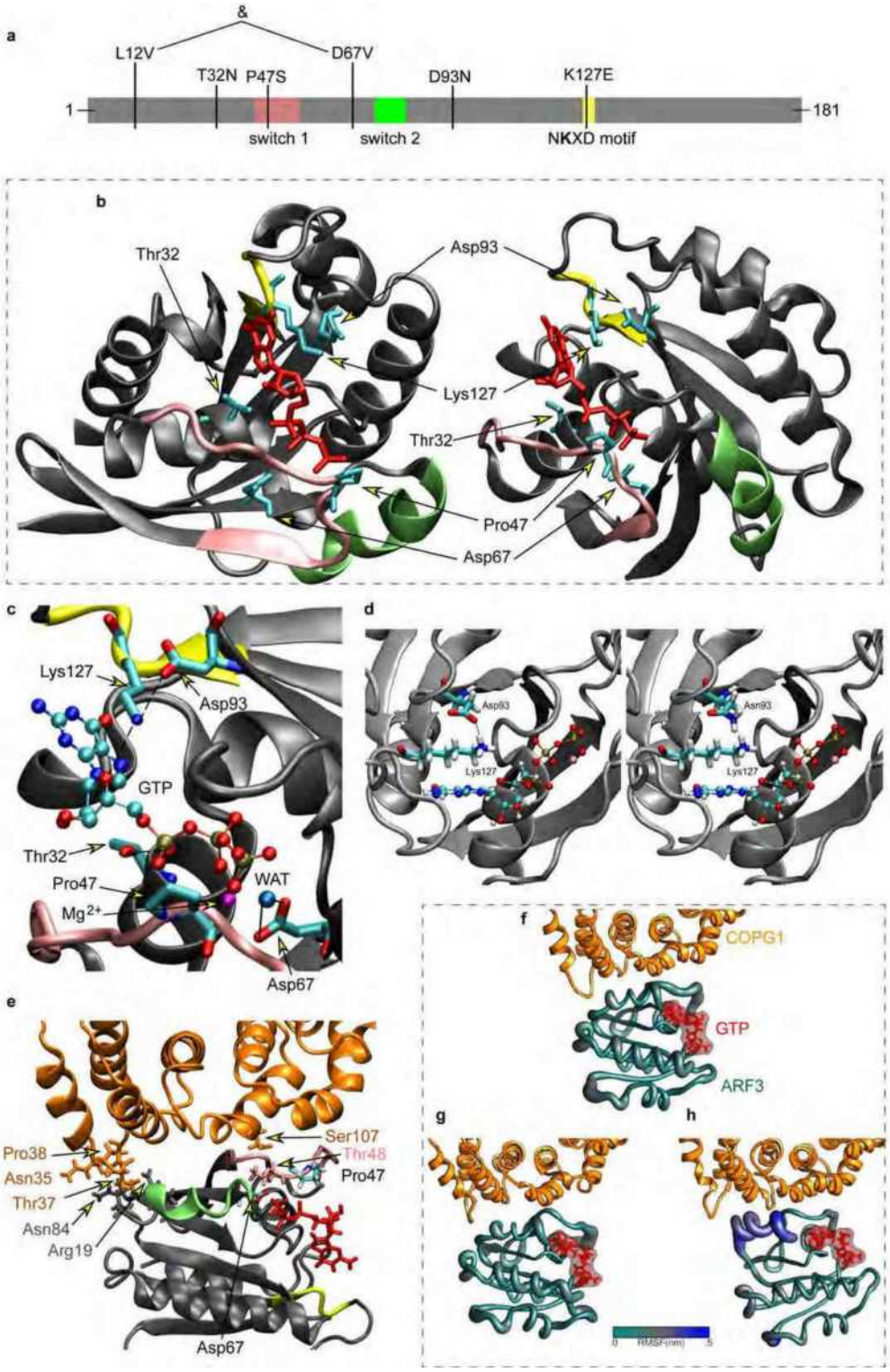
a
&
L12V
D67V
T32N
P47S
D93N
K127E
1
181
switch 1
switch 2
NKXD motif
b
Thr32
Asp93
Lys127
Thr32
Pro47
Asp67
c
Lys127
Asp93
GTP
Thr32
Pro47
WAT
Mg2+
Asp67
d
Asp93
Lys127
Asn93
Lys127
e
Ser107
Pro38
Thr48
Asn35
Pro47
Thr37
Asn84
Arg19
Asp67
f
COPG1
GTP
ARF3
g
h
RMSF(nm)

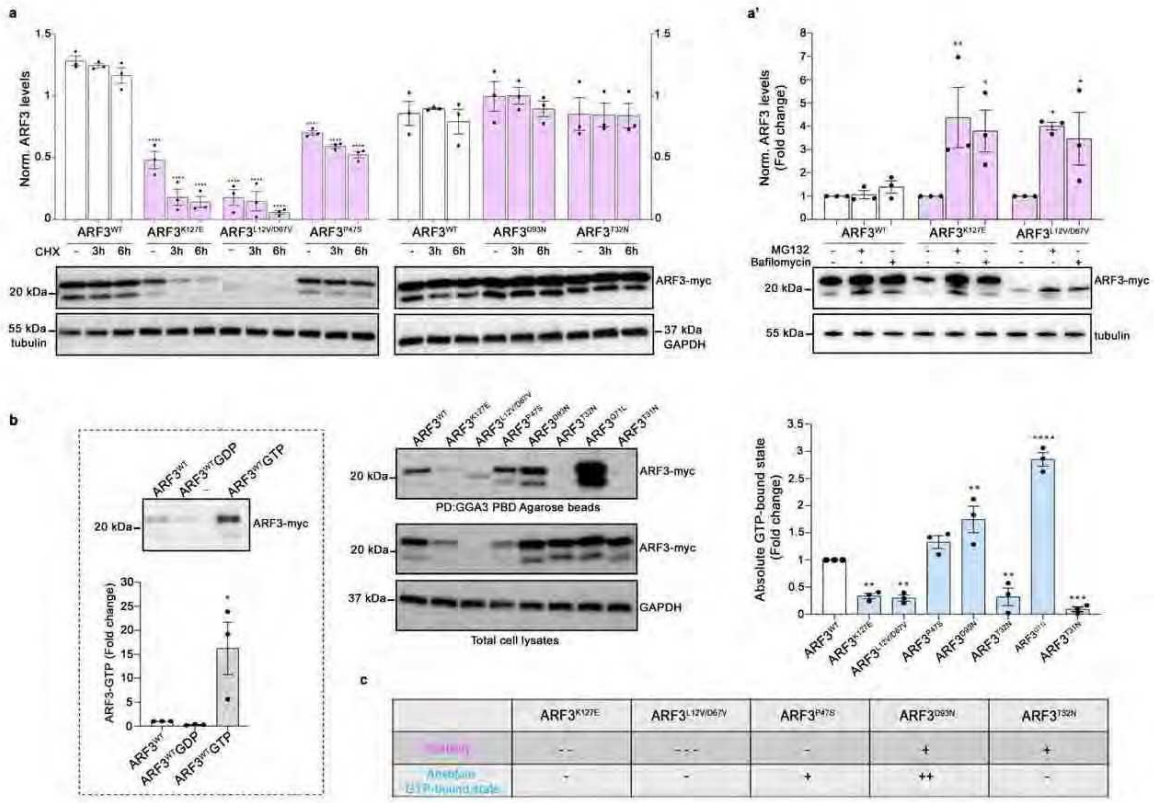

	ARF3K127E	ARF3L12V/D67V	ARF3R47S	ARF3D93N	ARF3T32N
Stability	- -	- - -	-	+	+
Amount GTP-bound state	-	-	+	++	-

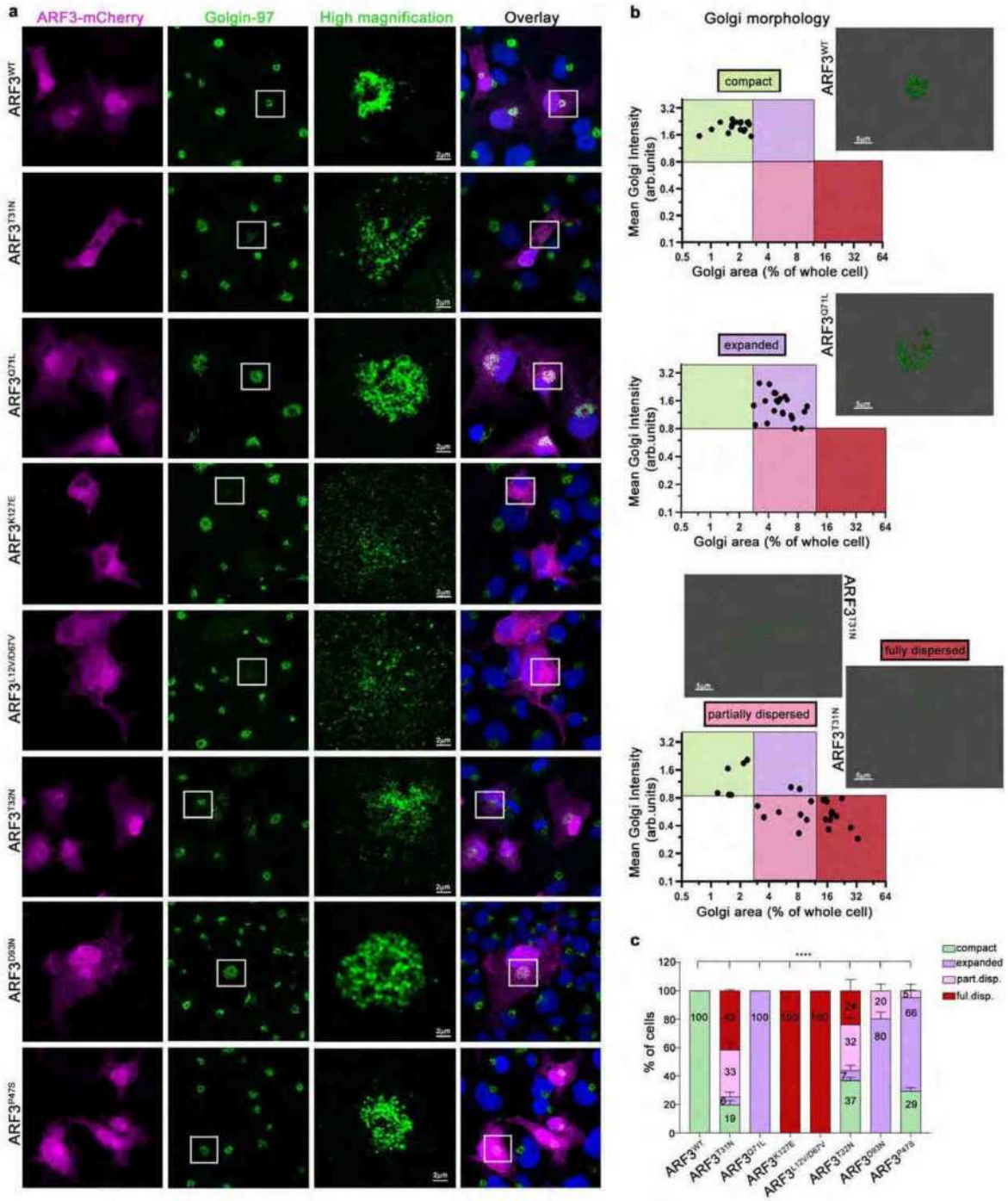
a
ARF3-mCherry
Golgin-97
High magnification
Overlay
ARF3WT
ARF3T31N
ARF3Q71L
ARF3K127E
ARF3L12V/D67V
ARF3T32N
ARF3D93N
ARF3P47S
b
Golgi morphology
compact
expanded
partially dispersed
fully dispersed
Mean Golgi Intensity (arb.units)
Golgi area (% of whole cell)
c
% of cells
compact
expanded
part.disp.
ful.disp.

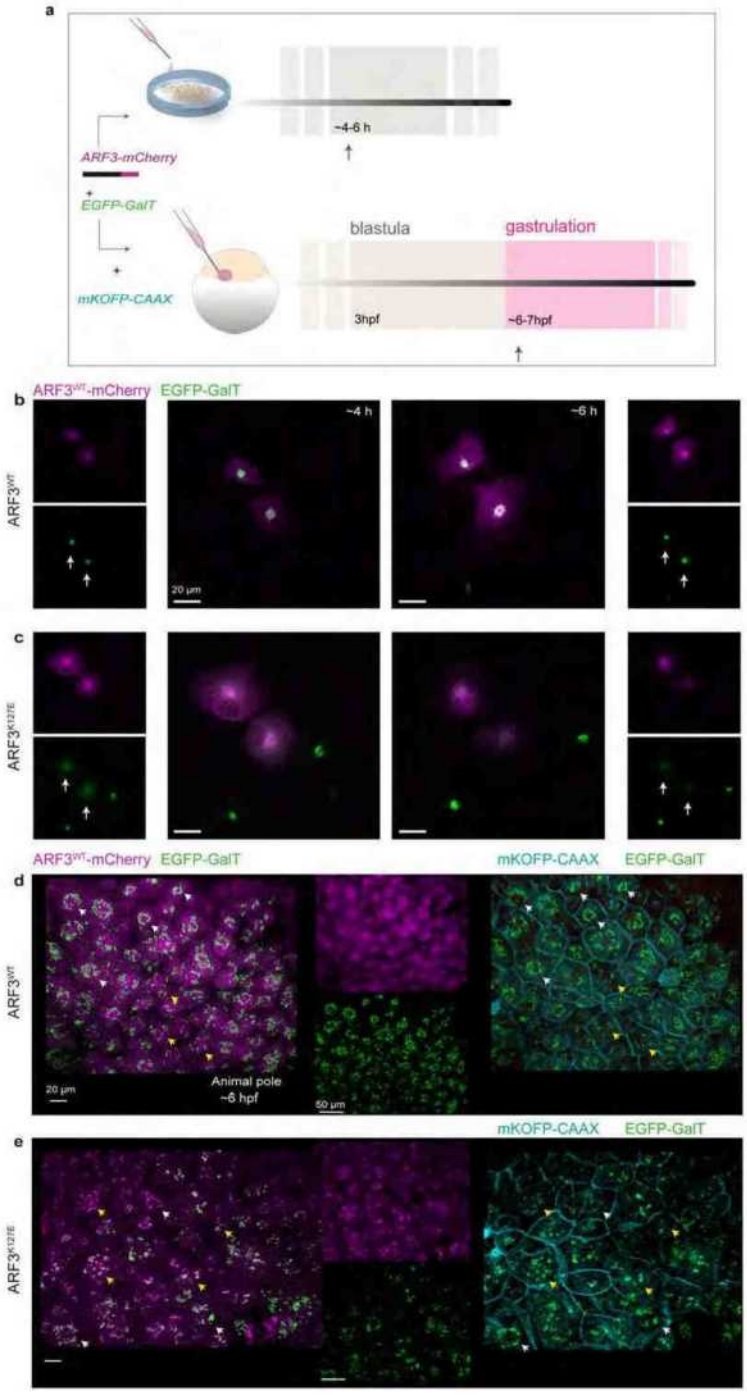
a
~4-6 h
ARF3-mCherry
EGFP-GalT
mKOFP-CAAX
blastula
gastrulation
3hpf
~6-7hpf
b
ARF3WT-mCherry EGFP-GalT
ARF3WT
~4 h
~6 h
20 µm
c
ARF3K12TE
d
ARF3WT-mCherry EGFP-GalT
mKOFP-CAAX EGFP-GalT
ARF3WT
20 µm
Animal pole
~6 hpf
50 µm
e
mKOFP-CAAX EGFP-GalT
ARF3K12TE

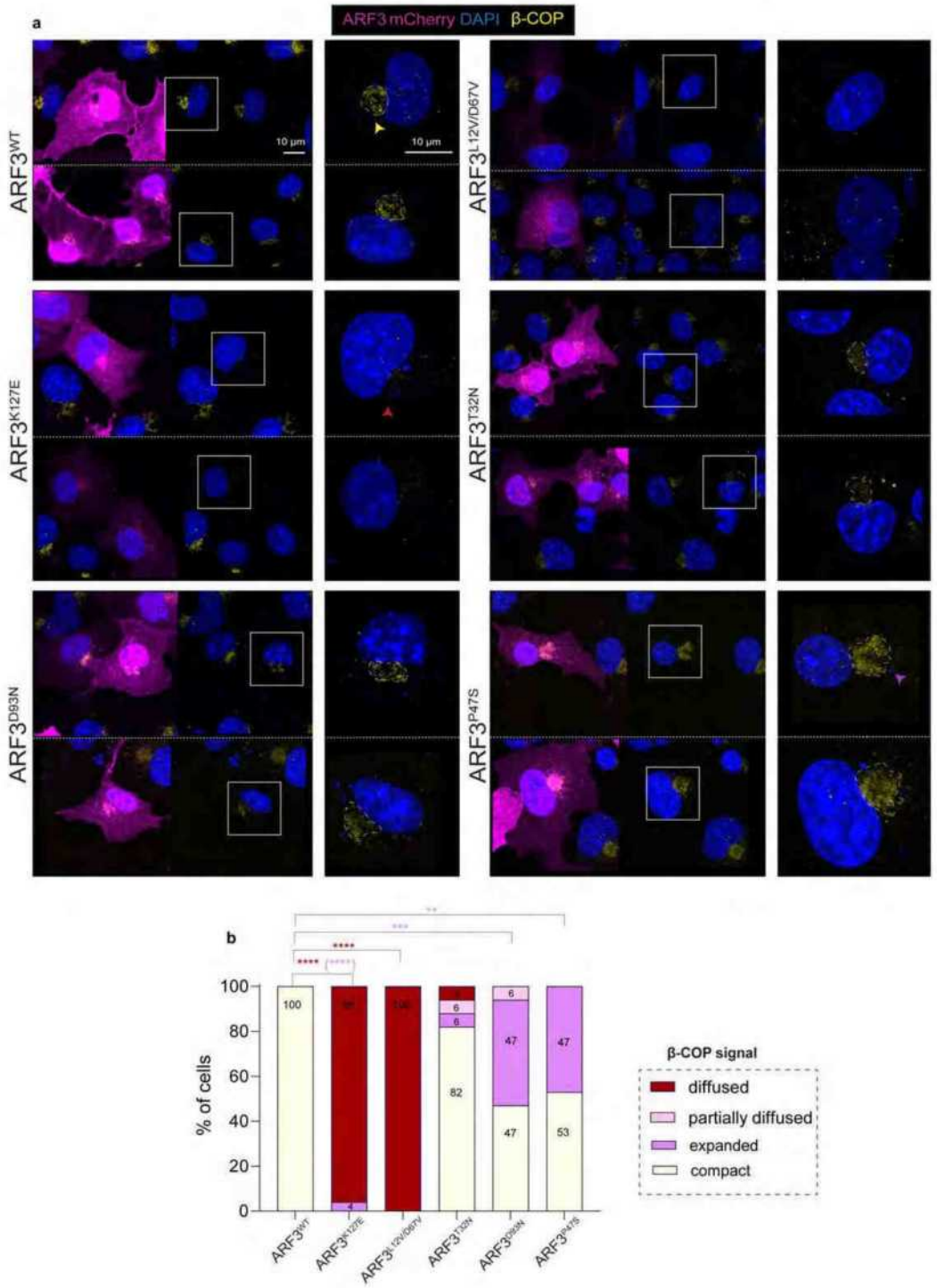
a
ARF3 mCherry DAPI β-COP
ARF3WT
ARF3L12V/D67V
ARF3K127E
ARF3T32N
ARF3D93N
ARF3P47S
10 µm
10 µm
b
% of cells
100
80
60
40
20
0
β-COP signal
diffused
partially diffused
expanded
compact
ARF3WT
ARF3K127E
ARF3L12V/D67V
ARF3T32N
ARF3D93N
ARF3P47S

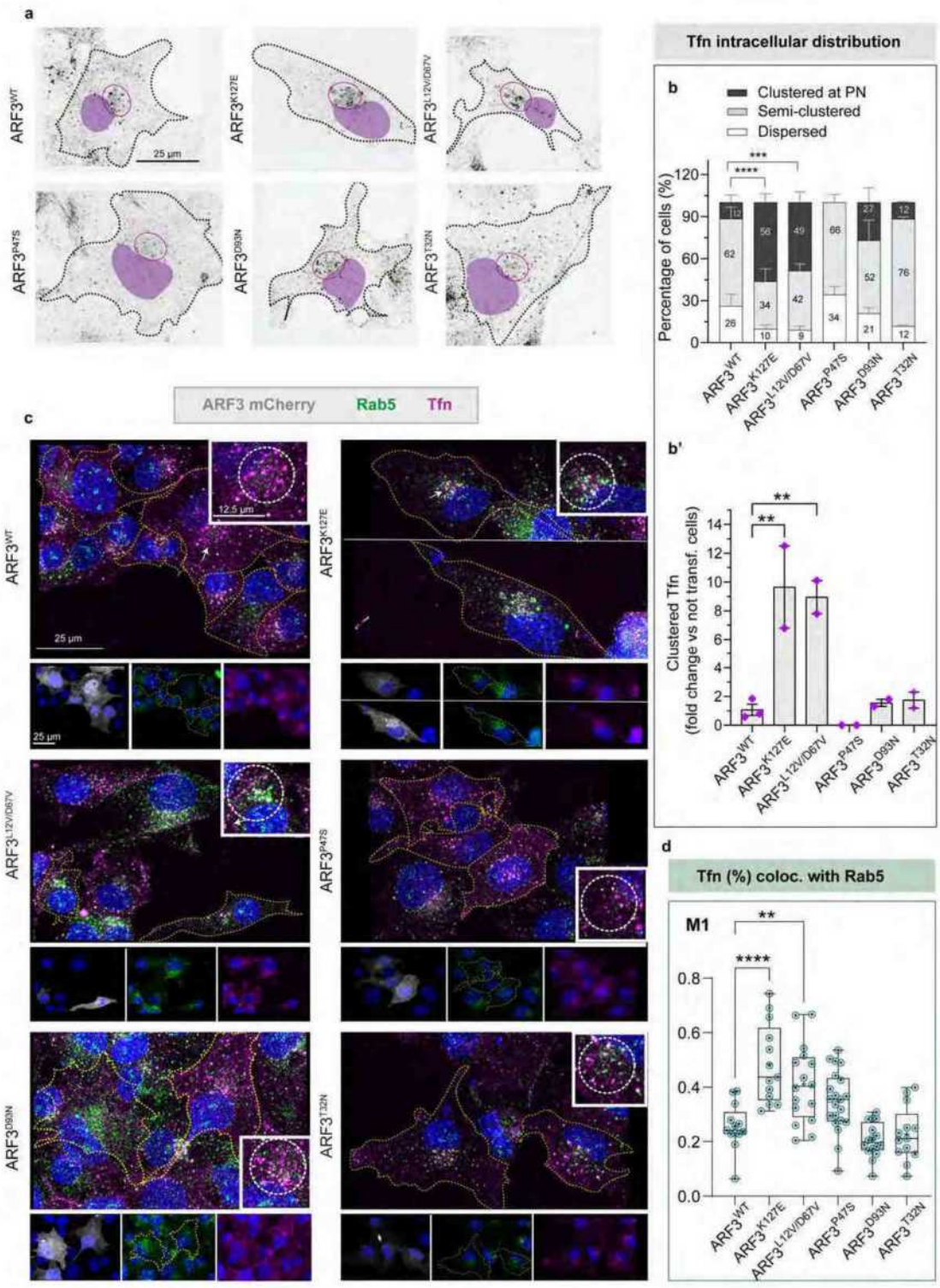
a
ARF3WT
ARF3K127E
ARF3L12V/D67V
ARF3P47S
ARF3D93N
ARF3T32N
25 µm
Tfn intracellular distribution
b
Clustered at PN
Semi-clustered
Dispersed
Percentage of cells (%)
b'
Clustered Tfn
(fold change vs not transf. cells)
ARF3 mCherry
Rab5
Tfn
c
12.5 µm
25 µm
d
Tfn (%) coloc. with Rab5
M1

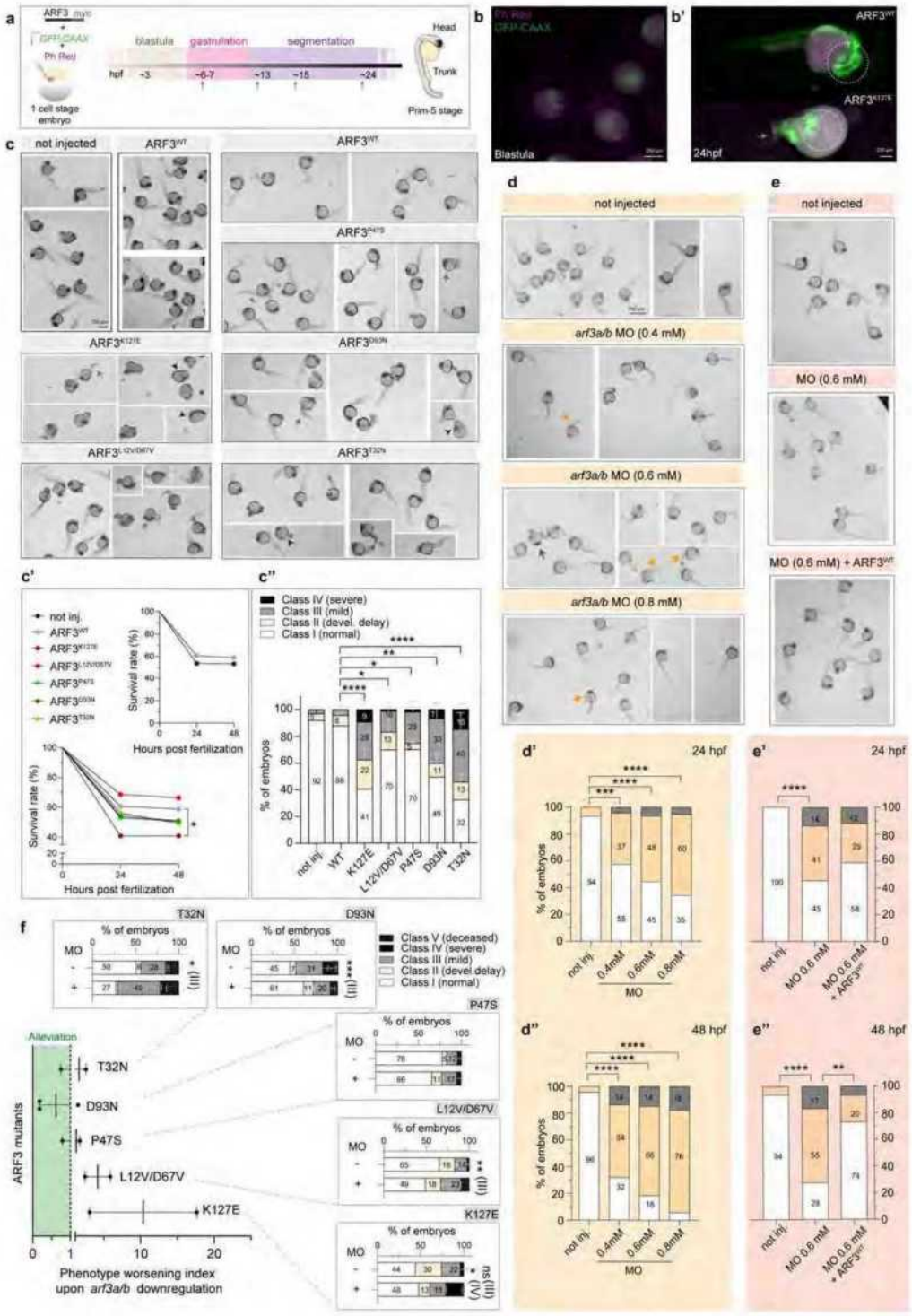
a
ARF3 (myc)
GFP-CAAX
Ph Rel
1 cell stage embryo
blastula
gastrulation
segmentation
hpf
~3
~6-7
~13
~15
~24
Head
Trunk
Prim-5 stage
b
Ph Rel
GFP-CAAX
Blastula
b'
ARF3WT
ARF3K127E
24hpf
c
not injected
ARF3WT
ARF3P47S
ARF3K127E
ARF3D93N
ARF3L12V/D67V
ARF3T32N
c'
not inj.
ARF3WT
ARF3K127E
ARF3L12V/D67V
ARF3P47S
ARF3D93N
ARF3T32N
Survival rate (%)
Hours post fertilization
c''
Class IV (severe)
Class III (mild)
Class II (devel. delay)
Class I (normal)
% of embryos
not inj.
WT
K127E
L12V/D67V
P47S
D93N
T32N
d
not injected
arf3a/b MO (0.4 mM)
arf3a/b MO (0.6 mM)
arf3a/b MO (0.8 mM)
e
not injected
MO (0.6 mM)
MO (0.6 mM) + ARF3WT
d'
24 hpf
% of embryos
not inj.
0.4mM
0.6mM
0.8mM
MO
e'
24 hpf
not inj.
MO 0.6 mM
MO 0.6 mM + ARF3WT
d''
48 hpf
e''
48 hpf
f
T32N
D93N
% of embryos
MO
Class V (deceased)
Class IV (severe)
Class III (mild)
Class II (devel.delay)
Class I (normal)
P47S
L12V/D67V
K127E
Alleviation
ARF3 mutants
T32N
D93N
P47S
L12V/D67V
K127E
Phenotype worsening index upon arf3a/b downregulation

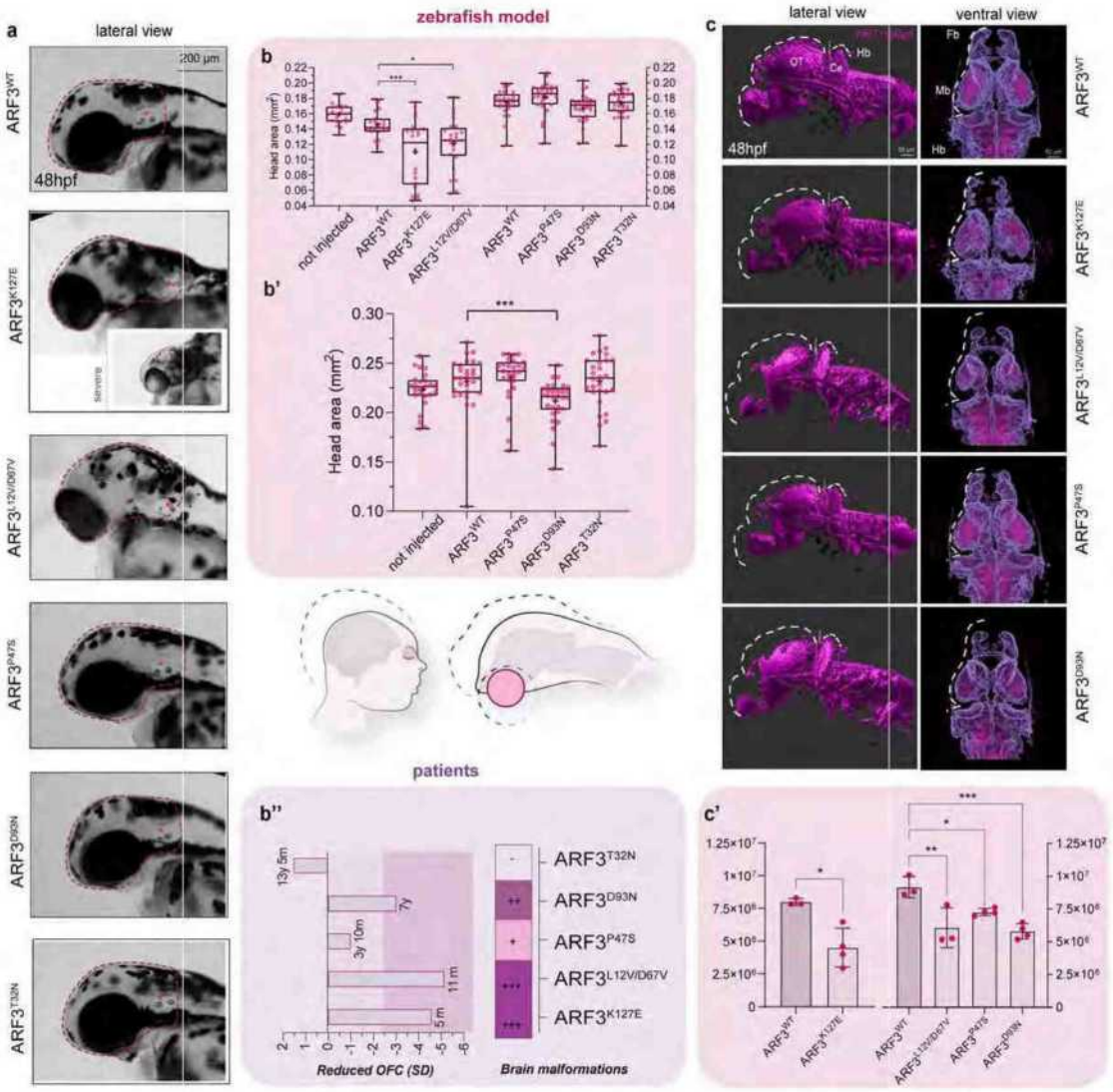
a
lateral view
200 µm
48hpf
ARF3WT
ARF3K127E
ARF3L12V/D67V
ARF3P47S
ARF3D93N
ARF3T32N
zebrafish model
b
Head area (mm²)
not injected
ARF3WT
ARF3K127E
ARF3L12V/D67V
ARF3P47S
ARF3D93N
ARF3T32N
b'
Head area (mm²)
c
lateral view
ventral view
48hpf
OT
Hb
Fb
Mb
patients
b''
13y 5m
7y
3y 10m
11 m
5m
Reduced OFC (SD)
Brain malformations
c'

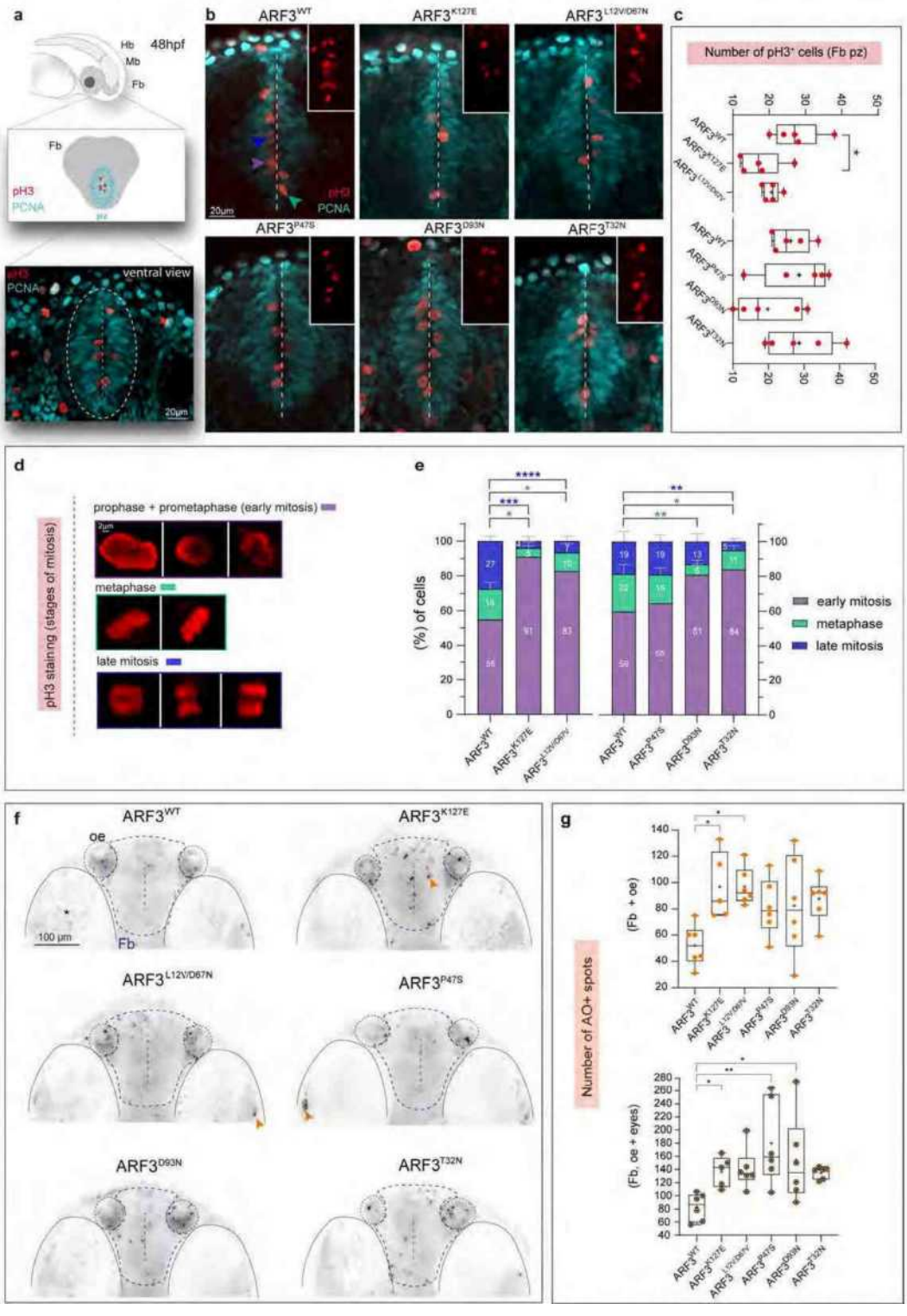
a
Hb
Mb
Fb
48hpf
pH3
PCNA
pz
ventral view
20µm
b
ARF3WT
ARF3K127E
ARF3L12V/D67N
ARF3P47S
ARF3D93N
ARF3T32N
c
Number of pH3+ cells (Fb pz)
d
pH3 staining (stages of mitosis)
prophase + prometaphase (early mitosis)
metaphase
late mitosis
e
(%) of cells
early mitosis
metaphase
late mitosis
f
oe
100 µm
Fb
g
Number of AO+ spots
(Fb + oe)
(Fb, oe + eyes)

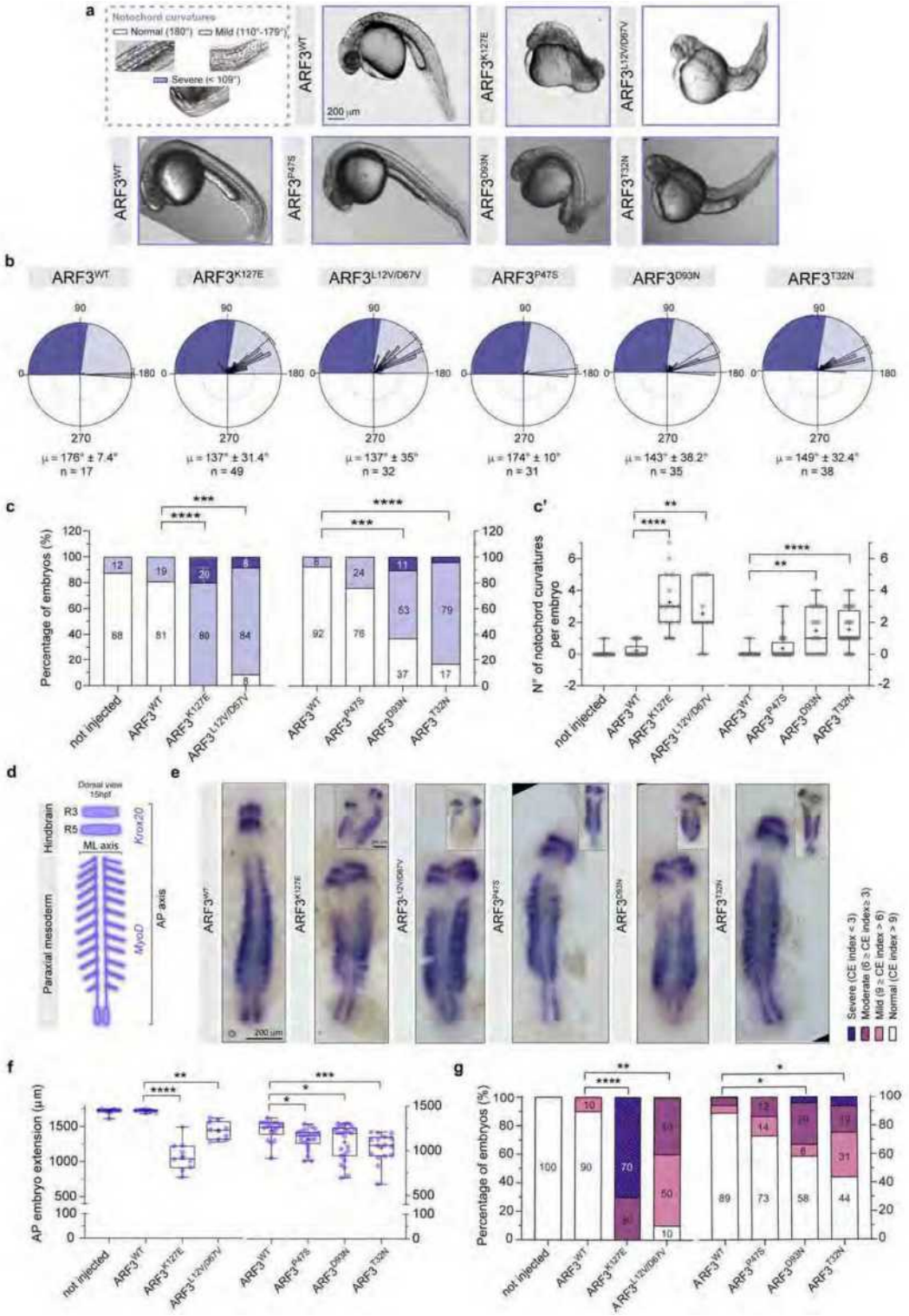
a
Notochord curvatures
Normal (180°)
Mild (110°-179°)
Severe (< 109°)
ARF3WT
ARF3K127E
ARF3L12V/D67V
ARF3P47S
ARF3D93N
ARF3T32N
200 µm
b
μ = 176° ± 7.4°
n = 17
μ = 137° ± 31.4°
n = 49
μ = 137° ± 35°
n = 32
μ = 174° ± 10°
n = 31
μ = 143° ± 38.2°
n = 35
μ = 149° ± 32.4°
n = 38
c
Percentage of embryos (%)
not injected
c'
N° of notochord curvatures per embryo
d
Dorsal view 15hpf
Hindbrain
R3
R5
ML axis
Krox20
MyoD
Paraxial mesoderm
AP axis
e
Severe (CE index < 3)
Moderate (6 ≥ CE index> 3)
Mild (9 ≥ CE index > 6)
Normal (CE index > 9)
f
AP embryo extension (µm)
g
Percentage of embryos (%)

3 DISCUSSION

RAS GTPases are molecular switches and cycle between active GTP-bound and inactive GDP-bound states [215]. In their active state, RAS GTPases associate with a multitude of effector proteins to induce a network of nuclear and cytoplasmic signaling pathways [44]. The RAS superfamily regulates various cellular processes, including proliferation, differentiation, migration, and apoptosis, in response to different extracellular stimuli [216]. The RAS/MAPK pathway is one of the most studied signaling cascades due to its essential role in many cellular functions, which are critical for normal development [217]. Mutations in genes that encode components of the RAS/MAPK pathway have been implicated in cancer and RASopathies [218]. We succeeded in biochemically characterizing ARF3 GTPases variants, as well as a HRAS mutant, that was linked with neurodegeneration disorders and Costello syndrome, respectively, to understand explicitly the molecular mechanisms underlying these disorders.

Decades of research on RHO GTPases have revealed outstanding characteristics such as diversity in their regulators, a wide range of their cellular targets, and substantial cross-talk and harmony, that lie beneath GTPases signal transduction pathways [219]. We were able to evaluate RHOGDI specificity for different RHO GTPases and proposed a detailed sketch for the GDI-RAC interaction and RAC displacement from the membrane.

The selectivity criteria of IQGAP1/2 proteins as downstream effectors for certain RHO GTPases were investigated using structural, mutational, and biochemical analyses. Furthermore, we investigated the other domains of IQGAPs in their interactions with CDC42, to unveil more about the scaffolding function of these multi-domain proteins, as well as molecular details of dysregulated signaling pathways.

3.1 ELECTROSTATIC FORCES MEDIATE THE SPECIFICITY OF RHO GTPASE-GDI INTERACTION

Previously, it has been shown that RHO GTPases are released from the membrane by GDI, and create a reservoir of inactivated RHO GTPases in the cytosol [206,220,221]. In addition, it has been demonstrated that non-prenylated RAC1 is incapable of binding GDI1, and GDI1 binds prenylated RAC1 and RHOA with a significantly higher affinity compared to non-prenylated RAC1 and RHOA [222,223].

Our study disclosed that the specific mode of GDI function only applies to a distinct subset of RHO GTPases, and we added additional details to the multi-step mechanism that promotes membrane extraction and the inhibition of RAC1 activation. We observed that both prenylated and non-prenylated RAC1 bind GDI1 in principally the same manner, and this is due to the specificity of GDIs for certain RHO GTPases, according to the data we obtained.

Our protein-protein interaction studies revealed that all three GDIs activities are nearly the same, and the slight difference in their affinity stems from variations in their cell-type specific expression patterns. GDI2 displayed a six-fold faster association rate constant for RAC2 in comparison to RAC1 and RAC3, and even in comparison to GDI1 and GDI3, GDI2 interacts with RAC2 slightly stronger. Under the same experimental conditions, we observed that all three GDIs demonstrated explicit specificity for RAC1, RAC2, RAC3, and RHOG, as well as RHOA. Several studies demonstrated that the mechanism of RHOGDI selective interaction with RHO GTPases is regulated by the interaction with certain receptors or post-translational modifications like SUMoylation, and phosphorylation [206,210,224,225].

However, our cell-free analyses indicate that there were potential gaps in the understanding of the selectivity of GDIs for RHO GTPases.

Analysis of sequence-structure-function relationships of RHO GTPase-RHOGDI interaction indicated that the C-terminal hypervariable region (HVR) of the RHO GTPases is an essential component that defines the specificity of GDIs activity. It has been shown that RAC1 with more positively charged residues (R/K) in its HVR is predominantly localized at the plasma membrane, however, CDC42 and RAC2 with a less positively charged HVR remain in the endomembrane [107]. The crystal structure of RAC1 and GDI uncovered that these positively charged residues in the HVR of RAC1 are positioned towards negatively charged residues in both the N-terminal arm and C-terminal Geranylgeranyl-binding domain of GDI1 [226]. Data from our kinetic analyses indicated that mutating the positively charged amino acids in RAC1 HVR to negatively charged residues results in the repulsion of the proteins and the hampering of the RAC1 and GDI1 interaction, as well as shifting the localization of RAC1 to the perinuclear structure. Considering RHOC with more positive charged residues and as a RHOGDI non-binder clarified that, in addition to the number of positive charges, the position of these basic residues in the C-terminal can change the fate of RHO GTPases interaction with RHOGDI.

Moreover, the substitution of negative charges for lysines or the deletion of N-terminal and C-terminal amino acids in GDI1 impeded the GDI1 interaction with both prenylated and non-prenylated RAC1. These findings confirm that the C-terminal Geranylgeranyl-binding domain and the N-terminal arm of GDI create an electrostatic pincer that grabs the RAC1 HVR and extracts the Geranylgeranyl moiety from the membrane.

Overall, we hypothesize that the GDI1 switch binding domain recognizes and interacts with switch regions of RAC1, then both the C-terminal Geranylgeranyl-binding domain and N-terminal arm of GDI1 initiate an electrostatic attraction towards the RAC1 hypervariable region and grab the RAC1 and steer it out of the membrane by locking the Geranylgeranyl moiety of RAC1 in the hydrophobic cavity of the Geranylgeranyl-binding domain of GDI1.

Deciphering the molecular basis underpinning RAC1 spatio-temporal regulation will help us to understand several diseases with the implication of RAC1 dysregulation and dysfunction, like cancer and neurodegeneration. Several pieces of evidence demonstrate that RHOGDIs is over-expressed in human cancers through dysregulation of RHO GTPases, and result in aggressive phenotypes, for instance, invasion and metastasis [227–229]. It is necessary to consider the cross-talk between RHOGDIs and several factors, such as phospholipids and other interacting proteins in a combined manner, to fully understand the molecular basis behind the disrupted RHOGDI-RHO GTPases interaction in the development of cancer.

In chapter V, we demonstrated our analyses on a generated pseudo-natural product called Rhonin, which is described as the first molecule ligand of RHOGDI1. We observed that Rhonin inhibits RHOGDI-mediated RAC1 extraction from liposomes. Moreover, Rhonin hindered RHOGDI-RAC1 Geranylgeranylated complex formation, by binding to RHOGDI. The wound healing assay demonstrated that Rhonin treatment changes the RHO GTPases localization from the plasma membrane to the endoplasmic membrane and inhibits cell migration.

Our findings provide a more complete picture to better understand the RAC1 extraction from the membrane promoted by GDI1 and highlight the effect of the RAC1 C-terminal region on its regulation and function.

3.2 Selectivity determinants of RHO GTPase binding to IQGAPs

IQGAPs are scaffold proteins, which are assigned to various subcellular sites and involved in multitudes of functions to guarantee the protein complex formation of several signaling molecules and ensure the specificity and efficiency of signal transduction [143]. RHO GTPases, in particular, CDC42 and RAC1 bind to IQGAP1 and assist IQGAP1 in its activities including intracellular adhesion [144,230]. However, the specificity of different IQGAP paralogs for various RHO GTPases remained unclear. In this study, we aimed to understand more accurately what criteria in RHO GTPases are crucial for IQGAP interaction.

We carried out a comprehensive interaction study for 14 RHO GTPases with the C-terminal 794 amino acids of IQGAP1 (IQGAP1 ^{C794}) and the C-terminal 795 amino acids of IQGAP2 (IQGAP2^{C795}) to clarify the selectivity determinants. The protein-protein interaction studies indicated that IQGAP1 and IQGAP2 bind selectively to CDC42 and RAC-like proteins. Although the switch regions have been described as the main binding sites, additional contact sites outside the switch regions are imperative for IQGAP binding. The switch regions are highly conserved in RHO GTPases, which are necessary but not sufficient for effector binding selectivity [135]. We compared the amino acid sequence of IQGAP binders versus IQGAP non-binders, and discovered four different hotspots, residues 25/26, 45/52, 74, and 85/88 are highly conserved and almost identical among IQGAP binders, yet vary in non-binders. These residues are enclosed to switch regions, positioned on the surface of the corresponding proteins, and are exposed for interaction. We checked the electrostatic properties of the selected hotspots and found out that they contain more negative net charges in IQGAP non-binders. The kinetic measurements showed that the mutation of these residues in CDC42 and RAC1-like proteins to equivalent residues to IQGAP non-binders like RHOA diminishes their binding affinity between 7- and 17-fold. These findings refer to the significance of these hotspots in RAC1 and CDC42 proteins binding to IQGAP.

To understand the located contacting regions between IQGAP1 and RAC1, we conducted a competitive binding assay, in which we analyzed the association of IQGAP1 with RAC1 in the presence and absence of an excess amount of RAC1 binding partners. Our competition assays revealed that IQGAP1 competes with DOCK2, p50GAP, and PAK1 to bind RAC1, which suggests that these proteins share an overlapping binding surface.

Overall, our study showed that additional distinct residues, besides those in switch regions, are required for RHO GTPases to enable them to associate with IQGAPs. Our study showed that the kinetic properties of IQGAP1 interaction with CDC42 and RAC1 are slightly different, and further analyses are needed to illuminate the correlation of these differences to their functional outcomes. IQGAPs modulate a broad spectrum of biological processes and they have become a drug target due to their regulatory role in cancer development.

Recently presented data from single molecule showed that IQGAP1 stabilizes the actin filaments, regulates the actin filament spatial organization, and also that the C-terminal half of IQGAP1 is required for full inhibition of actin filament growth [231]. Yet, the mechanistic framework for IQGAP interaction with CDC42 and RAC1 and the implication of these interactions in actin dynamics at the leading edge and cell migration requires further investigations.

3.3 CDC42-IQGAP INTERACTIONS SCRUTINIZED: NEW INSIGHTS INTO THE BINDING PROPERTIES OF THE GAP-RELATED DOMAIN

Like other multidomain proteins, IQGAPs use different domains to assemble various protein complexes at distinct cellular compartments [112,117]. For example, IQGAP1 interacts with actin filaments through its N-terminal CDH domain and IQ motifs interact with calmodulin [114,117,232]. It became widely accepted that the switch regions of CDC42 and RAC1 are associated with IQGAP1 GRD [54,145,233]. The published crystal structure of constitutively active CDC42 Q61L in complex with IQGAP2 GRD suggests that CDC42-IQGAP2 GRD binding is in a 4:2 stoichiometry [54]. That means two CDC42 proteins bind in a RASGAP interaction mode and the other two CDC42 proteins bind to extra domain sequences of GRDs [54]. However, different studies also showed that IQGAP RGCT mediates the high-affinity binding to switch regions of CDC42 and CDC42 can still bind to IQGAP1-ΔGRD [144,148,234]. To clarify this discrepancy in the CDC42-IQGAP interaction mode, we studied GRD interaction with CDC42 in detail through structural-functional analyses.

Our kinetic and equilibrium measurements demonstrated that both IQGAP1^{C794} and IQGAP2^{C795} (encompassing GRD, RGCT, and CT domain of IQGAP1 and 2, respectively) bind CDC42 mGDP- and mGppNHp-bound, yet with a higher affinity for mGppNHp-bound CDC42. Similar measurements indicated that IQGAP1 GRD and IQGAP2 GRD bind CDC42 with low affinity but in a nucleotide-independent manner. This data suggests that the RGCT domain associated directly with the switch regions of CDC42. To extend these findings, we evaluated the association of endogenous IQGAP1 full-length with purified CDC42 and RAC1 proteins. The pull-down analyses showed that IQGAP1 full-length binds both these GTPases, though binds weaker with the GDP-bound RAC1 and CDC42, than their GppNHp-bound forms.

Our equilibrium measurement data did not show a significant affinity loss for CDC42 variants carrying different mutations in switch I and II regions in interaction with GRD domains of IQGAP1 and 2. These findings propose that the association of CDC42 with IQGAP GRD is through other regions than switch regions.

Later, we tried to reveal the CDC42 contacting sites on IQGAP GRD by considering the CDC42 insert helix as its potential effector binding region. The kinetic data manifested that a mutation in the CDC42 insert helix results in a diminished GRD1 and CDC42 interaction, regardless of the nucleotide-bound states of CDC42 insert helix variants. Moreover, the pull-down results confirm that mutations in the CDC42 insert helix hinder IQGAP1 full-length binding. A recent study by Haspel *et al*. showed that the insert helix of CDC42 shows much larger conformational flexibility in GDP-bound CDC42 than in the GTP-bound form, and differences in conformational flexibility of GDP- and GTP-bound CDC42 Q61L are smaller [235]. Hence, we can consider the insert helix of CDC42 as a highly dynamic region, which even in its GDP-bound form does not lose its ability to bind to effectors.

Several previous studies suggested that CDC42 interaction is through the switch regions of this protein with the GRD domain of IQGAP [54,145]. One credible argument against these findings is using the constitutively active CDC42 variant Q61L, rather than using the CDC42 wild type. Therefore, we assessed IQGAP1 GRD binding to CDC42 Q61L in comparison to CDC42 wild type through equilibrium measurements and size exclusion chromatography (SEC). Our results confirmed that CDC42 Q61L binds IQGAP1 GRD and IQGAP2 GRD 50-fold stronger than the CDC42 wild type. In addition, the SEC analyses indicated that CDC42 Q61L and IQGAP1 GRD form a 2:1 stoichiometry, which is compatible with the previous

study for IQGAP2 GRD with CDC42 Q61L. However, our SEC data showed that the CDC42 wild type and IQGAP1 GRD form a 2:2 stoichiometry. The stoichiometric ratio for the wild-type form of a protein provides insights into the nature of protein interactions, which exist in a normal physiological state. It became clear that L61 is in direct contact with the GRD domain of IQGAP, since, unlike Q61, it is not involved in hydrogen bonding with a catalytic water molecule and is positioned toward the protein surface. Hence, CDC42 Q61L cannot be considered the best analog of CDC42 wild type, particularly in understanding the interaction network of downstream effectors.

The GRD domain of IQGAP does not show any RASGAP activity, even though there are structural similarities between the GRD and GAP domains of RASGAPs like GAP-334 and neurofibromin [145]. It would not be frugal for nature to create a GAP domain that acts only as an effector module and has a different mode of interaction than those true GAPs with GTP hydrolysis activity.

Overall, our findings verified 1st the role of IQGAP RGCT in mediating high-affinity binding to GTP-bound CDC42, and 2nd proposed the insert helix of CDC42 as the possible contacting site in interaction with the GRD domain of IQGAP. Further studies are needed to explain the significance of IQGAP GRD interaction with CDC42 in signal transduction and cellular processes.

3.4 Cutaneous manifestations in Costello syndrome: HRAS p. Gly12Ser affects RIN1-mediated integrin trafficking in immortalized epidermal keratinocytes

It was already known that GTP-bound HRAS binds RIN1 and enhances the activation of RAB5A GTPases and ABL1/2 tyrosine kinases, which are the two main signaling axes responsible for endosomal sorting and cytoskeletal dynamics [236–238]. To understand the molecular pathophysiology for dermatological findings in Costello syndrome, we examined the role of the HRAS-RIN1 signaling node, in the presence of constitutively active HRAS variants.

In the presence of HRAS wildtype, RIN1 as a GEF showed a 34-fold increase in its nucleotide exchange rate for RAB5A. The RIN1 nucleotide exchange rate for RAB5A was even significantly higher in the presence of HRAS G12S or HRAS G13E. Our findings imply that HRAS activity is critical for the RIN1-RAB5 signaling pathway. Given that GTP is far more abundant in cells than GDP, we conclude that RAB5A is most likely in an active GTP-bound form in the presence of HRAS G12S or HRAS G13E, in comparison with HRAS wildtype. Our data also indicated that HRAS G12S perturb the β1 integrin pools balance within the cell and cell surface. Since alterations in HRAS-RIN1 signaling lead to perturbation in integrin equilibrium, we conclude that this signaling pathway is accountable for the pathogenesis of epidermal findings in Costello syndrome.

3.5 Dominantly acting variants in ARF3 have disruptive consequences on Golgi integrity and cause microcephaly recapitulated in zebrafish.

A trio-based exome sequencing of individuals suffering from neurodegeneration diseases led to the identification of *de novo* mutations in ARF3. All amino acid substitutions including L12V, D67V, T32N, D93N, and K127E were conserved among ARF3 paralogs and orthologs, and three of them including D67V and K127E were also conserved in other RAS GTPases. The discovered variants altered residues that were previously linked to human diseases were driven by corresponding variants of the RAS superfamily.

To gain structural insights into the pathogenic mechanism of identified variants, we compared them with the published crystal structure of other RAS GTPases carrying the corresponding amino acid substitutions. Our findings indicated that all residues are clustered within or in the vicinity of the GTP/GDP binding pocket. For instance, D67 coordinates with Mg^{2+} ion through hydrogen bonds with a water molecule, which is required for GDP/GTP binding, and its substitution for Valine would significantly disrupt GDP/GTP binding. Similarly, K127 is part of the NKXD motif, which is located near the guanine moiety of GDP/GTP, and its substitution for glutamic acid perturbs the affinity for nucleotide binding.

The intrinsic and GEF stimulated-nucleotide exchange rates of all variants were evaluated using fluorescence polarization. It was striking that the intrinsic nucleotide exchange rates of D93N, as well as K127E variants, were considerably higher than for the wild type. These two variants showed a 15- to 18-fold higher intrinsic nucleotide exchange rate and reflected that no GEF is required to promote the nucleotide exchange reaction.

To establish a more detailed biochemical consequence of these mutations in ARF3 protein, we inspected the intrinsic GTP hydrolysis activity. Except for the D93N variant which showed a slight increase in GTP hydrolysis, the rest of the ARF3 variants indicated quite similar GTP hydrolysis rates compared to the ARF3 wild type.

Collectively, we revealed that discovered ARF3 variants are most likely accumulated in their GTP-bound state, which is very critical for their function, to maintain the Golgi integrity and subsequently affect normal brain development.

4 REFERENCES

1. Wennerberg, K.; Rossman, K.L.; Der, C.J. The Ras superfamily at a glance. *J. Cell Sci.* **2005**, *118*, 843–846, doi:10.1242/jcs.01660.

2. Vetter, I.R.; Wittinghofer, A. The Guanine Nucleotide-Binding Switch in Three Dimensions. *Science (80-.).* **2001**, *294*, 1299–1304, doi:10.1126/science.1062023.

3. Wittinghofer, A.; Scheffzek, K.; Ahmadian, M.R. The interaction of Ras with GTPase-activating proteins. *FEBS Lett.* **1997**, *410*, 63–67, doi:10.1016/S0014-5793(97)00321-9.

4. Bourne, H.R.; Sanders, D.A.; McCormick, F. The GTPase superfamily: conserved structure and molecular mechanism. *Nat. 1991 3496305* **1991**, *349*, 117–127, doi:10.1038/349117a0.

5. Ihara, K.; Muraguchi, S.; Kato, M.; Shimizu, T.; Shirakawa, M.; Kuroda, S.; Kaibuchi, K.; Hakoshima, T. Crystal Structure of Human RhoA in a Dominantly Active Form Complexed with a GTP Analogue. *J. Biol. Chem.* **1998**, *273*, 9656–9666, doi:10.1074/JBC.273.16.9656.

6. Wei, Y.; Zhang, Y.; Derewenda, U.; Liu, X.; Minor, W.; Nakamoto, R.K.; Somlyo, A. V.; Somlyo, A.P.; Derewenda, Z.S. Crystal structure of RhoA–GDP and its functional implications. *Nat. Struct. Biol. 1997 49* **1997**, *4*, 699–703, doi:10.1038/nsb0997-699.

7. Bos, J.L.; Rehmann, H.; Wittinghofer, A. GEFs and GAPs: Critical Elements in the Control of Small G Proteins. *Cell* **2007**, *129*, 865–877, doi:10.1016/j.cell.2007.05.018.

8. Willumsen, B.M.; Christensen, A.; Hubbert, N.L.; Papageorge, A.G.; Lowy, D.R. The p21 ras C-terminus is required for transformation and membrane association. *Nature* **1984**, *310*, 583–586, doi:10.1038/310583A0.

9. Casey, P.J.; Seabra, M.C. Protein Prenyltransferases. *J. Biol. Chem.* **1996**, *271*, 5289–5292, doi:10.1074/jbc.271.10.5289.

10. Choy, E.; Chiu, V.K.; Silletti, J.; Feoktistov, M.; Morimoto, T.; Michaelson, D.; Ivanov, I.E.; Philips, M.R. Endomembrane Trafficking of Ras. *Cell* **1999**, *98*, 69–80, doi:10.1016/S0092-8674(00)80607-8.

11. Ahearn, I.M.; Haigis, K.; Bar-Sagi, D.; Philips, M.R. Regulating the regulator: post-translational modification of RAS. *Nat. Rev. Mol. Cell Biol.* **2011**, doi:10.1038/nrm3255.

12. Marshall, C.J. Ras effectors. *Curr. Opin. Cell Biol.* **1996**, *8*, 197–204, doi:10.1016/S0955-0674(96)80066-4.

13. Macara, I.G.; Lounsbury, K.M.; Richards, S.A.; McKiernan, C.; Bar-Sagi, D. The Ras superfamily of GTPases 1 . *FASEB J.* **1996**, *10*, 625–630, doi:10.1096/FASEBJ.10.5.8621061.

14. McCormick, F.; Wittinghofer, A. Interactions between ras proteins and their effectors. *Curr. Opin. Biotechnol.* **1996**, *7*, 449–456, doi:10.1016/S0958-1669(96)80123-6.

15. Nauth, T.; Bazgir, F.; Voß, H.; Brandenstein, L.I.; Mosaddeghzadeh, N.; Rickassel, V.; Deden, S.; Gorzelanny, C.; Schlüter, H.; Ahmadian, M.R.; et al. Cutaneous manifestations in Costello syndrome: HRAS p.Gly12Ser affects RIN1-mediated integrin trafficking in immortalized epidermal keratinocytes. *Hum. Mol. Genet.* **2022**, *00*, 1–15, doi:10.1093/hmg/ddac188.

16. Wang, Y.; Waldron, R.T.; Dhaka, A.; Patel, A.; Riley, M.M.; Rozengurt, E.; Colicelli, J. The RAS Effector RIN1 Directly Competes with RAF and Is Regulated by 14-3-3 Proteins. *Mol. Cell. Biol.* **2002**, *22*, 916–926, doi:10.1128/MCB.22.3.916-926.2001/FORMAT/EPUB.

17. Han, L.; Colicelli, J. A human protein selected for interference with Ras function interacts directly with Ras and competes with Raf1. *Mol. Cell. Biol.* **1995**, *15*, 1318–1323, doi:10.1128/mcb.15.3.1318.

18. Plowman, S.J.; Hancock, J.F. Ras signaling from plasma membrane and endomembrane microdomains. *Biochim. Biophys. Acta* **2005**, *1746*, 274–283, doi:10.1016/J.BBAMCR.2005.06.004.

19. McCubrey, J.A.; Steelman, L.S.; Chappell, W.H.; Abrams, S.L.; Wong, E.W.T.; Chang, F.; Lehmann, B.; Terrian, D.M.; Milella, M.; Tafuri, A.; et al. Roles of the Raf/MEK/ERK pathway in cell growth, malignant transformation and drug resistance. *Biochim. Biophys. Acta* **2007**, *1773*, 1263–1284, doi:10.1016/J.BBAMCR.2006.10.001.

20. Shields, J.M.; Pruitt, K.; McFall, A.; Shaub, A.; Der, C.J. Understanding Ras: 'it ain't over 'til it's over'. *Trends Cell Biol.* **2000**, *10*, 147–154, doi:10.1016/S0962-8924(00)01740-2.

21. McKay, M.M.; Morrison, D.K. Integrating signals from RTKs to ERK/MAPK. *Oncogene* **2007**, *26*, 3113–3121, doi:10.1038/SJ.ONC.1210394.

22. Martinelli, S.; Krumbach, O.H.F.; Pantaleoni, F.; Coppola, S.; Amin, E.; Pannone, L.; Nouri, K.; Farina, L.; Dvorsky, R.; Lepri, F.; et al. Functional Dysregulation of CDC42 Causes Diverse Developmental Phenotypes. *Am. J. Hum. Genet.* **2018**, *102*, 309–320, doi:10.1016/j.ajhg.2017.12.015.

23. Saxton, R.A.; Sabatini, D.M. mTOR Signaling in Growth, Metabolism, and Disease. *Cell* **2017**, *168*, 960, doi:10.1016/J.CELL.2017.02.004.

24. Vanhaesebroeck, B.; Stephens, L.; Hawkins, P. PI3K signalling: the path to discovery and understanding. *Nat. Rev. Mol. Cell Biol. 2012 133* **2012**, *13*, 195–203, doi:10.1038/nrm3290.

25. Fruman, D.A.; Rommel, C. PI3K and Cancer: Lessons, Challenges and Opportunities. *Nat. Rev. Drug Discov.* **2014**, doi:10.1038/nrd4204.

26. Burke, J.E. Structural Basis for Regulation of Phosphoinositide Kinases and Their Involvement in Human Disease. *Mol. Cell* **2018**, *71*, 653–673, doi:10.1016/J.MOLCEL.2018.08.005.

27. Mendoza, M.C.; Er, E.E.; Blenis, J. The Ras-ERK and PI3K-mTOR pathways: cross-talk and compensation. *Trends Biochem. Sci.* **2011**, *36*, 320–328, doi:10.1016/J.TIBS.2011.03.006.

28. Sarbassov, D.D.; Guertin, D.A.; Ali, S.M.; Sabatini, D.M. Phosphorylation and regulation of Akt/PKB by the rictor-mTOR complex. *Science (80-.).* **2005**, *307*, 1098–1101, doi:10.1126/SCIENCE.1106148.

29. Liu, P.; Gan, W.; Chin, Y.R.; Ogura, K.; Guo, J.; Zhang, J.; Wang, B.; Blenis, J.; Cantley, L.C.; Toker, A.; et al. Ptdins(3,4,5) P3 - dependent activation of the mTORC2 kinase complex. *Cancer Discov.* **2015**, *5*, 1194–11209, doi:10.1158/2159-8290.

30. Fruman, D.A.; Chiu, H.; Hopkins, B.D.; Bagrodia, S.; Cantley, L.C.; Abraham, R.T. The PI3K Pathway in Human Disease. *Cell* **2017**, *170*, 605–635, doi:10.1016/J.CELL.2017.07.029.

31. Engelman, J.A. Targeting PI3K signalling in cancer: opportunities, challenges and limitations. *Nat. Rev. Cancer Vol.* **2009**, doi:10.1038/nrc2664.

32. Brown, E.J.; Albers, M.W.; Bum Shin, T.; Ichikawa, K.; Keith, C.T.; Lane, W.S.; Schreiber, S.L. A mammalian protein targeted by G1-arresting rapamycin–receptor complex. *Nat. 1994 3696483* **1994**, *369*, 756–758, doi:10.1038/369756a0.

33. Tartaglia, M.; Gelb, B.D. Disorders of dysregulated signal traffic through the RAS-MAPK pathway: phenotypic spectrum and molecular mechanisms. *Ann. N. Y. Acad. Sci.* **2010**, *1214*, 99–121, doi:10.1111/J.1749-6632.2010.05790.X.

34. Schubbert, S.; Shannon, K.; Bollag, G. Hyperactive Ras in developmental disorders and cancer. *Nat. Rev. Cancer 2007 74* **2007**, *7*, 295–308, doi:10.1038/nrc2109.

35. Tajan, M.; Paccoud, R.; Branka, S.; Edouard, T.; Yart, A. The RASopathy Family: Consequences of Germline Activation of the RAS/MAPK Pathway. *Endocr. Rev.* **2018**, *39*, 676–700, doi:10.1210/ER.2017-00232.

36. Chavrier, P.; Ménétrey, J. Toward a Structural Understanding of Arf Family:Effector Specificity. *Structure* **2010**, *18*, 1552–1558, doi:10.1016/J.STR.2010.11.004.

37. Liu, Y.; Kahn, R.A.; Prestegard, J.H. Article Structure and Membrane Interaction of Myristoylated ARF1., doi:10.1016/j.str.2008.10.020.

38. Donaldson, J.G.; Jackson, C.L. ARF family G proteins and their regulators: roles in membrane transport, development and disease. *Nat. Rev. Mol. Cell Biol. 2011 126* **2011**, *12*, 362–375, doi:10.1038/nrm3117.

39. Cherfils, J. Arf GTPases and their effectors: assembling multivalent membrane-binding platforms. *Curr. Opin. Struct. Biol.* **2014**, *29*, 67–76, doi:10.1016/J.SBI.2014.09.007.

40. D'souza-Schorey, C.; Chavrier, P. GTPase-activating protein Guanine nucleotide-exchange factor ARF proteins: roles in membrane traffic and beyond. *Nat. Rev. | Mol. CELL Biol.* **2006**, *7*, doi:10.1038/nrm1910.

41. Carlos Amor, J.; Harrison, D.H.; Kahn, R.A.; Ringe, D. Structure of the human ADP-ribosylation factor 1 complexed with GDP. *Nat. 1994 3726507* **1994**, *372*, 704–708, doi:10.1038/372704a0.

42. Adarska, P.; Wong-Dilworth, L.; Bottanelli, F. ARF GTPases and Their Ubiquitous Role in Intracellular Trafficking Beyond the Golgi. *Front. Cell Dev. Biol.* **2021**, *9*, 1977, doi:10.3389/FCELL.2021.679046/BIBTEX.

43. Gilbert, C.E.; Sztul, E.; Machamer, C.E.; Lippincott-Schwartz, J. Commonly used trafficking blocks disrupt ARF1 activation and the localization and function of specific Golgi proteins. *Mol. Biol. Cell* **2018**, *29*, 937, doi:10.1091/MBC.E17-11-0622.

44. Mosaddeghzadeh, N.; Ahmadian, M.R. The RHO Family GTPases: Mechanisms of Regulation and Signaling. *Cells 2021, Vol. 10, Page 1831* **2021**, *10*, 1831, doi:10.3390/CELLS10071831.

45. Jaffe, A.B.; Hall, A. Rho GTPases: Biochemistry and biology. *Annu. Rev. Cell Dev. Biol.* 2005, *21*, 247–269, doi: 10.1146/annurev.cellbio.21.020604.150721.

46. Etienne-Manneville, S.; Hall, A. Rho GTPases in cell biology. *Nature* 2002, *420*, 629–635, doi: 10.1038/nature01148.

47. Bishop, A.L.; Hall, A. Rho GTPases and their effector proteins. *Biochem. J.* **2000**, *348*, 241–255, doi:10.1042/0264-6021:3480241.

48. Hall, A. Rho GTPases and the Actin Cytoskeleton. *Science (80-.).* **1998**, *279*, 509–514, doi:10.1126/science.279.5350.509.

49. Raftopoulou, M.; Hall, A. Cell migration: Rho GTPases lead the way. *Dev. Biol.* 2004, *265*, 23–32, doi: 10.1016/j.ydbio.2003.06.003.

50. Hall, A. Rho family GTPases. Portland Press, 2012; Vol. 40, pp. 1378–1382, doi: 10.1042/BST20120103.

51. Wu, W.J.; Leonard, D.A.; Cerione, R.A.; Manor, D. Interaction between Cdc42Hs and RhoGDI Is Mediated through the Rho Insert Region *. *J. Biol. Chem.* **1997**, *272*, 26153–26158, doi:10.1074/JBC.272.42.26153.

52. Karnoub, A.E.; Der, C.J.; Campbell, S.L. The Insert Region of Rac1 Is Essential for Membrane Ruffling but Not Cellular Transformation. *Mol. Cell. Biol.* **2001**, *21*, 2847–2857, doi:10.1128/MCB.21.8.2847-2857.

53. Rose, R.; Weyand, M.; Lammers, M.; Ishizaki, T.; Ahmadian, M.R.; Wittinghofer, A. Structural and mechanistic insights into the interaction between Rho and mammalian Dia. *Nature* **2005**, *435*, 513–518, doi:10.1038/nature03604.

54. LeCour, L.; Boyapati, V.K.; Liu, J.; Li, Z.; Sacks, D.B.; Worthylake, D.K. The Structural Basis for Cdc42-Induced Dimerization of IQGAPs. *Structure* **2016**, *24*, 1499–1508, doi:10.1016/j.str.2016.06.016.

55. Thapar, R.; Karnoub, A.E.; Campbell, S.L. Structural and Biophysical Insights into the Role of the Insert Region in Rac1 Function†. *Biochemistry* **2002**, *41*, 3875–3883, doi:10.1021/BI0120087.

56. Wennerberg, K.; Der, C.J. Rho-family GTPases: It's not only Rac and Rho (and i like it). *J. Cell Sci.* **2004**, *117*, 1301–1312, doi:10.1242/jcs.01118.

57. Hodge, R.G.; Ridley, A.J. Regulating Rho GTPases and their regulators. *Nat. Rev. Mol. Cell Biol.* 2016, *17*, 496–510, doi: 10.1038/nrm.2016.67.

58. Wheeler, A.P.; Ridley, A.J. Why three Rho proteins? RhoA, RhoB, RhoC, and cell motility. *Exp. Cell Res.* **2004**, *301*, 43–49, doi:10.1016/J.YEXCR.2004.08.012.

59. Ridley, A.J. RhoA, RhoB and RhoC have different roles in cancer cell migration. *J. Microsc.* **2013**, *251*, 242–249, doi:10.1111/JMI.12025.

60. Wang, L.; Yang, L.; Luo, Y.; Zheng, Y. A novel strategy for specifically down-regulating individual Rho GTPase activity in tumor cells. *J. Biol. Chem.* **2003**, *278*, 44617–44625, doi:10.1074/JBC.M308929200.

61. Adamson, P.; Paterson, H.F.; Hall, A. Intracellular localization of the P21(rho) proteins. *J. Cell Biol.* **1992**, *119*, 617–627, doi:10.1083/jcb.119.3.617.

62. Vega, F.M.; Ridley, A.J. The RhoB small GTPase in physiology and disease. *Small GTPases* **2016**, *9*, 384–393, doi:10.1080/21541248.2016.1253528.

63. Guilluy, C.; Garcia-Mata, R.; Burridge, K. Rho protein crosstalk: another social network? *Trends Cell Biol.* **2011**, *21*, 718–726, doi:10.1016/J.TCB.2011.08.002.

64. Vega, F.M.; Fruhwirth, G.; Ng, T.; Ridley, A.J. RhoA and RhoC have distinct roles in migration and invasion by acting through different targets. *J. Cell Biol.* **2011**, *193*, 655–665, doi:10.1083/jcb.201011038.

65. Prendergast, G.C. Actin' up: RhoB in cancer and apoptosis. *Nat. Rev. Cancer* **2001**, *1*, 162–168, doi: 10.1038/35101096.

66. Liu, A.-X.; Cerniglia, G.J.; Bernhard, E.J.; Prendergast, G.C. RhoB Is Required to Mediate Apoptosis in Neoplastically Transformed Cells after DNA damage. *Source* **2001**, *98*, 6192–6197, doi: 10.1073/pnas.111137198.

67. Prendergast, G.C. Farnesyltransferase inhibitors: antineoplastic mechanism and clinical prospects. *Curr. Opin. Cell Biol.* **2000**, *12*, 166–173, doi:10.1016/S0955-0674(99)00072-1.

68. Van Aelst, L.; D'Souza-Schorey, C. Rho GTPases and signaling networks. *Genes Dev.* **1997**, *11*, 2295–2322, doi:10.1101/GAD.11.18.2295.

69. Fujisawa, K.; Madaule, P.; Ishizaki, T.; Watanabe, G.; Bito, H.; Saito, Y.; Hall, A.; Narumiya, S. Different regions of Rho determine Rho-selective binding of different classes of Rho target molecules. *J. Biol. Chem.* **1998**, *273*, 18943–18949, doi:10.1074/JBC.273.30.18943.

70. Sahai, E.; Marshall, C.J. ROCK and Dia have opposing effects on adherens junctions downstream of Rho. *Nat. Cell Biol. 2002 46* **2002**, *4*, 408–415, doi:10.1038/ncb796.

71. Maesaki, R.; Ihara, K.; Shimizu, T.; Kuroda, S.; Kaibuchi, K.; Hakoshima, T. The structural basis of Rho effector recognition revealed by the crystal structure of human RhoA complexed with the effector domain of PKN/PRK1. *Mol. Cell* **1999**, *4*, 793–803, doi:10.1016/S1097-2765(00)80389-5.

72. Dvorsky, R.; Blumenstein, L.; Vetter, I.R.; Ahmadian, M.R. Structural Insights into the Interaction of ROCKI with the Switch Regions of RhoA. *J. Biol. Chem.* **2004**, *279*, 7098–7104, doi:10.1074/jbc.M311911200.

73. Lim, W.G.; Tan, B.J.; Zhu, Y.; Zhou, S.; Armstrong, J.S.; Li, Q.T.; Dong, Q.; Chan, E.; Smith, D.; Verma, C.; et al. The very C-terminus of PRK1/PKN is essential for its activation by RhoA and downstream signaling. *Cell. Signal.* **2006**, *18*, 1473–1481, doi:10.1016/j.cellsig.2005.11.009.

74. Kühn, S.; Erdmann, C.; Kage, F.; Block, J.; Schwenkmezger, L.; Steffen, A.; Rottner, K.; Geyer, M. The structure of FMNL2–Cdc42 yields insights into the mechanism of lamellipodia and filopodia formation. *Nat. Commun.* **2015**, *6*, 1–14, doi:10.1038/ncomms8088.

75. Amano, M.; Ito, M.; Kimura, K.; Fukata, Y.; Chihara, K.; Nakano, T.; Matsuura, Y.; Kaibuchi, K. Phosphorylation and activation

of myosin by Rho-associated kinase (Rho-kinase). *J. Biol. Chem.* **1996**, *271*, 20246–20249, doi:10.1074/JBC.271.34.20246.

76. Kimura, K.; Ito, M.; Amano, M.; Chihara, K.; Fukata, Y.; Nakafuku, M.; Yamamori, B.; Feng, J.; Nakano, T.; Okawa, K.; et al. Regulation of myosin phosphatase by Rho and Rho-associated kinase (Rho- kinase). *Science (80-.).* **1996**, *273*, 245–248, doi:10.1126/science.273.5272.245.

77. Uehata, M.; Ishizaki, T.; Satoh, H.; Ono, T.; Kawahara, T.; Morishita, T.; Tamakawa, H.; Yamagami, K.; Inui, J.; Maekawa, M.; et al. Calcium sensitization of smooth muscle mediated by a Rho-associated protein kinase in hypertension. *Nat.* **1997**, *389*, 990–994, doi:10.1038/40187.

78. Watanabe, N.; Kato, T.; Fujita, A.; Ishizaki, T.; Narumiya, S. Cooperation between mDia1 and ROCK in Rho-induced actin reorganization. *Nat. Cell Biol.* **1999**, *1*, 136–143, doi:10.1038/11056.

79. Nakano, K.; Takaishi, K.; Kodama, A.; Mammoto, A.; Shiozaki, H.; Monden, M.; Takai, Y. Distinct Actions and Cooperative Roles of ROCK and mDia in Rho Small G Protein-induced Reorganization of the Actin Cytoskeleton in Madin-Darby Canine Kidney Cells. *Mol. Biol. Cell* **1999**, *10*, 2481–2491, doi: 10.1091/mbc.10.8.2481.

80. Insall, R.H.; Machesky, L.M. Actin Dynamics at the Leading Edge: From Simple Machinery to Complex Networks. *Dev. Cell* **2009**, *17*, 310–322, doi:10.1016/J.DEVCEL.2009.08.012.

81. Haataja, L.; Groffen, J.; Heisterkamp, N. Characterization of RAC3, a novel member of the Rho family. *J. Biol. Chem.* **1997**, *272*, 20384–20388, doi:10.1074/JBC.272.33.20384.

82. Haeusler, L.C.; Blumenstein, L.; Stege, P.; Dvorsky, R.; Ahmadian, M.R. Comparative functional analysis of the Rac GTPases. *FEBS Lett.* **2003**, *555*, 556–560, doi:10.1016/S0014-5793(03)01351-6.

83. Melzer, C.; Hass, R.; Lehnert, H.; Ungefroren, H. RAC1B: A rho GTPase with versatile functions in malignant transformation and tumor progression. *Cells* **2019**, *8*, 1–20, doi:10.3390/cells8010021.

84. Jordan, P.; Brazão, R.; Boavida, M.G.; Gespach, C.; Chastre, E. Cloning of a novel human Rac1b splice variant with increased expression in colorectal tumors. *Oncogene* **1999**, *18*, 6835–6839, doi:10.1038/sj.onc.1203233.

85. Schnelzer, A.; Prechtel, D.; Knaus, U.; Dehne, K.; Gerhard, M.; Graeff, H.; Harbeck, N.; Schmitt, M.; Lengyel, E. Rac1 in human breast cancer: overexpression, mutation analysis, and characterization of a new isoform, Rac1b. *Oncogene* **2000**, *19*, 3013–3020, doi:10.1038/sj.onc.1203621.

86. Fiegen, D.; Haeusler, L.C.; Blumenstein, L.; Herbrand, U.; Dvorsky, R.; Vetter, I.R.; Ahmadian, M.R. Alternative Splicing of Rac1 Generates Rac1b, a Self-activating GTPase. *J. Biol. Chem.* **2004**, *279*, 4743–4749, doi:10.1074/jbc.M310281200.

87. Dinauer, M.C. Regulation of neutrophil function by Rac GTPases. *Curr. Opin. Hematol.* **2003**, *10*, 8–15, doi:10.1097/00062752-200301000-00003.

88. Ambruso, D.R.; Knall, C.; Abell, A.N.; Panepinto, J.; Kurkchubasche, A.; Thurman, G.; Gonzalez-Aller, C.; Hiester, A.; DeBoer, M.; Harbeck, R.J.; et al. Human neutrophil immunodeficiency syndrome is associated with an inhibitory Rac2 mutation. *Proc. Natl. Acad. Sci. U. S. A.* **2000**, *97*, 4654–4659, doi:10.1073/pnas.080074897.

89. Kasper, B.; Tidow, N.; Grothues, D.; Welte, K. Differential expression and regulation of GTPases (RhoA and Rac2) and GDIs (LyGDI and RhoGDI) in neutrophils from patients with severe congenital neutropenia. *Blood* **2000**, *95*, 2947–2953, doi:10.1182/BLOOD.V95.9.2947.009K10_2947_2953.

90. Roberts, A.W.; Chaekyun, K.; Zhen, L.; Lowe, J.B.; Kapur, R.; Petryniak, B.; Spaetti, A.; Pollock, J.D.; Borneo, J.B.; Bradford, G.B.; et al. Deficiency of the hematopoietic cell-specific Rho family GTPase Rac2 is characterized by abnormalities in neutrophil function and host defense. *Immunity* **1999**, *10*, 183–196, doi:10.1016/S1074-7613(00)80019-9.

91. Dorseuil, O.; Reibel, L.; Bokoch, G.M.; Camonis, J.; Gacon, G. The Rac target NADPH oxidase p67phox interacts preferentially with Rac2 rather than Rac1. *J. Biol. Chem.* **1996**, *271*, 83–88, doi:10.1074/JBC.271.1.83.

92. Mizuno, T.; Kaibuchi, K.; Ando, S.; Musha, T.; Hiraoka, K.; Takaishi, K.; Asada, M.; Nunoi, H.; Matsuda, I.; Takai, Y. Regulation of the superoxide-generating NADPH oxidase by a small GTP-binding protein and its stimulatory and inhibitory GDP/GTP exchange proteins. *J. Biol. Chem.* **1992**, *267*, 10215–10218, doi:10.1016/S0021-9258(19)50005-9.

93. Eden, S.; Rohatgi, R.; Podtelejnikov, A. V.; Mann, M.; Kirschner, M.W. Mechanism of regulation of WAVE1-induced actin nucleation by Rac1 and Nck. *Nature* **2002**, *418*, 790–793, doi:10.1038/nature00859.

94. Chen, Z.; Borek, D.; Padrick, S.B.; Gomez, T.S.; Metlagel, Z.; Ismail, A.; Umetani, J.; Billadeau, D.D.; Otwinowski, Z.; Rosen, M.K. Structure and Control of the Actin Regulatory WAVE Complex HHS Public Access. *Nature* **2010**, *468*, 533–538, doi:10.1038/nature09623.

95. Millard, T.H.; Sharp, S.J.; Machesky, L.M. Signalling to actin assembly via the WASP (Wiskott-Aldrich syndrome protein)-family proteins and the Arp2/3 complex. *Biochem. J.* **2004**, *380*, 1–17, doi:10.1042/BJ20040176.

96. Machesky, L.M.; Mullins, R.D.; Higgs, H.N.; Kaiser, D.A.; Blanchoin, L.; May, R.C.; Hall, M.E.; Pollard, T.D. Scar, a WASp-related protein, activates nucleation of actin filaments by the Arp2/3 complex. *Proc. Natl. Acad. Sci. U. S. A.* **1999**, *96*, 3739–3744, doi:10.1073/pnas.96.7.3739.

97. Mullins, R.D.; Heuser, J.A.; Pollard, T.D. The interaction of Arp2/3 complex with actin: Nucleation, high affinity pointed end

capping, and formation of branching networks of filaments. *Proc. Natl. Acad. Sci. U. S. A.* **1998**, *95*, 6181–6186, doi:10.1073/PNAS.95.11.6181.

98. Innocenti, M.; Zucconi, A.; Disanza, A.; Frittoli, E.; Areces, L.B.; Steffen, A.; Stradal, T.E.B.; Di Fiore, P.P.; Carlier, M.F.; Scita, G. Abi1 is essential for the formation and activation of a WAVE2 signalling complex. *Nat. Cell Biol.* **2004**, *6*, 319–327, doi:10.1038/ncb1105.

99. Nobes, C.; Marsh, M. Dendritic cells: New roles for Cdc42 and Rac in antigen uptake? *Curr. Biol.* **2000**, *10*, R739–R741, doi:10.1016/S0960-9822(00)00736-3.

100. Ridley, A.J. Rho GTPases and actin dynamics in membrane protrusions and vesicle trafficking. *Trends Cell Biol.* **2006**, *16*, 522–529, doi:10.1016/J.TCB.2006.08.006.

101. Bokoch, G.M. Regulation of the phagocyte respiratory burst by small GTP-binding proteins. *Trends Cell Biol.* **1995**, *5*, 109–113, doi:10.1016/S0962-8924(00)88960-6.

102. Bosco, E.E.; Mulloy, J.C.; Zheng, Y. Rac1 GTPase: A "Rac" of All Trades. *Cell Mol Life Sci* **2009**, doi:10.1007/s00018-008-8552-x.

103. Olson, M.F. Rho GTPases, their post-translational modifications, disease-associated mutations and pharmacological inhibitors. *Small GTPases* **2018**, *9*, 203–215, doi: 10.1080/21541248.2016.1218407.

104. Goka, E.T.; Lippman, M.E. Loss of the E3 ubiquitin ligase HACE1 results in enhanced Rac1 signaling contributing to breast cancer progression. *Oncogene 2015 3442* **2015**, *34*, 5395–5405, doi:10.1038/onc.2014.468.

105. Abdrabou, A.; Wang, Z. Post-translational modification and subcellular distribution of Rac1: An update. *Cells* **2018**, *7*, 1–16, doi:10.3390/cells7120263.

106. CC, L.; R, R.-V.; CL, W. Novel mechanism of the co-regulation of nuclear transport of SmgGDS and Rac1. *J. Biol. Chem.* **2003**, *278*, 12495–12506, doi:10.1074/JBC.M211286200.

107. Michaelson, D.; Silletti, J.; Murphy, G.; D'Eustachio, P.; Rush, M.; Philips, M.R. Differential localization of Rho GTPases in live cells: Regulation by hypervariable regions and RhoGDI binding. *J. Cell Biol.* **2001**, *152*, 111–126, doi:10.1083/JCB.152.1.111/VIDEO-4.

108. Williams, C.L. The polybasic region of Ras and Rho family small GTPases: A regulator of protein interactions and membrane association and a site of nuclear localization signal sequences. *Cell. Signal.* **2003**, *15*, 1071–1080, doi:10.1016/S0898-6568(03)00098-6.

109. Lanning, C.C.; Daddona, J.L.; Ruiz-Velasco, R.; Shafer, S.H.; Williams, C.L. The Rac1 C-terminal Polybasic Region Regulates the Nuclear Localization and Protein Degradation of Rac1. *J. Biol. Chem.* **2004**, *279*, 44197–44210, doi:10.1074/JBC.M404977200.

110. Walch, A.; Seidl, S.; Hermannstädter, C.; Rauser, S.; Deplazes, J.; Langer, R.; Hann Von Weyhern, C.; Sarbia, M.; Busch, R.; Feith, M.; et al. Combined analysis of Rac1, IQGAP1, Tiam1 and E-cadherin expression in gastric cancer. *Mod. Pathol.* **2008**, *21*, 544–552, doi:10.1038/modpathol.2008.3.

111. Braga, V.M.M.; Machesky, L.M.; Hall, A.; Hotchin, N.A. The Small GTPases Rho and Rac Are Required for the Establishment of Cadherin-dependent Cell–Cell Contacts. *J. Cell Biol.* **1997**, *137*, 1421–1431, doi:10.1083/JCB.137.6.1421.

112. Abel, A.M.; Schuldt, K.M.; Rajasekaran, K.; Hwang, D.; Riese, M.J.; Rao, S.; Thakar, M.S.; Malarkannan, S. IQGAP1: Insights into the function of a molecular puppeteer. *Mol. Immunol.* **2015**, *65*, 336–349, doi:10.1016/j.molimm.2015.02.012.

113. Choi, S.; Anderson, R.A. IQGAP1 is a phosphoinositide effector and kinase scaffold. *Adv. Biol. Regul.* **2016**, *60*, 29–35, doi: 10.1016/j.jbior.2015.10.004.

114. Hedman, A.C.; Smith, J.M.; Sacks, D.B. The biology of IQGAP proteins: beyond the cytoskeleton . *EMBO Rep.* **2015**, *16*, 427–446, doi:10.15252/embr.201439834.

115. Nouri, K.; Timson, D.J.; Ahmadian, M.R. New model for the interaction of IQGAP1 with CDC42 and RAC1. *Small GTPases* **2020**, *11*, 16–22, doi: 10.1080/21541248.2017.1321169.

116. Mosaddeghzadeh, N.; Nouri, K.; Krumbach, O.H.F.; Amin, E.; Dvorsky, R.; Ahmadian, M.R. Selectivity determinants of rho gtpase binding to iqgaps. *Int. J. Mol. Sci.* **2021**, *22*, 12596, doi:10.3390/IJMS222212596/S1.

117. Smith, J.M.; Hedman, A.C.; Sacks, D.B. IQGAPs choreograph cellular signaling from the membrane to the nucleus. *Trends Cell Biol.* **2015**, *25*, 171–184, doi: 10.1016/j.tcb.2014.12.005.

118. Kuroda, S.; Fukata, M.; Nakagawa, M.; Fujii, K.; Nakamura, T.; Ookubo, T.; Izawa, I.; Nagase, T.; Nomura, N.; Tani, H.; et al. Role of IQGAP1, a target of the small GTPases Cdc42 and Rac1, in regulation of E-cadherin- mediated cell-cell adhesion. *Science* **1998**, *281*, 832–835, doi:10.1126/SCIENCE.281.5378.832.

119. Noritake, J.; Watanabe, T.; Sato, K.; Wang, S.; Kaibuchi, K. IQGAP1: a key regulator of adhesion and migration. *J. Cell Sci.* **2005**, *118*, 2085–2092, doi:10.1242/JCS.02379.

120. Miller, K.E.; Kang, P.J.; Park, H.O. Regulation of Cdc42 for polarized growth in budding yeast. *Microb. cell* **2020**, *7*, 175–189, doi:10.15698/MIC2020.07.722.

121. Etienne-Manneville, S. Cdc42 - The centre of polarity. *J. Cell Sci.* **2004**, *117*, 1291–1300, doi: 10.1242/jcs.01115.

122. Watson, J.R.; Owen, D.; Mott, H.R. Cdc42 in actin dynamics: An ordered pathway governed by complex equilibria and directional effector handover. *Small GTPases* **2016**, *8*, 237–244, doi:10.1080/21541248.2016.1215657.

123. Miki, H.; Sasaki, T.; Takai, Y.; Takenawa, T. Induction of filopodium formation by a WASP-related actin- depolymerizing protein N-WASP. *Nature* **1998**, *391*, 93–96, doi:10.1038/34208.

124. Symons, M.; J Derry, J.M.; mammalian cells, in; Karlak, B.; Jiang, S.; Lemahieu, V.; McCormick, F.; Francke, U.; Abo, A. Wiskott-Aldrich Syndrome Protein, a Novel Effector for the GTPase CDC42Hs, Is Implicated in Actin Polymerization CDC42Hs triggers induction of microspikes and filo. *Cell* **1996**, *84*, 723–734, doi: 10.1016/s0092-8674(00)81050-8.

125. Hemsath, L.; Dvorsky, R.; Fiegen, D.; Carlier, M.F.; Ahmadian, M.R. An electrostatic steering mechanism of Cdc42 recognition by Wiskott-Aldrich syndrome proteins. *Mol. Cell* **2005**, *20*, 313–324, doi:10.1016/j.molcel.2005.08.036.

126. Aspenstr¨om, P.; Aspenstr¨om, A.; Sa Fransson, A.˚; Saras, J. Rho GTPases have diverse effects on the organization of the actin filament system. *Biochem. J* **2004**, *377*, 327–337, doi: 10.1042/BJ20031041.

127. Farhan, H.; Hsu, V.W. Cdc42 and Cellular Polarity: Emerging Roles at the Golgi. *Trends Cell Biol.* **2016**, *26*, 241–248, doi:10.1016/J.TCB.2015.11.003.

128. Erickson, J.W.; Zhang, C.J.; Kahn, R.A.; Evans, T.; Cerione, R.A. Mammalian Cdc42 Is a Brefeldin A-sensitive Component of the Golgi Apparatus. *J. Biol. Chem.* **1996**, *271*, 26850–26854, doi:10.1074/JBC.271.43.26850.

129. Michaelson, D.; Silletti, J.; Murphy, G.; D'Eustachio, P.; Rush, M.; Philips, M.R. Differential Localization of Rho Gtpases in Live Cells. *J. Cell Biol.* **2001**, *152*, 111–126, doi:10.1083/jcb.152.1.111.

130. Nalbant, P.; Hodgson, L.; Kraynov, V.; Toutchkine, A.; Hahn, K.M. Activation of endogenous Cdc42 visualized in living cells. *Science (80-.).* **2004**, *305*, 1615–1619, doi:10.1126/SCIENCE.1100367.

131. Burbelo, P.D.; Drechsel, D.; Hall, A. A Conserved Binding Motif Defines Numerous Candidate Target Proteins for Both Cdc42 and Rac GTPases. *J. Biol. Chem.* **1995**, *270*, 29071–29074, doi:10.1074/JBC.270.49.29071.

132. Owen, D.; Mott, H.R. CRIB effector disorder: exquisite function from chaos. *Biochem. Soc. Trans.* **2018**, *46*, 1289–1302, doi:10.1042/BST20170570.

133. Leonard, D.A.; Satoskar, R.S.; Wu, W.J.; Bagrodia, S.; Cerione, R.A.; Manor, D. Use of a fluorescence spectroscopic readout to characterize the interactions of Cdc42Hs with its target/effector, mPAK-3. *Biochemistry* **1997**, *36*, 1173–1180, doi:10.1021/BI9622837.

134. Morreale, A.; Venkatesan, M.; Mott, H.R.; Owen, D.; Nietlispach, D.; Lowe, P.N.; Laue, E.D. Structure of Cdc42 bound to the GTPase binding domain of PAK. *Nat. Struct. Biol.* **2000**, *7*, 384–388, doi:10.1038/75158.

135. Dvorsky, R.; Ahmadian, M.R. Always look on the bright site of Rho: Structural implications for a conserved intermolecular interface. *EMBO Rep.* **2004**, *5*, 1130–1136, doi:10.1038/sj.embor.7400293.

136. Hart, M.J.; Callow, M.G.; Souza, B.; Polakis, P. IQGAP1, a calmodulin-binding protein with a rasGAP-related domain, is a potential effector for cdc42Hs. *EMBO J.* **1996**, *15*, 2997–3005, doi:10.1002/J.1460-2075.1996.TB00663.X.

137. Kuroda, S.; Fukata, M.; Kobayashi, K.; Nakafuku, M.; Nomura, N.; Iwamatsu, A.; Kaibuchi, K. Identification of IQGAP as a putative target for the small GTPases, Cdc42 and Rac1. *J. Biol. Chem.* **1996**, *271*, 23363–23367, doi:10.1074/JBC.271.38.23363.

138. Hedman, A.C.; Smith, J.M.; Sacks, D.B. The biology of IQGAP proteins: beyond the cytoskeleton . *EMBO Rep.* **2015**, *16*, 427–446, doi:10.15252/embr.201439834.

139. Brandt, D.T.; Grosse, R. Get to grips: steering local actin dynamics with IQGAPs. *EMBO Rep.* **2007**, *8*, 1019–1023, doi:10.1038/SJ.EMBOR.7401089.

140. White, C.D.; Erdemir, H.H.; Sacks, D.B. IQGAP1 and its binding proteins control diverse biological functions. *Cell. Signal.* **2012**, *24*, 826–834, doi:10.1016/j.cellsig.2011.12.005.

141. Watanabe, T.; Wang, S.; Kaibuchi, K. IQGAPS as key regulators of actin-cytoskeleton dynamics. *Cell Struct. Funct.* **2015**, *40*, 69–77, doi:10.1247/csf.15003.

142. Abel, A.M.; Schuldt, K.M.; Rajasekaran, K.; Hwang, D.; Riese, M.J.; Rao, S.; Thakar, M.S.; Malarkannan, S. IQGAP1: Insights into the function of a molecular puppeteer. *Mol. Immunol.* 2015, *65*, 336–349, doi: 10.1016/j.molimm.2015.02.012.

143. Pudewell, S.; Wittich, C.; Kazemein Jasemi, N.S.; Bazgir, F.; Ahmadian, M.R. Accessory proteins of the RAS-MAPK pathway: moving from the side line to the front line. *Commun. Biol.* **2021**, *4*, 696, doi:10.1038/s42003-021-02149-3.

144. Nouri, K.; Fansa, E.K.; Amin, E.; Dvorsky, R.; Gremer, L.; Willbold, D.; Schmitt, L.; Timson, D.J.; Ahmadian, M.R. IQGAP1 interaction with RHO family proteins revisited kinetic and equilibrium evidence for multiple distinct binding sites. *J. Biol. Chem.* **2016**, *291*, 26364–26376, doi:10.1074/jbc.M116.752121.

145. Kurella, V.B.; Richard, J.M.; Parke, C.L.; LeCour, L.F.; Bellamy, H.D.; Worthylake, D.K. Crystal structure of the GTPase-

activating protein-related domain from IQGAP1. *J. Biol. Chem.* **2009**, *284*, 14857–14865, doi:10.1074/jbc.M808974200.

146. Mosaddeghzadeh, N.; Pudewell, S.; Bazgir, F.; Kazemein Jasemi, N.S.; Krumbach, O.H.F.; Gremer, L.; Willbold, D.; Dvorsky, R.; Ahmadian, M.R. CDC42-IQGAP Interactions Scrutinized: New Insights into the Binding Properties of the GAP-Related Domain. *Int. J. Mol. Sci.* **2022**, *23*, 8842, doi:10.3390/IJMS23168842.

147. Hart, M.J.; Eva, A.; Evans, T.; Aaronson, S.A.; Cerione, R.A. Catalysis of guanine nucleotide exchange on the CDC42Hs protein by the dbloncogene product. *Nature* **1991**, *354*, 311–314, doi:10.1038/354311a0.

148. Swart-Mataraza, J.M.; Li, Z.; Sacks, D.B. IQGAP1 is a component of Cdc42 signaling to the cytoskeleton. *J. Biol. Chem.* **2002**, *277*, 24753–24763, doi:10.1074/jbc.M111165200.

149. Fukata, M.; Watanabe, T.; Noritake, J.; Nakagawa, M.; Yamaga, M.; Kuroda, S.; Matsuura, Y.; Iwamatsu, A.; Perez, F.; Kaibuchi, K. Rac1 and Cdc42 capture microtubules through IQGAP1 and CLIP-170. *Cell* **2002**, *109*, 873–885, doi:10.1016/S0092-8674(02)00800-0.

150. Lam, M.T.; Coppola, S.; Krumbach, O.H.F.; Prencipe, G.; Insalaco, A.; Cifaldi, C.; Brigida, I.; Zara, E.; Scala, S.; Di Cesare, S.; et al. A novel disorder involving dyshematopoiesis, inflammation, and HLH due to aberrant CDC42 function. *J. Exp. Med.* **2019**, *216*, 2778–2799, doi:10.1084/jem.20190147.

151. Takenouchi, T.; Kosaki, R.; Niizuma, T.; Hata, K.; Kosaki, K. Macrothrombocytopenia and developmental delay with a de novo CDC42 mutation: Yet another locus for thrombocytopenia and developmental delay. *Am. J. Med. Genet. Part A* **2015**, *167*, 2822–2825, doi:10.1002/AJMG.A.37275.

152. Murphy, N.P.; Mott, H.R.; Owen, D. Progress in the therapeutic inhibition of Cdc42 signalling. *Biochem. Soc. Trans.* **2021**, *49*, 1443–1456, doi:10.1042/BST20210112.

153. Yang, W.; Wu, P. fei; Ma, J. xing; Liao, M. jun; Xu, L. shan; Yi, L. TRPV4 activates the Cdc42/N-wasp pathway to promote glioblastoma invasion by altering cellular protrusions. *Sci. Reports* **2020**, *10*, 1–15, doi:10.1038/s41598-020-70822-4.

154. Nussinov, R.; Jang, H.; Gursoy, A.; Keskin, O.; Gaponenko, V. Inhibition of Nonfunctional Ras. *Cell Chem. Biol.* **2021**, *28*, 121–133, doi:10.1016/J.CHEMBIOL.2020.12.012.

155. Rossman, K.L.; Der, C.J.; Sondek, J. GEF means go: Turning on Rho GTPases with guanine nucleotide-exchange factors. *Nat. Rev. Mol. Cell Biol.* **2005**, *6*, 167–180, doi: 10.1038/nrm1587.

156. Goicoechea, S.M.; Awadia, S.; Garcia-Mata, R. I'm coming to GEF you: Regulation of RhoGEFs during cell migration. *Cell Adhes. Migr.* **2014**, *8*, 535–549, doi: 10.4161/cam.28721.

157. Cherfils, J.; Zeghouf, M. Regulation of small GTPases by GEFs, GAPs, and GDIs. *Physiol. Rev.* **2013**, *93*, 269–309, doi:10.1152/physrev.00003.2012.

158. Cherfils, J.; Chardin, P. GEFs: structural basis for their activation of small GTP-binding proteins. *Trends Biochem. Sci.* **1999**, *24*, 306–311, doi:10.1016/S0968-0004(99)01429-2.

159. Guo, Z.; Ahmadian, M.R.; Goody, R.S. Guanine nucleotide exchange factors operate by a simple allosteric competitive mechanism. *Biochemistry* **2005**, *44*, 15423–15429, doi:10.1021/bi0518601.

160. Klebe, C.; Prinz, H.; Wittinghofer, A.; Goody, R.S. The Kinetic Mechanism of Ran-Nucleotide Exchange Catalyzed by RCC1. *Biochemistry* **1995**, *34*, 12543–12552, doi: 10.1021/bi00039a008.

161. Lai, C.C.; Boguski, M.; Broek, D.; Powers, S. Influence of guanine nucleotides on complex formation between Ras and CDC25 proteins. *Mol. Cell. Biol.* **1993**, *13*, 1345–1352, doi:10.1128/MCB.13.3.1345.

162. Hutchinson, J.P.; Eccleston, J.F. Mechanism of nucleotide release from Rho by the GDP dissociation stimulator protein. *Biochemistry* **2000**, *39*, 11348–11359, doi:10.1021/bi0007573.

163. Heasman, S.J.; Ridley, A.J. Mammalian Rho GTPases: New insights into their functions from in vivo studies. *Nat. Rev. Mol. Cell Biol.* **2008**, *9*, 690–701, doi:10.1038/nrm2476.

164. Srivastava, S.K.; Wheelock, R.H.P.; Aaronson, S.A.; Eva, A. Identification of the protein encoded by the human diffuse B-cell lymphoma (dbl) oncogene. *Proc. Natl. Acad. Sci. U. S. A.* **1986**, *83*, 8868–8872, doi:10.1073/pnas.83.23.8868.

165. Liu, X.; Wang, H.; Eberstadt, M.; Schnuchel, A.; Olejniczak, E.T.; Meadows, R.P.; Schkeryantz, J.M.; Janowick, D.A.; Harlan, J.E.; Harris, E.A.S.; et al. NMR structure and mutagenesis of the N-terminal Dbl homology domain of the nucleotide exchange factor Trio. *Cell* **1998**, *95*, 269–277, doi:10.1016/S0092-8674(00)81757-2.

166. Jaiswal, M.; Dvorsky, R.; Ahmadian, M.R. Deciphering the molecular and functional basis of Dbl family proteins: A novel systematic approach toward classification of selective activation of the Rho family proteins. *J. Biol. Chem.* **2013**, *288*, 4486–4500, doi:10.1074/jbc.M112.429746.

167. Nimnual, A.S. Coupling of Ras and Rac Guanosine Triphosphatases Through the Ras Exchanger Sos. *Science (80-.).* **1998**, *279*, 560–563, doi:10.1126/science.279.5350.560.

168. Cook, D.R.; Rossman, K.L.; Der, C.J. Rho guanine nucleotide exchange factors: Regulators of Rho GTPase activity in development and disease. *Oncogene* **2014**, *33*, 4021–4035, doi: 10.1038/onc.2013.362.

169. Aspenström, P. Atypical Rho GTPases RhoD and Rif integrate cytoskeletal dynamics and membrane trafficking. *Biol. Chem.* **2014**, *395*, 477–484, doi: 10.1515/hsz-2013-0296.

170. Kunimura, K.; Uruno, T.; Fukui, Y. DOCK family proteins: Key players in immune surveillance mechanisms. *Int. Immunol.* **2020**, *32*, 5–15, doi: 10.1093/intimm/dxz067.

171. Shi, L. Dock protein family in brain development and neurological disease. *Commun. Integr. Biol.* **2013**, *6, doi: 10.4161/cib.26839.*.

172. Côté, J.F.; Motoyama, A.B.; Bush, J.A.; Vuori, K. A novel and evolutionarily conserved PtdIns(3,4,5)P3-binding domain is necessary for DOCK180 signalling. *Nat. Cell Biol.* **2005**, *7*, 797–807, doi:10.1038/ncb1280.

173. Meller, N.; Merlot, S.; Guda, C. CZH proteins: A new family of Rho-GEFs. *J. Cell Sci.* **2005**, *118*, 4937–4946, doi: 10.1242/jcs.02671.

174. Kukimoto-Niino, M.; Ihara, K.; Murayama, K.; Shirouzu, M. Structural insights into the small GTPase specificity of the DOCK guanine nucleotide exchange factors. *Curr. Opin. Struct. Biol.* **2021**, *71*, 249–258, doi:10.1016/J.SBI.2021.08.001.

175. Laurin, M.; Côté, J.F. Insights into the biological functions of Dock family guanine nucleotide exchange factors. *Genes Dev.* 2014, *28*, 533–547.

176. Nishikimi, A.; Kukimoto-Niino, M.; Yokoyama, S.; Fukui, Y. Immune regulatory functions of DOCK family proteins in health and disease. *Exp. Cell Res.* **2013**, *319*, 2343–2349, doi:10.1016/J.YEXCR.2013.07.024.

177. Scheffzek, K.; Ahmadian, M.R. GTPase activating proteins: Structural and functional insights 18 years after discovery. *Cell. Mol. Life Sci.* **2005**, *62*, 3014–3038, doi: 10.1007/s00018-005-5136-x.

178. Amin, E.; Jaiswal, M.; Derewenda, U.; Reis, K.; Nouri, K.; Koessmeier, K.T.; Aspenström, P.; Somlyo, A. V.; Dvorsky, R.; Ahmadian, M.R. Deciphering the molecular and functional basis of RHOGAP family proteins: A systematic approach toward selective inactivation of RHO family proteins. *J. Biol. Chem.* **2016**, *291*, 20353–20371, doi:10.1074/jbc.M116.736967.

179. Rittinger, K.; Taylor, W.R.; Smerdon, S.J.; Gamblin, S.J. Support for shared ancestry of GAPs . *Nature* **1998**, *392*, 448–449, doi: 10.1038/33043.

180. Scheffzek, K.; Ahmadian, M.R.; Wittinghofer, A. GTPase-activating proteins: Helping hands to complement an active site. *Trends Biochem. Sci.* 1998, *23*, 257–262, doi: 10.1016/s0968-0004(98)01224-9.

181. Scheffzek, K.; Lautwein, A.; Kabscht, W.; Ahmadian, M.R.; Wittinghofer, A. Crystal structure of the GTPase-activating domain of human p120GAP and implications for the interaction with Ras. *Nature* **1996**, *384*, 591–596, doi:10.1038/384591a0.

182. Scheffzek, K.; Ahmadian, M.R.; Kabsch, W.; Wiesmüller, L.; Lautwein, A.; Schmitz, F.; Wittinghofer, A. The Ras-RasGAP complex: Structural basis for GTPase activation and its loss in oncogenic ras mutants. *Science* **1997**, *277*, 333–338, doi:10.1126/science.277.5324.333.

183. Rittinger, K.; Walker, P.A.; Eccleston, J.F.; Smerdon, S.J.; Gamblin, S.J. Structure at 1.65 Å of RhoA and its GTPase-activating protein in complex with a transition-state analogue. *Nature* **1997**, *389*, 758–762, doi:10.1038/39651.

184. Garrett, M.D.; Self, A.J.; Van Oers, C.; Hall, A. Identification of distinct cytoplasmic targets for ras/R-ras and rho regulatory proteins. *J. Biol. Chem.* **1989**, *264*, 10–13, doi:10.1016/s0021-9258(17)31215-2.

185. Diekmann, D.; Brill, S.; Garrett, M.D.; Totty, N.; Hsuan, J.; Monfries, C.; Hall, C.; Lim, L.; Hall, A. Bcr encodes a GTPase-activating protein for p21rac. *Nature* **1991**, *351*, 400–402, doi:10.1038/351400a0.

186. Settleman, J.; Albright, C.F.; Foster, L.C.; Weinberg, R.A. Association between GTPase activators for Rho and Ras families. *Nature* **1992, doi: 10.1038/359153a0**.

187. Karnoub, A.E.; Weinberg, R.A. Ras oncogenes: split personalities. *Nat. Rev. Mol. Cell Biol.* **2008**, *9*, 517–531, doi:10.1038/NRM2438.

188. Yang, X.Y.; Guan, M.; Vigil, D.; Der, C.J.; Lowy, D.R.; Popescu, N.C. p120Ras-GAP binds the DLC1 Rho-GAP tumor suppressor protein and inhibits its RhoA GTPase and growth-suppressing activities. *Oncogene* **2009**, *28*, 1401–1409, doi:10.1038/onc.2008.498.

189. Bankaitis, V.A.; Mousley, C.J.; Schaaf, G. The Sec14 superfamily and mechanisms for crosstalk between lipid metabolism and lipid signaling. *Trends Biochem. Sci.* **2010**, *35*, 150–160, doi:10.1016/J.TIBS.2009.10.008.

190. Peck, J.; Douglas IV, G.; Wu, C.H.; Burbelo, P.D. Human RhoGAP domain-containing proteins: Structure, function and evolutionary relationships. *FEBS Lett.* **2002**, *528*, 27–34, doi:10.1016/S0014-5793(02)03331-8.

191. Minoshima, Y.; Kawashima, T.; Hirose, K.; Tonozuka, Y.; Kawajiri, A.; Bao, Y.C.; Deng, X.; Tatsuka, M.; Narumiya, S.; May, W.S.; et al. Phosphorylation by Aurora B converts MgcRacGAP to a RhoGAP during cytokinesis. *Dev. Cell* **2003**, *4*, 549–560, doi:10.1016/S1534-5807(03)00089-3.

192. Ligeti, E.; Dagher, M.C.; Hernandez, S.E.; Koleske, A.J.; Settleman, J. Phospholipids Can Switch the GTPase Substrate Preference of a GTPase-activating Protein. *J. Biol. Chem.* **2004**, *279*, 5055–5058, doi:10.1074/jbc.C300547200.

193. Bernards, A. GAPs galore! A survey of putative Ras superfamily GTPase activating proteins in man and Drosophila. *Biochim. Biophys. Acta - Rev. Cancer* **2003**, *1603*, 47–82, doi: 10.1016/s0304-419x(02)00082-3.

194. Sahai, E.; Marshall, C.J. RHO–GTPases and cancer. *Nat. Rev. Cancer* **2002**, *2*, 133–142, doi:10.1038/nrc725.

195. Vigil, D.; Cherfils, J.; Rossman, K.L.; Der, C.J. Ras superfamily GEFs and GAPs: Validated and tractable targets for cancer therapy? *Nat. Rev. Cancer* **2010**, *10*, 842–857, doi: 10.1038/nrc2960.

196. Kreider-Letterman, G.; Carr, N.M.; Garcia-Mata, R. Fixing the GAP: The role of RhoGAPs in cancer. *Eur. J. Cell Biol.* **2022**, *101*, doi:10.1016/J.EJCB.2022.151209.

197. Blumberg, P.; Kedei, N.; Lewin, N.; Yang, D.; Czifra, G.; Pu, Y.; Peach, M.; Marquez, V. Wealth of Opportunity - The C1 Domain as a Target for Drug Development. *Curr. Drug Targets* **2008**, *9*, 641–652, doi:10.2174/138945008785132376.

198. DerMardirossian, C.; Bokoch, G.M. GDIs: Central regulatory molecules in Rho GTPase activation. *Trends Cell Biol.* **2005**, *15*, 356–363, doi:10.1016/j.tcb.2005.05.001.

199. Leonard, D.; Hart, M.J.; Platko, J. V.; Eva, A.; Henzel, W.; Evans, T.; Cerione, R.A. The identification and characterization of a GDP-dissociation inhibitor (GDI) for the CDC42Hs protein. *J. Biol. Chem.* **1992**, *267*, 22860–22868, doi:10.1016/S0021-9258(18)50026-0.

200. Platko, J. V.; Leonard, D.A.; Adra, C.N.; Shaw, R.J.; Cerione, R.A.; Lim, B. A single residue can modify target-binding affinity and activity of the functional domain of the Rho-subfamily GDP dissociation inhibitors. *Proc. Natl. Acad. Sci. U. S. A.* **1995**, *92*, 2974–2978, doi:10.1073/PNAS.92.7.2974.

201. De León-Bautista, M.P.; Del Carmen Cardenas-Aguayo, M.; Casique-Aguirre, D.; Almaraz-Salinas, M.; Parraguirre-Martinez, S.; Olivo-Diaz, A.; Del Rocío Thompson-Bonilla, M.; Vargas, M. Immunological and functional characterization of RhoGDI3 and its molecular targets RhoG and RhoB in human pancreatic cancerous and normal cells. *PLoS One* **2016**, *11*, e0166370–e0166370, doi:10.1371/journal.pone.0166370.

202. Brunet, N.; Morin, A.; Olofsson, B. RhoGDI-3 regulates RhoG and targets this protein to the Golgi complex through its unique N-terminal domain. *Traffic* **2002**, *3*, 342–358, doi: 10.1034/j.1600-0854.2002.30504.x.

203. Boulter, E.; Garcia-Mata, R.; Guilluy, C.; Dubash, A.; Rossi, G.; Brennwald, P.J.; Burridge, K. Regulation of Rho GTPase crosstalk, degradation and activity by RhoGDI1. *Nat. Cell Biol.* **2010**, *12*, 477–483, doi:10.1038/NCB2049.

204. Ren, X.D.; Kiosses, W.B.; Schwartz, M.A. Regulation of the small GTP-binding protein Rho by cell adhesion and the cytoskeleton. *EMBO J.* **1999**, *18*, 578, doi:10.1093/EMBOJ/18.3.578.

205. Mosaddeghzadeh, N.; Kazemein Jasemi, N.S.; Majolée, J.; Zhang, S.C.; Hordijk, P.L.; Dvorsky, R.; Ahmadian, M.R. Electrostatic Forces Mediate the Specificity of RHO GTPase-GDI Interactions. *Int. J. Mol. Sci.* **2021**, *22*, doi:10.3390/IJMS222212493.

206. Garcia-Mata, R.; Boulter, E.; Burridge, K. The "invisible hand": Regulation of RHO GTPases by RHOGDIs. *Nat. Rev. Mol. Cell Biol.* **2011**, *12*, 493–504, doi: 10.1038/nrm3153.

207. Hoffman, G.R.; Nassar, N.; Cerione, R.A. Structure of the Rho family GTP-binding protein Cdc42 in complex with the multifunctional regulator RhoGDI. *Cell* **2000**, *100*, 345–356, doi:10.1016/S0092-8674(00)80670-4.

208. Maeda, M.; Matsui, T.; Imamura, M.; Tsukita, S.; Tsukita, S. Expression level, subcellular distribution and Rho-GDI binding affinity of merlin in comparison with ezrin/radixin/moesin proteins. *Oncogene* **1999**, *18*, 4788–4797, doi:10.1038/sj.onc.1202871.

209. Takahashi, K.; Sasaki, T.; Mammoto, A.; Takaishi, K.; Kameyama, T.; Tsukita, S.; Tsukita, S.; Takai, Y. Direct Interaction of the Rho GDP Dissociation Inhibitor with Ezrin/Radixin/Moesin Initiates the Activation of the Rho Small G Protein. *J. Biol. Chem.* **1997**, *272*, 23371–23375, doi:10.1074/jbc.272.37.23371.

210. Yamashita, T.; Tohyama, M. The p75 receptor acts as a displacement factor that releases Rho from Rho-GDI. *Nat. Neurosci.* **2003**, *6*, 461–467, doi:10.1038/nn1045.

211. Abiatari, I.; DeOliveira, T.; Kerkadze, V.; Schwager, C.; Esposito, I.; Giese, N.A.; Huber, P.; Bergman, F.; Abdollahi, A.; Friess, H.; et al. Consensus transcriptome signature of perineural invasion in pancreatic carcinoma. *Mol. Cancer Ther.* **2009**, *8*, 1494–1504, doi:10.1158/1535-7163.MCT-08-0755.

212. Ma, L.; Xu, G.; Sotnikova, A.; Szczepanowski, M.; Giefing, M.; Krause, K.; Krams, M.; Siebert, R.; Jin, J.; Klapper, W. Loss of expression of LyGDI (ARHGDIB), a rho GDP-dissociation inhibitor, in Hodgkin lymphoma. *Br. J. Haematol.* **2007**, *139*, 217–223, doi:10.1111/J.1365-2141.2007.06782.X.

213. Ding, J.; Huang, S.; Wu, S.; Zhao, Y.; Liang, L.; Yan, M.; Ge, C.; Yao, J.; Chen, T.; Wan, D.; et al. Gain of miR-151 on chromosome 8q24.3 facilitates tumour cell migration and spreading through downregulating RhoGDIA. *Nat. Cell Biol.* **2010**, *12*, 390–399, doi:10.1038/NCB2039.

214. Waldmann, H.; Akbarzadeh, M.; Flegel, J.; Patil, S.; Shang, E.; Narayan, R.; Buchholzer, M.; Jasemi, N.S.K.; Grigalunas, M.; Krzyzanowski, A.; et al. The Pseudo-Natural Product Rhonin Targets RHOGDI. *Angew. Chemie Int. Ed.* **2022**, doi:10.1002/anie.202115193.

215. Simanshu, D.K.; Nissley, D. V.; McCormick, F. RAS Proteins and Their Regulators in Human Disease. *Cell* **2017**, *170*, 17–33,

doi:10.1016/J.CELL.2017.06.009.

216. Colicelli, J. Human RAS Superfamily Proteins and Related GTPases. *Sci. STKE* **2004**, RE13, doi:10.1126/STKE.2502004RE13.

217. Hebron, K.E.; Hernandez, E.R.; Yohe, M.E. The RASopathies: from pathogenetics to therapeutics. *Dis. Model. Mech.* **2022**, *15*, doi:10.1242/DMM.049107.

218. Tidyman, W.E.; Rauen, K.A. The RASopathies: developmental syndromes of Ras/MAPK pathway dysregulation. *Curr. Opin. Genet. Dev.* **2009**, *19*, 230–236, doi:10.1016/J.GDE.2009.04.001.

219. Bar-Sagi, D.; Hall, A. Ras and Rho GTPases: A Family Reunion. *Cell* **2000**, *103*, 227–238, doi:10.1016/S0092-8674(00)00115-X.

220. Moissoglu, K.; Schwartz, M.A. Spatial and temporal control of Rho GTPase functions. *Cell. Logist.* **2014**, *4*, e943618, doi:10.4161/21592780.2014.943618.

221. Ugolev, Y.; Berdichevsky, Y.; Weinbaum, C.; Pick, E. Dissociation of Rac1(GDP)·RhoGDI complexes by the cooperative action of anionic liposomes containing phosphatidylinositol 3,4,5-trisphosphate, Rac guanine nucleotide exchange factor, and GTP. *J. Biol. Chem.* **2008**, *283*, 22257–22271, doi:10.1074/jbc.M800734200.

222. Newcombe, A.R.; Stockley, R.W.; Hunter, J.L.; Webb, M.R. The Interaction between Rac1 and Its Guanine Nucleotide Dissociation Inhibitor (GDI), Monitored by a Single Fluorescent Coumarin Attached to GDI. *Biochemistry* **1999**, *38*, 6879–6886, doi:10.1021/BI9829837.

223. Tnimov, Z.; Guo, Z.; Gambin, Y.; Nguyen, U.T.T.; Wu, Y.W.; Abankwa, D.; Stigter, A.; Collins, B.M.; Waldmann, H.; Goody, R.S.; et al. Quantitative analysis of prenylated RhoA interaction with its chaperone, RhoGDI. *J. Biol. Chem.* **2012**, *287*, 26549–26562, doi:10.1074/jbc.M112.371294.

224. DerMardirossian, C.; Rocklin, G.; Seo, J.Y.; Bokoch, G.M. Phosphorylation of RhoGDI by Src regulates Rho GTPase binding and cytosol-membrane cycling. *Mol. Biol. Cell* **2006**, *17*, 4760–4768, doi:10.1091/MBC.E06-06-0533.

225. Dransart, E.; Olofsson, B.; Cherfils, J. RhoGDIs revisited: Novel roles in Rho regulation. *Traffic* 2005, *6*, 957–966, doi: 10.1111/j.1600-0854.2005.00335.x.

226. Grizot, S.; Fauré, J.; Fieschi, F.; Vignais, P. V.; Dagher, M.C.; Pebay-Peyroula, E. Crystal structure of the Rac1 - RhoGDI complex involved in NADPH oxidase activation. *Biochemistry* **2001**, *40*, 10007–10013, doi:10.1021/bi010288k.

227. Wang, H.; Wang, B.; Liao, Q.; An, H.; Li, W.; Jin, X.; Cui, S.; Zhao, L. Overexpression of RhoGDI, a novel predictor of distant metastasis, promotes cell proliferation and migration in hepatocellular carcinoma. *FEBS Lett.* **2014**, *588*, 503–508, doi:10.1016/J.FEBSLET.2013.12.016.

228. Auguste, D.; Maier, M.; Baldwin, C.; Aoudjit, L.; Robins, R.; Gupta, I.R.; Takano, T. Disease-causing mutations of RhoGDIα induce Rac1 hyperactivation in podocytes. *Small GTPases* **2016**, *7*, 107–121, doi:10.1080/21541248.2015.1113353.

229. Cho, H.J.; Baek, K.E.; Yoo, J. RhoGDI2 as a therapeutic target in cancer. *Expert Opin Ther Targets* **2009**, *14*, 67–75, doi:10.1517/14728220903449251.

230. Grohmanova, K.; Schlaepfer, D.; Hess, D.; Gutierrez, P.; Beck, M.; Kroschewski, R. Phosphorylation of IQGAP1 modulates its binding to Cdc42, revealing a new type of Rho-GTPase regulator. *J. Biol. Chem.* **2004**, *279*, 48495–48504, doi:10.1074/jbc.M408113200.

231. Hoeprich, G.J.; Sinclair, A.N.; Shekhar, S.; Goode, B.L. Single-molecule imaging of IQGAP1 regulating actin filament dynamics. *Mol. Biol. Cell* **2022**, *33*, ar2, doi:10.1091/MBC.E21-04-0211/ASSET/IMAGES/LARGE/MBC-33-AR2-G006.JPEG.

232. Palani, S.; Ghosh, S.; Ivorra-Molla, E.; Clarke, S.; Suchenko, A.; Balasubramanian, M.K.; Köster, D.V. Calponin-homology domain mediated bending of membrane-associated actin filaments. *Elife* **2021**, *10*, doi:10.7554/ELIFE.61078.

233. Sila Ozdemir, E.; Jang, H.; Gursoy, A.; Keskin, O.; Li, Z.; Sacks, D.B.; Nussinov, R. Unraveling the molecular mechanism of interactions of the Rho GTPases Cdc42 and Rac1 with the scaffolding protein IQGAP2. *J. Biol. Chem.* **2018**, *293*, 3685–3699, doi:10.1074/jbc.RA117.001596.

234. Elliott, S.F. Biochemical analysis of the interactions of IQGAP1 C-terminal domain with CDC42. *World J. Biol. Chem.* **2012**, *3*, 53, doi:10.4331/wjbc.v3.i3.53.

235. Haspel, N.; Jang, H.; Nussinov, R. Active and Inactive Cdc42 Differ in Their Insert Region Conformational Dynamics. *Biophysj* **2021**, *120*, 306–318, doi:10.1016/j.bpj.2020.12.007.

236. Balaji, K.; Colicelli, J. Communicative & Integrative Biology RIN1 regulates cell migration through RAB5 GTPases and ABL tyrosine kinases. **2013**, doi:10.4161/cib.25421.

237. Tall, G.G.; Barbieri, M.A.; Stahl, P.D.; Horazdovsky, B.F. Ras-activated endocytosis is mediated by the Rab5 guanine nucleotide exchange activity of RIN1. *Dev. Cell* **2001**, *1*, 73–82, doi:10.1016/S1534-5807(01)00008-9.

238. Hu, H.; Bliss, J.M.; Wang, Y.; Colicelli, J. RIN1 is an ABL tyrosine kinase activator and a regulator of epithelial-cell adhesion and migration. *Curr. Biol.* **2005**, *15*, 815–823, doi:10.1016/J.CUB.2005.03.049.

ACKNOWLEDGEMENTS

Foremost, I would like to express my deepest appreciation to Reza, for giving me invaluable guidance throughout my Ph.D. Your unconditional support and meticulous scrutiny carried me throughout the stages of many projects. I shall never forget how much I grew up with your professional advice and criticism.

I want to thank Georg Groth for his support and constructive suggestions, which were determinant for the accomplishment of the work presented in this thesis.

I would like to express my thanks to Marco Tartaglia and Herbert Waldmann for opportunity allowing me to collaborate on those fascinating projects.

Special thanks to Jürgen Scheller, Roland Piekorz, and Radovan Dvorsky, who accompanied me during the time of my Ph.D. studies and gave me useful suggestions and advice. I would like to acknowledge the insightful comments of Doreen and Jens during many projects, which helped me to proceed easier.

I am also grateful to all members of the Institute of Biochemistry and Molecular Biology II, specially Mehrnaz, Fereshteh, and Petra for their kindness and continuous support.

Silke, simply your presence made this journey a memorable part of my life. I have coped with many challenges during my Ph.D. because of you. You have such a unique and strong character, and one of the precious assets I got during Ph.D. was the gift of knowing you. You are truly appreciated!

Maman and baba, thank you for teaching me that I needed a dream to chase after. I cannot thank you enough for all the sacrifices you have made for all of your children. Your encouragement and generosity warm my heart.

Noushin and Farzin, I will always remember how you took me in 7 years ago and took care of me like a family. Farzin, Thank you for our endless laughter. Noushin, you read me like a book and that's something wonderful. Thank you for everything you have done for me.

Robert, nobody has ever done so much to make me smile. I am so thankful to you for sticking around even when I was at my worst. You are truly the definition of ride or die. Thank you for your infinite love, devotion, and support. I could not have survived without you.

EIDESSTATTLICHE ERKLÄRUNG

Ich versichere an Eides Statt, dass die Dissertation von mir selbständig und ohne unzulässige fremde Hilfe unter Beachtung der „Grundsätze zur Sicherung guter wissenschaftlicher Praxis an der Heinrich-Heine-Universität Düsseldorf“ erstellt worden ist. Diese Dissertation wurde in der vorgelegten oder einer ähnlichen Form noch bei keiner anderen Institution eingereicht und es wurden bisher keine erfolglosen Promotionsversuche von mir unternommen.

Düsseldorf, den

_____

Niloufar Mosaddeghzadeh